SAPP XXV

25th Symposium on Application of Plasma Processes
and
14th EU-Japan Joint Symposium on Plasma Processing

Book of Contributed Papers

Štrbské Pleso, Slovakia

31 Jan - 5 Feb, 2025

Edited by G. D. Megersa, E. Maťaš, J. Országh, P. Papp, Š. Matejčík

Book of Contributed Papers: 25th Symposium on Application of Plasma Processes and 14th EU-Japan Joint Symposium on Plasma Processing, Štrbské Pleso, Slovakia, 31 January – 5 February 2025.

Symposium organised by Department of Experimental Physics, Faculty of Mathematics, Physics and Informatics, Comenius University in Bratislava and Society for Plasma Research and Applications in hotel SOREA TRIGAN***.

Editors: G. D. Megersa, E. Maťaš, J. Országh, P. Papp, Š. Matejčík

Publisher: Society for Plasma Research and Applications, Bratislava, Slovakia

Issued: January 2025, Bratislava, first issue

ISBN: 978-80-972179-5-2

URL: https://neon.dpp.fmph.uniba.sk/sapp/

Local Organizers

Department of Experimental Physics
Faculty of Mathematics, Physics and Informatics
Comenius University in Bratislava
Mlynská dolina F2
842 48 Bratislava, Slovakia
URL: http://www.fmph.uniba.sk/
Tel.: +421 2 602 95 686
Fax: +421 2 654 29 980

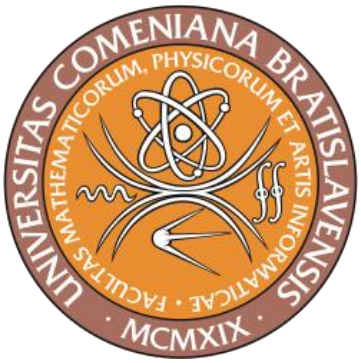

Society for plasma research and applications
Faculty of Mathematics, Physics and Informatics
Comenius University Bratislava
Mlynská dolina F2
842 48 Bratislava, Slovakia
E-mail: spvap@neon.dpp.fmph.uniba.sk
Tel.: +421 2 602 95 686

SPVAP

Local Organizing Committee

Peter Papp (chairman)
Štefan Matejčík
František Krčma
Juraj Országh
Ladislav Moravský
Peter Čermák
Matej Klas
Barbora Stachová
Emanuel Maťaš
Filip Pastierovič
Samuel Peter Kovár
Priyanka Kumari
Gadisa Deme Megersa
Enmily Garcia
Angel Pardo

International Scientific Committee

25th Symposium on Application of Plasma Processes

Prof. J. Benedikt	Christian-Albrechts-University, Kiel, Germany
Dr. R. Brandenburg	INP, Greifswald, Germany
Dr. T. Field	Queen's University, Belfast, United Kingdom
Prof. S. Hamaguchi	Osaka University, Japan
Dr. P. Hartmann	HUN-REN Wigner Research Centre for Physics, Budapest, Hungary
Prof. F. Krčma	Brno University of Technology, Brno, Czech Republic
Prof. N. Mason	School of Physical Sciences, University of Kent, United Kingdom
Prof. Š. Matejčík	Comenius University in Bratislava, Slovakia
Prof. J. Pawlat	University of Technology, Lublin, Poland
Prof. M. Radmilović-Radjenović	Institute of Physics, Belgrade, Serbia
Prof. P. Scheier	Leopold-Franzens University, Innsbruck, Austria

14th EU-Japan Joint Symposium on Plasma Processing

Prof. S. Hamaguchi	Osaka University, Japan
Prof. N. Mason	School of Physical Sciences, University of Kent, United Kingdom
Prof. Z. Petrović	Institute of Physics, Belgrade, Serbia

Reading Committee

Prof. Š. Matejčík	Comenius University in Bratislava, Slovakia
Prof. F. Krčma	Brno University of Technology, Brno, Czech Republic
Prof. N. Mason	University of Kent, United Kingdom
Assoc. Prof. P. Papp	Comenius University in Bratislava, Slovakia
Assoc. Prof. J. Országh	Comenius University in Bratislava, Slovakia
Assoc. Prof. V. Medvecká	Comenius University in Bratislava, Slovakia
Assoc. Prof. M. Klas	Comenius University in Bratislava, Slovakia
Assoc. Prof. P. Čermák	Comenius University in Bratislava, Slovakia
Dr. Vahideh Ilbeigi	Comenius University in Bratislava, Slovakia

Conference Topics

1. Electrical discharges and other plasma sources
2. Elementary plasma processes and plasma-chemical reactions
3. Theory and modelling of plasmas and plasma processes
4. Plasma-surface interactions
5. Plasma surface treatment for applications
6. Plasmas for nanomaterials
7. Plasma diagnostics
8. Ion mobility and mass spectrometry

Table of Contents

INVITED LECTURES

PLASMA-TREATED HYDROGELS: A THERAPEUTIC ALTERNATIVE IN PLASMA MEDICINE?

Cristina Canal[1,2,3]

[1]PlasmaMED Lab, Biomaterials, Biomechanics and Tissue Engineering Group, Department of Materials Science and Engineering and Institute for Research and Innovation in Health (IRIS), Universitat Politècnica de Catalunya ·BarcelonaTech (UPC), Av. Eduard Maristany 10-14, 08019 Barcelona, Spain.
[2]Barcelona Research Center in Multiscale Science and Engineering (CCEM), UPC, Barcelona, Spain.
[3]Centro de Investigación Biomédica en Red de Bioingeniería, Biomateriales y Nanomedicina (CIBER-BBN), Instituto de Salud Carlos III, Spain.
E-mail: cristina.canal@upc.edu

Plasma medicine, an emerging interdisciplinary field, explores the therapeutic potential of cold atmospheric plasma (CAP) for biomedical applications [1]. Two plasma treatment modalities have been under study in the last years: direct plasma treatment and indirect plasma treatment via plasma-treated solutions, usually saline solutions when designed for medical applications. In direct treatment, the therapeutic target (e.g., wound or tumor) is directly exposed to the plasma plume. Here all components of plasma, including short-lived RONS are locally delivered to the target. However, the extremely short penetration depth of plasma requires its access to the site. In contrast, in indirect treatment, CAP is used to treat a chemical solution to generate with RONS within it. This plasma-treated liquid can be used for local, minimally invasive treatment of internal targets / tumors. These plasma-treated liquids contain only the long-lived RONS from plasmas, and can be diluted in vivo by body fluids upon injection.

Hydrogels, with their high water content, biocompatibility, and tunable physical properties, present a unique platform for plasma-based therapies, as they can allow to overcome clinical limitations associated with direct plasma application and provide alternatives to plasma treated liquids [2]. This talk investigates the interplay between CAP and hydrogels, focusing on their potential as therapeutic alternatives in plasma medicine. We examine how plasma treatment modifies hydrogel properties, including their chemistry, mechanical characteristics, and bioactivity. The design of the hydrogel is a key step, and key findings highlight the generation of reactive oxygen and nitrogen species (RONS) within hydrogels due to plasma exposure, and key cytotoxic activity. The evidence of the immunogenicity of PTH will be presented, along with reported induced immunogenic cell death (ICD) in osteosarcoma cancer cells [3].

Plasma-treated hydrogels are an interesting platform as they can incorporate further entities in the system, and thus allow simultaneous delivery of other bioactive molecules or drugs. This capability broadens the potential applications of PTH. This presentation evaluates existing challenges, including scalability, standardization, and long-term effects, while proposing strategies for advancing this innovative therapeutic approach.

Plasma-treated hydrogels stand at the frontier of plasma medicine, poised to bridge the gap between advanced materials science and cutting-edge biomedical therapies. This talk aims to spark dialogue on their translational potential and inspire novel research directions.

1. References

[1] Tornin, J., C. Labay, F. Tampieri, M.P. Ginebra, and C. Canal 2021, *Nat Protoc.*, 16(6): p. 2826-2850.
[2] Zivanic, M., A. Espona-Noguera, A. Lin, and C. Canal, 2023, Adv Sci., 10(8): p. e2205803.
[3] M. Živanić, A. Espona-Noguera, H. Verswyvel, E. Smits, A. Bogaerts, A. Lin, C. Canal, 2024, *Adv. Funct. Mater.*, 34, 2312005.

DIFFUSE DBD AT ATMOSPHERIC PRESSURE: FROM PHYSICS STUDY TO APPLICATIONS

Naudé Nicolas[1], Belinger Antoine[1], Dap Simon[1]

[1]*LAPLACE, Université de Toulouse, CNRS, INPT, UPS, Toulouse, France*
E-mail: nicolas.naude@laplace.univ-tlse.fr

This contribution is dedicated to studying diffuse DBD at atmospheric pressure through electrical and optical diagnostics with spatial resolution. Subsequently, the use of this type of discharge for applications will be discussed, focusing on thin film coating.

1. Introduction

Dielectric Barrier Discharges (DBDs) are a type of atmospheric pressure discharge that can be used for a variety of applications, including surface modification, thin-film coating, sterilisation, treatment of gases, aerodynamic flow control, and energy-efficient lighting devices [1-3]. Depending on the gas, electrical parameters, and electrode configuration, these discharges can operate in either the classical filamentary mode or in a diffuse mode [4-5]. One the one hand, the filamentary mode can be too restrictive for some applications, such as surface coating. On the other hand, the conditions required to obtain a diffuse DBD can also be restrictive.

Diffuse DBDs at atmospheric pressure have been obtained in noble gases like helium, argon, neon, and nitrogen with a Penning admixture [5]. In nitrogen, the ionisation level is too low to allow the formation of a cathode fall. Consequently, the electrical field is quasi-uniform over the discharge gap, like low-pressure Townsend discharges, and the discharge that is obtained is called Atmospheric Pressure Townsend Discharge (APTD) [5]. Compared to Atmospheric Pressure Glow Discharge (APGD) obtained in noble gases, the conditions required to obtain an APTD are more often restrictive. For example, the APTD can be obtained only at low frequencies (from a few Hz to a few kHz, depending on the experimental conditions), and a production of seed electrons is necessary when the electric field is low to obtain the Townsend breakdown.

2. Study of Diffuse DBD in N_2 and N_2 oxygen species admixtures

The APTD obtained in N_2 and N_2 with O admixtures (O_2, N_2O, NO) have been intensively studied using electrical and optical diagnostics [6-7]. At atmospheric pressure, an important aspect is always to determine the discharge regime (filamentary or diffuse). Electrical measurements are more straightforward than optical measurements for doing that. They are also used to study the discharge behaviour. However, because of the dielectric presence, it is impossible to measure directly the electrical parameters of the discharge. Usually, the electrical parameters (gas gap voltage, discharge current, charge transferred within the discharge, discharge power, …) are calculated from the measured quantities (*e.g.* total current or charge) under usage of an electrical equivalent circuit [8-9]. Among other parameters, the electrical equivalent circuit depends on the DBD geometry. The key parameter for this approach is the determination of the discharge area, which is usually considered equal to the electrode surface as long as the discharge is homogeneous. However, even if the discharge seems to cover the electrodes uniformly, its electrical properties (current density, breakdown voltage, discharge duration, …) are not the same at any time and at any point on the surface. That's why it is preferable to talk about diffuse discharge rather than homogeneous discharge.

The spatial variation can be due to several factors like the dielectric surfaces or the gas flow circulation, as observed in a diffuse discharge ignited by Townsend breakdown in nitrogen [10]. Indeed, for a plan-to-plan DBD, when a gas flow is injected, the residence time of the gas increases as a function of the position from the gas inlet to the gas outlet. Thus, the species densities are not the same along the gas flow because of the kinetic processes and chemical reactions in the discharge [10]. Then, the discharge current and the gas voltage are not uniform along the spatial DBD dimensions. Therefore, the

determination of discharge current and gas voltage from macroscopic parameters of the DBD is often inaccurate. In the best case, the calculated values are spatially averaged but do not allow the interpretation of localised plasma treatment.

To have a more accurate characterization of the discharge behavior, a measurement of the local current density is required. To get a 2D mapping of the discharge electrical parameters, a dedicated setup was developed in which the ground electrode was prepared as a segmented electrode with 64 equally spaced square segments. The high voltage electrode remained full. This electrode is a 3x3 cm^2 square, while each square of the segmented electrode has a 3.44 mm side length, a distance of 350 mm spaced each segment (Figure 1). A prototype based on this experimental configuration together with a dedicated data acquisition system has been successfully validated by the comparison with short exposure time photos taken by a camera from above the discharge cell [11]. Then, it has been used to study the diffuse discharge (APTD) and shows the effect of a gas flow on the local electrical behavior of the discharge. In the case of diffuse DBDs with sinusoidal voltages at frequencies from 1 to 20 kHz, the temporal and spatial resolutions are high enough to characterise the discharge behaviour with sufficient spatial information. Figure 2 presents a 3D mapping of the surface power density obtained with the segmented electrode for a gas mixture of N_2 with 30 ppm of NO. We can clearly see the main influence of the gas flow on the breakdown voltage.

This electrode arrangement and measuring systems allows a 2D mapping of the discharge electrical parameters (discharge current, power dissipated, gas voltage, etc.) of Townsend but also of Glow discharges, hybrid or patterned regimes.

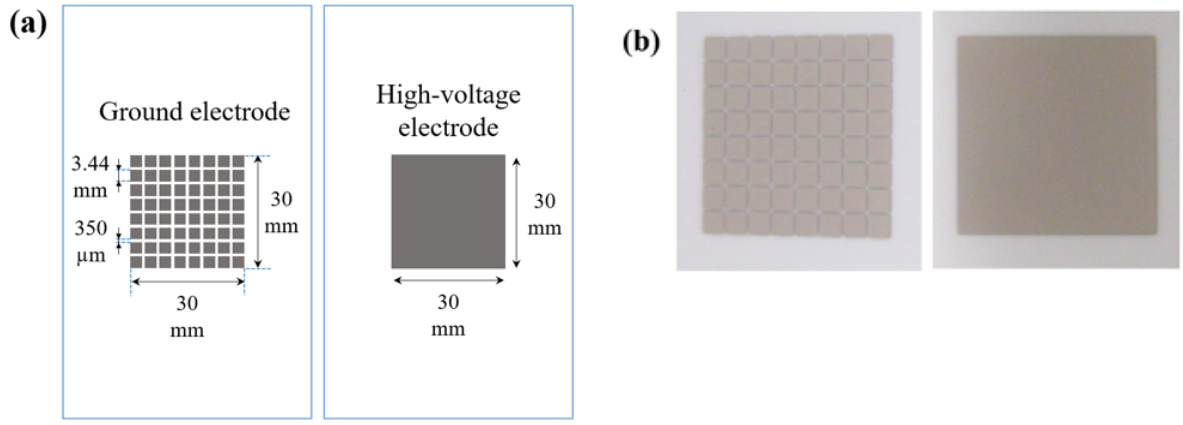

Fig. 1. Diagram (a) and photograph (b) of the segmented electrode and the high-voltage electrode.

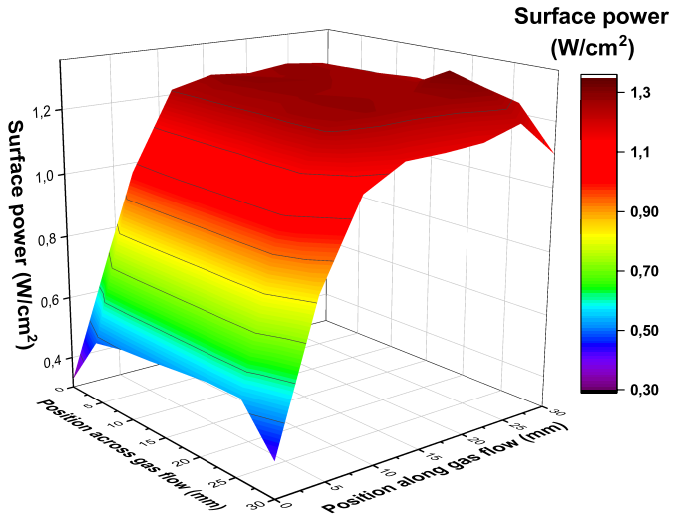

Fig. 2. 3D mapping of surface power density from measurements with the segmented electrode in N_2 + 30 ppm NO (gap=2 mm, 2 kHz, 17.12 kV_{pp}, 4 sLm).

3. Applications of APTD?

During the presentation, the use of an APTD for surface treatment applications will be discussed. We will first focus on thin-film coating using APTD. As an example, Figure 3 compares coatings realised with a filamentary discharge and a diffuse discharge for the same gas composition (N_2 with N_2O and HMDSO) and the same discharge power (10 W/cm^3). Then, we will also explore some other possibilities. Finally, solutions to improve discharge uniformity and power dissipation, to reduce the sensitivity to precursor concentration, and to increase deposition rate mainly in the case of discharges obtained in N_2 will be discussed.

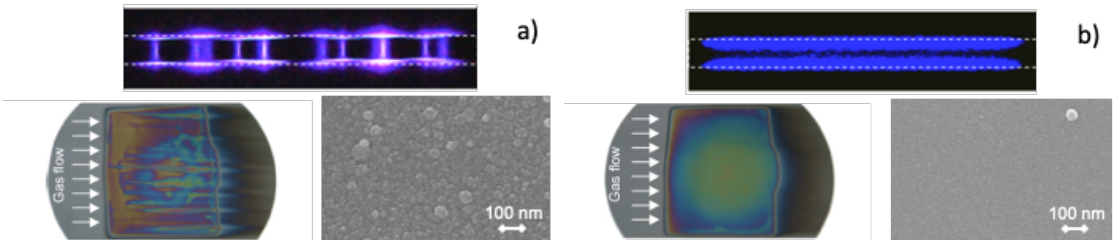

Fig. 3. Comparison of a coating realised with: a) a filamentary discharge and b) a diffuse discharge in N_2 with N_2O and HMDSO for the same discharge power (10 W/cm^3).

4. References

[1] S. Samukawa *et al.*, *J. Phys. D: Appl. Phys.* 45 (2012) 253001
[2] I Adamovich *et al.*, *J. Phys. D: Appl. Phys.* 55 (2022) 373001
[3] U. Kogelschatz, *Plasma Chem Plasma* P 23 (1), 1-46 (2003)
[4] R. Brandenburg, *Plasma Sources Sci. Technol.* (2017) 26 053001
[5] F. Massines *et al.*, *Eur. Phys. J. Appl. Phys.* 47, 22805 (2009)
[6] R. Brandenburg *et al.*, *J. Phys. D: Appl. Phys.* 38 (2005) 2187
[7] G. Dilecce *et al., Plasma Sources Sci. Technol.* (2007) 16 511
[8] A. V. Pipa *et al.*, *Rev Sci Instrum* 83 (11), 115112 (2012).
[9] F. Peeters *et al.*, *in Atmospheric Pressure Plasma - from Diagnostics to Applications*, edited by A. Nikiforov and Z. Q. Chen (IntechOpen Limited, London, UK, 2019)
[10] C. Tyl *et al.*, *J Phys D Appl Phys* 51 (35) (2018)
[11] C. Tyl *et al.*, *Review of Scientific Instruments* 2021, 92 (5), pp.053552

BREAKDOWN CHARACTERISTICS IN LOW GWP AND LOW ODP FREONS

Jelena Marjanović[1], Dragana Marić[1], Zoran Lj. Petrović[2,3]

[1]*Institute of Physics, University of Belgrade, Pregrevica 118, 11080 Belgrade, Serbia*
[2]*Serbian Academy of Sciences and Arts, Kneza Mihaila 35, 11001 Belgrade, Serbia*
[3]*School of Engineering, Ulster University, Jordanstown, County Antrim BT37 0QB, United Kingdom*
E-mail: sivosj@ipb.ac.rs

We present the results of breakdown measurements for three freons: 1,1,1,2-tetrafluoroethane (R134a, $C_2H_2F_4$), 2,3,3,3-tetrafluoropropene (HFO1234yf, $C_3H_2F_4$), and trans-1,3,3,3-tetrafluoropropene (HFO1234ze(E), $C_3H_2F_4$) in a centimeter-sized plan-parallel electrode system, under swarm conditions at low currents (~ 1 □A) and low pressures. Paschen curves and corresponding distributions of emission intensities at low current were recorded in the *pd* (pressure x electrode gap) range from 0.05 to 3 Torr cm, covering the region of Paschen minimum. We obtained an effective ionization coefficient of studied freons from the emission profiles for the *E/N* range 2.5 kTd to 23 kTd.

1. Introduction

The widespread use of fluorocarbons and sulphur hexafluoride (SF_6) has raised concerns regarding their emissions due to their detrimental environmental impact. These greenhouse gases have an extremely long atmospheric lifetime, high global warming potentials (GWP) and high ozone depletion potentials (ODP). The electrical industry, a major consumer of SF_6, is actively working to replace it with environmentally friendly insulation gases. Among the most promising alternatives are hydrofluoroolefins (HFOs), perfluoro-ketones (PFKs), and perfluoronitriles (PFNs). These synthetic compounds not only have significantly shorter atmospheric lifetimes compared to SF_6 [1, 2] but are also added in small concentrations to atmospheric gases, providing similar electrical strength as SF_6 [3-5]. However, the ideal SF_6 replacement in electrical gas insulation equipment must fulfil some relevant technical parameters such as maximum operating voltage, limited by the breakdown voltage, minimum operating temperature, boiling point, vapour pressure, toxicity, flammability, low GWP and ODP etc.

In recent years, many studies (dielectric breakdown experiments, swarm experiments) have been made to obtain the necessary data needed for a better understanding of the electrical and physical properties of new synthetic compounds and their mixtures [6-9]. Nonetheless, there is still a lack of essential data necessary for the development of environmentally friendly power equipment. The main objective of this work is to gather the elementary breakdown data (breakdown voltages at various reduced electric fields, effective ionization coefficients, secondary electron yields) that will contribute to the development of comprehensive sets of cross-sections and other discharge parameters in the energy range that are relevant to a wide array of applications.

2. Experimental setup

Breakdown measurements are done in a centimeter-sized plan-parallel electrode system, under swarm conditions at low currents (~ 1 mA) and low pressures (~0.05 – 3 Torr). The copper cathode and aluminium anode have a diameter of 5.4 cm, and the distance between them is set at 1.1 cm. The electrode system is placed in a narrow cylinder made of quartz glass, which allows the recording of side - on images of the discharge emission in a wide spectral range. We used a sensitive ICCD camera (Andor IStar DH720-18U-03) to capture light emission from discharges, and for spectrally resolved recordings, we employed optical band-pass filters. A more detailed description of the experimental procedure is given in [10, 11]. Measurements were done for three freons: 1,1,1,2-tetrafluoroethane (R134a, $C_2H_2F_4$), 2,3,3,3-tetrafluoropropene (HFO1234yf, $C_3H_2F_4$), and trans-1,3,3,3-

tetrafluoropropene (HFO1234ze(E), $C_3H_2F_4$). Figure 1 depicts a simplified schematic of the experimental set-up.

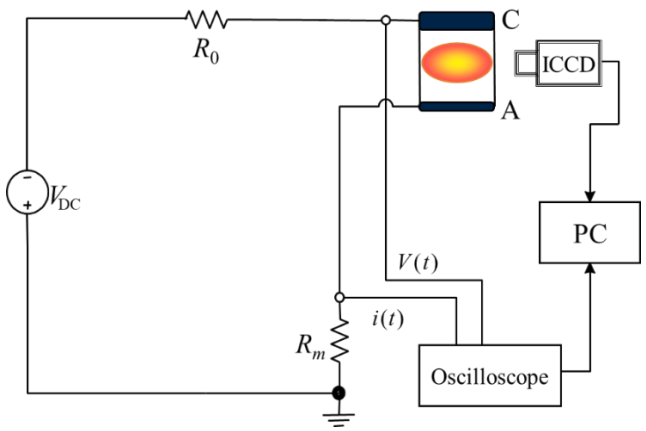

Fig. 1. Schematics of the experimental setup and the electrical circuit used in measurements. The discharge current is determined by measuring voltage drop on the resistor R_m, while R_0 limit the current.

3. Results

In Figure 2, we present the breakdown voltage dependence on the product of pressure (p) and interelectrode distance (d), commonly known as Paschen curves for 1,1,1,2-tetrafluoroethane (R134a, $C_2H_2F_4$), 2,3,3,3-tetrafluoropropene (HFO1234yf, $C_3H_2F_4$), and trans-1,3,3,3-tetrafluoropropene (HFO1234ze(E), $C_3H_2F_4$) in comparison with sulfur hexafluoride (SF_6) [12, 13]. The Paschen curves for all presented gases have a minimum at ~ 0.25 Torr cm. R134a exhibits the lowest breakdown voltages compared to HFOs and SF_6 under identical conditions.

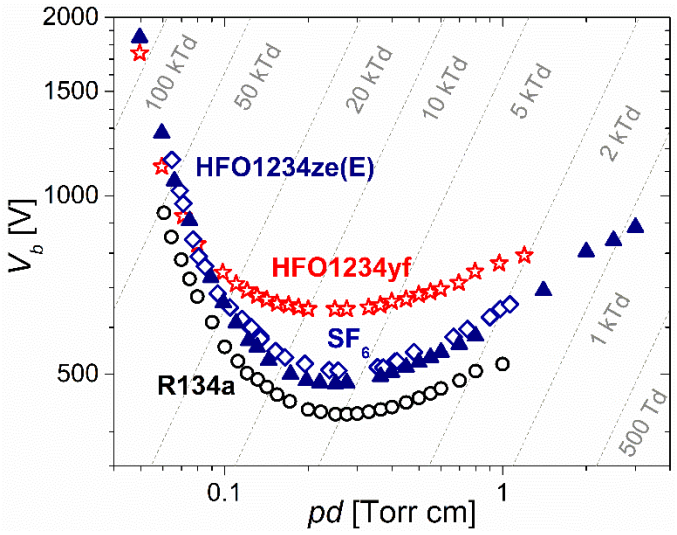

Fig. 2. Comparison of Paschen curves for 1,1,1,2-Tetrafluoroethane (R134a) (open circles), 2,3,3,3-Tetrafluoropropene (HFO1234yf) (open stars), trans-1,3,3,3-Tetrafluoropropene (HFO1234ze(E)) (solid triangles), and sulfur hexafluoride (SF_6) (open rhombs) [12, 13]. Curves have been obtained for an electrode distance of 1.1 cm.

While the breakdown voltage values for HFO1234ze(E) around the Paschen minimum are significantly lower than those for HFO1234yf, a shift towards higher pressures reveals a steeper increase in voltage for HFO1234ze(E) compared to HFO1234yf. At lower pressures, the voltage increase in the left-hand

branch of the Paschen curve, is comparable for both HFOs and aligns with the left-hand branch of SF_6. Observing the Paschen curves of SF_6 and HFO1234ze(E), it is evident that these gases align closely in breakdown voltages at both lower pressures (left-hand branch) and higher pressures (right-hand branch). One should keep in mind that surface processes dominantly influence the left-hand branch of the Paschen curve, while the right-hand branch is mainly shaped by the processes in gas [14].

Along with the breakdown measurements, we recorded the spatial distribution of discharge emission. We obtained the axial emission profiles (Fig. 3) for the range of reduced electric fields covered by the Paschen curve. The recordings of discharge spatial distribution are crucial because they can provide insights into the overall particle kinetics under various conditions [15-19]. In Steady State Townsend (SST) discharges, there are two distinguished regions, one an electron-dominated region observed near the anode, and another with significant emissions near the cathode that are generally due to the heavy particles excitation, such as fast neutrals, fast ions and metastables [16, 20, 21]. The recordings for all three studied freons reveal that the significant contribution to total emission originates from the heavy - particle excitation for all covered reduced electric fields (*E/N*) (examples shown in Fig. 3, integrated visual profiles). However, the Hα emission profile significantly changes its shape with the decrease of reduced electrical field (*E/N*). Around the Paschen minimum, for all showed freons, contribution to overall emission by electron excitation becomes significant, which is depicted with the maximum intensity in front of the anode (Fig. 3, Hα profiles at 0.3 and 0.25 Torr cm).

R134a

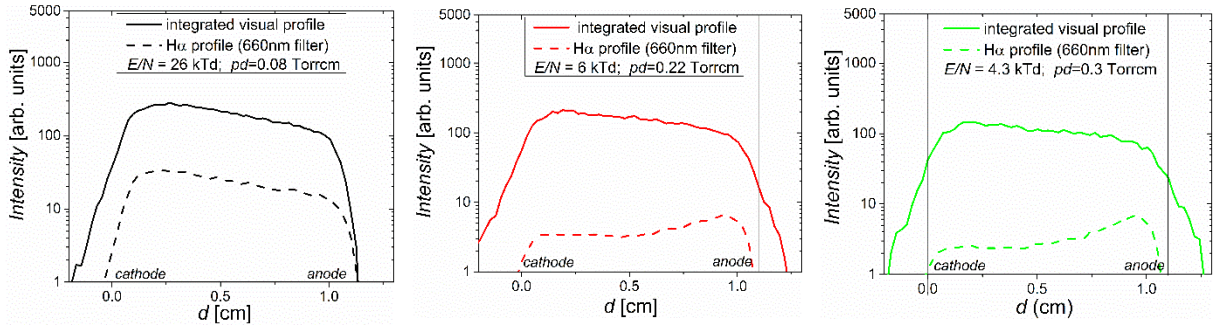

HFO1234yf

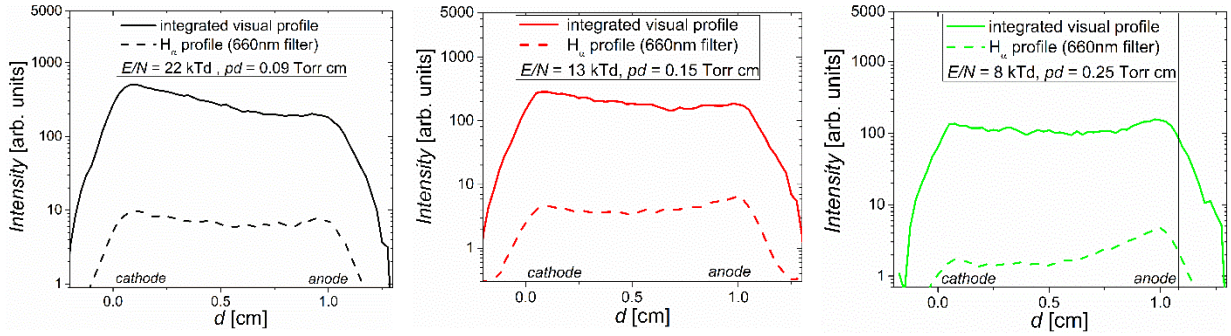

HFO1234ze(E)

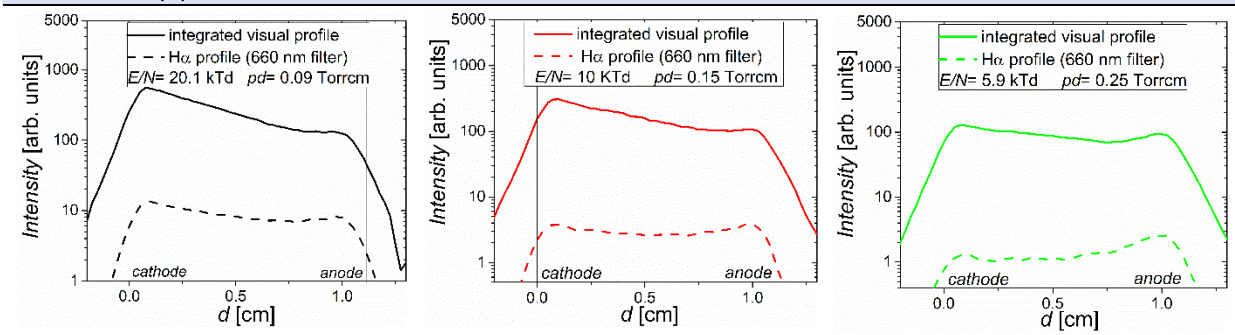

Fig. 3. Examples of the total (integrated visual) axial emission profiles and Hα axial emission profiles of R134a, HFO1234yf, and HFO1234ze(E) discharges, recorded for various reduced electric fields (*E/N*).

The effective ionization coefficients for the studied gases are determined from the axial emission profiles obtained in the spectrally resolved measurements by using band-pass optical filters [see ref. [10]]. Profiles are recorded for the low-current limit (no space charge) of the DC discharges in the Townsend/diffuse regime (breakdown conditions). In the case of HFO1234ze, we determined *α/N* coefficient from Hα axial emission profiles as they show only a small contribution of fast neutrals to excitation (an example shown in Fig. 4). The slope of exponential intensity growth (plotted in a semi - logarithmic scale) corresponds to the effective ionization coefficient α_{eff}/N [12, 22].

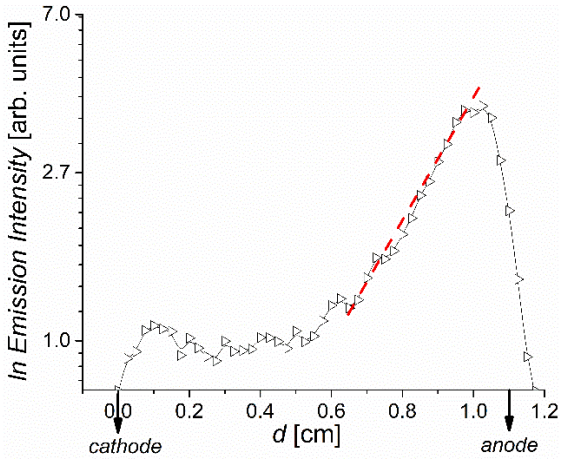

Fig. 4. Hα axial emission profile of low-current Townsend discharge recorded in HFO1234ze(E) for *pd* = 0.4 Torr cm, V_b = 504 V and *E/N* = 3.8 kTd at electrode distance of *d* = 1.1 cm. The plot of the emission profile in the semi-log scale reflects electron multiplication between the electrodes, and the profile slope (red dotted line) corresponds to the effective ionization coefficient.

In Figure 5, we present results for the reduced effective ionization coefficient for HFO1234ze(E) discharge and compare it with the results for R134a, HFO1234yf [10]. Results are obtained in the *E/N* range from 2.5 kTd to 23 kTd. For comparison, we also show effective ionization coefficients for SF_6 from the literature [23, 24]. The α_{eff}/N values for SF_6 in the *E/N* range of 2.5 kTd to 4 kTd are approximately twice as large as those for HFO1234ze(E) within the same range.

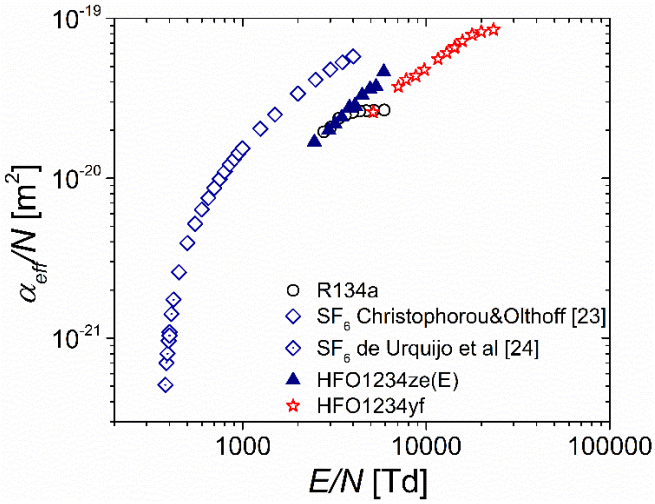

Fig. 5. The dependence of reduced effective ionization coefficient (α_{eff}/N) on the reduced electric field (*E/N*). Results obtained from our experiment for R134a (open circles), HFO1234yf (open stars), and

HFO1234ze(E) (solid triangles) are compared with data for SF_6 from Christophorou and Olthoff (open rhombs)[23] and de Urquijo et al (open rhombs with dots)[24].

HFO1234ze(E) and HFO1234yf gases show the high potential for insulation applications because of their high breakdown voltages and low effective ionization coefficients.. They cannot fully replace SF_6 in medium and high-voltage technologies. Still, they represent building blocks for understanding a new complex class of gases that is currently the most promising alternative to SF_6.

Acknowledgements

This research was supported by the Science Fund of the Republic of Serbia, Grant No. 7749560, project EGWIn. Zoran Lj. Petrović is grateful to the SASA project F155.

4. References

[1] Lin [1] L, Chen Q, Wang X, Zhang H, and Li H 2022 *High Voltage*, ***7***(6) 1069
[2] Christophorou L G, J. Olthoff K, and Green D S 1997 *Technical Note (NIST TN)* **1425** 1-44
[3] Seeger M, Smeets R, Ito H, Claessens M, Dullni E, Falkingham L, Franck C M, Gentils F, Hartmann W, Kieffel Y, Jia S, Jones G, Mantilla J, Pawar S, Rabie M, Robin-Jouan P, Schellekens H, Spencer J, Uchii T, Li X, Yan J, and Yanabu S 2017 *Electra* **291** 26–29
[4] Koch M and Franck C M 2015 *IEEE Transactions on Dielectrics and Electrical Insulation* **22**(6) 3260-3268
[5] Zhang B, Chen L, Li X, Guo Z, Pu Y, and Tang N 2020 *IEEE Transactions on Dielectrics and Electrical Insulation* **27**(4) 1187-1194
[6] Chachereau A et al. 2016 *Plasma Sources Sci. Technol*. **25** 045005
[7] Egüz E A et al. 2022 *J. Phys. D: Appl. Phys.* **55** 315203
[8] Egüz E A et al. 2023 *J. Phys. D: Appl. Phys*. **56** 395203
[9] Garland N A et al. 2024 *J. Phys. D: Appl. Phys.* **57** 245202
[10] Marjanović J, Marić D, and Petrović Z Lj 2024 *European Physical Journal D* **78**, 14
[11] Sivoš J, Marić D, Malović G, and Petrović Z Lj 2020 *European Physical Journal D* **74**(64) 1-10
[12] Marić D, Savić M, Sivoš J, Škoro N, Radmilović-Radjenović M, Malović G, Petrović Z Lj 2014 *Eur. Phys. J. D* **68** 155
[13] Steanović I 1998 *Osobine difuznih električnih pražnjenja u gasovima na niskom pritisku u režimu niskih struja* (Doctoral dissertation, School of Electrical Engineering, University of Belgrade)
[14] Phelps A V and Petrović Z Lj 1999 *Plasma Sources Sci. Technol*. **8** R21
[15] Ingold J. H. 1978 *Anatomy of the discharge in Gaseous Electronics: Electrical Discharges vol 1*, edited by Hirsh M and Oskam H J (Academic Press, New York, ISBN 0-12-349701-9)
[16] Petrović Z Lj and Phelps A V 2009 *Phys. Rev. E* **80** 016408
[17] Marić D, Kutasi K, Malović G, Donkó Z, and Petrović Z Lj 2002 *Eur. Phys. J. D* **21** 73
[18] Petrović Z Lj, Donkó Z, Marić D, Malović G, and Živanov S 2002 *IEEE Trans. Plasma Sci*. **30** 136
[19] Marić D, Hartmann P, Malović G, Donkó Z, and Petrović Z Lj 2003 *J. Phys. D: Appl. Phys*. **36** 2639
[20] Petrović Z Lj, Jelenković B M, and Phelps A V 1992 *Phys. Rev. Lett.* **68** 325
[21] Petrović Z Lj and Stojanović V 1998 *J. Vac Sci. Technol. A* **16** 329
[22] Malović G, Strinić A, Živanov S, Marić D, and Petrović Z Lj 2003 *Plasma Sources Sci. Technol.* **12** 1
[23] Christophorou L G and Olthoff J K 2000 *J. Phys. Chem. Ref. Data* **29**(3) 267–330
[24] Urquijo J et al. 2001 *J. Phys. D: Appl. Phys*. **34** 2151

DYNAMICS INDUCED BY ELECTRON COLLISIONS: GASES AND LIQUIDS

Juraj Fedor[1]

[1]*J. Heyrovský Institute of Physical Chemistry, Czech Academy of Sciences, Dolejškova 3, Prague, Czech Republic*
E-mail: juraj.fedor@jh-inst.cas.cz

I will discuss processes induced by impact of free electrons in systems with increasing degree of aggregation.

1. Gas phase targets

For gas-phase molecules, the motivation primarily comes from the fundamental aspects of quantum dynamics. In an electron-molecule collision system, resonances (states embedded in electronic continuum) can be formed and the nuclear dynamics on these states often leads to effects which are not commonly encountered in other types of vertical excitation (e.g., photoexcitaction), such as nuclear interference or non-locality. Experimentally, we use two-dimensional electron energy loss spectroscopy (2D EELS) to monitor the decay channels of resonances and to extract the dynamical information from these. I will describe the extremely non-Born-Oppenheimer dynamics in CO_2 [1] and contrasting dynamics in isolectronic anions [2].

2. Liquid microjets

I will also describe our current experiments on electron collisions with liquid microjets where the main goal is the implementation of EELS for liquid targets.

3. References

[1] J. Dvořák et al, Phys. Rev. Lett. **2022**, https://doi.org/10.1103/PhysRevLett.129.013401

[2] P. Nag et al., J. Phys. Chem. Lett. **2024**, https://doi.org/10.1021/acs.jpclett.3c03460

[3] P. Nag et al., J. Phys. B: At. Mol. Opt. Phys. **2024** https://doi.org/10.1088/1361-6455/ad0205

DISSOCIATING PURE AMMONIA WITH MICROWAVE DISCHARGES: A GLOBAL MODEL

M. Y. Awaji[1,2], L. Pentecoste[1], C. Noel[1], M. Belmahi[1], T. Gries[1], T. Belmonte[1]

[1]*Université de Lorraine, CNRS, IJL, F-54000 Nancy, France*
[2]*2Department of Physical Sciences, Physics Division, College of Science, Jazan University, P.O. Box 114, Jazan 45142, Kingdom of Saudi Arabia*

E-mail: thierry.belmonte@univ-lorraine.fr

A global model of microwave discharge in pure ammonia at reduced pressure (from 40 to 200 mbar) and moderate power (between 430 and 450 W) is presented. Satisfactory results are obtained, reproducing correctly the evolution of the electron density of the discharge as a function of the pressure without strong assumptions. Beyond 100 mbar, new phenomena are likely at stake, which could explain the difference observed between experimental and theoretical results.

1. Introduction

To combat the current energy and climate change crisis, sustainable fuels for energy storage should be synthesized from surplus energy ('power-to-X'). As technologies for producing hydrogen from seawater continue to advance [1, 2], the chemical storage of the hydrogen produced will be essential for many applications because of the extremely low density of hydrogen. The potential problems of safety and infrastructure costs associated with the storage of pure hydrogen are also an issue. Ammonia, identified as a promising energy vector, offers advantages in storage and transport over hydrogen. It capitalizes on existing global infrastructures, with approximately 20 million metric tons traded annually, contributing to a total production of 150 million tons annually. Microwave plasmas are recognized for their low cost and high throughput potential. The conversion of large quantities of ammonia—on the order of tons per day—is a realistic economic target, already being considered for CH_4, another promising hydrogen carrier [3]. Microwave plasmas are also preferred to low-temperature plasmas, like dielectric barrier discharges, because they possibly provide the heat required for catalyst activation without any external heating source.

In this study, we provide a macroscopic model of a pure ammonia plasma submitted to microwave excitation. The lack of accurate chemical pathways for a molecule as complex as NH_3 made us choose a simpler description of the plasma, reduced to the given of its permittivity. This quantity is related to the electron density, validation is provided through microwave interferometry measurements.

2. Experimental setup

The geometry of the reactor is depicted in Fig. 1. The plasma is generated within a custom-built resonant cavity, excited with microwaves operating at a frequency of 2.45 GHz, provided by a SAIREM power supply. The employed SAIREM GMP 12 KED C microwave generator has a capacity of delivering up to 1,200 W. The bent part of the WR-340 waveguide is used to connect the cavity with the water load, which prevents the source from damage caused by backstroke waves. Pure ammonia (99.9% purity, Air Liquide) was used as a working gas. The pressure range spanned from 40 to 200 mbar and two series of measurements were selected, corresponding to gas flows of 5 and 10 standard liters per minute (slm) and absorbed powers around 430-450 W. For the measurement of the electron density, a Ka-band Microwave Interferometer (MWI) 2650-A by Miwitron was used. With a frequency of 26.5 GHz, the critical electron density is 9×10^{12} cm^{-3}. Only electron densities of less than 3×10^{12} cm^{-3} typically could be measured. As the minimum measurable phase shift is 0.1°, for a plasma of a few centimetres, this places the minimum measurable density at a few 10^9 cm^{-3}.

Measuring the geometry of the plasma is done with a fast camera, which generally shows edges between the emissive and non-emissive zones that are relatively easy to define, but unfortunately depend on the camera's focus. As the focus is the same for all measurements, we had to assume that the plasmas were all in the same place, which is not strictly true and affects slightly the value of the established volume. The plasma fluctuates over time and its geometry was represented numerically by an ellipsoid. The assessed surface area of the cross-section is used to determine an equivalent radius leading to the same area for a disc. The radius is used in the calculation. The electron temperature was assessed by using 3 or 4 transitions of the Balmer series (H_α, H_β, H_γ and H_δ when available). They were recorded using a 550 mm monochromator (Jobin Yvon TRIAX 550) equipped with 3 diffraction gratings of 100, 1200 and 1800 lines/mm blazed at 450, 500 and 250 nm respectively. The gas temperature was determined from the average of the rotational temperatures of two molecular probes: N_2 and NH. The N_2 ($C^3\Pi_u$-$B^3\Pi_g$) second positive system and NH ($A^3\Pi$-$X^3\Sigma^-$) Ångström system overlap around 336-337 nm. Both contributions are disentangled by numerical modelling of the two spectra using homemade Python software.

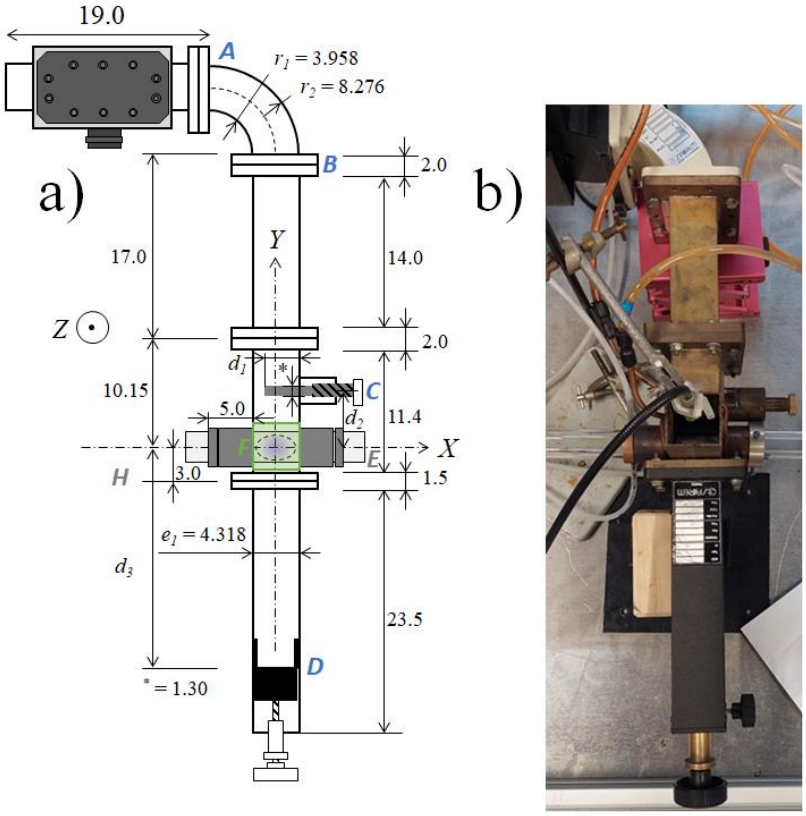

Fig. 1. a) Schematic of the microwave delivery system used for the microwave-discharge interaction model. Distances are in cm. Letters are used to locate the different parts of the system. The copper window enables the viewing of the plasma from the bottom and the top is perpendicular to the view plane and depicted in green. b) Picture of the experimental setup showing the WR-340 waveguide, the movable stub, the short-circuit piston, and the reactor tube. The height of the waveguide is 8.636 cm.

3. Modelling

To describe the model built, we give details about the geometry of the reactor, the equations solved for the propagation of the wave, the energy coupling with the plasma, the gas flow and heating, the boundary conditions, and the mesh used for the numerical resolution.

3.1 Geometry

The geometric characteristics and physical properties of the various domains making up the experimental setup are as follows:

Waveguide

A-D in Fig.1. We used a standard WR340 rectangular waveguide. The incident power imposed at the inlet port (one-port circuit [4]) represents the power delivered by the microwave generator operating at a fixed frequency of 2.45 GHz. It is different from the power delivered to the generator that converts the AC signal to a microwave signal with a yield of about 40%. The relative permittivity and relative permeability of the air in the waveguide are taken equal to 1.

Movable stub

C in Fig.1. There is only one movable stub. With the movable short-circuit piston at the end of the line, it gives 3 degrees of freedom, which is enough to match the microwaves with the load. It is modelled as a simple cylinder. It is made of an 11 cm long copper rod (3 cm smooth and 8 cm threaded) screwed on a copper cylinder of 4.3 cm long. Its length in the waveguide can vary from 0 to ~4 cm, depending on the simulated experimental conditions. The distance between the center of the discharge tube and the center of the stub can be adjusted but it is set at d_2=4.50 cm.

Fused silica (discharge) tube

E-H in Fig.1. The outer and inner radii of the fused silica tube are 1.4 cm and 1.3 cm respectively. The length of the quartz tube is set at 8 cm. The electromagnetic properties taken into account for fused silica are assumed to be lossless: ε_{fs} = 3.8 and μ_{fs} = 1. At the inlet, the gas flowrate is set to its nominal value (5 or 10 standard liters per minute). The temperature is set at 300 K. The effect of the swirl was neglected in this model. The gas flow is laminar. The Reynold number reaches a maximum value of 450. At the outlet, the pressure is considered as weak enough to enable the exhaust of the gas.

Short-circuit piston

D in Fig.1. The movable piston at the end of the line is used with the short-circuit piston to set the matching conditions. It is modelled by a flat wall which is a perfect electrical conductor (see boundary conditions). The distance between the center of the tube and this piston can vary from 5 cm to 15 cm, depending on the experimental conditions simulated.

Window

Green square *F* in Fig.1. The window above the cavity is modelled by a rectangular parallelepiped 4.318 cm wide, 4.318 cm high and 9.6 cm long. Although the window prevents any microwave leakage, we take it into account in our modelling because it influences the resonance conditions, in particular when the electronic concentration of the plasma is relatively low or in the absence of plasma.

Gas

The discharge tube is filled with ammonia. The change of the gas properties due to the cracking of the molecule is described hereinafter. Its electromagnetic characteristics are lossless and as follows: $\varepsilon_r = 1$ and $\mu_r = 1$.

Plasma

The geometry of the plasma is modelled by an ellipsoid of equatorial radius R_q (*x=0*) and polar radius R_p whose dimensions are defined experimentally by image analysis of plasma photographs. The relative permeability of the plasma is taken to be equal to 1. The relative permittivity of the plasma depends on its electron concentration and the effective electron-neutral collision frequency, as presented before. For the simulations, the electron-neutral collision frequency is considered to be constant throughout the plasma volume. The electron concentration is assumed to have a volume distribution represented by:

$$n_e(x,y,z) = n_e^0 \times \left\{1 - \left(\frac{y^2+z^2}{R_q^2} + \frac{x^2}{R_p^2}\right)\right\} \quad (1)$$

defined in the volume $\frac{y^2+z^2}{R_q^2}+\frac{x^2}{R_p^2}\leq 1$. Here, n_e^0 is the maximum value of the electron density, which lies in the center of the volume $V=\frac{4}{3}\pi R_q^2 R_p$. The average electron density is then:

$$\tilde{n}_e(x,r)=\frac{\pi}{6}n_e^0 \quad (2)$$

which can be used to define the electron distribution from the average electron density instead of the maximum electron density.

3.2 Wave propagation

The wave propagation in the waveguide adopts a TE_{01} mode and obeys the equation:

$$\vec{\nabla}\times\left(\vec{\nabla}\times\vec{E}\right)=\frac{\omega^2}{c^2}\left(1-j\frac{\sigma}{\omega\varepsilon_0}\right)\vec{E} \quad (3)$$

where $\vec{E}$ is the electric field, ω the microwave angular frequency, c the speed of light, σ is the electrical conductivity and ε_0 the permittivity of the free space. The plasma resistivity can be evaluated with the following expression:

$$\sigma=\frac{\varepsilon_0\omega_p^2}{(\tilde{\nu}_m+j\omega)}=\frac{n_e e^2}{m_e}\frac{\tilde{\nu}_m}{(\omega^2+\tilde{\nu}_m^2)}-j\frac{n_e e^2}{m_e}\frac{\omega}{(\omega^2+\tilde{\nu}_m^2)} \quad (4)$$

ω_p is the plasma angular frequency. $\tilde{\nu}_m$ is the effective electron-neutral collision frequency for momentum transfer. It is given by:

$$\tilde{\nu}_m=\int_0^\infty \frac{\nu_m\varepsilon^{3/2}}{(\nu_m^2+\omega^2)}\frac{df}{d\varepsilon}d\varepsilon\Big/\int_0^\infty \frac{\varepsilon^{3/2}}{(\nu_m^2+\omega^2)}\frac{df}{d\varepsilon}d\varepsilon \quad (5)$$

This quantity is evaluated by assuming a Maxwellian shape of the electron energy distribution function at an electron temperature of 0.5 eV, determined experimentally (see hereafter). The cross section needed for evaluating the electron-neutral collision frequency for momentum transfer ν_m is taken from [5].

ε_p and σ are related by:

$$\varepsilon_p=1+\frac{Im(\sigma)}{\varepsilon_0\omega}-j\frac{Re(\sigma)}{\varepsilon_0\omega}. \quad (6)$$

The input power in the discharge is related to the electric field in the whole plasma volume *vol_p* by:

$$W_p=\frac{1}{2}Re\left\{\int_{vol\_p}\tilde{E}\cdot\left(\sigma\tilde{E}\right)^* dV\right\} \quad (7)$$

This relation gives the magnitude of the electric field. The dissipated power in the cavity is given by:

$$W_d=W_p+\sum_{all\_walls}\int_{wall}\frac{\omega}{Q}\cdot\varepsilon_w\left|\tilde{E}\right|^2 dV. \quad (8)$$

where the second term represents the energy stored in the electromagnetic fields and dissipated in the cavity walls. Q is the quality factor of the cavity.

3.3 Gas flow and heating

The following Navier-Stokes equations in stationary mode are solved using the power deposited by the microwaves in the plasma volume:

$$\nabla\cdot\rho\vec{v}=0 \quad (9)$$

$$\nabla\cdot(\rho\vec{v}\otimes\vec{v}-\bar{\bar{\tau}})=-\vec{\nabla}P+\rho\vec{g} \quad (10)$$

$$\nabla\cdot\left(\rho C_p T\vec{v}-\lambda_T\vec{\nabla}\mathrm{T}\right)=S_{\mu w} \quad (11)$$

ρ the density, $\vec{v}$ the gas velocity, $\bar{\bar{\tau}}$ the stress tensor which is taken isotropic, P the pressure, g the gravitational acceleration, T the temperature, C_p the specific heat capacity, and λ_T the thermal conductivity. $\otimes$ is the dyadic product. $S_{\mu w}$ is the heat deposited by the microwaves in the plasma. It is treated as a source term. These equations are closed by the ideal gas law. The gas properties are those of ammonia up to 700 K and those of a mixture of 25vol.%N_2 / 75vol.%H_2 beyond this value.

3.4 Boundary conditions

Electromagnetic BC

When we assume that the walls of the experimental device are perfect electrical conductors, the following condition applies:

$$\vec{n}\times\vec{E}=\vec{0} \quad (12)$$

where $\vec{n}$ is the unit vector normal to the surface. This condition ensures that the tangential component of the magnetic field is zero. For the section of the guide that connects the generator to the reactor, we impose a port-type condition, which is a matched boundary condition. This matched boundary condition applies to boundaries that have no physical representation, such as the waveguide section. This boundary condition simulates a non-reflective boundary. In the eigenvalue problem posed, it translates into the following relation:

$$\vec{n} \times \left(\vec{\nabla} \times \vec{E}\right) - j\beta\vec{n} \times \left(\vec{E} \times \vec{n}\right) = 0 \quad (13)$$

Here, β is the wavenumber: $\beta = \omega / c$. At the gas inlet and gas outlet of the quartz tube and each end of the window, we also impose a port condition. When the problem concerns the calculation of powers, the port condition on the cross-section of the waveguide allows us to impose the incident power P_i via E_0. This results in the following relationship:

$$\vec{n} \times \left(\vec{\nabla} \times \vec{E}\right) - j\beta\vec{n} \times \left(\vec{E} \times \vec{n}\right) = -2j\beta\vec{n} \times \left(\vec{E}_{in} \times \vec{n}\right) \quad (14)$$

with $\left\|\vec{E}_{in}\right\| = E_0 \sin\left(\frac{\pi x}{a}\right)$.

The continuity of the tangential component is set at the wall of the fused silica tube.

Flow BC

The ammonia flow at the inlet of the fused silica tube is set by its standard flow rate, parallel to the boundary normal, and the tangential flow velocity is set to zero. The gas temperature is 300 K.

At the outlet of the fused silica tube, the gas exit is defined by the normal stress, which is taken here as equal to the absolute pressure. The tangential stress component is set to zero.

The fused silica tube is assumed to be non-catalytic, *i.e.* without any dissociation of NH_3. The gas velocity is set to zero. The heat flux Φ_h at the inner surface of the fused silica wall is defined by Fourier's law and the given thermal conductivity λ_T of fused silica as a function of the temperature (It varies from 1.35 to 2.52 W m^{-1} K^{-1}) from 300 to 1100 K [6]). The effect of radiation is neglected.

$$\Phi_h = -\lambda_T \vec{\nabla} T \cdot \vec{n} \quad (15)$$

The external temperature of the wall is set using an experimental profile measured with a pyrometer. Under severe conditions, the tube can melt, reaching about ~1950-1980 K.

3.5 Mesh and Resolution

To get reasonable calculation time, the geometry of the reactor was simplified. First, we chose to treat the ***AB*** section of the waveguide as linear, transforming the bent section into a straight section.

We used the symmetry of the reactor to model only half of it (the symmetry plane is the XY plane at Z=0). The complete mesh consists of 28381 domain elements (Fig. 2). d_1 and d_3 lengths in Fig. 1 were parametrized in the code and modified on demand.

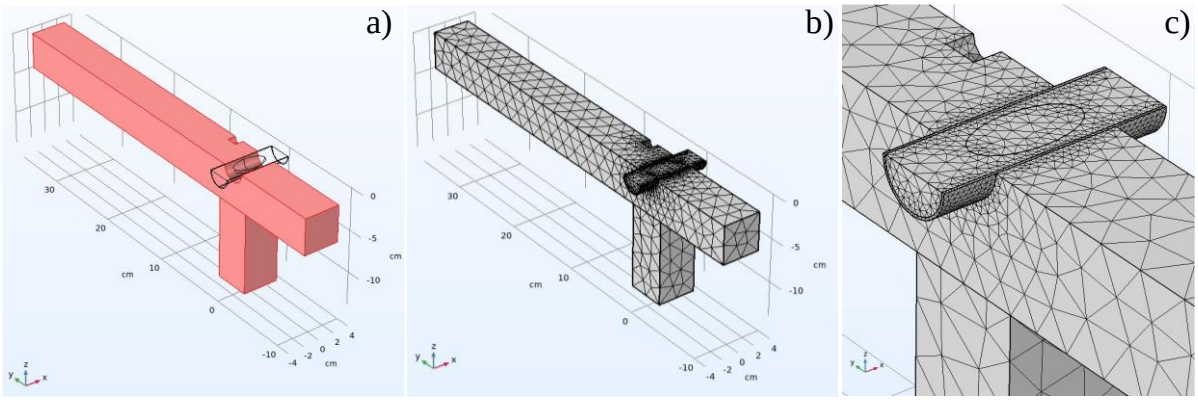

Fig. 2. The model reactor used for simulation. a) General 3D view showing the waveguide in pink, the quartz tube and the plasma ellipsoid inside. The stub appears as a hole on the right side closer to the inlet port. The short-circuit piston is the XZ square at Y=-12 cm. b) Mesh used for the simulation. c) Magnification of the view showing the mesh around the quartz tube and the plasma.

Equation 3 is solved numerically on the physical domain using Comsol Multiphysics® finite element software, which allows us to iterate over the geometric parameters and the electron concentration. To achieve our objective, two stages are necessary. The first is to determine the eigenvalue solution of Equation 3, which gives access to the cavity resonance frequency. The eigenvalue we are looking for f_{res} is linked to the pulsation by $\omega = 2\pi f_{res}$. The second is the resolution in E, giving access to the absorbed and reflected powers and the value of E. Eigenvalue resolution is used to determine the electron concentration at a specific frequency (2.45 GHz). The second step is applied once the concentration has been determined. It gives access to the value of the electric field in the plasma as well as the absorbed and reflected power.

3.6 Coupling

The propagation of the microwaves in the system defined by successive zones of distinct permittivity values leads to the development of a standing wave which deposits energy in absorbing media.
This amount of energy is calculated and used as a heat source to define the flow conditions, leading to a temperature distribution in the volume of the reactor tube. The multiphysics problem is then relatively simple as it does not require to implement a feedback loop between the Navier-Stokes equations and the Maxwell equations. The COMSOL Multiphysics Software [7] was used to solve the numerical problem.

4 Experimental results

We found out that, regardless of the conditions (pressure between 50 and 200 mbar, flow rates from 1.375 to 11.0 slm, and powers from 300 to 1000 W), the electron temperature consistently remains around 0.5 ± 0.1 eV. So, we set T_e = 0.5 eV for all conditions. The positions of the stub and the short-circuit piston were accurately measured and associated with the selected experimental conditions to define the reflected power and therefore the absorbed power for a given incident power, and with the geometry and volume of the plasma by image analysis for an average electron density measured by MWI. Results are presented in table 1. The data reported indicate that the effect of pressure on plasma parameters is not very significant overall. The volume decreases slightly (by around 40% at 5 slm) when the pressure is multiplied by 5. The rotational temperatures of the two probes vary by only 10% and the electron densities decrease by a factor of 3. It should also be noted that the positions of the impedance adjustment parameters are also virtually constant. To reproduce these results theoretically, we chose to vary only the electron density to reproduce the evolution of the temperature probe measurements. The consequences of this choice will be discussed later. To do this, we have to take into account the changes in $\tilde{\nu}_m$ with the various parameters on which the frequency depends. We can consider that the dependencies according to n_e were weak. By fixing T_e=0.5 eV over the whole pressure range, and considering a maximum gas temperature of the order of 2500 K, all that remains is to calculate the variation of $\tilde{\nu}_m$ with P. This is almost linear and is written as:

$$\tilde{\nu}_m[s^{-1}] = 1.84 \times 10^6 P[Pa] + 9.33 \times 10^8 \quad (16)$$

This allows us to calculate the permittivity of the medium as:

$$\varepsilon_p = 1 - a(P)\tilde{n}_e - ib(P)\tilde{n}_e \quad (17)$$

where $a(P)$ and $b(P)$ are two coefficients provided for each pressure. They can also be used to calculate the electrical conductivity values:

$$\sigma_p = \varepsilon_0 \omega b(P)\tilde{n}_e - i\varepsilon_0 \omega a(P)\tilde{n}_e \quad (18)$$

The results of these calculations are shown in Fig. 3. First of all, it is important to note that without any strong assumptions, it is possible to reproduce the values of the electron densities with an accuracy generally less than a factor of 2, which is very satisfactory. The discharge temperatures are necessarily very close to the theoretical values obtained since this criterion is used to define the value of the electron density in the code. We have chosen to limit ourselves to two significant digits for the value of n_e, which leads to small deviations in the gas temperature T_g.

Tab. 1. Raw data needed for the modelling of NH_3 plasmas. The plasma volume is treated as an ellipsoid (polar radius R_p and equatorial radius R_q).

	Pressure (mbar)	Injected power (W)	d_1 (mm)	d_3 (mm)	R_p (cm)	R_q (cm)	Volume (cm^3)	NH T_{rot} (K)	N_2 T_{rot} (K)	n_e^0 (cm^{-3})	$\tilde{n}_e$ (cm^{-3})
5 slm	40	430	15	135	3.45	0.824	9.81	2561	2645	2.79×10^{11}	1.46×10^{11}
	60	430	22	135	3.00	0.675	5.73	2835	2682	2.04×10^{11}	1.07×10^{11}
	80	430	22	135	2.55	0.720	5.53	2971	2814	1.90×10^{11}	9.97×10^{10}
	100	430	22	135	2.25	0.723	4.92	2996	2877	1.85×10^{11}	9.67×10^{10}
	200	430	21	130	1.65	0.802	4.44	2906	2891	8.90×10^{10}	4.66×10^{10}
10 slm	40	450	12	135	3.90	0.689	7.75	2618	2716	3.65×10^{11}	1.91×10^{11}
	60	450	11	135	3.60	0.666	6.69	2777	2703	3.21×10^{11}	1.68×10^{11}
	80	440	12	135	3.15	0.627	5.18	2897	2813	2.58×10^{11}	1.35×10^{11}
	100	440	14	135	2.70	0.598	4.05	2998	2831	2.10×10^{11}	1.10×10^{11}
	200	440	20	130	1.95	0.542	2.40	2918	2856	6.89×10^{10}	3.61×10^{10}

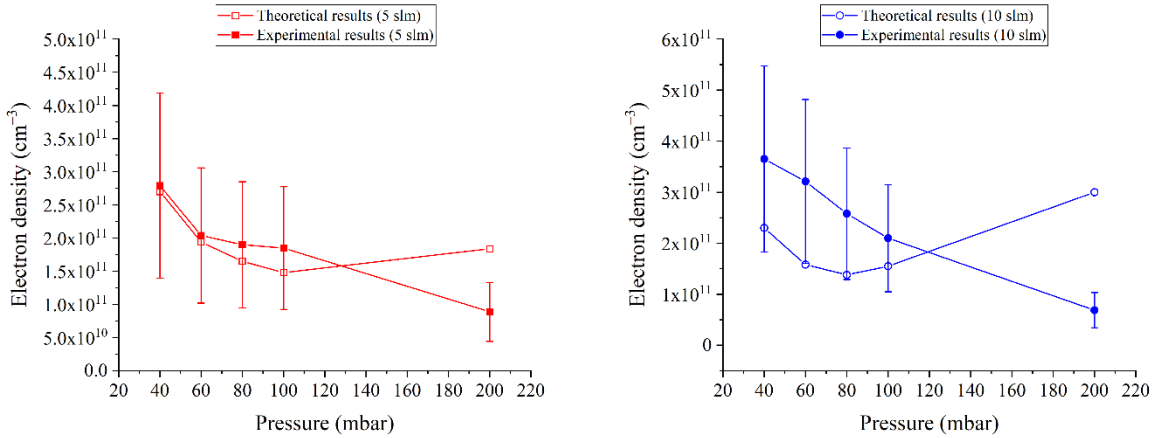

Fig. 3. Evolution of the electron density as a function of the pressure in the different conditions shown in Table 1. Left: 5 slm. Right: 10 slm.

For one condition (60 mbar and 10 slm), we provide the spatial evolution of selected parameters in Fig. 4. This shows the relevancy of the calculation in this case. The spatial distribution of the electric field strength is provided Figs. 4a and 4b. We observe the presence of a standing wave with a maximum absorption in the cavity. The gas temperature (Figs. 4c and 4d) varies from room temperature at the entrance of the tube, increases to its maximum value slightly farther than the plasma center due to the flow, and decreases next. We see in Figs. 4g and 4h that the gas temperature at the wall remains below the melting point of the fused silica tube. In Figs. 4e and 4f, we show the velocity field in the tube and the corresponding parabolic profile across the tube. In this condition, the maximum velocity reaches ~19 m s^{-1}. The flow, represented by arrows in the center of the tube and at the wall in Fig. 4g, is clearly laminar.

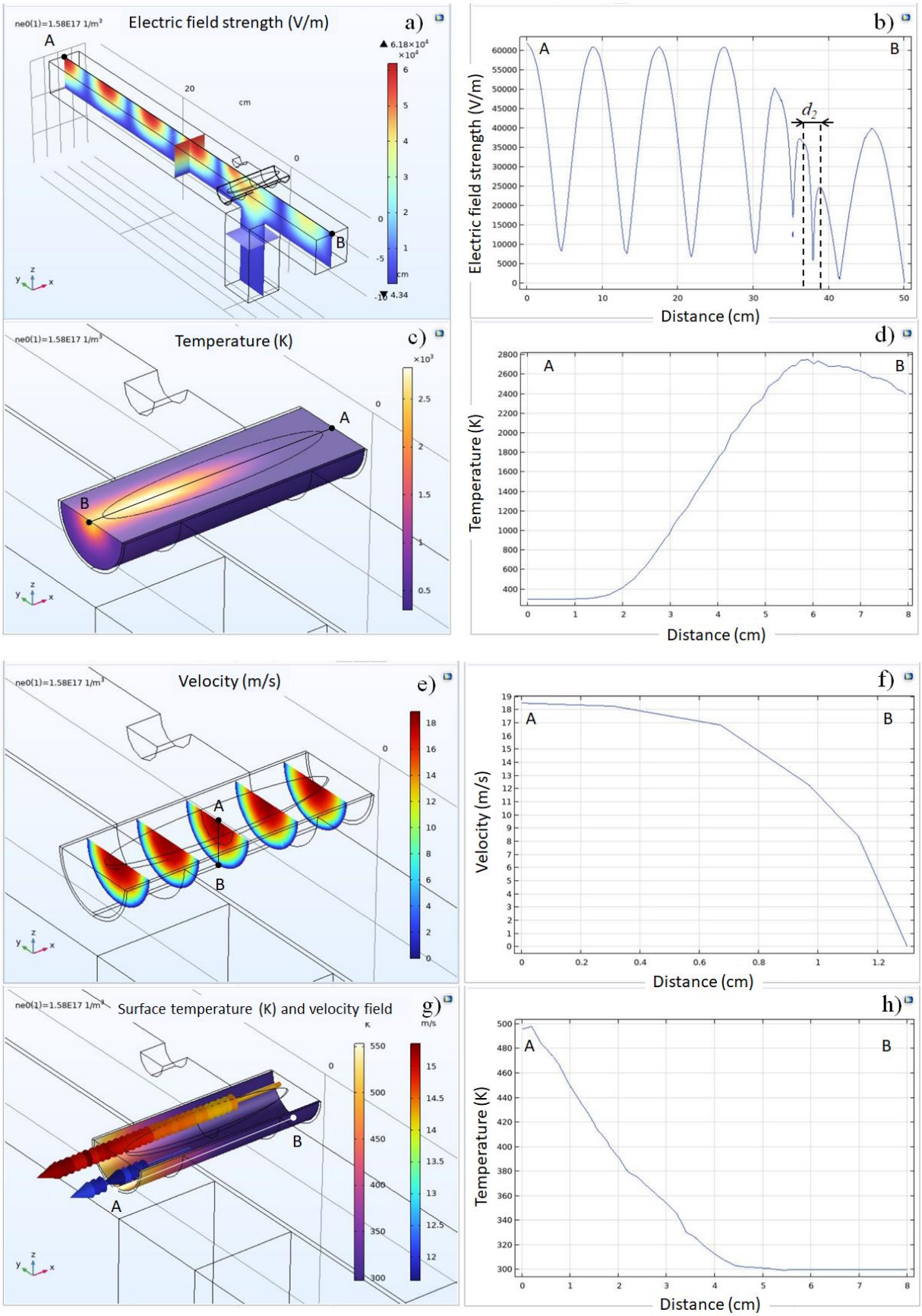

Fig. 4: Spatial evolution of some selected parameters. Left: 3D view. Right: line evolution along the AB segment shown in the 3D view. a) and b) Strength of the electric field. c) and d) Gas temperature. e)

and f) Gas velocity. g) and h) Gas temperature at the wall of the fused silica tube. In g), the flow is represented by arrows in the center of the tube and at the wall.

We note in Fig. 3 the presence of one condition (at 200 mbar, 10 slm), where the calculation result is far from the experimental data. For this particular condition, the value of n_e is significantly lower than the values determined at lower pressures. To understand this case, it was necessary to estimate the influence of the main parameters on the calculation results. To do this, we modified the input data for each parameter in the calculation to estimate the resulting change in n_e. Some parameters cannot be subject to a large error (such as d_1 or d_3), which leads to weak errors on $n_e^{0,th}$. Small variations in the pressure, which is still a fairly accurate control experimentally, do not significantly affect the electron density. Similarly, if we stay within the temperature range defined by the rotational probes, there is little change in $n_e^{0,th}$. The influence of volume is more important but still limited. With a 5% error on the 2 characteristic dimensions of the plasma, the volume only decreases by 0.95 cm^3 (14%), while the error on the electron density hardly exceeds 10%. When the power increases by 4.4%, the electron density decreases by 11%, which is close to 10% as well. The reason why the electron density decreases is because we consider a higher power per volume unit, which requires fewer electrons to dissipate the same energy. Varying the electron temperature leads to a weak effect on the electron density. To sum up, we observe that the changes of n_e due to variations of parameters within acceptable ranges of values never exceed 12%. This means that at 200 mbar, measurements made with the same accuracy as for other conditions are expected to be as reliable. So, there is probably a physical reason that explains the mismatch between the experimental and the theoretical data. Let's notice that this trend seems to start appearing around 100 mbar already. More experiments are now needed to understand the origin of this mismatch.

4. Conclusion

The global model described in this work shows how the microwaves are absorbed by the plasma and how the gas is heated in the case of pure ammonia under reduced pressure. The accuracy at the highest tested pressure decreases, likely because one important effect is neglected in this case. Deeper investigations are now needed to understand the origin of this behaviour.

5. References

[1] Jamesh M-I and Harb M 2020 *Mater. Sci. Energy Technol.* **3** 780.

[2] Dotan H, Landman A, Sheehan S W, Malviya K D, Shter G E, Grave D A, Arzi Z, Yehudai N, Halabi M, Gal N, Hadari N, Cohen C, Rothschild A and Grader G S 2019 *Nature Energy* **4** 786.

[3] Kelly S, Mercer E, De Meyer R, Ciocarlan R G, Bals S and Bogaerts A 2023 *J. CO_2 Utilization* **75** 102564.

[4] Zhang W 2019 « *Recherche numérique et expérimentale sur les propriétés de décharge et les caractéristiques de propagation électromagnétique dans les torches à plasma micro-ondes.* » PhD thesis, Toulouse

[5] Itikawa Y 2017 *J. Phys. Chem. Ref. Data* **46** 043103.

[6] Combis P, Cormont P, Gallais L, Hébert D, Robin L and Rullier J 2012 *Appl. Phys. Lett.* **101** 211908.

[7] COMSOL Multiphysics®,v. 6.3. www.comsol.com. COMSOL AB, Stockholm, Sweden.

LOW ENERGY ELECTRONS IN NANO-SCALE PROCESSING

Oddur Ingólfsson[1] et al.

[1]*Science Institute of the University of Iceland, Department of Chemistry, Dunhagi 3, 107 Reykjavík, Iceland*

E-mail: odduring@hi.is

In the current contribution the focus is on the role of low energy secondary electrons in nanotechnology, specifically, dissociative electron attachment (DEA) in the fabrication of carbon nano-membranes (CNMs) from self-assembled monolayers (SAMs) and in focused electron beam induced deposition (FEBID). The nature, selectivity and efficiency of the DEA process is discussed in general and specifically the potential of this process to enhance the selectivity and efficiency in two nanofabrication processes is discussed for two examples. The first being the targeted modification of biphenyls to enhance the DEA induced cross-linking efficiency in SAMs for the production CNMs. The second being DEA of the high performance FEBID precursor $HFe(Co)_3(CO)_{12}$, which is found to attach an electron up to above 20 eV incident electron energy leading to a single electron induced dissociation of all 12 CO ligands.

1. Secondary electrons in nano-scale fabrication

Where high-energy radiation interacts with matter, ionization and thus production of free electrons is bound to be significant. The energy distribution of these electrons depends on the nature and the energy of the initial radiation as well as the composition and phase of the material in question. Moreover, the electrons initially produced through the respective ionizing events are subjects to scattering events within the media they are produced in. These scattering events further influence their energy and spatial distributions and may also constitute secondary ionization processes leading to further electron production. For high-energy electron beams impinging on a solid surface, as is the case in focused electron beam induced deposition (FEBID) (typically 1-10 keV) [1-3] and in the production of carbon nano-membranes (CNMs) from self-assembled monolayers (typically 500 eV) [4,5], the secondary electron energy distribution typically peaks well below 10 eV, has a significant contribution at threshold (close to 0 eV) and a tail to higher energies. This is also the case in extreme ultra-violet lithography (EUVL) [6-8], except that here the extent of the high-energy tale is confined below the respective photon energy (about 90 eV for 13.5 nm photons). Thus, in such nano-technology fabrication approaches, low energy electrons are abundant and play a significant, if not a determining, role in the chemistry underpinning methods.

In turn, funded understanding of these processes may allow advantageous design of FEBID precursors, SAMs, and EUVL resist materials. This is especially true as the energy dependency, the efficiency and the nature of the initial electron induced reactions depends critically on the molecular composition of the respective matter and may thus be synthetically tailored to suit the intended application.

2. DEA in FEBID and the Production of CNMs from SAMs

In principle, electron induced bond rupture in the low energy range from about 0-100 eV may proceed through four distinctly different processes [9-14]:

Dissociative Ionization (DI);

$$AB + e^- \longrightarrow AB^{(\ddagger)+} + 2e^- \longrightarrow A^{(\ddagger)+} + B^{(\ddagger)} + 2e^- \quad (1)$$

Dissociative Electron Attachment (DEA);

$$AB + e^- \longrightarrow AB^{(\ddagger)-} \longrightarrow A^{(\ddagger)-} + B^{(\ddagger)} \quad (2)$$

Neutral Dissociation (ND);

$$AB + e^-(\varepsilon_1) \longrightarrow [AB]^* + e^-(\varepsilon_2 < \varepsilon_1) \longrightarrow A^{(\ddagger)} + B^{(\ddagger)} \quad (3)$$

Dipolar Dissociation (DD);

$$AB + e^-(\varepsilon_1) \longrightarrow [AB]^* + e^-(\varepsilon_2 < \varepsilon_1) \longrightarrow A^{(\ddagger)+} + B^{(\ddagger)-} \quad (4)$$

Here; (‡) signifies possible vibrational and/or electronic excitation, *denotes electronic excitation, and ε_1 and ε_2 represent the electron's initial and residual energy before and after the inelastic scattering process, respectively.

These processes are distinctly different, and while DEA is a resonant process that is typically confined to narrow energy ranges below 10 eV and generally has the highest cross section close to 0 eV, DI is a none-resonant process with an onset slightly above the ionisation limit of the respective molecules. The energy dependence of ND and DI, on the other hand, is determined by the underlying electronic excitations.

Not only the energy dependence of these processes, but also their extent and the nature of the fragments formed are distinctly different; while DEA predominantly leads to single bond cleavage and the formation of a closed shell anion and neutral radical, DI, leads to the formation of a closed shell cation and neutral radical(s), and results in a more extensive fragmentation as the incident electron energy increases. In ND, two or more neutral radical fragments are formed, but little experimental data is available on the extent of fragmentation in this process. Like DEA, however, single bond ruptures may be expected to be the most efficient ND processes. Finally, DD leads to the formation of an anionic and a cationic fragment.

Furthermore, the cross sections for these processes and the branching ratios for different dissociation paths depend critically on the respective molecular composition, which in turn opens opportunities to direct these in a favourable way by tailoring the initial electron induced bond rupture in the respective processes.

3. Dissociative Electron Attachment in FEBID and the Production of CNMs from SAMs

In the current contribution the focus is on dissociative electron attachment and potential means to use the efficiency and selectivity of this process to enhance and direct targeted nano-fabrication processes. Generally, the nature of the DEA process and its efficiency and selectivity is discussed before the potential role, and use of this process in nanofabrication is discussed for two examples. The first is the targeted chemical modification of biphenyls for the production CNMs from SAMs, where sensitization towards DEA through targeted halogenation was found to enhance the process significantly [15]. The second example describes DEA to an exceptionally high performance FEBID precursor $HFe(Co)_3(CO)_{12}$, which allows the deposition of high purity, magnetically well defined structures [16-18]. In DEA this precursor also shows extraordinary behaviour by electron attachment up to above 20 eV – about 12 eV above its ionisation energy. And, single electron induced dissociation of all 12 CO-ligands from the metallic core [18, 19].

Acknowledgements

This work was supported by the Icelandic Center of Research (RANNIS), the University of Iceland Research Fund and the COST Action CM1301; Chemistry for ELectron-Induced Nanofabrication (CELINA) and was conducted within the framework of the Marie Skłodowska-Curie Innovative Training Network 722149 - ELENA; Low energy ELEctron driven chemistry for the advancement of emerging Nano-fabrication methods.

4. References

[1] I. Utke, P. Hoffmann, J. Melngailis, J. Vac. Sci. Technol. B 26(4) (2008) 1197.

[2] W.F. van Dorp and C.W. Hagen, J. of Appl. Phys. 104 (2008) 081301.

[3] R.M. Thorman, R. Kumar. T.P., D.H. Fairbrother, O. Ingólfsson Beilstein J. Nanotechnol. 6 (2015) 1904

[4] A. Turchanin, Ann. Phys. (Berlin), 529 (2017) 1700168

[5] A. Turchanin, D. Weber, M. Büenfeld, C. Kisielowski, M. V. Fistul, K. B. Efetov, T. Weimann, R. Stosch, J. Mayer and A Gölzhäuser, ACS Nano 5(5), (2011), 3896-3904.
[6] Extreme Ultraviolet (EUV) Lithography V, Eds; O.R.Wood and E.M. Panning, Proc. of SPIE Vol. 9048 (2014) 90482Z.
[7] Banqiu Wu and Ajay Kumar, J. Vac. Sci. Technol. B 25 (2007) 1743
[8] J. Torok, R. Del Re, H. Herbol, S. Das, I. Bocharova, A. Paolucci, L.E. Ocola, C. Ventrice, E. Lifshin, G. Denbeaux, R.L. Brainard, J. Photopolym. Sci. Technol. 26 (2013) 625-634.
[9] Ingólfsson, O. (Ed), *Low-Energy Electrons Fundamentals and Applications*; Pan Stanford Publishing Pte. Ltd.: Singapore, The Republic of Singapore, 2019.
[10] H. Hotop, M.-W. Ruf, M. Allan, I. Fabrikant, Adv. Atom. Mol. Opt. Phys. 49 (2003) 85.
[11] I. Bald, J. Langer, P. Tegeder, O. Ingólfsson, Int. J. Mass Spectrom. 277 (2008) 4-25.
[12] C. R. Arumainayagam, H.-L. Lee, R. B. Nelson, D.R. Haines, R.P. Gunawardane, Surf. Sci Rep. 65 (2010) 1-44.
[14] E. Bohler, J. Warneke, P. Swiderek, Chem. Soc. Rev. 42 (2013) 9219-31.
[15] S. Koch, C. D. Kaiser, P. Penner, M. Barclay, L. Frommeyer. D. Emmrich, P. Stohmann, T. Abu-Husein, A. Terfort, D. H. Fairbrother, O. Ingólfsson and A. Gölzhäuser, *Beilstein J. Nanotechnol.* **2017,** *8,* 2562–2571.
[16] F. Porrati, M. Pohlit, J. Müller, S. Barth, F. Biegger, C. Gspan, H. Plank, and M. Huth, Nanotechnology, 26 (2015) 475701.
[17] Ragesh Kumar T P, P. Weirich, L. Hrachowina, M. Hanefeld, R. Bjornsson, H. R. Hrodmarsson, S. Barth, D. H. Fairbrother, M. Huth and O. IngólfssonBeilstein J. Nanotechnol. 9, (2018) 555–579
[18] T. P., R. K.; Barth, S.; Bjornsson, R.; Ingólfsson, O. Eur. Phys. J. D 70 (2016) 163.
[19] Kumar T P, R.; Bjornsson, R.; Barth, S.; Ingólfsson, O. Chem. Sci., 8 (2017) 5949–5952.

SPATIALLY AND TEMPORALLY RESOLVED ELECTRIC FIELD, CURRENT, AND ELECTRON DENSITY IN AN RF ATMOSPHERIC PRESSURE PLASMA JET BY E-FISH

Inna Orel[1], Nikita D. Lepikhin[1], Zoltán Donkó[1,2], Dirk Luggenhölscher[1], Uwe Czarnetzki[1]

[1]*Ruhr University Bochum, Institute for Plasma and Atomic Physics, 44780 Bochum, Germany*
[2]*Institute for Solid State Physics and Optics, HUN-REN Wigner Research Centre for Physics, 1121 Budapest, Hungary*
E-mail: inna.orel@rub.de

The work presents, to the best of our knowledge, the first ns-scale time and sub-mm-scale space resolved E-FISH measurements in an RF-APPJ similar to the COST-jet. The jet is operated in He with 0.5% N_2 admixture. The experimentally measured electric field is then used to estimate the time and space resolved absolute current density and electron density across the discharge assuming ions to be immobile. A comparison against an *ab initio* PIC/MCC simulation shows excellent agreement for the electric field and good agreement for the electron density.

1. Introduction

The electric field is one of the key parameters in a plasma. It is widely used as an input or output parameter in plasma simulations and thus its accurate experimental measurement is necessary to ensure the validity of simulation predictions. Although Radio Frequency Atmospheric Pressure Plasma Jets (RF-APPJ) are well known and thoroughly studied, accurate experimental measurements of their electric fields are lacking due to numerous experimental complications (e.g. helium-nitrogen discharge chemistry and miniature device sizes). Electric Field Induced Second Harmonic generation (E-FISH) is a laser-driven, non-invasive, non-resonant and spatio-temporally resolved technique that exploits the ability of a gaseous medium to convert two laser photons with wavelength λ to a single λ/2 photon in the presence of an external E-field [1]. In the present work, E-FISH is applied to measure the electric field across the inter-electrode gap of the RF-APPJ. This electric field is then used to obtain an estimate of the absolute current density and electron density from the homogeneity of the total current density. The experimental findings are confirmed by an *ab initio* PIC/MCC simulation.

2. Experimental setup

The discharge is driven between two flat stainless steel electrodes that are 1 mm thick and 20 mm long with an inter-electrode gap of 1.5 mm and covered from the sides by glass plates (similarly to [2]). A gas mixture of He:N_2 = 995:5 at a total flow rate of 1000 sccm is supplied via a through-hole in the back glass plate in the center of the inter-electrode gap. A sinusoidal high voltage waveform with a frequency of 13.56 MHz and an amplitude of 400 V (800 V peak-to-peak) generated by an RF power supply is applied to one of the electrodes of the jet via a homemade matching network and via a 50 Ohm coaxial cable, while the other electrode is grounded.
The emission of a Nd-YAG laser at 1064 nm with a 10 Hz repetition rate and a 100 ps pulse duration is used as a fundamental for the second harmonic generation (details in [3]). The laser beam with a 90 µm waist is focused by a plano-convex lens with a focal distance of 500 mm to the middle of the discharge gap. The generated second harmonic 532 nm beam is separated from the fundamental and focused onto a 100 µm pinhole before being guided to a photomultiplier tube to reduce the stray 532 nm light contribution. A fast photodiode with a rise time of about 200 ps is used to record the time instant of the laser pulse relative to the discharge. A precise synchronization is realized by measuring a Laplacian field at conditions without ignition of the discharge. The PMT data are sorted in 2 ns wide time bins with around 5000 shots per bin.

3. PIC/MCC simulation

The discharge is simulated using an electrostatic 1d3v (one dimensional in space and three dimensional in velocity space) PIC/MCC simulation which is based on the model from [4,5]. However, besides electrons, He^+, He_2^+, and N_2^+ ions, the present model also includes N_4^+ ions as in our more recent work [6,7].

4. Results

Figure 1 presents the electric field measured by E-FISH together with PIC/MCC simulation results at different distances from the grounded electrode (the powered electrode is located at 1500 µm). Excellent agreement is found between experiment and simulation across the entire inter-electrode gap, with respect to the overall waveform amplitude, shape and phase (measurements at distances below 840 µm are not shown here for clarity). Thereby, the *ab initio* PIC/MCC simulation is validated.

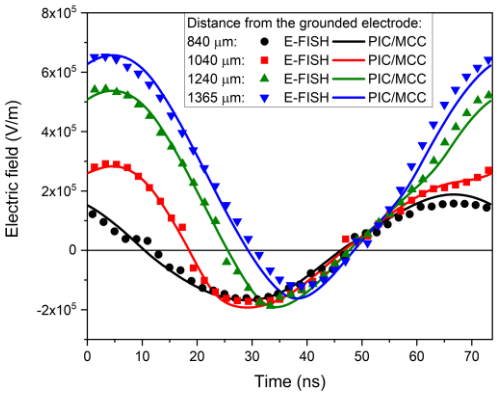

Fig. 1. Temporally resolved electric field across the RF-APPJ experimentally measured by E-FISH and calculated by PIC/MCC simulation. The error bars of the E-FISH electric field measurements estimated to be ±0.15 kV/cm are not shown.

The electron density and the current density are derived in the following way: The total current density is approximated by the sum of the displacement and conduction current density (neglecting the diffusion current). Since the current density is homogeneous across the discharge, the value in the center equals the value near the electrode. At the latter position, the conduction current can be neglected during times of maximum sheath potential, which leaves only the displacement current. Then the electron density in the center can be deduced by $n_e = (j_{electrode} - \varepsilon_0 \dot{E})/(e\mu E)$. Here, the electron density in the center is approximated as constant in time. In the present work, the electron mobility is calculated by BOLSIG+ [8].

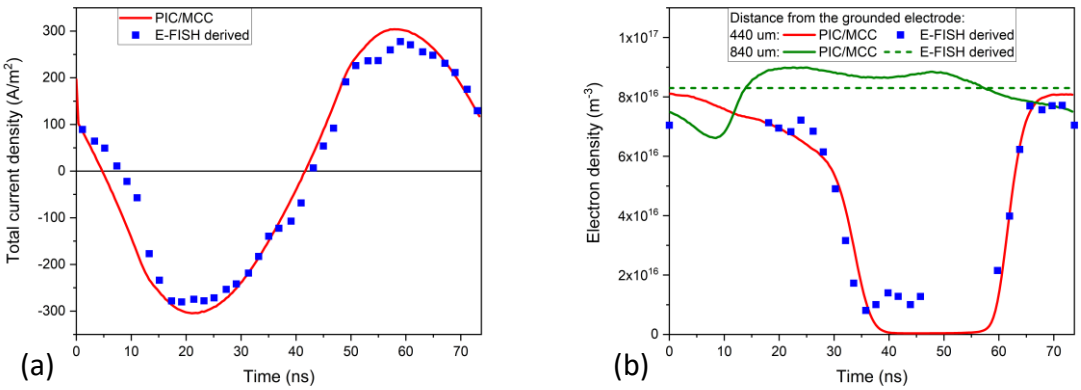

Fig. 2. Temporally resolved (a) total current density and (b) electron density calculated by PIC/MCC simulation and inferred from E-FISH electric field measurements, see text.

With the known electron density in the center, the total current density is also known at all times: $j_{total} = \varepsilon_0 \dot{E} + e n_e \mu E$. This allows to deduce now the temporally varying electron density at all locations in the discharge: $n_e = (j_{total} - \varepsilon_0 \dot{E})/(e\mu E)$. Very good agreement with PIC/MCC simulation is found.

5. Conclusions

The time and space resolved electric field in the RF-APPJ in a helium-nitrogen mixture was measured by E-FISH. The electric field allows the determination of the total current density and the spatially and temporally resolved electron density. The fact that the displacement current density at all points is of the same order as the conduction current density reveals the non-neutral nature of the discharge [5].

6. Acknowledgements

The work is supported by the DFG (German Science Foundation) in the frame of SFB1316 “Transient atmospheric plasmas — from plasmas to liquids to solids”.

7. References

[1] Dogariu A, Goldberg B M, O’Byrne S and Miles R B 2017 Phys. Rev. Applied 7(2) 024024
[2] Lepikhin N D, Luggenhölscher D and Czarnetzki U 2020 Journal of Physics D: Applied Physics 54 055201
[3] Orel I, Lepikhin N D, Luggenhölscher D, Czarnetzki U 2025 Electric field measurements in a He:N_2 atmospheric pressure RF plasma jet by E-FISH Plasma Sources Science and Technology (under revision)
[4] Hübner G, Bischoff L, Korolov I, Donkó Z, Leimkühler M, Liu Y, Böke M, Schulz-von der Gathen V, Mussenbrock T and Schulze J 2021 Journal of Physics D: Applied Physics 55 095204
[5] Klich M, Wilczek S, Donko Z and Brinkmann R P 2022 Plasma Sources Science and Technology 31 045003
[6] Kuhfeld J, Lepikhin N, Luggenhölscher D, Czarnetzki U and Donkó Z 2023 Plasma Sources Science and Technology 32 084001
[7] Lepikhin N, Kuhfeld J, Donkó Z, Luggenhölscher D and Czarnetzki U 2023 Plasma Sources Science and Technology 32 084002
[8] Hagelaar G J M and Pitchford L C 2005 Plasma Sources Science and Technology 14 722

ADVANCED DCSBD-BASED PLASMA TECHNOLOGIES FOR SURFACE MODIFICATIONS AND BIO-APPLICATIONS

Dušan Kováčik[1, 2], Richard Krumpolec[1], Jakub Kelar[1], Slavomír Sihelník[1], Jianyu Feng[1], Pedram Ghourchi Beigi[1], Leila Zahedi[1], Zlata Kelar Tučeková[1], Oleksandr Galmiz[1], František Zelenák[1], Ali Jamaati Kenari[1], Sandra Ďurčányová[2], Veronika Medvecká[2], Tomáš Homola[1], Mirko Černák[1], Anna Zahoranová[2]

[1]*Department of Plasma Physics and Technology, CEPLANT - R&D Center for Plasma and Nanotechnology Surface Modifications, Faculty of Science, Masaryk University, Kotlářská 267/2, 602 00 Brno, Czech Republic*

[2]*Department of Experimental Physics, Faculty of Mathematics, Physics and Informatics, Comenius University Bratislava, Mlynská dolina, 842 48 Bratislava, Slovakia*

E-mail: dusan.kovacik@mail.muni.cz

Within the invited lecture, atmospheric pressure plasma technologies for the surface treatment of materials based on Diffuse Coplanar Surface Barrier Discharge (DCSBD) will be presented. These have been developed since DCSBD's first construction in an operational form almost 25 years ago. Several of them have also been industrially tested in real production conditions. The DCSBD discharge has undergone several technical modifications to optimize the parameters of the generated plasma so that it is suitable for the treatment of a wide range of materials and, in recent years, also for bio-applications. The DCSBD discharge has also enabled the development of other plasma sources, such as MSDBD or a brand new DCSBD linear atmospheric pressure plasma jet. Due to the advantageous properties of the generated plasma, these plasma sources occupy a significant position among state-off-the-art commercial atmospheric sources of non-equilibrium plasma and compete with them in many respects.

1. Introduction

Dielectric barrier discharges (DBDs) offer a relatively simple method of generating a non-equilibrium (or non-thermal) plasma at atmospheric pressure, which can be used for surface treatment of materials, among other applications. However, the disadvantage remains the filamentary nature of the generated plasma resulted in non-uniform treatment and, in the case of thermal-sensitive materials, even in their damage. Among DBDs, the Diffuse Coplanar Surface Barrier Discharge (DCSBD) has gained a significant position due to the advantageous properties of generated plasma for the low-cost, uniform and possible large-area surface treatment of a wide range of materials. Over the almost 25 years since the DCSBD was developed, designed, and first constructed in a functional form as a source of large-area surface plasma (up to ~ 8 x 20 cm^2) by the research group of Prof. Černák at the Faculty of Mathematics, Physics and Informatics, Comenius University (FMPI CU) in Bratislava, it has undergone several technical modifications and optimization. The DCSBD technology was later adopted and advanced at the R&D Centre CEPLANT, Masaryk University, Brno, and commercialized by spin-off Roplass Ltd. It is characterized by generating a non-equilibrium plasma in the ambient air in a thin layer (~ 0.3 mm) of high-power density with a high representation of diffuse plasma, due to which it appears macroscopically homogeneous (Fig. 1a) without any stabilization by the flowing gas or admixture of noble gases [1]. DCSBD is robust and easily scalable, capable of operating in dusty and humid environments, predisposing it to direct deployment in industrial production lines. Although DCSBD can be used effectively for surface treatment, activation, cleaning or functionalization of various materials, and, in recent years, also for bio-applications involving bio-decontamination or treatment of plant seeds, it is particularly suitable for flat and flexible materials, possibly for bulk materials that can be directly exposed to the plasma at an effective distance of ~ 0.3 mm from the plasma unit. For more complex spatial objects, its use is limited or ineffective. This fact was the motivation at the CEPLANT centre for the development of similarly efficient plasma sources as DCSBD but with use for surface treatment of 3D and structured objects. This effort resulted in the development of two DCSBD-based

plasma sources, Multi-hollow Surface Dielectric Barrier Discharge (MSDBD) and a brand new DCSBD linear atmospheric pressure plasma jet (DCSBD linear APPJ) enabling effective remote treatment.

2. Potential application of DCSBD, MSDBD and DCSBD linear APPJ

As already pointed, the **DCSBD** was successfully used in research to optimise the surface treatment of various materials. It was tested for the high-speed activation (450 m/min) of the lightweight PP non-woven fabrics directly on the production line before subsequent coating with surfactants. Similarly, DCSBD plasma treatment can be used for surface activation of PP non-woven, serving as a substrate for the electrospun nanofibre layer to enhance its adhesion but also for the treatment of the nanofibre layer itself to make it hydrophilic with the utilization in the production of nanofibre membranes to enhance their water and air filtering performance properties. In connection with nanofibres, other research activity at the CEPLANT centre is also optimizing electrospun nanofibres for enhanced tissue engineering performance assisted by atmospheric pressure plasma and plasma-assisted calcination of inorganic nanofibers in the collaboration with FMPI CU. DCSBD plasma was also used for enhancement of the dyeability and antibacterial properties of cotton fabrics. The simple scalability of DCSBD technology enabling the treatment of large-area materials was tested in industrial conditions for the surface activation of float glass and processing of PVB and Ionoplast interlayers for performance improvement of laminated glass used in civil engineering. At the CEPLANT centre, intensive research is currently underway focused on the applications of reduced graphene oxide (rGO) prepared by DCSBD plasma-triggered ultrafast and environmentally friendly reduction of graphene oxide [2], e.g. for rGO-based membranes for water filters to remove pesticides, antibiotics or analgesics.

Half-DCSBD (HDCSBD) generating surface plasma (Fig. 1b) with half the area (~ 8 x10 cm^2) compared to standard DCSBD plasma unit is a unique approach to the DCSBD configuration manufactured by KYOCERA Inc. (Kyoto, Japan) but designed and protected by Masaryk University. This type of discharge can be easily implemented, e.g., in wide-format UV-digital printers to improve ink adhesion after short substrate plasma treatment [3] or in robotic arms to automate the surface treatment process as part of production lines.

Among the several possibilities for using **MSDBD**, it seems to be promising as a source of plasma (Fig. 1c) and plasma-generated species for remote plasma curing of polysilazane coatings with anti-soiling anti-corrosion properties. This plasma-based curing approach can replace the standard long-time (up to 7 days) and high temperature (>150˚C) curing methods and significantly reduce the processing time to short curing times, typically less than five minutes, and thus enhance productivity and energy efficiency. MSDBD has proven further as an effective plasma system for activating water-based medium for bacterial biofilm decontamination [4] as well as for soybean treatment aimed to enhance germination [5] or decrease the dustiness of coated seeds using plasma pre-treatment [6].

DCSBD linear APPJ presents a brand-new plasma source developed at CEPLANT and protected by the submitted patent application. It possesses all the advantages of DCSBD design, like robustness and virtually unlimited lifetime of the electrode system. It generates low-temperature afterglow plasma plume (AfPP) suitable for plasma modification of complex 3D surfaces of even temperature-sensitive materials. It uses standard air or nitrogen as a working gas, and the current configuration of the electrode system enables it to generate a linear AfPP of 50 mm width (Fig. 1d). Effective treatment distance is 1-20 mm in open-air environment and at least 50 mm in closed N2-filled chamber. The efficiency of this unique linear jet was verified by comparison with the commercial plasma curtain system (ULD-60, AcXys Technologies) for the surface treatment of polycarbonate. The low-temperature nature of the afterglow plasma was confirmed by the treatment of temperature-sensitive materials such as BOPP foil, ionoplast polymer, and thick PP nonwoven fabrics, but especially in the complex study of pea seeds treatment as a biological object to improve their germination in collaboration with FMPI CU.

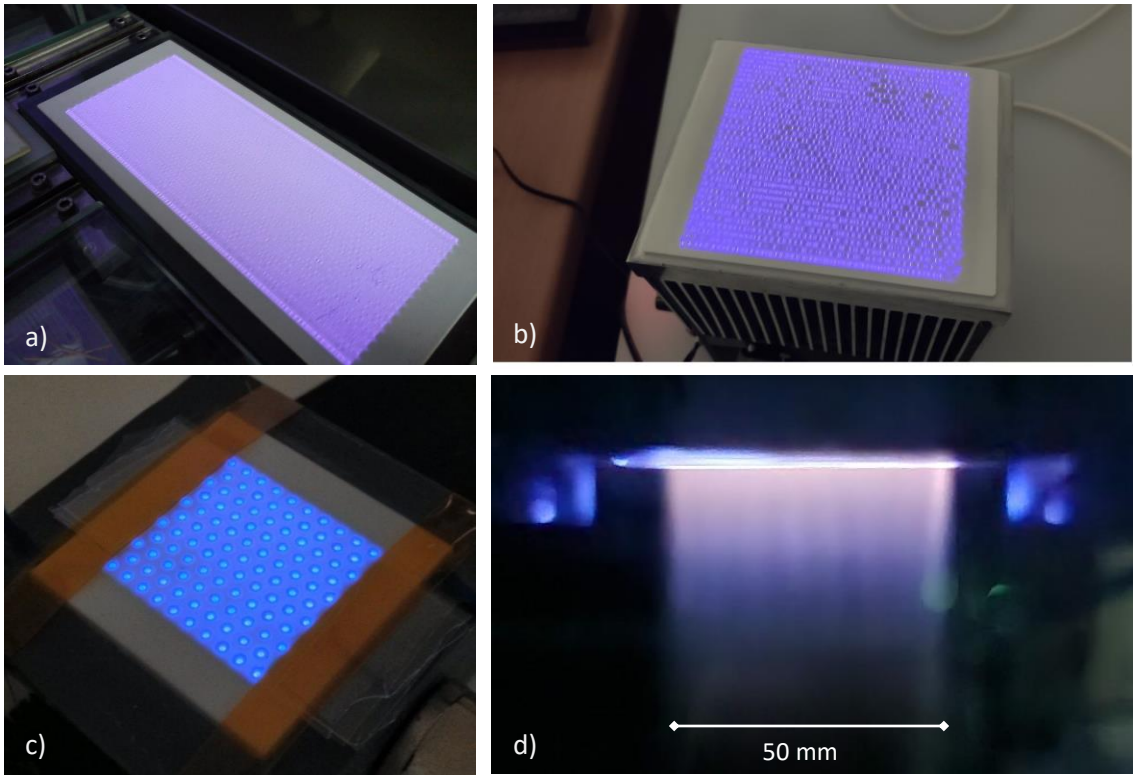

Fig. 1. The photos illustrating plasma generated at atmospheric pressure by DCSBD in ambient air (a), HDCSBD during the heating up period in ambient air (b), MSDBD in flowing air (c), and DCSBD linear APPJ operating into N_2 filled chamber (d).

Acknowledgment: This research has been supported by the project LM2023039 funded by the Ministry of Education, Youth and Sports of the Czech Republic as well as by the Slovak Research and Development Agency under the contract No. APVV-21-0147.

3. References

[1] Černák M, Černáková Ľ, Hudec I, *et al.* 2009 *Eur. Phys. J. Appl. Phys.* **47** 22806.
[2] Zelenák F, Kováčová M, Moravec Z, *et al.* 2023 *Carbon* **215** 118436.
[3] Fleischer M, Kelar Tučeková Z, Galmiz O, *et al.* 2024 *Nanomaterials* **14** 426.
[4] Kelar Tučeková Z, Vacek L, Krumpolec R, *et al.* 2021 *Molecules* **26** 910.
[5] Ďurčányová S, Slováková Ľ, Klas M, *et al.* 2023 *Plasma Chem Plasma Process* **43** 1863–1885.
[6] Slavíček P, Štěpánová V, Fleischer M, *et. al.* 2023 *Plasma Chem Plasma Process* **43** 1887–1906.

PLASMA-BASED MICROFABRICATION TECHNOLOGY FOR CHARGE CONTROL METHODS IN PATHOLOGICAL SPECIMENS TO DETECT VIRUS PARTICLE USING SEM AND AFM.

Sanae Ikehara[1,2], Kazuhiko Azuma[1], Syota Ohki[1], Hiroki Kondo[3,4], Yoko Iizumi[2], Toshiya Okazaki[2], Masaru Hori[4], Komei Baba[5], Yuzuru Ikehara[1, 2]

[1] Department of Pathology, Graduate School of Medicine, Chiba University 1-8-1 Inohana, Chuo-ku, Chiba, Japan [2], Natl. Inst. Industrial Sci. and Tech. (AIST), Tsukuba, Japan, [3] Kyusyu Univ. Kyusyu, Japan, [4] Nagoya Univ. Nagoya, Japan,[5]DLC Research Institute LLC, Nagasaki, Japan.

E-mail:yuzuru-ikehara@chiba-u.jp

Nanoimaging technology has progressed alongside the growing integration of silicon-based circuits. Short abstract of the contributed paper. However, the direction of progression on nanoimaging has not been well fitted with the life science heading to understand homeostasis and pathogenesis of cells and tissues.. Short abstract of the contributed paper. Short abstract of the contributed paper. (10pt font size).

1. Main text.

Nanoimaging technology has progressed alongside the growing integration of silicon-based circuits. In the case of a scanning electron microscope (SEM), achieving nanoimaging with a resolution of less than 1 nm has become possible with the invention of the in-lens method. On the other hand, the resolution of the transmission electron microscope (TEM) is up to 40.5 picometers due to the advancements in aberration correction and scanning transmission electron microscopy technology. The advancement of these nanoimaging technologies has responded to the growing demands on integrating silicon-based circuits in evaluating and verifying nano-microfabrication results, such as lithography, thin film deposition, and etching.

The direction of progression on nanoimaging has not been well fitted with the life science heading to understand homeostasis and pathogenesis of cells and tissues. For example, in research on the SARS-Cov2 virus (COVID-19) infection, it is hard to visualize the infected viruses by SEM in Formalin-Fixed Paraffin-Embedded (FFPE) specimens on glass slides that are widely used for diagnosis on surgical pathology. Currently, no suitable methods for marking virus particles using antibody staining exist, and the resolution is insufficient to capture both the virus particles and the antibody reactions. The latter limitation is due to charging effects and the low-level emission of secondary electrons from the organic molecules that comprise tissues. Additionally, as TEM can only observe ultra-thin sections made from epoxy resin, it does not meet the needs of these analyses performed on glass slides. Therefore, our goal in advancing nanoimaging is to acquire morphological information for analysing pathological conditions interpreted within the context of physiological functions and tissue remodelling using glass slide specimens.

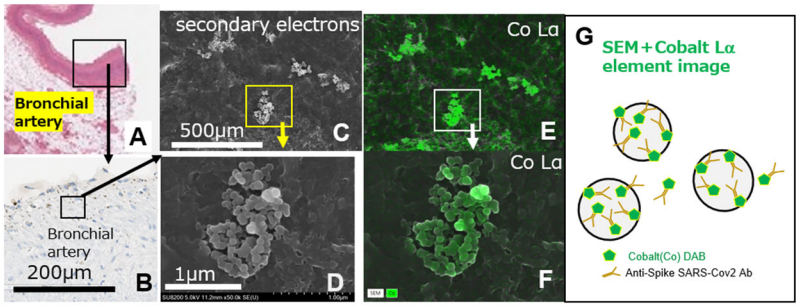

Fig.1 Analysis results of autopsy lung tissue from a case of SARS-Cov2 virus infection. A is HE staining. B is immunostaining for SARS-Cov2 spike protein on the wall of the bronchial artery. C and D are secondary electron images. E and F are elemental imaging results obtained by acquiring Lα-rays of Cobalt (Co) using EDX. G. Image of the antigen-antibody reaction performed to visualize the SARS-Cov2 virus. Modified from [1] and [7] .

Following the research investigating the characteristics and dynamics of the plasma generated by dielectric barrier discharge, we have established a method for observing thin sections of FFPE on glass slides using SEM [1-5]. Notably, because we discovered that proteins in solution could be transferred

from the liquid phase to the solid phase by receiving an electric charge from the plasma, we tried to use the plasma generated by dielectric barrier discharge to extend the nanoimaging in the Life Science area. Indeed, the discover of phenomena that ion-induced phase transitions from plasma was a clue to increase the emission efficiency of secondary electron scattering from FFPE specimens on glass slides by carbon-based plasma treatment[4-6].

At the symposium, we will introduce the phenomenon of the reaction of FFPE specimens on glass slides with a carbon-based plasma produced by dielectric barrier discharge, which reduces charging and improves secondary electron emission efficiency in SEM observation. Moreover, we will also outline the establishment of a virus labeling method using antibody staining, which the carbon-based plasma treatment can do. In addition, we will introduce the results of identifying SARS-Cov2 virus infection by observing thin-sectioned FFPE on glass specimens using SEM[7] and AFM, and we want to discuss the possibility that this developed technology will become a milestone on the path to medical and pathological research.

2. Acknowledgement

This work was supported by the JST-Moonshot R&D (No. JPMJMS2025) and Grants-in-Aid for Scientific Research (20K08351, 23K07455), AMED-CREST (No. JP20gm1210003).

3. References

[1] Sanae Ikehara, Ikehara Y: To perform electron microscope analysis using spatial omics analysis. Clinical immunology & allergoloy 2024, 82:385-90.

[2] Ikehara S, Sakakita H, Ishikawa K, Akimoto Y, Yamaguchi T, Yamagishi M, Kim J, Ueda M, Ikeda J-i, Nakanishi H, Shimizu N, Hori M, Ikehara Y: Plasma Blood Coagulation Without Involving the Activation of Platelets and Coagulation Factors. Plasma Processes and Polymers 2015, 12:1348-53.

[3] Ikehara Y, Sakakita H, Shimizu N, Ikehara S, Nakanishi H: Formation of Membrane-like Structures in Clotted Blood by Mild Plasma Treatment during Hemostasis. Journal of Photopolymer Science and Technology 2013, 26:555-7.

[4] Ogata H, Akita S, Ikehara S, Azuma K, Yamaguchi T, Maimaiti M, Maezawa Y, Kubota Y, Yokote K, Mitsukawa N, Ikehara Y: Calcification in Werner syndrome associated with lymphatic vessels aging. Aging (Albany NY) 2021, 13:25717-28.

[5] Wakai K, Azuma K, Iwamura C, Maimaiti M, Mikami K, Yoneda K, Sakamoto S, Ikehara S, Yamaguchi T, Hirahara K, Ichikawa T, Nakayama T, Ikehara Y: The new preparation method for paraffin-embedded samples applying scanning electron microscopy revealed characteristic features in asthma-induced mice. Sci Rep 2022, 12:9046.

[6] Okano M, Hirahara K, Kiuchi M, Onoue M, Iwamura C, Kokubo K, Hishiya T, Morimoto Y, Ikehara Y, Murakami A, Ebihara N, Nakayama T: Interleukin-33-activated neuropeptide CGRP-producing memory Th2 cells cooperate with somatosensory neurons to induce conjunctival itch. Immunity 2022, 55:2352-68.e7.

[7] Iwamura C, Hirahara K, Kiuchi M, Ikehara S, Azuma K, Shimada T, Kuriyama S, Ohki S, Yamamoto E, Inaba Y, Shiko Y, Aoki A, Kokubo K, Hirasawa R, Hishiya T, Tsuji K, Nagaoka T, Ishikawa S, Kojima A, Mito H, Hase R, Kasahara Y, Kuriyama N, Tsukamoto T, Nakamura S, Urushibara T, Kaneda S, Sakao S, Tobiume M, Suzuki Y, Tsujiwaki M, Kubo T, Hasegawa T, Nakase H, Nishida O, Takahashi K, Baba K, Iizumi Y, Okazaki T, Kimura MY, Yoshino I, Igari H, Nakajima H, Suzuki T, Hanaoka H, Nakada TA, Ikehara Y, Yokote K, Nakayama T: Elevated Myl9 reflects the Myl9-containing microthrombi in SARS-CoV-2-induced lung exudative vasculitis and predicts COVID-19 severity. Proc Natl Acad Sci U S A 2022, 119:e2203437119.

Drift velocity of charged particles in gases: General relationship between drift velocities in position and velocity spaces

Toshiaki Makabe

Faculty of Science & Technology, Keio University, 3-14-1 Hiyoshi, Yokohama 223-8522, Japan

E-mail: makabe@keio.jp
(December 27, 2024 Makabe/)

Abstract.

We discuss the theoretical expression of the drift velocity of charged particles (i.e., positive and negative ions as well as electrons) from the perspective of the distinct statistical characteristics in position and velocity spaces. A qualitative difference between the drift velocities, $\boldsymbol{V}_{d\mathrm{R}}$ in position space and $\boldsymbol{V}_{d\mathrm{V}}$ in velocity space emerges, as commonly recognized, in the presence of non-conservative collisions that the number of the charged particle is not conserved. This paper confirms that $\boldsymbol{V}_{d\mathrm{R}}$, incorporating a corrected term in position space, is equivalent to the phase-space expression of the charged particle with a small density gradient under a cold gas approximation using the Boltzmann equation. Numerically predicted drift velocities in the literature for charged particles in gases allow us to categorize their relative magnitudes with respect to $\boldsymbol{V}_{d\mathrm{R}} \gtrless \boldsymbol{V}_{d\mathrm{V}}$ in the range of reduced electric field E/N previously studied. We discuss the disparity between $\boldsymbol{V}_{d\mathrm{R}}$ and $\boldsymbol{V}_{d\mathrm{V}}$ based on the energy dependence of the non-conservative collision. It is noteworthy that the present argument is irrespective of the degree of anisotropy in the velocity distribution of the charged particle.

Key words: drift velocity, drift velocity in position and velocity spaces, relationship between the bulk and the flux drift velocities, Boltzmann equation, density gradient expansion of the distribution.

1. Introduction

An important yet limited number of theoretical studies concerning charged-particle transport in gases have analyzed the impact of the production and loss processes in collision with a neutral molecule. We have two types of statistical procedures to study the particle transport. These are described in position and velocity spaces, respectively. The phase space Boltzmann equation enables us to interrelate both quantities consistently. One of the most well-known transport parameters is drift velocity. The flux drift velocity $\boldsymbol{V}_{d\mathrm{V}}$ has been studied in velocity space, while the bulk drift velocity $\boldsymbol{V}_{d\mathrm{R}}$ has been explored in position space as a function of reduced field E/N in gases. Here, E is the electric field and N the gas number density.

In the late 1970s, Tagashira *et al* initially highlighted the discrepancy between $\boldsymbol{V}_{d\mathrm{R}}$ and $\boldsymbol{V}_{d\mathrm{V}}$ as a function of E/N in the presence of electron impact ionization and/or attachment through electron swarm analysis using the Boltzmann equation [1]. In the early 1990s, the physical origin of the correction to the flux drift term $\boldsymbol{V}_{d\mathrm{V}}$, aiming to represent $\boldsymbol{V}_{d\mathrm{R}}$, was elucidated by Robson [2]. In the past few decades, numerical studies at the Institute of Physics, Belgrade [3], James Cook University [4], Hokkaido University [5, 6] and elsewhere predicted the disparity in the magnitudes of $\boldsymbol{V}_{dR}$ and $\boldsymbol{V}_{dV}$ as a function of E/N in gases for negative ions, positive ions, and electrons, respectively. These discrepancies are induced by the presence of non-conservative collisions that the number of the charged particle is not conserved.

Isolated charged particles traveling in gases under an external field exhibit a Gaussian-like distribution in position space and a non-Maxwellian distribution in velocity space under quasiequilibrium conditions. In thermal equilibrium, specifically, Maxwell velocity distribution is established. Charged particle transport under an influence of binary collisions with a neutral molecule in an external field is categorized into classical statistics, the Boltzmann equation which interrelates transport in velocity and position spaces [7]. A bulk plasma region with a relatively high effective field $(E(t)/N)_{eff}$ is known to exist in a low-temperature radiofrequency plasma in electronegative gases [8, 9]. Non-conservative collisions causing $\boldsymbol{V}_{d\mathrm{R}} \neq \boldsymbol{V}_{d\mathrm{V}}$ appear mostly at high E/N. We have few arguments about the influence of the shape of the non-conservative collision cross section on the relationship between $\boldsymbol{V}_{d\mathrm{R}} \gtrless \boldsymbol{V}_{d\mathrm{V}}$ as a function of E/N. It will be important to discuss the general characteristics of the drift velocity of the charged particle at high E/N influenced by the non-conservative collision.

The purpose of this paper is to integrate the relationship between $\boldsymbol{V}_{d\mathrm{R}}$ and $\boldsymbol{V}_{d\mathrm{V}}$ of the charged particles, namely electrons, negative ions, and positive ions in gases based on the phase-space Boltzmann equation. At the same time, we will show that $\boldsymbol{V}_{d\mathrm{R}}$ with the corrected term in position space by Tagashita *et al* [1] corresponds to the phase-space expression by Shimura and Makabe [10], and Maeda *et al* [11].

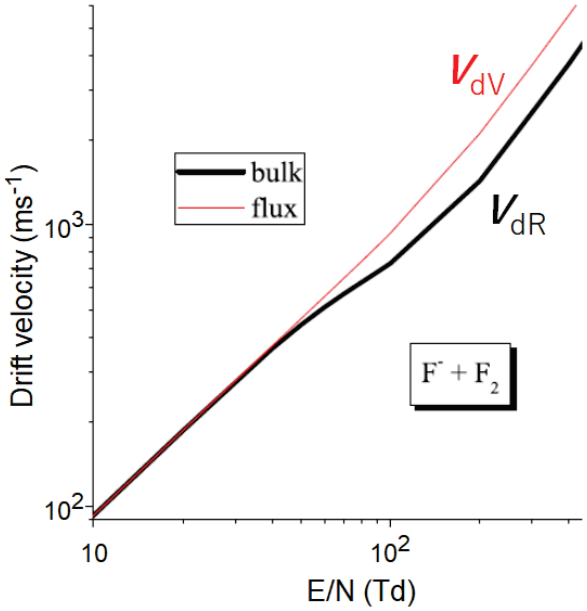

Figure 1. Example of the drift velocity of F^- in F_2 as a function of E/N, obtained from Monte Carlo simulation. The discrepancy between $\boldsymbol{V}_{d\mathrm{R}}$ and $\boldsymbol{V}_{d\mathrm{V}}$ is clearly demonstrated. Reproduced from [12].

2. Development of the theoretical drift velocity

The drift velocities of positive and negative ions, as well as electrons, in gases have been studied numerically for the past 20 years in a system that includes a distinction between $\boldsymbol{V}_{d\mathrm{R}}$ and $\boldsymbol{V}_{d\mathrm{V}}$ under the presence of non-conservative collisions with neutral molecules. Figure 1 illustrates one of the numerical outcomes depicting the drift velocity of negative ions F^- in F_2 obtained by Monte Carlo simulation [12].

Table 1 outlines the conventional definition and assessment methods of the drift velocity of electrons in gases. That is, [a] and [b] in Table 1 provide the drift velocity in position and velocity spaces, namely $\boldsymbol{V}_{d\mathrm{R}}$ and $\boldsymbol{V}_{d\mathrm{V}}$, commonly referred to as bulk and flux drift velocities, respectively [2]. In particular, the theoretical $\boldsymbol{V}_{d\mathrm{R}}$ in [a] is the expression with a correction term in position space [1]. The theoretical connection between $\boldsymbol{V}_{d\mathrm{R}}$ and $\boldsymbol{V}_{d\mathrm{V}}$ in phase space is expressed in radio frequency (rf) fields in [c] in Table 1 [11]. Subsequently, this relationship in [c] is validated in a direct current (dc) field [13, 14].

3. Nonconservative collision term of charged particles

3.1. Conservation and nonconservation of charged particles at collisions

The transport of charged particles in gases is described by the Boltzmann equation [16]

$$\frac{\partial}{\partial t}g(\boldsymbol{v},\boldsymbol{r},t)+\boldsymbol{v}\cdot\frac{\partial}{\partial \boldsymbol{r}}g+\frac{e\boldsymbol{E}(t)}{m}\cdot\frac{\partial}{\partial \boldsymbol{v}}g=J(g,F). \tag{1}$$

Table 1. Definition of the drift velocity of electrons. R_{effi} is the effective ionization rate. $g^0(\boldsymbol{v},t)$ is normalized to unity. Other symbols are described in the text.

Physical space	Definition	Procedure	Ref.
[a]			
in position space	$\boldsymbol{V}_{d\mathrm{R}}(t) = \frac{\mathrm{d}}{\mathrm{d}t}<\boldsymbol{r}(t)> = \frac{\mathrm{d}}{\mathrm{d}t}\int_{\boldsymbol{r},\boldsymbol{v}} \boldsymbol{r} g(\boldsymbol{v},\boldsymbol{r},t)\mathrm{d}\boldsymbol{v}\mathrm{d}\boldsymbol{r}$	experiment	[13, 15]
under $n_e(\boldsymbol{r},t)$	$\boldsymbol{V}_{d\mathrm{R}}(t) = \boldsymbol{V}_{d\mathrm{V}}(t) + \frac{1}{n(t)}\int_{\boldsymbol{r}}(\boldsymbol{r}-\boldsymbol{r}_0)R_{effi}(\boldsymbol{r},t)n(\boldsymbol{r},t)\mathrm{d}\boldsymbol{r}$	theory	[1]
[b]			
in velocity space	$\boldsymbol{V}_{d\mathrm{V}}(t) = <\boldsymbol{v}(t)> = \int_{\boldsymbol{v}} \boldsymbol{v} g^0(\boldsymbol{v},t)\mathrm{d}\boldsymbol{v}$	theory	[7]
under uniform n_e		simulation	
[c]			
in phase space	$\boldsymbol{V}_{d\mathrm{R}}(t) = \boldsymbol{V}_{d\mathrm{V}}(t) + N\int_{\boldsymbol{v}}[Q_i(v)-Q_a(v)]v\boldsymbol{g}^1(\boldsymbol{v},t)\mathrm{d}\boldsymbol{v}$	theory	[10]
under small ∇n_e			[11]

Here, $g(\boldsymbol{v},\boldsymbol{r},t)$ represents the density distribution, i.e., the velocity distribution of charged particles as a function of velocity $\boldsymbol{v}$, position $\boldsymbol{r}$, and time t. $\int g(\boldsymbol{v},\boldsymbol{r},t)\mathrm{d}\boldsymbol{v}$ yields the local number density $n(\boldsymbol{r},t)$. e and m denote the charge and mass of the charged particle. $J(g,F)$ represents the binary collision term of a charged particle with a molecule having a velocity distribution $F(V)$, and $J(g,F)$ depends linearly on $g(\boldsymbol{v})$. In the present paper, we consider the external uniform field $\boldsymbol{E}$. The collision term $J(g,F)$ comprises a particle-conserving component J_{con} and a non-conserving component J_{noncon}, characterized by

$$\int_{\boldsymbol{v}} J_{con}(g,F)\ \mathrm{d}\boldsymbol{v} \quad = 0, \tag{2}$$

$$\int_{\boldsymbol{v}} J_{noncon}(g,F)\ \mathrm{d}\boldsymbol{v} \gtrless 0. \tag{3}$$

$J_{noncon}(g,F)$ is determined by collisional birth and death processes represented through the collision cross section, $Q_{birth}(v)$ and $Q_{death}(v)$. Most of the collision cross sections exhibit a threshold energy and escalate as energy increases within an interesting range for the charged particle. When charged particles are ejected into a gas from the point $\boldsymbol{s}_0$ at $t = 0$ in an external field E, a weakly skewed Gaussian-like distribution $n(\boldsymbol{r},t)$ forms at $t > t_0$ (see figure 2). Here t_0 corresponds to a relaxation time. The forefront of $n(\boldsymbol{r},t)$ exposed to the diffusion heating has a local mean energy $\langle\epsilon(\boldsymbol{r},t)\rangle$ greater than the value at the peak position $\boldsymbol{r}_0$ of $n(\boldsymbol{r},t)$ [17, 18]).

Next we summarize the production and loss processes of the charged particles, namely electrons, negative ions, and positive ions in gases [19].

3.2. Electron birth and death processes

In the binary collision between an electron e and a neutral molecule AB, ionization and electron attachment form $J_{noncon}(g,F)$:

$$\mathrm{e} + \mathrm{AB} \rightarrow \mathrm{AB}^+ + \mathrm{e} + \mathrm{e} \quad \text{(ionization)}, \tag{4}$$

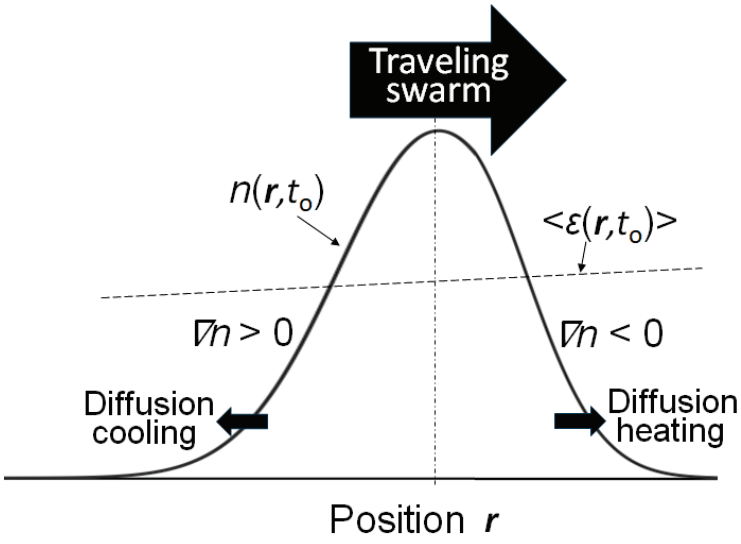

Figure 2. An isolated traveling swarm of charged particles with number density $n(\boldsymbol{r}, t_0)$ at time t_0 in gases in an external field. $< \epsilon(\boldsymbol{r}, t_0 >$ is the local mean energy.

$$\mathrm{e} + \mathrm{AB} \rightarrow \mathrm{A}^- + \mathrm{B} \quad \text{(dissociative electron attachment)}, \tag{5}$$

$$\mathrm{e} + \mathrm{AB} \rightarrow \mathrm{AB}^- \quad \text{(nondissociative electron attachment)}. \tag{6}$$

3.3. Negative ion death processes

Negative ion A^- is lost by

$$\mathrm{A}^- + \mathrm{AB} \rightarrow \mathrm{A} + \mathrm{AB} + \mathrm{e} \quad \text{(collisional detachment)}, \tag{7}$$

$$\mathrm{A}^- + \mathrm{AB} \rightarrow \mathrm{A} + \mathrm{AB}^- \quad \text{(asymmetric charge transfer)}. \tag{8}$$

3.4. Positive ion death process

Positive ion A^+ is lost by

$$\mathrm{A}^+ + \mathrm{AB} \rightarrow \mathrm{A} + \mathrm{AB}^+ \quad \text{(asymmetric charge transfer)}. \tag{9}$$

3.5. Ion recombination and photo detachment

Moreover, in an activated low-temperature plasma, positive and negative ion recombination can occur. For example, the reaction:

$$\mathrm{A}^- + \mathrm{AB}^+ \rightarrow \mathrm{A} + \mathrm{AB} \quad \text{(ion pair recombination)}, \tag{10}$$

takes place in a high density bulk plasma in electronegative plasma. Of course, the gas-phase recombination process is contingent on the number densities of both positive and negative ions [19]. Additionally, negative ion loss can be induced by a photon $\mathrm{h}\nu$ with frequency ν.

$$\mathrm{A}^- + \mathrm{h}\nu \rightarrow \mathrm{A} + \mathrm{e} \quad \text{(photo detachment)}. \tag{11}$$

4. Theoretical relationship between $\boldsymbol{V}_{dR}$ and $\boldsymbol{V}_{dV}$

We begin the discussion regarding the drift velocity of charged-particles in position space following the methodology of Tagashira *et al* [1] and Sugawara *et al* [6], which elucidated the relationship between $\boldsymbol{V}_{d\mathrm{R}}$ and $\boldsymbol{V}_{d\mathrm{V}}$ for electrons in gases. However, our ultimate objective diverges from the approach taken by Tagashira *et al* [1]. We derive the general formula connecting $\boldsymbol{V}_{d\mathrm{R}}$ and $\boldsymbol{V}_{d\mathrm{V}}$ for charged particles, applicable to negative and positive ions, and electrons.

The drift velocity in position space $\boldsymbol{V}_{d\mathrm{R}}$ is defined as the center of mass velocity of the swarm consisting of charged particles (j=1, ...,$\mathrm{N_{cp}}(t)$) positioned at $\boldsymbol{r}_j$ at time t considering the birth and death collision interactions with neutral molecules.

$$\begin{aligned}
\boldsymbol{V}_{d\mathrm{R}}(t) &\equiv \frac{\mathrm{d}}{\mathrm{d}t}\Big(\frac{1}{N_{\mathrm{cp}}(t)}\sum_{j=1}^{Ncp}\boldsymbol{r}_j(t)\Big), \qquad (12)\\
&= \frac{\mathrm{d}}{\mathrm{d}t}\Big(\frac{1}{n(t)}\int_{\boldsymbol{r},\boldsymbol{v}}\boldsymbol{r}g(\boldsymbol{v},\boldsymbol{r},t)\mathrm{d}\boldsymbol{v}\mathrm{d}\boldsymbol{r}\Big),\\
&= \frac{1}{n(t)}\frac{\partial}{\partial t}\int_{\boldsymbol{r},\boldsymbol{v}}\boldsymbol{r}g(\boldsymbol{v},\boldsymbol{r},t)\mathrm{d}\boldsymbol{v}\mathrm{d}\boldsymbol{r}\\
&\quad -\Big(\frac{1}{n(t)}\int_{\boldsymbol{r},\boldsymbol{v}}\boldsymbol{r}g(\boldsymbol{v},\boldsymbol{r},t)\mathrm{d}\boldsymbol{v}\mathrm{d}\boldsymbol{r}\Big)\times\frac{1}{n(t)}\frac{\partial}{\partial t}\int_{\boldsymbol{r},\boldsymbol{v}}g(\boldsymbol{v},\boldsymbol{r},t)\mathrm{d}\boldsymbol{v}\mathrm{d}\boldsymbol{r},\\
&= \frac{1}{n(t)}\int_{\boldsymbol{r},\boldsymbol{v}}(\boldsymbol{r}-\boldsymbol{r}_0)\frac{\partial}{\partial t}g(\boldsymbol{v},\boldsymbol{r},t)\mathrm{d}\boldsymbol{v}\mathrm{d}\boldsymbol{r}, \qquad (13)
\end{aligned}$$

where $\boldsymbol{r}_0 = \int \boldsymbol{r}g(\boldsymbol{v},\boldsymbol{r},t)\mathrm{d}\boldsymbol{r}\mathrm{d}\boldsymbol{v}/n(t)$ is the center of mass position of charged particles with density $n(\boldsymbol{r},t)$ at t. In equation (13), $\frac{\partial}{\partial t}g(\boldsymbol{v},\boldsymbol{r},t)$ is represented by the Boltzmann equation (1). Then, taking into account equations (2) and (3):

$$\begin{aligned}
\boldsymbol{V}_{d\mathrm{R}}(t) &= -\frac{1}{n(t)}\int_{\boldsymbol{r},\boldsymbol{v}}(\boldsymbol{r}-\boldsymbol{r}_0)\Big(\boldsymbol{v}\cdot\frac{\partial}{\partial\boldsymbol{r}}g+\frac{e\boldsymbol{E}(t)}{m}\cdot\frac{\partial}{\partial\boldsymbol{v}}g-J(g,F)\Big)\mathrm{d}\boldsymbol{v}\mathrm{d}\boldsymbol{r},\\
&= \frac{1}{n(t)}\int_{\boldsymbol{r},\boldsymbol{v}}\Big(\boldsymbol{v}g(\boldsymbol{v},\boldsymbol{r},t)\mathrm{d}\boldsymbol{r}\Big)\mathrm{d}\boldsymbol{v}+\frac{1}{n(t)}\int_{\boldsymbol{r},\boldsymbol{v}}(\boldsymbol{r}-\boldsymbol{r}_0)J_{noncons}(g,F)\mathrm{d}\boldsymbol{v}\mathrm{d}\boldsymbol{r}. \qquad (14)
\end{aligned}$$

The nonconservative collision processes, namely birth and loss processes, are commonly detailed in Sec. 3.2, 3.3, and 3.4. Here, we express $g(\boldsymbol{v},\boldsymbol{r},t)$ in the form of a density gradient expansion of $n(\boldsymbol{r},t)$ [20, 21]

$$g(\boldsymbol{v},\boldsymbol{r},t) = g^0(\boldsymbol{v},t)n(\boldsymbol{r},t)+\boldsymbol{g}^1\cdot(-\nabla_r)n(\boldsymbol{r},t)+O((-\nabla_r)^2 n), \qquad (15)$$

where,

$$\int \boldsymbol{g}^{\mathrm{k}}(\boldsymbol{v},t)\mathrm{d}\boldsymbol{v} = 1 \quad (\mathrm{k}=0), \quad \text{or} \quad 0 \quad (\mathrm{k}\geq 1). \qquad (16)$$

In particular, the second term on the right-hand side of equation (15) shows the influence of the diffusion heating and cooling on the local energy under Gaussian like $n(\boldsymbol{r},t)$ as

illustrated in figure 2. Then, the first term on the right-hand side of equation (14) specifies the drift velocity in velocity space, called the flux drift velocity,

$$\boldsymbol{V}_{d\mathrm{V}}(t) \equiv \frac{1}{n(t)} \int_{\boldsymbol{r},\boldsymbol{v}} \Big(\boldsymbol{v} g(\boldsymbol{v},\boldsymbol{r},t) \mathrm{d}\boldsymbol{r} \Big) \mathrm{d}\boldsymbol{v} = \int_{\boldsymbol{v}} \boldsymbol{v} g^0(\boldsymbol{v},t) \mathrm{d}\boldsymbol{v}. \tag{17}$$

When the charged particle having a small density gradient is transported in a cold gas ($T_g = 0$) with the velocity distribution, approximated by $F(V) = N\delta(V)$ with number density N, the second term in equation (14) can be expressed as

$$\begin{aligned}
&\frac{1}{n(t)} \int_{\boldsymbol{r},\boldsymbol{v}} (\boldsymbol{r} - \boldsymbol{r}_0) J_{noncons}(g,F) \mathrm{d}\boldsymbol{v}\mathrm{d}\boldsymbol{r} \\
&\quad = \frac{N}{n(t)} \int_{\boldsymbol{r},\boldsymbol{v}} (\boldsymbol{r} - \boldsymbol{r}_0) \Big(Q_{birth}(v) - Q_{death}(v) \Big) v \\
&\qquad\qquad \times \Big(g^0(\boldsymbol{v},t) n(\boldsymbol{r},t) - \boldsymbol{g}^1 \cdot \frac{\mathrm{d}}{\mathrm{d}\boldsymbol{r}} n(\boldsymbol{r},t) \Big) \mathrm{d}\boldsymbol{v}\mathrm{d}\boldsymbol{r}, \\
&\quad = -\frac{N}{n(t)} \int_{\boldsymbol{r},\boldsymbol{v}} (\boldsymbol{r} - \boldsymbol{r}_0) \Big(Q_{birth}(v) - Q_{death}(v) \Big) v \boldsymbol{g}^1(\boldsymbol{v},t) \cdot \frac{\mathrm{d}}{\mathrm{d}\boldsymbol{r}} n(\boldsymbol{r},t) \mathrm{d}\boldsymbol{r}\mathrm{d}\boldsymbol{v}, \\
&\quad = -\frac{N}{n(t)} \int_{\boldsymbol{v}} \Big(Q_{birth}(v) - Q_{death}(v) \Big) v \boldsymbol{g}^1(\boldsymbol{v},t) \cdot \Big\{ \\
&\qquad\qquad \int_{\boldsymbol{r}} \frac{\mathrm{d}}{\mathrm{d}\boldsymbol{r}} \Big((\boldsymbol{r} - \boldsymbol{r}_0) n(\boldsymbol{r},t) \Big) \mathrm{d}\boldsymbol{r} - \int_{\boldsymbol{r}} \frac{\mathrm{d}}{\mathrm{d}\boldsymbol{r}} (\boldsymbol{r} - \boldsymbol{r}_0) n(r,t) \mathrm{d}\boldsymbol{r} \Big\} \mathrm{d}\boldsymbol{v}, \\
&\quad = N \int_{\boldsymbol{v}} \Big(Q_{birth}(v) - Q_{death}(v) \Big) v \boldsymbol{g}^1(\boldsymbol{v},t) \mathrm{d}\boldsymbol{v}.
\end{aligned} \tag{18}$$

As a result, we describe the relationship between $\boldsymbol{V}_{d\mathrm{R}}(t)$ and $\boldsymbol{V}_{d\mathrm{V}}(t)$ as

$$\boldsymbol{V}_{d\mathrm{R}}(t) = \boldsymbol{V}_{d\mathrm{V}}(t) + N \int_{\boldsymbol{v}} \Big(Q_{birth}(v) - Q_{death}(v) \Big) v \boldsymbol{g}^1(\boldsymbol{v},t) \mathrm{d}\boldsymbol{v}. \tag{19}$$

Equation (19) is equal to the expression of the drift velocity of electrons in the presence of a small density gradient [10, 11]. It is noted that the drift velocity in position space $\boldsymbol{V}_{d\mathrm{R}}(t)$ is equal to the value in velocity space $\boldsymbol{V}_{d\mathrm{V}}(t)$ in the case of only number-conserving collisions of the charged particle.

5. Validation

First, we discuss an isolated charged-particle swarm characterized by the number density $n(\boldsymbol{r},t)$ and the velocity distribution $g(\boldsymbol{v},\boldsymbol{r},t)$ under an external field E and neutral number desnity N as depicted in figure 2. The local mean energy $\langle \epsilon(\boldsymbol{r},t) \rangle$ as a function of $\boldsymbol{r}$ and t under cold gas approximation is expressed from equation (15) as

$$\langle \epsilon(\boldsymbol{r},t) \rangle = \int_{\boldsymbol{v}} \frac{1}{2} m v^2 g^0(\boldsymbol{v},t) n(\boldsymbol{r},t) \mathrm{d}\boldsymbol{v} - \int_{\boldsymbol{v}} \frac{1}{2} m v^2 \boldsymbol{g}^1(\boldsymbol{v},t) \mathrm{d}\boldsymbol{v} \cdot \frac{\mathrm{d}}{\mathrm{d}\boldsymbol{r}} n(\boldsymbol{r},t). \tag{20}$$

$\langle \epsilon(\boldsymbol{r},t) \rangle$ at the forefront of the swarm with $\mathrm{d}n(\boldsymbol{r},t)/\mathrm{d}\boldsymbol{r} < 0$ experiences heating through the diffusion flow in contrast to the value at the peak, $\nabla_{\boldsymbol{r}} n(\boldsymbol{r},t) = 0$. That is, the relation

$$-\Big(\int_{\boldsymbol{v}} \frac{1}{2} m v^2 \boldsymbol{g}^1(\boldsymbol{v},t) \mathrm{d}\boldsymbol{v} \Big) \cdot \frac{\mathrm{d}n(\boldsymbol{r},t)}{\mathrm{d}\boldsymbol{r}} > 0, \tag{21}$$

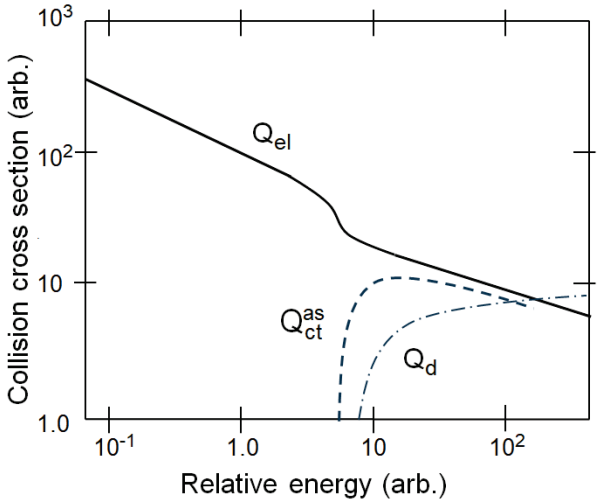

Figure 3. A set of model cross sections for negative ions in a neutral molecule.

is satisfied. Expression (21) leads the relation

$$\int_{\boldsymbol{v}} (Q_{birth}(v) - Q_{death}(v))\ v\boldsymbol{g}^1(\boldsymbol{v},t)\mathrm{d}\boldsymbol{v} > 0, \tag{22}$$

in equation (19), as long as $(Q_{birth}(v) - Q_{death}(v))$ increases in proportional to $v^{\mathrm{h}}(\mathrm{h} \geq 1)$ at the range of E/N previously investigated (see Table 2). As a result, the following general relationship will be established in equation(19):

$$\boldsymbol{V}_{d\mathrm{R}} > \boldsymbol{V}_{d\mathrm{V}},\ \text{under } \mathrm{Q_{birth}} > \mathrm{Q_{death}} \text{ at an interesting range of E/N}, \tag{23}$$

$$\boldsymbol{V}_{d\mathrm{R}} = \boldsymbol{V}_{d\mathrm{V}},\ \text{under } \mathrm{Q_{birth}} = \mathrm{Q_{death}} \text{ at an interesting range of E/N}, \tag{24}$$

$$\boldsymbol{V}_{d\mathrm{R}} < \boldsymbol{V}_{d\mathrm{V}},\ \text{under } \mathrm{Q_{birth}} < \mathrm{Q_{death}} \text{ at an interesting range of E/N}. \tag{25}$$

A limited number of numerical results are available to validate the above relation. We explore systems where either $Q_{birth}(v)$ or $Q_{death}(v)$ exists along with elastic collisions, as detailed in the literature (see Table 2). A set of model cross sections for negative ions in a gas is shown in figure 3. In this context, Q_{el}, Q_{ct}^{as}, and Q_d represent the cross sections for elastic collision, asymmetric charge transfer, and electron detachment, respectively. In particular, electron detachment, acting as the death process for negative ions, has a threshold energy, which leads to the difference between $\boldsymbol{V}_{d\mathrm{R}}$ and $\boldsymbol{V}_{d\mathrm{V}}$ at high E/N as predicted by the numerical simulation.

When both $Q_{birth}(v)$ and $Q_{death}(v)$ exhibit distinct threshold energies, the situation becomes rather complicated. In fact, in an electron swarm having ionization and electron attachment cross sections, $Q_i(v)$ and $Q_a(v)$ with threshold energies, ϵ_i and ϵ_a, the accumulated theoretical data indicate the relationship where $\boldsymbol{V}_{d\mathrm{V}} > \boldsymbol{V}_{d\mathrm{R}}$ appears at the lower range of E/N [23], whereas $\boldsymbol{V}_{d\mathrm{V}} < \boldsymbol{V}_{d\mathrm{R}}$ is found at higher E/N. The effect of the three-body electron attachment as a function of pressure [24] on $\boldsymbol{V}_{d\mathrm{R}}$ and $\boldsymbol{V}_{d\mathrm{V}}$ is investigated in O_2 by using a multi term solution of the Boltzmann equation [25]. As expected, the drift velocity subject to the three-body electron attachment cross section

Table 2. General characteristics of the drift velocity of charged particles.

System	Examples	Cross section	Relation	Ref.
e/M	e/Ar	$Q_{\rm i}$	$V_{d\rm R} > V_{d\rm V}$	[22]
	e/CH_4	$Q_{\rm i}$	$V_{d\rm R} > V_{d\rm V}$	[10]
	e/CO	$Q_{\rm a},\ Q_{\rm i}$	$V_{d\rm R} > V_{d\rm V}$	[14]
	e/H_2O	$Q_{\rm a},\ Q_{\rm i}$	$V_{d\rm R} > V_{d\rm V}$	[4]
	e/HBr	$Q_{\rm a},\ Q_{\rm i}$	$V_{d\rm R} < V_{d\rm V}$ (low E/N)	[23]
	e/HBr	$Q_{\rm a},\ Q_{\rm i}$	$V_{d\rm R} > V_{d\rm V}$ (high E/N)	[23]
	e/O_2	$Q_{\rm a},\ Q_{\rm a3},\ Q_{\rm i}$	$V_{d\rm R} < V_{d\rm V}$ (low E/N)	[25]
	e/CF_4	$Q_{\rm a},\ Q_{\rm i}$	$V_{d\rm R} > V_{d\rm V}$	[26]
	e/C_4H_8O	$Q_{\rm a},\ Q_{\rm i}$	$V_{d\rm R} > V_{d\rm V}$	[27]
A^-/M	O^-/O_2	$Q_{\rm d},\ Q_{\rm ct}^{\rm as}$	$V_{d\rm R} < V_{d\rm V}$	[5]
	F^-/Ar	$Q_{\rm d}$	$V_{d\rm R} < V_{d\rm V}$	[28]
	F^-/F_2	$Q_{\rm d}$	$V_{d\rm R} < V_{d\rm V}$	[12]
	F^-/CF_4	$Q_{\rm d}$	$V_{d\rm R} < V_{d\rm V}$	[3]
	CF_3^-/CF_4	$Q_{\rm d}$	$V_{d\rm R} < V_{d\rm V}$	[3]
A^+/M	Ar^+/Ar	$Q_{\rm ct}^{\rm s}$	$V_{d\rm R} = V_{d\rm V}$	[29]
	Ar^+/BF_3	$Q_{\rm ct}^{\rm as}$	$V_{d\rm R} < V_{d\rm V}$	[29]
	CF_3^+/CF_4	$Q_{\rm d}$	$V_{d\rm R} < V_{d\rm V}$	[30, 31]

$Q_{a3}(v)$ in O_2 at very low E/N shows the relation, $\boldsymbol{V}_{d\rm R} \ll \boldsymbol{V}_{d\rm V}$. In fact, the difference between $\boldsymbol{V}_{dV}$ and $\boldsymbol{V}_{dR}$ increases with increasing pressure [24].

In particular, the reaction becomes very complex, as discussed in [30, 31], when a polyatomic reactive ion has a collision with a polyatomic molecule. The distinction between $\boldsymbol{V}_{d\rm V}$ and $\boldsymbol{V}_{d\rm R}$ in the electron swarm, as shown in Table 2, can be elucidated in equation (19) by recognizing that electrons are lost through dissociative electron attachment at low energies and generated through ionization at high energies. It should be noted that the degree of anisotropy in $g(\boldsymbol{v}, t)$ of the charged particle in velocity space [32, 33] has no influence on the above discussion regarding $\boldsymbol{V}_{d\rm V}$ and $\boldsymbol{V}_{d\rm R}$.

6. Summary

We have deduced that $\boldsymbol{V}_{d\rm R}$, incorporating the correction term in position space for electrons by Tagashira *et al* [1] in the presence of the non-conservative collision, is consistent with the phase-space formulation by Shimura and Makabe [10], and Maeda *et al* [11] under the conditions of

(i) a small density gradient of electrons of order $O((-\nabla_r)^{\rm k} n_e : {\rm k} \geq 2)$, and

(ii) cold gas approximation ($T_g = 0$).

In addition, we note that the general relationship (19) between $\boldsymbol{V}_{d\rm R}$ and $\boldsymbol{V}_{d\rm V}$ hold true not only for electrons but also for negative ions and positive ions in gases. A qualitative

difference between $\boldsymbol{V}_{d\mathrm{R}}$ and $\boldsymbol{V}_{d\mathrm{V}}$ becomes evident in the presence of nonconservative collisions of charged particles. However, both quantities are equal in the conservative collisions. Note that the cold gas approximation remains valid to investigate the transport of the charged particle with a relatively high threshold energy at collision. The relationship between $\boldsymbol{V}_{d\mathrm{R}}$ and $\boldsymbol{V}_{d\mathrm{V}}$ is independent of the anisotropy of the velocity distribution of the charged particle as shown in the derivation [32, 33].

The present argument is valid in the hydrodynamic regime for rf-$E(t)/N$ as well as dc-E/N. The distribution $\boldsymbol{g}^1(\boldsymbol{v},t)$ as a function of E/N in equation (19) necessitates awaiting a study utilizing the Boltzmann equation of the charged-particle [34, 35]. The ongoing compilation of data regarding $\boldsymbol{V}_{d\mathrm{R}}$ and $\boldsymbol{V}_{d\mathrm{V}}$ persists for charged particles in variety of neutral gases. Such data are indispensable for numerical simulations of transient gas discharges and non-equilibrium plasmas.

Finally, we reach the following physical understanding of the charged particle transport theory on the basis of the density gradient expansion procedure of the Boltzmann equation. The second term $\boldsymbol{g}^1(\boldsymbol{v},t)$ in the density gradient expansion of $g(\boldsymbol{v},\boldsymbol{r},t)$ in equation (15) has two important meanings;

(i) Diffusion tensor with two different components, perpendicular and transverse coefficients, is defined as a function of $\boldsymbol{g}^1(\boldsymbol{v},t)$ as elucidated in the late 1960s [21].

(ii) Each of drift velocities, $\boldsymbol{V}_{d\mathrm{R}}$ and $\boldsymbol{V}_{d\mathrm{V}}$, defined in position and velocity spaces is connected through $\boldsymbol{g}^1(\boldsymbol{v},t)$ as analyzed in the present study.

Acknowledgments

The motivation for the present study was brought about through a discussion with H. Sugawara at Hokkaido University and Z. Lj. Petrovic at the Serbian Academy of Sciences and Arts.

7. References

[1] Tagashira H, Sakai Y and Sakamoto S 1977 *J. Phys. D: Appl. Phys.* **10** 1051
[2] Robson R E 1991 *Aust. J. Phys.* **44** 685
[3] Petrovic Z Lj, Raspopovic Z M, Stojanovic V D, Jovanovic J. V, Malovic G, Makabe T, and de Urquijo J 2007 *Appl. Surf. Sci.* **253** 6619
[4] Ness K F, Robson R E, Brunger M J, and White R D 2012 *J. Chem. Phys.* **136** 024318
[5] Okada I, Sakai Y, Tagashira H, and Sakamoto S 1978 *J. Phys. D* **11** 1107
[6] Sugawara H, Tagashira H and Sakai Y 1997 *J. Phys. D* **30** 368
[7] Kumar K, Skullerud H R, and Robson R E 1980 *Aust. J. Phys.* **33** 343
[8] Makabe T 2019 *Jpn. J. Appl. Phys.* **58** 110101
[9] Makabe T 2023 *J. Phys. D.* **56** 045203
[10] Shimura N and Makabe T 1992 *J. Phys. D* **25** 751
[11] Maeda K, Makabe T, Nakano N, Bzenic S, and Petrovic Z Lj 1997 *Phys. Rev. E* **55** 5901
[12] Stojanovic V, Raspopovic Z, Jovanovic J, Nikitovic Z and Petrovic Z Lj 13 2013 *EPL* **101** 45003
[13] Vass M, Korolov I, Loffhagen D, Pinhao, and Donko Z 2017 *Plasma Sources Sci. Technol.* **26** 065007

[14] Dujko S, Bosnjakovic D, Vass M, Hartmann P, Korolov I, Pinhao N R, Loffhagen D and Donko Z 2023 *Plasma Sources Sci. Technol.* **32** 025014
[15] Huxley L G H and Crompton R W 1974 *The Diffusion and Drift of Electrons in Gases* (New York, John Wiley & Sons)
[16] Sturrock P A 1994 *Plasma Physics, An introduction to the theory of astrophysical, geophysical, and laboratory plasmas* (New York, Cambridge University Press)
[17] Suvakov M, Petrovic Z Lj, Marler J P, Buckman S J, Robson R E, andMalovic G 2008 *New J. Phys.* **10** 053034
[18] Raspopovic Z M 2023 *Phys. Rev. E* **108** L053202
[19] Makabe T and Petrovic Z Lj 2016 *Plasma Electronics: Applications in Microelectronic Device Fabrication* (2nd edn) (Boca Raton, CRC Press)
[20] Wannier G H 1953 *Bell Syst. Tech. J.* **32** 170
[21] Skullerud H R 1969 *J. Phys. B* **2** 696
[22] Casey M J E, Stokes P W, Cocks D G, Bosnjakovic D, Simonovic I, Brunger M J, Dujko S, Petrovic Z Lj, Robson R E and White R D 2021 *Plasma Sources Sci. Technol.* **30** 035017
[23] Sasic O, Dujko S, Makabe T and Petrovic Z Lj 2012 *Chem. Phys.* **398** 154
[24] Taniguchi T, Tagashira H, Okada I and Sakai Y 1978 *J. Phys. D* **11** 2281
[25] Dujko S, Ebert U, White R D and Petrovic Z Lj 2011 *Jpn. J. Appl. Phys.* **50** 08JC01.
[26] Rabie M and Franck C M 2016 *Comput. Phys. Comm.* **203** 268.
[27] Garland N A, Brunger M J, Garcia G, de Urquijo J and White R D 2013 *Phys. Rev. A* **88** 062712
[28] Nikitovic Z, Raspopovic Z, Stojanovic V, and Jovanovic J 2014 *EPL* **108** 35004
[29] Nikitovic Z D and Raspopovic Z M 2021 *Eur. Phys. J. D* **75** 118
[30] Jovanovic J V, Stojanovic V, Rspopovic Z, de Urquijo J, and Pterovic Z Lj 2019 *Plasma Sources Sci. Technol.* **28** 045006
[31] Georgieva V, Bogaerts A and Gijbels R 2003 *J. Appl. Phys.* **93** 2369
[32] Makabe T, Misawa K and Mori T 1981 *J. Phys. D* **14** 199
[33] Diomede P and Longo S 2008 *IEEE Trans. Plasma Sci.* **36** 1600
[34] Makabe T and Mori T 1984 *J. Phys. D* **17** 699
[35] Shimada T, Nakamura Y, Petrovic Z Lj and Makabe T 2003 *J. Phys. D* **36** 1936

HYBRID FLUID/MC SIMULATIONS OF RADIO-FREQUENCY ATMOSPHERIC PRESSURE PLASMA JETS

Mate Vass[1,2], Peter Hartmann[2], Zoltan Donko[2], Ihor Korolov[1], Julian Schulze[1], Thomas Mussenbrock[1]

[1]*Chair of Applied Elecltrodynamics and Plasma Technology, Ruhr-University Bochum, 44780 Bochum, Germany*

[2]*Institute for Solid State Physics and Optics, HUN-REN Wigner Research Centre for Physics, 1121 Budapest, Hungary*

E-mail: vass@aept.rub.de

A hybrid fluid-MC (fluid-kinetic) simulation method is applied to describe the COST reference microplasma jet operated in a He/O_2 mixture (99.5/0.5) driven by a tailored voltage waveform consisting of four consecutive harmonics with a base frequency of f_b=13.56 MHz. The simulation method, which makes use of the disparate timescales in atmospheric pressure plasmas, is capable of describing electrons fully kinetically while offering a significant speedup compared to, e.g., PIC/MCC simulations. It is shown that the efficiency of generating certain neutral radicals in the plasma depends on the phase of the even harmonics, which is a direct consequence of the control of the Electron Energy Probability Function (EEPF), offered by voltage waveform tailoring. The simulation results are also verified by experimental data (using Two Photon Absorption Laser Induced Fluorescence Spectroscopy).

1. Introduction

Atmospheric pressure radio-frequency (RF)-driven microplasma jets have a wide range of industrial applications, most notably in plasma medicine, owing to their ability to generate reactive oxygen and nitrogen species (RONS) [1,2]. The efficient generation of such radicals, which is of high importance in optimizing these systems, can only be done if a firm scientific understanding of the underlying physical and chemical processes is available. It has been shown that using multi-frequency excitation waveforms (Voltage Waveform Tailoring) enables the control of the Electron Energy Probability Function, providing a way of controlling the plasma chemistry [3]. In this work we use a spatially 1D fluid-MC (fluid-kinetic) hybrid simulation method to demonstrate how Voltage Waveform Tailoring affects the EEPF in the COST reference microplasma jet [4] operated in a He/O_2 mixture. Furthermore, we show how a judicious adjustment of the voltage waveform can enable control over which radical species is most efficiently generated.

2. Computational method

The computational method used in this work is a fluid-kinetic hybrid simulation that leverages the disparate timescales of the underlying physical processes in atmospheric pressure plasmas. This approach provides a fully kinetic description of the electrons while offering a significant speedup compared to other kinetic simulation methods, e.g., PIC/MCC [5]. The method is based on a fluid module, that solves the continuity equation assuming a drift-diffusion approximation for both charged particles (electrons and ions) as well as neutrals, and Poisson's equation for the electrostatic potential. Owing to the timescale difference between reactions generating charged particles and neutrals, a time slicing approach is utilized. The kinetic description of the electrons comes from a separate Monte Carlo module, where the spatio-temporal rates of the electron impact processes are calculated based on the available cross sections and the spatio-temporal distribution of the electric field, which is taken from the fluid module. The resulting electron impact rates are then fed back to the fluid module where they act as source/loss terms for the respective continuity equations. The two modules are iterated - typically every 100 RF cycles simulated by the fluid module - until convergence is reached, which usually requires a few thousand RF cycles.

The He/O_2 discharge model consists of 7 charged species (electrons, He^+, O_2^+, O^+, O^-, O_2^- and O_3^- ions) and 8 neutral species (O, He*, O(^{1}D), O_2(v=1-4), O_2($a^1\Delta$), O_2($b^1\Sigma$), O_3, O_3(v)), where He* is an aggregate species of He(2^1S) and He(2^3S). The electron impact cross sections and the chemical reaction set can be found in [5]. The fluid module assumes a Local Field Approximation where the mobility and diffusion coefficients are precalculated using a Monte Carlo simulation. The surface model of the electrodes includes electron reflection and ion induced secondary electron emission [5].

In the simulations a constant pressure of 10^5 Pa and a constant background gas temperature of T_g = 350 K was assumed. The gas mixture was set to 99.5/0.5 He/O_2. The gap length of the jet is L=1 mm, with a total volume of V=30 mm^3.

3. Results

The excitation waveform used in this work is synthesized from four consecutive harmonics with a base frequency of f_b=13.56 MHz, including a free parameter, the phase φ:

$$\phi(t) = \sum_{k=1}^{4} \phi_k \cos(2\pi k f_b t + \varphi_k), \quad (1)$$

where the amplitudes ϕ_k are (160, 120, 80, 40) V and the phases φ_k are (0 φ+π,0, φ+π). The resulting voltage waveform for various phase values over two RF cycles is shown in Fig. 1.(a). As the phase varies between 0 and 2π, the waveform transitions continuously from a ``valleys'' to a ``peaks'' shape.

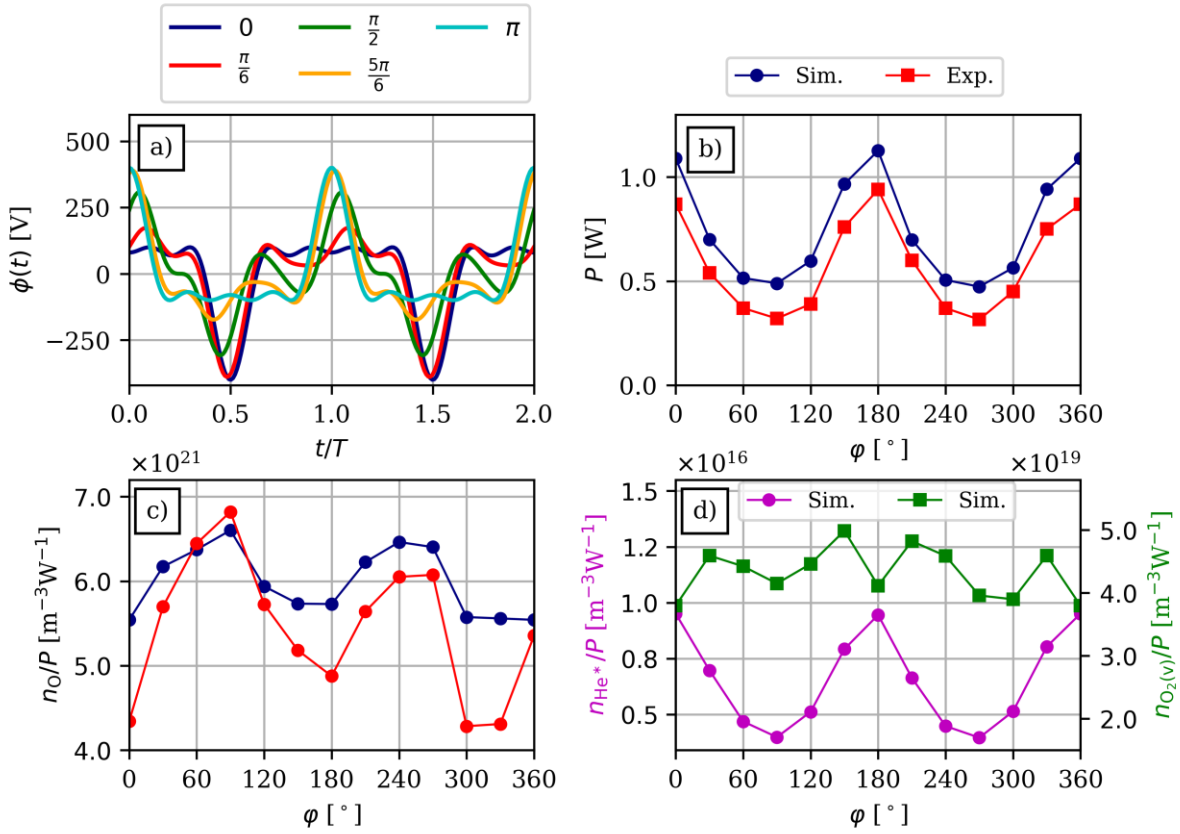

Fig. 1. Excitation waveform, ϕ(t), for various phase values, φ, (a), measured and computed total power, P as a function of the phase (b), measured and computed energy efficiency of generation of atomic oxygen (c) of helium metastables, He* and of vibrationally excited oxygen, O_2(v=1-4) as a function of the phase (d).

Since the voltage amplitudes were kept constant, the total power deposited into the plasma exhibits a phase dependence, as shown in panel (b): both simulation (calculated as mean power times the plasma volume) and experiment (based on [6]) show a good agreement, with the minor discrepancy arising from the simulation being spatially one dimensional. In the following three different neutral radicals are investigated: helium metastables, He*, atomic oxygen, O, and vibrationally excited oxygen, O_2(v=1-4). Each of these species is primarily generated by electron impact processes, but their threshold energies are significantly different: 20 eV for Helium metastables, 4.2 eV for atomic oxygen and 0.19 eV for vibrationally excited oxygen [7].

Since the power has a phase dependence, the energy efficiency, defined as the mean density divided by the power, will also exhibit a phase dependence. Panel (c) presents both simulation results and experimental data for the energy efficiency of atomic oxygen generation (the latter derived from TALIF measurements [6]). As shown in the figure, the maximum energy efficiency for atomic oxygen generation occurs at 90 degrees.

In contrast to this, the energy efficiency of generation of helium metastables (panel (d)) reaches its minimum at 90 degrees and achieves its maximum at 0 or 180 degrees, corresponding to the commonly applied ``valleys'' and ``peaks'' waveforms, respectively. For vibrationally excited oxygen, there is little variability in energy efficiency over the interval studied here.

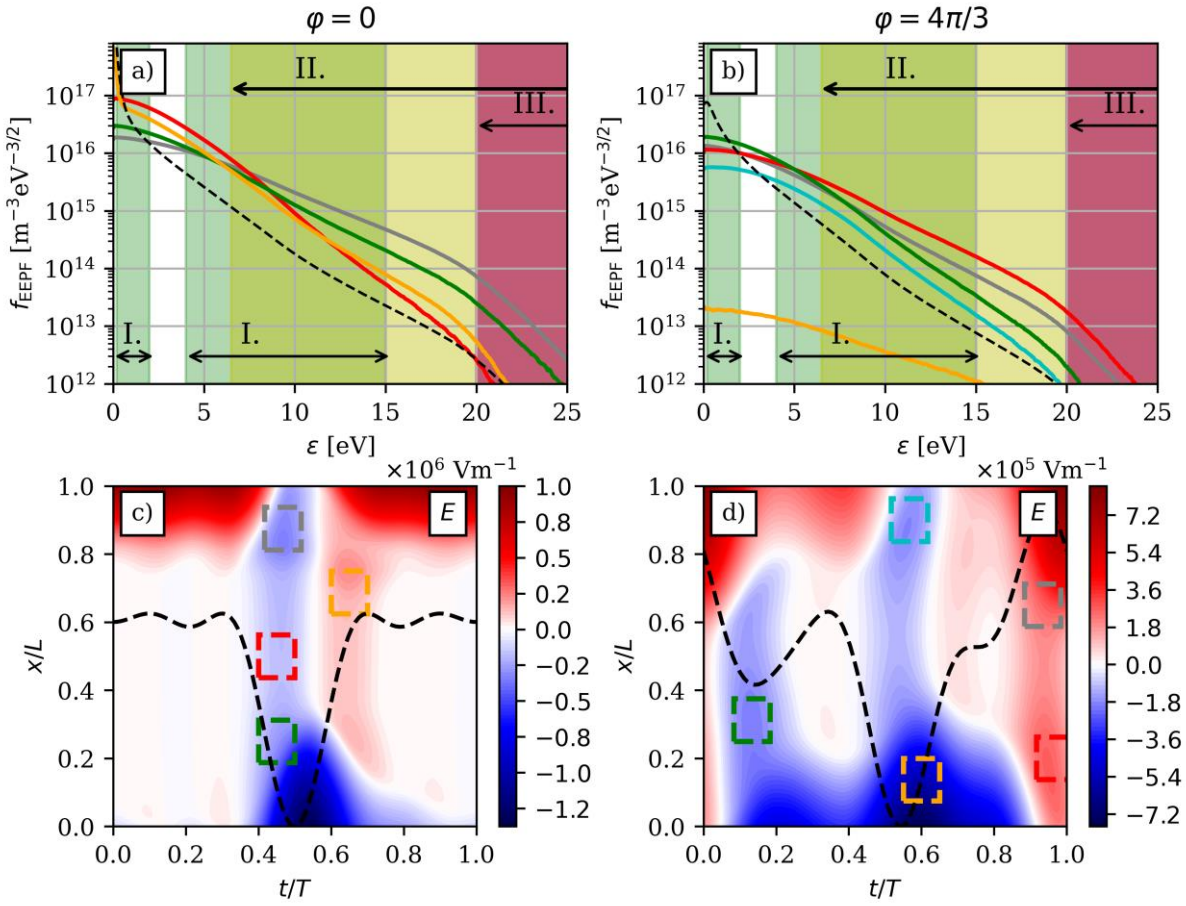

Fig. 2. Electron Energy Probability Function (EEPF) for φ=0 (a) and φ=$4\pi/3$ (b) calculated in different spatiotemporal regions of interest, and spatiotemporal distribution of the electric field for these phase values (c, d). The colored lines in panels (a, b) correspond to EEPFs calculated in the spatiotemporal regions denoted by the same colors in panels (c, d). The dashed black lines in panels (a, b) represent the average EEPF. The regions I-III. indicate the energy where the cross sections for electron impact processes that generate vibrationally excited oxygen, atomic oxygen, and helium metastables, respectively, are non-negligible. The dashed black lines in panels (c, d) show the excitation waveform.

To uncover why this family of waveforms allows control over which radical is most efficiently generated, Fig. 2 shows the Electron Energy Probability Functions (EEPFs, first row) and the spatio-temporal distribution of the electric field (second row) for two phase values: φ=0, where helium metastables are generated most efficiently and $\varphi=4\pi/3$, where atomic oxygen generation is more prominent. The colored lines in panels (a, b) correspond to EEPFs calculated in the spatio-temporal regions of interest (ROIs) indicated by the same color in the second row. The dashed black lines in panel (a, b) represent the mean EEPF. The energy regions I-III., highlighted in color, indicate the electron energy ranges where the cross sections for electron impact processes that generate vibrationally excited oxygen, atomic oxygen, and helium metastables, respectively, are non-negligible. The black dashed lines in panels (c, d) denote the excitation waveform.

As seen in panel (a), the EEPFs exhibit significant variations depending on the ROI. In regions of high electric field, especially near the ``peak'' of the waveform, the EEPFs display a populated high energy tail, which facilitates the efficient generation of helium metastables that require a threshold energy of 20 eV. In the case of $\varphi=4\pi/3$ (panel d), the excitation waveform contains multiple, smaller ``peaks'', resulting in a decreased electric field. Consequently, the high energy tail of the EEPFs becomes depleted. Nevertheless, the electric field remains sufficient to ensure a substantial EEPF value in region II, which supports efficient atomic oxygen generation (which has a threshold energy of only 4.2 eV). Furthermore, the overall power decreases for $\varphi=4\pi/3$, creating the condition where atomic oxygen is generated more efficiently than helium metastables. Thus, for the investigated family of voltage waveforms, the ability to control the generation efficiency of specific radicals with distinct electron energy thresholds arises because waveforms with multiple ``peaks'' redistribute the power across the discharge region, favoring the generation of species with lower energy thresholds.

It is important to note that, although the presented results were obtained for a specific gas mixture and focused on the generation of selected neutral species, the findings are generalizable. Similar results are expected under different discharge conditions and for other neutral species, provided that their electron energy thresholds differ and the EEPF is influenced by the applied voltage waveform.

Acknowledgements

Funding by the German Research Foundation (DFG) in the framework of the CRC 1316, projects A4, A5, A6 and B2, the DFG research Project MU 2332/12-1, and by the Hungarian National Research, Development and Innovation Office via Grant NKFIH 134462 is gratefully acknowledged.

4. References

[1] Von Woedtke T, Reuter S, Masur K and Weltmann K D 2013 *Phys. Rep.* **530** 291–320
[2] Dharini M, Jaspin S and Mahendran R 2023 *Food Chem.* **405** 134746
[3] Korolov I *et al.* 2021 *Plasma Sources Sci. Technol.* **30** 095013
[4] Golda J *et al.* 2016 *J. Phys. D: Appl. Phys.* **49** 084003
[5] Vass M *et al.* 2024 *Plasma Sources Sci. Technol.* **33** 015012
[6] Korolov I *et al.* 2021 *J. Phys. D: Appl. Phys.* **54** 125203
[7] Vass M *et al.* 2024 *Plasma Sources Sci. Technol.* **33(**11) 11LT01

LOW-PRESSURE PLASMA POLYMERIZATION FOR EMERGING FUNCTIONAL MATERIALS

Paula Navascués[1], Dirk Hegemann[1]

[1] *Empa, Swiss Federal Laboratories for Materials Science and Technology, Plasma & Coating group*
E-mail: paula.denavascues@empa.ch

Low-pressure plasma polymerization provides a versatile platform for functionalizing advanced materials. In this regard, plasma polymer films (PPFs) deposited via the polymerization of hexamethyldisiloxane (HMDSO) [1] exhibit versatile wettability and nanoporosity control. By varying plasma operating parameters (e.g., additional gases, applied power, reactor configuration, etc.) siloxane-based coatings ranging from hydrophobic to hydrophilic with different volumetric nanoporosity can be obtained [2]. Plasma polymerization, performed at room temperature, allows deposition onto sensitive substrates such as polymers, carbon-based nanofibers, and scaffolds, enabling functionalization for advanced applications in medicine and biology. Despite decades of study in the field of plasma-enhanced chemical vapor deposition (PECVD), further research is still needed to unravel the reaction mechanisms of plasma polymer formation, especially with 3D materials featuring complex geometries commonly used in the mentioned applications [3]. In this regard, nanoporous plasma polymer films hold promise for biomaterial functionalization. With rising bacterial and viral threats, new antimicrobial methods are needed. One approach involves surfaces that generate and release reactive oxygen species (ROS) without leaching substances. This talk will explore plasma technology's role in developing functionalized metal oxide catalytic materials through deposition and oxidation processes. The reactive gas environment facilitates defect sites for ROS formation, while nanoporous plasma polymer SiOx films control ROS release. The permeation of H_2O and O_2 molecules through the functional polymeric cover layer allows ROS production at the interface between the metal oxide and the PPF and controls their delivery. ROS delivery—such as superoxide anion (O_2•–) and singlet oxygen ($^1O_2$)—can be fine-tuned by the plasma-deposited SiOx layer thickness [4]. This plasma-based approach yields antimicrobial surfaces effective against bacteria and murine hepatitis virus, without cytotoxicity, expanding plasma's potential in plasma medicine. Additionally, hydrophobic HMDSO-derived PPFs can also functionalize similar ROS-releasing surfaces. While maintaining antimicrobial activity, the functional layer defines surface wettability, rendering it hydrophobic rather than hydrophilic and making it ideal for applications such as combating biofilm formation. This talk will discuss how the integration of catalytic surfaces with HMDSO-derived plasma polymer films facilitates the precise control of ROS delivery, paving the way for innovative functional materials for applications ranging from therapy to sustainability.

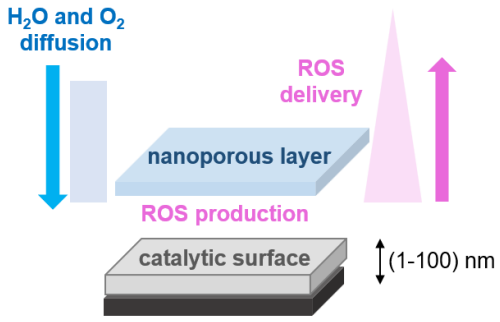

Fig. 1. A nanoporous functional layer deposited on top of a catalytic surfaces producing reactive oxygen species (ROS) allows the precise controlled of ROS to the environment.

References

[1[2] P. Navascués, U. Schütz, B. Hanselmann, D. Hegemann, Nanomat. 14(2), 195; (2024) https://doi.org/10.3390/nano14020195
[3] P. Navascués, M. Buchtelová, L. Zajíčková, P. Rupper, D. Hegemann, Appl. Surf. Sci., 645, 158824 (2023) https://doi.org/10.1016/j.apsusc.2023.158824.
[4] P. Navascués, F. Kalemi et al. Under review (2025), https://arxiv.org/abs/2411.01219.

INVESTIGATING STABLE SURFACE MODIFICATIONS OF FLUOROPOLYMERS BY ATMOSPHERIC PRESSURE NITROGEN DISCHARGE

Jacopo Profili[1,2]

[1] *Laboratoire de Procédés et Matériaux Avancés (LPMA), Département de biologie, chimie et géographie, Université de Québec à Rimouski (UQAR), Rimouski, QC, Canada*
[2] *Département de Génie des Mines, de la Métallurgie et des Matériaux, Faculté des Sciences et de Génie, Université Laval, Québec, QC, Canada.*

E-mail: jacopo_profili@uqar.ca

This work provides insights into plasma-surface interactions during atmospheric pressure plasma treatment of fluorinated ethylene propylene (FEP), enabling the observation of surface modifications over time. These results demonstrate the possibility to produce a highly stable surface modification with minimal hydrophobic recovery, a characteristic often absent in atmospheric pressure plasma treatments. While conventional modifications (reduced contact angle and increased hydrophilicity) were observed, notably higher fluorine content remained on the treated surfaces, suggesting that complete fluorocarbon removal is not essential for achieving hydrophilicity. Furthermore, the modified surfaces exhibited strong resistance to aging, maintaining high hydrophilicity even after rigorous scrub testing. Adhesion testing, comparing plasma-treated samples to conventionally chemically etched polymers, revealed similar or superior adhesion strengths. These findings pave the way for novel, tailored atmospheric pressure surface modifications of fluoropolymers, particularly for applications in medical devices.

1. Introduction

Fluoropolymers (FPs), valued for their non-stick, waterproof, and chemically resistant properties, often require surface modification to ensure adhesion in composite materials or medical devices [1]. While existing methods include wet-chemical treatments [2] (which use hazardous reagents and can damage material properties) and low-pressure plasma processes [3] (limited by batch processing and vacuum requirements), atmospheric pressure plasma offers a promising alternative. This approach eliminates the need for expensive vacuum equipment, reduces maintenance, and enables treatment of larger substrates, offering a cleaner, safer, and more cost-effective solution for industrial applications. This work investigates the modification of fluorinated ethylene propylene (FEP) films using an atmospheric pressure nitrogen dielectric barrier discharge (DBD) plasma. Modified samples were characterized using AFM, XPS, T-peel testing, wettability measurements, and scrub-washing (ASTM D-2486 – 17) to evaluate modification stability.

2. Experimental conditions

The discharge cell employed a plane-to-cylinder configuration with a metallic electrode (15 cm x 1 cm x 6 cm) separated by a few mm N_2 injection slot and a 15 cm cylindrical ground electrode. Surface chemistry of FEP films was analyzed using a PHI 5600-ci XPS (Physical Electronics, MN, USA) with a 45° take-off angle and a 0.5 mm² detection area. Survey spectra (1200-0 eV) were acquired using an Al X-ray source (1486.6 eV, 300 W) with charge neutralization, while high-resolution C1s spectra were obtained using a Mg X-ray source (1253.6 eV, 300 W) without charge neutralization and a 5.85 eV pass energy. Curve fitting, using Gauss-Lorentz peak fitting and a Shirley baseline, was performed with Multipak software, referencing each spectrum to the CF2 signal at 292.0 eV. Surface topography was analyzed using a Dimension 3100 AFM (Digital Instruments, Santa Barbara, CA, USA) in tapping mode with an etched silicon tip (OTESPA, tip radius <10 nm). Topography was evaluated over 5 x 5 µm areas using Nanoscope software, and surface roughness was quantified using the root mean square roughness (Rrms) parameter. Modification stability was assessed via scrub-washing (ASTM D-2486 –

17) using an Elcometer 1720 Abrasion & Washability Tester (USA) with nylon brush (KT001720P030) and sponge (KT001720P073) abrasives, a 100 g load, and varying cycles using water or acetone.

3. Results

Contact angle measurements revealed that plasma treatment of FEP reduced the water contact angle from 109.4° ± 1.3° (untreated) to 102.1° ± 1.3° and the diiodomethane contact angle from 83.6° ± 0.5° (untreated) to 79.2° ± 1.4°, resulting in an increased surface energy (from 16.5 ± 1.1 mN/m to 19.1 ± 1.1 mN/m). XPS analysis showed an increase in the C/F ratio from 0.60 (untreated) to approximately 0.7 after treatment, along with the introduction of nitrogen and oxygen, indicating defluorination and the creation of new functional groups. High-resolution C1s XPS spectra revealed the appearance of C-O, C–C/C-N, and C-CFx/CO-CFx bonds after treatment, in addition to the CF3, CF2, and CF bonds present in untreated FEP. AFM analysis showed a decrease in surface roughness (RMS-Ra) from 7.1 ± 0.6 nm (untreated) to 3.6 ± 0.3 nm after plasma treatment. T-peel tests demonstrated a significant increase in peel strength after plasma treatment. Importantly, this enhanced adhesion persisted after scrub-washing (ASTM D-2486 – 17) with various solvents (water and acetone, using both brush and sponge), even showing increased adhesion in some cases after scrubbing. This suggests that the plasma treatment creates a robust surface modification resistant to aging and removal by scrubbing. The adhesion of the plasma-treated FEP was comparable to or greater than that of conventionally chemically etched FEP. These results indicate that atmospheric pressure plasma treatment can create stable and effective surface modifications on fluoropolymers for applications such as medical devices.

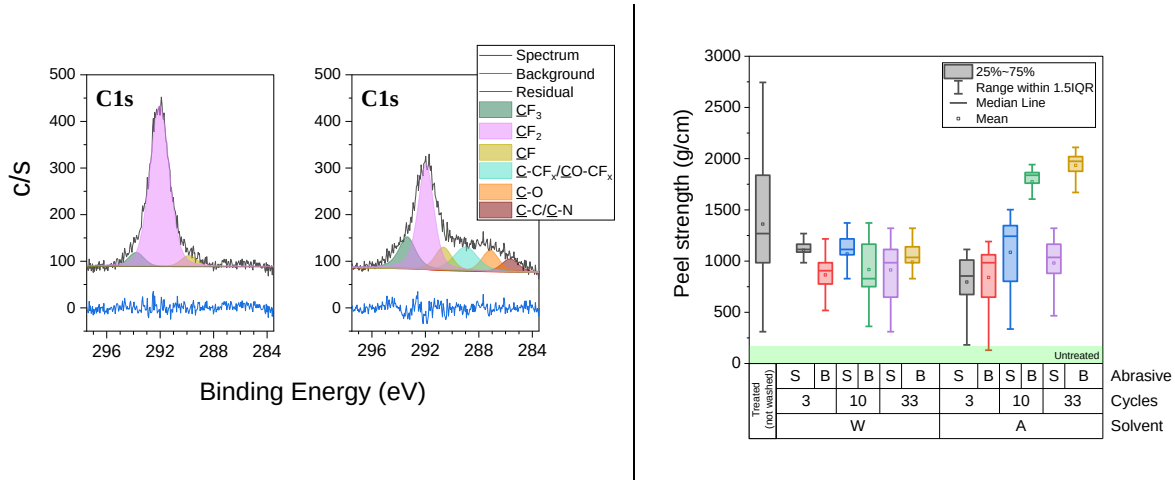

Fig. 1. (Left) XPS HR of C1s region of: a) FEP untreated; b) FEP plasma treated. (Right) peel strength obtained by peel test of samples (W: water; A: acetone; B: brush; S: sponge)

Experiments investigated the surface modification and adhesion changes of samples treated with an atmospheric pressure N_2 discharge. The treatment resulted in increased surface roughness and the presence of new oxygen- and nitrogen-containing functional groups. These modifications proved resistant to scrub-washing. Varying the polymer's exposure to the discharge (e.g., scroll speed) resulted in different degrees of modification (results not shown).

4. References

[1] S. Ebnesajjad, Fluoroplastics Volume 1: Non-Melt Processible Fluoropolymers - The Definitive User's Guide and Data Book, 2nd ed. 2015.

[2] I. Mathieson, D. M. Brewis, and R. A. Cayless, "Pretreatments of Fluoropolymers," J. Adhes., vol. 46, no. 1994, pp. 49–56, 1994

[3] Y. Ohkubo et al., "Drastic Improvement in Adhesion Property of Polytetrafluoroethylene (PTFE) via Heat-Assisted Plasma Treatment Using a Heater," Sci. Rep., vol. 7, no. 1, pp. 1–9, 2017, doi: 10.1038/s41598-017-09901-y.

RADIATION CHEMISTRY PROCESSES ON THE SURFACES OF ICY MOONS IN THE PLASMA ENVIRONMENT OF GIANT PLANETS

Z. Juhász[1], D. V. Mifsud [1,2], Z. Kaňuchová[3], P. Herczku[1], S. T. S. Kovács[1], G. Lakatos[1,4], K. K. Rahul[1], R. Rácz[1], B. Sulik[1], S. Biri[1], I. Rajta[1], I. Vajda[1], S. Ioppolo[5], R. W. McCullough[6], G. Richards[7], N. J. Mason[1,2]

[1]*HUN-REN Institute for Nuclear Research (ATOMKI), Debrecen H-4026, Hungary*

[2]*Centre for Astrophysics and Planetary Science, School of Physics and Astronomy, University of Kent, Canterbury CT2 7NH, United Kingdom*

[3]*Astronomical Institute, Slovak Academy of Sciences, Tatranská Lomnica SK-059 60, Slovakia*

[4]*Doctoral School of Chemistry, University of Debrecen, Egyetem Tér 1, Debrecen H-4032, Hungary*

[5] *Centre for Interstellar Catalysis, Department of Physics and Astronomy, Aarhus University, Aarhus DK-8000, Denmark*

[6]*Department of Physics and Astronomy, School of Mathematics and Physics, Queen's University Belfast, Belfast BT7 1NN, United Kingdom*

[7]*School of Physical Sciences, The Open University, Milton Keynes MK7 6AA, United Kingdom*

E-mail: zjuhasz@atomki.hu

We have studied ion irradiation-induced chemical changes in laboratory ice analogues mimicking the surfaces of icy moons in the outer Solar System. We have explored the possible creation mechanisms of sulphur-bearing compounds and simple organic molecules that are of contemporary interest in light of recent and future space missions.

1. Introduction

Jupiter's plasma environment is one of the most intriguing plasma laboratories in our Solar System. The whole system is fed by plasma sources predominantly from within the magnetosphere with some contributions from outside. The volcanic moon Io is the strongest internal source with smaller contributions from Europa and possibly from other moons, as well as the ionosphere of Jupiter [1]. ESA's *Jupiter Icy Moons Explorer* (JUICE) mission is to explore Jupiter's complex environment in depth. Embedded in Jupiter's inner magnetosphere, icy moons interact strongly with the surrounding plasma. *Voyager* and *Galileo* data have shown that these moons are constantly bombarded by electrons and energetic ions (H^+, C^{n+}, O^{n+} and S^{n+}). Similarly, the surface of Enceladus is constantly irradiated by Saturn's magnetospheric plasma, which consists of a variety of charged particles including water-group ions over a wide energy range.

The intense irradiation of the surface ice is the main driver of the formation of thin lunar atmospheres and may be crucial in shaping the properties of the oceans beneath the icy crusts. However, details on the surface irradiation processes and their impact on the environment are poorly understood. These processes, which may be essential for the origin of life, are simulated in the laboratories at ATOMKI to understand their intricacies [2]. In particular, we have investigated the radiolytic sulphur chemistry on Europa arising as a result of the ion irradiation of the surface; for instance, we have investigated the irradiation of ices on top of a solid sulphur layer, as well as the implantation of reactive sulphur ions into various oxygen-bearing molecular ices [3]. A surface ice analogue of Enceladus, made by mixing different molecules, was also processed by ions to explore whether the molecules regarded as indicators for habitability, which were found in Enceladus plumes, could be created in this way [4].

2. Sulphur chemistry at surface of Europa

Sulphur dioxide has been detected in the surface of Europa but its formation mechanisms have not been identified so far [5]. This motivated us to check whether sulphur ion implantation into ices made of molecules other than water could be the source of SO_2. Analogous investigations on water ice

already gave negative results; instead the efficient formation sulphuric acid was observed [6]. Sulphur ion implantation in CO_2 ice (which has been observed on Europa [7]) indeed resulted in the formation SO_2, but only at 20 K, which is too cold with respect to ambient temperatures on the surface of Europa (Figure 1). At 70 K, no sulphur-bearing molecules were formed, which therefore suggest that sulphur implantation into surface ice is not an efficient SO_2 formation mechanism on Europa.

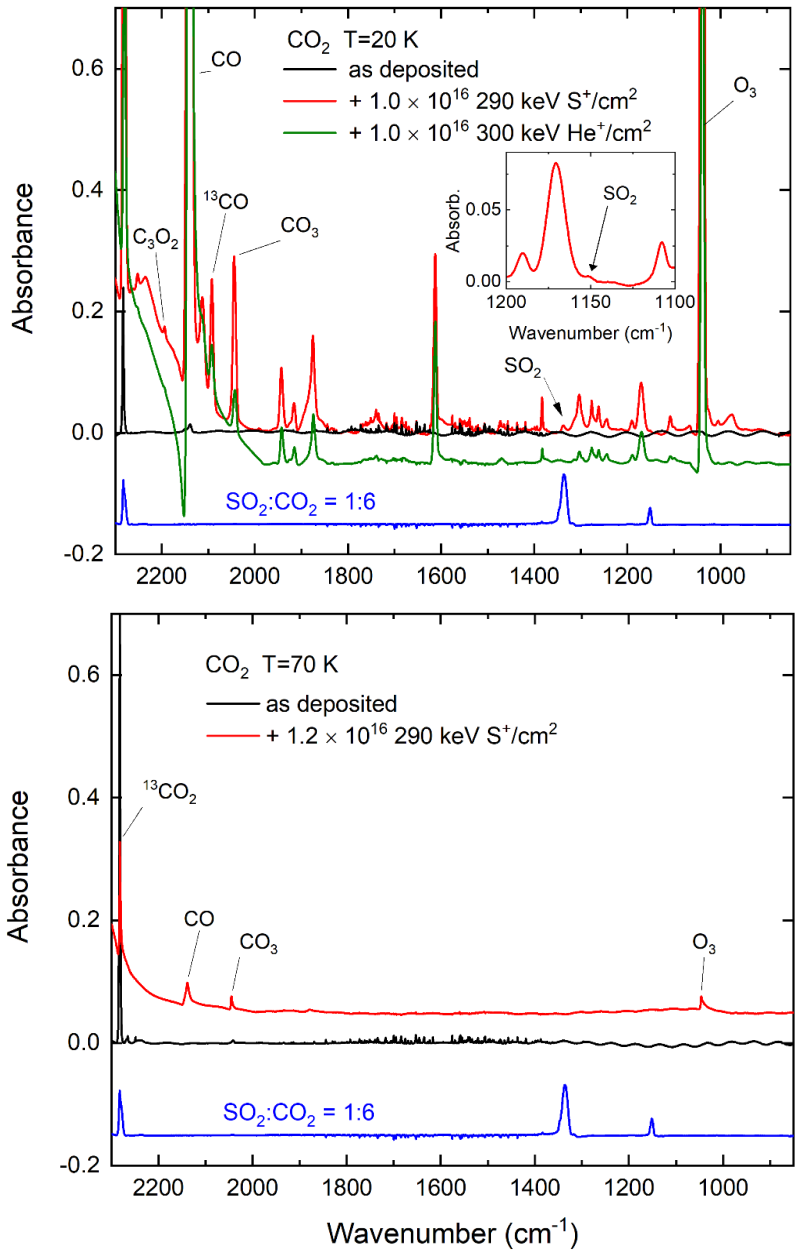

Fig. 1. Fourier-transform mid-infrared (FTIR) spectra of condensed CO_2 before (black trace) and after (red trace) the implantation of 290 keV S^+ ions at 20 K and 70K. Also shown are the FTIR spectra acquired during control experiments, including an unirradiated CO_2:SO_2 (6:1) ice mixture at 20 K (blue trace) and a CO_2 ice after the implantation of 300 keV He + ions at 20 K (green trace).

This has led us to investigate refractory sulphur layers, which may also exist in the surface of icy moons. We covered them with ice layers from the most common molecules present on the lunar surfaces and in their atmospheres. As Fig. 2 shows, the most intensive SO_2 formation was found in experiments in which O_2 ice on top of sulphur was processed by He+ ions. This experiment was performed at 20 K,

since at 70 K the oxygen layer sublimes very efficiently; but for a CO_2 ice layer we could perform the experiment at 70 K and observed significant SO_2 production at this Europa-relevant temperature.

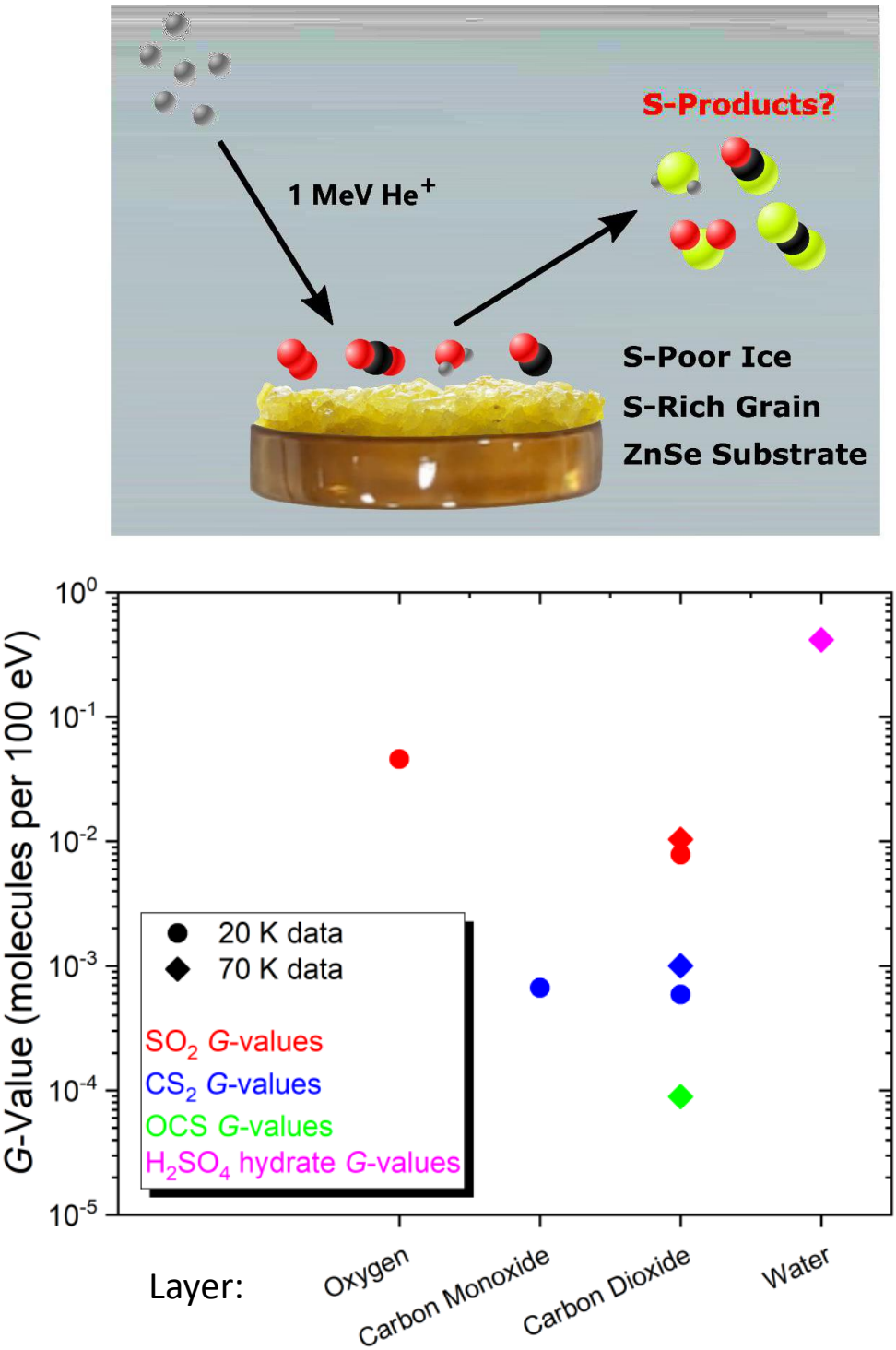

Fig. 2. Obtained *G*-values (number of produced molecules per 100 eV deposited energy) for the sulphur-bearing products observed as a result of irradiating different ices on top of allotropic sulphur using 1 MeV He+ ions. Note that circles represent data points acquired at 20 K, while diamonds represent those acquired at 70 K.

3. Water-group ion irradiation studies on Enceladus ice analogues

Surface ice analogues of Enceladus composed of H_2O:CO_2:CH_4:NH_3 (approximate stoichiometry of 7:1:1:1) were prepared and irradiated different water group ions, including O^+, O^{3+}, OH^+, and H_2O^+ ions. We have observed the creation of simple compounds such as CO and OCN^- due to irradiation, and most experiments also formed NH_4^+; while post-irradiative heating produced carbamic acid, ammonium carbamate, and an alcohol (likely methanol or ethanol) in most experiments (Fig 3.) Our results have important implications for radiation-driven chemistry on Enceladus; although none of the radiolytic products observed in our laboratory experiments has been detected on the icy surface of Enceladus, some have been detected within its plumes. Our research shows that irradiative processes may play a role in that environment and, therefore, caution is advised when searching for evidence of biosignatures in Enceladus' plumes.

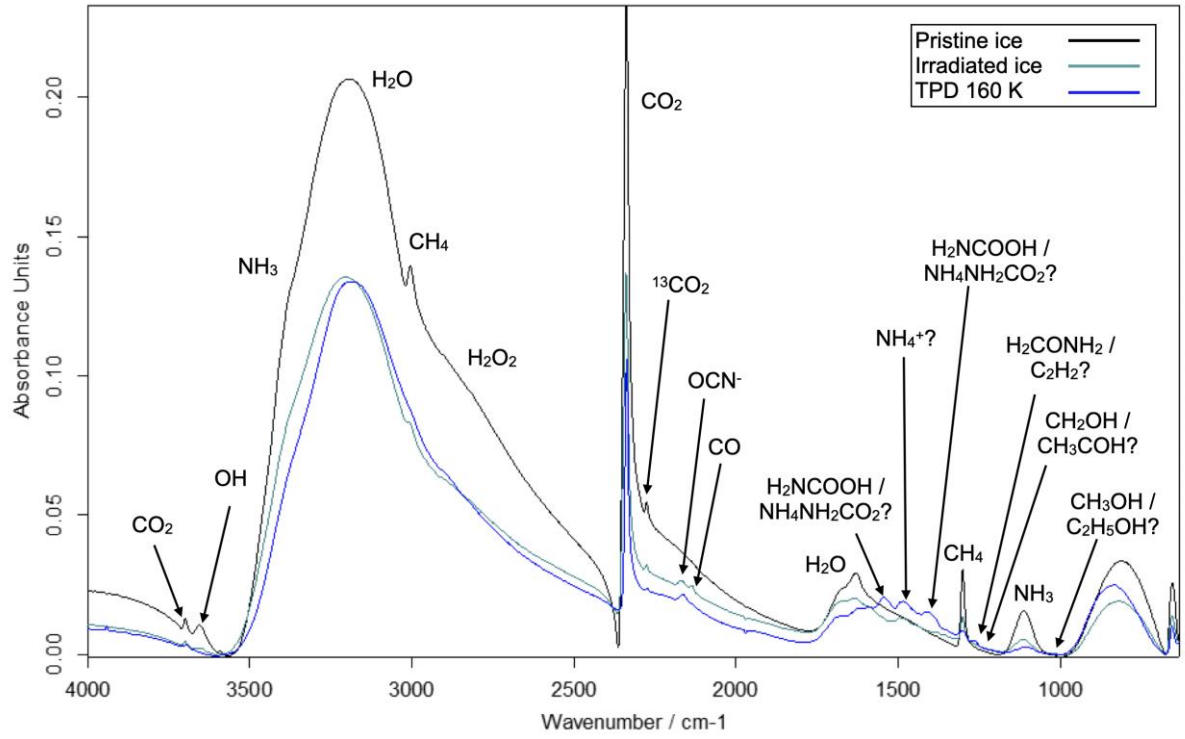

Figure 3: FTIR spectra for irradiation of an Enceladus surface ice analogue with 45-keV O^{3+}, before and after irradiation, and during the TPD at 160 K.

4. Acknowledgement

The authors acknowledge support from the Europlanet 2024 RI which has been funded by the European Union's Horizon 2020 Research Innovation Programme under grant agreement no. 871149. This work has also received support from the European Union and the State of Hungary; co-financed by the European Regional Development Fund through grant GINOP-2.3.3-15-2016-00005. Support has also been received from the Research, Development, and Innovation Fund of Hungary through grant no. K128621. This paper is also based on work from the COST Action CA20129 MultIChem, supported by COST (European Cooperation in Science and Technology).

Duncan V. Mifsud is the grateful recipient of a University of Kent Vice-Chancellor's Research Scholarship. The research of Zuzana Kaňuchová is supported by the Slovak Grant Agency for Science (grant no. 2/0059/22) and the Slovak Research and Development Agency (contract no. APVV-19-0072). Zoltán Juhász is grateful for the support of the Hungarian Academy of Sciences through the János Bolyai Research Scholarship. Sergio Ioppolo acknowledges support from the Danish National Research Foundation through the Centre of Excellence 'InterCat' (grant agreement no. DNRF150), as well as from the Royal Society.

5. References

[1] Bolton S J et al. 2015 *Space Sci. Rev.* ***192*** 209–236.
[2] Herczku P et al. 2021 *Rev. Sci. Inst.* ***92*** 8.
[3] Mifsud D V et al. 2022 *Geophys. Res. Lett.* ***49*** 24.
[4] Peter J S, Nordheim T A, and Hand K P 2024. *Nature Astronomy* **8** 164-173.
[5] Carlson R W, Anderson M S, Mehlman R, & Johnson R E 2005 *Icarus* **177(2**) 461–471.
[6] Strazzulla G, Baratta G A, Leto G, & Gomis O 2007 *Icarus* **192(2**) 623–628.
[7] Trumbo S K and Brown M E 2023 *Science* **381** 1308-1311.

SWARMS OF IONS IN VARIABLE ELECTRIC FIELD - POSSIBLE ANALYTICAL APPLICATION

Jarosław Puton[1], Krzysztof Piwowarski[1], Jarosław Ławreńczyk[1], Izabela Wolańska[1]

[1]*Institute of Chemistry, Military University of Technology, Gen S. Kaliskiego Str. 2, 00-908 Warsaw, Poland*
E-mail: jaroslaw.puton@wat.edu.pl

The paper concerns a simple radioionization detector intended for analytical applications. The theoretical model of the detector is based on the ion balance equations for a variable electric field. The calculation results are compared with experimental data obtained from measurements performed using the constructed detector model.

1. The influence of ionization chamber filling on the signal – an old idea for gas analysis

A typical way of using ionization chambers is to measure the radiation field. In this case, the chamber filling is constant, and the signal measured continuously or pulsed contains information about the dose rate or energy left in the gas by the charged particle or ion [1]. However, over a hundred years ago it was noticed [2,3] that if the radiation field is constant, the electrical signal generated in the chamber depends on the composition of the gas filling it. This effect can be used in analytical applications. The basic way of such use was to measure the current at a constant supply voltage. Considerations on the theory of processes occurring in such detectors were based on the so-called system of ionization chamber equations including ion balance equations and Gauss's law [4,5]. In the 1950s and 1960s, a number of ionization detector designs were developed, mainly for chromatography [6,7]. Probably the most famous of them were the flame ionization detector (FID) and the electron capture detector (ECD). Soon after, ion mobility spectrometers (IMS detectors) appeared and dominated the on-site detection of hazardous materials [8]. Simple ionization detectors with an internal radioactive source found some applications in equipment for detecting chemical warfare agents (CWA). Unlike older designs, they used a variable electric field and the signal was an average current value. The theoretical description of such detectors can be found in few works [9,10].
Despite the significant advantages of IMS detectors, there is a need for sensors with simpler structures that function as indicators that generate alarm signals in the event of the appearance of chemical substances with specific properties (e.g. high proton affinity). In connection with this, attempts are being made to use detectors with a variable field in new devices for detecting contamination [11]. This paper is devoted to research on a simple detector in which detection is based on a signal generated by oscillating ion swarms. The aim of the paper is to develop elements of the theory of such a detector, as well as to perform tests of its usefulness in analytics.

2. Modeling of ion concentration distributions and calculating the detector signal

A simplified diagram of the detector construction, which was the object of the research, is shown in Fig. 1. The detector consists of two electrodes and a housing. The cylindrical outer electrode is used to supply the detector with an alternating voltage in the shape of a symmetrical square wave. The central electrode is used to measure the detector signal (current). On the surface of central electrode, a 63-Ni isotope source is placed for ionization of the gas. The effective ionization range for this source (approx. 0.7 cm) is significantly smaller than the radius of the outer electrode (1.5 cm). Both electrodes are placed in a grounded housing. Fig. 1 also shows the method of powering and measuring signal of the model detector.

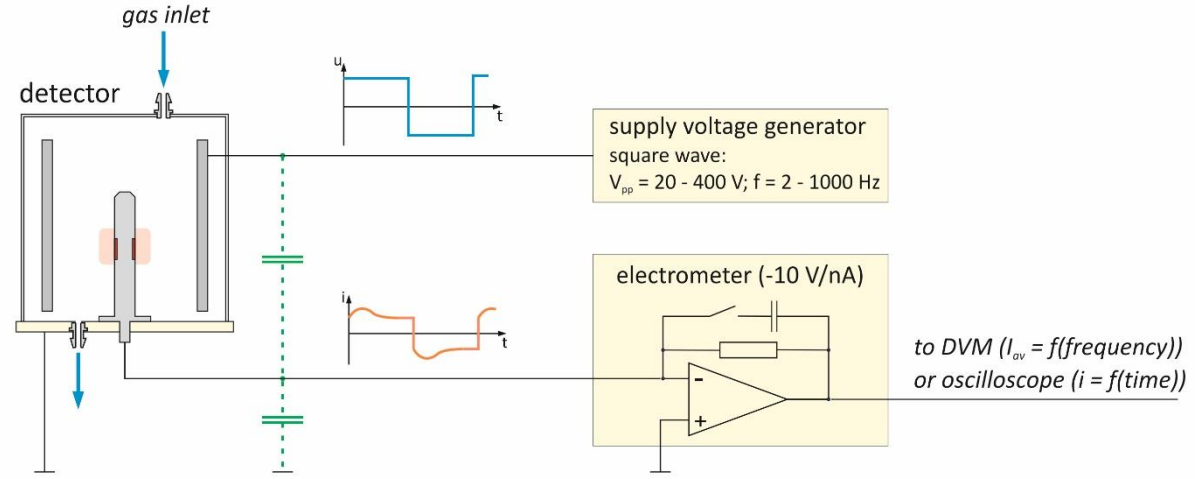

Fig. 1. Detector sketch, power supply and signal measurement method.

The mathematical description of the phenomena occurring in the gas filling the detector is based on the ion balance equations. The balance equation for the i-th type of ions has the form:

$$\frac{\partial n_i}{\partial t} = -div(n_i \boldsymbol{v_i}) + div\left(D_i grad(n_i)\right) + P_i - L_i \qquad (1)$$

where: n_i – concentration of i-th type of ions
$\boldsymbol{v}_i$ – velocity of i-th type of ions, $\boldsymbol{v}_i = \boldsymbol{u} + K_i \boldsymbol{E}$
D_i – diffusion coefficient of i-th type of ions
P_i – generation of i-th type of ions (ionization, ion-molecule reactions)
L_i – losses of i-th type of ions (recombination, ion-molecule reactions.)
$\boldsymbol{E}$ – electric field intensity, $div\boldsymbol{E} = (1/\varepsilon\varepsilon_0)\rho$
ρ – electric charge density
ε, ε_0 – dielectric constant (relative and for the vacuum)
$\boldsymbol{u}$ – gas velocity
K_i – mobility of i-th type of ions

The simplicity of the above system of equations is very deceptive. There are as many equations as there are types of ions. The electric field is generated by the electrode system and the spatial distributions of charge carriers. The loss and production terms couple the equations. In real devices, the geometry of the electrode system is not ideal. It is therefore necessary to ignore selected processes occurring in reality. Solving simplified problems allows us to explain some phenomena observed in measurement results. The basic simplification that was adopted for modeling the phenomena in the detector under consideration was the occurrence of an external electric field of relatively high intensity in the detector. This allowed us to ignore the effects related to diffusion, recombination and the influence of the space charge on the electric field between the electrodes. In addition, it was assumed that considering one-dimensional cylindrical geometry is sufficient to describe the phenomena. With such assumptions, the balance equations for positive and negative ions take the form:

$$\frac{\partial n_+}{\partial t} = N(r) + \frac{1}{r}\frac{K_+ V_0}{ln(R_0/r_0)}\frac{\partial n_+}{\partial r} \qquad (2)$$

$$\frac{\partial n_-}{\partial t} = N(r) - \frac{1}{r}\frac{K_- V_0}{ln(R_0/r_0)}\frac{\partial n_-}{\partial r} \qquad (3)$$

where $N(r)$ is the specific ionization, i.e. the number of ions pairs produced by radiation emitted from the source in a unit of volume in 1 s.

In the steady state for a constant voltage V_0, stable distributions of concentrations of both types of ions are obtained. In the case of supplying the detector with an alternating voltage, of the shape as in Fig. 1, a solution of equations (2) and (3) for the time after switching the polarization should be found. Such a solution can be obtained numerically or through relatively simple calculations based on the principle of conservation of charge. Example solutions illustrating the movement of ions when the polarization of the supply voltage changes are shown in Fig. 2.

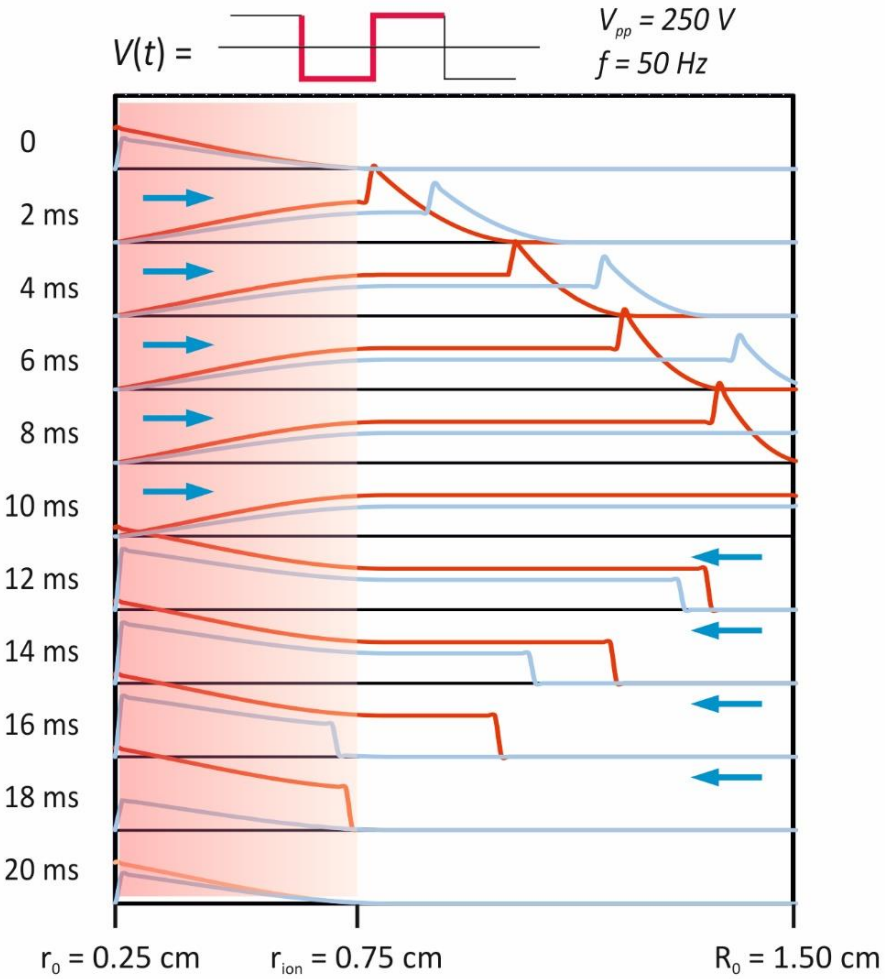

Fig. 2. Time dependent concentration distributions for positive ions (K = 1.6 (red) and 2.2 (blue) $cm^2V^{-1}s^{-1}$)

The detector signal is a time-dependent current. Its magnitude results both from the collection of ions by the electrodes and from the induction of current by time-varying charge distributions between the electrodes. A simple method of calculating the current in an external circuit is to use the principle of conservation of energy, according to which the work done by the electric field in moving an ion must be equal to the energy taken from the external circuit:

$$i_{\pm}(t)V_0 dt = \pm eE(r)dr \tag{4}$$

For positive and negative ions with mobilities K_+ and K_- moving in an electric field of cylindrical geometry, the formula for calculating the current is:

$$i_{\pm}(t) = \frac{2\pi ehK_{\pm}V_0}{(\ln(R_0/r_0))^2}\int_{r_0}^{R_0}\frac{1}{r}n_{\pm}(r,t)dr \tag{5}$$

3. Measurement results

Formula (5) allowed to calculate the time-dependent detector current when supplied with an alternating voltage of relatively low frequency, i.e. such that the distribution of ion concentrations in the space between the detector electrodes is completely established in a time equal to half the period. The correctness of the model assumptions can be confirmed by comparing theoretical predictions with measurement results (Fig. 3).

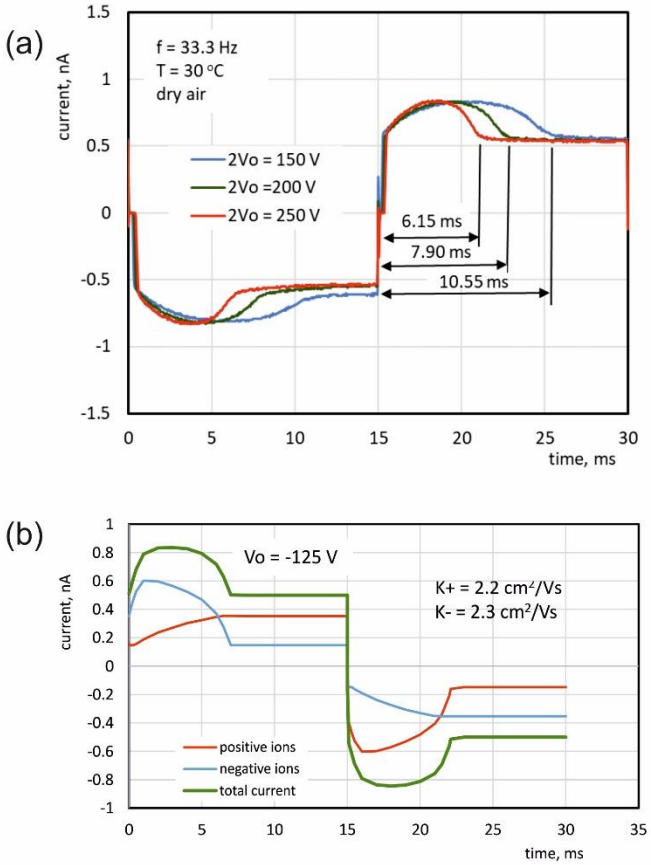

Fig. 3. Measured (a) and theoretically determined (b) dependence of the detector current on time.

Comparison of experimentally determined dependencies of current on time with calculation results allows us to state that the theoretical description of ion transport in the detector is correct. Two characteristic ranges are visible in the time dependencies shown in Fig. 3. Immediately after changing the polarity of the supply voltage, an ion current pulse is observed. The duration of this pulse depends on the amplitude of the supply voltage. It can be proven that the pulse duration corresponds to the time of flight of ions between the detector electrodes. After the pulse ends, the absolute value of the ion current is the same for both polarities of the supply voltage and is about 0.5 nA. This value corresponds to the saturation current measured in static conditions.

The measurement results shown in Fig. 3a indicate the potential use of the detector in analytical applications. The pulse duration (transient state after polarization change) depends on the voltage amplitude. It should be expected that this is the result of the dependence of ion velocity on the electric field intensity. However, the ion velocity also depends on mobility. Therefore, the duration of the transient state should be different for different ions. To verify this prediction, measurements of the time dependencies of the current were performed for methyl salcylate (MS) and dimethyl methylphosphonate (DMMP). These two compounds are known CWA symulants. MS is responsible for the change in mobility of positive and negative ions. DMMP is a phosphoorganic CWA imitator with high proton affinity and causes a decrease in the mobility of positive ions. The results of the studies carried out for MS and DMMP are shown in Fig. 4.

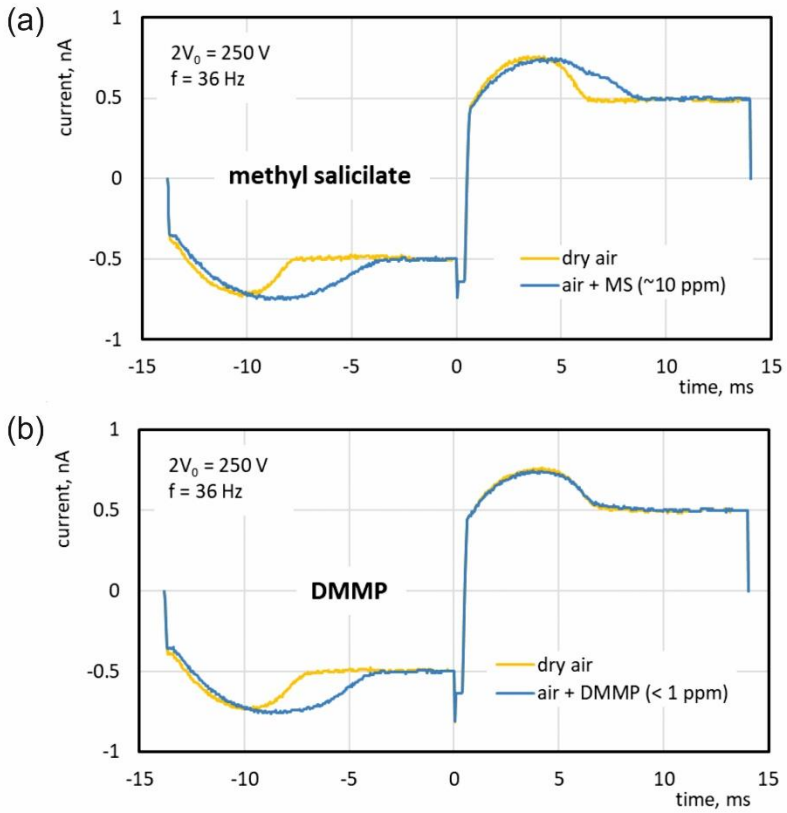

Fig. 4. Time dependence of the detector current measured for methyl salicylate (a) and dimethyl methylphosphonate (b).

4. Conclusion

The current waveforms shown in Fig. 4 indicate that the signal from a simple cylindrical detector contains information about the mobility of charge carriers occurring in the space between the electrodes. This effect can be used to determine the presence of compounds with high proton affinity or the ability to create stable, heavy negative ions in the air. Of course, the method does not provide the analytical possibilities provided by the IMS detector with a drift chamber. However, the method and design solution are very simple and can be used to build cheap detectors generating an alarm signal, which will be the basis for performing further, more detailed tests in a given location.

5. Acknowledgments

This work was founded by Polish National Centre of Research and Development (project number DOB-SZAFIR/09/A/010/01/2021).

6. References

[1] Knol G.F., Radiation Detection and Measurement, 4th ed.; John Wiley & Sons, Inc., 2010.
[2] Mie G., Der elektrische strom in ionisierter luft in einem ebenen kondensator Ann. Phys., Lpz. 13 (1904) 857–89.
[3] Zeleny J., The distribution of mobilities of ions in moist air, Phys. Rev. 34 (1929) 310-334.
[4] Seeliger R., Beitrag zur theorie der elektrizitätsleitung in dichten gasen Ann. Phys., Lpz. 33 (1910) 319–81.

[5] Novkovič D., Miloševič Z., Subotič K., Manič-Kudra S., Numerical solutions of differential equations of a cylindrical ionization chamber, Phys. Med. Biol. 41 (1996) 725–741.
[6] Lovelock J.E., Ionization methods for the analysis of gases and vapours, Anal. Chem. 33 (1961) 162-178.
[7] Poole C.F., Ionization-based detectors for gas chromatography, J. Chromatogr. A 1421 (2015) 137–153.
[8] Eiceman G. A., Karpas Z., Hill H.H. Jr., Ion Mobility Spectrometry, 3 ed.; CRC Press, 2013.
[9] Milinkovič S.A., Milanko O.S., Ionization chamber as a gas sensor: Organophosphorus compound detection, Anal. Chim. Acta 331 (1996) 233-238.
[10] Milinkovič S.A., Miniature sensor cell for gaseous and aerosol air pollutants, Mediterranean Conference on Embedded Computing, MECD – 2012, Bar, Montenegro.
[11] Technical Specifications - Polimaster PM 2012M Operation Manual, https://www.manualslib.com/manual/2761255/Polimaster-Pm-2012m.html?page=10#manual (2024).

MULTISCALE SIMULATION OF PLASMA-BASED DEPOSITION PROCESSES

Masaaki Matsukuma

Tokyo Electron Technology Solutions Limited
E-mail: masaaki.matsukuma@tel.com

An example of simulation flow for a thin film deposition is described. The importance of consistent data and simulation technology through the atomic scale to chamber scale is shown.

Recent semiconductor devices have not only undergone simple miniaturization but have also undergone significant changes in materials and structures. For example, 3D structures, including FinFET, this approach not only saves space but also enhances performance through reduced interconnect delays and improved power management. About the materials innovations, traditional silicon-based semiconductors are being supplemented or replaced with materials such as gallium nitride (GaN), silicon carbide (SiC), and other two-dimensional materials like graphene and transition metal dichalcogenides. These materials can improve performance in terms of speed, power efficiency, and thermal management. In this trend of semiconductor device evolution, manufacturing processes and equipment are also being required to evolve.

This presentation will provide an overview of the simulations being carried out to develop the technology for depositing desired thin films on the latest complex device structures. The process involves analyzing the decomposition and polymerization reactions of the source gases, simulating their transport and distribution within the chamber, and finally simulating the film formation process within the fine pattern. From this series of simulations, we can predict the performance of our manufacturing equipment and processes.

However, the speed of semiconductor device evolution has accelerated in recent years, and we need to work backwards from the desired device and process performance to select materials and develop equipment and processes that will achieve these. This is not an easy task, especially when it comes to inverse problems. We have accumulated a wide range of data and simulation results and are working to overcome this challenge with the aid of machine learning. In this presentation, I would like to present my concerns and hope to receive advice from academia.

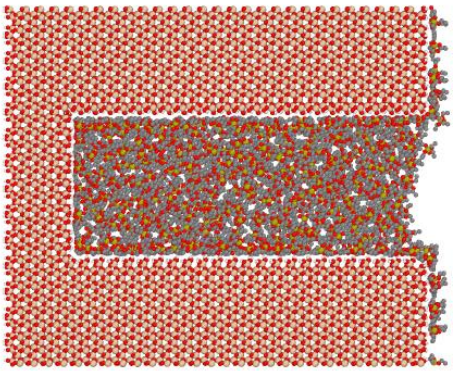

Fig. 1. Gapfill for a lateral trench

HOT TOPICS

INDOOR AIR CLEANING BY NON-THERMAL PLASMA AND PHOTOCATALYSIS

Thomas Vazquez[1], Aleksandra Lavrikova[1], Dalimír Wiedermann[2], Jan Babic[2], and Zdenko Machala[1]

[1]*Division of Environmental Physics, Faculty of Mathematics, Physics and Informatics, Comenius University Bratislava, Mlynská dolina, 842 48 Bratislava, Slovakia*
[2]*IQ Capital s.r.o., Banská Bystrica, Slovakia*
E-mail: machala@fmph.uniba.sk

Indoor air contains many harmful compounds (chemical pollutants, pathogenic aerosols, tobacco smoke, etc.). We use non-thermal atmospheric plasma in a dielectric barrier discharge configuration and UV-induced photocatalysis for the treatment of polluted indoor air. The main advantage of using these two technologies is their capability to destroy and mineralize pollutants to inert gases, contrary to traditional filters that just trap them. We target to decompose chemical pollutants and pathogenic bio-aerosols, at high gas flow rates (>300 L/min) for a real scale use, which is the main challenge of this study.

1. Introduction

Indoor air contains many harmful components (chemical pollutants, bacteria, pathogenic aerosols, tobacco smoke, etc.) that can cause respiratory, cardiovascular, and oncological diseases under long-term exposure. Hospital-acquired infections are also spread through air contaminants [1]. Finding an innovative technology that would efficiently remove all kinds of airborne pollutants without producing harmful by-products and with a low energy cost would be not only a major advance for public health but would also help prevent the spread of airborne pathogens such as in the case of the recent COVID-19 pandemic. The goal of this work is to assess the efficacy of non-thermal plasma (NTP) dielectric barrier discharge combined with UV-A induced photocatalysis for the removal of volatile organic compounds (VOCs) and inactivation of aerosol-borne bacteria at a high gas flow rate. NTP and photocatalysis have proven their capabilities to decompose or inactivate a broad range of harmful compounds present in indoor air. Moreover, combining these two techniques may offer a very effective hybrid air decontamination device, as studies suggest a synergetic effect [2].

2. Experiment

We designed an indoor air decontamination device that combines a Dielectric Barrier Discharge (DBD) for the NTP generation (Fig. 1), and a TiO_2 coating which is activated on-demand by UV-A LEDs. The device uses a very short residence time of the pollutant in the reactor: the gas flow rate was set above 300 L/min and uses a single-pass method to determine the pollutant reduction.

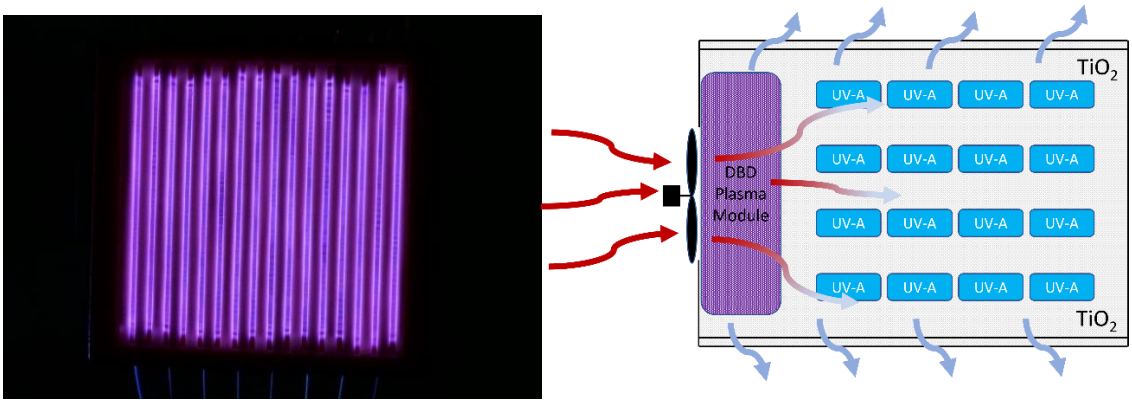

Fig. 1. Photo of the DBD module and schematic of the air decontamination device combining DBD and UV-A induced photocatalysis.

The chemical analysis of the VOC contaminants (formaldehyde) and the gaseous species produced by the DBD was performed by FTIR absorption spectroscopy (Shimadzu IRSpirit-X spectrometer) using a 542 cm absorption path gas cell equipped with ZnSe windows. Single-pass of the bio-contaminated water aerosols through the reactor was set at a high gas flow rate (>300 L/min). The aerosol-borne bacteria *E. coli* and *S. aureus* were collected on Petri dishes for 30 seconds and evaluated by microbiological thermostatic cultivation.

3. Results and discussion

The removal efficiency of about 40% was reached for the formaldehyde concentration, as shown in Fig. 2, and it slightly decreased with the air flow rate. We also monitored the concentration of ozone generated by the DBD, which is not desired for human exposure, thus it must be decomposed by the photocatalytic process before exiting the reactor.

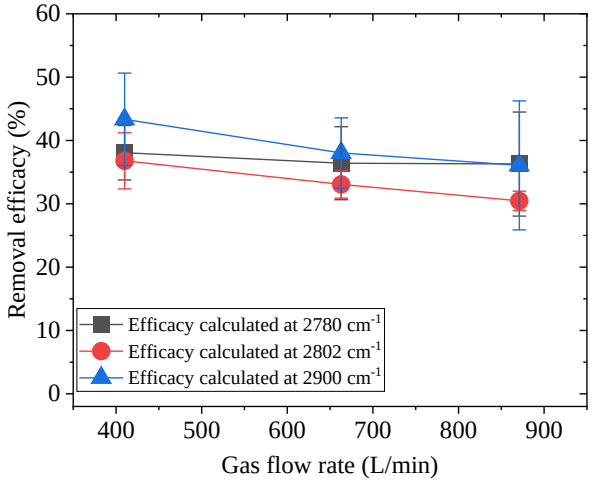

Fig. 2. Removal efficacy of formaldehyde (HCHO) in a single pass vs. gas flow rate, measured by infrared absorption spectra at three different wavenumbers typical for HCHO absorption.

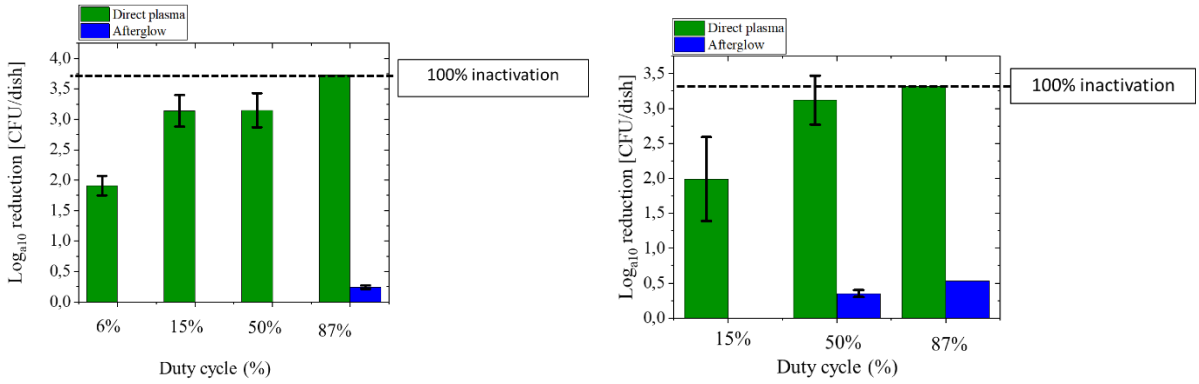

Fig. 3. DBD effects on water aerosol-borne *E. coli* (left) and *S. aureus* (right) bacteria at various duty cycles of the power supply.

The obtained results of the decontamination of bio-aerosols are also very promising. We reached 3,73 log (99.98%) and 3,32 log (99.95%) reduction for the inactivation of water aerosol-borne *E. coli* and *S. aureus,* respectively. 100% inactivation for both bacteria was achieved with a power supply duty cycle set at 87%, and high inactivation was achieved even at a low duty cycle with lower ozone production [3].

4. Conclusions

We developed a new design for indoor air decontamination allowing for better efficacy of air chemical (formaldehyde) and biological (*E. coli* and *S. aureus* bacteria) contaminants. It employs combined effects of DBD plasma and UV-A activated TiO_2 photocatalysis. The device is applicable for high gas flow rates (>300 L/min). It enables complete mineralization of organic pollutants to H_2O and CO_2. As the NTP technology, it produces a strong oxidant ozone, which helps to remove the pollutants and pathogens. On the other hand, ozone is an undesirable product to be emitted into the indoor air, thus has to be removed by the photocatalytic effect. High inactivation of both organic chemical pollutants (40%) and airborne bio-pathogens (up to 100%) was achieved at a low specific input energy and very high gas flow rates. This combined NTP-photocatalysis technology can be applied in all sorts of indoor settings, including hospitals and public spaces, as well as in potential manned space missions.

5. Acknowledgments

This work was funded by the EU NextGenerationEU through the Recovery and Resilience Plan for Slovakia under the project No. 09I03-03-V03-00033 and by the Slovak Research and Development Agency grants APVV-22-0247, APVV-17-0382, and APVV-20-0566.

6. References

[1] Sikora A, Zahra F. Nosocomial Infections. StatPearls Publishing; 2024
[2] Zhang Y et al. 2022, *Catalysis Communications* 172, 106535
[3] Vazquez T, Lavrikova A, Wiederman D, Babic J, Machala Z. 2025, *J. Electrostat., under preparation*

ELECTRICAL DISCHARGES IN CAPILLARY TUBES AND HONEYCOMB MONOLITHS

Karol Hensel, Gokul Selvaraj, Richard Cimerman, Mário Janda

Division of Environmental Physics,
Faculty of Mathematics, Physics and Informatics, Comenius University, Bratislava, Slovakia
E-mail: hensel@fmph.uniba.sk

Summary of our results on generation of discharges in glass capillary tube(s) and ceramic honeycomb monolith. Reactor and materials of various geometry, several power supplies of both polarities were tested. Electrical and optical diagnostic of the discharges was performed, and their chemical activity tested.

1. Summary

Atmospheric pressure plasmas generated by electrical discharges are often used for air pollution control. The common discharge types are corona and dielectric barrier discharges (DBD) generated in gases or on dielectric surfaces. They can be also generated inside cavities and pores of materials, such as foams, pellets, beads, or tubes [1]. It is very interesting from the point of view of plasma catalysis as the interaction of the plasma with (catalytic) materials can be utilized to enhance associated chemical processes.

This contribution summarizes the results on generation of discharges in a single capillary tube, a bundle of capillary tubes as well as ceramic honeycomb monolith. Electrical and optical measurements were performed in various geometry (diameter, length, cpi), feed gases (air, N2, O2, H2O) and power supplies (AC, DC, pulsed) of both polarities. Electrical diagnostics included oscilloscopic measurements and power consumption evaluation. The optical diagnostics included optical emission spectroscopy and measurements of discharge propagation velocity. Chemical activity was monitored by FTIR spectroscopy.

The discharge in a single capillary tube was investigated to understand a fundamental mechanism of its formation and propagation [2]. The propagation velocity increased with the decreasing tube diameter. It was found 4.3×10^7 and 9.9×10^7 cm/s for 1 and 0.2 mm diameter, respectively. Onset and breakdown voltages increased with the decreasing tube diameter, while stable discharge generation was improved by extending its length. Propagation velocity was higher for smaller tube diameters and higher O2 content. Tests with a bundle of capillary tubes were performed to assess the overall stability and spatial homogeneity of the discharge. The discharges were generated by a DC high voltage, eventually assisted by auxiliary AC driven discharges in a pellet bed [1] or in a multihollow DBD [3]. The homogeneity and the stability largely depended on the discharge polarity, ballasting resistor, and feed gas humidity. At last, the discharges generated directly in ceramic honeycombs of various geometry (length, cpi) were tested. They were also briefly subjected to the investigations of its plasma chemical activity (generation of O3 and NOx removal). Tentative results were quite promising and are expected to be further improved in systems with honeycombs supported by various catalysts.

The work was supported by Slovak Research and Development Agency grant APVV-20-0566 and Scientific Grant Agency VEGA grant 1/0822/21 and funded by the EU NextGenerationEU through the Recovery and Resilience Plan for Slovakia under the project No. 09I03-03-V04-00092.

2. References

[1] K. Hensel, Eur. Phys. J. D 54, 141 (2009)
[2] K. Hensel et al. XXXII ICPIG, Iasi, Romania (2015)
[3] R. Cimerman et al. Int. J. Plasma Environ. Sci. Technol. 15, e01003 (2021)

TRACE ELEMENTS DETECTION AND CF ELEMENTAL ANALYSIS OF WATER BY LIBS FOR ENVIRONMENTAL CONTROL- COMPARISON OF SURFACE ASSISTED, ACOUSTIC LEVITATION AND NE METHODS.

Pavel Veis[1], Jairo C. Peralta[1], Sanath J. Shetty[1], Matej Veis[1], Dhanada V.S. [1], Neelmani[1] and Ivan A. Urbina[1]

[1]*Faculty of Math., Phys. and Informatics, Comenius Univ., Mlynská dol. F2, 84248 Bratislava, Slovakia*
E-mail: pavel.veis@fmph.uniba.sk

Elemental analysis of water circulating in nature (e.g., water from springs, lakes, rivers, polluted groundwater near environmental contaminants, and wastewater released from factories) is highly important. Pure natural water primarily contains elements such as C, N, O, H, alkali metals, alkaline earth metals, and other trace elements essential for life. However, pollutants like heavy metals or other elements introduced through industrial environmental pollution may also be present (e.g., Cd, Pb). Monitoring these elements in groundwater is crucial for assessing water quality.
Laser-Induced Breakdown Spectroscopy (LIBS) is a method offering rapid detection and quantification of all elements present in natural water samples, including heavy metal pollutants, which is critically important for environmental protection and public health.
Elemental analysis of water samples using LIBS remains challenging due to issues such as splashing and plasma quenching by water products [1]. Several LIBS-based methods have been developed to address these challenges, such as surface-enhanced (SE) or surface-assisted (SA) LIBS, where liquid droplets are dried on a solid surface [2,3,4], or using absorption in zeolites to capture pollutants from water samples [5].
Acoustic levitation (AL) of isolated droplets, achieved by creating an ultrasonic standing wave in an acoustic resonator, is a sampling technique that enables LIBS analysis of liquids without contact with a solid substrate [6,7]. In this method, controlled evaporation using CW-IR laser radiation leads to the preconcentration of water samples around hundred times. Another method for enhancing the LIBS signal of water-based samples is nanoparticle (NP) enhancement (NE). This technique is often combined with SE or SA LIBS methods. Recently, our group used this approach to compare different beverages (drinking water, wine, beer) by employing varying concentrations of three different types of spherical metal nanoparticles (Au, Ag, Cu) [8]. Additionally, NE-LIBS combined with AL was utilized in our group to analyze heavy metals (Cd, Pb) in water using Ag nanoparticles.
These two liquid LIBS analysis methods (SA LIBS and LIBS AL), both with and without NP enhancement, will be compared for the elemental analysis of various types of water- and alcohol-based liquids using time-resolved, broadband UV-NIR Echelle-based spectroscopy. Recent results regarding the limit of detection (LOD) for boron in water samples using the LIBS AL method will also be presented [9].

Acknowledgement. Funded by the EU NextGenerationEU through the Recovery and Resilience Plan for Slovakia under the project No. 09I03-03-V03-00033.

References

[1] Keerthi K, Unnikrishnan V K, et al., *Optics and Laser Technology* **147** (2022) 107622.
[2] Aguirre M A, Legnaioli S, Palleschi V, et al *Elemental analysis by SE LIBS*…, SCAB **79–80** (2013) 88.
[3] Bocková J, Veis P, Yu J, et al. *Determination of Metal Elements in Wine…*Appl. Spectr. **71**(2017) 1750.
[4] Bocková J, Marín Roldán A, Yu J, Veis P, Applied Optics **57** (2018) 8272.
[5] Horňáčkova M, Veis P, et al. *Heavy Metals Detection in Zeolites Using LIBS…*, Atoms **7** (2019) 98.
[6] Peralta J, et al., *Opt Lett*, **43** (2018) 2260.
[7] Peralta J, Veis P, et al., *LIBS signal enhancement from liquids… ,Proc. LIBS conf*. Bari 2022
[8] Dhanada V S, Neelmani, Veis P et al, to be published.
[9] Shetty S J, Peralta J, Urbina I A, Veis P, et al, *submitted* in SCAB 2024.

THE EFFECT OF NITROGEN ADDITION TO ARGON ON THE Ar $1s_5$ AND $1s_3$ METASTABLE ATOM DENSITIES AND Ar SPECTRAL EMISSION IN A CAPACITIVELY COUPLED PLASMA

Z. Donkó[1,4], P. Hartmann[1], Ts. V. Tsankov[2], U. Czarnetzki[3], F. J. Arellano[4], S. Hamaguchi[4]

[1]*HUN-REN Wigner Research Centre for Physics, Budapest, Hungary*
[2]*Laboratoire de Physique des Plasma (LPP), CNRS, Sorbonne Universite, École Polytechnique, Institut Polytechnique de Paris, Palaiseau, France*
[3]*Ruhr University Bochum, Faculty of Physics and Astronomy, Experimental Physics V, Germany*
[4] *Division of Materials and Manufacturing Science, Graduate School of Engineering, Osaka University, 2-1 Yamadaoka, Suita, Osaka, 565-0871 Japan*
Email: donko.zoltan@wigner.hun-ren.hu

The effect of nitrogen admixture to argon gas, on the densities of the Ar $1s_5$ and $1s_3$ metastable atoms and the intensities of Ar 2p→1s spectral lines (in Paschen notation) radiated by a capacitively coupled plasma is investigated experimentally and by a coupled particle simulation of the discharge and a fluid model for the excited Ar atoms that includes radiative transitions.

1. Introduction

Light emission is a basic property of electrical discharges that can be used to reveal information about the plasma characteristics, like the electron density and the electron temperature, provided that a connection between certain spectral line intensities or their ratios and these properties is established. In our previous studies, we have used a collisional-radiative model (CRM) to predict line intensities in an Ar capacitively coupled plasma (CCP) based on the computation of the electron density and the electron energy probability function (EEPF) using particle-in-cell / Monte Carlo collisions (PIC/MCC) simulation [1]. Subsequently, we have realized an iterative solution of (i) a PIC/MCC simulation extended by electron-impact processes between 30 excited Ar levels [2] to compute all electron-impact reaction rates and (ii) a diffusion-reaction-radiation (DRR) model to derive the densities of the Ar atoms in the various excited levels based on the rates obtained in the PIC/MCC simulation [3]. The simulation model has been experimentally validated based on measurements of the spatial distributions of the Ar $1s_5$ metastable atoms at various conditions [2]. In the present study both the experiments and simulations are extended to gas mixtures containing small amounts of nitrogen. The effect of this admixture on the characteristics of a capacitively coupled plasma is investigated, including the densities of the Ar metastable atoms as well as the intensities of the spectral lines belonging to the 2p→1s system of Ar.

2. Experimental setup

The discharge cell, situated inside a vacuum chamber, is composed of two flat disc stainless steel electrodes placed 4 cm apart. The plasma is created with a 13.56 MHz Tokyo HY- Power RF-150 generator and using a Tokyo HY-Power MB- 300 matching network, see figure 1. The peak-to-peak value of the RF voltage is fixed at V_{pp} =300 V and the results are reported for a gas pressure range of 2.5 – 40 Pa, for N_2 contents between 0% and 5%. The Ar $1s_5$ and $1s_3$ metastable atom densities and the gas temperature are determined using Tunable Diode Laser Absorption Spectroscopy. We measure the absorption on the Ar(1s5 → 2p6) transition at a wavelength of 772.376 nm and on the Ar(1s3 → 2p2) transition at wavelength of 772.421 nm using a laser diode of type Toptica LD-0773-0075-DFB-1 driven by a control unit Toptica DLC DFB PRO L. The laser light passes through the plasma along its diameter, at the middle of the electrode gap and is detected at the other side of the chamber by a

photodiode. To perform proper background subtraction, detector signals were recorded with and without discharge, both with laser on and off states. Assuming dominating Doppler broadening, the amplitude of the absorption provides information about the line-integrated metastable atom density, while the width of the line conveys information about the gas temperature.

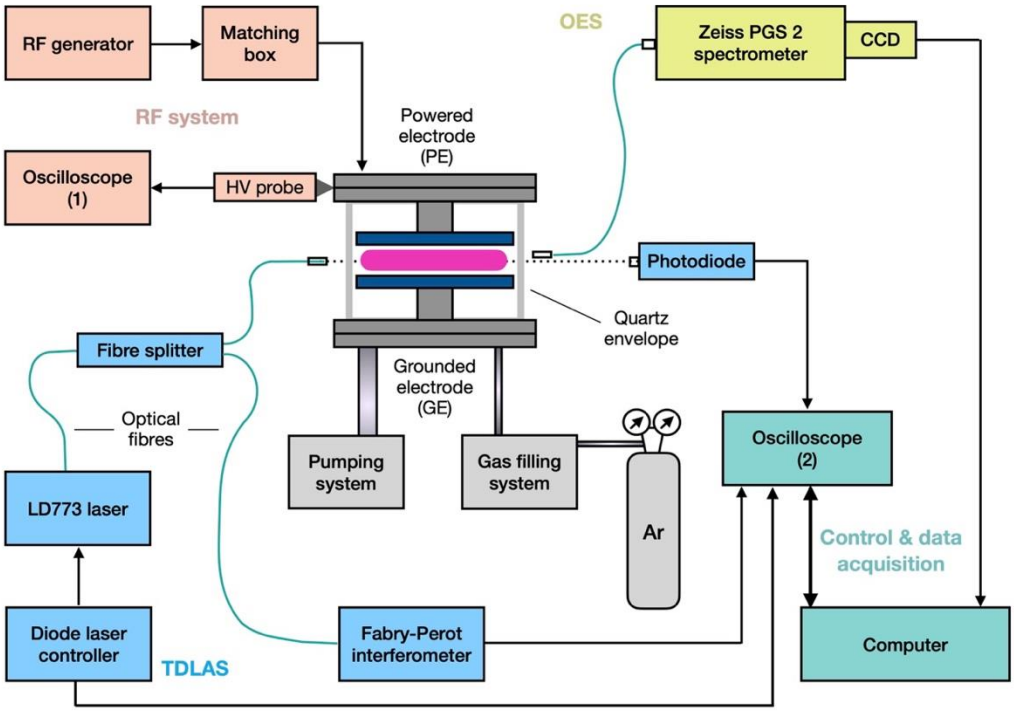

Fig. 1. The scheme of the experimental system [2].

For the intensity measurements of the 2p→1s Ar transitions we use a Carl Zeiss Jena PGS-2 spectrometer equipped with a Greateyes ELSEs 2k512 BI UV3 detector. Light emitted from the central, ≈1 cm-diameter region of the plasma is captured with an optical fiber oriented perpendicularly to the principal axis of the discharge. Relative sensitivity calibration of the system is performed with an RS-15 Total Flux Calibration Light Source having a certified calibration report (that specifies the radiant flux of the lamp as a function of the wavelength in the range between 300 nm and 1100 nm) provided by Gamma Scientific.

3. Computational model

The numerical studies are based on a hybrid computational framework [1,2] that was originally developed for pure Ar gas. It consists of (i) a Particle-in-Cell / Monte Carlo Collisions (PIC/MCC) code that includes Ar atoms in several excited levels in addition to the ground-state Ar atoms as targets for electron-impact collisions, thereby accounting for all direct and stepwise excitation and ionization, as well as de-excitation electron collisions, and (ii) a Diffusion-Reaction-Radiation (DRR) code that solves the diffusion equations of Ar atoms in the excited levels, considering their sources and losses, which includes the rates of the electron-impact processes (obtained in the PIC/MCC module) as well as the rates of the radiative transitions between the various levels. The two modules are executed iteratively.

Here, this model is extended: the PIC/MCC simulation part of the computational framework contains as well electron-N_2 molecule collisions, collisions of N_2^+ ions with N_2 and Ar, as well as of Ar^+ ions with N_2 molecules. In the DRR part of the model, quenching reactions of N_2 with Ar $1s_5$ and $1s_3$ metastable atoms are incorporated with rate coefficients adopted from [4].

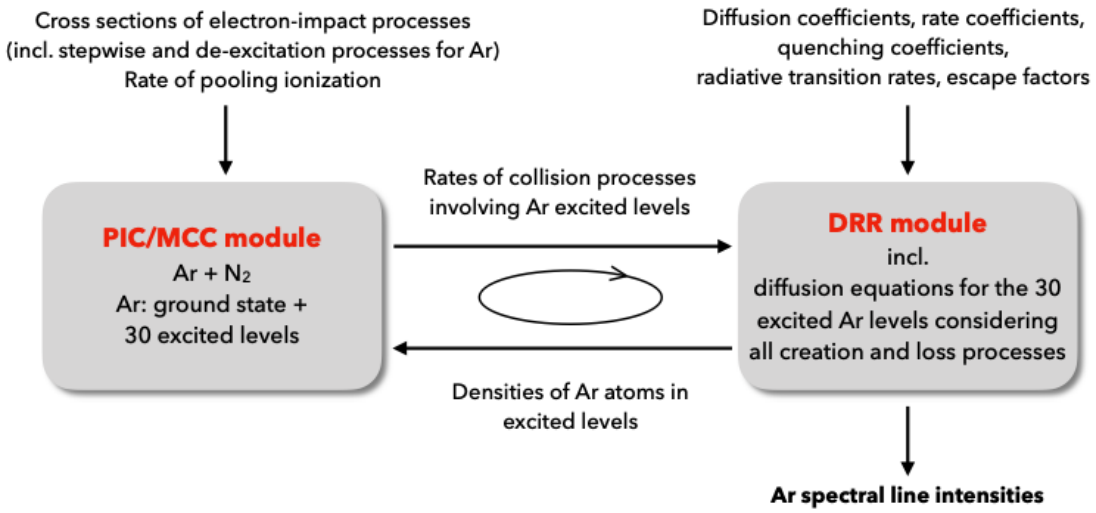

Fig. 2. The scheme of the computational framework [3].

4. Results

Figure 3 shows the results of the TDLAS measurements and the numerical calculations for the Ar $1s_5$ and $1s_3$ densities at the center of the plasma, as a function of pressure and N_2 content of the gas. In pure Ar discharges and at low pressure, the densities of both metastable species increase with pressure. With further increase of the pressure, their densities slightly decrease. This is due to the development of a dip of the density in the center as production of the excited species moves nearer to the electrodes with increasing pressure (see [2]). The Ar $1s_5$ atom density is approximately an order of magnitude higher as compared to the Ar $1s_3$ atom density. The effect of N_2 content increases with increasing pressure, at 2.5 Pa, the metastable atom densities decrease only by about a factor of 2 when the N_2 content reaches 5%, but at 40 Pa pressure, this decay amounts about two orders of magnitudes.

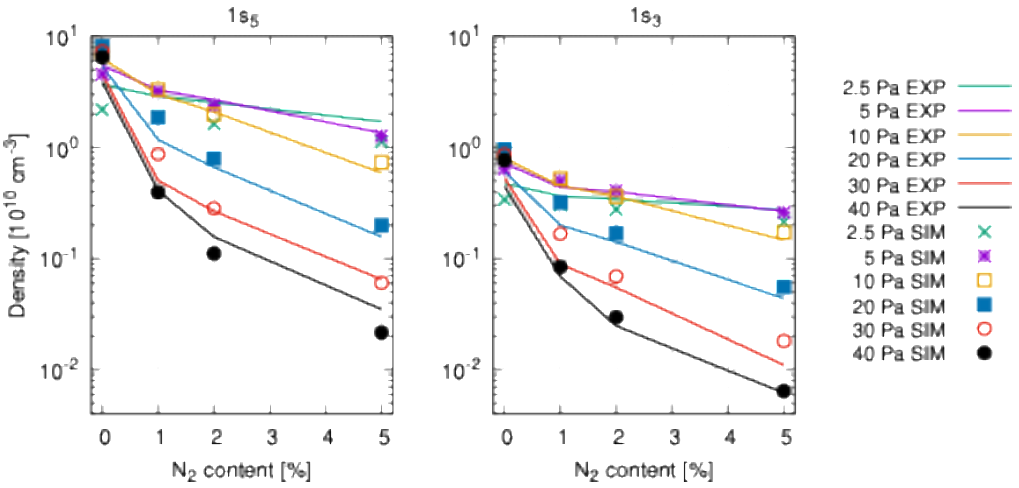

Fig. 3. Experimental ("EXP") and computational ("SIM") results for the dependence of the densities of Ar metastable species on the N_2 admixture concentration.

The intensity distributions of a subset of Ar 2p→1s spectral lines, obtained in the experiments and derived from the modeling calculations are displayed in figure 3, for various pressures and nitrogen contents. The measured line intensities are normalized as $I_\lambda = I_{\lambda,\,meas} / \Sigma\, I_{\lambda,\,meas}$, i.e., we ensure that the intensities add up to one. The same normalization is also applied to the calculated intensities.

The increasing N_2 content has different effect on individual lines, e.g. (i) the 750.4 nm line exhibits an increasing relative intensity, (ii) for the 811.5 nm line we observe the opposite effect: the intensity

decreases, (iii) the 763.5 nm line shows an increasing intensity at low pressure and is nearly the same intensity at higher pressure, regardless of the N_2 content in the gas. These changes are closely linked to the varying contributions of the direct / stepwise excitation processes: the 750.4 nm line is primarily excited by direct electron impact of the ground-state Ar atoms, while the 811.5 nm line is known to be preferentially excited by stepwise excitations under the conditions when an appreciable amount of metastable Ar atoms is present. As the density of metastable atoms is strongly decreased with increasing N_2 concentration, the stepwise excitation processes become less important, leading to a decrease of the intensities of spectral lines that are preferentially excited via this channel. This explains the behavior of the 811.5 nm line observed. The increase of the intensity of the 750 nm line is a consequence of the decrease of the intensities of other lines since we use normalized intensities. The experimental and computational line intensities show quite good agreement over the whole range of pressures and nitrogen contents.

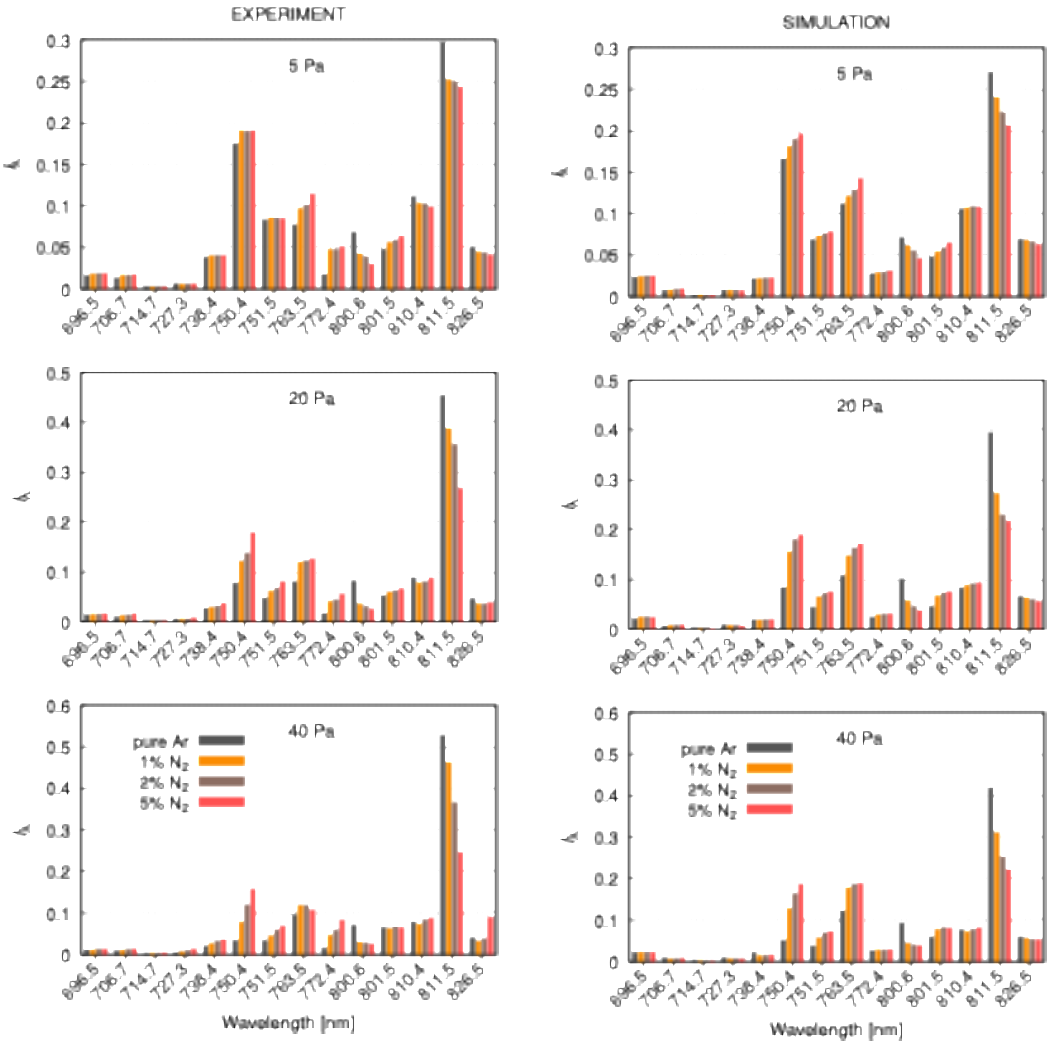

Fig. 4. Measured (left) and computed (right) relative intensities of Ar 2p→1s spectral lines at the center of the discharge, for various pressures and nitrogen contents.

5. Conclusion

A capacitively coupled radio-frequency discharge in Ar and in Ar-N_2 mixtures was investigated both experimentally and computationally. The densities of Ar metastable species and the intensities of Ar 2p→1s spectral lines were compared, as a function of the N_2 admixture concentration. A good agreement was found for both of these characteristics. N_2 was found to lead to a decay of the densities of the Ar metastable species, due to the modification of the electron energy distribution function and

due to the direct quenching reaction with these species. The intensities of the individual spectral lines were found to be influenced to different extents by the metastable atom densities, therefore the (relative) intensities of various lines follow specific trends as the N_2 admixture concentration increases.

6. Acknowledgments

This work was supported by the National Office for Research, Development and Innovation (NKFIH, Hungary) via Grant K134462, The Japan Ministry of Education, Culture, Sports, Science and Technology (MEXT) and the Japan International Cooperation Agency (JICA) Innovative Asia. Z D and S H are grateful for being supported in part by the Mercator Fellowship program within the SFB1316 'Transient atmospheric plasmas: from plasmas to liquids to solids' as well as Osaka University International Joint Research Promotion Programs (Type A+), the Japan Society of the Promotion of Science (JSPS) Grants-in-Aid for Scientific Research(S) 15H05736 and (A) 21H04453, JSPS Core-to-Core Program JPJSCCA2019002, and Japan Science and Technology Agency (JST)'s 'Adopting Sustainable Partnerships for Innovative Research Ecosystem (ASPIRE)' Grant Number JPMJAP2321. Ts V Ts and U C acknowledge support within the SFB1316 'Transient atmospheric plasmas: from plasmas to liquids to solids'.

7. References

[1] Arellano F J, Gyulai M, Donkó Z, Hartmann P, Tsankov Ts V, Czarnetzki U, Hamaguchi S 2023 *Plasma Sources Science and Technology* **32** 125007.

[2] Donkó Z, Hartmann P, Korolov I, Schulenberg D, Rohr S, Rauf S, Schulze J 2023 *Plasma Sources Science and Technology* **32** 065002.

[3] Donkó Z, Tsankov Ts V, Hartmann P, Arellano F J, Czarnetzki U, Hamaguchi S 2024 *Journal of Physics D: Applied Physics* **57** 375209.

[4] Le Calvé J, Gutcheck R A, Dutuit O 1977 *Chemical Physics Letters* **47** 470.

PLASMA TECHNOLOGY AS AN EFFICIENT TOOL TO IMPROVE SEED GERMINATION AND PROVIDE ADHESION OF PROTECTIVE POLYMER COATINGS ON SEEDS

Petra Šrámková, Anna Zahoranová

Department of Experimental Physics, Faculty of Mathematics, Physics and Informatics, Comenius University Bratislava, Mlynská dolina, 842 48 Bratislava, SR
E-mail: petra.sramkova@fmph.uniba.sk

In agricultural research, the application of non-thermal plasma (NTP) to seeds leads to an improvement in germination and viability and has a decontaminating effect on undesirable microorganisms on the seed coat. In addition, plasma activation leads to higher wettability and thus better adhesion of dressings or pesticides to the naturally hydrophobic seed coat. We used this strategy to apply a special polysaccharide coating to the seed surface, which gradually supplies the seeds with water in the early germination stage. This contribution gives an insight into the experimental concept and describes our motivation and hypotheses. In addition, the first results of the application of plasma to seeds are presented.

Seed coating is a common pre-sowing process in which the seed is covered with auxiliary materials to improve handling, protection and nutrient delivery[1]. Many different chemicals and additives must be used in this process to achieve the correct coating. Besides different fertilizers and pesticides, additives called "binders" with adhesive properties are used to ensure proper adhesion of these active ingredients to the seed surface and their retention. However, the negative impact of all employing synthetic substances on the environment is alarming and it is important to minimise their use. This can be achieved through the adoption of innovative green technologies such as plasma treatment[2]. Irradiating the seeds with non-thermal plasma (NTP) leads to an improvement in germination and viability and, in addition, the plasma has a decontaminating effect that minimises unwanted microorganisms on the seed coat. It was already demonstrated that the treatment of seeds with dielectric barrier discharge under optimal conditions can reduce the amount of fungicide used 50-90% without affecting the physiology of the seed[3].

In very similar way we aim to use plasma treatment of seeds to activate their waxy-like, hydrophobic surface to enable adhesion of the applied superabsorbent polymer (SAP) to eliminate the use of binders and fillers in seed coating. Plasma, as a very effective, non-invasive and environmentally friendly tool, can efficiently improve the adhesion of the applied SAP and create a porous layer capable of storing large amounts of water on the surface of the seed. The SAPs most used in agriculture are polyacrylates and polyacrylamides, which degrade very slowly in the soil and therefore pose a significant environmental risk[4]. To minimise the environmental impact, our partial goal is to develop polysaccharide-based SAPs that degrade naturally.

So far, we have analysed and compared two different plasma sources operating at atmospheric pressure in ambient air and their effects on model seeds - diffuse coplanar surface barrier discharge (DCSBD) and Piezobrush PZ3. DCSBD has been widely studied in agricultural research for treatment of various seed types[5,6], while Piezobrush PZ3 was used for seed treatment for the first time. Our contribution summarizes the whole experimental concept, describes our motivation and hypotheses and presents the first results.

Funded by the EU NextGenerationEU through the Recovery and Resilience Plan for Slovakia under the project No. 09I03-03-V04-00143.

References

[1] Pedrini S, Merritt D J, Stevens J and Dixon K 2017 *Trends Plant Sci.* **22**, 106–116.
[2] Bilea F, Garcia-vaquero M, Magureanu M *et al.* 2024 *Crit. Rev. Plant Sci.* **43**, 428–486.
[3] Hoppanová L, Medvecká V, Dylíková J *et al.* 2020 *Acta Chim. Slovaca*, **13**, 26–33.
[4] Wilske B, Bai M, Lindenstruth B *et al.* 2014 *Environ. Sci. Pollut. Res.* **21** 9453–9460.
[5] Zahoranová A, Henselová M, Hudecová D *et al.* 2016 *Plasma Chem. Plasma Process.* **36** 397.
[6] Tomeková J, Švubová R, Slováková Ľ *et al.* 2024 *Plasma Chem. Plasma Process.* **44** 487–507.

MOLECULAR DYNAMICS SIMULATIONS OF SILICON NITRIDE ATOMIC-LAYER DEPOSITION OVER A NARROW TRENCH STRUCTURE

Abdullah Y. Jaber, Jomar U. Tercero, Tomoko Ito, Kazuhiro Karahashi,

Kazumasa Ikuse, Michiro Isobe, and Satoshi Hamaguchi

Division of Materials and Manufacturing Science,
Graduate School of Engineering, Osaka University
E-mail: hamaguch@ppl.eng.osaka-u.ac.jp

MD simulations for PE-ALD processes of SiN over a trench structure are performed when the gap is closing and the two facing sidewalls are approaching each other. The transport of gaseous species in a closing gap is typically described as Knudsen diffusion, but when the gap distance approaches the atomic scale, the transport becomes closer to diffusion in solids.

1. Background

Molecular dynamics (MD) simulations were performed to study the surface reaction mechanisms in plasma-enhanced atomic layer deposition (PE-ALD) of silicon nitride (SiN). In a typical SiN PE-ALD process, silicon (Si) and chlorine (Cl) containing precursors such as dichlorosilane (DCS) SiH_2Cl_2 are adsorbed on the surface in the first half-cycle, and then, in the second half-cycle, Cl atoms are removed and SiN is formed by the exposure to nitrogen (N_2) / hydrogen(H_2) or ammonia (NH_3) plasmas.[1] In the first half-cycle, the precursor adsorption is self-limiting due to the surface termination by Cl atoms. In the subsequent half-cycle, the plasma-based process removes Cl atoms from the surface and terminates it with N and H atoms. An earlier study [2] experimentally examined the Cl removal process in the second half cycle, focusing on Cl-passivated Si surfaces, rather than Cl-terminated SiN surfaces, with incident N_2^+ ions using ion beam experiments. Accompanying molecular dynamics (MD) simulations also reproduced the experimental observations with high accuracy. Furthermore, the MD simulations also showed that H radicals played the dominant role in removing Cl atoms by forming HCl molecules.

2. SiN ALD over a trench structure

Extending the earlier study of SiN ALD over a flat Si surface, we performed MD simulations for PE-ALD processes of SiN over a trench structure when the gap is closing and the two facing sidewalls are approaching each other. Under such conditions, H radicals generated by the plasma in the second half-cycle must be transported through the closing gap and reach the bottom of the trench to remove Cl atoms left over in the preceding half-cycle. The simulation results of the gas-phase transport in such a narrow gap show that the transport changes from Knudsen diffusion to diffusion in a solid material.

3. References

[1] K. Arts, S. Hamaguchi, T. Ito, K. Karahashi, H. C. M. Knoops, A. J. M. Mackus, and W. M. M. E. Kessels, “Foundations of atomic-level plasma processing in nanoelectronics,” Plasma Sources Sci. Tech., 31, 103002 (2022).

[2] T. Ito, H. Kita, K. Karahashi, and S. Hamaguchi, “Low-energy ion irradiation effects on chlorine desorption in plasma-enhanced atomic layer deposition (PEALD) for silicon nitride,” Jpn. J. Appl. Phys. 61 SI1011 (2022).

STABILITY OF METAL-ORGANIC FRAMEWORKS IN NON-THERMAL ATMOSPHERIC PLASMA

Alexander Quack[1], Hauke Rohr[2], Kerstin Sgonina[1], Norbert Stock[2,3], Jan Benedikt[1,3]

[1]*Institute of Experimental and Applied Physics, Kiel University*
[2]*Institute of Inorganic Chemistry, Kiel University*
[3]*Kiel Nano, Surface and Interface Science (KINSIS), Kiel University*
E-mail: benedikt@physik.uni-kiel.de

The stability of nine metal-organic frameworks (MOFs) in direct contact with non-thermal atmospheric plasma has been thoroughly tested at several temperatures and prolonged times. These MOFs have been carefully selected to test the effect of the MOF morphology and the selection of the metal centers and organic linkers on their stability. The set of stable MOFs have been identified as potential candidates for catalyst development.

1. Introduction

MOFs are a relatively new class of porous crystalline materials combining metal centers connected by organic linkers and offer large flexibility regarding their composition, porosity and large surface area and they are studied to be used for example in CO_2 capture or conversion [1]. Several works utilizing MOFs in the plasma catalysis processes have been published recently [2,3] indicating that MOFs are compatible with reactive plasmas, profiting from their low operation temperature. However, the MOF stability in NAP has not yet been studied in a systematic way.

2. MOF Stability study

Therefore, a dielectric barrier discharge (DBD) reactor (Fig. 1) has been developed to enable the characterization of the MOF interaction with plasma in H_2/N_2 or H_2/CO_2 mixtures. The plasma has been operated at 10-17 kV_{pp}/21 kHz with heating up to 200 °C. The used system is designed with a large contact area between plasma and MOF and without a necessity to use pellets. The gas exhaust is analyzed by mass spectrometry. A transparent electrode (indium tin oxide) enables to monitor the plasma operation during the treatment. Nine MOFs have been treated by plasma: **ZIF 8** $[Zn(C_4H_5N_2)_2]$, **ZIF 67** $([Co(C_4H_5N_2)_2])$, **MAF 5** $([Zn(C_5H_7N_2)_2])$, **MAF 6** $([Zn(C_5H_7N_2)_2])$, **ZIF-7** $([Zn(C_7H_5N_2)_2]\cdot 1DMF)$, **ZIF 71** $([Zn(C_3HCl_2N_2)_2])$, **CAU 10** $([Al(OH)(m\text{-}H_2BDC)]\cdot nH_2O)$, **CAU 24** $([M_6O_4(OH)_8(H_2O)_4(TCPB)_2]$, M=Ce/Zr), **UiO 66** $([Zr_6O_4(OH)_4(p\text{-}BDC)_6]\cdot nH_2O)$. Their stability has been studied by performing powder X-ray diffraction (XRD), sorption measurements, IR absorption spectroscopy and elemental analysis before and after the treatment.

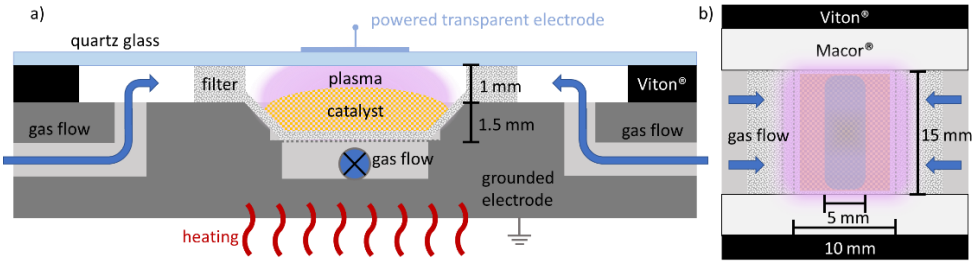

Fig. 1. Sketch of the used DBD reactor.

3. References

[1] J. Gandara-Loe *et al.*, React. Chem. Eng. **6** (2021) 787
[2] H. Chen *et al.*, AIChE Journal. **66** (2020) e16853
[3] F. Gorky *et al.*, ACS Appl. Mater. Interfaces **13** (2021) 21338

PLASMA PROCESSING OF POLYMER NANOFIBERS FOR ENHANCED IMMOBILIZATION OF LIGNIN NANO/MICROPARTICLES

L. JANŮ[1], N. SOUAWDA[1], M. JANŮŠOVÁ[1], J. MEDALOVÁ[2], P. RYŠÁNEK[3], D. DUDAY[4], J. S. THOMAN[4], R. ANAND[4], D. COLLARD[4], L. ZAJÍČKOVÁ[1,5]

[1]*CEITEC, Brno University of Technology, Brno, Czech Republic*
[2]*Dept of Experimental Biology, Faculty of Science, Masaryk University, Brno, Czech Republic*
[3]*J. E. Purkyně University, Ústí nad Labem, Czech Republic*
[4]*Luxembourg Institute of Science and Technology (LIST), Luxembourg*
[5]*Dept. Condensed Matter Phys., Faculty of Science, Masaryk University, Brno, Czech Republic*
E-mail: lenkaz@physics.muni.cz

We report different plasma modifications of polycaprolactone nanofibrous (NF) mats, treatment in oxygen plasma and deposition of amine or carboxyl plasma polymer films, with the aim to create a surface promoting the adhesion of lignin nano/microparticles. The plasma-processed mats and the mats soaked in solutions with differently sized lignin particles were investigated by X-ray photoelectron spectroscopy and electron scanning microscopy. Even untreated NF mats proved to have a capability to immobilize lignin particles. However, washing the mats with lignin particles proved that plasma polymer coatings have significant advantage of creating stable bonds with lignin.

1. Introduction

The advantage of polymer nanofibers forming nonwoven mats is their large surface area, high porosity, and good pore interconnectivity. It makes them highly suitable as base materials for delivery of active substances, filtration, or as breathable dressings. Processing of synthetic polymers overcomes the complexities associated with natural polymeric materials; however, synthetic materials exhibit low surface free energy and inertness. In the case of biomedical applications, a surface modification leading to improved wettability is needed [1,2]. If nanofibers are used as a matrix for delivering drugs or nano/micro-particles added after the nanofiber synthesis, the surface chemistry has to be tuned for a reactivity enabling immobilization of desired compounds or particles on the surface [3].

Previously, we demonstrated a successful modification of nanofibrous mats by coating them with nitrogen or oxygen-containing plasma polymers [4,5]. Such coatings can be efficiently used for immobilization of biomolecules as demonstrated by the construction of biosensors [6,7] or covalent binding the platelet-rich blood plasma [8]. Here, we take the advantage of combining polymer nanofibrous mats with such reactive surfaces for immobilization of lignin nano/microparticles. It is motivated by a high abundance of lignin that is renewable phenolic biopolymer with versatile chemistry, exhibiting antibacterial, antioxidant, anti-inflammatory and UV-blocking properties. Moreover, technologies allowing synthesis of lignin micro or nanoparticles enhanced the potential lignin applications, providing advantages over the bulk material.

2. Experimental Details

The plasma modifications were carried out in the low-pressure capacitively coupled radio frequency discharges (13.56 MHz) ignited between two parallel plate electrodes inside the stainless steel chamber. The substrates, i.e. polymer nanofibrous mats and polished Si pieces, were placed on the bottom electrode connected to the radio frequency (RF) generator via a matching box containing a capacitor, blocking the DC current through the circuit.

A large plasma reactor (R2) was used for plasma polymerization from cyclopropylamine (CPA) vapors (2 sccm) mixed with argon (28 sccm). In this case, the bottom RF electrode was 420 mm in diameter.

The RF power was 100 W and the discharge was operated in the pulsed mode using the duty cycle of 33 % and the repetition frequency of 500 Hz. The pressure was 50 Pa. Before the deposition, NFs were sputter-cleaned in Ar discharge of similar parameters for 5 min.

The oxygen plasma treatment and plasma polymerization from CO_2/C_2H_4 gas mixture were carried out in a smaller plasma reactor (R4) with parallel plate electrodes, 210 mm in diameter. To limit the etching, the pressure during the oxygen treatment was as high as 50 Pa. The discharge was ignited at 20 W.

The deposition from CO_2/C_2H_4 in R4 was performed accordingly to previously proposed double layer by Hegemann *et al.* [9]. The highly cross-linked base layer was prepared at the RF power of 70 W and 2:1 CO_2:C_2H_4 ratio. Then, a less crosslinked layer with more functional groups was deposited on the top at 20 W and 6:1 CO_2:C_2H_4 ratio. The pressure was kept at 10 Pa. Before the deposition, NFs were sputter-cleaned in an Ar discharge at 50 W for 5 min.

Polycaprolactone (PCL) nanofibrous mats were electrospun from the PCL dissolved in a 2:1 mixture of acetic and formic acids (14 wt.%) with INOSPIN Mini device (Inocure, Praha, Czech Republic) based on needle spinning. The electrospinning conditions have been optimized previously by Kupka *et al.* [10] and adapted to INOSPIN Mini device. The applied voltage was +40 kV on the needle and -10 kV on the collecting electrode. The electrode distance was 155 mm. The nanofibers (NFs) were collected on a polypropylene nonwoven textile placed on the collecting electrode - a cylinder rotating with the speed of 20 rpm.

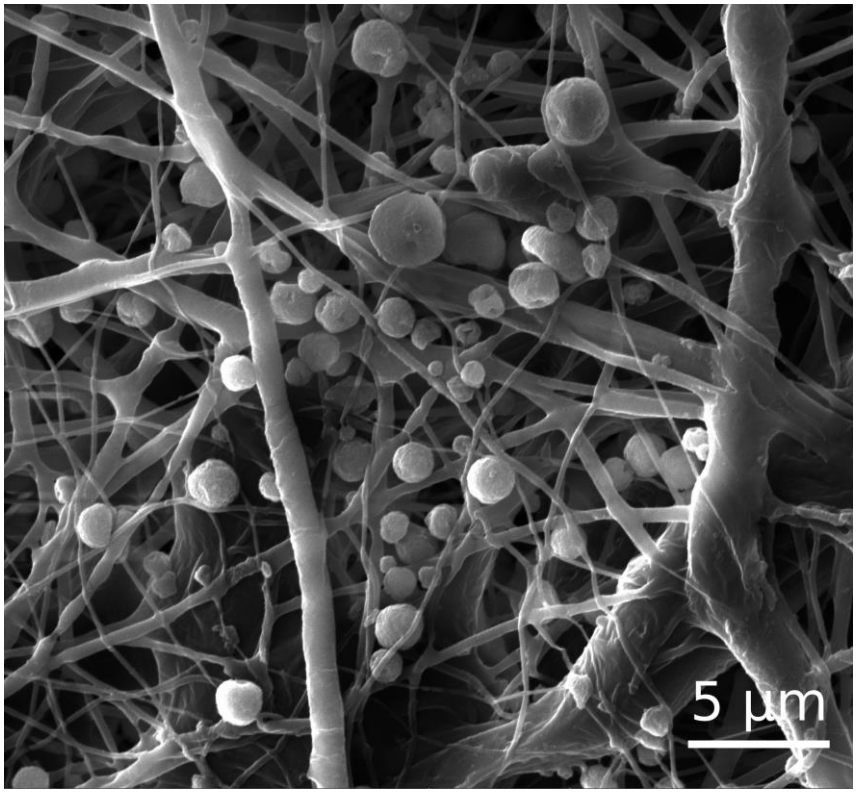

Fig. 1. Plasma-processed polymer nanofibers with immobilized lignin microparticles.

The immobilization of lignin particles on pristine and plasma-modified PCL mats was performed by a wet process employing colloid of lignin particles dispersed in distilled water. NF mats were soaked in

the colloid for a short time (about 5 s), pulled out, and let dry. The materials were investigated with scanning electron microscopy (SEM) and X-ray photoelectron spectroscopy before and after washing.

3. Results and Conclusions

Plasma treatment in oxygen discharge had to be carefully tuned not to melt and etch the NF mat structure. Treatment time of 2 min was evaluated as a trade-off condition between too high damage and induced surface changes by the formation of additional oxygen-containing groups on the PCL surface. Although the change of the elemental composition obtained by XPS was only minor, the pronounced change was detected by water contact angle. SEM revealed roughening of the NF surfaces due to plasma etching.

The deposition time of amine PP from CPA/Ar was set to 47 min to achieve 250 nm thick film on the Si substrate. The deposition time for the bottom cross-linked layer from CO_2/C_2H_4 was 5 min, followed by 1 min deposition of top functional layer. It led to 80 nm thick film in total on the Si substrate. Untreated nanofibers had an average diameter of 240 ± 10 nm. In both deposition experiments, the thicknesses of nanofibers increased but the not as much as expected from the film thickness on the flat Si. The side film thicknesses on the fibers were roughly 5x lower. Interestingly, particles of 460 ± 10 nm in diameter were created during CO_2/C_2H_4 deposition and were recognizably attached to NFs. Moreover, carboxyl-PP coated NFs exhibited pronounced wrinkled morphology which was not seen for amine-PP coated or untreated NFs. XPS analyses proved in both the depositions that PCL fibers were coated by the corresponding film.

Even untreated NF mats proved to have a capability to immobilize lignin particles. However, washing the mats with lignin particles proved that plasma polymer coatings have significant advantage of creating stable bonds with lignin.

4. References

[1] Bacakova, L., Filova, E., Parizek, M., Ruml, T., Svorcik, V. Modulation of cell adhesion, proliferation and differentiation on materials designed for body implants. *Biotechnol. Adv.* **29** (2011) 739.

[2] Nemcakova I., Blahová L., Rysanek P., Blanquer A., Bačáková L., Zajíčková L., Behaviour of Vascular Smooth Muscle Cells on Amine Plasma-Coated Materials with Various Chemical Structures and Morphologies, I*nternational Journal of Molecular Sciences* **21** (2020) 9467.

[3] Yoo H. S., Kim T. G., Park T. G., Surface-functionalized electrospun nanofibers for tissue engineering and drug delivery, *Advanced Drug Delivery Reviews*, **61**(12) (2009) 1033-1042.

[4] Manakhov A., Nečas D., Čechal J., Pavliňák D., Eliáš M., Zajíčková L., Deposition of stable amine coating onto polycaprolactone nanofibers by low pressure cyclopropylamine plasma polymerization, Thin Solid Films 581 (2015) 7-13

[5] Manakhov A., Kedroňová E., Medalová J., Černochová P., Obrusník A., Michlíček M., Shtansky D., Zajíčková L., Carboxyl-anhydride and amine plasma coating of PCL nanofibers to improve their bioactivity, Materials & Design 132 (2017) 257-265

[6] Makhneva E., Farka Z., Skládal P., Zajíčková L., Cyclopropylamine plasma polymer surfaces for label-free SPR and QCM immunosensing of Salmonella, Sens. Actuator B-Chem. 276 (2018) 447-455

[7] Makhneva E., Farka Z., Pastucha M., Obrusník A., Horáčková V., Skládal P., Zajíčková L., Maleic anhydride and acetylene plasma copolymer surfaces for SPR immunosensing, Anal. Bioanal. Chem. 411 (2019) 7689-7697

[8] Miroshnichenko S., Timofeeva V., Permykova E., Ershov S., Kiryukhantsev-Korneev P., Dvořáková E., Shtansky D., Zajíčková L., Solovieva A., Manakhov A., Plasma-Coated Polycaprolactone Nanofibers with Covalently Bonded Platelet-Rich Plasma Enhance Adhesion and Growth of Human Fibroblasts, Nanomaterials 9 (2019) 637-655

[9] Rupper, P., Vandenbossche, M., Bernard, L., Hegemann, D., and Heuberger, M., Composition and stability of plasma polymer films exhibiting vertical chemical gradients. Langmuir 33 (2017) 2340.
[10] Kupka V., Dvořáková E., Manakhov A., Michlíček M., Petruš J., Vojtová L., Zajíčková L., Well-Blended PCL/PEO Electrospun Nanofibers with Functional Properties Enhanced by Plasma Processing, Polymers 12(1403) (2020) 16.

ATMOSPHERIC PRESSURE CHEMICAL IONIZATION STUDY OF SULPHUR-CONTAINING COMPOUNDS BY ION MOBILITY SPECTROMETRY AND MASS-SPECTROMETRY

Ladislav Moravský[1,2], Arian Fateh Borkhari[1], Samuel Peter Kovár[1], Peter Papp[1], Alexey Yu. Adamov[2], Alexey A. Sysoev[2], Štefan Matejčík[1,2]

[1]*Department of Experimental Physics, Comenius University in Bratislava, 84248 Bratislava, Slovakia*
[2]*Molecular Physics Department, National Research Nuclear University, Moscow Engineering Physics Institute, 115409 Moscow, Russia*
E-mail: ladislav.moravsky@fmph.uniba.sk

To study the atmospheric pressure chemical ionization of selected sulphur-containing hydrocarbons Thiophene C_4H_4S, 2-Methyl thiophene C_5H_6S, and 2,5-Dimethyl thiophene C_6H_8S, in negative polarity the ion mobility spectrometry (IMS) and IMS combined with time-of-flight mass spectrometer (IMS-TOF MS) techniques were used in the dry air at 403 K drift gas temperature. The dominant reaction ions (RI) were $CO_3^-(H_2O)_{0,1}$, $CO_4^-(H_2O)_{0,1}$ and $O_2^-(H_2O)_{1,2}$. The ionization resulted in the appearance of CHS^- ions for all substances.

1. Introduction

One of the affordable and reliable energy resources that are currently considered is petroleum oils from fossil-based materials [1]. The molecular mixture in petroleum comprises different categories of hydrocarbons (alkanes, naphthenes, and aromatic compounds) with five- or six-carbon member rings and polar compounds. The main unfavourable impurity in petroleum oils is the presence of polar compounds containing hetero-atoms mostly composed of nitrogen, oxygen, and sulphur-containing species. To reach better quality of petroleum all these compounds must be removed, or their quantities reduced [2-4]. In crude oil, one of the most abundant constituents is sulphur-containing compounds such as thiols and heterocyclic compounds, and their detailed structural characterization is of particular interest. In some cases, the sulphur content in crude oil can be as high as 10% [5]. The petroleum analysis is quite difficult due to sulphur-containing compounds which exhibit high reactivity, absorptivity, and adsorptivity. These components are also mainly responsible for catalyst poisoning and the corrosion of petroleum pipelines [6]. In the oil industry, their better identification and reduction could be helpful to achieve a higher quality of oil, as well as cheaper transportation processes and cost reduction achieved for refining. Besides, sulphur-containing compounds have environmental and human health presenting high exposure risk factors [4]. The present work aims to detect and identify three selected sulphur-containing hydrocarbons by IMS-MS at negative polarity at sub-atmospheric pressure.

2. Experimental part

Ion mobility spectrometer

In this work, the homemade ion mobility spectrometer (IMS) with an atmospheric pressure chemical ionisation (APCI) source based on point-to-ring corona discharge (CD) has been used. During measurements, the IMS was operated in negative polarity mode at sub-atmospheric pressure (680 mbar) due to the capillary inlet´s simple sampling of volatile organic compounds. The operating parameters of IMS are summarized in Table 1.

Gases and chemicals

As a drift gas in IMS, we used a laboratory air cleaned by our self-designed circulation vacuum system with additional moisture traps (Agilent) and containers filled with activated carbon and potassium permanganate-impregnated activated alumina spheres (Alphasorb). In the case of sample flow, non-purified lab air was constantly sucked in with sample vapour (10 $mL.min^{-1}$). The three organosulfur compounds were supplied from Sigma-Aldrich with the following purities: Thiophene (C_4H_4S) 99%, 2-Methyl thiophene (C_5H_6S) 98% and 2,5-Dimethylthiophene (C_6H_8S) 98.5%. The vapours of the thiophenes were introduced into the reaction region of the IMS through a sample inlet. The thiophenes were placed in a glass syringe (about 3 mg, 1 drop). To achieve an equilibrium between the gas and the liquid phase we waited at least 20 minutes. Afterwards, the syringe was connected via a capillary with the sample inlet. Using a syringe pump (Kent Scientific), the sample was introduced into the reaction region of the IMS with a pre-set flow rate.

Tab.1. Parameters of IMS used in the experiment.

Operating Parameters	Unit
IMS drift tube length	11.9 cm
Electric field intensity	672 $V.cm^{-1}$
IMS operating pressure	680 mbar
IMS operating temperature	403 K
Drift gas flow	800 $mL.min^{-1}$
Sample gas flow	10 $mL.min^{-1}$
CD current	10 µA
Shutter grid pulse width	80 µs
Shutter grid frequency	50 z

3. Results

The negative corona discharge in IMS produces three types of Reactant Ions (RI) in drift gas. In contrast with IMS spectra, where we observe only two ion mobility peaks (one strong and one weak), in MS we observe many of them, from which O_2^-, CO_3^- and CO_4^- ions and their water clusters are the most important. We measured the IMS spectra of RI at drift gas temperature 403K and observed one lower peak at K_0 = 2.54 $cm^2.V^{-1}.s^{-1}$ corresponds to ion $CO_3^-.(H_2O)_n$ (n = 0, 1)and one higher peak at K_0 = 2.43 $cm^2.V^{-1}.s^{-1}$ corresponds to ions $CO_4^-.(H_2O)_n$ (n = 0, 1) and $O_2^-.(H_2O)_n$ (n = 1, 2) (Figure 1a.). We confirmed the formation of $O_2^-.(H_2O)_n$ (50 and 68 m/z), $CO_3^-.(H_2O)_n$ (60 and 78 m/z) and $CO_4^-.(H_2O)_n$ (76 and 94 m/z) by a mass spectrometer (MS) (Figure 1b.). In addition to RI in MS spectra, we saw other ions with lower intensities. We identified the ions with 46, 62, 64, 123 and 125 m/z which correspond to NO_2^-, NO_3^-, $NO_2^-.H_2O$, and $CO_3^-.HNO_3$ and $NO_3^-.HNO_3$ ions respectively.

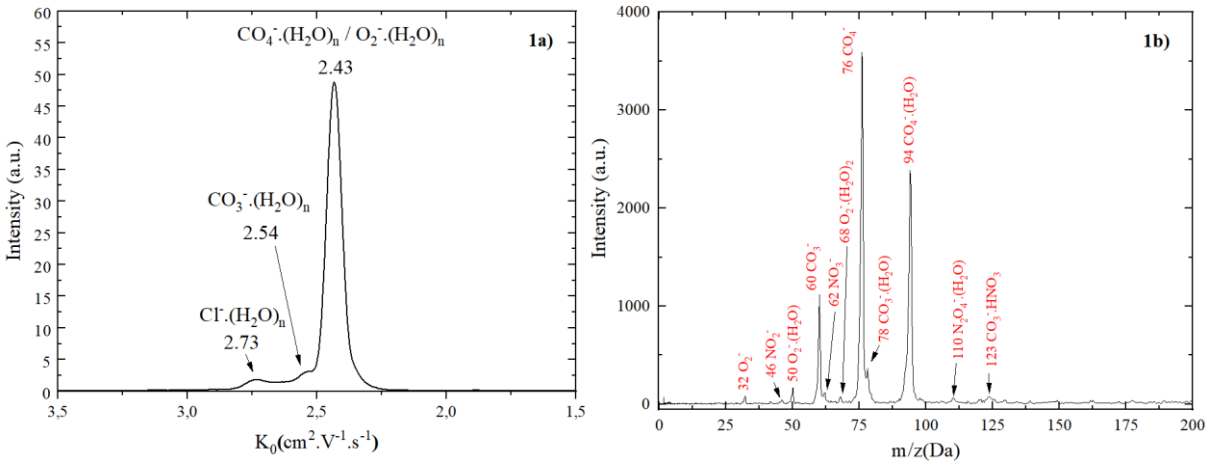

Fig. 1. The IMS (1a) and the MS (1b) spectra of RI at 403K.

The IMS measurement of three investigated compounds is shown in Figure 2. For Thiophene, we observed an intensity increase of $CO_3^-.(H_2O)_n$ (K_0 = 2.55 $cm^2.V^{-1}.s^{-1}$). Besides that, a new clear peak has formed with reduced ion mobility value K_0 = 2.30 $cm^2.V^{-1}.s^{-1}$. In the case of 2-Methyl thiophene, a very strong peak has formed with K_0 = 2.74 $cm^2.V^{-1}.s^{-1}$, unfortunately, it corresponds to $Cl^-.(H_2O)_n$ (n = 1, 2). The chloride evaporates very intensively from the sample, and it causes their higher concentration in IMS and MS spectra. We identified only two sample peaks for 2,5-Dinethyl thiophene with K_0 = 2.16 and 2.26 $cm^2.V^{-1}.s^{-1}$.

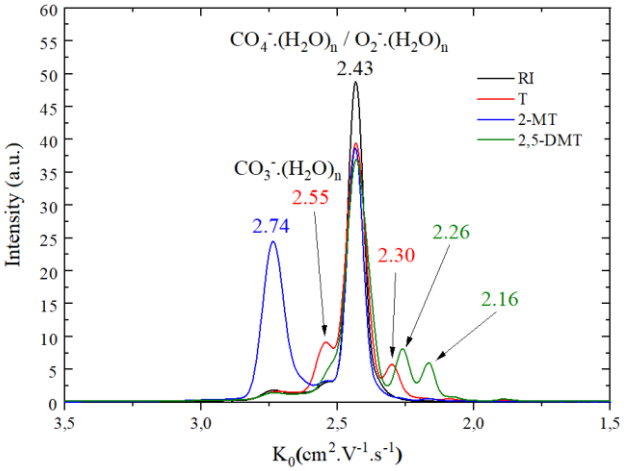

Fig. 2. The IMS spectra of samples at 403K.

The MS spectra for these three samples are shown in Figures 3, 4 and 5. Figure 3 corresponds to Thiophene, and we identified five negative ions except RI. Three ions with m/z = 87, 99 and 127 have a low intensity, while the intensity of ions with m/z = 96 and 112 are much higher. We identified ions with m/z = 87 and m/z = 96 as $C_4H_7S^-$ and $C_2H_4S^-.(H_2O)_2$ / $CO_3^-.(H_2O)_2$ from previous measurement. The other ions are not clearly identified, but we assume them as $CHS^-.(H_2O)_3$ (m/z = 99), $CO_4^-.(H_2O)_2$ (m/z = 112).

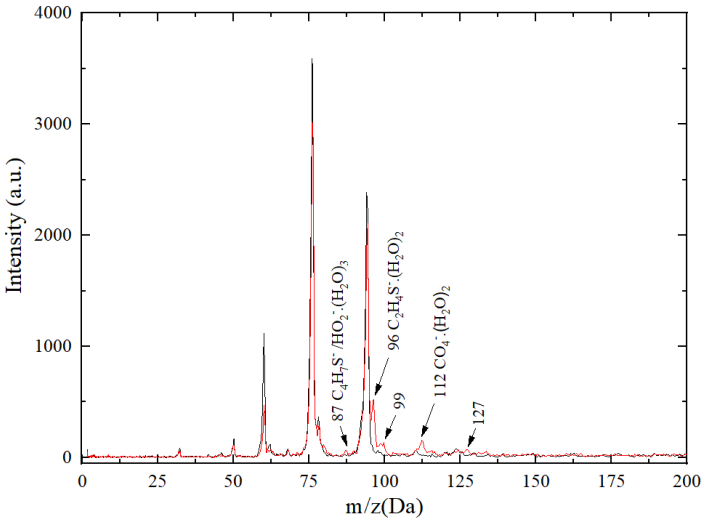

Fig. 3. The IMS spectra of Thiophene at 403K

In the case of 2-Methyl thiophene, we confirmed our statement about IMS spectrum. The IMS peak with K_0 = 2.74 $cm^2.V^{-1}.s^{-1}$ is corresponds to $Cl^-.(H_2O)_n$ (n = 1, 2), and we detect all six of them with mass 35, 37, 53, 55, 71 and 73 (Figure 4). Besides these ions, we detect another five ions with masses 45, 81, 87, 112 and 113. Ions with m/z = 45, 81 and 87 we assigned to CHS^-, $CHS^-.(H_2O)_2$ and $C_4H_7S^-$ respectively. While ion with m/z = 112 and 113 we identified as $CO_4^-.(H_2O)_2$ and an unknown ion.

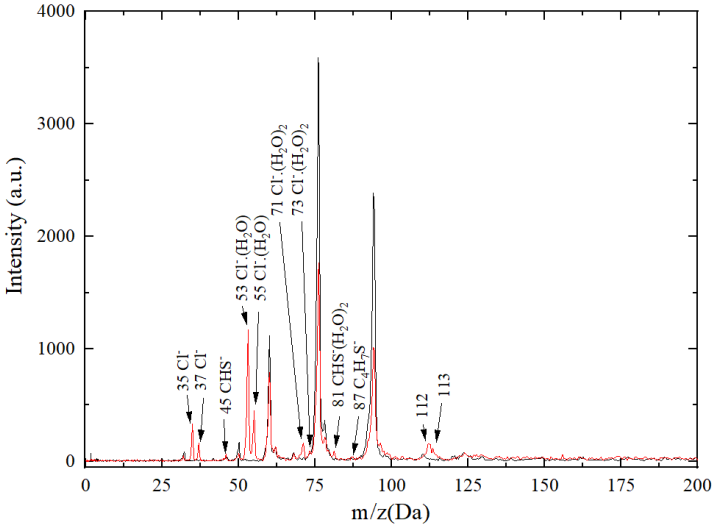

Fig. 4. The IMS spectra of 2-Methyl thiophene at 403K

The clearest MS spectrum with high-intensity peaks has 2,5-Dimethyl thiophene (Figure 5). We identify ions with mass 45, 63 and 81 which are assigned to $CHS^-.(H_2O)_n$ (n = 0, 1, 2), ions with mass 62, 78 and 96 ($C_2H_6S^-$, $C_2H_4S^-.(H_2O)_{1,2}$) and with mass 85 and 87 $C_4H_5S^-$ and $C_4H_7S^-$. Very high intensity has two ions with m/z = 91 and 92, which we identified as $CH_2S.CHS^-$ and $CH_2S.CH_2S^-$ (or $C_2H_3S.O_2^-$ and $C_2H_4S.O_2^-$). The last two ions with lower intensity (m/z = 105 and 112) were identified as $C_2H_4S.CHS^-$ and $C_6H_8S^-$.

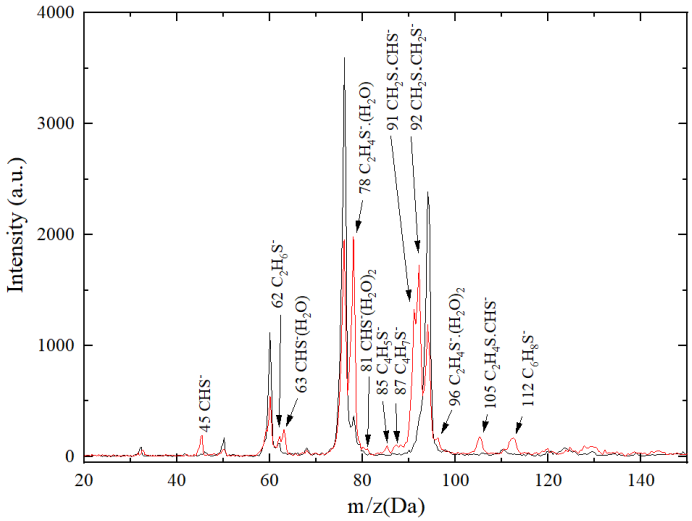

Fig. 5. The IMS spectra of 2,5-Dimethyl thiophene at 403K

Acknowledgement:

This work was supported by the Slovak Research and Development Agency APVV-19-0386, APVV-22-0133, APVV-23-0522 and the Slovak Grant Agency for Science (contract no. VEGA 1/0553/22). We acknowledge support from the MEPhI Academic Excellence Project in 2019-2022.

4. References

[1] Acter, T., Solihat, N.N., Kim, S. et al. *Anal Bioanal Chem* **412,** 243–255 (2020).

[2] Li, S.-m.; Pang, X.-q.; Jin, Z.-j.; Li, M.-w., *Diqiu Huaxue* 2001, **30** (4), 347-352.

[3] Farrington, J. W.; Quinn, J. G., *Estuarine Coastal Mar. Sci*. 1973, **1** (1), 71-9.

[4] Hossein Maleki, Samaneh Ghassabi Kondalaji, Mahdiar Khakinejad, and Stephen J. *Energy & Fuels* 2016 **30** (11), 9150-9161

[5] Hua, R. X.; Wang, J. H.; Kong, H. W.; Liu, J.; Lu, X.; Xu, G. W., *Journal of Separation Science* 2004, **27** (9), 691-698.

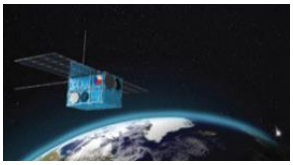

HANKA – CUBESAT SPACE DUST ANALYSER WITH PLASMA ION SOURCE

J. Žabka[1*], Y. Zymak[1,2], M. Malečková[1], M. Polášek[1], B. Cherville[1], J. Jašík[1], A. Spesyvyi[1], M. Lacko[1], M. Kashkoul[1], M. Nezvedová[1], N. Sixtová[1]

[1] *J. Heyrovský Institute of Physical Chemistry, CAS, Dolejškova 3, 182 23 Prague 8, Czechia*
[2] *ELI Beamlines, Institute of Physics, CAS, Na Slovance 2, Prague 182 21, Czechia*
[*] *Corresponding author:* jan.zabka@jh-inst.cas.cz

The application of mass spectrometry for asteroid exploration has recently become a hot topic. Mass spectrometry can be used both in orbit and on the asteroid's surface for the analysis of space dust, micrometeorites, and particles from larger objects.

The ***HANKA*** (***H***motnostný ***AN***alyzér pre ***K***ozmické ***A***plikácie) space instrument is a high-resolution mass spectrometer based on an electrostatic ion trap, which is a principal component of commercial instruments [1] established in biology and medicine research, the so-called Orbitrap™, and the space CosmOrbitrap prototype (developed by LPC2E Orleans [2]). ***HANKA*** will bring this new technology into space to combine a small CubeSat space version of this high-mass resolution ion trap analyzer, with a velocity/charge detector and a hypervelocity impact ionization source.

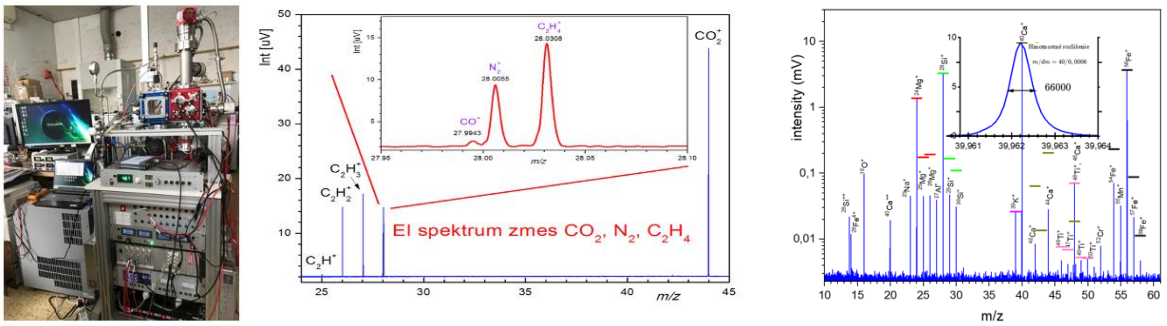

Fig. 1. ***HANKA*** – laboratory prototype, the data: EI source [3] and plasma source -Martian meteorite

Based on the results obtained on the laboratory prototype, a miniature version of the high-resolution space mass spectrometer - ***HANKA*** - will be constructed.

The proposed parameters of the module ***HANKA*** are:

Resolution: up to 50 000 at *m/z* 200

Mass Range: 2 - 3000*m/z*

Power: 10 W

Dimension: 200x200x100 mm (4U)

Weight: 6kg

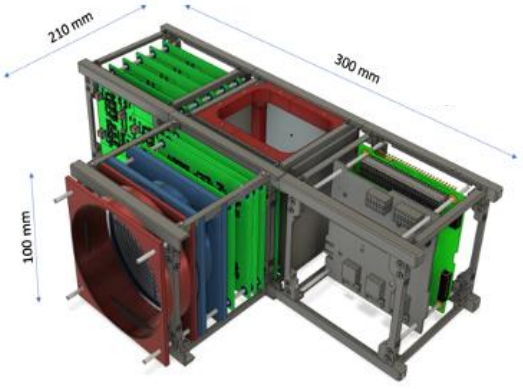

Fig. 2. ***HANKA*** – Cubesat version

Acknowledgments: This work was supported by the Czech Science Foundation (grant No. 21-11931J and 25-19508L)

References

[1] Makarov, A.; *Anal. Chem*. **2000,** 72, 1156–1162.
[2] Briois C., Thissen R., Thirkell L., et al.; *Planet Space Sci.* **2016**, 131, 33-45.
[3] Zymak Y., Zabka J., Polášek M., et al.; al.; *Aerospace* **2023**, 10(6), 522.

ATMOSPHERIC PRESSURE PLASMA TREATMENT AND FUNCTIONALIZATION OF GLASS SURFACE FOR RELIABLE ADHESIVE BONDING

Zlata KELAR TUČEKOVÁ[1], Jakub Kelar[1], Petra Šrámková[1], Dávid Brodňanský[1], Michal Fleischer[1], Yasmina Boutar[2], Zdeněk Sokol[2], Jan Kudláček[3], Martina Eliášová[2] & Mirko Černák[1]

[1]*Department of Plasma Physics and Technology, Faculty of Science, Masaryk University, Kotlářská 2, 611 37 Brno, Czech Republic*

[2]*Department of Steel and Timber Structures, Faculty of Civil Engineering, Czech Technical University in Prague, Thákurova, 166 29 Prague 6, Czech Republic*

[3]*Department of Manufacturing Technology, Faculty of Mechanical Engineering, Czech Technical University in Prague, Technická 4, 166 07 Prague 6, Czech Republic*

E-mail: zlata.tucekova@mail.muni.cz

This contribution presents the results of the plasma effect on glass using Diffuse Coplanar Surface Barrier Discharge (DCSBD) generated in ambient air at atmospheric pressure. Short DCSBD plasma treatment improved the glass adhesion and surface-free energy. Scanning electron and atomic force microscopy revealed negligible morphological changes on the glass surface.

1. Introduction

Glass load-bearing structural elements are currently used more often in civil engineering. However, due to the brittle fracture of glass, it is necessary to design these structures with sufficient reliability. Adhesive joints have several advantages over mechanical glass connectors commonly used in construction. Adhesives can eliminate thermal bridges and provide a more uniform stress distribution along the connection without weakening the bonded material.

Various chemical methods have been developed for cleaning and activating glass surfaces before adhesive bonding. Recently, these methods have been substituted by glass surface cleaning and activation using ambient (humid) air plasma. Such an approach is considered much faster, technically simpler, and more environmentally friendly than the traditional chemical methods. For example, it eliminates the need for the so-called primer interlayer, where the primer is usually considered a heavy chemical with significant environmental impact.

This work aims to improve adhesion by improving glass surface cleaning, activation, and functionalization by atmospheric pressure plasma generated by diffuse coplanar surface barrier discharge (DCSBD). Moreover, controlled adhesion improvement was tested by utilizing surface silanization after plasma pre-treatment of glass.

2. Experimental Design

We studied the DCSBD plasma treatment in ambient air for several seconds up to one minute. The plasma was generated with a frequency of 15 kHz and an input power of 400 W. The flat glass substrates were treated in a dynamic regime at an effective distance of 0.3 mm [1].

The DCSBD plasma effect was evaluated by contact angle and surface free energy measurements (Theta Lite, BIOLIN SCIENTIFIC) and peel-test adhesion measurement (TA.XTplusC Texture Analyser, STABLE MICROSYSTEMS). Scanning electron microscope (Mira3, TESCAN) and atomic force microscope (Ntegra Prima, NT-MDT) investigated morphological changes on the glass surface.

The glass-to-glass adhesion at elevated temperatures was tested with respect to the artificial ageing of adhesive bonding due to the environment. The project partners at CTU Prague carefully selected and provided tested substrates (different float-glass, heat-treated and tempered glass) and tested transparent adhesives [2].

3. Result Description

The DCSBD provided float glass surface activation and cleaning after 1 second of treatment. Homogeneous hydrophilization of the surface was achieved on the air side of the glass, and the water contact angle decreased on the tin side. However, fast aging of the treatment was shown as wettability recovery after 24 hours on the tin side. The contact angle on the air side increased to approx. 50-80% of the reference value after 24 hours. Both polar and dispersive components of surface-free energy increased after the treatment. The increase in the polar component indicated the creation of polar functional groups on the glass, whereas the increase in the dispersive component often indicates the formation of non-polar functional groups and surface roughness change. The adhesive force did not change significantly on the air side for all treatment times (1-60 seconds). However, the adhesive force on the tin side increased by approx. 3,5 times, and its value remained stable after 24 and 168 hours. The wetting, the surface free energy component and chemical changes after DCSBD plasma treatment are well described in [3] in the case of float glass.

Other tested glass surfaces were low-iron glasses branded or so-called Clear Vision. Another, Clear Lite glass, was also provided as tempered and heat-strengthened types. The surface free energy of all glass samples increased on both sides of the glass after 1 second of DCSBD treatment. On the Clear Vision and Clear Lite glass types, the adhesive force increased after 10 seconds of treatment on the tin side (3,8-2,8 times) and 1 second on the air side (2,3-1,2 times). The adhesive force improvement was observed on both sides after 1 second of treatment of heat-strengthened Clear Vision glass, and it was more pronounced and stable after 10 seconds (increase 5 times). The tempered Clear Lite glass needed more than 5 seconds of treatment for adhesive force improvement (approx. 3 times).

Furthermore, tensile and shear tests were performed on bulk-cured adhesive samples and bonded glass-to-glass block shear specimens at room temperature, 40 °C, and 80 °C. The results showed that increasing temperatures decreased tensile and shear strength [4]. The same effect was observed for glass joints pre-treated by DCSBD plasma. We observed a negligible increase in the shear strength at room temperature after pre-treatment. Nowadays, we are testing the process of stable polar group incorporation by utilizing silanol groups on the joint surfaces before glueing. The silanization process uses (3-Aminopropyl)triethoxysilane on a DCSBD pre-treated surface, which is indicated by an increased surface contact angle. Moreover, the formation of C-N, C-NH^{3+} and C-NH_2 groups confirmed the successful silanization of the tested glass surfaces. However, the further interaction of functionalized surfaces with adhesives and their influence on sheer strength must be tested thoroughly.

4. Conclusion

The DCSBD plasma is very effective for cleaning, activating, and functionalizing the glass surface. We observed different effects of DCSBD on the air and tin sides of the tested glass surfaces, whereas the contact angle and surface energy aged within the first 24 hours after the treatment. The adhesion force was improved and stable after ≥10 seconds of DCSBD treatment. However, to improve the sheer strength of glass-to-glass joints further, stable polar group incorporation is needed by utilizing a silanization process or controlled plasma processing atmosphere.

5. Acknowledgement

This research was supported by project No. GA23-06016S, funded by the Czech Science Foundation (GAČR) and supported by project LM2023039, funded by the Ministry of Education, Youth and Sports of the Czech Republic.

6. References

[1] Černák M et al. 2009 *Eur. Phys. J. Appl. Phys.* **47**, 22806.
[2] Boutar Y et al. 2023 *Int. J. Adhes. Adhes.* **127** 103526.
[3] Sihelník S et al. 2023 *Surf.Interfaces* **40** 103080.
[4] Boutar Y et al. 2024 *Challenging Glass Conference Proceedings* **9** 497.

IN-SITU DIAGNOSTIC OF ELECTROSPRAY BY RAMAN LIGHT SHEET MICROSPECTROSCOPY

Mário Janda[1], Kasidapa Polprasarn[2], Pankaj Parek[1], David Pai[2]

[1]*Faculty of mathematics, physics and informatics, Comenius University in Bratislava, Slovakia*
[2]*Laboratoire de Physique des Plasmas, CNRS, Sorbonne Université, École Polytechnique, Institut Polytechnique de Paris, Palaiseau, France*
E-mail: janda1@uniba.sk

Cold atmospheric plasma with aerosol generated by electrospray process presents enormous potential for innovations in agriculture, environmental science, and medicine. However, further research is needed to address the challenges of *in-situ* diagnostics of electrospray aerosol particles exposed to plasma. Here we present a study of an electrospray characterized by *in-situ* Raman light sheet microspectroscopy, with a focus on the detection of NO_3^-.

1. Introduction

Aerosols, comprising tiny solid particles or liquid droplets suspended in gas, play significant roles in various environmental, health, and technological contexts [1]. On the other hand, artificially generated aerosols are utilized in various industries, particularly in healthcare [2]. Still more sustainable aerosol technologies are needed to balance the efficiency with the environmental safety. Plasma-activated aerosol (PAA), often referred to as plasma-activated mist or fog [3], is the combination of cold plasma with micrometric aerosol particles. The extremely high surface/volume ratio of water aerosol microdroplets allows harvesting ultrashort-lived reactive species from plasma that have a relatively small impact in processes generating plasma activated water in batch mode, due to their short depth of penetration. Thus, PAA have been reported to achieve extremely high yields of reactive species production [4].

The number and variety of PAA system configurations are rapidly growing but three common aerosol generator systems are usually used, pneumatic, piezoelectric and electrospray (ES) systems [5]. The production of the aerosol mist usually takes place before its treatment by plasma, except for the case of the electrospray, in which the same needle at high voltage can produce at the same time and location both the droplets and the plasma (e.g. transient spark discharge [6]). When a sufficiently high voltage is applied on the capillary (or nozzle), with a liquid flowing through it, the effective surface tension of the liquid starts to decrease due to the presence of an electric field, causing charge separation inside the liquid. This implies the volume of the forming droplets to decrease. When a critical voltage is reached, the shape of the droplet changes to conical, referred to as a Taylor cone [7]. Finally, a jet emerges from the tip of the Taylor cone and breaks into smaller droplets due to various instabilities. [8, 9].

Combining cold atmospheric plasma with aerosol technology presents enormous potential for innovations in agriculture, environmental science, medicine, and industrial pollution control. However, to fully realize the potential of plasma-aerosol systems, further research is needed to address the challenges of diagnostics, stability, and scale-up. Here we present study of ES by *in-situ* monitoring of the Taylor cone, water filament and microdroplets using Raman light sheet microspectroscopy [10], with a focus on detection of NO_3^-.

2. Experimental setup

Figure 1 shows a schematic of the experimental setup for the generation of the water microdroplets by ES process. The setup consists of a reactor, a water supply unit, a DC high voltage (HV) power supply, and electrical diagnostic tools.

To generate an electrospray, a syringe pump (KD Scientific Legato 110) continuously delivers deionized water (100-500 µl/min) or standard NO_3^- solutions (0.5-25 mM) to the reactor through

a blunt hollow stainless steel needle (nozzle) with an inner diameter of 0.5 mm and an outer diameter of 0.7 mm. The needle, acting as the anode, is connected to an HV power supply (FUG Elektronik) via a 13 MΩ ballast resistor. The applied voltage (6-17 kV) is monitored using a DC HV probe (Agilent N2771A) and the signal is processed by a digital oscilloscope (Rohde & Schwarz RTO2024, 2 GHz bandwidth).
The applied high voltage of positive polarity must exceed 5 kV to generate a sufficiently strong electric field between the tip of the needle (anode) and the grounded wire electrode (cathode) to form the electrospray of charged water microdroplets. The gap between the two electrodes is 16 mm, and the diameter of the grounded stainless steel wire electrode is 2 mm.

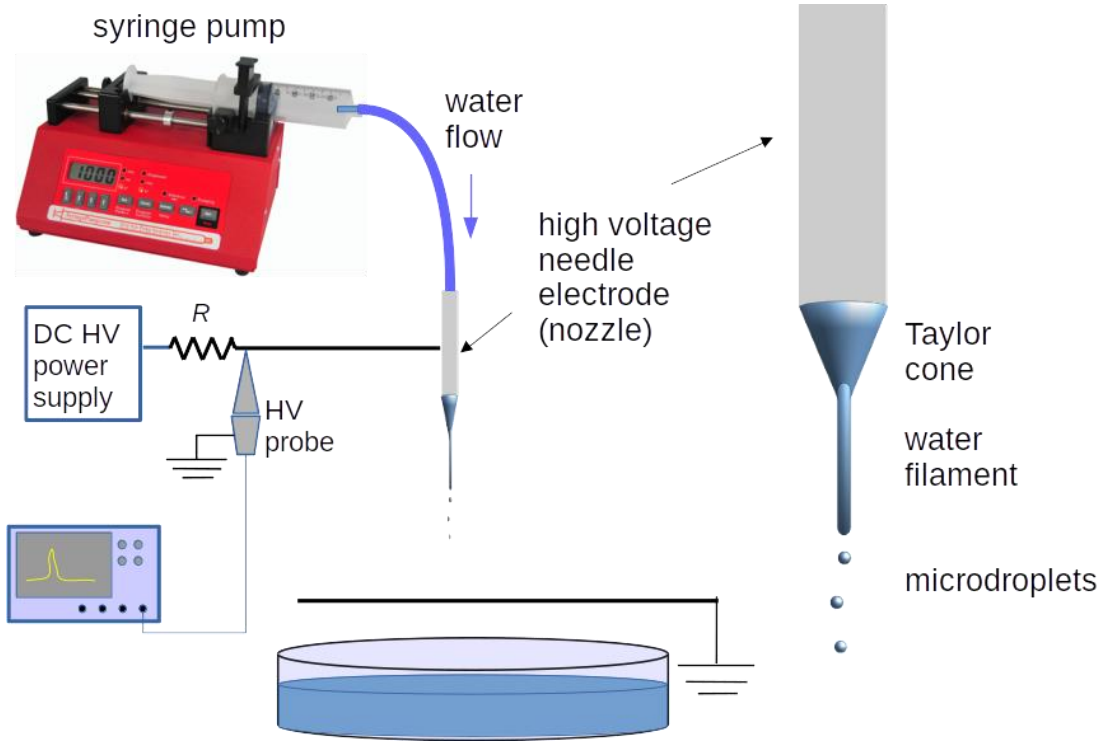

Fig. 1. Simplified schematic of the electrospray setup.

The Raman spectrometer is nearly identical to the system described in Ref. [10]. As shown in Figure 2, a diode-pumped solid-state laser (Elforlight Spot) produced pulses at 532 nm of 2 ns duration at a repetition frequency of 30 kHz, with the average power measured to be 452 mW. The beam first passed through an expander, followed by a variable power attenuator consisting of a rotating half-wave plate combined with a polarizing beamsplitter. The beam underwent vertical focusing upon passing through a cylindrical lens. Upon reflection off a dichroic mirror (Semrock RazorEdge), the beam focused horizontally via a 10X microscope objective (Mitutoyo M Plan Apo and working distance 34 mm). The focus point did not change during the experiments, but the ES reactor was placed on a 3D micrometric positioning system and it was thus possible to focus at different positions below the nozzle.
During in situ measurements, the laser was stable in power to within 3% with a jitter of 1 ns, as measured by a power meter and photodiode placed behind the dichroic mirror. The backscattered light was filtered through the dichroic mirror and then a notch filter (Semrock StopLine). The parallel component of the Raman signal was focused onto the entrance slit of a monochromator (Acton SP2500i, f/6.5 and focal length 0.5 m) coupled with an intensified CCD camera (Princeton Instruments PIMAX 4) mounted at the exit plane of the monochromator.
A delay generator (Stanford Research Systems DG645) synchronized the triggering of the camera gating and the laser. The camera gate duration was 30 ns. Number of accumulations per exposure,

exposures per frame, and camera gain, were adjusted for each measurement to provide and acceptable trade-off between the signal-to-noise ratio and acquisition time.
An additional Tungsten lamp or a LED lamp was used to visualize the target using a CMOS camera (Zelux 1.6 MP Color) during the alignment process. For the alignment we used a cw laser (Laser Quantum Gem).

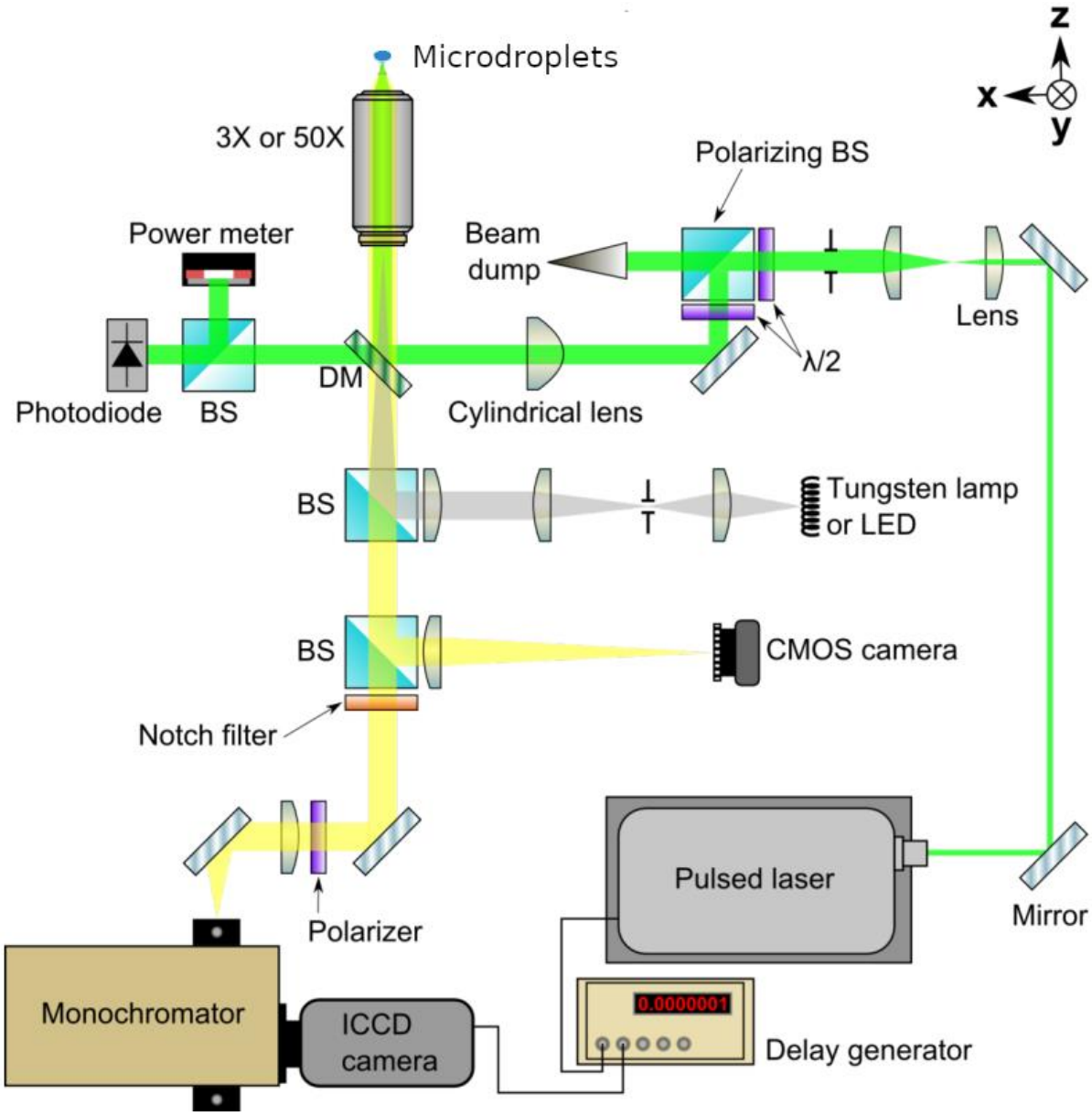

Fig. 2. Top-view schematic diagram of the in situ Raman microspectrometer. The abbreviations are as follows: half-wave plates (λ/2), beamsplitters (BS), dichroic mirror (DM).

3. Results and Discussion

A 3D micrometric positioning system enabled us to focus the laser beam at different positions below the nozzle. Thus we were able to test the possibility of getting Raman signal from all three stages of the electrospray: the Taylor cone, filament and microdroplets (depicted on Figure 1). As an example, Figure 3 shows a camera image of the ES water filament with the reflection from the cw laser used for alignment (green color). We used the objective with 10x magnification, and the area of the camera chip is 4.95 x 3.33 mm (1440x1080 pixels). Based on these numbers, the estimated width of the water filament, as indicated in Figure 3, is approximately 130 µm.

At an applied voltage of 6.5 kV (6 kV at the needle), we obtained a relatively stable ES mode, and thus also relatively stable reflection and backscattering of the laser beam. We were able to record Raman spectra with good signal to noise ratio from both the Taylor cone and from the water filament formed below the Taylor cone. Further away, where the filament disintegrates into microdroples, the signal decreases significantly. Figure 4 shows the decrease of Raman signal intensity as a function of distance from the end of the Taylor cone.

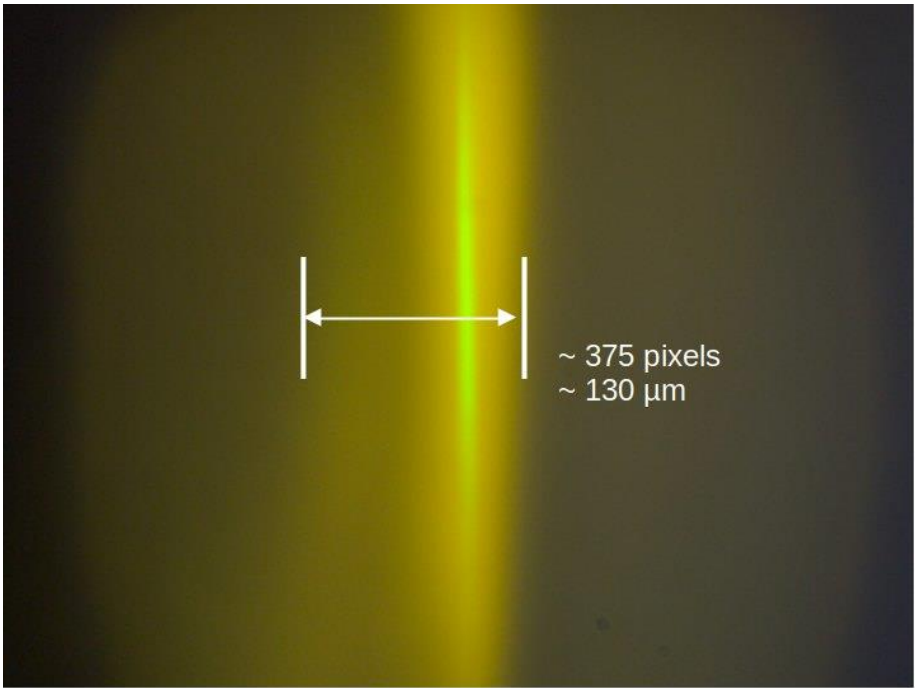

Fig. 3. A camera image of ES water filament with reflection of alignment cw laser (green color), water flow rate of 300 µl/min, applied voltage of 6.5 kV (6 kV at the needle, as measured by HV probe).

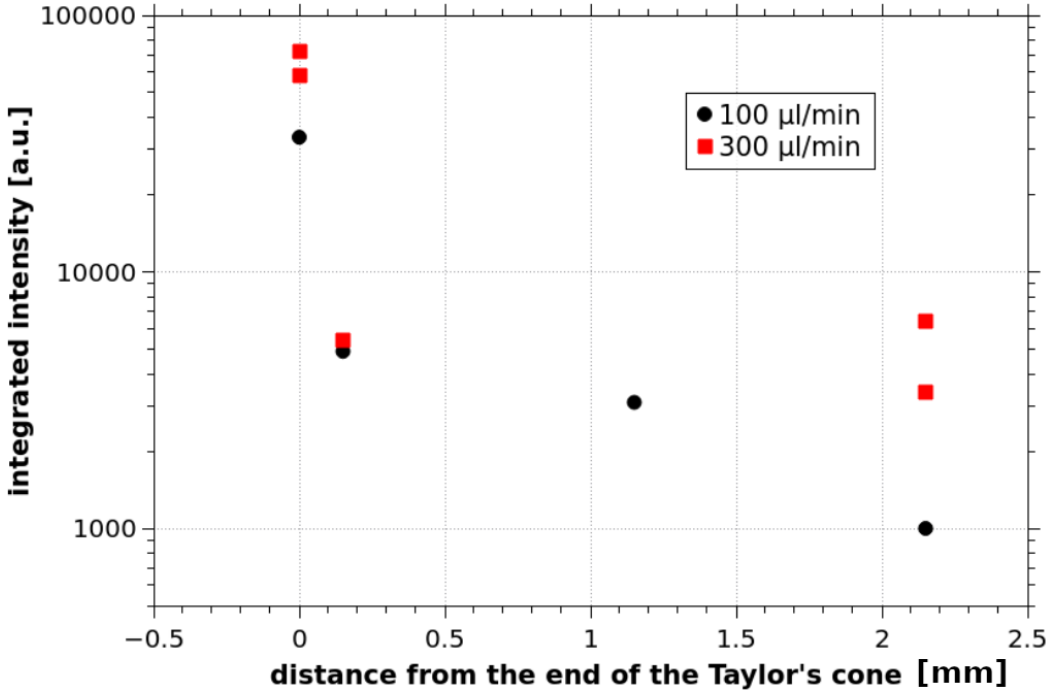

Fig. 4. Integrated intensity of the Raman signal (scattering by H_2O, wavenumbers 2600-4000 cm^{-1}) as a function of the measurement position, two different water flow rates.

The signal in Figure 4 is integrated over the wavenumbers 2600-4000 cm^{-1} corresponding to the Raman scattering by H_2O molecules (-OH stretch). Note that the formation (dripping) of microdroplets from the filament is not synchronized with the laser pulses. Moreover, the formed microdroplets do not follow the same path and only some of them can interact with the laser beam. This can explain significant decrease of the signal further away from the Taylor cone, in the zone of microdroplets.

Despite this fact, it was possible to obtain Raman spectra also from light scattered by the micdrodroplets, and it was even possible to see peak corresponding to the NO_3^- symmetric stretch mode near 1050 cm^{-1}. Figure 5 shows normalized background corrected Raman spectra of 5 mM NO_3^- solution, measured at three different positions (Taylor cone, filament, droplets). With normalization, it is possible to see different S/N when measuring at three different positions. In the case of spectra measured at the Taylor cone or in the filament, the NO_3^- peak is well visible and the detection limit is probably around concentration of 1 mM. In the case of the signal from droplets, the NO_3^- peak is also visible, but it is comparable to the noise level.

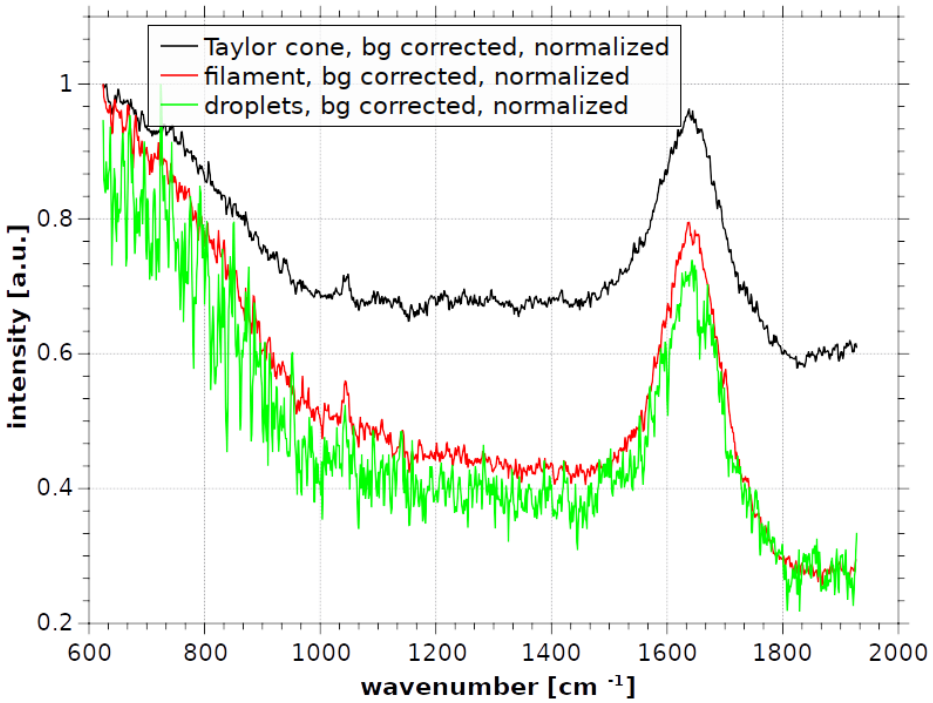

Fig.5. Normalized Raman spectra measured at three different positions, water flow rate of 300 µl/min, 6 kV at the needle, 5 mM NO_3^- solution.

4. Conclusions

We have shown that *in-situ* monitoring of the Taylor cone, water filament and microdroplets by using Raman light sheet microspectroscopy is possible. This technique can be also used to monitor NO_3^- in ES microdroplets. However, the detection limit needs to be improved from about 1-5 mM to much lower values, so that this technique can be used for probing the gradual increase of the NO_3^- in the microdroplets exposed to the plasma. This could be probably achieved by using the coherent anti-Stokes Raman scattering technique.

Acknowledgment: Funded by the EU NextGenerationEU through the Recovery and Resilience Plan for Slovakia under the project No. 09I03-03-V03-00033 EnvAdwice, and by APVV Agency bilateral grant SK-FR-22-0014.

5. References

[1] Anlimah, F, Gopaldasani V, MacPhail C and Davies B 2023 *Environ Sci Pollut Res* **30** 54407–54428.
[2] Rogliani P et al. 2017 *Respiratory Medicine* **124** 6–14.
[3] Aceto, D et al. 2024 Atmospheric Pressure, Low Temperature Plasma applications for decontamination of agrifood products, ESCAMPIG XXVI, Brno, Czech Republic, July 9–13.
[4] Locke B R and Shih K-Y 2011 *Plasma Sources Sci. Technol* **20** 034006.
[5] Janda M, Stancampiano A, di Natale F and Machala Z 2024 Short Review on Plasma-Aerosol Interactions, *Plasma Process. Polym.,* e2400275. https://doi.org/10.1002/ppap.202400275
[6] Machala Z et al. 2013 *Plasma Process. Polym.* **10** 649–659.
[7] Taylor G 1964 *Proc. R. Soc. Lond. A* **280** 383–97
[8] Cloupeau M and Prunet-Foch B 1990 *J. Electrostat.* **25** 165–84
[9] Hartman R P A et al. 2000 *J. Aerosol Sci.* **31** 65-95.
[10] Pai D Z 2021 *J. Phys. D: Appl. Phys.* **54** 355201.

MEMORY EFFECT IN PULSED MICRODISCHARGES

Matej Klas, Mária Maťašová, Peter Čermák, Štefan Matejčík

Department of Experimental Physics, Faculty of Mathematics, Physics and Informatics, Comenius University, Mlynská dolina, 842 48 Bratislava, Slovakia
E-mail: matej.klas@fmph.uniba.sk

This study investigates the correlation between successive breakdowns in vacuum microdischarges. Breakdown voltages were generated using a pulsed electric field with a rate of 10^{10} V/s under single-pulse and pulse-burst regimes. The correlation patterns of successive breakdowns were analyzed based on pulse duration and the minimum power required to maintain vacuum discharge. Measurements were performed with electrode distance of 10 µm using palladium, copper and tungsten electrode.

1. Introduction

Successive pulsed breakdowns observed in a vacuum are not random processes but are influenced by the value of the previous breakdown [1]. To graphically represent this memory effect, the dependency U_i vs. $U_{i+1}-U_i$ is proposed. This plot reveals a unique pattern that illustrates the evolution of breakdowns, highlighting both the cyclic behavior and the transition region. The transition region separates the area where the breakdown voltage tends to increase from the area where subsequent breakdowns decrease. In this study, we focus on the discharge parameters responsible for the transition region. Specifically, we analyze pulse duration and the minimal power required to maintain the discharge from a statistical perspective, aiming to identify the cause of this memory effect.

2. The experimental setup

The schematic of the apparatus is shown in Figure 1. The electrodes were situated in a vacuum chamber (p ~1.10-4Pa) in sphere to plane geometry, ensuring quasi-uniform electric field. The sphere electrode represents the cathode with a diameter of approximately 5 mm.

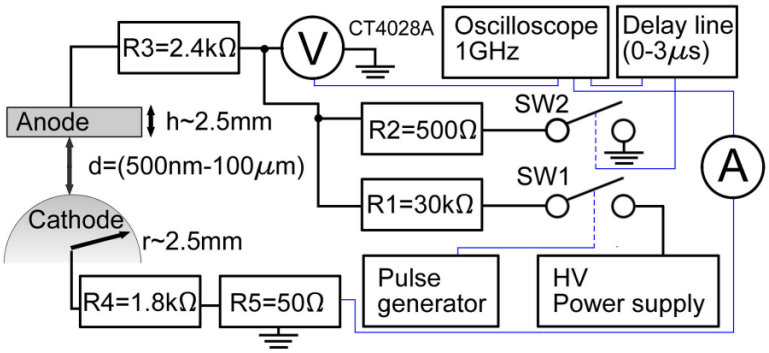

Fig. 1. Schematic of the electrical circuit

The anode was connected via a series of resistors to a pulse signal, generated by switching (S1-Behlke HTS 181-01-C) the high voltage (HV) from power supplies (Spellman SL 150). The second switch (S2-Behlke HTS 121-03) was inserted to enhanced turn of the system and was triggered with a delay after the breakdown was reached. The voltage was measured by an HV probe (Tektronix P6015A) while the current was measured across a 50-ohm resistor connected in series with the cathode. Waveforms were recorded using a digital oscilloscope (Teledyne LeCroy Wavesurfer 510). The 0µm separation was established by monitoring the electrical resistance (R3+R4+R5). Prior to the measurements, the electrodes were conditioned with pulse breakdowns [2-3].

3. Results and discussion

The observed results, presented as scatter density plots, reveal distinct relationships between successive breakdowns for different electrode materials. In single-pulse (SP) mode, similar patterns were observed for palladium, copper (Fig. 2), and gold electrodes. However, in the burst mode, the patterns varied depending on the electrode material. In case of copper electrodes, the pattern strongly depended on the order of the successive breakdown pulses. In contrast, for palladium electrodes, the pattern remained stable regardless of the selected pulse regime. Further analysis of pulse duration and the minimal power required to sustain discharges indicates dynamic changes in the vacuum microdischarges process as the breakdown threshold is approached.

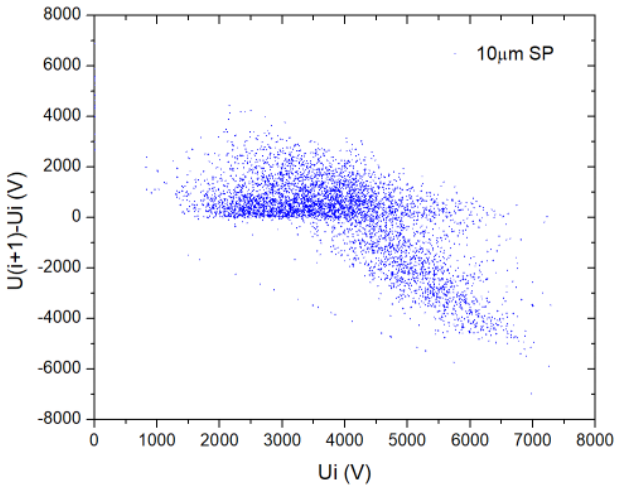

Fig. 2. The observed pattern of the dependency U_i vs. $U_{i+1}-U_i$ for the copper electrode in single-pulse mode.

Acknowledgments

The authors acknowledge partial support from Slovak Research and Development Agency under project Nr. APVV-23-0522 and from Slovak Grant Agency for Science VEGA Nr. 1/0553/22.

4. References

[1] Mat'ašová, M., Klas, M., Čermák, P., Radmilović-Radjenović, M., Petrovič, P., Satrapinskyy, L., Matejčík, Š. Vacuum 222 (2024) 112998.

[2] Klas, M., Čermák, P., Borkhari, A. F., Satrapinskyy, L., Matejčík, Š., Radjenović, B., & Radmilović-Radjenović, M. Vacuum (2021) 110327.

[3] Beukema G.P., Physica (1972) 259-274.

STREAMER PROPAGATION DYNAMICS IN A NANOSECOND PULSED SURFACE DIELECTRIC BARRIER DISCHARGE IN HELIUM-NITROGEN MIXTURES

Ihor Korolov[1], Gerrit Hübner[1], Nils Schoeneweihs[1], Dominik Filla[1], Sebastian Wilczek[2], Máté Vass[1], Thomas Mussenbrock[1]

[1] *Chair of Applied Electrodynamics and Plasma Technology, Ruhr-University Bochum, 44780 Bochum, Germany*
[2] *TH Georg Agricola University, 44787 Bochum, Germany*
E-mail: korolov@aept.rub.de

An atmospheric pressure surface dielectric barrier discharge in helium–nitrogen mixtures is investigated using phase-resolved optical emission spectroscopy and 2D fluid simulations. Good qualitative agreement is observed between experiments and simulations. The discharge structure varies between filamentary and homogeneous depending on the microsecond or nanosecond voltage pulse applied. The propagation of the homogeneous surface ionization wave is analysed for different nitrogen admixtures, pressures, and voltages.

Non-thermal plasma discharges are an emerging technology with diverse applications, including plasma medicine [1], agriculture [2], and ozone generation [3]. Among these, dielectric barrier discharges (DBDs), a type of non-thermal atmospheric-pressure plasma, stand out due to their unique chemical and physical properties, making them ideal for biomedical and environmental applications [4]. DBDs operate at near-room temperature, as the dielectric barrier prevents the formation of high-temperature arcs. A notable subclass of DBDs is surface dielectric barrier discharges (SDBDs), where two electrodes are separated by a dielectric barrier, restricting the discharge to the surface of the dielectric. Twin SDBD electrodes, featuring symmetric electrodes on both sides of a dielectric barrier, have demonstrated potential in catalysis and VOC conversion [5,6]. While previous studies have investigated streamer behaviour under microsecond and nanosecond voltage pulses [7], the dynamics of nanosecond surface discharges, particularly their impact on VOC conversion and catalytic processes, remain insufficiently explored.

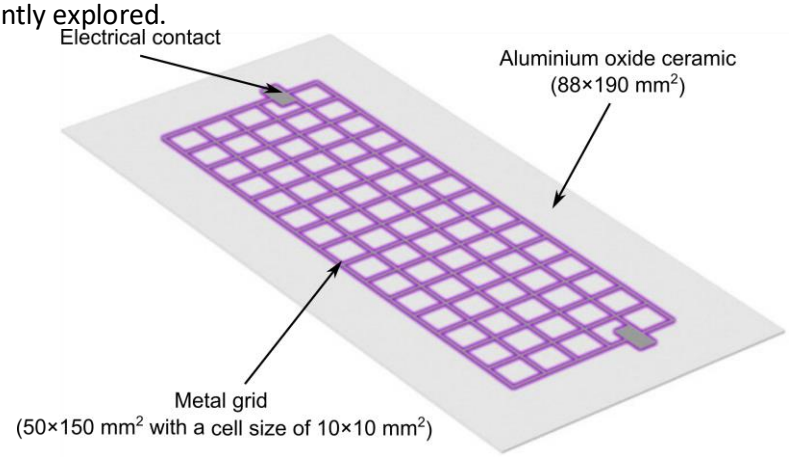

Fig. 1. Sketch of the SDBD electrode configuration. A metal grid functions as a powered electrode, with the counter grounded electrode situated on the opposite side.

In this work a twin SDBD electrode (see Figure 1) driven by a micro- and ns-voltage-pulse operated in helium and nitrogen at various pressures, is analysed through experiments using Phase Resolved Optical Emission Spectroscopy (PROES) and two-dimensional fluid simulations using the *nonPDPSIM* code [8]. A good agreement is observed between the experimental findings and the simulations. With

measurements taken on both the powered and grounded sides of the twin SDBD electrode, it is demonstrated that the discharge of the twin SDBD electrode transitions from a filamentary streamer mode under microsecond-driven operation to a diffusive mode when driven by nanosecond pulses, due to the significantly different rise times of the applied voltage (~3 kV/µs vs ~3 kV/ns), see Figure 2.

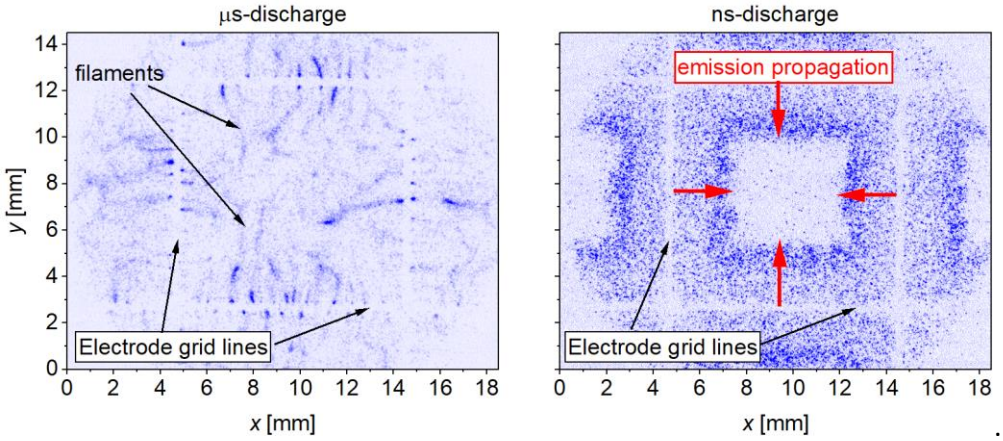

Fig. 2. Experimental measurements performed with intensified CCD camera. Left panel: data obtained for µs-voltage pulses at 12 kVpp captured for an individual pulse using the gate width of 1000 ns. Right panel: data obtained for single pulse of ns-discharge, the gate width is set to 5 ns. The four red arrows pointing towards the center show the direction of the emission propagation. Gas mixture: He/N_2 = 90/10 at 1 atm.

From the temporal excitation plots of the ns-discharge, the velocities of positive and negative streamers are determined for various nitrogen admixtures. Since the streamer velocity directly impacts the distribution of reactive species, flow dynamics, and energy deposition, understanding the factors influencing this velocity is critical for optimizing VOC conversion using the twin SDBD electrode.
Simulations reveal that the positive streamer on the powered side of the twin SDBD electrode does not directly interact with the dielectric. Instead, it hovers above it due to the significant role of photoionization in its propagation within this gas mixture. In contrast, the negative streamer primarily propagates through electron impact ionization, making it independent of photoionization. As a result, it can directly interact with the dielectric and form surface charges.
This understanding is pivotal for enhancing VOC conversion efficiency using catalytic surfaces with twin SDBD electrodes. Additionally, the observed effects of varying the applied voltage pulse, pressure, and gas mixture on streamer discharge formation and propagation provide opportunities to control key factors such as reactive species distribution, flow dynamics, energy deposition, and streamer interaction with dielectric or catalytic materials.

Acknowledgements: This work was supported by the German Research Foundation in the frame of the collaborative research center SFB 1316, projects A5 and A7.

Reference

[1] Laroussi M 2018 *Plasma Medicine: A Brief Introduction, Plasma* **1** 47–60
[2] Domonkos M, Tichá P, Trejbal J and Demo P 2021 *Applied Sciences* **11** 4809
[3] Yuan D, Ding C, He Y, Wang Z, Kumar S, Zhu Y and Cen K 2017 *Plasma Chemistry and Plasma Processing* **37** 1165–1173
[4] Guo Y, Liu P, Zhang L, Peng S, Wang X, Luo H and Wu G 2021 *Applied Physics Letters* **119** 061601
[5] Peters N, Schücke L, Ollegott K, Oberste-Beulmann C, Awakowicz P and Muhler M 2021 *Plasma Processes and Polymers* **18** 202000127
[6] Schücke L et al. 2020 Plasma Sources Science and Technology **29** 114003

[7] Nguyen-Smith R T, Böddecker A, Schücke L, Bibinov N, Korolov I, Zhang Q Z, Mussenbrock T, Awakowicz P and Schulze J 2022 *Plasma Sources Science and Technology* **31** 035008
[8] Hübner G, Wilczek S, Schoeneweihs N, Filla D, Mussenbrock T and Korolov I 2024 *Journal of Physics D: Applied Physics* **58** 065201

GENERATION OF REACTIVE SPECIES VIA SURFACE DIELECTRIC BARRIER DISCHARGE IN DIRECT CONTACT WITH WATER

Oleksandr Galmiz[1,2], Richard Cimerman[1], Mário Janda[1] and Zdenko Machala[1]

[1]*Division of Environmental Physics, Faculty of Mathematics, Physics and Informatics, Comenius University in Bratislava, Mlynská dolina, 842 48 Bratislava, Slovakia*
[2]*Department of Plasma Physics and Technology, Faculty of Science, Masaryk University, Kotlářská 267/2, 611 37 Brno*
E-mail: oleksandr.galmiz@uniba.sk

Surface dielectric barrier discharge (SDBD) ignited directly from the liquid electrodes at the 3-phase gas/liquid/solid interface represents a novel approach in both water and polymer surface treatment methods. This study investigates the gaseous and liquid-phase reactive oxygen and nitrogen species (RONS) generated by this discharge. The impact of the discharge power and treatment duration on the concentration of these species in both gas and liquid is explored.

1. Introduction

Plasma-activated water (PAW) in general is a type of water that has been in contact/treated with a plasma discharge. PAW has shown potential uses in numerous emerging applications, such as e.g. enhancement of seed germination, plant growth, selective treatment of cancer cells, wound healing, food preservation, inactivation of bacteria, viruses, fungi, etc. [1–4]. The versatility of PAW lies in its remarkable chemical activity, resulting from its interaction with non-equilibrium plasma. Plasma discharges in liquids or over their surface generate reactive oxygen and nitrogen species (RONS), such as radicals, ions, and excited molecules (e.g., ·O, ·OH, O_3, N_2^-, O_2^-).

Traditional surface dielectric barrier discharge (SDBD) systems generate plasma along a thin dielectric surface layer but do not directly reach the water. This limits the concentration of short-lived, highly reactive species like ·OH and ·O radicals. In this study, we address these limitations by employing a liquid electrode system that enables SDBD ignition directly from the liquid surface [5,6]. Although the plasma-water contact is confined to the dielectric tube's perimeter, the system is scalable and adaptable for specific applications. Besides water activation, this configuration also supports cleaning and surface treatment of dielectric materials, with potential uses in material processing and medicine. This study investigates the reactive species formation (H_2O_2, O_3, NO_2^-, NO_3^-) in tap water measured by using UV-VIS absorption spectroscopy. Additionally, Fourier transform infrared (FTIR) absorption spectroscopy was employed to measure concentrations and production yields of plasma-generated gas-phase species. The spatial evolution of O_3 in the liquid phase was also analyzed through the UV-VIS *in-situ* spectroscopy.

2. Experimental setup

To simulate the triple-phase interface (plasma-liquid-solid) under stable conditions, a thin glass test tube with a 10 mm diameter and a 0.5 mm wall thickness was used. The liquid inside the test tube served as the high-voltage electrode and was connected to a power supply generating a sinusoidal voltage waveform. The Petri dish bath, which grounded the system, completed the circuit, as depicted in figure 1. A more detailed explanation of the discharge could be found in [5] where a similar principle of the discharge was used. The high-voltage sine waveform had an amplitude range of 0 to 20 kV and could be adjusted to frequencies between 23 and 30 kHz depending on the reactor configuration and used liquids. Power was delivered to the liquid electrodes through a high-voltage resonance generator (Lifetech-300W) paired with a function generator (FY3200S-24M).

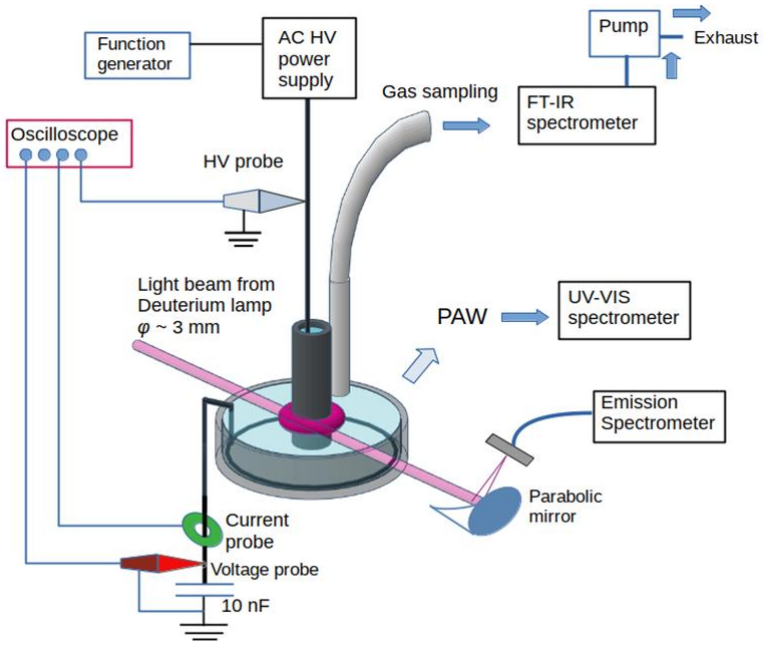

Fig. 1. Schematic of the experimental assembly for the SDBD treatment of water around the glass tube with the *in-situ* UV-VIS absorption diagnostics.

The chemical analysis of gaseous species produced by the SDBD was performed by FTIR absorption spectroscopy (Shimadzu IRSpirit-X spectrometer) using a 542 cm absorption path gas cell equipped with ZnSe windows. To determine spatial distributions of reactive species concentrations around the glass tube inserted in the treated water in the reactor, the in-situ measurements using the UV-VIS absorption spectroscopic technique were performed (figure 1). By using the UV–VIS absorption spectroscopy (Shimadzu UV-1800) the main aqueous species such as hydrogen peroxide H_2O_2, nitrite NO_2^- and nitrate NO_3^- were detected and their absolute concentrations were evaluated.

3. Results and discussion

The production of ozone (O_3) is often desirable due to its strong oxidizing properties, making it suitable for a range of applications. However, when plasma discharge interacts with a liquid, nitrogen oxides (NO_x) can dissolve, forming nitrites NO_2^- and nitrates NO_3^-, which are valuable for biomedical and agricultural purposes. The presence of water or humidity in the gas phase significantly influences the composition and concentrations of gaseous products, as well as the discharge properties and electrical characteristics. Therefore, understanding the production trends of gaseous species under various conditions is essential before employing the discharge in liquid-contact applications.

Figure 2 presents the infrared absorption spectrum of gaseous species generated by the discharge. Under the studied conditions, only O_3, N_2O, and N_2O_5 were detected. Notably, other expected species, such as NO, NO_2, HNO_2, and HNO_3, were absent from the spectra. The absence of NO and NO_2 suggests that either their concentrations were below the detection limits of the setup (approximately 7 ppm for NO and 1.5 ppm for NO_2), or they underwent rapid oxidation into N_2O_5, facilitated by O_3 [7]. The results indicate that the discharge operated primarily in an O_3-dominated mode, with negligible formation of NO, NO_2, HNO_2, and HNO_3 in the gas phase across all tested conditions.

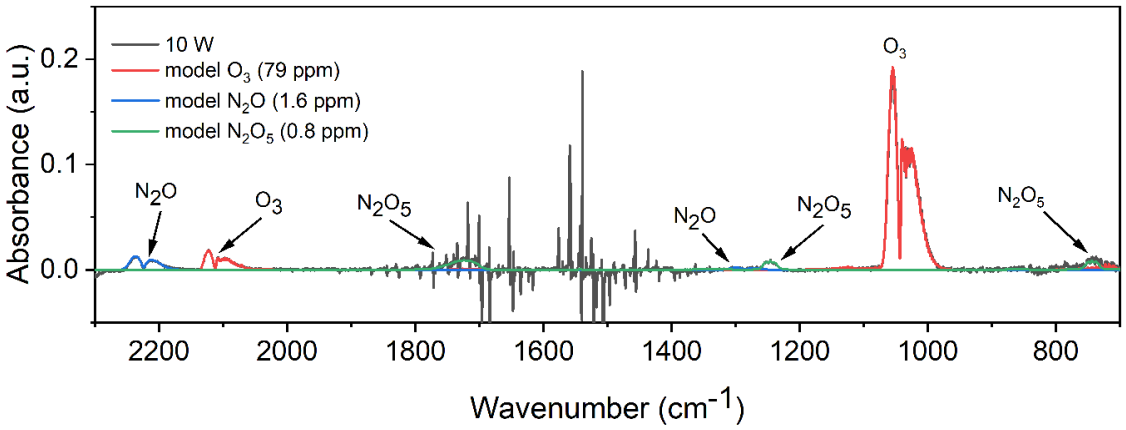

Fig. 2. Infrared absorption spectrum of gaseous products of the discharge at discharge power of 10 W. The modeled spectra of O_3, N_2O, and N_2O_5 corresponding to respective species concentrations are also presented.

Figure 3 illustrates the concentrations of RONS in tap water following the plasma treatment at varying applied powers and treatment durations. The results demonstrate that the reactor configuration highly influences RONS production. When compared to values reported in the literature, the proposed system exhibits comparable or even superior efficiency in RONS generation.

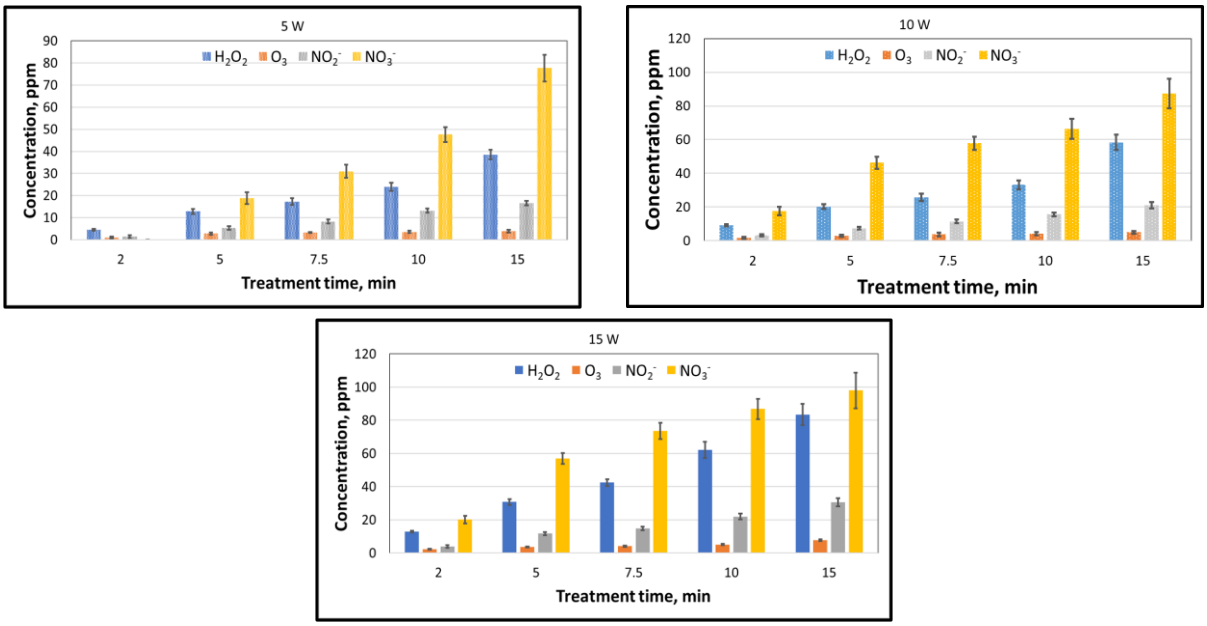

Fig. 3. Concentrations of RONS generated in the PAW outside the dielectric tube for different discharge powers.

4. Conclusions

This study employed a novel plasma setup to generate PAW, and the resulting chemical changes in both the gas and liquid phases were analyzed using various spectroscopic measurement techniques. The results showed high efficiency in the generation of reactive oxygen and nitrogen species, with ozone being the dominant product in the gas phase. The dominance of O_3 likely drives the conversion of reactive nitrogen species to N_2O_5.

The high concentration of N_2O_5 in the gas phase could explain the prevalence of nitrate ions among the RONS observed in the PAW. However, it is also possible that the observed NO3- is primarily formed from nitric acid. Since HNO_3 is readily soluble in water, it would explain its low concentrations

measured in the gas phase. Further research is needed to definitively determine the primary source of NO_3^- in the PAW.
The implementation of the surface dielectric barrier discharge (SDBD) at the gas/liquid/solid interface introduces an innovative approach to dielectric surface modification, and water treatment marking a contribution to the scientific literature with multiple environmental and biomedical applications.

Acknowledgments
This work was funded by the EU NextGenerationEU through the Recovery and Resilience Plan for Slovakia under the project No. 09I03-03-V04-00094, the Marie S. Curie Action Postdoctoral Fellowship under Horizon Europe with grant agreement number 101066764 and by the project LM2023039 funded by the Ministry of Education, Youth and Sports of the Czech Republic.

5. References

[1] Puač N, Škoro N, Spasić K, Živković S, Milutinović M, Malović G and Petrović Z L 2018 Activity of catalase enzyme in Paulownia tomentosa seeds during the process of germination after treatments with low pressure plasma and plasma activated water *Plasma Processes and Polymers* **15** e1700082.
[2] Schmidt A, Bekeschus S, Wende K, Vollmar B and von Woedtke T 2017 A cold plasma jet accelerates wound healing in a murine model of full-thickness skin wounds *Exp Dermatol* **26** 156–62.
[3] Woedtke T Von, Oehmigen K, Brandenburg R, Hoder T, Wilke C, Hähnel M and Weltmann K Plasma-liquid-interactions : chemistry and antimicrobial effects 39–40.
[4] Rathore V, Patel D, Shah N, Butani S, Pansuriya H and Nema S K 2021 Inactivation of Candida albicans and Lemon (Citrus limon) Spoilage Fungi Using Plasma Activated Water *Plasma Chemistry and Plasma Processing* **41** 1397–414.
[5] Galmiz O, Pavlinak D, Zemanek M, Brablec A and Cernak M 2016 Study of surface dielectric barrier discharge generated using liquid electrodes in different gases *J Phys D Appl Phys* **49** 065201.
[6] Galmiz O, Pavliňák D, Zemánek M, Brablec A and Černák M 2017 Hydrophilization of outer and inner surfaces of Poly(vinyl chloride) tubes using surface dielectric barrier discharges generated in ambient air plasma *Plasma Processes and Polymers* **14** e1600220.
[7] Cimerman R and Hensel K 2023 Multi-hollow Surface Dielectric Barrier Discharge: Production of Gaseous Species Under Various Air Flow Rates and Relative Humidities *Plasma Chemistry and Plasma Processing* **43** 1411–33.

YOUNG SCIENTISTS' LECTURES

COLD PLASMA AS AN APPROACH TOWARDS ALTERNATIVE TREATMENT OF *OTITIS EXTERNA*

Kristína Trebulová[1], Augusto Stancampiano[4], Eric Robert[4], Marek Moravčík[1], František Krčma[1]

[1]*1Brno University of Technology, Faculty of Chemistry, Purkyňova 118, 612 00 Brno, Czech Republic*

[2] *GREMI, UMR7344 CNRS/University of Orleans, 14 Rue d'Issoudun, 45067 Orléans, France*

E-mail: trebulovakristina@gmail.com

This work studies the interaction of cold atmospheric-pressure plasma (CAP), specifically the plasma gun [1], with the selected surface materials for decontamination purposes. Special attention is brought to an alternative treatment of otitis externa in dogs. Otitis externa or so-called swimmer´s ear, is a condition that causes an inflammation of the external ear canal. One of the factors causing this disease are microorganisms. An increasing resistance of microorganisms to antimicrobial drugs urges the researchers to find new alternative treatment methods. Thus, the antimicrobial effects of CAP on bacteria and yeasts and their combination were studied.

1. Plasma decontamination

As model microorganisms, gram-negative bacteria Escherichia coli and gram-positive Staphylococcus aureus, Staphylococcus epidermidis and the yeast Candida glabrata were chosen. Several experiments were carried out on the different surfaces for individual bacteria (*E. coli*, *S. epidermidis*), yeast (*C. glabrata*) and even their coculture (yeast with bacteria). The treatment of coculture and the use of different inoculation substrates moves us closer to real life situation, where the ear canal is contaminated by a mixture of different microbes interacting with each other. Metabolic activity and the viability of the microbial species after different treatments were evaluated. For the testing of the metabolic activity the MTT assay modified for bacterial cells was used. This modified protocol was inspired by several studies done on use of MTT assay for different microbial species [1, 2, 3]. For the evaluation of overall viability standard plate count and optical density measurement were used. Several experiments were also evaluated in cooperation with HexTech research s.r.o in the software Aurora using AI-powered image recognition (like examples on Fig. 1). The use of these different test helped to study the antimicrobial efficacy on different surface material (the agar, the pork skin and the polylactic acid polymers) and in liquid suspension.

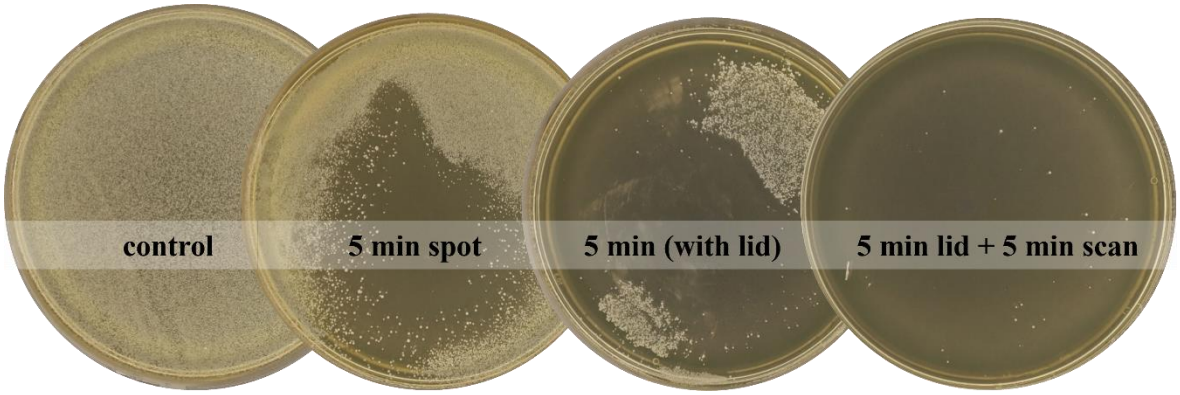

Figure 1: Example of the plasma decontamination tested on S. epidermidis, where:
***5 min spot** = treatment on one spot for 5 minutes, **5 min (with lid)** = treatment on one spot for 5 minutes in enclosed area, where the lid of the Petri dish (with a small hole for the plasma capillary) was put on the Petri dish during the treatment, **5 min lid + 5 min scan** = combination of enclosed area treatment for 5 minutes followed by 5 min scan of the whole surface of the Petri dish*

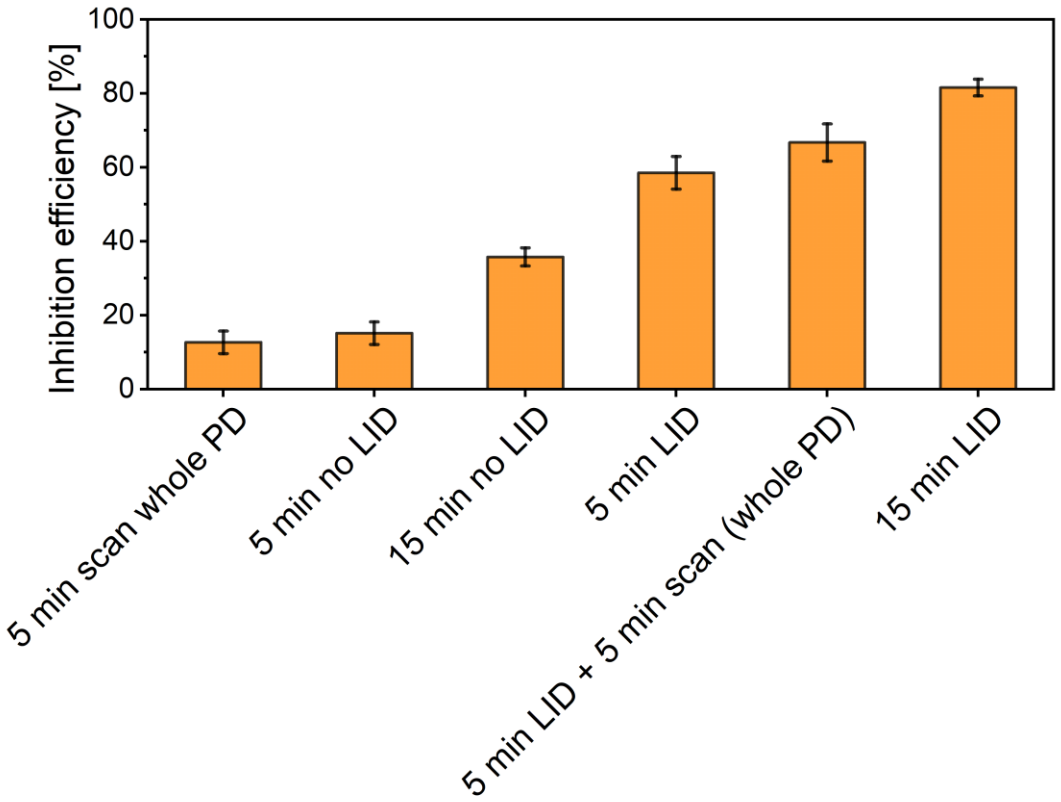

Figure 2: Overview of the plasma treatment efficacy in the decontamination of microbial co-culture (E. coli, S. epidermidis, C. glabrata), were the inhibition efficacy is evaluated as the decontaminated area of a Petri dish (d = 90 mm) compared to the conrol samples, were the whole surface of the Petri dish was covered by the microbial cells.

2. Plasma-target interaction

The antimicrobial efficacy was studied also in context with the plasma characteristics. In addition to classic plasma diagnostics including the optical emission spectroscopy or looking at the plasma with the ICCD camera, different ozone measurements were done to support the estimations about the inhibition mechanisms. The combined action of short-lived species in cooperation with the long-lived species was studied and several treatment modes were established to achieve the most efficient decontamination. The composition of the plasma gas was also studied in relation to the antimicrobial efficacy, were the addition of oxygen and nitrogen to the plasma gas was tested. To study the fluid dynamics Schlieren imaging was performed, and the most optimal treatment conditions were established. The experiments were done on different surface materials (the agar, the pork skin and the polylactic acid polymers) to study the interactions of the plasma gun with the different targets (Fig. 3).

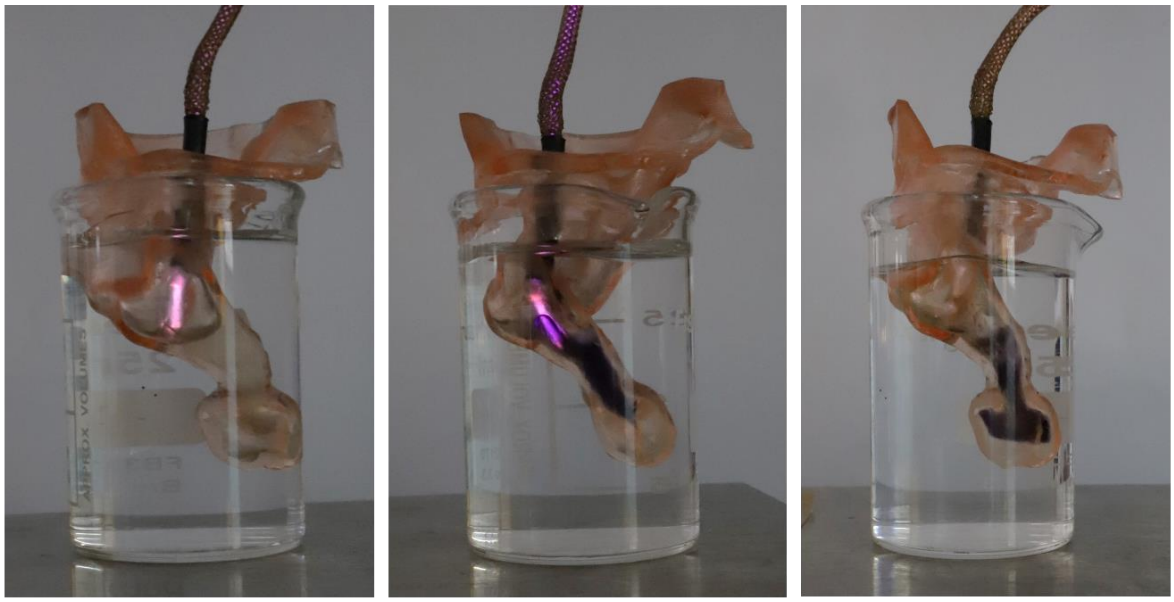

Beginning of the plasma treatment (1s) | *During the plasma treatment (20 s)* | *Diffusion of RONS in the liquid after the plasma treatment (30 s)*

Fig. 3. The visualization of RONS diffusion into the liquid using the chemical reaction of potassium iodide and starch to produce dark blue colour upon oxidation.

3. References

[1] Robert, E.; Sarron, V.; Riès, D.; Dozias, S.; Vandamme, M.; Pouvesle, J.-M. Characterization Of Pulsed Atmospheric-Pressure Plasma Streams (Paps) Generated By A Plasma Gun. *Plasma Sources Science and Technology* 2012, *21*, doi:10.1088/0963-0252/21/3/034017.

[2] Grela, E.; Kozłowska, J.; Grabowiecka, A. Current Methodology Of Mtt Assay In Bacteria – A Review. *Acta Histochemica* 2018, *120*, 303-311, doi:10.1016/j.acthis.2018.03.007.

[3] Benov, L.; Giuffrè, A. Effect Of Growth Media On The Mtt Colorimetric Assay In Bacteria. *PLOS ONE* 2019, *14*, doi:10.1371/journal.pone.0219713.

[4] Oh, Y.J.; Hong, J. Application Of The Mtt-Based Colorimetric Method For Evaluating Bacterial Growth Using Different Solvent Systems. *LWT* 2022, *153*, doi:10.1016/j.lwt.2021.112565.

Acknowledgement

This work was supported by the COST Actions CA20114 and CA19110 and Erasmus+. The authors would also like to acknowledge the Veterinary University in Brno for their expertise and advice in the development of the target models and to our collaborators from HexTech research s.r.o for their help with data processing.

PLASMA-CATALYTIC GAS TREATMENT: THE ROLE OF PELLET-SHAPED MATERIAL IN PACKED-BED DBD REACTORS

Richard Cimerman[1], Jakub Roubíček[1], Jana Kšanová[1],
L. Satrapinskyy[2], K. Hensel[1]

[1]*Division of Environmental Physics, Faculty of Mathematics, Physics, and Informatics, Comenius University, Bratislava, Slovakia*
[2]*Department of Experimental Physics, Faculty of Mathematics, Physics, and Informatics, Comenius University, Bratislava, Slovakia*
E-mail: richard.cimerman@fmph.uniba.sk

This study explores the role of solid pellet-shaped material in plasma-catalytic packed-bed DBD reactors for gas treatment applications. Different pellet-shaped materials, with varying catalytic properties, were tested, demonstrating their distinct influence on the efficiency of gas treatment. Additionally, the results indicated a significant influence of pellet-shaped materials' properties on the electrical characteristics of the reactors. The results emphasize the crucial role of material selection and its properties in optimizing plasma-catalytic gas treatment systems, especially for removing hydrocarbons and converting CO_2 from gas mixtures.

1. Introduction

Packed-bed dielectric barrier discharge (DBD) reactors are widely recognized for their applications in nonthermal plasma (NTP) gas treatment [1]. These reactors typically have a cylindrical geometry and are filled with solid packing materials, often in the form of small spherical or cylindrical pellets. When these materials possess catalytic properties, packed-bed DBD reactors offer a simple but effective combination of NTP and catalysis, i.e., plasma catalysis. Optimizing their performance requires a detailed understanding of how the pellet-shaped material influences both the chemical processes and the electrical characteristics of the discharge. This study investigates the impact of various pellet-shaped materials with distinct catalytic properties on the efficiency of packed-bed DBD reactors for gas treatment. Specifically, it examines the removal (conversion) of various model pollutants, where naphthalene ($C_{10}H_8$) and toluene (C_7H_8) represent organic gaseous pollutants (hydrocarbons), in contrast to carbon dioxide (CO_2), a major inorganic pollutant contributing significantly to climate change.

2. Methodology

In this work, NTP was generated by cylindrical packed-bed DBD reactors that were powered by an AC high voltage with a fixed frequency of 1 kHz at various energy densities (up to 2400 J/l) using various carrier gases (ambient/synthetic air or dry/humid N_2). The reactors were filled with various pellet-shaped materials depending on the gas treatment application. For the removal of naphthalene and toluene, titanium dioxide TiO_2, platinum or palladium coated on alumina Pt-, Pd/Al_2O_3, barium titanate $BaTiO_3$, zirconium dioxide ZrO_2, alumina Al_2O_3 and glass beads were used [2, 3], while titanium dioxide TiO_2, barium titanate $BaTiO_3$, zirconium dioxide ZrO_2, silicon dioxide SiO_2 and magnesium oxide MgO were tested for CO_2 conversion. In addition to examining the eventual catalytic properties of the materials, the effects of their dielectric constant (5–4000), shape (cylindrical vs. spherical), size (Φ 3–5 mm), and specific surface area (SSA; 37–150 m^2/g) were also investigated. Moreover, a combination of different packing materials in a single reactor was also studied. Both gaseous and solid products of toluene, naphthalene, and CO_2 conversion were analyzed by the Fourier-transform infrared absorption (FTIR) spectrometry. The surface of the pellet-shaped materials before and after the use was analysed by scanning electron microscopy (SEM) equipped with energy-dispersive X-ray (EDX) spectroscopy. In addition to the chemical effects of the packed-bed DBD reactors, their electrical characteristics were also examined. Out of them, discharge power, amplitudes, and numbers of

current pulses, reactor capacitances and transferred charges were evaluated based on detailed oscilloscopic measurements and analysis of Lissajous figures.

3. Results and discussion

The study demonstrated that key material parameters (i.e., dielectric constant, shape, size, and SSA) significantly influence the dominant discharge mode (surface or filamentary) in the packed-bed DBD reactor, thereby determining its electrical characteristics. This discharge mode directly impacts reactor performance; however, materials that are efficient for one application may not perform equally well for another. For instance, Figure 1 compares the naphthalene removal efficiency (Fig. 1a), toluene removal efficiency (Fig. 1b) and CO_2 conversion efficiency (Fig. 1c) for reactors filled with various pellet-shaped materials. In all experiments, the reactor without any material (DBD alone) exhibited the lowest efficiency. While all packed-bed DBD reactors outperformed the empty DBD configuration, their efficiency varied significantly depending on the material used. The reactor filled with $BaTiO_3$ achieved the highest CO_2 conversion efficiency but was the least effective for naphthalene removal. In contrast, TiO_2 material showed the highest naphthalene removal efficiency, while its toluene removal and CO_2 conversion performance were among the lowest.

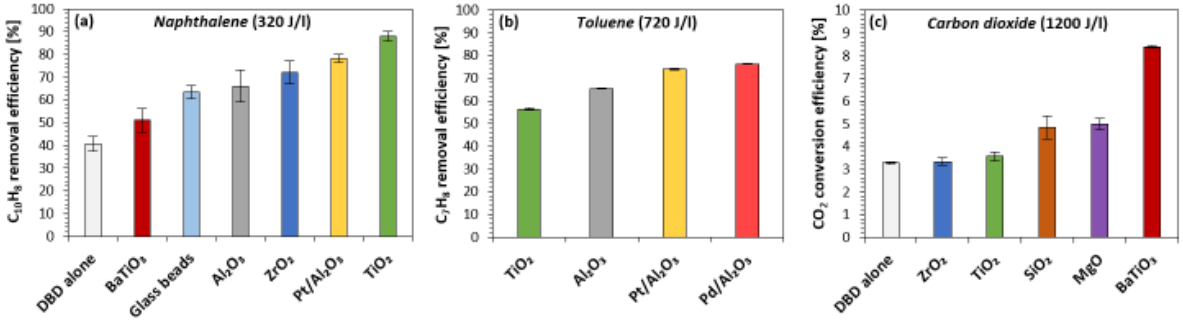

Fig. 1. Naphthalene removal efficiency (a), toluene removal efficiency (b) and CO_2 conversion efficiency (c) for different packed-bed DBD reactors filled with various materials.

Finally, the electrical characteristics of the packed-bed DBD reactors were strongly influenced by the properties of the pellet-shaped materials. However, the removal/conversion efficiencies of the model pollutants showed no direct correlation with these characteristics, suggesting a significant role of surface catalytic processes.

4. Conclusions

This research highlights the pivotal role of material selection in plasma catalysis. The findings reveal that a material highly efficient for one application, such as CO_2 conversion, may perform poorly in another, such as hydrocarbon removal. By examining the interplay between material properties, discharge characteristics, and pollutant removal efficiency, this work provides valuable insights for optimizing plasma-catalytic systems aimed at sustainable gas treatment solutions.

5. Acknowledgements

Funded by the EU NextGenerationEU through the Recovery and Resilience Plan for Slovakia under the project No. 09I03-03-V04-00092. The authors also express their gratitude to Mária Maťašová (Cíbiková) and Diana Priškinová (Račková) for their assistance with the experiments.

6. References

[1] Chen H L, Lee H M, Chen S H, Chang M B 2008 *Ind. Eng. Chem. Res.* **47** 2122–2130.
[2] Cimerman R, Račková D, Hensel K 2018 *J. Phys. D. Appl. Phys.* **51** 274003.
[3] Cimerman R, Cíbiková M, Satrapinskyy L, Hensel K 2020 *Catalysts* **10** 1476.

ELECTRON INDUCED FLUORESCENCE OF CARBON MONOXIDE

Barbora Stachová[1], Enmily Loelbis Garcia Angulo[1], Juraj Országh[1], Samuel Peter Kovár[1], Peter Papp[1], Dennis Bodewits[2], Steven Bromley[2], Štefan Matejčík[1]

[1]*Department of Experimental Physics, Faculty of Mathematics, Physics and Informatics, Comenius University in Bratislava, Slovak Republic*
[2]*Department of Physics, Auburn University, Alabama, USA*
E-mail: barbora.stachova@fmph.uniba.sk

The fluorescence of carbon monoxide – CO was studied in a crossed electron and molecule beam experiment using optical emission spectroscopy. CO is one of the dominant carbon bearing molecules in the Universe. The emission spectrum following electron impact on CO was measured at 50 eV within the wavelengths of 300 - 1000 nm. The emission bands of CO dominate this spectral region at energies below 20 eV, while the signal from CO^+ is dominant above this energy. Excitation-emission functions of several emission bands were measured as well, and their threshold energies were estimated.

1. Introduction

Inelastic collisions of molecules with low energy electrons are of great importance and occur across the whole Universe [1]. They often result in excitation and subsequent emission of radiation as excited particles de-excite, referred to as electron induced fluorescence. Emission spectroscopy is one of the tools that can be used to acquire knowledge on electron induced fluorescence. The results can serve as a reference data for the analysis of astronomic spectra, discharge spectra, they act as an input for theoretical modelling of complex systems such as atmospheric processes, discharges and other research or industrial applications.

This work is focused on electron induced fluorescence of carbon monoxide. Carbon monoxide is one of the dominant molecules in the Universe, especially on extra-terrestrial bodies such as comets or centaurs. The $A^2\Pi - X^2\Sigma^+$ transition of CO^+ is prominent in emission spectra of the cometary comae and is referred to as the Comet Tail system. The diagnostic of these cometary volatiles is a necessity for solar system formation models [2]. CO is also present in interstellar gas clouds which are the precursors of star formation. It is commonly used as a tracer of H_2 in the interstellar medium, which is difficult to observe on its own as it lacks a permanent dipole moment [3]. It is also an important compound of planetary atmospheres, such as Mars or Venus.

There are several papers on electron impact excitation of carbon monoxide. Many are focused solely on the Comet Tail system of CO^+ such as [4] because of its dominance in higher energy spectra. In 2019, Ajello et al. [5] also measured the far ultraviolet (VUV) emission spectrum of CO and CO_2 induced by electrons with the kinetic energy of 30 and 100 eV. They have identified the Fourth Positive system of CO and the optically forbidden atomic transition of O ($^5S^0 - {}^3P$) and also measured their emission cross-sections. A comprehensive review of the literature on the band spectrum of CO was compiled by [6]. It consists of critically evaluated numerical data on band positions, molecular constants, energy levels and potential energy curves. A critical review of the process of dissociation of a wide range of oxygen containing molecules including CO following electron impact was concluded by [7]. The dissociation mechanisms include dissociative ionisation, attachment and excitation.

The aim of this research is to extend this collection of data on the transitions and absolute emission cross sections and to obtain more information on the processes that occur in the experiment.

2. Experimental apparatus

The experimental apparatus utilized in this work is based on a crossed electron and molecular beams method and is further described in a previous publication [8]. A monochromatic electron beam is generated by a trochoidal electron monochromator placed in a vacuum chamber. This electron beam interacts with a molecular beam formed by an effusive capillary perpendicularly to the electron beam.

The background pressure of the vacuum chamber is about 10^{-8} mbar and the pressure of the molecular beam is set to sustain binary collisions – one electron with one molecule. One of many products of electron-molecule interactions are particles that are excited, which subsequently emit radiation as they de-excite. These are the subject of our research. An optical system is used to guide the emitted radiation out of the vacuum chamber and focus it into the entrance slit of a Czerny-Turner optical monochromator. Two detectors - a Hammamatsu photomultiplier (PMT) or a CCD (CCD) camera are used for the detection and quantification of the emission passing through the optical monochromator. The photomultiplier operates in the wavelength region of 185 – 700 nm. It collects the signal from one small wavelength interval defined by optical resolution of the monochromator at a time. The CCD camera is sensitive in 270 – 1100 nm wavelength range. It detects light from approximately 80 nm wide wavelength interval at once. The scheme of the experimental apparatus is shown in Fig. 1.

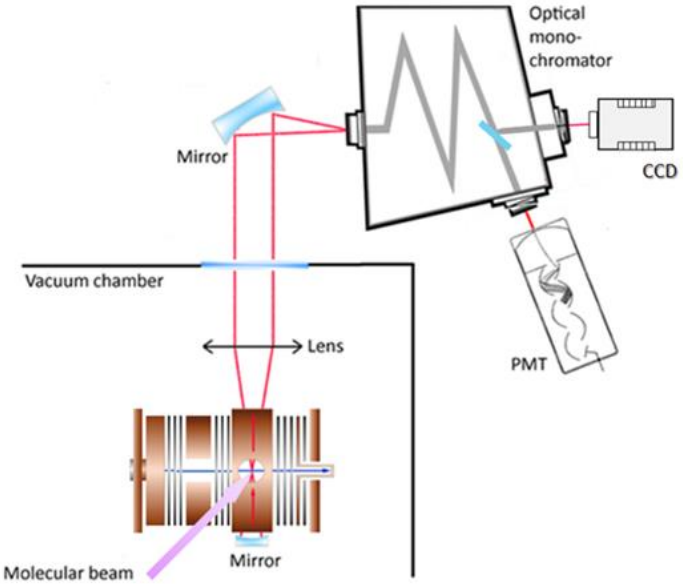

Fig. 1. The scheme of the experimental apparatus for electron induced fluorescence. Blue - electron beam, red - fluorescence signal, violet - molecular beam.

3. Experimental results

The emission spectrum containing emission bands of neutral and ionized molecule of CO as well as its fragments was obtained as a result of electron impact on this molecule. The overview emission spectrum was measured in the wavelengths within 300 – 1000 nm at 50 eV electron energy and is depicted in Fig. 2. and Fig. 3. The spectrum is not calibrated for apparatus sensitivity. This spectral region is dominated by the Comet Tail system of CO^+ ($A^2\Pi - X^2\Sigma^+$) spreading over the wavelengths from 300 to 750 nm. A few emission bands of the Baldet – Johnson system of CO^+ ($B^2\Sigma - A^2\Pi^+$) were identified as well. The emission lines of C I and O I were observed in the higher wavelength region and are identified in Fig. 3. Along with the emission bands of ionized CO^+, the spectrum also contains several emission bands of neutral CO. These bands spread along the whole spectral region, but at 50 eV their intensity is much weaker than of the Comet Tail system, so they are hard to distinguish.

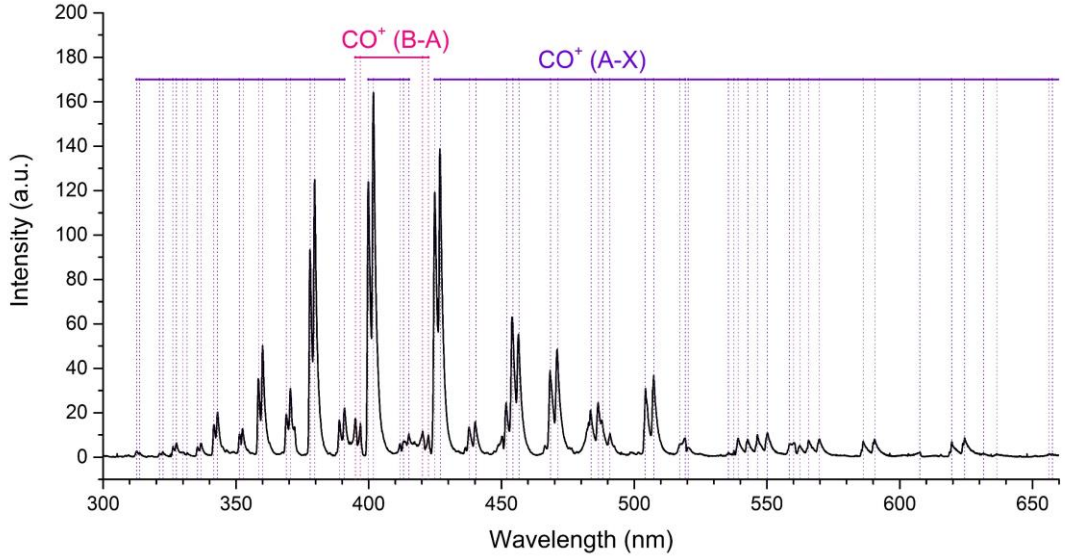

Fig. 2. The emission spectrum of CO measured by CCD camera at 50 eV within 300 – 660 nm.

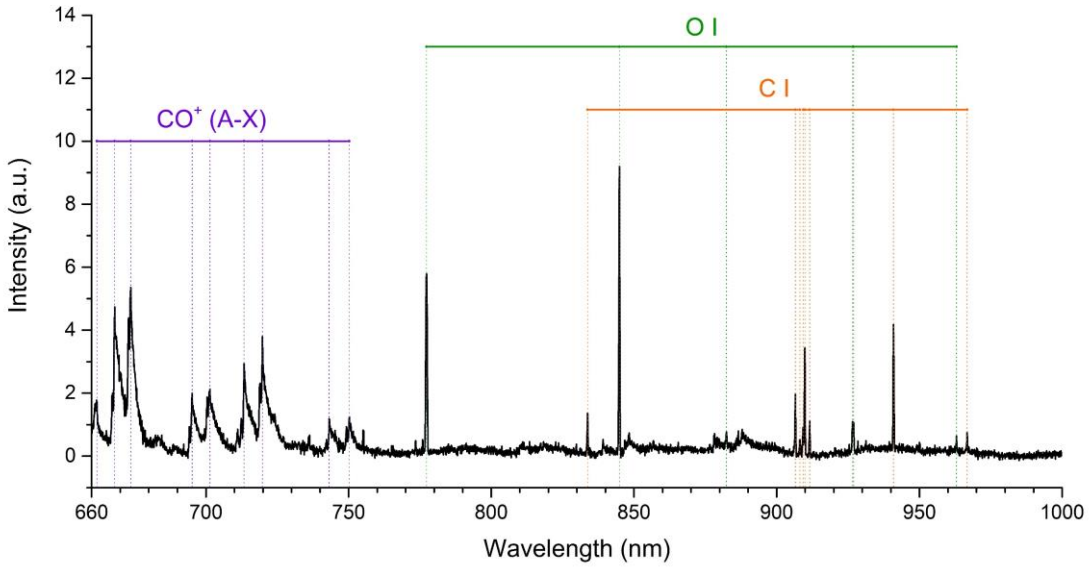

Fig. 3. The emission spectrum of CO measured by CCD camera at 50 eV within 660 – 1000 nm.

Additionally, the excitation-emission functions of selected transitions were measured in the electron energy range within 5 – 100 eV. Fig. 4.a) show the excitation-emission function of the First Negative system of CO^+ ($B^2\Sigma - X^2\Sigma$) at 230.3 nm with its threshold energy at 20.0 eV. The signal from the Third Positive system of CO ($b^3\Sigma^+ - a^3\Pi$) was measured at 297.2 nm and is depicted in Fig. 4.b). The threshold energy of this transition was determined at 10.6 eV. Fig.4.c) shows signal from two excitation-emission functions measured at 402.2 nm. It consists of the emission from the Asundi system of CO ($a'^3\Sigma^+ - a^3\Pi$) and the Comet Tail system of CO^+ ($A^2\Pi - X^2\Sigma^+$) with their thresholds at 10.2 eV and 18.0 eV respectively. The excitation emission function of the Ångström system of CO ($B^1\Sigma^+ - A^1\Pi$), depicted in Fig.4.d), was measured at 451.1 nm. Its threshold energy was determined at 9.5 eV.

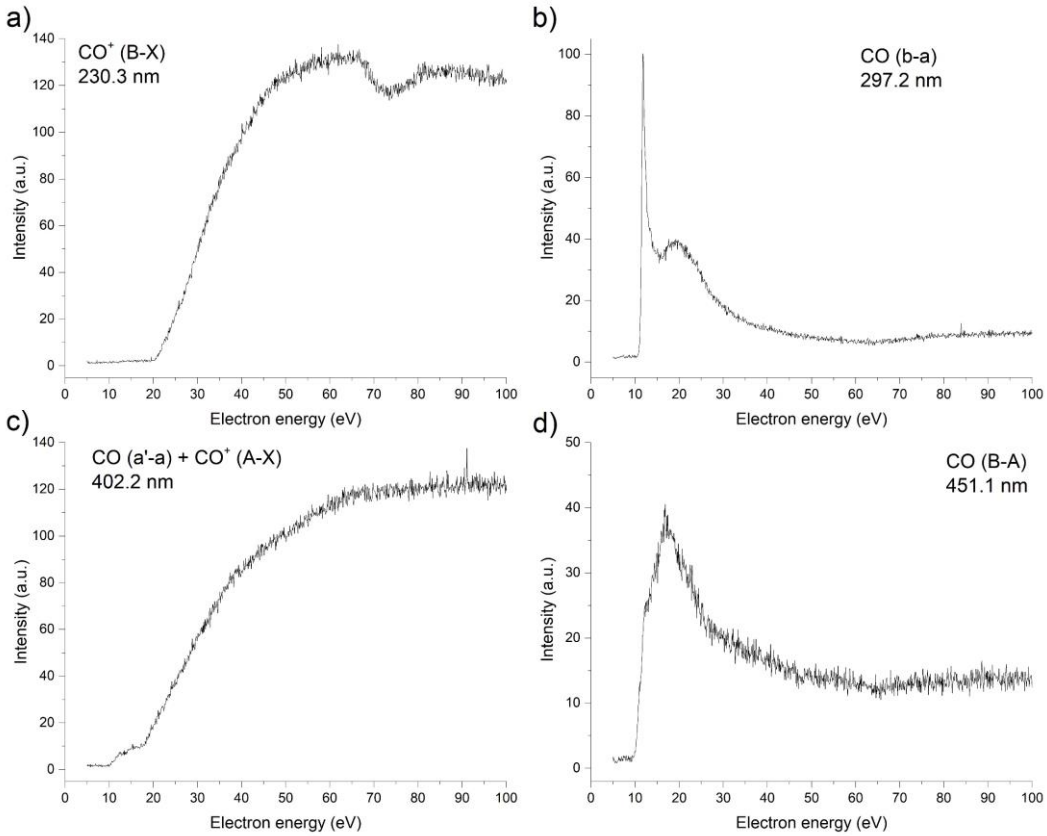

Fig. 4. Excitation-emission functions: a) CO^+ ($B^2\Sigma - X^2\Sigma$) at 230.3 nm, b) CO ($b^3\Sigma^+ - a^3\Pi$) at 297.2 nm, c) CO ($a'^3\Sigma^+ - a^3\Pi$) combined with CO^+ ($A^2\Pi - X^2\Sigma^+$) at 402.2 nm, d) CO ($B^1\Sigma^+ - A^1\Pi$) at 451.1 nm.

4. Conclusion

Electron induced fluorescence of carbon monoxide was studied in a crossed-beam experiment. The emission spectrum at 50 eV in the wavelength range of 300 – 1000 nm was measured and analysed. The spectrum shows a prominent emission of the Comet Tail system of CO^+ ($A^2\Pi - X^2\Sigma^+$) along with a few emission bands of the Baldet – Johnson system of CO^+ ($B^2\Sigma - A^2\Pi^+$) and the emission lines of C I and O I. The excitation-emission functions of chosen transitions of both CO and CO^+ were measured as well and their threshold energies were estimated. Further research will be focused on a 3D spectral electron energy map which will consist of the emission spectra measured at energies ranging from 5 to 100 eV with small energy steps. This data will give the information about the excitation-emission functions of all of the individual transitions in the spectra and their threshold energies. The data will be calibrated to absolute values of the emission cross sections, which will make it suitable as reference data for astrophysical research.

Acknowledgements. This work was supported by the Slovak Research and Development Agency under the Contracts no. SK-PL-23-0050, APVV-19-0386 and APVV-23-0522, Slovak grant agency VEGA under projects nr. 1/0489/21 and 1/0553/22. This project has received funding from the European Union's Horizon 2020 research and innovation programme under grant agreement No 871149.

5. References

[1] Ingólfsson O 2019 *Low-Energy Electrons; Fundamentals and Applications.* doi: 10.4324/9780429058820.

[2] Roth L et al. 2021 *Nature Astronomy.* **5** 1043–1051.

[3] Bodewits D et al. 2016 *The Astronomical Journal.* **152** 130.
[4] Holland R F and Maier II W B 1972 *The Journal of Chemical Physics.* **56** 11.
[5] Ajello J M et al. 2019 *Journal Geophysical Research: Space Physics*. **124** 4 2954–2977.
[6] Krupenie P H 1966 *The Band Spectrum of Carbon Monoxide. National Standard Reference Data Series.* ***3****.*
[7] McConkey J W et al. 2008 *Physics Reports*. **466** 1–3 1–103.
[8] Országh, J, Danko M, Čechvala P, Matejčík Š 2017 *The Astrophysical Journal.* ***841*** 17 (10pp).

EFFECT OF DILUTION OF H_2/CH_4 MICROWAVE MICROPLASMA WITH ARGON FOR IMPROVED GAS PHASE NUCLEATION OF NANODIAMONDS

Joel Jeevan[1, *], Abdoulaye Constant Siby[1], Arvind K. Bhakta[1,2], Michael Redolfi1, Khaled Hassouni[1], Swaminathan Prasanna[1]

[1]*LSPM-CNRS, UPR 3407, Université Sorbonne Paris Nord, 99 avenue J.B. Clément, 93430, Villetaneuse, France*

[2]*Universite Paris Cite, CNRS UMR-7086, ITODYS, 15 Rue Jean-Antoine de Baïf, 75251, Paris, France*

[*]E-mail : joel.jeevan@lspm.cnrs.fr

A microwave microplasma (MWMP) torch using $Ar/H_2/CH_4$ as the working gas was used to synthesize nanodiamonds (NDs) along with trace amount of amorphous carbon nanostructures. In this study, plasma parameters such as the microwave power, operating pressure, H_2/CH_4 ratio were fixed by varying Ar concentration. The plasma was characterized extensively using optical emission spectroscopy (OES) and pico-second two absorption laser induced fluorescence (ps-TALIF) to obtain local plasma parameters such as n_e, T_g and n_H. It was found that injection of argon increases hydrogen atom density (nH) by one order of magnitude to $10^{17}cm^{-3}$ with gas temperature increasing up to 1700 K. The effect of Argon in a H_2 rich plasma on the gas-phase nucleation of nanodiamond was studied by correlating the plasma characteristics with the synthesized nanomaterials characterized by Raman spectroscopy and scanning electron microscopy (SEM). In spite of the increase in gas temperatures, high H-atom densities ensured higher yield of sp^3 fraction of the synthesized nanostructures. Moreover, this increase in sp^3 fraction positively correlates with high C_2 emission, indicating that the increased nucleation of nanodiamonds was due to higher concentration of carbon radicals in Argon plasmas.

1. Introduction

Nanodiamonds (NDs) are one of numerous types of carbon nanostructures, including nano-sized amorphous carbon, fullerenes, carbon nano tubes, onions, and rods, to mention few[1–4]. They are sp^3 - hybridized carbon structures at nanoscale dimension (1 to 100 nm). Diamonds at nanoscale can be of various forms such as pure-phase diamond films, diamond nanoparticles, 1-D diamond nanorods and 2-D diamond nanoplatelets [5]. The most pure ND grains can have almost pristine crystalline structure with traces of non-diamond carbon. They have tremendous potential in biomedicals, tribology, optical sensors, electronics, quantum computing, tissue engineering, photovoltaics, and a variety of environmental applications such as waste water treatment [6–10].

NDs were first synthesized using detonation by researchers from USSR long back in July 1963 [11–13]. They have improved thermal stability and mechanical properties, henceforth the research has shifted its focus to their synthesis and modification [14]. Extensive research has been conducted to discover several ND synthesis methods, such as laser ablation, ion irradiation of graphite, ultrasound cavitation, high energy ball milling of high pressure high temperature diamond microcrystals, plasma enhanced chemical vapour deposition, and so on[15–19]. Each of these methods has its own limitations and requires a precursor version of diamond, at least in small amounts depending on whether it is top-bottom or bottom-top mode of synthesis. In contrary, there are rising number of studies that have reported the gas-phase nucleation of ND and are technologically interesting[20–27].

Jia et al.,2023 [28] discussed the gas phase nucleation of NDs while using H_2 and CH_4 as the primary gas precursors in a microwave microplasma torch (MWMP). Later, Siby et al.,2024 [29] have verified the gas phase nucleation of ND in a hydrogen rich atmosphere and discussed the importance of hydrogen atom in the molecular growth of diamond. The key findings of these papers were that ND nucleation enhances in high concentration of hydrogen atoms which was measured using ps-TALIF[30], and a high concentration of hydrocarbon species in the plasma could alter the molecular growth pathway from sp^3 feasibility to sp^2 species such as polyaromatic hydrocarbons(PAHs) and polyacetylenes. The gas temperature T_g should be moderate, as graphitic phase is more stable and diamond graphitization occurs at higher temperatures. [28,31].

In order to support nucleation of nanodiamonds, it is important to develop a hydrocarbon plasma chemistry in the presence of substantial H-atom density under moderate temperatures. A very good supply of key carbon radicals such as CH_3· , and C_2 dimer would be a key-factor[28,32,33] while minimizing alternative molecular pathways such as PAHs and polyacetylenes. Studies have also shown that noble gases increase the dissociation rate of methane, as well as hydrogen and other hydrocarbon molecules, thus increasing the concentration of key carbon radicals and therefore increasing the deposition rate [34]. Ar in addition to hydrogen is known to induce a supersaturation effect of H-atom and ions in the system [35]. This study thus attempts on making the plasma more reactive and richer by addition of Ar to the precursor gases and study its effects on the quality and yield of the nanodiamonds in the collected carbon nanostructures.

2. Materials and methodology

Experimental setup

Details of the experimental setup are discussed elsewhere [28,29]. In this study, the working gas was a varied combination of $Ar/H_2/CH_4$. The operating pressure and microwave power were set to 100 mBar and 90 Watts, respectively.

Material characterization

The synthesized carbon nanostructures were collected on a Si substrate placed downstream the MWMP torch and were directly characterized using Raman spectroscopy and SEM. Raman spectroscopy was conducted using HR800 spectrometer equipped with a Peltier-cooled CCD detector (Horiba Jobin Yvon) with back- scattering configuration coupled to a 473 nm laser, whose spectral and spatial resolutions were 0.25 cm^{-1} and 5 µm, respectively. SEM analysis was conducted using a ZEISS SUPRA 40VP and a field emission ZEISS ULTRA plus microscopes, operating at 5 kV.

Plasma characterization

The plasma was extensively characterized using OES and ps-TALIF to obtain plasma parameters such as n_e, T_g and n_H. OES was carried out using a 1m Jobin-Yvon THR 1000 spectrometer with 1800 grooves per mm grating blazed at 250 nm. The spectrometer is associated with Horiba DPM-HVH photomultiplier tube. The signal acquisition was carried out using a 40 µm slit opening. The gas temperature was assumed equal to the rotational temperature of the ($G^1\Sigma^+$, $v = 0$) level and determined from the rotational structure of the $G^1\Sigma_g^+ \rightarrow B^1\Sigma_U^+(0, 0)$ transition [36]. Electron density was inferred from the stark broadening of the *Hγ* line ($n = 5$ to $n = 2$). The C_2 Swann band (0, 0) transition ($d^3\Pi_g \rightarrow a^3\Pi_u$) at 516 nm in varying conditions were also recorded. H-atom density was measured using ps-TALIF, whose experimental methodology has been detailed elsewhere [30].

3. Results

We observed a slight increase in n_e in the range of 1 to 4× 10^{13} cm^{-3} when argon was introduced in the feed gas. However, the T_g measured (figure 1a) from the rotational structure of the $G^1\Sigma_g^+ \rightarrow B^1\Sigma_U^+(0, 0)$ transition, increases significantly from 1200 K in the absence of argon in the feed gas to 1700 K for 20 sccm Ar in the feed gas. From figure 1b, it is clear that H-atom density, n_H, increases by 1 order of magnitude when argon is injected in the plasma. The simultaneous increases of n_e, T_g and n_H indicate that the increase of argon concentration in the feed gas results in an enhanced plasma excitation and reactivity, which would therefore impact the hydrocarbon chemistry in the plasma.

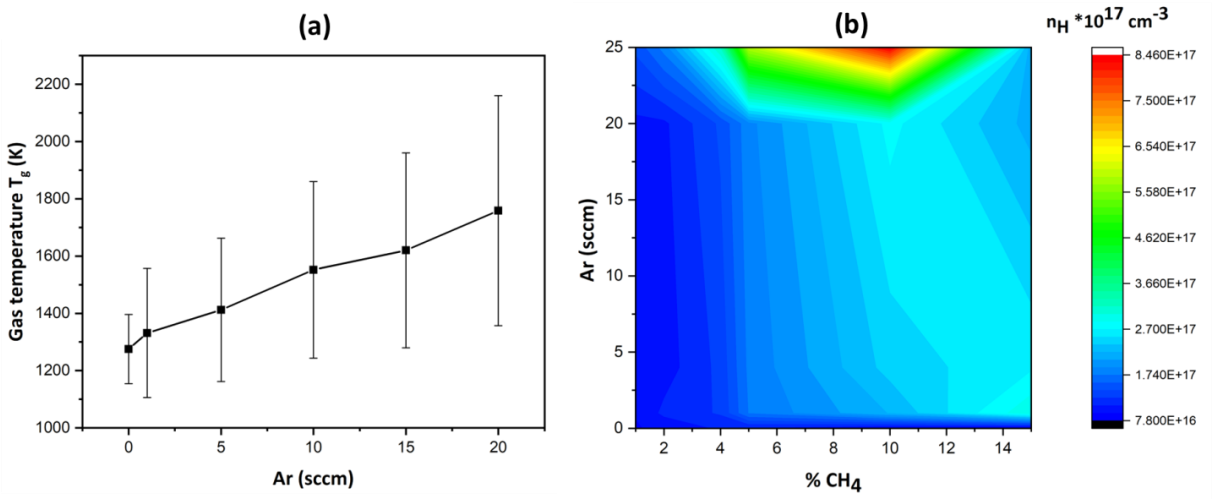

Fig. 1. Plasma characterization for (a) Gas temperature measurement and (b) Hydrogen atom density with varying Ar concentration.

As a consequence, the amount of carbon nanostructures increased significantly with addition of Ar. The SEM image of the as-synthesized carbon nanostructures with 20 sccm Ar is shown in figure 2b. It was found that the morphology of these deposits are quite different from nanostructures generated without argon in the feed gas. The particles produced in an Ar diluted plasma were much larger (possibly due to agglomeration), ~ 30-45 nm size as against ~ 10 nm size in Ar less plasma. It is observed that the effective deposit density per area also (calculated from the SEM images) increases from 2.75 $A^{\circ -2}$ for Ar less plasma to 3.75 $^{\circ}A^{-2}$corresponding to 20 sccm flow rate of Ar. It appears therefore that argon improves both particle growth and particle nucleation, which is likely due to an enhanced production of key carbon radicals and molecular growth chemistry that govern nucleation kinetics, respectively.

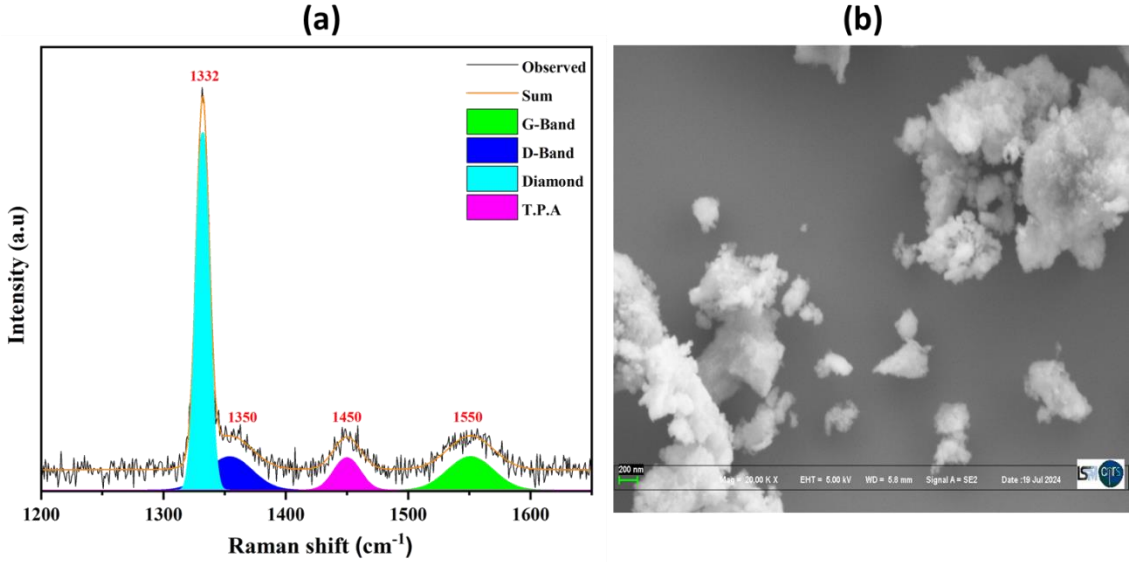

Fig. 2. Material Characterization via (a) Raman spectrsoscopy and, (b) SEM microscopy of as-synthesized nanostructures.

The significant Raman features (figure 2a) observed in the as-synthesized samples were well in accordance with the previous publications on Raman characterization of ND[29,37,38]. The key features observed were as follows: -

- The sharp peak at 1332 cm^{-1} corresponds to diamond which is sp^3 hybridized.

- The band around 1350 cm^{-1} corresponds to D - band often related to disorder and amorphous carbon which is sp^2.
- The band near 1450 cm^{-1} corresponds to transpolyacetylene which is sp^2 hybridized.
- The band near 1550 cm^{-1} corresponds to G band which is indicative of graphitic impurity(sp^2) present in the samples.

Raman spectroscopy was also used to compute the sp^3 of the synthesized carbon nanostructures, figure 3a shows the effect of Ar injection on the sp^3 fraction of the material at various conditions. It was found out using the following formula [29,39]:

$$\%sp^3 = \frac{60I_{dia}}{60I_{dia}+\Sigma I_{non-dia}} * 100 \quad (1)$$

In spite of increase in T_g, the increase in H-atom densities might have stabilized diamond formation thus avoiding graphitization [28]. Figure 3b shows a very interesting result with regard to C_2 swann band emissions, which are indicative of C_2 densities. This emission (figure 3b) shows a direct relationship with the sp^3 fraction depicted in figure 3a. The region of contour plot with maximum C_2 intensity corresponds to the condition with the maximum sp^3 fraction in our regime of investigation (c.f Figure 3a). This suggests that C_2 dimer can play a key role in the molecular growth of ND in MWMP torch, which is in agreement with Jia et al. [28].

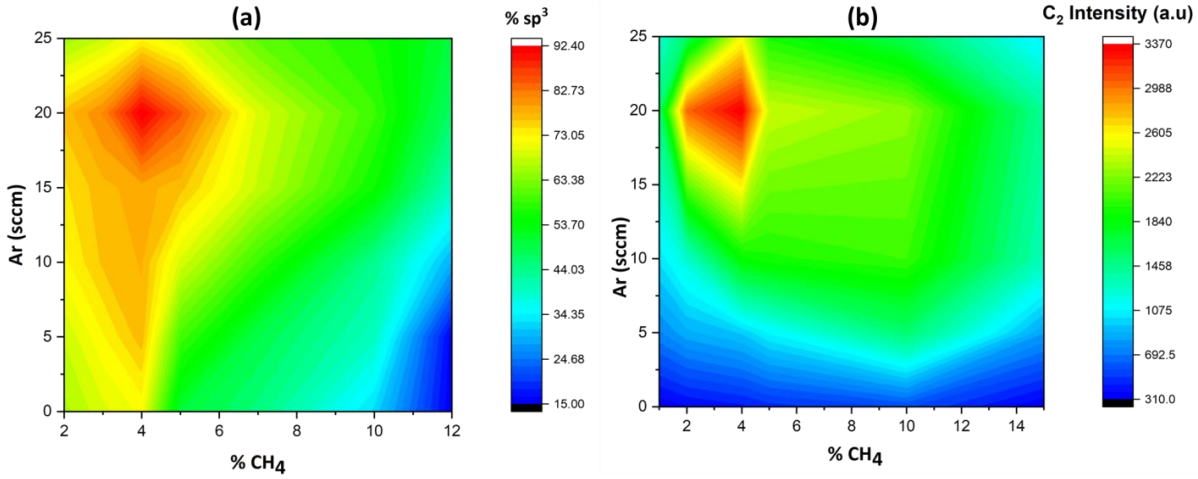

Fig. 3. sp^3 fraction and emission intensity of C_2 swann band intensity as a function of Ar concentration.

4. Discussion

This paper examined the effect of Ar injection to H_2/CH_4 plasma on ND nucleation. In the investigated regime, the best NDs are nucleated at 100 mBar pressure with 90 Watt of injected microwave power with a total flowrate of 120 sccm, having the gas composition as 96 sccm of H_2, 4 sccm of CH_4 and 20 sccm of Ar.

This study is indicative that both H-atom and C_2 dimer are important for ND nucleation. We have found a direct correlation between intensity of C_2 Swann band emisson to sp^3 fraction. This means that C_2 dimer has a strong role to play in ND nucleation. The importance of C_2 in ND nucleation has been discussed by other researchers as well. Gruen et al.[33] observed almost a linear relationship between diamond growth rate and intensity of C_2 swann band emissions in Ar, H_2 and CH_4 plasma. According to Gruen et al., the C_2 is energetically favourable to form diamond as C_2 insertion in CH as well as CC bonds have low activation energy. Dolmotov had also proposed a C_2 led molecular growth mechanism involving cyclohexane as one of the key building blocks of ND nucleation in detonation conditions, but

cyclohexane is also a precursor in sp^2 carbons[40,41]. Even though we advocate the role of C_2 dimer as a building block in ND nucleation phenomena, it is obvious that other sp^3 nucleation routes through CH_3 and the sp^2 growth pathways may also co-exist.

The n_H is observed to increase with concentration of Ar in the plasma. It is known that, H-atom concentration could have strong influence in improving the sp^3 fraction because it is often associated with hydrogen abstraction reaction resulting in formation of CH_3· radicals. In addition to it, from our observations in the figure 1b and figure 3a, suggests that a very high concentration of H-atom does not necessarily increase the sp^3 fraction, rather there is an optimum level of H-atom for sp^3 growth. In particular, hydrogen abstraction reactions also initiates the hydrogen abstraction acetylene addition (HACA) processes, which are thought to be the primary pathway in soot creation, acetylene, a crucial chemical precursor in soot formation, is also a by-product of hydrogen abstraction reactions[42,43]. Shao et al., discussed about a different role of H-atom, the author claims that in a H-atom rich atmosphere, the hydrogen abstraction reactions readily generate aryl radicals which can enhance soot formation[44,45]. A very high H-atom density could therefore result in increased sp^2 fraction and may be detrimental to the nucleation of diamond which is sp^3 hybridized [46].

In conclusion, ND nucleation can occur through multiple pathways dictated by favorable kinetics due to optimum quantities of H-atoms along with key carbon radicals such as C_2.

5. Acknowledgment

This work was funded by the French Agence Nationale de la Recherche (ANR), under grants ANR-22-CE51- 0013 (project NANODIAPLAS) and ANR-22-CE51-0027-02 (project ULTRAMAP), Labex SEAM (ANR-10-LABX-0096; ANR-18-IDEX0001, LA01PRASAN233690LSPMXR) and IDF regional project SESAME DIAGPLAS. One of the authors (Khaled Hassouni) acknowledges the support of the Institut Universitaire de France.

6. References

[1] Georgakilas V, Perman J A, Tucek J, and Zboril R 2015 *Chem. Rev.* **115** 4744–4822.
[2] Manasa G, Mascarenhas R J, Bhakta A K, and Mekhalif Z 2020 *Electroanalysis* **32** 939–948.
[3] Manasa G, Mascarenhas R J, Bhakta A K, and Mekhalif Z 2021 *Michrochemical Journal* **160** 105768.
[4] Bhakta A K, Kumari S, Hussain S, Belkhiri S, Lo M, Mascarenhas R J, Delhalle J, and Mekhalif Z2021 *Emergent Materials* **4** 403–411.
[5] Zamani Y, Ghazanfari H, Erabi G, Moghanian A, Fakic B, Hosseini S M, and Mahammod B P 2021 *Journal of composites and compounds.*
[6] McGuinness L P, Yan Y, Stacey A, Simpson D A, Hall L T, Maclaurin D, Prawer S, Mulvaney P, Wrachtrup P, Caruso F, Scholten R E, and Hollenberg L C L 2011 *Nature Nanotechnology* **6** 358–363.
[7] Zhang Q, Mochalin V N, Neitzel L, Knoke I Y, Han J, Klug C A, Zhou J G, Lelkes P I, and Gogotsi Y. 2011 *Biomaterials* **32** 87–94.
[8] Mochalin V, Shenderova O, Ho D, and Gogotsi Y 2020 *Jenny Stanford Publishing*. ISBN 978-0-429-39903-9.
[9] Karishma B R, Manasa G, Bhakta A K, Maiyalagan T, Mascarenhas R J, and Shetti N P 2023 *Colloids and Surfaces B: Biointerfaces* **227** 113363.
[10] Manasa G, Bhakta A K, Mascarenhas R J, and Shetti N P 2023 *Michrochemical Journal* **191** 108778.
[11] Danilenko V V 2004 *Physics of the Solite State* **46** 595–599.
[12] Volkov K V, Danilenko V V, and Elin V I 1990 *Plenum Publishing Corporation* **26** 366–368.
[13] Dolmatov V V 2007 *Russian Chemical Reviews* **76** 339–360.
[14] Zhang Y, Rhee K Y, and Park S-J 2017 *Composites Part B: Engineering* **114** 111–120.
[15] Amans D, Chenus A.-C., Ledoux G, Dujardin C, Reynaud C, Sub- lemontier O, Masenelli-Varlot K, and Guillois O 2009 *Diamond and Related Materials* **18** 177–180.
[16] Boudou J-P, Curmi P A, Jelezko F, Wrachtrup J, Aubert P, Sennour M, Balasubramanian G, Reuter

R, Thorel A, and Gaffet E 2009 *Nanotechnology* **20** 235602.
[17] Daulton T L, Kirk M A, Lewis R S, and Rehn l E 2001 *Nuclear Instruments and Methods in Pysics Research Section: Beam Interactions with Materials and Atoms* **175–177** 12–20.
[18] Gicquel A, Hassouni K, Silva F, and Achard J 2001 *Current Applied Physics* **1** 479–496.
[19] Khachatryan A K, Aloyan S G, May P W, Sargsyan R, Khachatryan V A, and Baghdasaryan V S 2008 *Diamond and Related Materials* **17** 931–936.
[20] Alekseev N I, Khadutin V S, and Khmelnitskii I K 2021 *Structure of Matter and Quantum Chemistry* **95** 2444–2453.
[21] Badzian A R and DeVries R C 1988 *Materials Research Bulletin* **23** 385–400.
[22] Derjaguin B V and Fedoseev D V 1994 *Progress in Surface Science* **45** 81–83.
[23] Kamo M, Sato Y, Matsumoto S, and Setaka N 1983 *Journal of Crystal Growth* **62** 642–644.
[24] Kumar A, Lin P A, Xue A, Hao B, Yap Y K, and R. Sankaran M 2013 *Nature* **4** 2618.
[25] Nikhar T and Baryshev S V 2024 *AIP Advances* **14** 045334.
[26] Frenklach M, Kematick R, Huang D, Howard W, Spear K E, Phelps A W, and Koba R 1989 *Journal of Applied Physics* **66** 395–399.
[27] Rebrov A K 2017 *Physics-Uspekhi* **60** 179.
[28] Jia Z, Fermi Y, Siby A, Brinza O, Hassouni K, and Prasanna S 2022 *Plasma Processes and Polymers* **20** 2200180.
[29] Siby A C, Bhakta A K, Jeevan J, Sun X, Decorse P, Ammar S, Hassouni K, and Prasanna S *Nucleation of nanodiamonds in H-atom rich microplasma*. URL https://hal.science/hal-04764588.
[30] Siby A, Stefas D, Agha Y, Invernizzi L, Gazeli K, Lombardi G, Hassouni K, and Prasanna S 2024 *Physics of Plasmas* **31** 033506.
[31] Vita A D, Galli G, Canning A, and Car R 1996 *Applied Surface Science* **104-105** 297–303.
[32] De´ak P, Giber J, and Oechsner H 1991 *Surface Science* **250** 287–290.
[33] Gruen D M, Zuiker C D, Krauss A R, and Pan X 1995 *Journal of Vaccum Science and Technology* A **13** 1628-1632.
[34] Zhu W, Inspektor A, Badzian A R, McKenna T, and Messier R 1990 *Journal of Applied Physics* **68** 1489–1496.
[35] Baranauskas V, Ceragioli H J, Peterlevitz A C, Tosin M C, and Durrant S F 2000 *Thin Solid Films* **377–378** 303–308.
Goyette A N, Jameson W B, Anderson L W, and Lawler J 1998 *Journal of Physics D: Applied Physics* **29** 1197–1201.

MAPPING RADICAL FLUXES WITH THERMOCOUPLE PROBES

A. Herrmann[1,2], D. de Graaf[1], P. Krebauma, S. Bera[1], M.N. Tsampas[1] M.C.M. van de Sanden[1,3]

[1]*Dutch Institute for Fundamental Energy Research (DIFFER), Eindhoven, The Netherlands;*
[2]*Queen's University Belfast, School of Maths and Physics, United Kingdom;*
[3]*Eindhoven Institute for Renewable Energy Systems (EIRES), Eindhoven University of Technology Eindhoven, The Netherlands*
E-mail: a.herrmann@qub.ac.uk

Understanding the radical flux of e.g. reactive oxygen and nitrogen species is essential for advancing the medical applications of plasma, as these species play a pivotal role in the effects of plasma-based treatments. Radical probes are an in-situ, low-cost method for radical flux or density measurements in plasma afterglows. They are based on a calorimetric principle. Radicals recombine exothermically on a catalytic surface on the tip of a temperature sensor, e.g. a thermocouple. The measured temperature is translated to a heat flux from catalytic recombination reactions through a heat flux analysis of the system. Knowing the heat flux from recombination, the radical density can be calculated[1]. The use of a dual thermocouple probe allows plasma heating to be distinguished from recombination heating; a second *reference* thermocouple without the catalytic surface is placed next to the active, *catalytic* thermocouple[2].

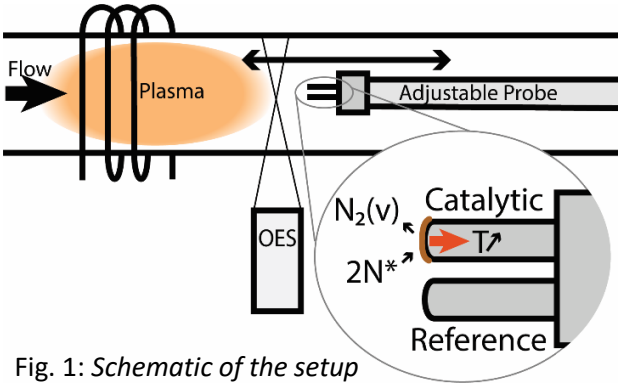

Fig. 1: *Schematic of the setup*

We performed an extensive heat flux analysis of the dual thermocouple setup combining thermal imaging with temperature measurements of the probe inside the reactor and found that adding a heat sink to the thermocouples with a third thermocouple measuring the sink temperature reduces ambiguity in the evaluation. Additionally to the thermocouple probe, we quantified Nitrogen density through optical emission spectroscopy, using the first positive system[3], where we observed an overpopulation of high vibrational states of N_2(B,v=11) in the afterglow.

Fig. 1 shows a schematic of the setup. The thermocouple probe is mounted on an adjustable feedthrough, and the OES fiber is on a rail parallel to the quartz tube, permitting a scan of the entire reactor. Mapping the N density through the entire reactor enables us to analyze the reaction rates of recombination in the gas phase as well as give an estimate on the lifetimes of the radicals at the measured pressure and flow rates.

Acknowledgments

This project is part of the European project ORACLE, which has received funding from the European Union's Horizon 2020 Research and Innovation Programme under grant agreement No 101022738.

References

[1] Mozetic, M., Vesel, A., Cvelbar, U. et al. *Plasma Chem Plasma Process 26*, 103–117 (2006).

[2] Qerimi, D., Shchelkanov, I., et al. *Journal of Vacuum Science & Technology A*., 39. 023003 (2021).

[3] F J J Peeters et al *Plasma Sources Sci. Technol.* 24 045006 (2015).

ATMOSPHERIC PRESSURE PLASMA POLYMERIZATION FOR FUNCTIONAL COATING APPLICATIONS

Sandra Ďurčányová[1], Michal Stano[1], Pedram Ghourchi Beigi[2], Dušan Kováčik[1,2]

[1]*Comenius University in Bratislava, Faculty of Mathematics, Physics and Informatics, Department of Experimental Physics, Mlynská dolina, 842 48 Bratislava, Slovakia*
[2]*Department of Plasma Physics and Technology, CEPLANT, Faculty of Science, Masaryk University, Kotlářská 2, 602 00 Brno, Czech Republic*
E-mail: sandra.durcanyova@fmph.uniba.sk

This contribution deals with atmospheric pressure plasma polymerization of hexamethyldisiloxane as a method of preparing hydrophobic layers on glass. The plasma-polymerized layers were characterized using ATR-FTIR, SEM and WCA measurements. Long-term chemical stability of the layers was studied via ageing tests.

1. Introduction

Plasma polymerization (PP) is a technique for depositing thin, functional, polymer-like coatings by activating gaseous or liquid monomers in the presence of non-thermal plasma. The highly reactive plasma species, such as ions, electrons, radicals and excited molecules, interact with a gaseous or liquid monomer present in the working gas, initiating polymerization and facilitating layer deposition directly onto substrates without the need for solvents, catalysts, or additional curing steps [1]. Unlike conventional polymerization, which often requires complex chemical processes and produces toxic waste, PP is more environmentally friendly and allows fine-tuning of layer properties by adjusting different process parameters. This enables the formation of layers with unique chemical and physical properties. With the appropriate selection of working conditions, plasma-polymerized layers have the potential to be mechanically and chemically resistant, insoluble, thermally stable, homogeneous, with a high degree of monomer cross-linking, and adhere well to different types of surfaces [2]. PP can be carried out under various pressure regimes, with atmospheric pressure offering notable advantages in scalability, operational simplicity and cost-effectiveness compared to vacuum systems.
Examples of plasma sources used for PP at atmospheric pressure include most notably dielectric barrier discharges (DBDs) and plasma jets. These systems vary in their ability to generate uniform plasma, manage gas flow dynamics, and produce different reactive species, which influences the quality and functionality of the deposited coatings. The properties of plasma-polymerized layers are determined by the interplay of parameters such as the working gas composition and flow rate, exposure time, substrate material, temperature, electrode configuration, input power and many more. This high degree of flexibility allows for the creation of layers tailored to specific applications, such as protective, hydrophobic, or anti-corrosive coatings. However, reproducibility remains a key challenge, as minor variations in these parameters can lead to significant inconsistencies in layer properties. This is why PP research focused on understanding the deposition mechanisms, as well as determining the parameters which play the key role in improving layer properties, remains a relevant topic.
In recent years, there has been research mainly focused on PP implemented using plasma jets [3,4], with a lack of direction of research towards the use of other plasma sources. However, a great disadvantage of plasma jets is their relatively small volume of plasma, resulting in long treatment times and the inability to treat larger areas at once. For many applications, other types of plasma sources would be more suitable, where it is not necessary to scan the sample with a thin plasma jet beam. There is also a lack of comprehensive research on PP, where the influence of several parameters simultaneously on various properties of the resulting layers would be compared and clarified.

Using different types of plasma sources to carry out PP on different substrates along with varying working conditions can improve our understanding of the fundamental processes underlying PP and help identify optimal methods for specific practical applications.

In previous research in the field of PP at atmospheric pressure, carried out at our department, a Diffuse Coplanar Surface Barrier Discharge (DCSBD) was used as a plasma source for PP. The anti-corrosion properties of plasma-polymerized layers prepared from the HMDSO monomer (pp-HMDSO layers) on the surface of aluminum were investigated in the work [5]. The protective effect of these layers has been demonstrated, however, their stability over time has not been investigated. The work [6] studied pp-HMDSO layers deposited on glass, and confirmed their hydrophobic stability, but only in the interval of 120 hours.

2. Experiment

Our work investigates atmospheric-pressure PP of hexamethyldisiloxane (HMDSO) using DCSBD to deposit hydrophobic layers on glass. We focused on how the exposure time, temperature and substrate affect the resulting layer properties. Post-treatment, i.e. plasma treatment of already deposited layers without supplying the monomer to the working gas, was also studied, as it poses a way to further refine the layers and achieve even better functionality or durability [7]. The input power of the DCSBD plasma source was 300 W. The working gas was prepared in the following way: nitrogen flowed into a bubbler filled with liquid HMDSO, and the HMDSO-enriched nitrogen was then mixed with pure nitrogen in the desired ratio through two mass flow controllers. The relative flow was 15.8 (8 slm of nitrogen + 1.5 slm of HMDSO-enriched nitrogen). Distance between the sample and the DCSBD surface was kept at 0.34 mm.

The pp-HMDSO layers were analyzed using surface diagnostics such as water contact angle (WCA) measurements, attenuated total reflectance Fourier-transform infrared spectroscopy (ATR-FTIR) and scanning electron microscopy (SEM) to assess their hydrophobicity, chemical composition, and morphology. Additionally, ageing tests were performed to assess the long-term stability of the layers up to 7 weeks after deposition. To characterize the properties of the PP process, we determined the electrical efficiency of the DCSBD discharge (dependence of real power delivered into the discharge on input power) generated in the working gas and measured the liquid monomer consumption per minute and per deposited layer. Our findings describe the influence of some of the critical process parameters on layer properties and suggest new options to improve the deposition process to achieve reproducible, homogeneous functional coatings.

This work was financially supported by the Comenius University Grant No. UK/3098/2024.

3. References

[1] Friedrich J 2012 *The Plasma Chemistry of Polymer Surfaces: Advanced Techniques for Surface Design*, Wiley-VCH, Weinheim
[2] Yasuda H 1981 *Journal of Polymer Science: Macromolecular Reviews* 16 199
[3] Trinh Q H 2019 *Surface and Coatings Technology* **361** 377
[4] Silva L L G 2022 *Brazilian Journal of Physics* **52**(4) 114
[5] Bónová L 2012 *Chem. Listy* **106** 1431
[6] Krumpolec R 2012 *WDS'12 Proceedings of Contributed Papers* **24**
[7] Bour J 2008 *Plasma Processes and Polymers* **5**(8) 788

PLASMA TREATMENT OF WASTEWATER: A PROMISING APPROACH TO PLANT FERTILIZATION

Ludmila Čechová[1,2], Plamena Marinova[3], Evgenia Benova[4], Tomáš Vozár[2], Pavel Pořízka[1], Jozef Kaiser[1], Zdenka Kozáková[2], František Krčma[2]

[1]*Central European Institute of Technology, Brno University of Technology, Purkyňova 123, 60200 Brno, Czech Republic*

[2]*Faculty of Chemistry, Brno University of Technology, Purkyňova 118/464, 612 00 Brno, Czech Republic*

[3]*University of Forestry, Faculty of Forest Industry, 10 Kliment Ohridski Blvd, Sofia, 1756, Sofia, Bulgaria*

[4]*Sofia University "St. Kliment Ohridski", Clean&Circle Center of Competence, 8 Dragan Tsankov Blvd., Sofia, Bulgaria*

E-mail: Ludmila.cechova@vut.cz

Plasma technology for treatment of water is a new and promising technology that started to be developed more than 10 years ago. There is a significant progress regarding the technology and construction of different plasma devices designed specifically for interaction of plasma with liquids. However, these technologies now have to be tested in regards of reactive oxygen and nitrogen species (RONS) production and the subsequent effect of RONS enriched water on plants.

1. Introduction

Plasma treatment of water and the product of plasma treatment called Plasma Activated Water (PAW) has gained a significant attention in the recent years. The PAW, produced by direct or indirect plasma treatment of water, contains reactive oxygen and nitrogen species (RONS) that are transported from gaseous plasma into the water through plasma-liquid interaction. These short-lived RONS interact with the water molecules and generate long-lived RONS, such as hydrogen peroxide, nitrates and nitrites. These molecules contribute to PAW's fertilizing properties, as well as it's antibacterial properties. Nitrogen serves as an important nutrient for plant growth and photosynthesis, while hydrogen peroxide can enhance seed germination [1].

In the past studies, PAW prepared from distilled and tap water was tested. However, plasma-treated wastewater could also present a promising application as an eco-friendly fertilizer. Wastewater often contains essential nutrients such as phosphorus, magnesium, and calcium, which are vital for plant growth but are not products of plasma treatment. Plasma can also help with water disinfection and decompose organic substances [2].

This study utilized three plasma systems specifically designed for plasma-liquid interaction: (i) dielectric barrier discharge with a liquid electrode, (ii) a microwave cold atmospheric plasma jet above the water surface and (iii) new microwave plasma source Beta device (Clean&Circle Centre of Competence, University of Sofia, Bulgaria). Concentrations of NO_2^- and NO_3^- in plasma treated wastewater were measured using UV-VIS spectroscopy, revealing variations in PAW composition between the systems. A toxicity test was conducted to evaluate the impact of treated wastewater on plants by measuring the germination rate and root length of melon seeds *Cucumis melo* after five days. Additionally, plants of salad *Lactuca sativa* were grown in hydroponic system with either plasma treated tap water and wastewater. The effect of plasma treated tap water and wastewater was observed in changes of growth, chlorophyll content and elemental uptake. The spatial distribution of nutrients was determined using Laser-Induced Breakdown Spectroscopy (LIBS), a technique that analyses optical emissions from laser-induced plasma. LIBS enables spatially resolved bioimaging of

plant samples and has become a valuable tool for detecting the precise distribution of contaminants such as heavy metals, nanoparticles, and microplastics [3].

2. References

[1] Puač N, Gherardi M, Shiratani M 2018 *Plasma Processes Polym.* **15** 1700174
[2] Takeuchi N and Yasuoka K 2021 *Jpn. J. Appl. Phys.* **60** SA0801
[3] Brennecke T, Čechová L, et al. 2023 *Spectrochim. Acta Part B: At. Spectroscopy* **205** 106684

THERMAL DEGRADATION OF BIODEGRADABLE POLYMERS STUDIED BY IMS TECHNIQUE

Emanuel Maťaš[1], Ivan Chodák[2], Štefan Matejčík[1]

[1]*Department of Experimental Physics, Comenius University, Mlynská dolina F2, 84245 Bratislava, Slovakia*

[2]*Polymer Institute SAS, Dúbravská cesta 9, 845 41 Bratislava, Slovakia*

E-mail: emanuel.matas@fmph.uniba.sk

Ion mobility spectrometry (IMS) was applied to monitor the thermal degradation of biodegradable polymers including polyhydroxybutyrate (PHB), polybutylene adipate terephthalate (PBAT), and polylactic acid (PLA). The IMS method enabled the identification of thermal degradation products as well as the determination of the threshold temperatures at which degradation became detectable: 40 °C for PHB, 25 °C for PBAT, and 80 °C for PLA

1. Introduction

Biodegradable polymers have attracted attention in recent years due to their potential to alleviate environmental issues caused by plastic waste. These materials are specifically designed to degrade through microbial activity, breaking down mainly to water, carbon dioxide, and biomass [1, 2]. Commonly studied biodegradable polymers include natural polymers like cellulose, rubber and starch, synthetic polymers such as polybutylene adipate terephthalate (PBAT) and polylactic acid (PLA), as well as microbial polymers like polyhydroxybutyrate (PHB) [2]. These polymers find extensive applications in packaging, agriculture, and biomedical fields [2-6].

Thermal degradation plays a crucial role in determining the performance and end-of-life behaviour of biodegradable polymers [2]. Understanding their thermal stability and degradation pathways is vital for optimizing functionality and ensuring environmental sustainability. Unlike conventional polymers, biodegradable polymers generally exhibit lower thermal resistance, making it essential to study their thermal properties. This knowledge is critical for facilitating the transition from traditional polymers to more environmentally friendly alternatives [1].

Standard methods for the quantitative analysis of polymer thermal degradation include thermogravimetric analysis (TGA) and thermal volatilization analysis (TVA) [1-3]. While highly accurate, these techniques are often time-demanding and require lengthy experimental procedures. For qualitative analysis, techniques such as Fourier-transform infrared (FTIR) spectroscopy and mass spectrometry (MS) are widely employed to identify degradation products and chemical changes in polymers.

In this study, we utilized ion mobility spectrometry (IMS) in combination with MS for the rapid qualitative analysis of the thermal degradation of PHB, PBAT and PLA.

2. Results and Discussion

The IMS device (Advanced IMS, MaSa Tech s.r.o.) for monitoring the thermal degradation of biodegradable polymers was operated in positive polarity, with an electric field intensity of 547.6 $V.cm^{-1}$ in the drift tube. The drift gas flow rate was maintained at 700 mL/min, while the drift tube operating at a pressure of 700 mbar and a temperature of 373K. The sample flow rate was set at 20 mL/min.

For identification of products generated during the thermal degradation of polymers, a time-of-flight MS (TOF-MS) was used. Samples of biodegradable polymers, specifically PHB, PBAT and PLA were

provided by the Polymer Institute of the Slovak Academy of Science. Small amounts of each sample (100 mg) were placed into vials. Prior recording an IMS spectrum a sample of polymer was kept for 30 min at a earlier set temperature, in order to establish equilibrium conditions. After this period 3 ml of the headspace of the vial was injected into the IMS for analysis and IMS spectrum was recorded. This procedure was carried out for temperatures 25, 40, 60, 80, 90, 100 °C for all studied polymers.

The IMS spectra recorded for different temperatures of PHB are presented in Figure 1. Peaks with reduced ion mobilities of 2.39 and 2.21 $cm^2.V^{-1}.s^{-1}$ (black line – RI) correspond to spectrum of reactant ions generated in purified carrier gas, specifically water cluster ions of NO^+ and H_3O^+, respectively. After polymer headspace injection, new peaks appeared in the IMS spectra. Ion peak with a reduced ion mobility of 2.52 $cm^2.V^{-1}.s^{-1}$ represents ammonia ions NH_4^+. Additional peaks with ion mobilities of 2.05, 1.98, 1.89, 1.8 and 1.72 $cm^2.V^{-1}.s^{-1}$ were detected and their intensities were increasing with the headspace temperature of the sample. It was observed that the intensity of NO^+ decreased rapidly, probably due to the formation of new ions via NO^+ ionization pathways. According to the present experiment, the thermal degradation of the PHB started at temperature 40°C, when the peaks described above were detected first time (blue line). In the Figure 1, the IMS spectrum of PHB recorded at 25 ˚C is not depicted, as it was identical with the spectrum of RI.

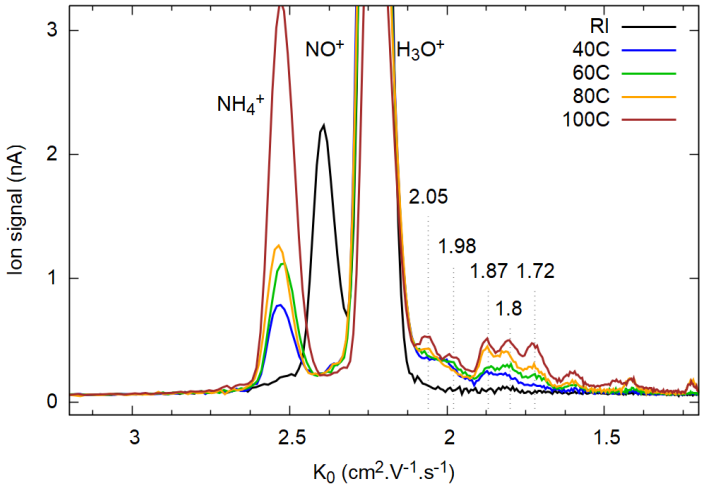

Fig. 1. IMS spectra of reactant ions (RI) and PHB at heating temperatures of 40, 60, 80 and 100 °C.

The thermal degradation of PHB is well documented in the literature, where crotonic acid was identified as a key degradation product [2, 3]. The IMS spectrum of crotonic acid standard, recorded using the above-described method is depicted in Figure 2. The IMS spectrum of PHB recorded at headspace temperature of 100 °C is compared with the IMS spectrum of crotonic acid, recorded at headspace temperature of 25˚C. The spectrum of crotonic acids exhibits four peaks with reduced ion mobility of 2.05, 1.98, 1.8 and 1.72 $cm^2.V^{-1}.s^{-1}$, which are identical with the ion peaks generated by thermal degradation of PHB. Additional minor peaks present in the IMS spectra of PHB could be attributed to polymer admixtures or impurities in the sample.

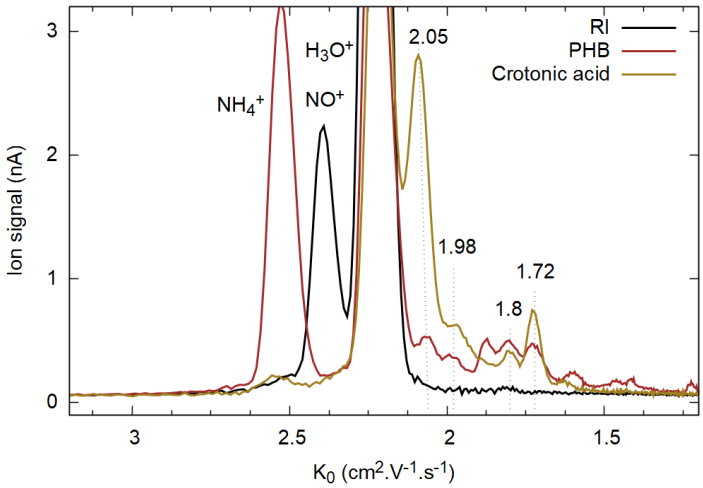

Fig. 2. IMS spectra of PHB at a heating temperature of 100 °C and crotonic acid at room temperature.

The IMS spectra of PBAT polymer recorded at different headspace temperatures are presented in Figure 3. Inspection of the Figure indicates that products of thermal degradation of the PBAT polymer are visible already at room temperature of 25 °C (Figure 3. blue line). Two dominant degradation peaks with reduced ion mobilities of 1.95 and 1.53 cm^2.V^{-1}.s^{-1} were detected, accompanied by several less pronounced features. Mass spectrometric (MS) analysis revealed that these peaks have m/z 91, 109 and 127, which can be attributed to protonated 1,4-butanediol ion (M.H$^+$, m/z 91,) and its water clusters (M.H$^+$.(H_2O), m/z 109,) and (M.H$^+$.(H_2O)$_2$, m/z 127, M.H$^+$.(H_2O)$_2$). These ions are associated with the IMS peak with a reduced ion mobility of 1.95 cm^2.V^{-1}.s^{-1}. The second peak with the ion mobility of 1.53 cm^2.V^{-1}.s^{-1} is according to the MS analysis protonated dimer of 1,4-butanediol (M_2.H$^+$, m/z 181). Given the chemical structure of PBAT, detection of 1,4-butanediol was expected, as this molecule constitutes a significant part of PBAT composition.

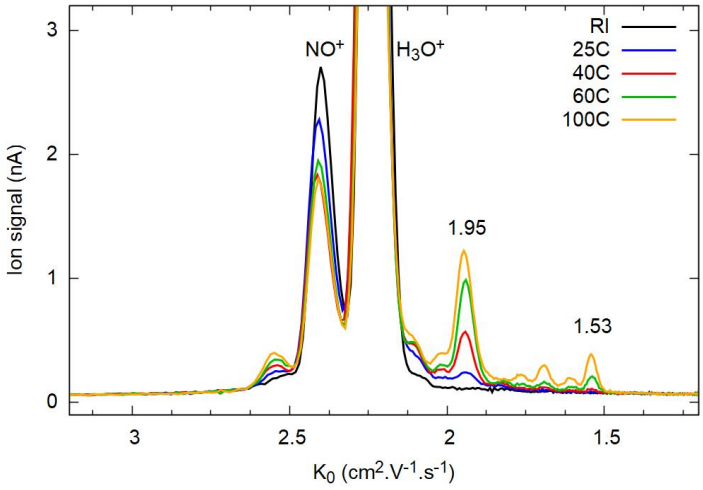

Fig. 3. IMS spectra of PBAT at a heating temperature of 25, 40, 60 and 100 °C.

The polymer PLA showed the best thermal stability of the studied polymers. The first degradation products were detected at headspace temperature of 80˚C (Figure 4. red line). IMS spectra recorded at lower headspace temperatures did not show any degradation products. The degradation efficiency of PLA strongly increases between 90 and 100 °C. The IMS spectrum of PLA, shown in Figure 4, revealed one significant peak with a reduced ion mobility of 1.63 cm^2·V^{-1}·s^{-1}. MS analysis identified the corresponding ion with m/z 145 and 163, attributed to protonated lactic acid with three and four

attached water ($M.H^+.(H2O)_{3,4}$). Additionally, IMS spectrum indicates that in the ionization are involved the NO^+ ions similar to PHB.

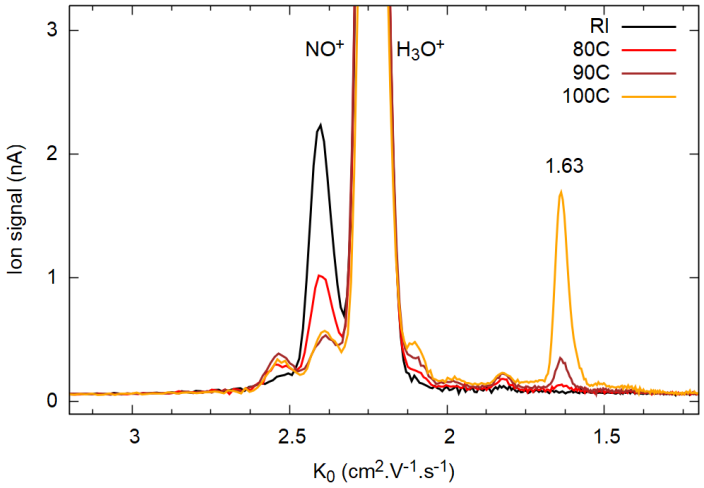

Fig. 4. IMS spectra of PLA at a heating temperature of 80, 90 and 100 °C.

3. Conclusions

The IMS was used for real-time analysis of the processes of thermal degradation of biodegradable polymers. This technique has enabled fast and sensitive detection of degradation products, their identification and has potential also for quantitative evaluation of the degradation process. Compared to traditional techniques, it offers a significant advantage, especially in terms of measurement time. Moreover, IMS is not limited to detecting biodegradable polymers; it can also be applied to analyse conventional, commonly used plastics, thereby offering a valuable tool for monitoring, and assessing the environmental impact of these materials.

Acknowledgments. The present studies were partially supported by the Slovak Grant Agency for Science VEGA Nr. 1/0489/21 and VEGA Nr. 1/0553/22, Slovak Research and Development Agency under project Nr. APVV-19-0386, Nr. APVV-22-0133 and Nr. APVV-23-0522.

4. References

[1] Calmon-Decriaud A, Bellon-Maurel V, and Silvestre F 1998 *Review and perspectives*. *Blockcopolymers-Polyelectrolytes-Biodegradation*, **135** 207.
[2] Scott, G. et. col 2010 *Dordrecht: Springer Netherlands* 1.
[3] Albertsson A. C. 1993 *Journal of Macromolecular Science Part A* **30** 757.
[4] European Bioplastics, Bioplastics − Facts and Figures. 2013 *http://en.european-bioplastics.org/wp-content/uploads/2013/publications* p. 5.
[5] Doppalapudi S. Jain A. Khan W. and Domb A J 2014 *Polymers for Advanced Technologies* **25** 427.
[6] Ulery B. D. Nair L. S. and Laurencin C. T. 2011 *Journal of polymer science Part B: polymer physics* **49** 832.

POSTER PRESENTATIONS

THE TEMPERATURES OF HELIUM AND AIR-FED ATMOSPHERIC PRESSURE PLASMA JETS

Louise Daly[1], Amy Jennings[1], Daniel Simpson[1], Conn Ritchie[2], Thomas Thompson[2], Brendan Gilmore[2], Tom Field[1]

[1]Centre for Light Matter Interactions, School of Mathematics and Physics, Queen's University Belfast, Belfast, BT7 1NN, N. Ireland, UK

[2] School of Pharmacy, Queen's University Belfast, Belfast, BT7 1NN, N. Ireland, UK

E-mail: t.field@qub.ac.uk

Temperatures of helium and air fed atmospheric pressure plasmas jets have been measured. Preliminary results show that under similar conditions the helium jets may have slightly higher temperatures, which was not expected.

1. Introduction

The temperatures of different atmospheric pressure plasma jets have been measured spectroscopically and with a thermocouple. The work is part of a project to develop air-fed plasma jets with antimicrobial activity. It is critical that the output temperature of the plasma/gas mixture is close to room temperature in applications where living tissue is treated. Helium is a wonderful gas to work with because it breaks down at relatively low applied voltage and the gas generally remains close to room temperature. The low breakdown voltage of helium and the low temperature are due to the excited states of atomic helium lying so high in energy that they are close to the ionisation energy. By contrast, the components of air have many excited states with a great range of energies; close to the ground state are excited rotational and vibrational states which can be excited by low energy electrons to heat the gas. Thus, it is a challenge to form a plasma jet with air feed gas and maintain a low gas temperature.

Two different plasma jet systems have been investigated; a dielectric barrier discharge helium jet[1] and a new air-fed jet. Gas temperatures have been measured spectroscopically and with a thermocouple. At this very preliminary point in the analysis it appears that with similar conditions the helium jets may be slightly higher in temperature than the air jets, which is somewhat unexpected.

IONIZATION-ATTACHMENT INSTABILITY IN AN O_2 CCRF PLASMA

Peter Hartmann[1], Ranna Masheyeva[1,2,3], Mate Vass[1,4], Murat Myrzaly[2], Chong-Biao Tian[4,5], Karlygash Dzhumagulova[2,3], Julian Schulze[4], Zoltán Donkó[1]

[1]*Institute for Solid State Physics and Optics, HUN-REN Wigner Research Centre for Physics, 1121 Budapest, Hungary*

[2]*Research Institute of Experimental and Theoretical Physics, Al-Farabi Kazakh National University, 050040 Almaty, Kazakhstan*

[3]*Department of General Physics, Satbayev University, 050000 Almaty, Kazakhstan*

[4]*Chair of Applied Electrodynamics and Plasma Technology, Faculty of Electrical Engineering and Information Sciences, Ruhr University Bochum, 44801 Bochum, Germany*

[5]*Key Laboratory of Materials Modification by Laser, Ion, and Electron Beams (Ministry of Education), School of Physics, Dalian University of Technology, 116024 Dalian, China*

E-mail: hartmann.peter@wigner.hu

In this study, we investigate the ionization-attachment plasma instability in a symmetric capacitively coupled plasma (CCP) reactor operated in oxygen gas [1]. This instability is characterized by periodic fluctuations in plasma parameters, such as the emitted light intensity, electron density, etc. These dynamics are particularly relevant in industrial plasma applications, such as etching and semiconductor processing, where stability and precision are critical.

We have combined experimental measurements and numerical simulations to explore how operating conditions – pressure, voltage amplitude, and the secondary electron emission coefficient (SEEC, γ) – influence the onset and characteristics of this plasma instability.

1. Experiments

We performed experiments using our Budapest Cell v.3 symmetric CCP reactor with flat stainless steel electrodes placed at 2.5 cm distance, housed in a quartz cylinder. The reactor was filled with high-purity oxygen (4.5 grade) at pressures ranging from 50 Pa to 350 Pa, regulated using a flow controller and a needle valve. The powered electrode was driven by a 13.56 MHz radio-frequency (RF) generator, with voltage amplitudes varying from 250 V to 700 V. Optical emission from the plasma was monitored with a photodetector and a high-bandwidth oscilloscope. Additionally, spatial light intensity distributions were recorded using a CCD camera. The schematic of the experimental setup is shown in in Fig. 1.

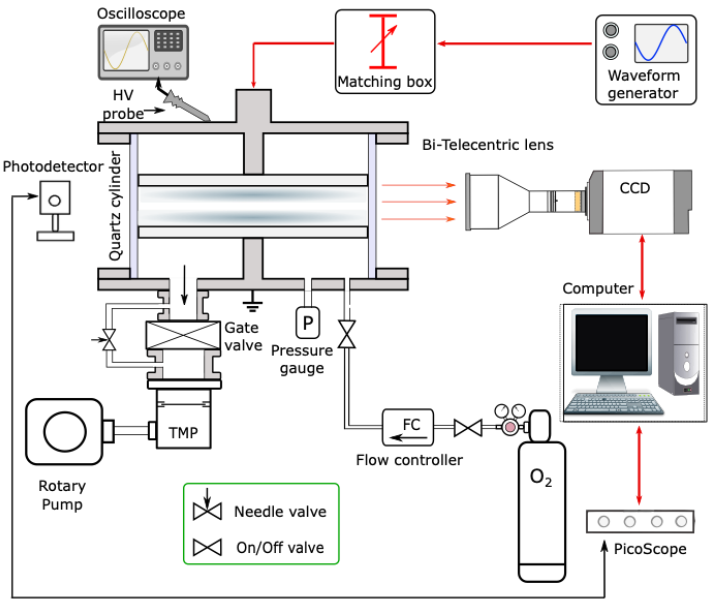

Fig. 1. Schematic of the experimental setup

During the experiments, we observed periodic fluctuations in light intensity – indicative of plasma instability – at pressures above 50 Pa within specific voltage ranges. As shown in Fig. 2(a), these ranges shifted with pressure, broadening and decreasing in central value as the pressure increased. At 100 Pa, for instance, the instability occurred in a voltage amplitude range of 655±30 V, with a peak oscillation frequency of 0.25 kHz. Below 50 Pa, no instabilities were observed.

The spatial distribution of light emission also showed distinct characteristics: a bulk region of emission and additional peaks near the electrodes, as shown in figure 2(b). We identified these near-electrode peaks as resulting from dissociative excitation of oxygen molecules due to collisions with energetic O_2^+ ions [1]. With increasing voltage, the relative intensity of bulk emission decreased, while near-electrode peaks became more pronounced.

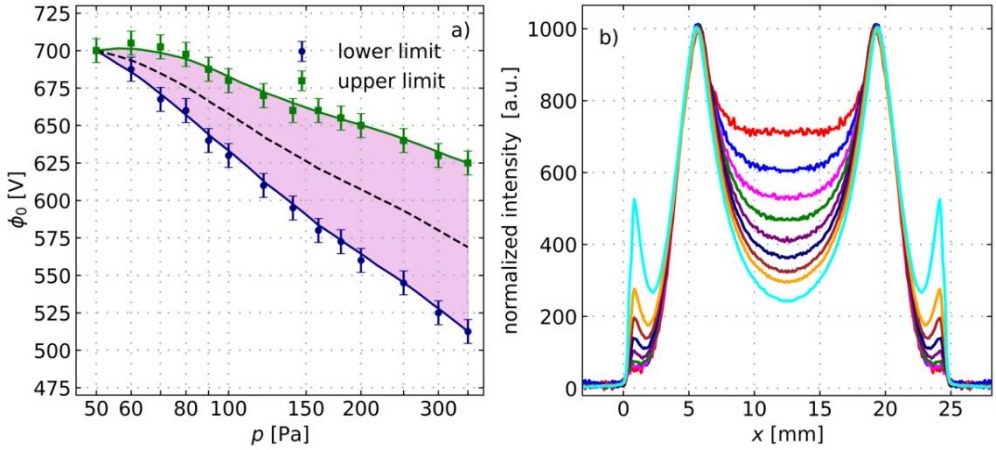

Fig. 2. (a) Voltage region of instability as a function of the pressure in the center of the instability region; (b) normalized axial light intensity distributions at p = 100 Pa pressure and different voltages.

2. PIC/MCC simulation

To interpret our experimental findings, we performed numerical simulations using a spatially one-dimensional, three-dimensional velocity space (1d3v) Particle-In-Cell with Monte Carlo Collisions (PIC/MCC) model. This approach allowed us to simulate the kinetics of electrons, positive molecular ions (O_2^+), and negative atomic ions (O^-) under similar conditions to our experiments. The SEEC (γ) was treated as a variable parameter to match the experimental results.

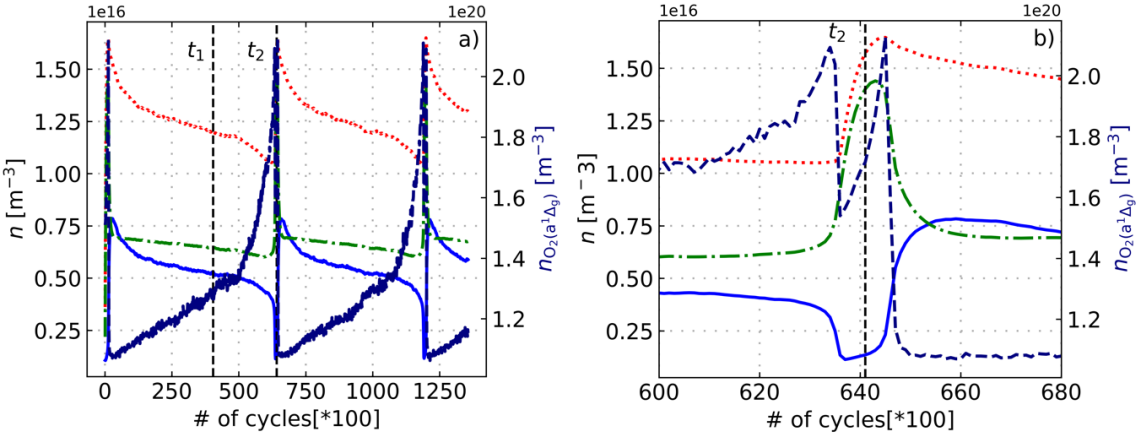

Fig. 3. Time evolution of the density of plasma species: e^- O_2^+ O^- $O_2(a^1\Delta_g)$. Discharge conditions: 100 Pa pressure, 600 V Voltage amplitude at 13.56 MHz, γ = 0.0042.

Figure 3 shows the computed time evolution of the active plasma particles (electrons, ions, and molecules in the delta metastable excited level). We successfully reproduced the experimentally observed oscillation frequency of 0.25 kHz by setting γ = 0.0042 and reducing the voltage amplitude to

600 V, accounting for possible measurement uncertainties. The simulations revealed that the instability originates from a feedback loop: an increase in electron density (during natural fluctuations) lowers electron temperature, reducing ionization while altering attachment rates. If the attachment rate declines more rapidly than the ionization rate, the combined effect can result in an effective increase in electron density. This positive feedback leads to periodic oscillations in electron density, electron temperature, and reaction rates [2].

Our simulations also uncovered a periodic shift in the plasma's electron power absorption modes during the instability cycles. At certain times, the plasma operated in the Drift-Ambipolar (DA) mode, where the bulk electric field drives ionization. At other times, it transitioned to a Detachment-Induced (DI) mode, dominated by processes near the sheath edges [3]. These transitions correlated with shifts in reaction rates for ionization, dissociative attachment, and associative detachment, contributing to the observed oscillations.

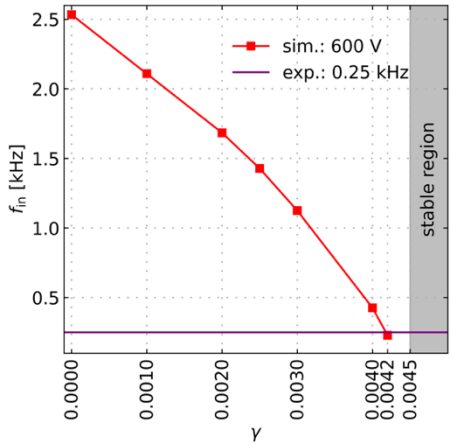

Fig. 4. Computed dependence of the instability frequency on the γ parameter at fixed voltage amplitude of 600 V.

Further, as shown in figure 4, we found that increasing the SEEC decreased the frequency of the instability. This result highlights the sensitivity of plasma behavior to surface properties, such as γ, and the role of secondary electrons in driving instabilities. Our findings suggest that γ can be determined computationally by matching computed and experimentally observed oscillation frequencies, providing a new diagnostic method for surface-plasma interactions.

3. Conclusions

Through a combination of experiments and simulations, we have demonstrated that the ionization-attachment instability in oxygen CCPs is highly dependent on operating conditions and surface properties. By varying the SEEC parameter γ, we matched experimental and computational results, revealing the underlying feedback mechanisms and the periodic transitions in electron power absorption modes. These findings advance our understanding of plasma instabilities and offer a pathway for optimizing CCP systems in industrial applications, such as semiconductor manufacturing and surface treatments.

4. Acknowledgements

This work was supported by the National Office for Research, Development and Innovation (NKFIH) via Grant K134462, by the German Research Foundation via the SFB 1316, project A4, as well as project 428942393, and by the Grant No. AP19679536 of the Ministry of Science and Higher Education of the Republic of Kazakhstan.

5. References

[1] Küllig C et.al. 2012 *Contributions to Plasma Physics* **52** 836-846

[2] Küllig C, Wegner T and Meichsner J 2015 *Physics of Plasmas* **22** 043515

[3] Tian C-B *et al* 2024 *Plasma Sources Sci. Technol.* **33** 075008

DEVELOPMENT ANTIBACTERIAL ATMOSPHERIC PRESSURE PLASMA JET

Amy Jennings[1], Kamila Shojaa[1], Daniel Simpson[1], Louise Daly[1],
Thomas Thompson[2], Brendan Gilmore[2], Tom Field[1]
[1]*Centre for Light Matter Interactions, School of Mathematics and Physics, Queen's University Belfast, Belfast, BT7 1NN, N. Ireland, UK*
[2] *School of Pharmacy, Queen's University Belfast, Belfast, BT7 1NN, N. Ireland, UK*
E-mail: ajennings12@qub.ac.uk

Preliminary results of antimicrobial effect of a new air fed atmospheric pressure plasma jet are presented.

1. Introduction

Atmospheric pressure plasma jets (APPJs) have medical applications, particularly in dermatology and inactivation of bacteria [1] and further applications being investigated, for example, in destruction of cancer cells. The DIN specification 91315 for characterising a plasma jet used in medical application has established a foundation for the development of medical applications.

Many atmospheric pressure jets use helium as the feeding gas due to easy ionisation and low temperatures, however, helium is expensive. The subject of this presentation is the development of an air fed atmospheric pressure plasma jet (APPJ) for bacterial inactivation. The project is at an early stage, but a new jet has been developed.

2. Results

Some preliminary bacterial inactivation measurements have been made with the new jet, which are shown in figure 1. Some inactivation of bacteria is visible in figure 1, but it is hoped that the effectiveness of the jet can be improved and optimised.

The results show that bacterial inactivation with an air jet is possible, but we do not see the desired 4 log reduction in population with the current prototype. Other issues will also need to be addressed, such as ensuing the output of the gas from the jet is below 40°C to allow treatment of living tissue. Elevated temperatures could, however, be ok for killing bacteria on medical devices that can tolerate higher temperatures.

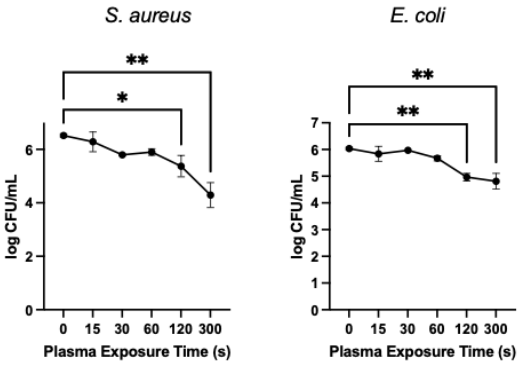

Fig. 1. The amount of microbial cells left after different times bacteria was exposed to air APPJ.

3. References

[1] Brandenburg, R., Ehlbeck, J., Stieber, M., et al., Contributions to Plasma Physics, 47 (2007), 72-79. 10.1002/ctpp.200710011 1

CYCLIC PLASMA-CATALYTIC SYSTEM OF CATALYST DEACTIVATION AND REGENERATION APPLIED FOR VOC REMOVAL

Jana Kšanová[1], Richard Cimerman[1], Christian Oberste-Beulmann[2], Oleksandr Galmiz[1], Peter Švec[3], Karol Hensel[1]

[1]*Division of Environmental Physics, Comenius University, Bratislava, Slovakia*
[2]*Laboratory of Industrial Chemistry, Ruhr University Bochum, Bochum, Germany*
[3]*Institute of Physics, Slovak Academy of Sciences, Bratislava, Slovakia*
E-mail: jana.ksanova@fmph.uniba.sk

This study examines a cyclic system of catalyst deactivation and regeneration used for toluene removal via plasma catalysis. The system, tested with various catalysts, shows that plasma-regenerated catalysts exhibit higher toluene removal efficiency compared to those non-regenerated. The findings highlight the potential of nonthermal plasma as an economical and efficient solution for VOC removal and catalyst regeneration.

1. Introduction

Volatile organic compounds (VOCs) are major contributors to one of the most pressing global environmental issues - air pollution. A promising approach to their removal from the air is through catalysis. However, catalysts are often subject to deactivation (i.e., losing their catalytic activity) by use. This deactivation of the catalysts is mainly caused by the adsorption of undesired reaction products on their surface resulting in their limited lifetime. As a result, the catalysts need to be regularly replaced or regenerated. Replacement of the catalysts produces waste and conventional regeneration requires high temperatures. Both high temperatures and waste production are associated with high costs. Although the regeneration of the deactivated catalysts (i.e., restoring their catalytic activity) is a more appropriate approach to extend their lifetime, conventional (thermal) methods of catalyst regeneration are often insufficient. Therefore, it is necessary to search for new or improve existing regeneration methods. An innovative way of removing VOCs from the gas [1, 2] as well as regeneration of catalysts deactivated by the undesired products, such as those from the VOC removal process [3], involves utilizing nonthermal plasma in these processes.

2. Methodology

In our research, we focused on testing a cyclic system that, in the first step, removes a model pollutant (toluene) from the air using plasma catalysis (a combination of nonthermal plasma with catalysis) followed by, in the second step, the catalyst regeneration using the nonthermal plasma in oxygen. The regenerated catalyst was then reused in the toluene removal process. A cycle of toluene removal with subsequent catalyst regeneration was repeated three times for two different catalysts (TiO_2 and $Pt/\gamma Al_2O_3$). Each toluene removal process lasted 180 min with a fixed discharge power of 6 W, while regeneration lasted 120 min with a fixed discharge power of 3 W. In order to evaluate the regeneration efficiency, three cycles of toluene removal without subsequent regeneration were also performed. The toluene removal efficiencies achieved with regenerated and non-regenerated catalysts were compared. Gaseous oxidation products of both the toluene removal process and catalyst regeneration were monitored using Fourier-transform infrared (FTIR) spectroscopy. In addition, the efficiency of plasma regeneration in one 120 min cycle was compared with other regeneration methods, including ozone and thermal regeneration of the same duration. Moreover, sequential plasma catalyst regeneration (i.e. regeneration for 40 min cycles + mixing of pellets, repeated 3 times) was tested, too. To evaluate the regeneration efficiency, time courses of concentrations of gaseous regeneration products (CO_2, CO, HCOOH) were evaluated. The catalysts were analyzed by thermogravimetric analysis (TGA) and scanning electron microscopy (SEM). The chemical identification of solid undesired products

adsorbed on the surface of the catalysts was carried out by gas chromatography coupled with mass spectrometry (GC-MS).

3. Results and discussion

A Figure 1 shows a comparison of the toluene removal efficiency achieved by two different catalysts (TiO_2 and $Pt/\gamma Al_2O_3$) over three cycles, comparing regenerated and non-regenerated catalysts. The achieved toluene removal efficiency is higher for the $Pt/\gamma Al_2O_3$ than for the TiO_2 in each individual cycle. This result was expected due to the higher catalytic activity and high oxidation properties of $Pt/\gamma Al_2O_3$. The results show that the toluene removal efficiency mostly decreases with an increasing number of cycles for both regenerated and non-regenerated catalysts due to gradual catalyst deactivation caused by the adsorption of solid undesired products. However, regenerated catalysts exhibit higher toluene removal efficiency across all cycles than those non-regenerated. Therefore, the catalyst regeneration partially restores their catalytic activity.

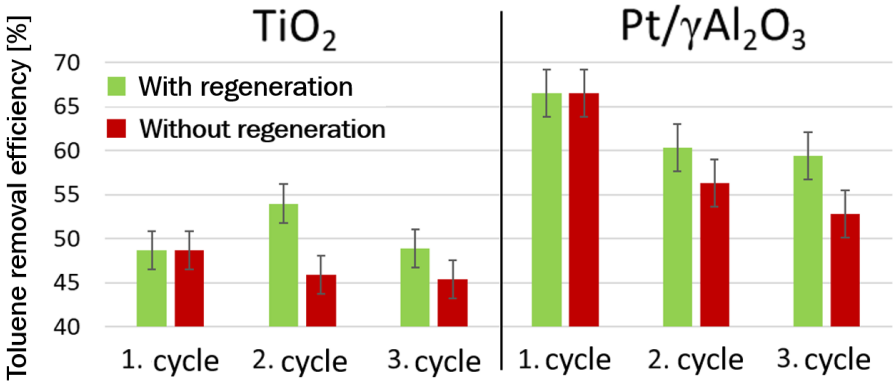

Fig. 1. Comparison of toluene removal efficiency for cycles with and without regeneration for TiO_2 (left) and $Pt/\gamma Al_2O_3$ (right).

Moreover, plasma catalyst regeneration in one cycle was compared to ozone, thermal and sequential plasma catalyst regeneration. The results show that both plasma and plasma sequential regenerations are more effective than ozone or thermal regeneration; with plasma sequential regeneration being the most effective.

4. Conclusion

Investigation of cyclic system of catalyst deactivation in a plasma catalytic toluene removal followed by its regeneration demonstrates that plasma-regenerated catalysts maintain higher toluene removal efficiency in each cycle, compared to those non-regenerated. This indicates that plasma regeneration restored catalytic activity, offering a cost-effective and efficient alternative.

5. Acknowledgements

This work was supported by Slovak Research and Development Agency grants APVV-20-0566, Slovak Grant Agency VEGA 1/0822/21, Excellent Grant of Comenius University Bratislava UK/3061/2024 and funded by the EU NextGenerationEU through the Recovery and Resilience Plan for Slovakia under the project No. 09I03-03-V04-00092 and 09I03-03-V03-00033.

6. References

[1] Cimerman R, Račková D and Hensel K 2018 *Journal of Physics D: Applied Physics* **51**, 274003.
[2] Cimerman R, Cíbiková M, Satrapinskyy L and Hensel K 2020 *Catalysts* **10**, 1476.
[3] Hossain M M, Mok Y S, Nguyen D B, Ahmed D R, Saud S and Heo I 2020 *Chemical Engineering Research and Design* **164** 299–310.

COMPARISON OF THE MAGNETRON AND THE SOLID-STATE MICROWAVE GENERATOR POWERED SURFACE-WAVE DISCHARGES

Kinga Kutasi[1], Nevena Puač[2], František Krčma[3]

[1] *HUN-REN Wigner Research Centre for Physics, POB 49, H-1525 Budapest, Hungary*
[2] *Institute of Physics, University of Belgrade, Pregrevica 118, 11080 Belgrade, Serbia*
[3] *Faculty of Chemistry, Brno University of Technology, Purkyňova 118, 612 00 Brno, Czechia*
E-mail: kutasi.kinga@wigner.hu

It is shown, that the microwave generators used to power the discharges strongly influence the operation mode, the static and dynamic filamentation of the surfatron launched surface-wave microwave discharges.

1. Discharge set-up

The surface-wave microwave discharge investigated is ignited with the use of the surfatron surface-wave launcher (Sairem, Surfatron 80). The surfatron is a coaxial waveguide terminated by a short-circuit plunger at one end, and by a launching gap at the other end, as shown in Fig. 1. The discharge is generated in a quartz tube coaxially positioned into the surfatron body. The microwave field is coupled into the surfatron with a capacitive coupler. The electric field coupled into the coaxial body is normal to the cylindrical surfaces, which is changed by the circular gap into an azimuthally symmetric field distribution similar to that of an m = 0 mode wave. As a consequence, with the gas breakdown a surface-wave can be launched, which will sustain the discharge. Under steady-state conditions the surface-wave sustaining the discharge propagates on the boundary of the plasma column and the dielectric as long as the electron density in the plasma exceeds the critical electron density [1]. The two different type of discharges [2,3] have been powered with a CoberMuegge microwave generator (2450 MHz ±10 MHz, 300 W) based on magnetron and a Sairem solid-state generator, respectively. The variable elements of the surfatron: the coupling capacitance, the gap and body sizes allow the impedance matching and thus the minimization of the reflected power. Due to the structure of the gap, which shapes the electric field coupled into the surfatron and makes possible the launching of the surface-wave, the discharge is expected to operate in a (0,0) mode, with a central discharge filament. The present work investigates the operation mode and filamentation of the discharges powered with the two type of generators, respectively.

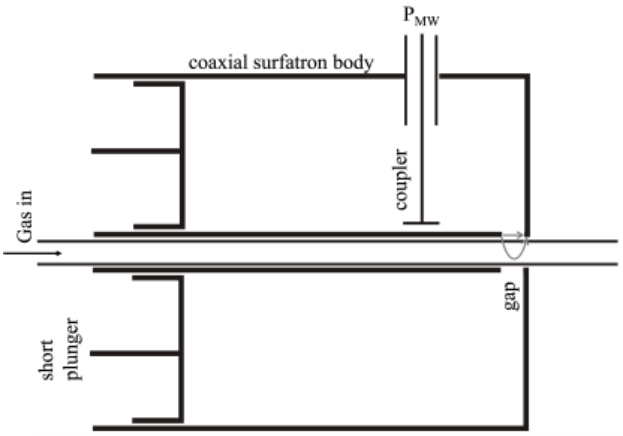

Fig. 1. The structure of the surfatron.

2. Operation modes

The work focuses on two discharge configurations, in what concerns the length of the quartz tube emerging from the surfatron body. The quartz tube, on whose boundary the surface-wave propagates, confines the plasma column. However, depending on the gas flow rate, input power and length of the quartz tub, the plasma column can emerge from the quartz tube. In this case the surface-wave can further propagate on the boundary of the plasma column and the ambient air, as long as the electron density in the plasma exceeds the critical electron density. Given the length of the quartz tubes, the effect of the gas flow rate and the input power on the discharge operation is discussed in the followings.

Fig. 2 shows the CCD images of the discharges confined in a 44 mm and 14 mm long quartz tubes at 24 W input power under different gas flow rates in the case of magnetron generator. The images are recorded Allied Vision Prosilica GX1050 camera and by using a band pass filter with transmission in the 450-650~nm range. At the 24 W input power, which insures a quasi-stable operation of the discharge, in the case of the 44 mm tube the plasma column extends to the end of the tube even at the lowest 0.5 slm gas flow rate and it exceeds it with the increase of flow rate. With shortening the quartz tube and keeping the power constant we observe a strong decrease of the plasma column due to the influx of the air into the discharge. With the increase of the gas flow rate, and thus diminishing of the air diffusion into the plasma core the increase of the plasma column is achieved outside of the quartz tube. As mentioned before, here the discharge is sustained by the surface-wave propagating along the boundary of the plasma column and the surrounding air as dielectric.

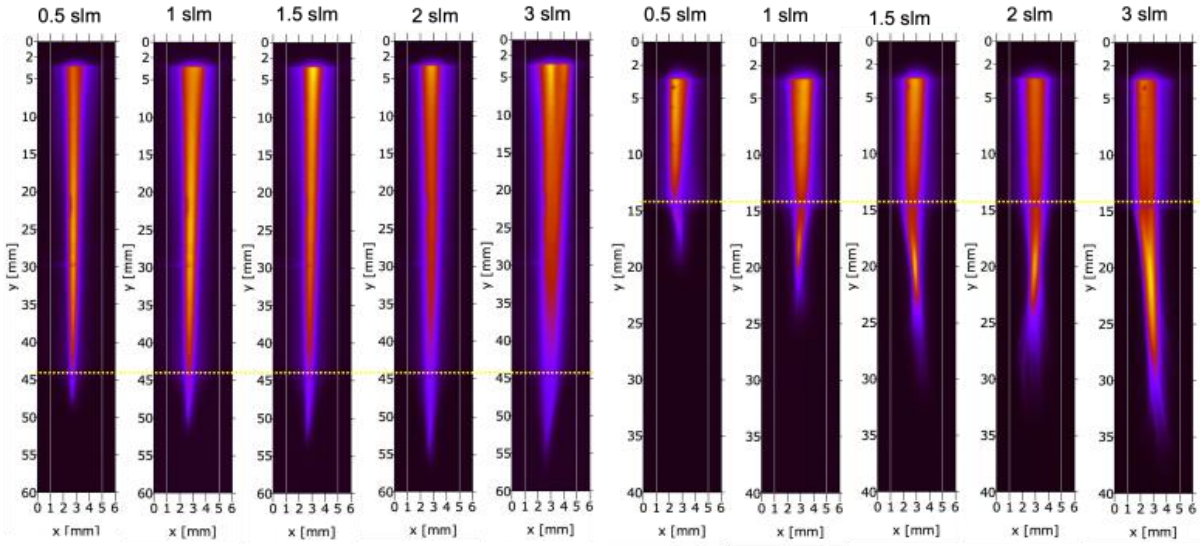

Fig. 2. The CCD images of the discharges confined in a 44 mm and 14 mm long quartz tube at 24 W input power under different gas flow rates in the case of the magnetron generator. Exposition time is 13 ms.

Regarding the effect of the power, images are shown for the 2 slm gas flow rate in Fig. 3. in the case of the magnetron generator powered discharge. At the lowest 15 W an unstable discharge is obtained with dynamic filaments. With increasing power the stability of the discharge increases and a quasi-stable discharge is achieved at 24 W. With the further power increase the filamentation of the discharge occurs. Two static filaments are developed, which tend to unite into a one single filament as distancing from the launching gap.

In the case of the solid-state generator powered discharge significantly different behaviour is observed, as shown in Fig.4. In this case the discharge is attached to the tube wall under every condition, regardless of the number of filaments. On the other hand, the filaments are always static, no dynamic movement – the creation and collapse – of the filaments occurs. Furthermore, significantly shorter discharge filaments are obtained, and the discharge operates in significantly different power ranges. While in the case of the magnetron generator powered discharge the plasma column fills a 50 cm tube at power as low as 20 W, in the case of the solid-state generator this occurs at about 50 W at the lowest 0.5 slm gas flow rate. In the case of the solid-state generator powered discharge the second filament develops at 38 W, and while at the lowest gas flow rate the two filaments tend to unite with the increase of the power, at the higher 2 slm gas flow rate the two filaments are stable. As the power is coupled into two different filaments, the overall plasma column becomes significantly shorter than in the case of the magnetron generator powered discharge.

With decreasing the length of the quartz tube, as mentioned in previously, the plasma column extends the discharge tube and it is strongly influenced by the air diffused into the plasma core. In the

case of the discharges confined in shorter tubes a very similar behaviour is observed as in the case of the longer tubes as a function of the power for both power generators, see Fig. 5. The main difference is the shorter plasma column due to the presence molecular gases. Furthermore, in the case of the magnetron generator powered discharge in the shorter tube no static double filaments occur, and while the developed two filaments always unite, in the case of the solid-state generator powered discharge the two stable static filaments do not unite.

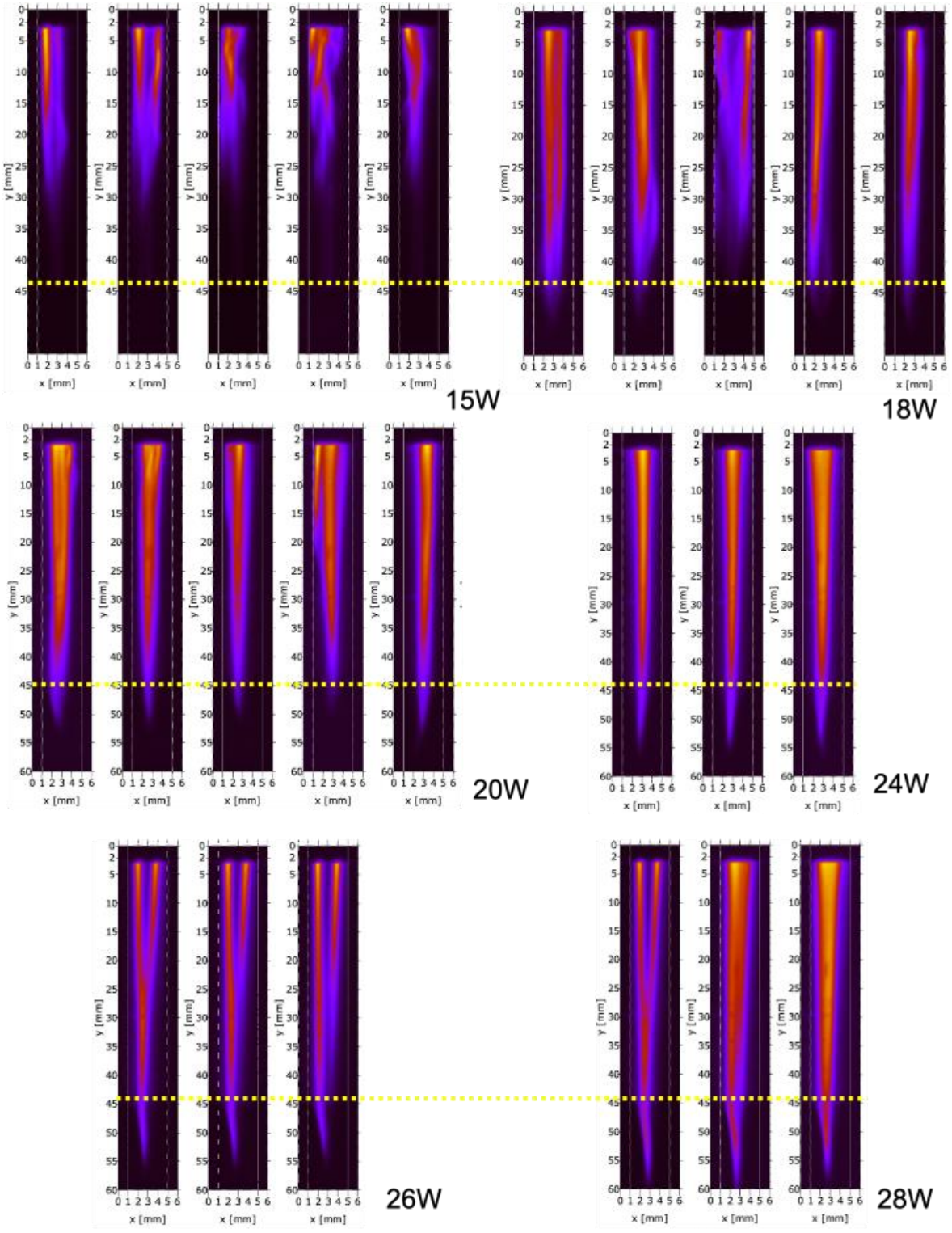

Fig. 3. The CCD images of the 2 slm Ar discharge confined in a 44 mm quartz tube at different input powers in the case of the magnetron generator. Exposition time is 13 ms.

The difference between the discharges powered with the two microwave generators is believed to originate from the power delivery of the power supplies, which is yet to be proven.

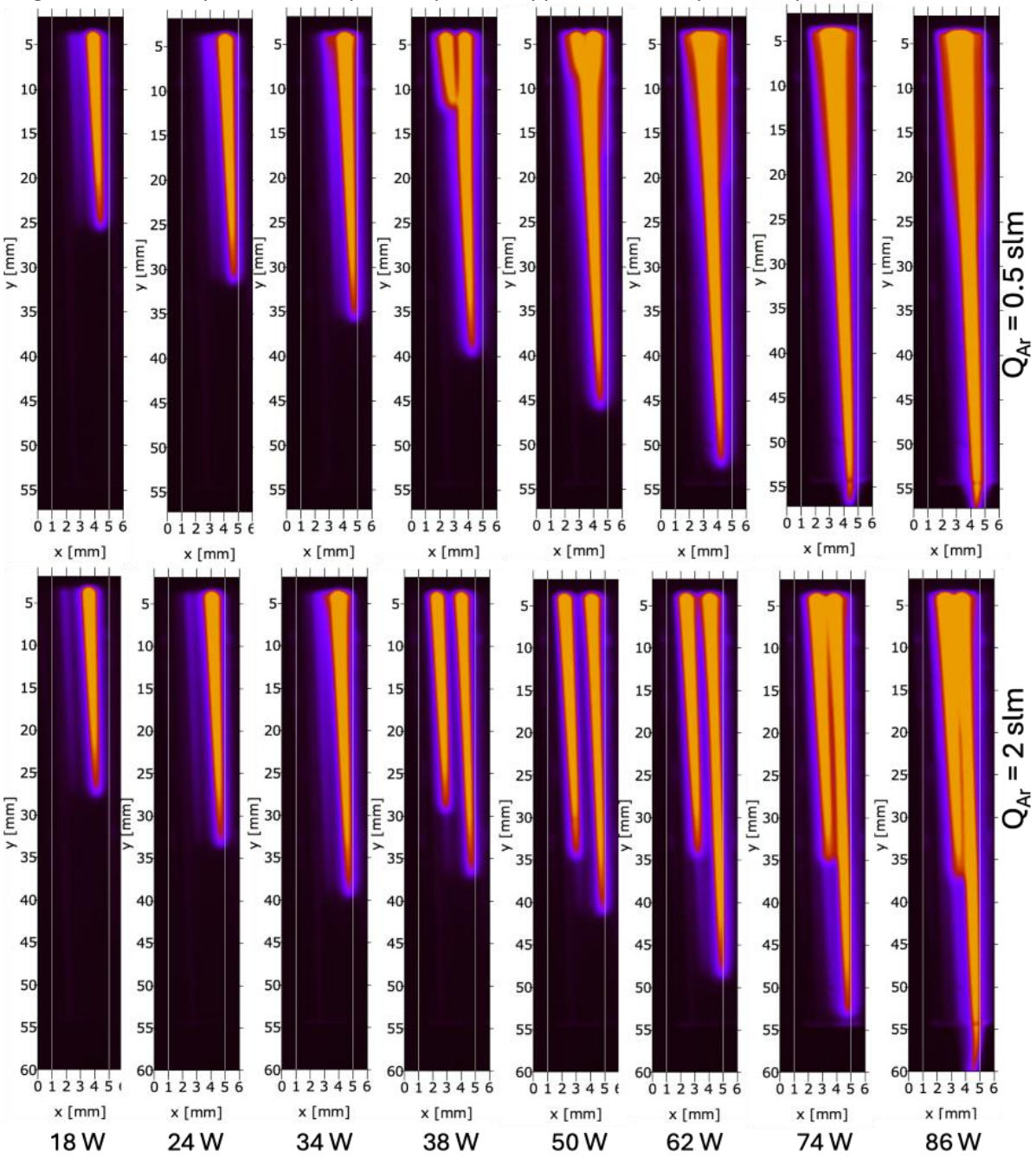

Fig. 4. The CCD images of the discharge confined in a 55 mm quartz tube at different input powers in the case of the solid-state microwave generator. Exposition time is 300 ms.

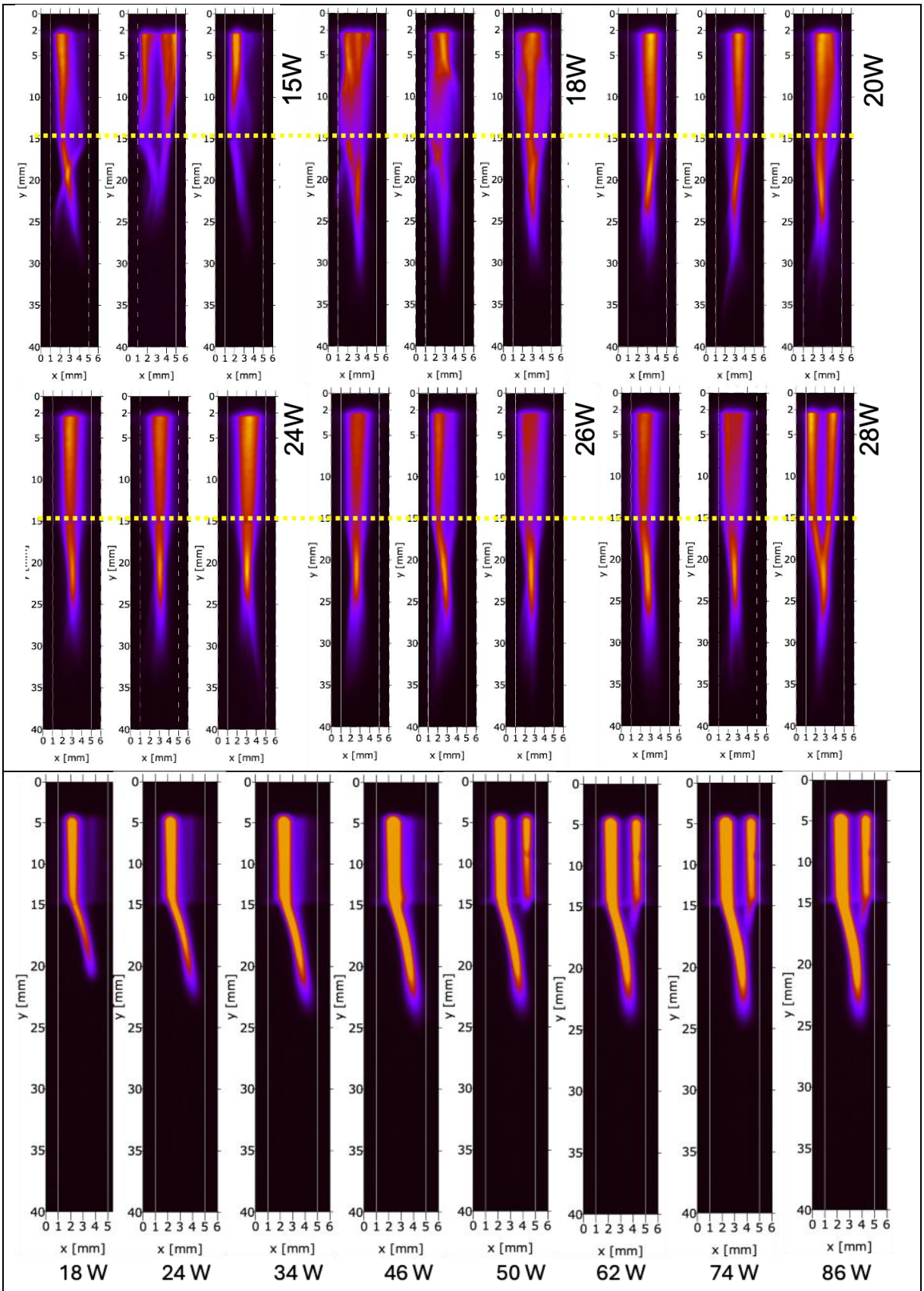

Fig. 5 The CCD images of the 2 slm Ar discharge confined in a 14 mm and 15 mm quartz tubes, respectively, at different input powers in the case of the magnetron and the solid-state generator (lower panel).

Acknowledgement
The work has been supported by Hungarian NKFIH Science Founds K-132158 and COST Action CA19110.

3. References
[1] Moisan M and Zakrzewski Z 1991 *J. Phys. D: Appl. Phys.* **24** 1025.
[2] Kutasi K *et al.* 2019 Plasma Sources Sci. Technol. **28** 095010. ; Kutasi K *et al.* 2023 *Plasma Process. Polym.* **20** 2200143.
[3] Krčma F *et al.* 2018 *J. Phys. D: Appl. Phys.* **51** 414001.

ON THE IN-SITU DETERMINATION OF THE EFFECTIVE SECONDARY ELECTRON EMISSION COEFFICIENT IN LOW PRESSURE CAPACITIVELY COUPLED RADIO FREQUENCY DISCHARGES BASED ON THE ELECTRICAL ASYMMETRY EFFECT

Ranna Masheyeva[1,2], Peter Hartmann[1], Lan-Yue Luo[3], Karlygash Dzhumagulova[2,4], Yong-Xin Liu[5], Julian Schulze[6], Zoltán Donko[1]

[1] *Institute for Solid State Physics and Optics, HUN-REN Wigner Research Centre for Physics, 1121 Budapest, Hungary*
[2]*Department of General Physics, Satbayev University, 050013 Almaty, Kazakhstan*
[3]*Department of Engineering Physics, Tsinghua University, 100084 Beijing, China*
[4]*Research Institute of Experimental and Theoretical Physics, Al-Farabi Kazakh National University, 050040 Almaty, Kazakhstan*
[5]*Key Laboratory of Materials Modification by Laser, Ion, and Electron Beams (Ministry of Education), School of Physics, Dalian University of Technology, Dalian 116024, China*
[6]*Chair of Applied Electrodynamics and Plasma Technology, Faculty of Electrical Engineering and Information Sciences, Ruhr University Bochum, 44801 Bochum, Germany*
E-mail: masheyeva.ranna@gmail.com

We present a method for the determination of the effective ion-induced secondary electron emission coefficient (SEEC, γ) based on the DC self-bias voltage generation due to the Electrical Asymmetry Effect when a capacitively coupled radio frequency plasma is driven by two consecutive harmonics of a base radio frequency signal. By measuring the DC self-bias voltage experimentally and conducting Particle-in-Cell/Monte Carlo Collision (PIC/MCC) simulations combined with a diffusion-reaction-radiation (DRR) code for excited argon (Ar) dynamics, we determine γ by matching results of experiments and simulations for self-bias voltages. For an Ar plasma and stainless steel (St.St.) electrodes, we find γ ≈ 0.07, consistent with literature values. This method is adaptable to various gases, electrode materials, and discharge conditions, offering a robust approach to determine the effective SEEC.

1. Introduction

Capacitively Coupled Plasmas (CCPs) driven by radio frequency (RF) waveforms are widely used in surface modification, layer deposition, and etching, particularly in microelectronics [1,2]. Due to the use of RF excitation, the processing of non-conducting materials is also possible, expanding the range of applications. In such systems, the plasma and the surrounding surfaces interact dynamically: the plasma can modify the surface properties, while the surfaces, in turn, influence the plasma characteristics. These interactions are characterized by surface coefficients, such as the effective ion-induced secondary electron emission coefficient γ and the elastic electron reflection coefficient, R, which play a critical role in determining the plasma behavior.

Accurate knowledge of these coefficients is essential for reliable simulations and optimization of plasma processes [3,4]. While γ describes the emission of secondary electrons due to ion, metastable, or photon impacts, R accounts for the elastic reflection of electrons. These coefficients depend on particle energies, electrode materials, and discharge conditions, yet data availability is often limited, or values are derived from high-vacuum based beam impact experiments [5], which significantly differ from practical CCP conditions.

To address the lack of data for γ and R, several methods have been developed to determine these surface coefficients in situ. These methods combine experimental measurements of plasma characteristics with numerical simulations, where some parameters accessible in experiments are calculated as a function of the surface coefficients. The best match between measured and computational data determines the coefficients. In [6], the spatio-temporal distribution of the

electron-impact excitation rate in argon CCPs was used, where changes in the excitation patterns were linked to the effective secondary electron yield, γ. In [7], electron density and the ion flux-energy distribution were also measured to determine both γ and R. In [8], energy-resolved ion mass spectrometry was applied to analyze the bimodal peak structure of the ion flux-energy distribution, enabling the determination of γ for stainless steel and aluminum oxide electrodes. In our paper [9], we have proposed an alternative method to determine γ via the measurement of the DC self-bias voltage, η, that develops in a geometrically symmetric CCP because of the Electrical Asymmetry Effect (EAE) [3] when a multi- frequency waveform

$$\phi_0(t) = \sum_{k=1}^{N_H} \phi_k \cos(k2\pi f_1 t + \theta_k), \quad (1)$$

is supplied by the generator to the plasma. Due to the EAE, the voltage drop over the plasma becomes

$$\phi(t) = \phi_0(t) + \eta\,. \quad (2)$$

Here, N_H is the number of harmonics, f_1 the 'base' radio frequency, ϕ_k and θ_k are the amplitude and the phase of the k-th harmonic, respectively. From the results of the dependence of η on the SEEC, γ, and the reflection coefficient, R, we concluded in [9] that the method is not easily applicable for the determination of R, but has a good prospect for the measurement of γ in situ. Here, we demonstrate the application of this method for the measurement of the SEEC in an Ar CCP operated with stainless steel electrodes [10].

2. Experimental and computational methods

In our experiments, we aim to measure the DC self-bias voltage generated in a geometrically symmetric CCP source operated with dual frequency excitation, using a waveform defined by eq. (1). The experimental conditions have been carefully chosen to (i) enable precise measurements of the RF discharge voltage waveform and (ii) maximize the effect of secondary electron emission on the measured DC self-bias voltage. The conditions include the base frequency, f_1, the number of harmonics, N_H, in the excitation waveform, the amplitudes of these harmonics, ϕ_1, ϕ_2 , and the gas pressure, p. A detailed description of the experimental setup and the description of the parameter selection can be found in our published work [10]. Here, we provide a brief description.

The experiments are conducted in a simplified CCP cell, referred to as the XS Cell, which consists of a glass cylinder with an inner diameter of 92 mm and two stainless steel electrode plates separated by a distance of L = 27.5 mm. To enhance the influence of secondary electron emission on the discharge characteristics, including the DC self-bias, we opted for a lower-frequency operation compared to the typical base frequency of 13.56 MHz. To further constrain the frequency range, we limited the number of harmonics to N_H = 2. Accordingly, the excitation waveform is defined as: $\phi_0(t) = \phi_1 \cos(\omega t) + \phi_2 \cos(2\omega t + \theta)$, with voltage amplitudes ϕ_1 = 150 V, ϕ_1 = 0.5V_1, and base frequency values of f_1 = 2 MHz and 4 MHz were chosen. The phase angle θ serves as the control parameter for adjusting the DC self-bias. The argon gas pressures of 40 Pa and 80 Pa are chosen as we expect a larger effect of the secondary electron emission on DC self-bias at higher pressures.

We use the computational approach developed in [11], which consists of a PIC/MCC module and a DRR (Diffusion-Reaction-Radiation) module. The PIC/MCC module traces the motion of electrons and Ar^+ ions in the background gas, that consists of ground-state Ar atoms and Ar atoms in 30 excited levels. The DRR module computes the spatial density distributions of Ar atoms in these excited levels, based on the rates of the electron-impact collision processes obtained in the PIC/MCC module and the rates of the radiative transitions. The calculations also take into account pooling ionization between the excited atoms, electron-impact stepwise ionization from the excited levels, quenching of the excited levels by neutrals, as well as diffusion losses. The detailed description of the method can be found in [11].

The PIC/MCC simulation considers a one-dimensional spatial geometry: the plasma forms between two plane and parallel electrodes; one of these, situated at $x = 0$, is powered by a waveform taken from experimental recordings for enhanced precision. The other electrode, located at $x = L$, is grounded. The approach adopts an equidistant numerical grid with N_g= 512 points for the calculation of the electric potential and the densities of the charged species. These quantities are computed at discrete values of the time, separated by $\Delta t = T/N_t$ where N_t is the number of time steps within a base RF period $T = 1/f_1$. Depending on the pressure and the base frequency f_1, we use N_t = 18 000 ... 72 000 time steps. These parameters fulfill the relevant stability criteria of the PIC/MCC method.
At the electrode surfaces, two processes are considered: (i) Ar^+ ions arriving at the surface induce the emission of a secondary electron with a probability that is expressed by the secondary electron yield, γ. (ii) Electrons reaching the electrodes undergo an elastic reflection event with a probability R, for which we adopt the value 0.7 based on [7]. The DC self-bias voltage resulting from the use of N_H = 2 harmonics is determined in an iterative manner. At the initialization of the simulation, $\eta = 0$ V is set. After executing the simulation for a given number of RF cycles, the currents of the electrons and argon ions reaching each electrode are compared. Depending on the balance of electron and ion currents, the DC self-bias voltage is changed by a small quantity. This procedure is continued until η reaches a converged value and the time-averaged charged particle currents to each of the two electrodes balance.

3. Results and discussion

The measurements and the simulations are carried out for Ar gas at pressures of p = 40 Pa and 80 Pa, for base frequency values of f_1 = 2 MHz and 4 MHz, voltage amplitudes ϕ_1 = 150 V and ϕ_2 = 75 V, and for an electrode gap of L = 2.75 cm. In the computations, we use a range of effective secondary electron yield values, $0 \leq \gamma \leq 0.2$, and the elastic reflection coefficient of the electrons R = 0.7.

Four sets of experimental results for the dependence of the DC self-bias voltage, η, on the phase angle, θ, are shown in figure 1 as solid lines. The shape of the η curves matches well the previous results [12]. The extrema of the bias voltage are around of $|\eta| \sim$ 42-47 V, depending on the discharge conditions. At θ = 0° and 180°, figure 1 also shows the DC self-bias voltage values obtained from the PIC/MCC simulations at p = 80 Pa, f_1 = 4 MHz, for γ values of 0, 0.1, and 0.2. These data points indicate that (i) the magnitude of the self-bias voltage decreases with increasing γ in agreement with the findings of [9] and that (ii) the effective secondary electron yield is in the $0 \leq \gamma \leq 0.1$ domain for the p = 80 Pa and f_1 = 4 MHz parameter combination.

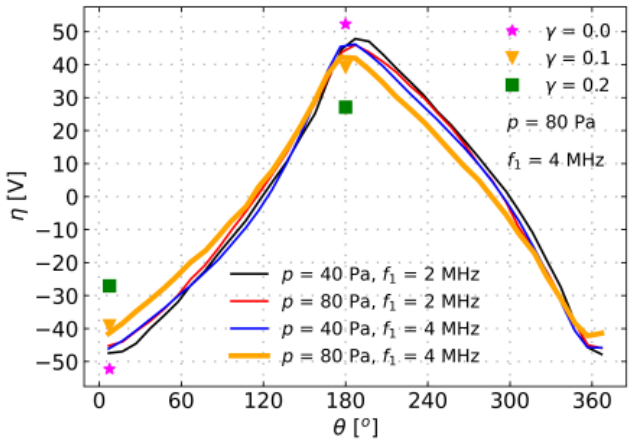

Fig. 1. Experimentally measured DC self-bias voltage as a function of the phase angle θ (solid lines) for p = 40 Pa and 80 Pa, f_1 = 2 MHz and 4 MHz (and L = 2.75 cm, ϕ_1 = 150 V, ϕ_2 = 75 V). The discrete data points show the computed DC self-bias voltages at θ = 0° and 180° for p = 80 Pa and f_1 = 4 MHz, for γ values of 0, 0.1, and 0.2.

Figure 2 illustrates the dependence of the computed DC self-bias voltage on γ for the two values of the base frequency, f_1 = 2 MHz (a) and f_1 = 4 MHz (b), at pressures of 40 Pa and 80 Pa. The experimental DC self-bias voltage values for the respective cases are represented by the dashed horizontal lines, while the numerical results are shown as symbols. The intersections of the latter and the horizontal lines identify the corresponding γ values, which are marked by thin gray vertical lines. For the conditions covered here, we find γ= 0.07 $\pm$ 0.012 which is in good agreement with the findings of previous studies, including the determination of the SEEC by matching simulation results with (i) experimentally measured ion energy distribution functions [8] and (ii) the spatio-temporal distributions of the electron-impact excitation rate, obtained experimentally by phase resolved optical emission spectroscopy (PROES) [7].

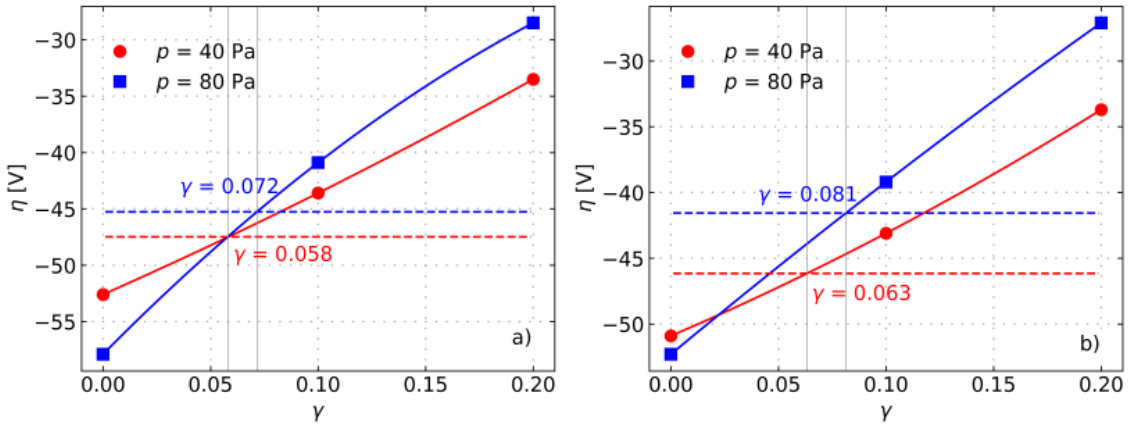

Fig. 2. Computed DC self-bias voltage at θ = 0° as a function of γ (solid lines with symbols). Discharge conditions: Ar, p = 40 and 80 Pa, f_1 = 2 MHz (a) and 4 MHz (b), ϕ_1 = 150 V and ϕ_2 = 75 V, L = 2.75 cm. The dashed horizontal lines correspond to the experimental data (red: 40 Pa, blue: 80Pa) for the DC self-bias. The solid lines are parabolic fits to the computed η values.

Figure 3 compares the measured DC self-bias voltage with the computed one over the whole domain of the phase angle θ for the γ =0.07 value at p = 80 Pa and f_1 = 4 MHz. The measured and computed curves exhibit a very good agreement, confirming the consistency of the model and the correctness of the effective secondary electron yield of approximately 0.07.

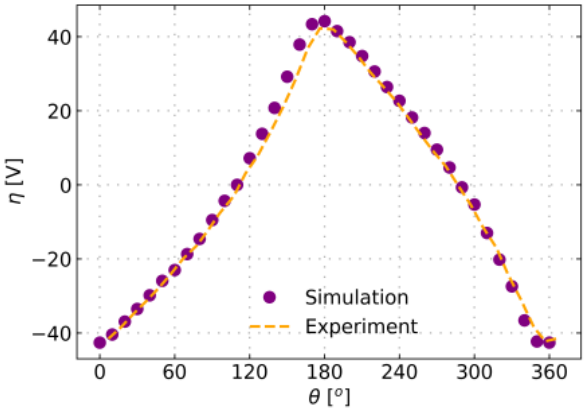

Fig.3. Measured and computed $\eta(\theta)$ curves for γ = 0.07. Discharge conditions: Ar, p = 80 Pa, L = 2.75 cm, f_1 = 4 MHz, ϕ_1 = 150 V and ϕ_2 = 75 V, R = 0.7.

Overall, this method represents a robust approach for determining γ in capacitively coupled plasmas, exhibiting potential for precise in-situ measurement of this critical parameter. It should, however, be kept in mind that the accurate measurement of the RF voltage amplitudes is a strict requirement for this technique. If this is ensured, then our method provides an easier access to the effective SEEC as

compared to some other approaches, like γ-CAST, as implementation of the PROES diagnostics could be impossible in practical plasma processing equipment. Future studies and laboratory experiments will further validate and expand upon this method, exploring different electrode materials and gases across various physical settings and discharge operating conditions.

Acknowledgments

This work was supported by the National Office for Research, Development and Innovation (NKFIH) via Grant K134462, by the Grant No.AP19679536 of the Ministry of Science and Higher Education of the Republic of Kazakhstan and by the German Research foundation via Grant 428942393. We thank Ihor Korolov and János Sárközi for their help in the RF measurements techniques.

4. References

[1] Makabe T and Petrović Z L 2014 *Plasma Electronics: Applications in Microelectronic Device Fabrication* (London: Taylor and Francis) **26**.
[2] Chabert P and Braithwaite N 2011 *Physics of Radio-Frequency Plasmas* (Cambridge University Press).
[3] Heil B G, Czarnetzki U, Brinkmann R P and Mussenbrock T 2008 *Journal of Physics D: Applied Physics* **41** 165202.
[4] Kawamura E, Vahedi V, Lieberman M and Birdsall C 1999 *Plasma Sources Science and Technology* **8** R45.
[5] Phelps A and Petrovic Z L 1999 *Plasma Sources Science and Technology* **8** R21.
[6] Daksha M, B Berger, E Schuengel, Korolov I , Derzsi A, Koepke M, Donkó Z and Schulze J 2016 *J. Phys. D Appl. Phys.* **49** 234001.
[7] Schulenberg D A, Korolov I, Donkó Z, Derzsi A and Schulze J 2021 *Plasma Sources Sci. Technol.* **30** 105003.
[8] Schulze C, Donkó Z, Benedikt J 2022 *Plasma Sources Sci. Technol.* **31** 105017.
[9] Masheyeva R U, Dzhumagulova K N, Myrzaly M, Schulze J and Donkó Z 2021 *AIP Advances* **11** 075024.
[10] Masheyeva R U *et al* 2025 *J. Phys. D: Appl. Phys.* **58** 045208.
[11]Donkó Z, Hartmann P, Korolov I, Schulenberg D, Rohr S, Rauf S and Schulze J 2023 Plasma Sources Science and Technology 32 065002.
[12] Donkó Z, Schulze J, Heil B and Czarnetzki U 2008 *Journal of Physics D: Applied Physics* **42** 025205.

STATISTICAL CHARACTERZATION OF VACUUM MICRODISCHARGES GENERATED IN HIGH PULSED ELECTRIC FIELDS

Mária Maťašová[1], Matej Klas[1], Peter Čermák[1], Štefan Matejčík[1]

[1]*Department of Experimental Physics, Faculty of Mathematics, Physics and Informatics, Comenius University, Mlynská dolina, 842 48 Bratislava, Slovakia*

E-mail: maria.cibikova@fmph.uniba.sk

The main objective of this work is the statistical analysis of microgap vacuum breakdowns generated in a high pulsed electric field between palladium, gold and platinum electrodes set in the sphere-to-plane geometry. High-voltage pulses with a ramp speed of 10^7 kV/s were applied to an electrode gap of 10 µm. The breakdown voltages were determined in the saturated state after conditioning the electrode surfaces. The observed memory effect, plotted as the dependency of $V_{B(i+1)} - V_{Bi}$ vs V_{Bi}, showed a different behaviour between consecutively generated breakdowns for the noble metals.

1. Introduction

The characterization of microdischarges generated at high pressures poses technical challenges due to the complex nature of field emission phenomena resulting from fast ionization processes within the discharge region. For this reason, low pressure can be more beneficial for investigation of microgap breakdown processes where the impact of the carrier gas can be neglected. The first attempts to investigate microgap breakdowns generated in vacuum were made in 1950s by Boyle, Germer and Kisliuk [1]. Over time, various materials (tungsten, copper, etc.) in different conditions (electrode separation, regime of electric signal, pressure, etc.) were investigated in numerous papers [2-4]. However, despite them, the breakdown initiation mechanisms are still unclear and under research. For this reason, we decided also to investigate them and in our previous work, the focus was on the vacuum microgap breakdowns generated in dc or pulsed regimes for stainless steel and corresponding field emission analysis [5,6]. Currently, the vacuum microgap breakdowns for palladium and other noble metals, which are characterized by good corrosion resistance, are under our investigation, mostly from the statistical point of view. The statistical characterization for palladium was successfully provided and recently published [7]. In this work we will focus on palladium, gold, and platinum.

2. The experimental setup

Scheme of our experimental setup is shown in Fig. 1. The vacuum ~ 10^{-4} Pa was secured by a system of turbomolecular pump with dry forepump for pre-vacuum. The electrodes were arranged in sphere-to-plane configuration inside the vacuum chamber. The metal sphere, with a diameter of approximately 5 mm, served as the cathode, while the plane anode was connected through resistors to a high-voltage power supply. The system operated in a pulsed regime, controlled by a function generator. The voltage ramp speed of the generated pulse was 10^7 kV/s and electrode gap size for all measurements was set to 10 µm. The 0 separation was determined by measuring of $R_{2+}R_3$ Ω using an ohmmeter. The required gap size was set using micrometer head.

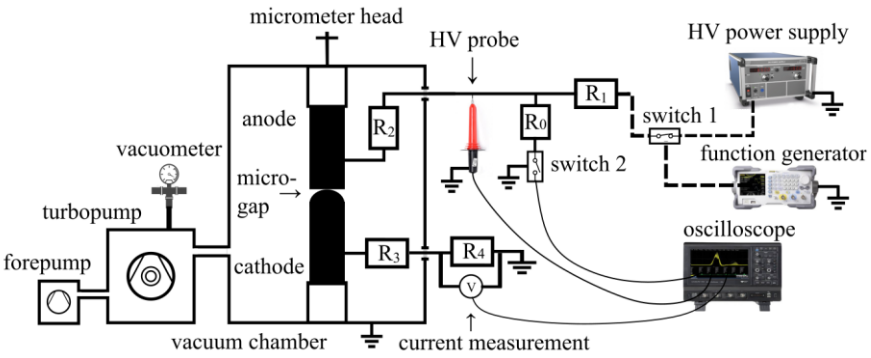

Fig. 1. The scheme of experimental setup for generation of vacuum microgap breakdowns in pulsed regime.

3. Results and discussion

Before conducting experiment, the conditioning of electrodes is necessary [1-7]. The conditioning process represents the cleaning of electrode surface from various impurities by successive breakdowns. In the following Fig. 2 the evolution of breakdown voltages during conditioning for palladium, gold and platinum is shown with the gap size of 10 µm.

From Fig. 2 it can be observed that during conditioning the breakdown voltage increased up to the saturated state where their values were determined, respectively ~ 3.5 kV for palladium, ~ 4 kV for gold and ~ 4.4 kV for platinum. These measurements confirmed the need of conditioning before breakdown voltage V_B determination as noticed in the works [1-5]. From Fig. 2 we can also deduced that for different materials, various numbers of breakdowns are required to reach the saturated state.

The statistical analysis was performed in saturated state for a sample over 10 000 breakdown sequences. In each breakdown sequence (pulse burst) with the length of several µs, several breakdowns were generated, as shown in Fig. 3 (illustration for palladium).

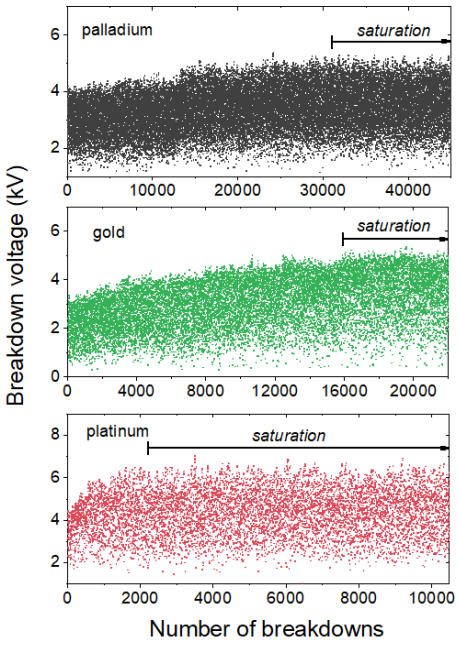

Fig. 2. Conditioning process.

The objective of the statistical analysis was the prove the relationship between two consecutive breakdowns. The correlation of $V_{B(i+1)} - V_{Bi}$ versus V_{Bi} where $i = 0, 1, 2, 3$ is the number of breakdown in the sequence was determined. At first, the breakdown pairs 1-0 (i = 0) for all materials were investigated. Corresponding dot density plots of correlation $V_{B1} - V_{B0}$ versus V_{B0} are shown in Fig. 4. These plots demonstrate that the consecutive breakdowns are not accidentally generated, but follow the pattern shown in Fig. 4. They differ with material. In the case of palladium, the maximum dot density is concentrated in in the positive part of y-axis, as well as in the case of gold. It indicates that for these materials the increase in breakdown voltage for first breakdown pair (1-0) is dominant. In the case of platinum, the pattern seems to have the same shape as the palladium, but the maximum point concentration is located in the negative side of y-axis what represents the decrease in breakdown voltage after first breakdown occurring. When the analysis of other breakdown pairs (2-1, 3-2, 4-3) was made, the maximum dot density was observed still in the positive side of y-axis. In general, we can conclude that the „cascading rise" of breakdown voltage, when multiple breakdowns are consecutively generated, is dominant. This suggests that, in the case of the microgap vacuum breakdown mechanism, the observed memory effect is related to surface conditions and modifications occurring during breakdown generation.

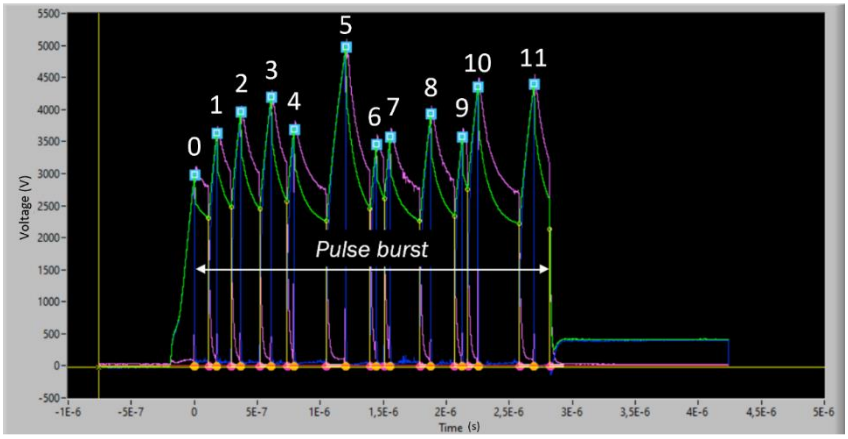

Fig. 3. The breakdown sequence (pulse burst) with several breakdowns for palladium.

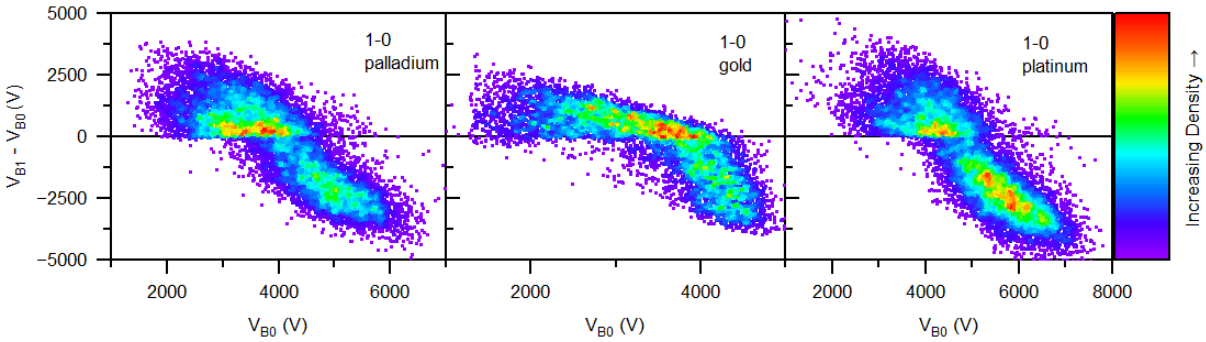

Fig. 4. The dot density plots breakdown pair 1-0 ($V_{B1} - V_{B0}$ versus V_{B0}) for palladium, gold and platinum.

Acknowledgments.

The authors acknowledge partial support from Slovak Grant Agency for Science VEGA Nr. 1/0553/22, Slovak Research and Development Agency under project Nr. APVV-23-0522.

4. References

[1] Boyle, W.S. Kisliuk, P. Germer, L.H. *J. Appl. Phys.* **26 (6)** (1955) 720–725.

[2] Dyke, W. P., & Trolan, J. K. (1953). Field emission: Large current densities, space charge, and the vacuum arc. Physical Review, **89(4)**, 799.

[3] Utsumi, T. *J. Appl. Phys*. **38(7)** (1967) 2989-2997.

[4] Zouache, N., & Lefort, A. *IEEE Trans. Dielectr. Electr.* **4(4)** (1997) 358-364.

[5] Klas, M., Matejčík, Š., Radjenović, B., & Radmilović-Radjenović, M. *EPL* ***95*****(3)** (2011) 35002.

[6] Klas, M., Čermák, P., Borkhari, A. F., Satrapinskyy, L., Matejčík, Š., Radjenović, B., & Radmilović-Radjenović, M. *Vacuum* (2021) 110327.

[7] Mat'ašová, M., Klas, M., Čermák, P., Radmilović-Radjenović, M., Petrovič, P., Satrapinskyy, L., & Matejčík, Š. *Vacuum* ***222*** (2024) 112998.

ELECTRON INDUCED DISSOCIATIVE EXCITATION OF FORMAMIDE

Enmily García[1], Barbora Stachová[1], Natalia Tańska[2], Wojciech Breguła[2], Marek Moravčík[3], František Krčma[3], Štefan Matejčík[1], Juraj Országh[1]

[1]*Department of Experimental Physics, Faculty of Mathematics, Physics and Informatics, Comenius University in Bratislava, Mlynská dolina F2, Bratislava, Slovakia*
[2]*Faculty of Applied Physics and Mathematics, Gdańsk University of Technology, Narutowicza 11/12, Gdańsk, Poland*
[3]*Faculty of Chemistry, Brno University of Technology, Purkyňova 118/464, Brno, Czech Republic*
E-mail: enmily.garcia@fmph.uniba.sk

Formamide, the simplest amide, is an interesting system to study due to its C=O double bond and C-N peptide bond. Its diverse chemistry includes functional groups and chemical bonds found in key biomolecules, making it a candidate as a potential precursor to life, many biochemical studies propose it likely played a crucial role in the context of the origin of life on our planet. The emission spectrum following electron impact on formamide is studied in a crossed-beam experiment. The spectra were measured at three slit widths of 100 and 300 μm, all at 50eV, within a wavelengths range of 280 to 1000 nm, to achieve optimal ratio of signal intensity and resolution. In the emission spectra, several lines and bands could be successfully identified, where the most prominent excited species that found were the hydrogen Balmer series, the nitrogen triplet system NH, the excited CH radical in the A and B electronic states, and atomic oxygen.

1. Introduction

Electron-induced fluorescence (EIF) is a technique enabling studying the electronic, vibrational, and rotational states of molecules through the principle of optical emission spectroscopy due to the emission of products from electron-molecule collisions; significantly important in several fields, such as interstellar chemistry (nebulae, stars, comets) [1].

Emission spectroscopy is an analytical method allowing the study of electron-molecule collisions producing excited species, which is especially important for astrophysics, particularly in space exploration, as it enables remote analysis of planetary atmospheres, cometary comas, and nebulas irradiated mainly by nearby stars [2]. The secondary electrons generated in photoionization reactions further interact with gas molecules and emission generated through these reactions provide insights into the molecular composition and processes active in these interstellar bodies.

In recent years, it has become evident that the chemistry of interstellar bodies is not confined to the gas phase. A significant portion of their mass resides in condensed matter, primarily in refractory dust grains or dust coated with volatile molecular ice mantles. Alternatively, ice-coated dust can accumulate on larger objects, growing in size up to that of comets. This process is of great interest to astrobiology, as comets are believed to play a role in delivering water and essential organic compounds to planetary surfaces. Such deliveries, including those to early Earth, could have occurred at a critical time, potentially contributing to prebiotic processes that led to the emergence of life [3].

Formamide (NH_2CHO) has been identified as a potential precursor to a wide variety of organic compounds essential for life, and many biochemical studies propose that it likely played a crucial role in the origin of life on Earth. First, it has an amide functional group (-N−C(=O)-), which is necessary to form chains of aminoacids and build up proteins; and second, it has been identified as a key precursor of a large variety of prebiotic molecules. Its first detection in space was reported in 1971 in the Sagittarius B2 region (Sgr B2), the most massive star-forming region in our galaxy. Additionally, its detection in comets, that retained their chemical composition from the birth of the Solar System, raises the question of whether a significant amount of formamide may have been exogenously delivered to the young Earth around four billion years ago [4-5].

The data from previous research on electron-induced fluorescence of formamide are insufficient or practically non-existent for studying extraterrestrial bodies. This study aims to expand the database of

absolute emission cross sections and provide detailed information on the processes occurring during the experiments.

2. Experimental Apparatus

The experimental apparatus used in this work is based on a crossed electron and molecular beams method and is further described in a previous publication [6]. Trochoidal electron monochromator located in a vacuum chamber generates a monochromatic electron beam. The electron beam interacts with a perpendicular molecular beam formed by an effusive capillary. The background pressure of the vacuum chamber is ~10^{-8} mbar and the pressure of the molecular beam is set to sustain binary interactions – one electron with one molecule. One of the products of electron-molecule interactions are excited species. These are unstable and emit radiation as they de-excite. The emitted radiation is collected by a UV fused silica lens and guided out of the vacuum chamber to a parabolic mirror, which focuses this radiation to the entrance slit of a Czerny-Turner optical monochromator. To maximise the detected signal, a spherical mirror is placed opposite to the collecting lens with its focus at the centre of collision. To acquire signal from the emitted radiation, an Andor iDUS 420 CCD camera is used. The CCD camera is sensitive to 300 – 1100 nm wavelength range and can obtain signal from an approximately 85 nm interval of wavelengths.

3. Experimental results and discussion

In a first step of this experiment, the emission spectrum of formamide was measured using different slit widths (100 μm and 300 μm which correspond to spectral resolution 0.4 nm and 1 nm), at 50eV electron energy. Comparing the experimental results allows us to determine the optimal measurement parameters for analyzing formamide, aiming the best resolution to identify the peaks and bands corresponding to the emission excitation of all possible fragmentations of the compound. The first emission spectrum, obtained with a slit width of 100 µm, was measured in the wavelengths within 300 – 950 nm. Meanwhile, the emission spectra with slit width of 300 µm was measured over a shorter wavelength range within 300 – 500 nm.

Comparing the emission spectra obtained, several emission lines were identified. In the spectrum 100 µm slit width, it is possible to observe the emission line corresponding to H_α as well as the oxygen emission line in the IR wavelength region, O I ($3p^3P\text{-}s^3S^0$), as shown in figure 1. In both spectra, the most prominent emission line corresponds to the nitrogen triplet system NH ($A^3\Pi\text{-}X^3\Sigma$), and the rest of the hydrogen's Balmer series from H_β to H_η, were also identified along with the CH ($B^2\Sigma\text{-}X^2\Sigma$), CH ($A^2\Delta\text{-}X^2\Pi$) and CN ($B^2\Sigma\text{-}X^2\Sigma$) bands, as shown in figure 2 [7 – 8].

Formamide is a liquid under typical temperature and pressure conditions at the Earth's surface. It is volatile and has a relatively low boiling point. However, conducting measurements of this compound proved to be more challenging than anticipated, as it condenses easily, leading to blockages in the system. Therefore, it is crucial to properly regulate the temperature of each individual component of the system to prevent condensation and subsequent blockages. At the same time, it is necessary to identify the ideal conditions to maintain a sufficiently high pressure that ensures a reasonable signal intensity.

The results presented are preliminary and help to clarify the most suitable parameters for working with this type of sample, allowing us to achieve clear, well-defined, stable, and reproducible results. We will continue working by repeating the measurements until the optimal working conditions are determined. Subsequently, a more comprehensive study of this molecule will be conducted, obtaining the emission spectrum after electron beam collisions at different electron energies ranging from 5 to 100 eV, covering the wavelength range from 280 to 1000 nm.

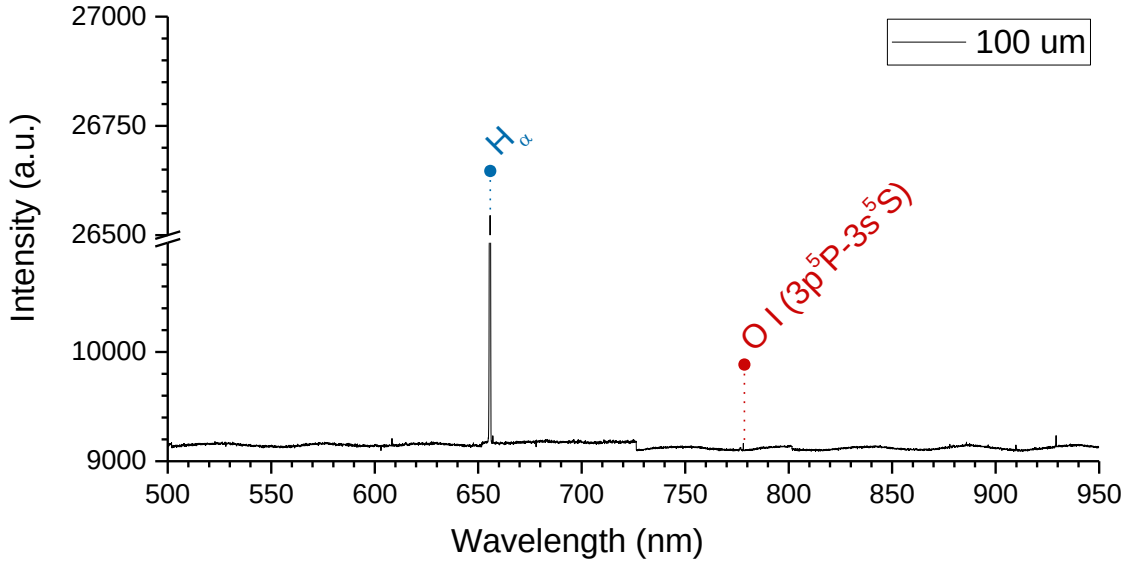

Fig. 1. The emission spectrum of Formamide measured by CCD camera at 50 eV electron energy with slit width of 100 μm, from 500 to 950 nm.

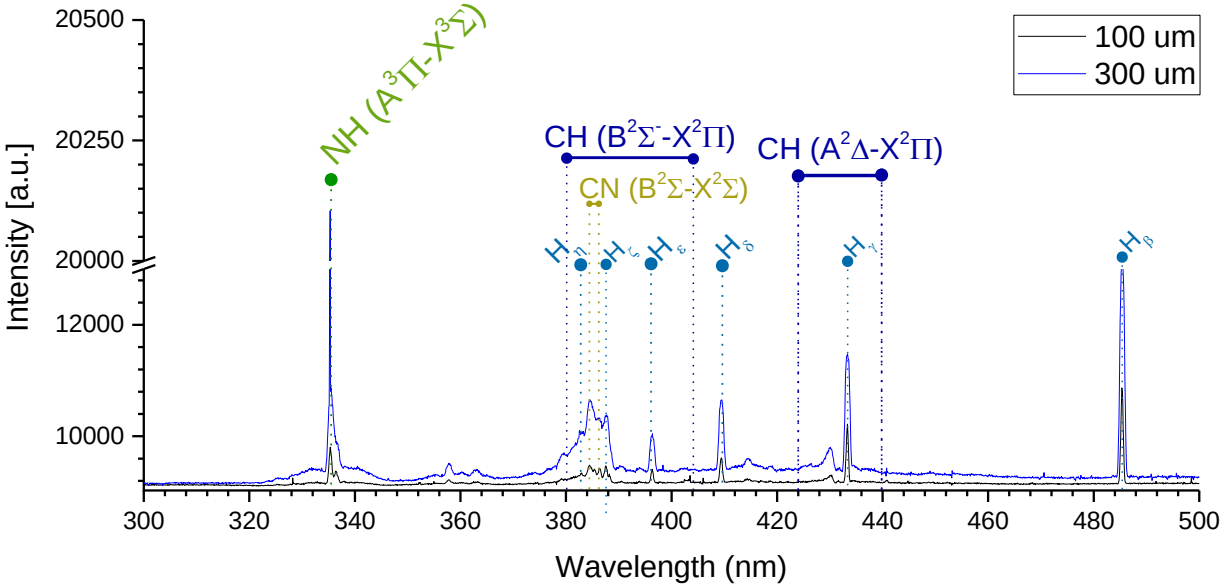

Fig. 2. The emission spectrum of Formamide measured by CCD camera at 50 eV electron energy with slit widths of 100 μm and 300 μm, from 300 to 500 nm.

4. Acknowledgements

This work was supported by the Slovak Research and Development Agency under the Contracts no. SK-PL-23-0050 and APVV-23-0522, Slovak grant agency VEGA under project nr. 1/0553/22. This project has received funding from the European Union's Horizon 2020 research and innovation programme under grant agreement No 871149. Funded by the EU NextGenerationEU through the Recovery and Resilience Plan for Slovakia under the project No. 09I01-03-V04-00047.

5. References

[1] J. Blasko, J. Országh et al., *Spectral electron energy map of electron impact induced emission of nitrogen*, Eur. Phys. J. D.,2023, 77:22.

[2] D. Bodewits, J. Országh, J. Noonan, M. Ďurian a Š. Matejčík, The Astrophysical Journal, 2019, 885 (16pp) 167.

[3] Woon D., *Ab Initio Quantum Chemical Studies of Reactions in Astrophysical Ices. 4. Reactions in Ices involving HCOOH, CH_2NH, HCN, HNC, NH_3, and H_2O*, International Journal of Quantum Chemistry, Vol. 88, 226–235, 2002.

[4] A. López-Sepulcre et al., *Interstellar Formamide (NH2CHO), a Key Prebiotic Precursor*, ACS Earth Space Chem, 2019, 3, 2122-2137.

[5] C. Kahane et al., *Detection of formamide, the simplest but crucial amide, in solar-type protostar*, The Astrophysical Journal Letters, &63:L38 (5pp), 2013.

[6] Országh, J., Danko, M., Čechvala, P., Matejčík, Š., Dissociative Excitation of Acetylene Induced by Electron Impact: Excitation-emission Cross-sections. *The Astrophysical Journal,* 841:17, (10pp), 2017.

[7] Luque J and Crosley D R, *LIFBASE: Database and Spectral Simulation Program (Version 1.5)* Tech. rep. SRI International, 1999.

[8] Pearse R W B and Gaydon A G, *The Identification of Molecular Spectra,* 4th ed (Halsted Press, John Wiley and Sons,Inc), 1976.

THERMAL PLASMA GASIFICATION

Michal Hlína[1], Tomáš Mates[2], Dominik Kralik[1], Alan Mašláni[1], Jakub Pilař[1], Jafar Fathi[1], Maksym Buryi[1]

[1]*Institute of Plasma Physics of the Czech Academy of Sciences, U Slovanky 2525/1a, 182 00 Prague 8*
[2]*Institute of Physics of the Czech Academy of Sciences, Cukrovarnická 10/112, 162 00, Prague 6*
E-mail: hlina@ipp.cas.cz

Thermal plasma gasification is a technology that utilizes high-temperature plasma to convert organic and inorganic materials into synthesis gas (syngas) and slag. There are several possibilities how produce thermal plasma. An argon-water arc plasma torch and a microwave plasma torch are utilized for these purposes at the Institute of Plasma Physics, and their characteristics have been compared.

1. Introduction

Microwave, arc discharges, and radio frequency sources can all produce thermal plasmas when they pass through a gas stream where gas molecules are ionized due to high temperatures. Thermal plasmas are relatively dense with rather lower electron energy in comparison with other plasmas [1]. Ionization for plasmas in thermal equilibrium is given by Saha equation [2]. Thermal equilibrium in the case of plasmas means that electrons, ions, and gas molecules and atoms are at the same temperature while cold plasmas usually feature hotter electrons than other elements. Thermal plasmas at atmospheric pressure possess high energy densities, making them well-suited for specific applications such as material processing (plasma spraying, nanoparticles synthesis), gasification-pyrolysis, fuel conversion and environmental applications (air and water purification, carbon capture conversion).

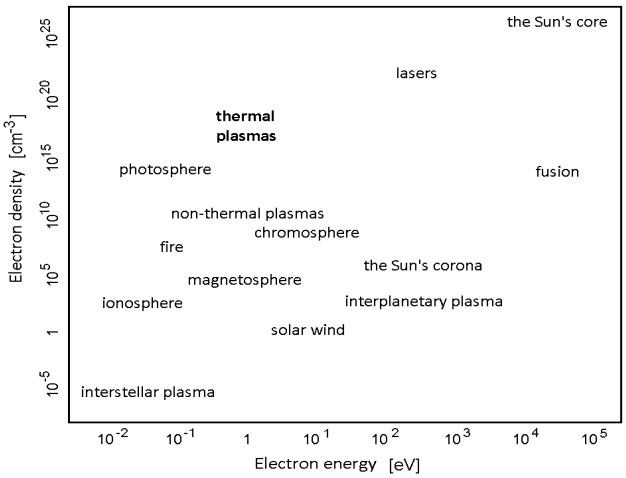

Fig. 1. Classification of Plasma by Electron Density and Energy [1].

Advantages of using thermal plasma originate from high temperatures leading to high reaction constants, reduction of reaction volumes and the options for proper reaction pathways in general, while disadvantages spring from high operating costs, limited scalability, and lifetime of electrodes in the case of arc plasma sources.

2. Arc plasma torch

An arc plasma torch (WSPH) used at Institute of Plasma Physics (IPP) for the purposes of gasification was patented on the same place and is characterized by several unique features. A cathode is protected against corrosion by an argon flow, but the main part of the arc is stabilized by a water

vortex and an anode is presented by water-cooled copper disc. Produced plasma has very low mass rate of ionized argon/water mixture with extremely high temperature (up to 20 000 K), maximum input power is 150 kW [3].

3. Microwave plasma torch

A microwave plasma torch (MW) utilised as the source of energy for gasification uses air as a working gas and was supplied by company Muegge (Germany). The torch consists of four major components which are: an AC power supply, a water-cooling system, a 950 MHz microwave generator and a 3-stub tuner. Maximum input power is 100 kW.

4. Experimental

The inlet of treated material and the plasma torch are mounted at the top of a 220 L reactor with ceramic thermal insulation of 400 mm thickness. Produced gas is quenched, filtered, flows through a water ejector, where the underpressure in the reactor in controlled and subsequently is burnt in the flare with a propane butane stabilizing burner. Temperatures range between 1000°C and 1200°C during experiments. A sampling probe for composition measurements was located at the reactor output and was cooled down by passage through the quenching chamber. A quadrupole mass spectrometer Pfeiffer Vacuum Omnistar GSD 301 with direct inlet and Matrix MG01 spectrometer Bruker Optik GmbH were used as gas analyzers. A freezing unit had to be placed into the sampling line to avoid water condensation. Polypropylene (PP) was treated by both torches and the results were compared.

5. Comparison of arc and microwave plasma torches

The WSPH torch produces 18 g/s of Ar/H_2O plasma, whereas the MW torch uses air as its working gas, with a mass rate nearly 70 times higher (1250 g/s) than that of the WSPH torch. This leads to enormous dilution by N_2 of produced syngas in the case of the MW torch, but the usage of different working gases (H_2O vapour, O_2, CO_2 or their mixtures) would lead to the production of synthetic gas with more advantageous composition [4].

Tab. 1. Comparison of arc plasma (WSPH) and microwave plasma (MW) torch, gasification of polypropylene (PP)

	syngas composition								operational parameters			
	CO	CO2	Ar	O2	CH4	H2	N2	NO/NO2	CO2	air	PP	P
	slm								slm		kg/h	kW
WSPH	46,80	3,60	10,20	0,11	1,70	37,58	0	0	129	0	7	138
MW	2,99	12,29	1,06	1,63	0,59	0,97	80,40	0,05	0	1016	7	40

High Ar concentration in the case of the WSPH torch is caused by externally adding of 50 slm of Ar for calibration purposes. The Ar concentration originated just from Ar presented in plasma would form approximately 1 %.

Due to its lower power and higher plasma mass flow rate, the MW torch has a much lower plasma temperature, which was expected to result in increased concentrations of hydrocarbons such as CH_4 and C_2H_2. However, measurements did not support this hypothesis.

Syngas composition and basic operational parameters are summarized in Tab. 1.

6. Acknowledgement

Financial support from the Technological Agency of the Czech Republic (Project No. TN02000069) is gratefully acknowledged.ob

7. References

[1] Peratt A L 1966 *Ap&SS*. **1/2** 93 (163)
[2] Saha M N 1920 *Phil. Mag.* **6** 40 (238)
[3] Hrabovsky M 2006 *IEEE Trans. Plasma Sci* 34
[4] Shin D H 2013 *Surf. Coat. Technol.* **228** S520-S523.

ON MECHANISM OF REACTIVE NITROGEN SPECIES FORMATION IN NEGATIVE POLARITY HIGH PRESSURE GLOW DISCHARGE

Mário Janda[1], Nenad Selaković[2], Olivera Jovanović[2], Neda Babucić[2], Nikola Škoro[2], Oleksandr Galmiz[1], Nevena Puač[2]

[1]*Faculty of mathematics, physics and informatics, Comenius University in Bratislava, Slovakia*
[2]*Institute of Physics, University of Belgrade, Belgrade, Serbia*
E-mail: janda1@uniba.sk

Mass spectroscopy (MS) was used for detection of oxygen and nitrogen species produced by negative polarity high pressure glow discharge (HPGD). Atomic O and N species as well as nitrogen oxides NO and NO_2 were detected. It was not possible to detect ions generated in the discharge directly. As shown by chemical kinetic model, concentration of negative ions is negligible in HPGD because of elevated temperature. Chemical kinetic model was also used to study formation pathways of species detected by MS.

1. Introduction

Electrical discharges can generate chemically active non-equilibrium plasmas, where electrons have significantly higher energy than ions and neutral particles. Among the many types of electrical discharges, low-pressure glow discharges are one of the most common and fundamental, often used for illumination [1]. While less common and well-known than their low-pressure counterparts, high pressure glow discharges (HPGD) offer the possibility of removing organic pollutants from exhaust gases [2]. Furthermore, their stability and efficiency in generating nitric oxide from air make them useful for nitrogen fixation [3].

HPGD can be ignited between a high-voltage metal electrode and a water surface, with the second electrode submerged [4]. This configuration, in combination with the generation of nitrogen oxides in the gas phase, makes HPGD suitable for generating plasma-activated water [5].

Plasma-activated water (PAW) is water that has been exposed to plasma. This exposure infuses the water with reactive oxygen and nitrogen species (RONS), such as hydrogen peroxide, nitrates, and nitrites, which temporarily alter the water's chemical properties and make it useful in many applications in food, agriculture, and biomedicine [6, 7]. These possibilities have made PAW a hot topic in the low-temperature plasma community in recent years.

Despite many studies and obtained results, further research is crucial for a better understanding of the formation mechanisms of reactive species, such as nitrogen oxides, and for assessing the role of different gas-phase species in the formation of aqueous RONS in PAW. From a practical point of view, this knowledge will allow for increased energy efficiency and selectivity with respect to the desired products when generating PAW. For this reason, the formation of RONS by HPGD is studied in this paper, using mass spectrometry (MS) and chemical kinetic modelling. For MS measurements we used molecular beam mass spectrometer (MBMS) that can sample from atmospheric pressure enabling to directly access chemical species created in the plasma. In principle the MBMS can detect both neutral and ionic species but in this study we focused to neutrals.

2. Experimental setup

A schematic diagram of the experimental apparatus is shown in Figure 1. The high pressure glow discharge was generated by a DC high voltage (HV) power supply (Glassmann PSIWH 20R25) with negative polarity output, capable of delivering up to 20 kV. The power supply was connected to the cathode via a 1 MΩ series resistor (R) to limit current. This power supply can also operate as a stabilized current source, providing up to 30 mA.

The cathode consisted of a stainless steel needle with a flat tip and an outer diameter of 0.7 mm. The discharges were generated in dry air from the pressure cylinder (purity 5.0), flowing along the cathode

towards the anode with the gas flow rate of 0.3-0.45 slm, controlled by mass controller (Bronkhorst F201-EV).
For diagnostics of neutral species, a grounded steel ring with an inner diameter of about 4 mm and an outer diameter of about 8 mm served as the anode. This ring was positioned 5 mm in front of the entrance to the mass spectrometer, which had an orifice diameter of 100 µm. For the measurements the mass spectrometer front plate with the orifice was grounded. The cathode-anode gap distance was maintained at 3 mm.
The electrical potential between the cathode and ground was measured using a high voltage probe (Tektronix P6015A) connected to a digital oscilloscope (Keysight MSOX 3024T).
The MBMS used for measurements (Hiden Analytical HPR 60) was operating in two modes- RGA (Residual Gas Analyzer) mode, that provides data on the mass spectra of neutrals in the range 0–100 amu; and MID scan, when the device is set to monitor the temporal changes of selected species. In both cases, for the detection of neutral species a ionization chamber was active with the electron energy set to 70 eV. The MBMS has an internal shutter – Swagelok that allows recording of the background signal coming from the gas phase inside the device.

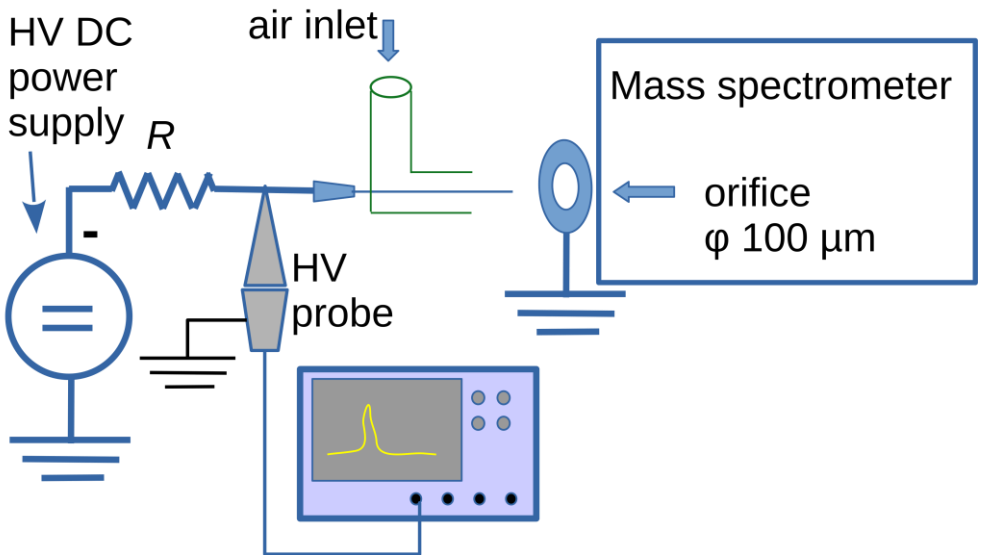

Fig. 1. A schematic diagram of the experimental apparatus.

3. Chemical kinetic model

The aim of the chemical kinetic model is to calculate density evolution of studied species interacting via defined set of chemical reactions. For this purpose we used ZDPlasKin module [8] that includes a Fortran 90 version of the VODE solver for numerical solution of system of ordinary differential equations [9]. Authors of ZDPlasKin also provide a ready-to-use list of plasma chemical processes in nitrogen-oxygen mixtures with all necessary rate coefficients [10]. This set of reactions (version 1.03) includes ~650 chemical reactions among 53 species.
The rate constants of reactions between heavy species from this list are calculated from the thermodynamic gas temperature T_g. The rate constant for electron impact reactions must be calculated from electron energy distribution function (EEDF) obtained by solving the Boltzmann equation for free electrons. The ZDPlasKin package includes a Bolsig+ solver [11] for this purpose. A set of required electron scattering cross sections was taken from the LXCat project database [12].
Finally, ZDPlasKin module requires use of additional subroutines written by user for comprehensive control of simulation conditions, e.g., changes in the gas temperature, pressure and reduced electric field. Our physical model has two parts, glow discharge and afterglow. The afterglow part has to be included because in some experiments, the gas from the discharge did not enter the mass spectrometer directly, but there was a 5 mm gap between the grounded ring electrode and orifice.

For modeling of GD we used constant temperature T_g = 2000 K, constant pressure of 1 atmosphere and constant reduced electric field strength E_n = 60 Td. We also used constant electron density n_e = 10^{12} cm^{-3}. These values were estimated based on previous experimental observations of HPGD [13]. In order to take into account diffusion of species our of the discharge plasma channel and mixing with the surrounding ambient air, we included a primitive diffusion model in our code. After each calculation step with duration Δt, concentration of each heavy particle n_i is decreased by Δn_i calculated as

$$\Delta n_i = -\alpha_{diff} n_i \Delta t, \quad (1)$$

where α_{diff} is coefficient representing diffusion of particles out of the plasma channel. To keep constant pressure (total density of particles), the removed particles were replaced by N_2 and O_2 molecules (ratio 4:1). This simulates mixing with the ambient air.

In the second part of the model, an afterglow period of 0.2 s, the reduced electric field strength decreased exponentially to 3 Td with a time constant of 20 ns. Electrons concentration was calculated dynamically along with the densities of all other species, rather than being held constant. Mixing with the surrounding air continued during the afterglow phase, leading to a calculated decrease in gas temperature. Electron diffusion was also incorporated, with a diffusion coefficient ten times higher than that of the heavy particles.

4. Results and Discussion

HPGD was generated with discharge current of either 2.1 mA, or 3 mA. The applied voltage was -3 kV and -4 kV, respectively. The discharge voltage (across the gap) decreased from ~1.3 kV to ~1.15 kV when the HPGD current increased from 2.1 mA to 3 mA. Mass spectra of produced neutral species were measured for both discharge currents. The obtained spectra had the same species visible for both currents so in Figure 2 we present the data recorded for 3 mA.

The data shows only species created in the plasma as the background signal, recorded in plasma off conditions, was subtracted. The most abundant species created in the discharge were atoms of H,N and O and reactive species OH, H_3O, NO, H_2O_2 and N_2O.

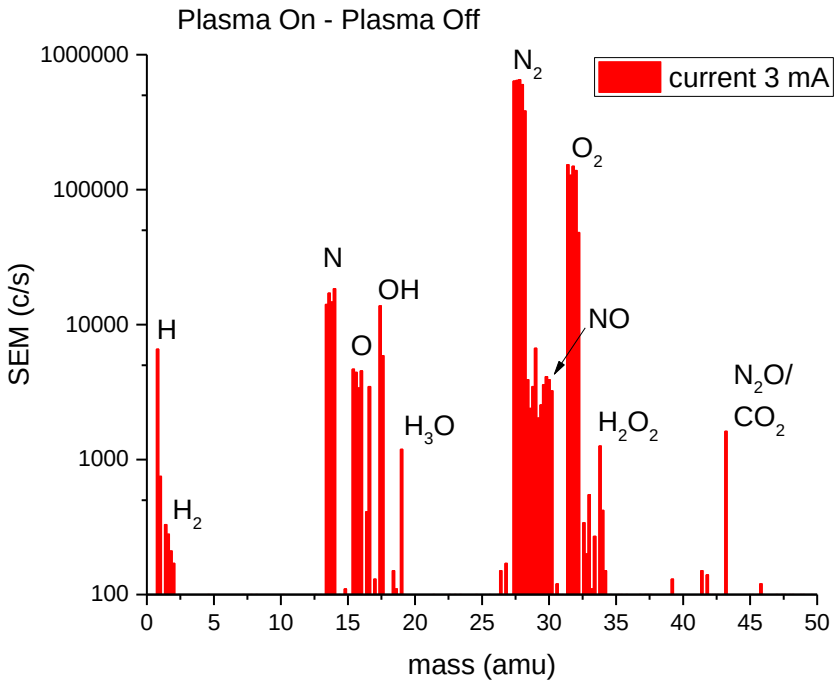

Fig. 2. Mass spectra of neutral species measured for current 3 mA.

In the MID scan mode, we monitored temporal changes in the nitrogen species NO, N_2O and NO_2 important for PAW generation. In Figure 3 we show recorded signals for these species with respect to different measurements conditions. Measurements were conducted with Swagelok open and with Swagelok closed. Swagelok open represents the sum of foreground and background species, while Swagelok closed corresponds to background species only. For the first 6 minutes of recording the discharge was off so variations in the signal is only due to processes inside the device. Once the discharge is ignited, increase in NO and NO_2 signals was due to the species created in the discharge. Obviously, creation of N_2O species was not large so the signal did not change after discharge inception.

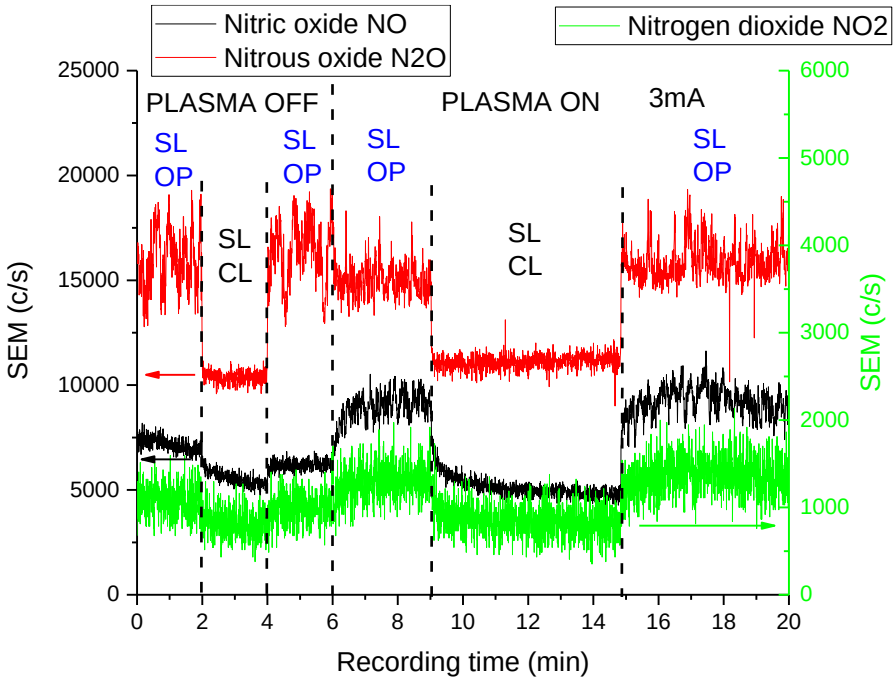

Fig. 3. MID-scan of NO, NO_2 and N_2O species without and with the discharge operating in front of the MS orifice with addition of synthetic air. Discharge current was 3 mA. Measurements were perforemed with Swagelok closed (SL CL) and open (SW OP).

In summary, the experimental data confirmed generation of N, O, NO and NO_2 by HPGD. Chemical kinetic model using ZDPlasKin module was used to explain their formation. As for example, Figure 4 shows time evolution of N, O, NO, NO_2 and O_3 species concentrations in the glow discharge. This calculation was performed with $\alpha_{diff} = 2\ s^{-1}$.

Our model incorporates diffusion, but the employed calculation approach is simplified, and the exact value of the diffusion coefficient remains unknown. Instead, we utilize a parameter, α_{diff}, to represent the diffusion rate. We performed several calculations with α_{diff} ranging from 0.1 to 10 s^{-1}. Since α_{diff} influences the calculated steady-state concentrations of species in the plasma, we cannot definitively determine the actual concentrations of the studied species in the HPGD. However, we observed that α_{diff} in studied range does not significantly affect the ratio of concentrations of various RONS or their production pathways.

Figure 4 demonstrates that the concentrations of all studied RONS reach a steady state after approximately 0.2 ms, remaining constant thereafter. This steady state arises from a balance between production (through chemical reactions) and removal (via chemical reactions and diffusion). Consequently, we analyzed the reaction pathways separately for the initial phase of the simulation and for the subsequent steady state.

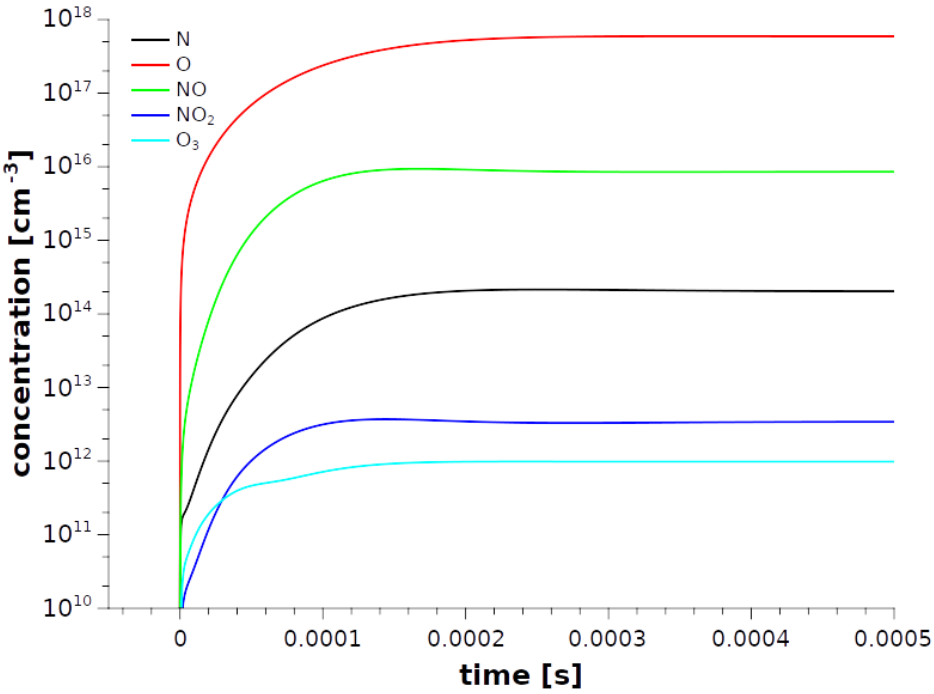

Fig. 4. Time evolution of N, O, NO, NO_2 and O_3 species concentration; calculated with $\alpha_{diff} = 2\ s^{-1}$.

In the initial phase (Figure 5), O atoms are mainly produced by reactions of O_2 with electronically excited molecular nitrogen species N_2* (the most important being $N_2(B^3\Sigma)$, and by electron impact dissociation of O_2 molecules:

$N_2^* + O_2 \rightarrow N_2 + O + O,$ (2)
$e + O_2 \rightarrow e + O + O.$ (3)

Contribution of other reactions, such as

$N + O_2 \rightarrow O + NO$ (4)

on O atoms production is already quite small.
In the later steady state phase, the production reactions (2-4) are compensated by O atoms recombination reactions

$O + O + M\ (M = O, O_2, N_2) \rightarrow O_2 + M.$ (5)

In this simplified O production/removal mechanism we omitted reactions between O, $O(^1D)$ and $O(^1S)$ species. An equilibrium between these species is achieved quickly, with O representing more than 99.9% of them.
N atoms are produced mostly by these two reactions:

$O(^1D) + NO \rightarrow O_2 + N,$ (6)
$N_2(a`^1) + NO \rightarrow N_2 + N + O.$ (7)

There is also a third important reaction producing N atoms, electron impact dissociacion of N_2, but it plays an important role at the very beginning of the simulation ($t < 50\ \mu s$), when there is still not enough NO molecules for N generation by equations (6) and (7).

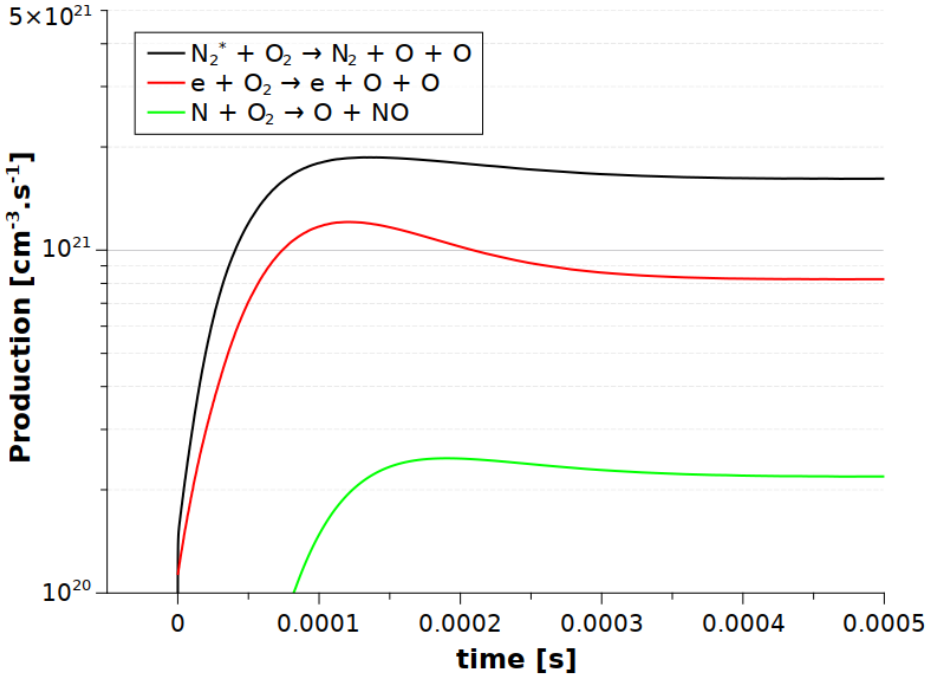

Fig. 5. Production of O atoms during the initial phase of the simulation; calculated with α_{diff} = 2 s^{-1}.

In steady state, the removal of NO molecules by N (equations (6) and (7)) is compensated by NO production via reaction

$N + O_2 \rightarrow O + NO.$ (8)

Reactions (6-8) all involve NO, they are crucial not only for N production and losses, but they also influence the density of NO. Reaction (8) is actually the most important for NO production (Figure 6). The other two important reactions are

$N_2(A^3) + O \rightarrow NO + N(^2D),$ (9)
$N(^2D) + O_2 \rightarrow NO + N.$ (10)

In the steady state, the production of NO is compensated by its removal (Figure 7) via reactions (6), (7), (11) and (12)

$NO + N(^2D) \rightarrow N_2 + O,$ (11)
$NO + N \rightarrow N_2 + O.$ (12)

NO_2 is produced almost eclusively by reaction (13) and removed by reaction (14)

$O + NO + M \rightarrow NO_2 + M\ (N_2, O_2),$ (13)
$O + NO_2 \rightarrow NO + O_2.$ (14)

Steady state NO_2 concentration $[NO_2]$ can be therefore easily calculated as $[NO_2] = k_{13}.[NO]/k_{14}$, assuming balance between NO_2 production and destruction by reactions (13) and (14). In this formula, [NO] is steady state concentration of NO, k_{13} and k_{14} are rate coefficients of reactions (13) and (14), respectively. At 2000 K, the ratio of these two rate coefficients is 7.3×10^{-4} and it explains why the steady state concentration of NO_2 is much lower than the concentration of NO (Figure 4).

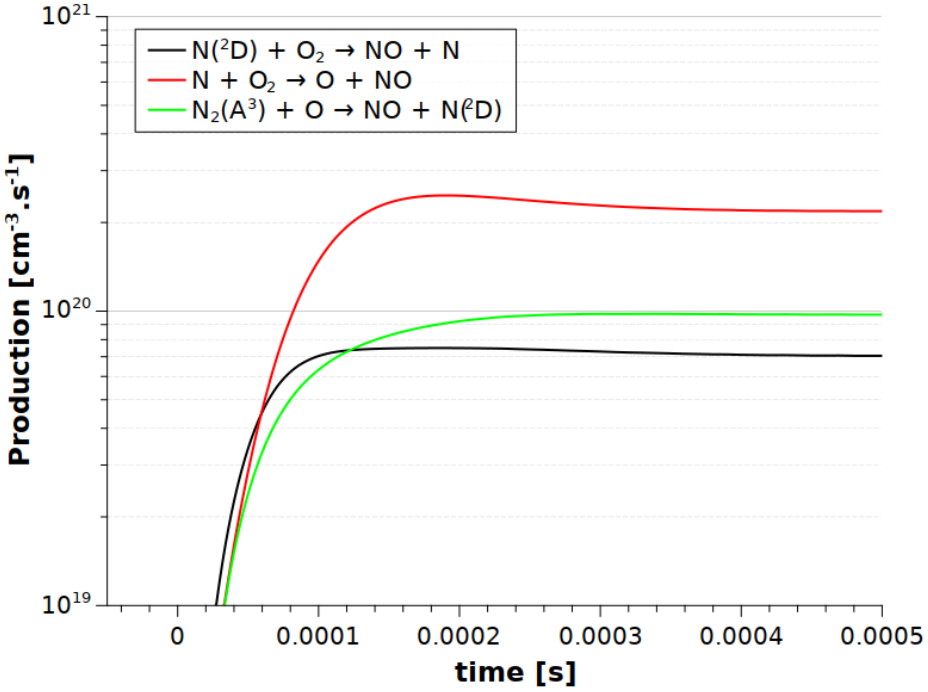

Fig. 6. Main reactions responsible for production of NO molecules; calculated with α_{diff} = 2 s^{-1}.

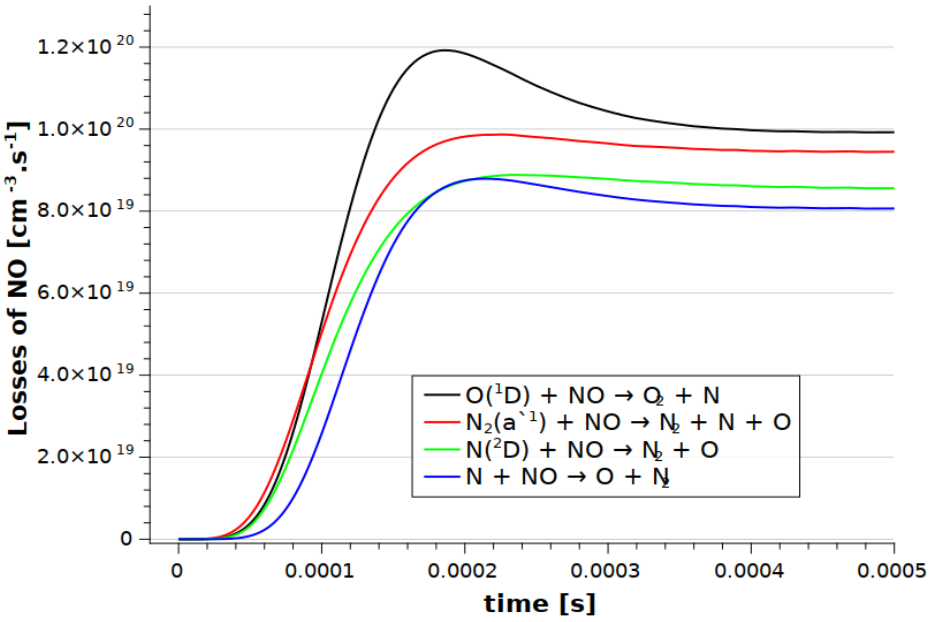

Fig. 7. Main reactions responsible for losses of NO molecules; calculated with α_{diff} = 2 s^{-1}.

Based o *ex-situ* measurements of the gas after treatment by glow discharge, the concentration of NO is higher than the concentration of NO_2, but the difference is not so significant [3]. Final NO and NO_2 concentration is mainly determined by reactions in the gas after leaving the discharge zone (afterglow). Figure 8 shows time evolution of gas temperature and N, O, NO and NO_2 species concentrations in the discharge afterglow, calculated with α_{diff} = 10 s^{-1}. The concentration of atomic species (N and O) decreases rapidly. While the NO concentration decreases slowly, the NO_2 concentration increases, despite mixing with the ambient air. Consequently, the difference between NO and NO_2 concentrations decreases in the discharge afterglow.

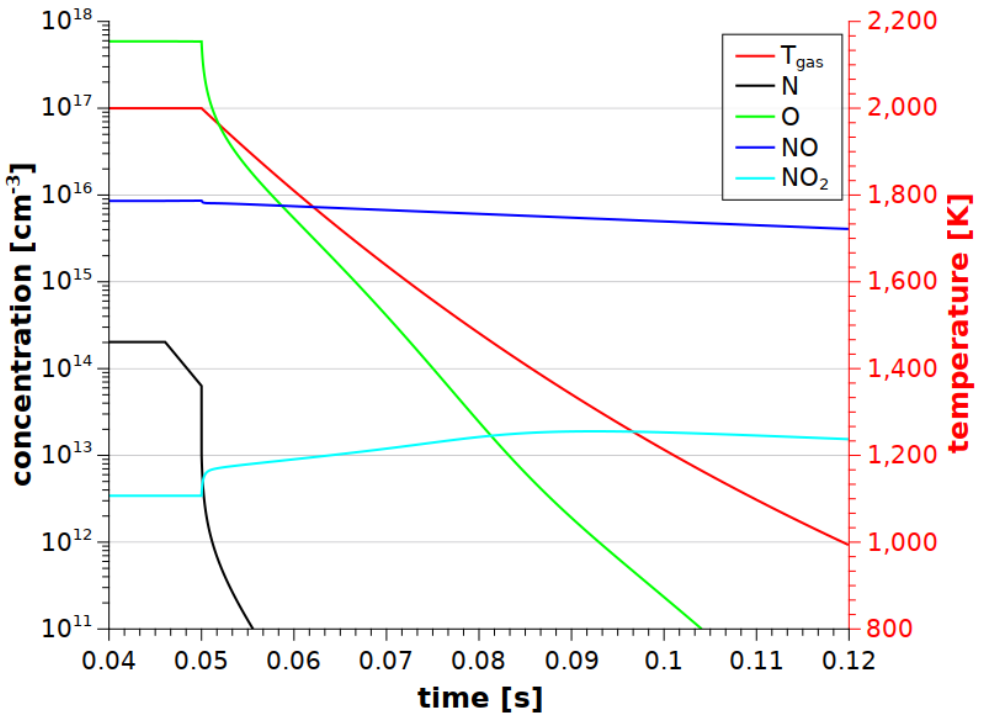

Fig. 8. Time evolution the gas temperature and N, O, NO and NO_2 species concentrations; calculated with α_{diff} = 10 s^{-1}.

A stable signal from ions directly generated by the HPGD was not detected by mass spectrometry. This can be attributed to two main factors. Firstly, the HPGD migrated on the surface of the orifice plate that served as anode, making its position relative to the spectrometer's gas entrance (a 100 µm orifice) highly variable. A stable ion signal could only be observed if the HPGD was positioned directly above this orifice, which occurred only randomly and occasionally. Secondly, even with the discharge positioned stably above the orifice, ion detection remains challenging. Positive ions are repelled from the anode, and the concentration of negative ions within the HPGD is relatively low, according to the kinetic model. The dominant negative ion, O^-, has a concentration of approximately 10^{10} cm^{-3}, two orders of magnitude lower than the electron concentration. This low negative ion concentration may be due to the elevated gas temperature in the HPGD plasma channel.

5. Conclusions

Fixation of nitrogen from the air, converting it into reactive compounds, remains a significant challenge and a hot topic within the low-temperature plasma community. High-pressure glow discharges offer a stable and efficient means to generate nitrogen oxides, key precursors for nitrogen fixation. This study investigates the mechanisms of nitrogen oxide generation in an HPGD using a combined approach of mass spectrometry and chemical kinetic modeling.

Mass spectrometry provided insights into the types of reactive oxygen and nitrogen species produced, while the kinetic model simulated the complex chemical reactions within the plasma. Our findings shed light on the dominant reaction pathways on nitrogen oxide formation. However, further research is crucial to refine our understanding. Future experimental work should focus on improving the detection and quantification of reactive species, particularly ions. Model enhancements are also necessary, including a more accurate representation of diffusion processes and the discharge afterglow phase. Furthermore, incorporating additional chemical reactions involving water molecules will enable us to explore the crucial role of humidity in the generation of nitrogen oxides, nitric acid, and nitrous acid. This comprehensive approach promises to advance our knowledge of nitrogen fixation using HPGD

and pave the way for the development of efficient and sustainable plasma-based technologies for fertilizer production and other applications.

Acknowledgement: Supported by the project of bilateral cooperation between Republic of Serbia and Republic of Slovakia 2024-2025 (project no. 337-00-3/2024-05/07 and APVV SK-SRB-23-0043); grant of the Ministry of Science, Technological Development and Innovations no. 451-03-68/2024-14/200024; and VEGA project No. 1/0596/22.

6. References

[1] Claude G 1913 *The Engineering Magazine* **115** 271–274.
[2] Machala Z, Laux C O and Kruger C H 2005 *IEEE Trans. Plasma Sci. - Special Issue on Plasma Images* **33** 320-321.
[3] Janda M, Hensel K, Machala Z and Field T A 2023 *J. Phys. D Appl. Phys.* **56** 485202
[4] Janda M, Machala Z, Morvová M, and Morva I 2008 *Orig. Life Evol. Biosph.* **38** 23-35
[5] Pai D Z 2021 *Journal of Physics D: Applied Physics* **54** 355201
[6] Rathore V, Tiwari B S and Nema S K 2021 Plasma Chem Plasma Process. **42** 109-129
[7] Chen Z, Xu R-G, Chen P and Wang Q 2020 *IEEE Trans. Plasma Sci.* **48** 3455–3471.
[8] Pancheshnyi S et al. 2008 Computer Code ZDPlasKin, Univ. Toulouse, Toulouse, LAPLACE, CNRS-UPS-INP, France. [Online]. Available: https://www.zdplaskin.laplace.univ-tlse.fr
[9] Brown P N, Byrne G D and Hindmarsh A C 1989 *SIAM J. Sci. Stat. Comput.* **10** 1038–1051
[10] kinet_N2_O2_v1.03 2015 [Online]. Available: http://www.zdplaskin.laplace.univ-tlse.fr/wp-content/uploads/2015/08/kinet_N2_O2_v1.03.inp
[11] Hagelaar G J M and Pitchford L C 2005 Plasma Sources Sci. Technol. **14** 722-733
[12] Pancheshnyi S et al. 2012 *Chem. Phys.* **398** 148–153.
[13] Machala Z et al. 2007 *J. Molec. Spectrosc.* **243** 194-201.

LOW ENERGY ELECTRONS INTERACTION WITH ACETONE $(CH_3)_2CO$ IN THE UV-VIS SPECTRAL REGION

G. D. Megersa[1], B. Stachová[1], E. L. Garcia Angulo[1], Š. Matejčík[1], B. Michalczuk[2], J. Országh[1]

[1]*Department of Experimental Physics, Faculty of Mathematics, Physics, and Informatics, Comenius University in Bratislava, Mlynská Dolina, 842 48 Bratislava*

[2]*Institute of Chemical Sciences, Faculty of Science, University of Siedlce, 3 Maja 54, 08-110 Siedlce, Poland*

Email: gadisa.deme@fmph.uniba.sk

Various studies have explored different aspects of electron-molecule interactions, which are fundamental processes in plasma chemistry, atmospheric reactions, astrophysics, and cometary science. Acetone occurs naturally in the human body, plants, and the atmosphere, and is also synthesized as a manufactured chemical used in cleaning products, paints, coatings, pharmaceuticals, and more [1]. Acetone is also an organic compound detected in extraterrestrial environments, including interstellar space, protoplanetary disks, and the surfaces of comets. For example, Douglas N. Friedel et al. (2005) reported the detection of interstellar acetone in the Orion-KL hot core, a high-mass star-forming region [2]. In 2017, a study on the evolution of cometary nuclei surfaces confirmed the presence of acetone and methanol through the sublimation of ice in the presence of organic volatiles [3]. The detection of significant abundances of acetone in various extra-terrestrial environments, such as comets, interstellar space, and planetary atmospheres, has significant implications for chemical processes, prebiotic chemistry, and astrobiology. Therefore, understanding the elementary processes and kinetics of electron-impact reactions on acetone is essential. In astronomy, the accurate description of emission spectra is particularly important, as most astronomical objects are primarily studied using emission spectroscopy.

Several studies have examined the fluorescence of acetone induced by various sources. The shape of the emission spectrum can reveal whether the emission is induced by electrons, photons, or other sources and provides insights into the excitation reaction energy. For example, Damon and Daniels [4] were the first to report fluorescence in acetone vapor when exposed to ultraviolet light from a mercury arc. T. Tran et al. investigated the fluorescence of acetone induced by a laser at pressures ranging from 1 to 15 atm [5]. However, only a few studies have explored the electron-impact spectrum of acetone. Our study focuses on the interaction of acetone molecules with low-energy electrons (10–100 eV) using emission spectroscopy in the UV-Vis spectral region. Electron-induced fluorescence (EIF) is a phenomenon that occurs during inelastic collisions of low-energy electrons with molecules based on a crossed electron and molecular beams method. At the Laboratory of Electron-Induced Fluorescence (LEIF) at Comenius University in Bratislava, optical emission spectra of acetone species under electron impact are currently being reported. The most prominent spectral features in the emission spectrum of acetone ($(CH_3)_2CO$) were measured in the wavelength range of 280 – 950 nm at 50 eV electron energy, including the hydrogen Balmer series lines Hα at 656.3 nm and H_β at 486 nm, the Swan system of C_2 ($d^3\Pi g–a^3\Pi u$) within 460–472 nm, and the CH ($A^2\Delta–X^2\Pi$) emission band observed in the range of 415–445 nm as shown in Fig. 1. These processes involve photon emission following electron-impact excitation and the subsequent de-excitation of excited particles. The emphasis is on spectral analysis and the determination of emission cross-sections. The primary objective of this work is to obtain data on the electron-induced fluorescence of acetone molecules in a crossed-beam experiment, which are key components in many extraterrestrial environments and may play a crucial role in astrophysics.

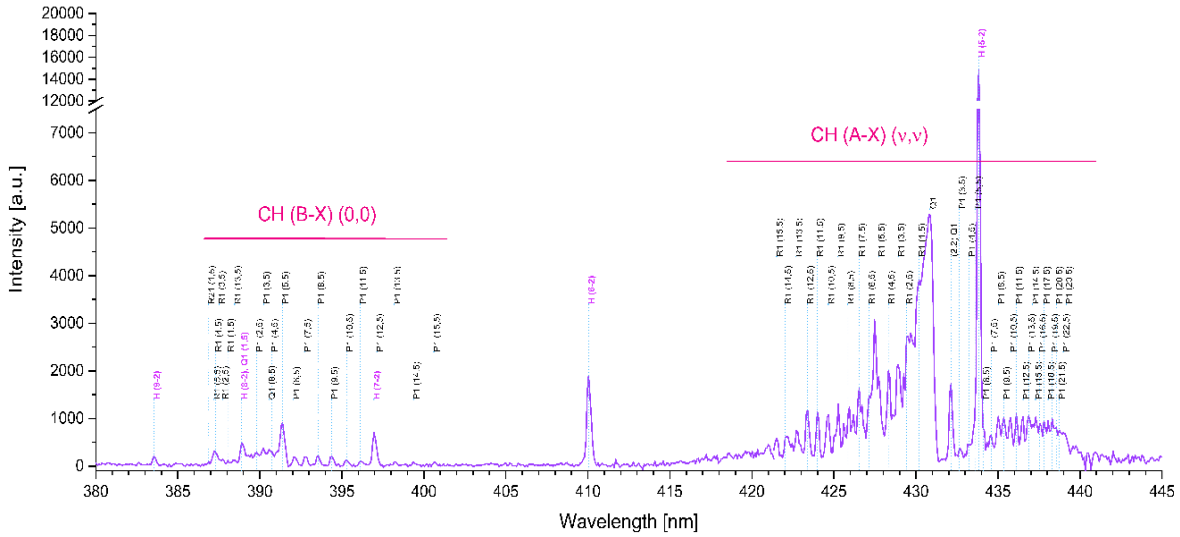

Fig. 1. The emission spectrum of $(CH_3)_2CO$ measured by CCD camera at 50 eV electron energy. All transitions were assigned according to the LIFBASE spectroscopic tool [6].

Acknowledgments

This work was supported by the Slovak Research and Development Agency under Contract no. SK-PL-23-0050, APVV-19-0386, and APVV-23-0522, Slovak grant agency VEGA under projects nr. 1/0489/21 and 1/0553/22. This project has received funding from the European Union's Horizon 2020 research and innovation programme under grant agreement No 871149. Funded by the EU Next Generation EU through the Recovery and Resilience Plan for Slovakia under the project No. 09I01-03-V04-00047. The work has been supported by the Polish National Agency for Academic Exchange. Grant Number: BPN/BSK/2021/1/00040/U/00001.

References

[1] M. P. Kalapos, "Acetone," in Encyclopedia of Toxicology: Third Edition, Elsevier, 2014, pp. 36–39. doi: 10.1016/B978-0-12-386454-3.00995-7.

[2] Friedel, Douglas N., L. E. Snyder, Anthony J. Remijan, and B. E. Turner. "Detection of interstellar acetone toward the Orion-KL hot core." The Astrophysical Journal 632, no. 2 (2005): L95.

[3] Kossacki, Konrad J., Jacek Leliwa-Kopystynski, Piotr Witek, Aleksander Jasiak, and Adrian Dubiel. "Sublimation of cometary ices in the presence of organic volatiles." Icarus 294 (2017): 227-233.

[4] Luckey, George W., A. B. F. Duncan, and W. Albert Noyes Jr. "The Fluorescence of Acetone Vapor1." The Journal of Chemical Physics 16, no. 4 (1948): 407-410.

[5] Tran, Thao, Yash Kochar, and Jerry Seitzman. "Measurement of Acetone Fluorescence and Phosphorescence at High Presssures and Temperatures." In 44th AIAA Aerospace Sciences Meeting and Exhibit, p. 831. 2006.

[6] J. Luque and D. R. Crosley, "Lifbase," Database and spectral simulation (version 2.1), vol. 99–009. SRI International Report MP.

WATER EMISSION INDUCED BY LOW-ENERGY ELECTRON IMPACT

Juraj Országh[1], Dennis Bodewits[2], Barbora Stachová[1], Štefan Matejčík[1]

[1]*Department of Experimental Physics, Comenius University in Bratislava, Slovakia*
[2]*Department of Physics, Auburn University, Alabama, USA*
E-mail: juraj.orszagh@uniba.sk

Electron induced excitation reactions of water were studied by means of optical emission spectroscopy in the spectral range between 200 nm and 800 nm in crossed beams experiment. Excited water cation H_2O^+, fragments OH, OH^+ and H and O were identified in the spectrum. For most intensive transition the cross sections and threshold energies were determined.

1. Introduction

Electron induced processes are abundant in various environments from space, planetary atmospheres through industry to laboratory. In astrophysics using the optical emission spectroscopic methods they can act as remote probe of physical properties of environments since every molecule or atom has a unique spectrum.

Analysis of the data from the Rosetta mission to comet 67P/Churyumov-Gerasimenko shown that the emission from the comet coma is induced mostly by electron impact outside the 2 AU pre-perihelion [1]. The emission fades if the comet is within 2 AU of the Sun. The effect can be caused by increased concentration of water in the coma leading to different energy distribution of electrons [2]. To assess such effect, it is necessary to thoroughly study the electron impact fluorescence of water including the cross sections in laboratory conditions as current data are incomplete or insufficient.

2. Experiment

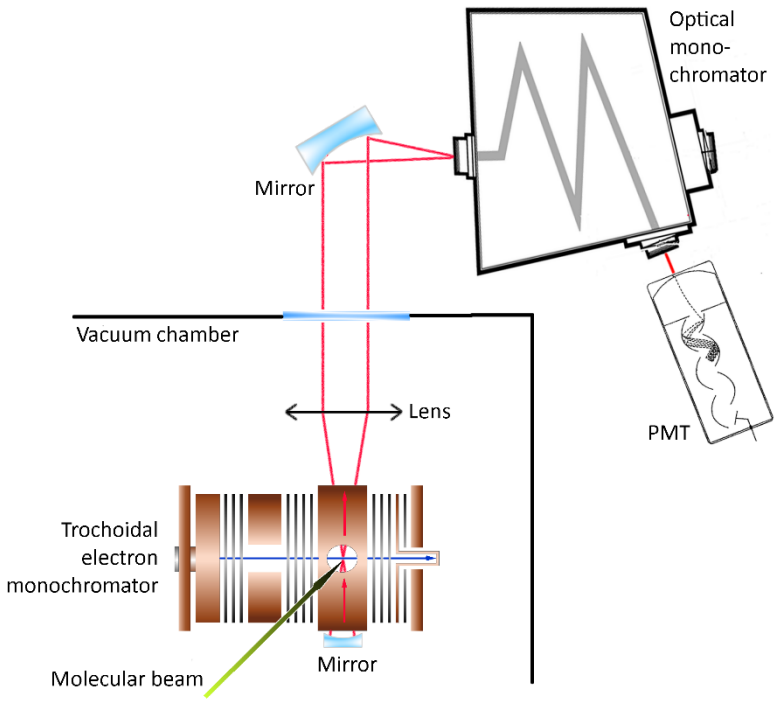

Fig. 1. Experimental apparatus

The apparatus used for the experiment was described in detail in previous publication [3] and is schematically depicted in figure 1. It utilized crossed beams configuration. The sources of electron (trochoidal electron monochromator) and molecular beams (effusive capillary) are in a vacuum

chamber with background pressure of ~ 10^{-8} mbar. The experiments were carried out at ~ $1.5x10^{-4}$ mbar. We have checked the linearity of the spectral line intensities on the pressure so that the single collision conditions were maintained [4]. The fluorescence radiation was collected by an optical system located perpendicularly to the crossing beams which focused the fluorescence signal onto the entrance slit of the Oriel Cornerstone 260 Czerny-Turner ¼ m optical monochromator. After passing through the optical monochromator, the signal was detected by a low-noise, Peltier-cooled photomultiplier working in the photon counting regime. The measurement was done in two modes: spectral measurement at constant electron energy or cross section measurement at specific wavelength corresponding to one deexcitation. The energy of the electron beam was absolutely calibrated by introducing a mixture of N_2 and H_2O into the apparatus and by measuring the intensity profile of the N_2 ($C^3\Pi_u$–$B^3\Pi_g$)(0–0) band at 337 nm which exhibits relatively sharp maximum at 14.1 eV [5] and intensity profile of H_β line. Subsequently the profile of H_β line was aligned with the same measurement in pure water vapours to calibrate the electron energy.

3. Results and discussion

The spectral region between 200 nm and 900 nm has been studied. The spectrum shown in the figure 2 is corrected for the spectral sensitivity of the experimental device. In the spectrum measured at electron energy 50eV the emission corresponding to deexcitation of atomic hydrogen (Balmer series), OH ($A^2\Sigma^+$-$X^2\Pi$), OH^+ ($A^3\Pi$-$X^3\Sigma^-$) and H_2O^+ ($\tilde{A}^2A_1$-X^2B_1) have been detected. The spectral bands corresponding to OH, OH^+ and H_2O^+ were identified according to the [6] and [7].

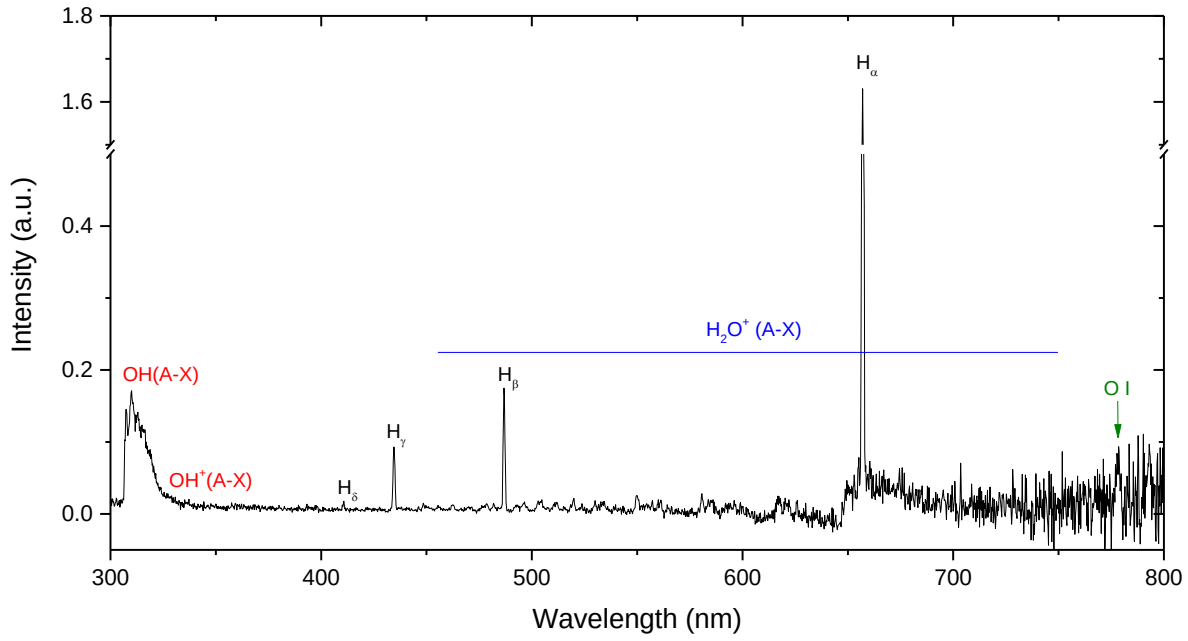

Fig. 2. Emission spectrum of water induced by 50 eV electrons impact.

In the spectral region above 800 nm no line nor band has been identified. One of the reasons can also be relatively low detector sensitivity. The O I ($3s^5S^0$ – $3p^5P$) at 777 nm line is very faint, almost hidden within the detector noise. The detail of the OH (A-X) transition is shown in the figure 3 including the region below 300 nm. All the detected water cation band correspond to the various vibrational transitions of H_2O^+ (A-X) and are present between 450 nm and 750 nm.

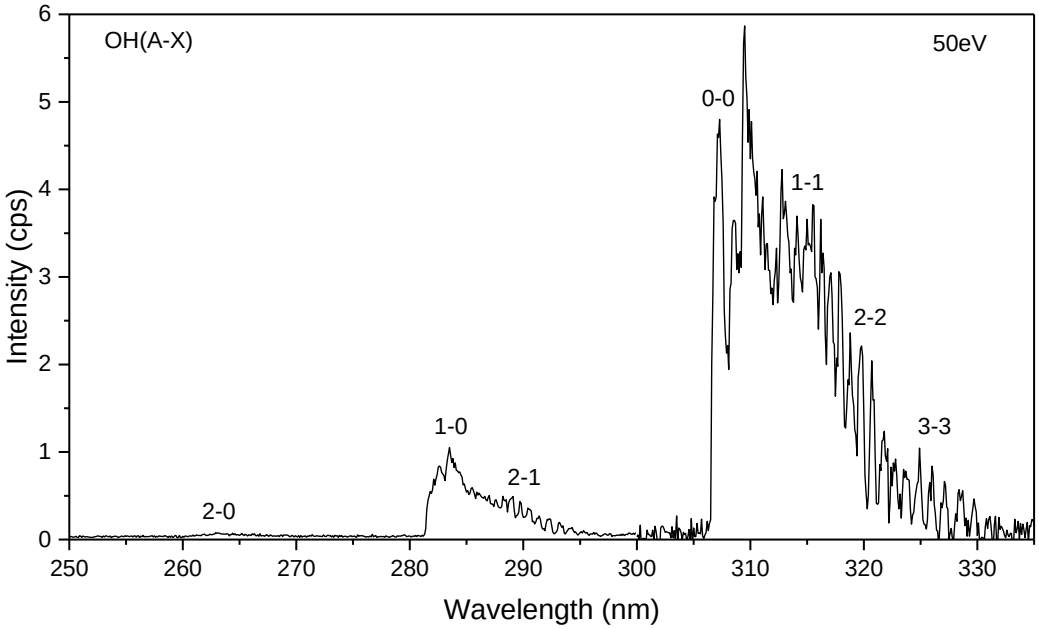

Fig. 3. Emission spectrum showing the detail of OH (A-X) transition measured at 50 eV electrons impact.

Apart from the spectral measurement the cross sections for the most intensive transitions were determined as well. The curves for Balmer's series were measured for transition H (3-2) to H (7-2). For each cross section the threshold energy was determined by simple fitting procedure. These values were compared to theoretical thresholds based on enthalpy of formation. The cross section curve for H (4-2) transition is shown in the figure 4.

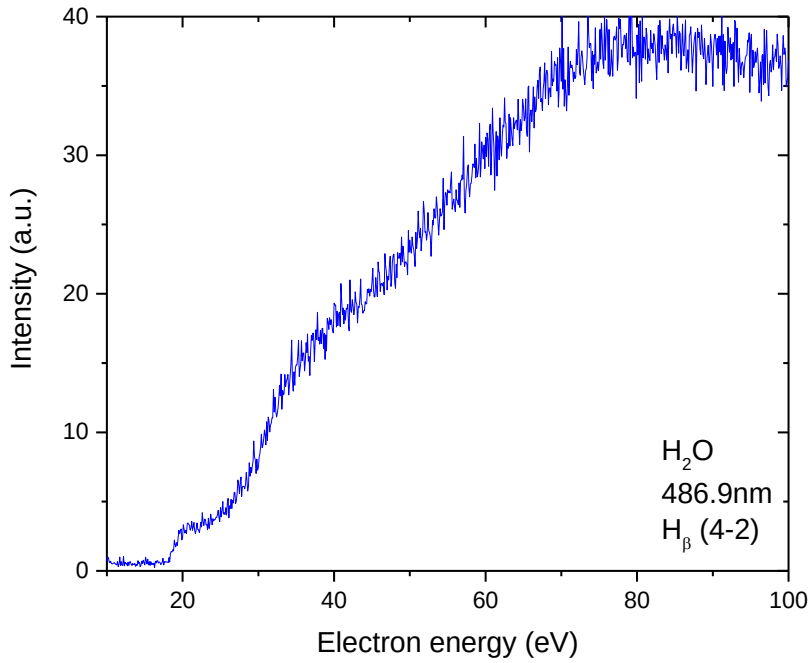

Fig. 4. Cross section curves of OH (A-X), OH+ (A-X), H2O+ (A-X) and H (4-2) transitions.

From the curve shape it is evident that there are three distinct thresholds. These correspond to different generation channels of excited hydrogen atoms in the electron-molecule reaction. Similar shape can be seen in case of other Balmer's series lines as well.

Acknowledgments

This work was supported by the Slovak Research and Development Agency under the Contracts no. SK-PL-23-0050 and APVV-23-0522. Funded by the EU NextGenerationEU through the Recovery and Resilience Plan for Slovakia under the project No. 09I01-03-V04-00047. JO would like to thank for support by the J. William Fulbright Commission for Educational Exchange in the Slovak Republic, within the Fulbright Visiting Scholar Program.

4. References

[1] Feldman P D et al. 2015 *Astronomy and Astrophysics* **583** A8.
[2] Bodewits D et al. 2016 *The Astronomical Journal* **152**, 130.
[3] Danko M et al. 2013 *Journal of Physics B: Atomic, Molecular and Optical Physics* **46** 045203.
[4] Filippelli A R et al. 1994 *Advances in Atomic, Molecular, and Optical Physics* **33** 1.
[5] Orszagh et al. 2012 *Nucl. Inst. Meth. B* **279** 76.
[6] Müller U et al. 1993 *Z. Phys. D* **25** 167.
[7] Tsuji M et al. 1988 *Chem. Phys. Lett.* **147** 6.

POTENTIAL ENERGY CURVES OF SPECTROSCOPICALLY RELEVANT EXCITED STATES OF CARBON MONOXIDE: A COMPUTATIONAL STUDY

Samuel Peter Kovár[1], Peter Papp[1]

[1]*Department of Experimental Physics, Faculty of Mathematics, Physics and Informatics, Comenius University in Bratislava, Mlynská dolina F2, 842 48 Bratislava*

E-mail: kovar23@uniba.sk

The aim of this work is to capture excited energy curves of carbon monoxide molecule using highly precise ab-initio method CASSCF. The main goal is providing set of data, consisting mainly of vertical transition energies, which can help interpreting absorption and fluorescence spectra of CO molecule, initiated with electron impact.

1. Introduction and experimental motivation

Precise knowledge of molecular potential energy surfaces (PES) is of crucial for any spectroscopic measurements as it enables identification of starting and final electronic state corresponding to excitation or deexcitation of studied molecule. Applications of spectroscopic measurements include, but are not limited to, determining presence, concentration, and reactions of carbon monoxide in astronomical objects as their distance from the Earth disqualifies most other diagnostic methods. Based on this motivation, electron-induced fluorescence (EIF) data were collected at Comenius University in Bratislava; however, these data lack a precise quantitative description of the excited states. Recent theoretical approaches dealing with dynamic and static correlations to HF can be employed to uncover the detailed information required for EIF.

2. Methodology presented in this work

Excited electronic states of CO were previously studied by Dora and Tennyson [1] using state averaged CASSCF(10,10). In this work we will examine alternative approach using SA-CASSCF(8,7) with starting orbitals obtained via natural bond orbital (NBO) analysis of MP2 [2] optimized wavefunction. Converged SA-CASSCF [3][4] wavefunctions are afterwards treated with NEVPT2 [5][6]. Final single point energies will be presented consisting of CASSCF energy extrapolated to complete basis set (CBS) and NEVPT2 correction at aug-cc-pV5Z level. All calculations are performed using ORCA 5.0.4 [7] quantum chemistry package and NBO7 [8] program.

Although smaller active space of CASSCF implies meaningful description of limited number of excited states, this approach proved advantageous in several ways. Firstly, we were able to obtain PES for wide range of interatomic distances from 0.85 Å up to 3.00 Å, equally for the ground and first 11 excited states, giving the possibility to uncover the repulsive states from the stable PES. Additionally, due to the nature of state averaged calculation, crossings of electronic states with same irreducible representation and spin multiplicity lead to sharp steps in the potential energy curves. Since these crossing appear primarily at higher energies, we were able to avoid most of them, thus obtaining smooth energy curves. Finally, reduced computational cost made perturbation treatment possible allowing us to capture part of dynamical correlation energy as well.

For extrapolation technique we considered CBS limit of to be given by expression [9]:

$$E_{\infty}^{tot} = E_{\infty}^{CAS} + E_{\infty}^{dc} \quad (1)$$

This split of total extrapolated single point energy E_{∞}^{tot} into CAS component E_{∞}^{CAS} which captures Hartree-Fock energy and non-dynamical correlation and E_{∞}^{dc} component which corresponds to dynamical correlation is necessary due to different rates at which these components converge with respect to the cardinal number of basis set [9]. For E_{∞}^{CAS} we chose 3-point extrapolation scheme [10] :

$$E_X^{CAS} = E_{\infty}^{CAS} + Aexp(-\beta x) \quad (2)$$

Where X is hierarchical number approximately equal to the cardinality of basis set [11], A and β are parameters to be fitted. Correction scheme specifically proposed for dynamical correlation [11] exists,

however it contains method specific parameters, which are not available for NEVPT2, thus dynamical part of correlation was not extrapolated.
While our results are generally in good agreement with findings of Dora and Tennyson [1], we were unable to replicate some of qualitative properties of lower lying excited electronic states - most notably B 1Σ+ and avoided crossing of two 3Σ+ states. These differences are likely due to the choice of smaller active space in our work.

3. Acknowledgements

This work was supported by the Slovak Research and Development Agency under the Contract no. APVV-22-0522 and the Slovak Grant Agency for Science (contract no. VEGA 1/0553/22). This work was supported in part through the Comenius University in Bratislava CLARA@UNIBA.SK high-performance computing facilities, services and staff expertise of Centre for Information Technology (https://uniba.sk/en/HPC-Clara). SPK would like to acknowledge the Comenius University in Bratislava for the extraordinary scholarship awarded to master student to support these studies and the presentation of results at international conference.

4. References

[1] A. Dora and J. Tennyson, "Electron collisions with CO molecule: Potential energy curves of higher lying CO-resonant states," *Journal of Physics B: Atomic, Molecular and Optical Physics*, vol. 53, no. 19, 2020, doi: 10.1088/1361-6455/aba5b0.

[2] M. J. Frisch, M. Head-Gordon, and J. A. Pople, "A direct MP2 gradient method," *Chem Phys Lett*, vol. 166, no. 3, 1990, doi: 10.1016/0009-2614(90)80029-D.

[3] R. H. A. Eade and M. A. Robb, "Direct minimization in MC SCF theory. The quasi-newton method," *Chem Phys Lett*, vol. 83, no. 2, 1981, doi: 10.1016/0009-2614(81)85480-2.

[4] C. Kollmar, K. Sivalingam, B. Helmich-Paris, C. Angeli, and F. Neese, "A perturbation-based super-CI approach for the orbital optimization of a CASSCF wave function," *J Comput Chem*, vol. 40, no. 14, 2019, doi: 10.1002/jcc.25801.

[5] Y. Guo, K. Sivalingam, and F. Neese, "Approximations of density matrices in N-electron valence state second-order perturbation theory (NEVPT2). I. Revisiting the NEVPT2 construction," *Journal of Chemical Physics*, vol. 154, no. 21, 2021, doi: 10.1063/5.0051211.

[6] C. Kollmar, K. Sivalingam, Y. Guo, and F. Neese, "An efficient implementation of the NEVPT2 and CASPT2 methods avoiding higher-order density matrices," *Journal of Chemical Physics*, vol. 155, no. 23, 2021, doi: 10.1063/5.0072129.

[7] F. Neese, F. Wennmohs, U. Becker, and C. Riplinger, "The ORCA quantum chemistry program package," *Journal of Chemical Physics*, vol. 152, no. 22, 2020, doi: 10.1063/5.0004608.

[8] E. D. Glendening *et al.*, "NBO 7.0. ," 2018, *Theoretical Chemistry Institute, University of Wisconsin, Madison*: 7.0.

[9] A. J. C. Varandas, "Extrapolating to the one-electron basis-set limit in electronic structure calculations," *Journal of Chemical Physics*, vol. 126, no. 24, 2007, doi: 10.1063/1.2741259.

[10] D. Feller, "The use of systematic sequences of wave functions for estimating the complete basis set, full configuration interaction limit in water," *J Chem Phys*, vol. 98, no. 9, 1993, doi: 10.1063/1.464749.

[11] F. N. N. Pansini, A. C. Neto, and A. J. C. Varandas, "Extrapolation of Hartree–Fock and multiconfiguration self-consistent-field energies to the complete basis set limit," *Theor Chem Acc*, vol. 135, no. 12, 2016, doi: 10.1007/s00214-016-2016-4.

KINETICS OF OZONE PRODUCTION BY SURFACE PROCESSES

Vera Mazankova[1], David Trunec[2]

[1]*Department of Mathematics and Physics, Faculty of Military Technology, University of Defence, Kounicova 65, 662 10 Brno, Czech Republic*

[2]*Department of Plasma Physics and Technology, Faculty of Science, Masaryk University, Kotlarska 2, 611 37 Brno, Czech Republic*

E-mail: vera.mazankova@unob.cz

This contribution is dedicated to address the gap in knowledge regarding the determination of ozone production rates on silica surfaces, which are commonly encountered in both laboratory and industrial plasma systems. By investigating the interactions between plasma species and silica surfaces, this study aims to provide a better understanding of the mechanisms underlying ozone production, with a focus on surface-bound reactions. This research not only helps to clarify the fundamental processes of plasma-surface interaction but also holds potential for improving the efficiency and control of ozone generation in practical applications.

1. Introduction and theory

Plasma-surface interactions play a crucial role in a wide range of discharge phenomena and are particularly significant in the processes of ozone formation and destruction. These interactions are especially important in the afterglow phase of a direct current (DC) low-pressure discharge in pure oxygen (O_2) [1], as well as in dielectric barrier discharges (DBDs) at atmospheric pressure [2]. Despite their importance, the rates or probabilities associated with these surface reactions remain largely unknown or poorly understood, which limits the ability to accurately model and control these processes. Understanding of these rates is critical for optimizing various applications, such as ozone generation and environmental plasma-based technologies.

When a solid surface comes into contact with an oxygen discharge or ozone, the surface rapidly becomes coated with adsorbed atomic oxygen (O) species, as well as molecular oxygen (O_2) species. These adsorbed species play a key role in subsequent surface reactions, particularly in the formation of ozone (O_3). Ozone generation at the surface can occur through two primary reaction mechanisms: the Langmuir-Hinshelwood (LH) mechanism and the Eley-Rideal (ER) mechanism. The LH mechanism is described by reaction

$$O_{2S} + O_S \rightarrow O_3 + 2S, \quad (1)$$

where O_S and O_{2S} are adsorbed oxygen atoms and molecules, respectively, S is the vacant site. The ER mechanism is described by reaction

$$O_2 + O_S \rightarrow O_3 + S, \quad (2)$$

where O_2 is molecule arriving at the surface from gas phase.

In the LH mechanism, both reactants O_S and O_{2S} are adsorbed onto the solid surface before reacting to form ozone. The reaction proceeds via a two-step process: First, atomic oxygen interacts with molecular oxygen adsorbed on the surface, creating an unstable O_3* intermediate, which then desorbs as ozone from the surface. This mechanism relies on the surface's ability to adsorb and activate the reactant species, allowing them to collide and react in close proximity to the surface. The efficiency of the LH mechanism is heavily influenced by the nature of the surface, the surface coverage of the reactants, and the temperature, as these factors affect the availability and reactivity of the adsorbed species.

In contrast, the ER mechanism involves one of the reactants being adsorbed on the surface, while the other remains in the gas phase. Specifically, an adsorbed atomic oxygen species (O_S) reacts with a gas-phase molecule of O_2, leading to the formation of ozone. This reaction mechanism does not

require both reactants to be adsorbed simultaneously on the surface. The ER mechanism typically occurs when one of the reactants (such as O) is in a highly reactive state, allowing it to react with gas-phase molecules that impinge on the surface.
Both mechanisms are essential for understanding the formation of ozone on solid surfaces, particularly in low-pressure oxygen discharges or when ozone is present in the system. The relative importance of the LH and ER mechanisms depends on factors such as the surface properties, temperature, pressure, and the specific conditions of the discharge. By examining these surface reaction pathways, it is possible to gain deeper insights into the conditions that maximize ozone production and better control the outcomes of plasma-based processes.

2. Experimental

Surface processes were studied in the experimental set-up shown in Fig.1.

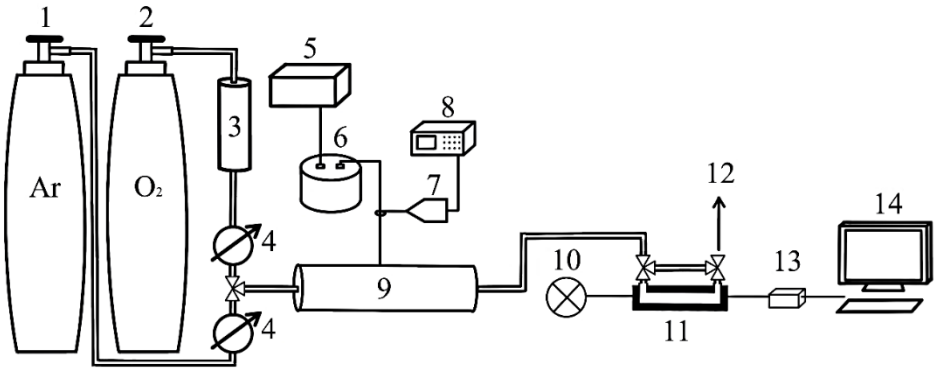

Fig. 1. – argon bottle, 2 – oxygen bottle, 3 – zeolites, 4 – mass flow controllers, 5 – high voltage generator, 6 – transformer, 7 – high voltage probe, 8 – oscilloscope, 9 – ozonizer, 10 – light source, 11 – measuring cuvette, 12 – gas outlet, 13 – spectrometer, 14 – PC.

The inner surface of the cuvette was exposed to ozone for a period of 5 minutes, allowing for thorough interaction between the surface and the ozone species. Following this treatment, the ozone was evacuated from the cuvette, and the chamber was subsequently filled with a mixture of oxygen (O_2) and argon (Ar) in varying ratios. This controlled gas mixture created a specific environment for studying the subsequent surface reactions. To monitor the time-dependent formation of products resulting from these surface interactions, absorption spectroscopy was employed. This technique enabled precise measurement of the concentration of the species formed by surface reactions over time. By carefully analyzing the absorption spectra, the dynamics of the surface reactions, as well as the influence of the gas mixture composition and exposure conditions, could be investigated in detail. The data obtained from these measurements provide valuable insights into the kinetics of the surface processes and the factors that govern the formation of reactive oxygen species under varying conditions.

3. Results and discussion

The results are shown in Fig. 2. For short reaction time the ozone concentration increases linearly, when the ozone concentration increases above $2 \cdot 10^{14}$ cm^{-3} also the destruction processes of ozone occur. When the cuvette is filled by argon only, the ozone originated by LH processes only. If the oxygen is added to the argon, the ozone is created also by ER mechanism and the increase of ozone concentration is faster and the final ozone concentration is also higher, see Fig. 2. The ozone concentration produced by LH mechanism is described by equation

$$n(O_3) = \frac{2}{R} \cdot \frac{n_0^2(O_S) \cdot k \cdot t}{1 + n_0(O_S) \cdot k \cdot t} \quad , \tag{3}$$

where R is the cuvette radius, $n_0(O_S)$ is the initial surface concentration of adsorbed O atoms, k is the rate coefficient and t is the time. For short times this equation (3) reduces to

$$n(O_3) = \frac{2}{R} \cdot n_0^2(O_S) \cdot k \cdot t \,. \quad (4)$$

So, the initial slope of time dependence of ozone concentration is $a = \frac{2}{R} \cdot n_0^2(O_S) \cdot k$. The slopes are shown in Fig. 3.

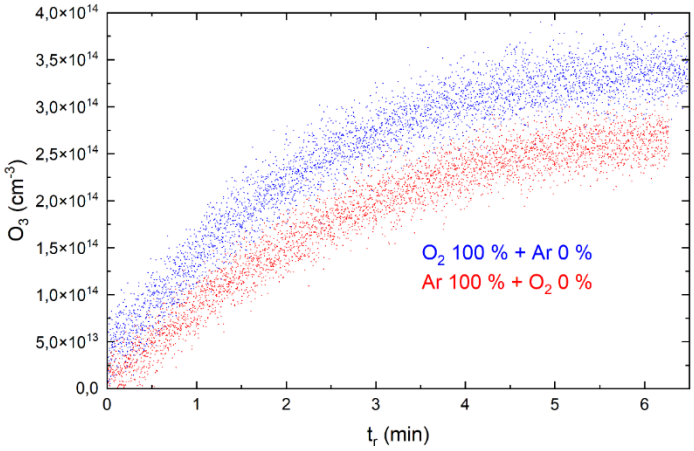

Fig. 2. The dependence of ozone concentration on reaction time.

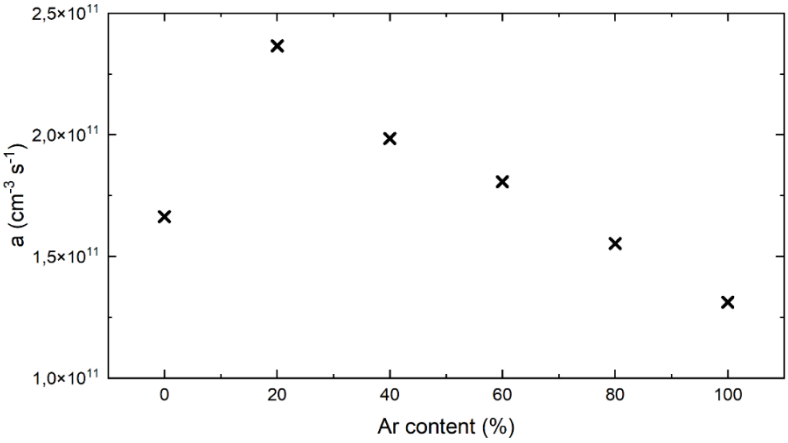

Fig. 3. The dependence of the initial slope on argon content in the mixture.

We assumed that the surface concentration of active sites is 10^{16} cm^{-2} and one half of these sites is occupied by atomic oxygen and second half is occupied by molecule oxygen. Under this assumption the rate coefficient derived from these slopes is 1.56 $\cdot 10^{-20}$ cm^{-2}s^{-1} for LH mechanism and for ER mechanism is 1.0 $\cdot 10^{-28}$ cm^{-2}s^{-1}.

4. References

[1] Booth J P et al 2023 *Plasma Sources Sci. Technol.* **32** 095016.
[2] Meyer M, Foster J and Kushner M J 2023 *Plasma Sources Sci. Technol.* **32** 085001.

Acknowledgement
This research work was supported by the Project for the Development of the Organization "DZRO Military autonomous and robotic systems" under Ministry of Defence and Armed Forces of Czech Republic.

EFFECTS OF PLASMA-BASED DISINFECTION METHODS ON THE SURFACE INTEGRITY OF TEFLON

Naomi Northage[1,2], Stéphane Simon[1], Vasyl Shvalya[2], Martina Modic[2], Thorsten Juergens[3], Sascha Eschborn[3], Malcolm J. Horsburgh[4], James L. Walsh[2,5]

[1]*Centre for Plasma Microbiology, Department of Electrical Engineering and Electronics, University of Liverpool, Liverpool, L69 3GJ, UK*

[2] *Laboratory for Gaseous Electronics, Jožef Stefan Institute, Ljubljana 1000, Slovenia*

[3]*R&D Endoscopy Reprocessing Systems, Olympus Surgical Technologies Europe, Olympus Winter & Ibe GmbH, Kuehnstraße 61, 22045 Hamburg, Germany*

[4]*Infection Biology & Microbiomes, Institute of Infection, Veterinary and Ecological Sciences, University of Liverpool, Liverpool, L69 7BE, UK*

[5]*York Plasma Institute, School of Physics, Engineering & technology, University of York, York, YO10 5DQ, UK*

E-mail: naomi.northage@ijs.si

This study evaluates the impact of cold atmospheric pressure plasma disinfection methods on Teflon endoscopic test pieces. Plasma-based methods, including PAD, showed superior antibiofilm efficacy, achieving a 7.30 log reduction in biofilms within 5 minutes. Minimal changes to surface composition and morphology were observed, indicating that plasma methods are effective without compromising Teflon's structural integrity.

1. Introduction

The narrow lumens within flexible endoscopes provide an ideal environment for biofilm formation, leading to the potential for cross-contamination and infection transmission. Current disinfection methods, such as the use of peracetic acid, are often inadequate in removing biofilms and their long-term use may cause damage to the delicate materials of endoscopic devices [1]. Cold atmospheric pressure plasma (CAP) and plasma activated liquids (PALs) have emerged as promising alternatives for high-level disinfection, showing significant antimicrobial potential [2], [3]. This study investigates the effects of CAP and PALs on the surface integrity of Teflon, a common material used in the inner channels of flexible endoscopes, and compares their efficacy against a commercially available peracetic acid-based disinfection method.

2. Experimental Setup

A flow system was developed to contaminate endoscopic test pieces with mixed-species biofilm using four clinically relevant bacterial species, through repeated cycles of cultivation and rinsing. A low-temperature surface barrier discharge (SBD) device was designed to generate four plasma-based disinfection methods: gas plasma (GAS), plasma-activated water (PAW), a combination of GAS + PAW, and plasma-activated disinfectant (PAD). The contaminated test pieces were exposed to each disinfection method for 5 minutes, and antibiofilm activity was compared to a commercially available peracetic acid-based disinfectant. To assess potential surface damage from the disinfection process, surface composition and morphology were analysed using X-ray photoelectron spectroscopy (XPS), Fourier transform infrared spectroscopy (FTIR), and atomic force microscopy (AFM).

3. Results

All four plasma-based disinfection methods had minimal effects on the surface composition and roughness of the Teflon endoscopic test pieces, as evidenced by XPS and AFM analyses. XPS results showed minor changes in the surface chemistry, with slight increases in C-F_2 peaks and minor decreases in C-F and C-F_3 peaks across all plasma treatments, suggesting that the surface underwent

only minor chemical modifications (Fig 1). Oxygen and fluorine peaks confirmed that plasma treatment did not lead to significant surface functionalization, with only minor increases in oxygen content observed in treated samples. AFM analysis revealed minimal changes in surface roughness, with no significant difference between the control and plasma-treated test pieces. Minor surface changes were found, but no greater than those seen for peracetic acid. These findings were supported by ATR-FTIR spectra, which showed no observable changes in the chemical structure after plasma treatments.

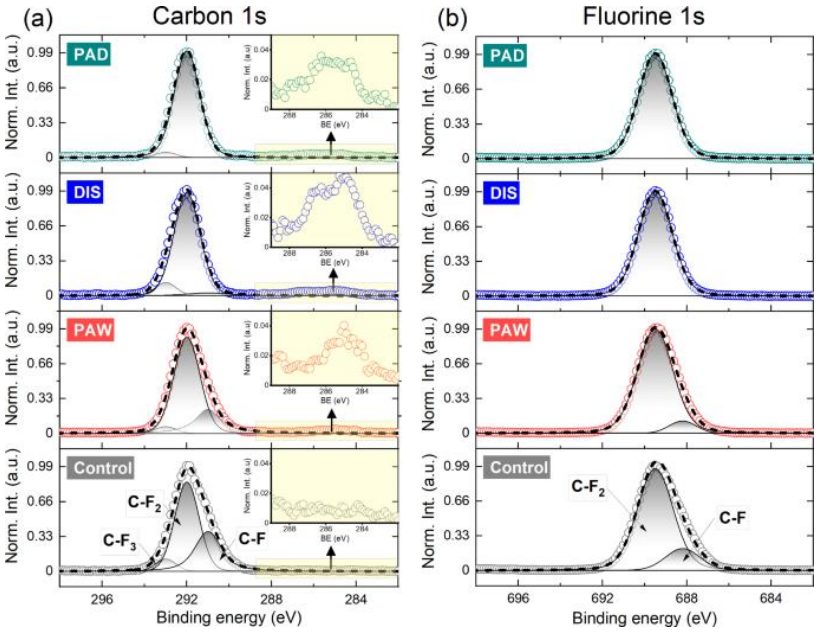

Fig 1. XPS analysis of the chemical composition of the Teflon endoscopic test pieces. Data presented shows high-resolution XPS spectra for carbon 1s (**a**) and fluorine 1s (**b**) with corresponding peak fittings.

4. Conclusion

This study demonstrates that plasma-based methods are effective in disinfecting endoscopic test pieces without causing significant damage to the surface composition or roughness of Teflon materials. The minimal chemical and morphological changes observed with plasma treatments were comparable to those induced by peracetic acid, indicating that CAP and PALs can serve as viable alternatives for disinfection without compromising the integrity of sensitive medical devices. Further investigation into the long-term effects and potential for routine use of CAP and PALs in endoscope reprocessing is warranted.

5. References

[1] G Kampf 2014 *World J Gastrointest Endosc* 6 390.
[2] N O'Connor, O Cahill, S Daniels, S Galvin and H Humphreys 2014 *Journal of Hospital Infection* 88 59–65.
[3] R C Hervé, M G Kong, S Bhatt, H-L Chen, E E Comoy, J-P Deslys, T J Secker, and C W Keevil 2023 *Journal of Hospital Infection* 136 100–109.

COMPARATIVE STUDY OF PLASMA TREATMENT OF PEA SEEDS WITH DIFFERENT GERMINATION USING TWO PLASMA SOURCES

Anna Zahoranová[1], Sandra Ďurčányová[1], Petra Šrámková[1], Renáta Švubová[2], Monika Bathóová[2], Dominik Kostoláni[2], Stanislav Kyzek[3], Eliška Gálová[3], Dušan Kováčik[1]

[1] *Department of Experimental Physics, Faculty of Mathematics, Physics and Informatics, Comenius University Bratislava, Mlynská dolina, 842 48 Bratislava, Slovakia*

[2] *Department of Plant Physiology, Faculty of Natural Sciences, Comenius University Bratislava, Mlynská dolina, Ilkovičova 6, 842 15 Bratislava, Slovakia*

[3] *Department of Genetics, Faculty of Natural Sciences, Comenius University Bratislava, Mlynská dolina, Ilkovičova 6, 842 15 Bratislava, Slovakia*

E-mail: sandra.durcanyova@fmph.uniba.sk

In our comparative study, we evaluated the effect of cold atmospheric pressure plasma (CAPP), generated in ambient air at atmospheric pressure, on the germination and growth parameters of pea seeds. Pea seeds (*Pisum sativum* L. var. Saxon) with natural germination of 90% and reduced germination of 50% were used. The CAP plasma was generated using a DCSBD plasma source and, for comparison, a prototype reactor with two DCSBD-plasma panels placed inside the chamber. To assess the effect of plasma at different treatment times (10, 20, 30 seconds) with both plasma sources, we determined several physiological germination parameters: imbibition rate, percentage of germination, germination index, seed and seedling vitality index, and seedling length index. Additionally, the impact of plasma treatment on DNA damage in pea seedlings was evaluated. Plasma-induced surface modifications were studied using surface diagnostic techniques such as water contact angle measurement to determine wettability, ATR-FTIR spectroscopy and XPS to assess potential changes in chemical composition and surface bonding.

1. Introduction

Agriculture is currently facing new challenges due to increasing demand for staple food production in the context of worsening climate change, drought, and shrinking areas of quality land. Maintaining the production of basic agricultural crops requires new approaches, preferably with limited/without the use of harmful chemicals [1]. As confirmed by the results of extensive research, the use of cold atmospheric pressure plasma (CAPP) in seed surface treatment leads to several positive changes in seed germination, growth parameters and, in addition, leads to the reduction of unwanted pathogens on the surface of seeds [2,3]. CAPP treatment of seeds for practical applications in agriculture has recently become the subject of significant research efforts. The advantage of CAPP is its low-temperature character, which enables the treatment of heat-sensitive biological material, minimizes the use of chemicals, and does not require vacuum equipment but uses ambient air as the working gas [4]. For the successful application of plasma technologies directly in companies involved in the production of seeds, it is necessary to develop equipment capable of treating larger amounts of seeds in a continuous production line. In our study, we compared the plasma treatment of seeds using the so-called diffuse coplanar surface barrier discharge (DCSBD) in standard laboratory configuration and a prototype with 2 DCSBD-plasma panels, which can treat larger quantities of seeds at once.

2. Experiment

The plasma treatment in our experiments was carried out using two plasma devices (Fig.1):

a) the reactor, where the DCSBD [5] plasma panel was placed on a laboratory orbital shaker to achieve the homogeneous movement of the seeds (the rotating speed was 330 rpm). The electrodes were powered by high voltage (peak-to-peak 20 kV) with a frequency of ~15 kHz (HV generator VF 700, Lifetech s.r.o., CZ) and isolated and cooled by a dielectric oil flowing system, and

b) the prototype reactor with 2 DCSBD-plasma panels (PP) placed inside the chamber with a mechanical device for turning the seeds, cooling oil circuit and HV power supplies similarly with the same value of high voltage (peak-to-peak 20 kV), as well as of the frequency (~15 kHz).

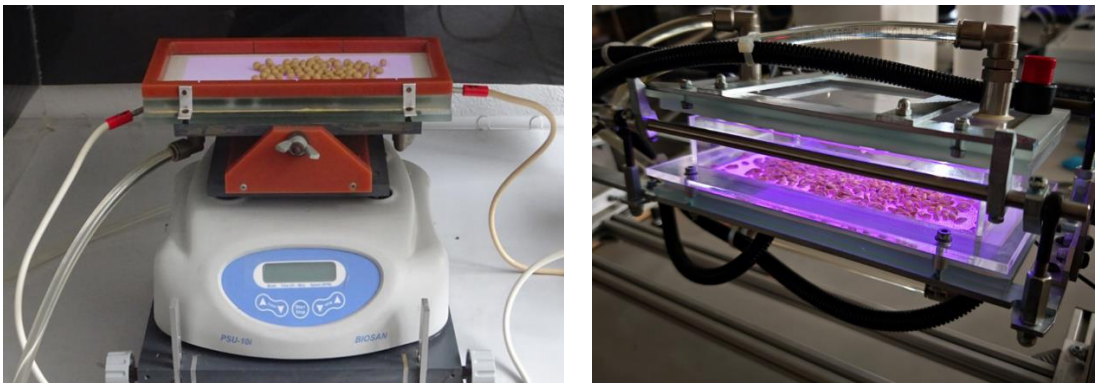

Fig. 1. Plasma sources used in plasma treatment of pea seeds, DCSBD plasma source (left), prototype reactor with 2 DCSBD-plasma panels (right).

Dried pea seeds (*Pisum sativum* L.) var. Saxon obtained from the Central Control and Testing Institute in Agriculture in Bratislava, Slovakia with naturally good germination (90%) and reduced germination (50%) were used in this study as biological material for the plasma treatment. The plasma treatment of the seeds (untreated control and plasma-treated variants, 30 seeds for each variant in four repetitions) was performed at an input power of 400 W, and plasma treatment times were 5, 10, 20 and 30 s (eventually also 60 s for hydrophilicity changes assessment of the seeds).

3. Experimental Results

Surface diagnostics – WCA

Changes in water contact angle values (Fig.2) indicate changes in surface energy of seeds after plasma treatment. Increased hydrophilicity helps better water uptake, which is a prerequisite for starting the germination process. The comparison of the two different DCSBD configurations showed that the homogeneity of the treatment at the low plasma exposure times (5 s) was lower in the case of the prototype reactor due to insufficient mixing of the seeds.

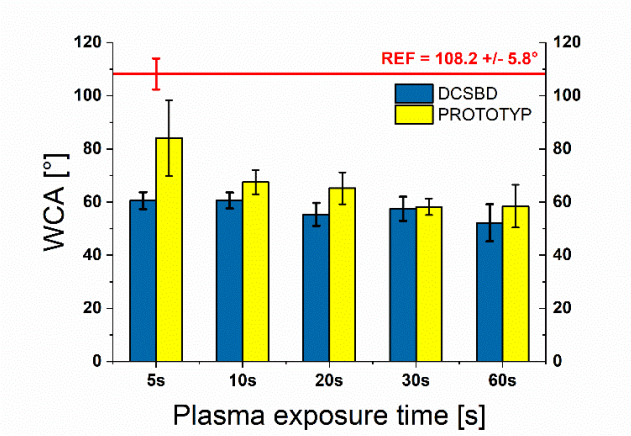

Fig. 2. Water Contact Angle changes for reference (REF =108.2° ± 5.8°) and plasma treated (using PP-prototype reactor and DCSBD plasma source) pea seeds with 90% germination for treatment times of 5, 10, 20, 30, 60 s.

Imbibition, Germination and Growth Parameters of pea seeds

Dry pea seeds (30 seeds for each variant) were weighed on an analytical scale and soaked in sterile distilled water for 1 h at room temperature. The imbibed seeds were blotted dry, weighed again and wrapped in moist sterile filter paper. The rolls were cultivated in a dark room in an incubator at the temperature of 24 ± 2 °C for 5 days. The number of germinated seeds was counted during the cultivation. After 5 days, the length and weight of shoots and roots of young seedlings were measured. This data was used to calculate the imbibition rate and many growth parameters (Percentage of Germination (%), Germination Potential (%), Germination Index, Seeds Vitality Index, Seedlings Vitality Index and Seedlings Length Index).

The imbibition rate is the amount of water uptake measured after 1 hour after plasma treatment. As illustrated (Fig. 3), plasma treatment increased the amount of water, the value of which also varies depending on the germination of seeds, poorly germinating seeds (50%) absorbed an increased amount of water. However, the differences between DCSBD and the PP-prototype in the water uptake were not observed.

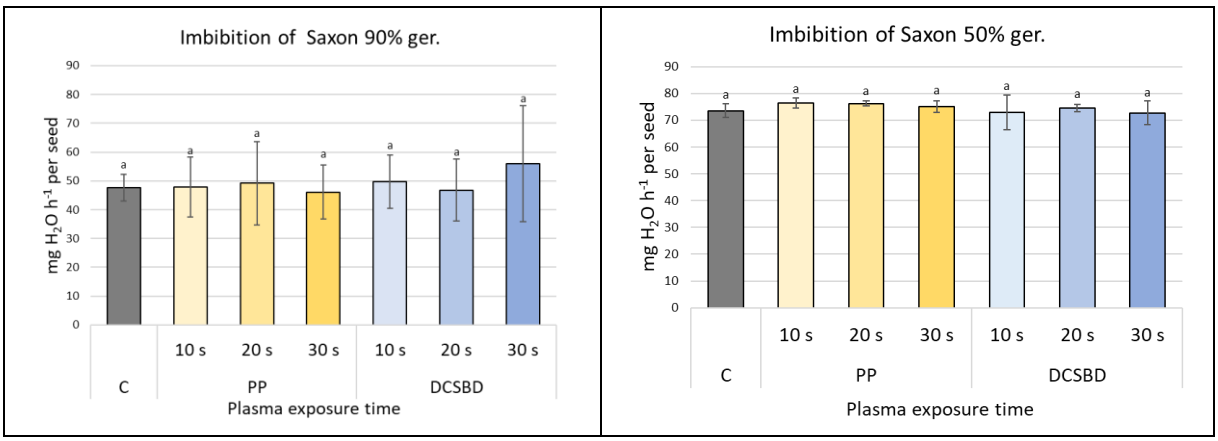

Fig. 3. Changes in water uptake (in mg on 1 seed) for reference (C) and plasma treated (using PP-prototype reactor and DCSBD plasma source) pea seeds with 90% and 50% germination for treatment times of 10, 20, 30 s.

One of the monitored growth parameters was the Seed Vitality Index. As can be observed from these results (Fig. 4), even relatively low plasma exposure times significantly improve growth parameters. Even in the case of low germination (50%), plasma exposure can significantly improve growth values and, in this case, surprisingly, the best improvement occurs at the shortest plasma exposure time (10 s).

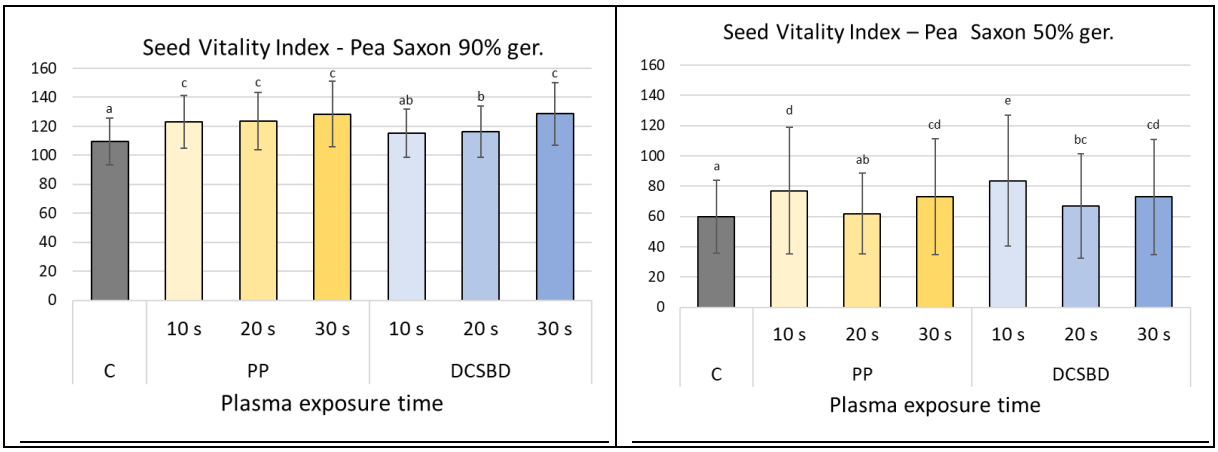

Fig.4. Changes in Seeds Vitality index for reference (C) and plasma treated (using PP- prototype reactor and DCSBD plasma source) pea seeds with 90% and 50% germination for treatment times of 10, 20,

30 s, (Seed Vitality index (%) = ((length of roots of 5-day-old seedlings + length of shoots of 5-day-old seedlings) x Percentage of germination)/100).

DNA damage

The alkaline comet assay tests (single cell alkaline gel electrophoresis) on pea seedlings after plasma treatment were performed to determine the level of DNA damage compared to reference samples [6]. The results varied with respect to the germination of the pea seeds. At 90% germination, the level of DNA damage was slightly higher than the reference sample in the case of DCSBD plasma treatment, but DNA damage was lower in the case of using the prototype reactor with 2 DCSBD-plasma panels. For samples with 50% germination, DNA damage varied approximately at the reference level.

4. Conclusions

We compared the effect of plasma generated by two plasma sources (DSCBD and a prototype reactor with 2 DCSBD-plasma panels) on several parameters of pea seeds with high (90%) and reduced (50%) germination rates. Based on the results, we conclude that the plasma reactor constructed using DCSBD technology is also suitable for in-line processing of plant seeds and grains under atmospheric pressure of ambient air. Due to the high surface and volume density of the plasma, extremely short treatment times in the order of seconds are sufficient. Both plasma configurations proved to be comparably effective in improving growth parameters. Furthermore, we observed that even when the natural germination of the seeds was high, plasma treatment led to an increase in the growth parameters of the seedlings (shoot length and weight, as well as root length). Monitoring the degree of DNA damage in plasma-treated seedlings revealed slight differences depending on the initial germination rate of the seeds. When peas with 90% germination were treated, the level of DNA damage was lower when using the prototype reactor.

Acknowledgment: This work was supported by the Slovak Research and Development Agency under the contract No. APVV-21-0147.

5. References

[1] Arora NK 2019 *Environ Sustain* **2** 95–96
[2] Waskow A, Howling A, Furno I 2021 *Front. Phys.* **9** 1–23
[3] Randeniya LK, De Groot GJJB 2015 *Plasma Process Polym* **12** 608–623
[4] Šimek M, Homola T 2021 *Eur Phys* J D **75** 210
[5] Černák M, Černáková L, Hudec I, et al 2009 *EPJ Appl Phys* **47** 22806
[6] Tomeková J, Kyzek S, Medvecká V *et al.* 2020 *Plasma Chem Plasma Process* **40** 1571–1584

EFFECT OF LOW-TEMPERATURE ATMOSPHERIC PRESSURE PLASMA ON GERMINATION, GROWTH PARAMETERS AND DECONTAMINATION OF RADISH SEEDS

Mohamed Khalaf [1], Silvia Mošovská[2], Veronika Medvecká[1]

[1] *Department of Experimental Physics, Faculty of Mathematics, Physics and Informatics, Mlynská Dolina F1, 842 48 Bratislava, Slovak Republic*

[2] *Department of Nutrition and Food Quality Assessment, Faculty of Chemical and Food Technology, Slovak University of Technology, Radlinského 9, 812 37 Bratislava, Slovak Republic*

E-mail: mohamed.fawwaz@fmph.uniba.sk

Cold atmospheric plasma (CAP) is utilized in agriculture as a practical, cost-effective, and ecologically friendly way to improve seed production. In addition, cold plasma treatment significantly lowers pathogen infection on seed surfaces. Reactive oxygen and nitrogen species in the plasma play a vital role in pathogen disinfection as they can disrupt the cell membrane of microorganisms and can increase the oxidative stress [1]. Radish seeds are known for their fast germination and growth of plants but also for sprouting, which are popular for the purpose of improvement of germination rate and growth parameters. We measured germination rate, the length of roots and shoots, Seedling vitality index I (mm), and Root: shoot ratio I from treated and untreated seeds. In addition, we observed the effect of plasma for inhibition of typical bacteria contaminating sprouts (*Escherichia coli* and *Salmonella* Enteritidis).

1. Experimental

- ***Plasma source and plasma treatment:***

Diffuse coplanar surface barrier discharge was used for plasma treatment of radish seeds. This plasma source is a unique type of coplanar dielectric barrier discharge. It generates low-temperature plasma with high ratio of diffuse part without the need of reduced pressure or special working gas (e.g. mixture of noble gases). The plasma with significantly high power density (80 W/cm^3) is generated in thin layer (cca 0.5 mm of the active plasma) in discharge area of 8x20cm^2, which allows treatment of high amount of material in short time [2, 3] . The radish seeds were treated for different exposure times in the range of 5s to 300 s according to the purpose and effect of plasma.

- ***Description of germination and growth parameters experiments:***

Radish seeds (Raphanus sativus) in bio quality intended for sprouting (Sonnentor, Austria, origin of seeds - Italy) was ordered from Vitaland market.

50 seeds from each group were soaked in distilled water for 30 minutes at room temperature. These seeds were then evenly distributed, without touching, in a Petri dishes covered with wet thin paper (25 in each), and 4 mL of water was added to achieve the moisture conditions required for germination. After 24 hours, the number of germinated seeds was counted, and after 5 days, the length of shoots and roots of young seedlings were measured. The obtained data were used to determine germination parameters, germination (%), seedling vitality index I (mm), and root-shoot ratio I [4] .

- ***Description of microbio experiments:***

The decontamination effect of plasma treatment was tested against bacterial strain E. coli CCM 3988 and S. enterica subs. enterica serovar Enteritidis CCM 4420 (the Collection of Microorganisms, Masaryk University, Brno, Czech Republic). Survivor bacteria were determined by surface plating (250µl) of appropriate aliquots on a Mueller-Hinton agar. The plates were incubated for 24h at 37°C and then the colony forming units (CFU) were counted. The results were expressed as log10CFU/g and the detection limit of this method was 1.0 log10CFU/g.

2. Results

The germination of treated and non-treated radish seeds was observed for 5 days. Fig.1 shows the germinated seeds of plasma-treated and untreated after 24 hr. Statistical analysis showed that there were no significant differences in seed germination rate for a short treatment time (5,10, and 15 s) and non-treated seeds. However, Inhibition of germination was observed after treatment with plasma for longer time (30s,60S, and 120 s). For seedling vitality index I (mm) and Root: shoot ratio that give induction about the quality of young seedlings, our result showed that no differences between treated seeds for short time and non-treated.

On the other hand, obtained results indicated the sensitivity of tested microorganisms inoculated onto the surface of radish seeds to DSCBD treatment. The devitalization effect increased with exposure time. E. coli was more sensitive to the plasma treatment than S. Enteritidis (Fig. 2). The microbial reduction level of more than 4 log10 was achieved already in 90s of samples exposure in plasma. A significant increase in the reduction of S. Enteritidis was observed for 120s (4.1 log10) plasma exposure. Subsequently, a CFU reduction was mitigated.

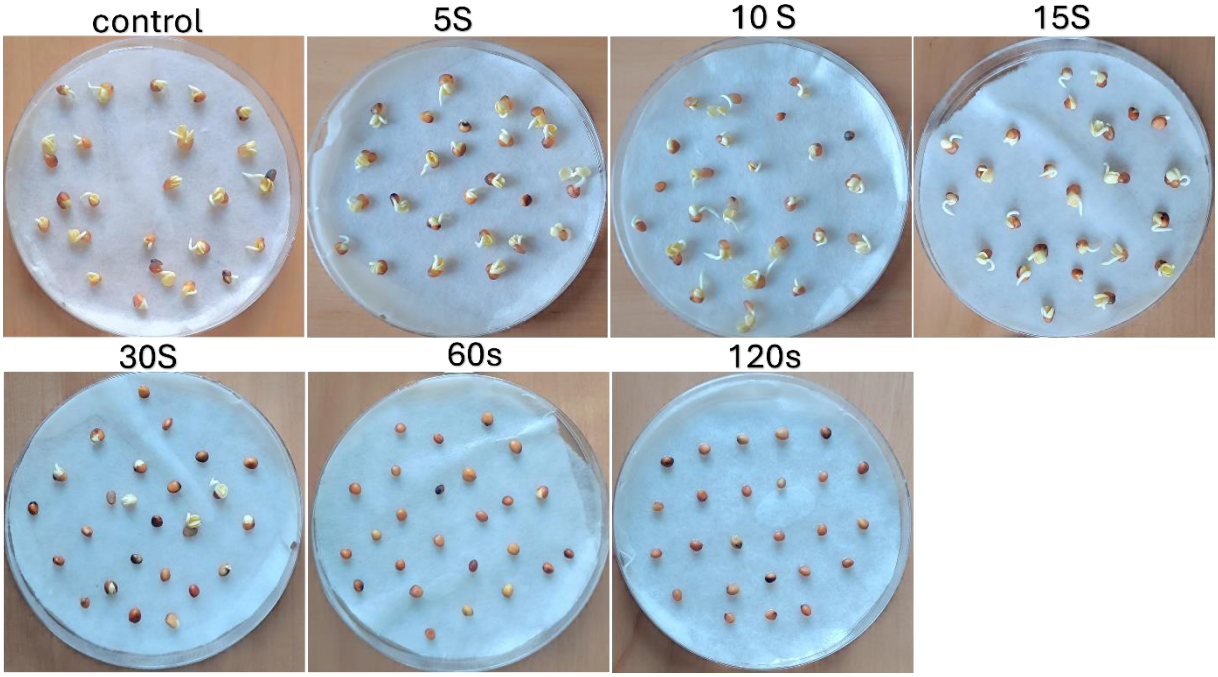

Fig. 1. Seeds germination of Twenty-five seeds in each petri dish for all groups after 24 hr.

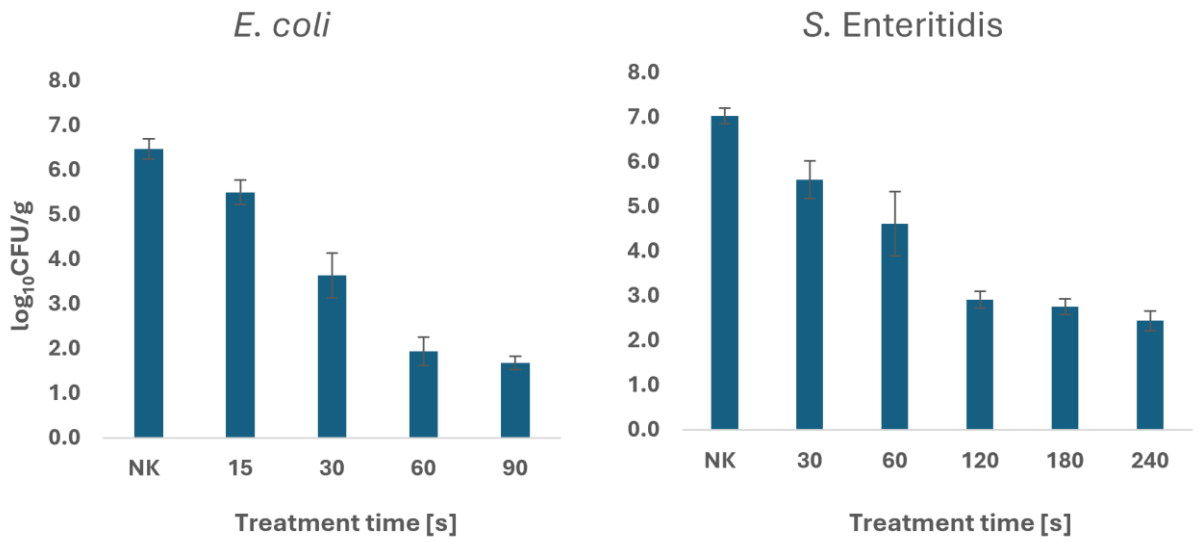

Fig. 2. Decontamination effect of DCSBD plasma against *E. coli and S. Enteritidis* inoculated on radish seeds

3. Conclusion

Our study examined the effects of plasma doses on germination of radish seeds and on E. coli and S. Enteritidis inactivation into seed surfaces. The findings revealed that E. coli was more sensitive to plasma treatment than S. Enteritidis, and the devitalization effect increased with exposure time. Furthermore, our findings showed that short plasma treatments have no negative impacts on seed germination. However, higher doses (30 S) had a negative impact and (60 S or more) entirely inhibited germination.

4. Acknowledgements

This work was supported by the Slovak Grant Agency No. 1/0688/22, No. 1/0515/21, and the Slovak Research and Development Agency under the contract No. APVV-21-0147.

5. References

1. Šimončicová, Juliana, Svetlana Kryštofová, Veronika Medvecká, Kamila Ďurišová, and Barbora Kaliňáková. 2019. Technical applications of plasma treatments: current state and perspectives. *Applied Microbiology and Biotechnology* 103: 5117–5129. https://doi.org/10.1007/s00253-019-09877-x.
2. Mošovská, Silvia, Veronika Medvecká, Noémi Halászová, Pavol Ďurina, Ľubomír Valík, Anna Mikulajová, and Anna Zahoranová. 2018. Cold atmospheric pressure ambient air plasma inhibition of pathogenic bacteria on the surface of black pepper. *Food Research International* 106: 862–869. https://doi.org/https://doi.org/10.1016/j.foodres.2018.01.066.
3. Medvecká, Veronika, Silvia Mošovská, Anna Mikulajová, Ľubomír Valík, and Anna Zahoranová. 2020. Cold atmospheric pressure plasma decontamination of allspice berries and effect on qualitative characteristics. *European Food Research and Technology* 246: 2215–2223. https://doi.org/10.1007/s00217-020-03566-0.
4. Božena, ŠERÁ. 2023. Methodological contribution on seed germination and seedling initial growth tests in wild plants. *Notulae Botanicae Horti Agrobotanici Cluj-Napoca* 51: 13164.

Application of DCSBD as a Low-Temperature Plasma Source for Polymer Processing

S. Gahramanli, P. Šrámková, A. Zahoranová

Department of Experimental Physics, Faculty of Mathematics, Physics and Informatics, Comenius University in Bratislava, Mlynská dolina, 842 48 Bratislava
E-mail: sahila.gahramanli@fmph.uniba.sk

This study explores the use of Diffuse coplanar surface barrier discharge (DCSBD) as a low-temperature plasma source for the surface modification of polymers, specifically polyamide (PA), polypropylene (PP), and polycarbonate (PC). The water contact angle (WCA) measurement was employed to assess the changes in surface wettability following plasma treatment. Results revealed a notable decrease in the contact angle for all three polymers, indicating an increase in surface energy. The DCSBD treatment effectively enhanced surface properties, which could potentially improve the adhesion, coating, and printing capabilities of these polymers. This work highlights the efficacy of DCSBD as a non-thermal plasma treatment technique for polymer surface modification.
Keywords: DCSBD, polymers, plasma-based treatment, water contact angle.

1. Introduction

Surface modification of polymers is essential for enhancing their properties, such as improving adhesion, wettability, and chemical reactivity, which are critical for various industrial applications. One effective approach for surface modification is the use of atmospheric pressure plasma, a non-thermal and environmentally friendly technique that alters surface characteristics without affecting the bulk material [1]. Among the various plasma techniques, diffuse coplanar surface barrier discharge (DCSBD) has emerged as a highly efficient plasma source due to its high power density, uniform plasma distribution, and capability to treat polymers at low temperatures [2].

The primary objective of this study is to assess the changes in the water contact angle (WCA) and chemical changes of polymer surfaces treated with DCSBD plasma at different exposure times. By exploring how treatment time influences surface energy, this research aims to provide valuable insights into optimizing plasma treatment parameters for enhancing polymer surface properties. Understanding these relationships is crucial for improving polymer performance in various applications such as coatings, printing, and adhesion [3].

2. Methodology

Polyamide (PA6), polypropylene (PP) and polycarbonate (PC) materials were selected due to their different wetting properties. Polymer sheets, 1 mm thick, were obtained from TechPlasty, s.r.o. (Žilina, SR). Samples measuring 1.5 x 4 cm were cleaned in an ultrasonic cleaner using isopropyl alcohol, acetone, and distilled water (10 minutes per solvent). They were then dried with nitrogen flow to eliminate contaminants. DCSBD was employed under optimized settings (400 W, 15 kHz) in atmospheric air. It delivered uniform treatment with a surface power density of 1–3 W/cm². Samples were secured on a 5 x 5 cm holder with adhesive and positioned using Kapton tape to ensure a precise 0.3 mm gap.

3. Results and Discussion

3.1 WCA outcomes following plasma treatment with DCSBD

This research examines the effects of DCSBD plasma treatment on the surface properties of polyamide (PA), polypropylene (PP), and polycarbonate (PC) polymers by measuring changes in water contact angle (WCA). The treatment times of 1, 3, 5, 10, 20, and 30 seconds were applied. Results

revealed a significant reduction in WCA for all three polymers, indicating improved surface wettability and increased surface energy. The most notable changes occurred after 10 seconds of plasma exposure, with further reductions in WCA observed up to 20 seconds. Beyond 20 seconds, there were no significant changes in surface properties (Fig. 1 and Tab. 1).

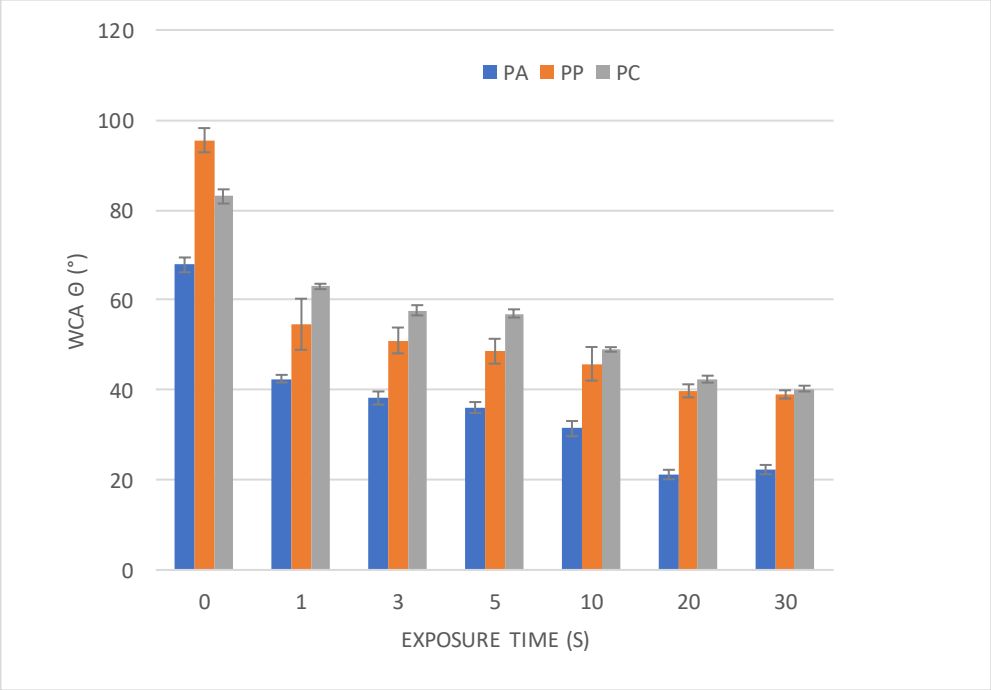

Fig. 1. WCA of DCSBD treated polymers (PA, PP, PC) at different exposure times.

The results of the water contact angle in different exposure times are shown in the table below.

Tab. 1. The results of WCA in different exposure time.

	Reference	1 s	3 s	5 s	10 s	20 s	30 s
PA	67.8±1.64	42.5±0.85	38.2±1.46	36.1±1.21	31.4±1.69	21.2±1.05	22.3±1.03
PP	95.5±2.69	54.6±5.68	51.0±2.87	48.6±2.76	45.8±3.74	39.8±1.45	39.0±0.92
PC	83.0±1.58	63.0±0.60	57.7±1.14	57.0±0.91	49.0±0.51	42.4±0.77	40.3±0.64

These findings highlight the effectiveness of DCSBD as a method to enhance the hydrophilicity of PA, PP, and PC surfaces, making it suitable for applications such as adhesion promotion, coating, and surface functionalization.

3.2 Impact of Ageing on Polymer Surface Properties

The effect of aging on the surface properties of polymers and the changes in wettability with time were investigated (Fig. 2 and Tab. 2). Polyamide (PA), polypropylene (PP) and polycarbonate (PC) were plasma treated for 3 s and the water contact angle (WCA) was measured immediately after treatment and then after 1, 3 days and 1, 2, 3 and 4 weeks of aging. The results show that there are significant changes in the surface properties over time. PA showed a gradual increase in WCA from 42.9° immediately after treatment to 54.4° after 4 weeks slowly reaching the reference value (67.8±1.64). PP showed a more stable surface with small increases in WCA from 53.7° to 57.7° during the aging period. In contrast, PC showed the most significant change and WCA increased from 48.2° to 67.4° immediately after 4 weeks.

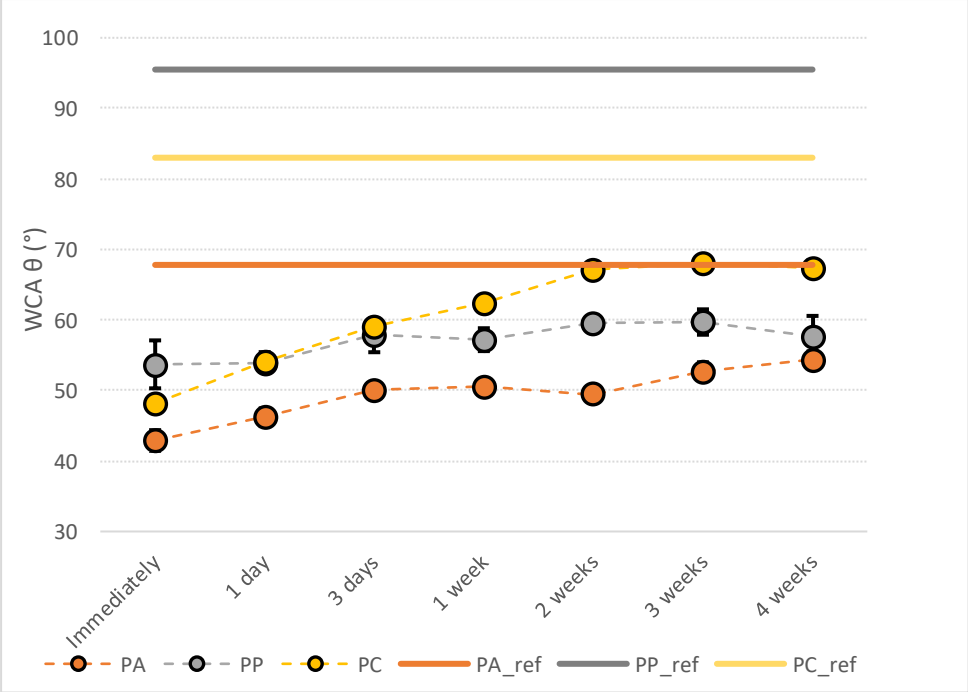

Fig. 2. Ageing results by WCA (DCSBD treated polymers - PA, PP, PC, exposure time – 3s).

Tab. 2. Water Contact Angle (WCA) of plasma-treated polymers (PA, PP, PC) at various ageing times.

	Immediately	1 day	3 days	1 week	2 weeks	3 weeks	4 weeks	ref
PA	42.9±1.47	46.2±1.25	50.0±0.98	50.5±0.98	49.5±0.96	52.7±1.29	54.4±1.14	67.8±1.64
PP	53.7±3.40	53.9±1.26	57.8±2.38	57.2±1.62	59.5±1.21	59.7±1.80	57.7±2.87	95.5±2.69
PC	48.2±0.59	54.1±1.33	59.0±0.95	62.3±0.71	67.1±1.15	68.0±0.91	67.4±1.06	83.0±1.58

These results suggest that ageing rate is different for different polymeric substrate and depends on chemical and physical properties of the appropriate polymer substrate. Understanding these changes and correlations between the plasma treatment conditions, properties of the substrate and storing conditions is crucial for predicting the long-term performance of plasma-treated polymers in various applications.

4. Conclusion

This study highlights the effectiveness of DCSBD plasma treatment in enhancing the surface properties of polyamide (PA), polypropylene (PP), and polycarbonate (PC) polymers. The reduction in water contact angle (WCA) across all polymers indicates a significant improvement in surface wettability and energy, with optimal results achieved after 10–20 seconds of plasma exposure. Aging tests revealed that surface properties evolve over time, with PA losing improved wettability the fastest, PP maintaining relatively stable properties, and PC increasing in hydrophobicity. These results emphasize the potential of DCSBD for various applications, such as improving adhesion, coatings, and surface functionalization, while also highlighting the importance of considering aging effects in long-term applications.

5. References

[1] Van Deynse A, Morent R, and De Geyter N 2016 *Polymer Sci.* 506-516.

[2] Černák M, Hudec I, Kováčik D, and Zahoranová A 2009 *Eur. Phys. J. Appl. Phys.* 47(2) 22806.

[3] Štěpánová V, Šrámková P, Sihelník S, Stupavská M, Jurmanová J, and Kováčik D 2021 *Vacuum* **183** 109887.

FUTURE TO FACILE SEEDING TECHNOLOGY: FROM NANODIAMOND TO NANOCRYSTALLINE DIAMOND FILM

Joel Jeevan[1,*], Sarah Al Zeibak[1], Arvind K. Bhakta[1,2], Fabien enedic[1], Michael Redolfi[1], Khaled Hassouni[1], Swaminathan Prasanna[1]

[1]*LSPM-CNRS, UPR 3407, Université Sorbonne Paris Nord, 99 avenue J.B. Clément, 93430, Villetaneuse, France*

[2]*Universite Paris Cite, CNRS UMR-7086, ITODYS, 15 Rue Jean-Antoine de Baïf, 75251, Paris, France*

[*]E-mail : joel.jeevan@lspm.cnrs.fr

Nanocrystalline diamond (NCD) films are materials of immense potential in a variety of application, advancements and modification in synthesis methods of NCD have been always topic of interests to researchers throughout the globe. In this work silicon wafer was treated with a unique homemade microwave microplasma (MWMP) torch with Ar/H_2 as the working gases. This resulted in formation of carbon nanostructures over the silicon wafer. Plasma parameters such as the microwave power, operating pressure, ratio and flowrate of 96/4/50 ratio of $H_2/CH_4/Ar$ was used for seed synthesis. This was later used as seed to grow nanocrystalline diamond (NCD) film using microwave plasma assisted chemical vapour deposition - distributed antenna array (MWPACVD-DAA). Raman spectroscopy, and Scanning electron microscopy (SEM) were key for material characterization. The SEM micrographs of carbon deposits on silica substrate show visible growth of diamond films following the MWPACVD of the seed. The Raman spectra of the samples before and after growth show noticeable enhancement of the diamond peak around 1332 cm^{-1}. The synthesised film thickness was measured to be in the range of 12 to 15 nm. A maximum purity of 98.47 % of sp^3 carbon was achieved from the synthesized ND.

1. Introduction

NDs are one of numerous types of carbon nanostructures, including nano-sized amorphous carbon, fullerenes, carbon nanotubes, onions, and rods, to mention a few [1]. They are sp^3-hybridized carbon structures at nanoscale dimensions (1 to 100 nm) and consist of pure-phase diamond films, diamond particles, 1-D diamond nanorods, and 2-D diamond nanoplatelets. The purest ND grains can have almost pristine crystalline structure with traces of non-diamond carbon. According to the literature, transmission electron microscopy (TEM) of NDs are polyhedra consisting of a diamond core comprising of sp^3 carbon which may be wrapped with graphitic sp^2 or amorphous carbon. They have tremendous potential in biomedicals, tribology, optical sensors, electronics, quantum computing, photovoltaics, and a variety of environmental applications.

NDs were first synthesized using detonation by researchers from USSR long back in July 1963. They have improved thermal stability and mechanical properties of NDs, research has shifted its focus to their synthesis and modification. Extensive research has been conducted to discover several ND synthesis methods, such as laser ablation, ion irradiation of graphite, ultrasound cavitation, high energy ball milling of high pressure high temperature diamond microcrystals, PACVD and so on. PACVD have lot of advantages compared to other synthesis methods. Compared to other methods, PACVD has a much lower temperature range. MWPACVD is the most effective of all the PACVD since it can provide high density plasma, which is necessary for NCD synthesis. The high density MW plasma boosts the concentration of active species in smaller volume which result in improved film growth than other methods. MWPACVD also offers the possibility of NCD growth in wide range of substrate materials. Eventhough MWPACVD has its own advantages compared to other methodologies it requires a precursor version of diamond, at least in small amounts as a seed to grow into NCD film.

Zixian et al., 2022 discussed a novel methodology of plasma synthesis with gas phase nucleation of ND without any diamond precursor using a MWMP torch [2]. H_2 and CH_4 were used as the primary

gas and carbon source respectively. The studies were carried out using an injected microwave power range between 30 W and 90 W. No significant Raman signals of ND were observed when the power was 30 W; it was only observed when the injected power was above 70 W. In (Arvind et al., 2024, Emergent Materials, submitted) the authors prepared a concentrated solution of ND in isopropanol, and then dropcasted it into a Si wafer to grow NCD film from it using a MWPACVD-DAA. It validates the gas phase nucleation of nanodiamond in a MWMP torch and reassures that ND synthesis here is not due to any surface phenomena. This gave the motivation to explore a new approach to grow NCD film which no longer requires commercially bought ND seeds. In this study, efforts were made to synthesize ND on a Si wafer using the mentioned MWMP torch with less than half the power with greater yield. This makes the process more energy-efficient and opens a possibility of reducing the overall experimental duration for ND seed generation. It was possible due to the use of Ar gas which promotes nucleation. The preliminary experiments on this are successful that paves the way to the possible incorporation of a MWMP torch into a MWPACVD-DAA reactor which can result in in-situ ND seed synthesis followed by NCD film growth.

2. Experimental Setup

The experimental setup is described elsewhere, in this study a pressure of 100 mBar with 45 watt of microwave power having gas composition of 96/4 sccm of H_2/CH_4 respectively with 50 sccm of Ar[1].

3. Results and Conclusions

The synthesied material where extensively characterised using Raman spectroscopy and scanning electron microscopy (refer figure 1).

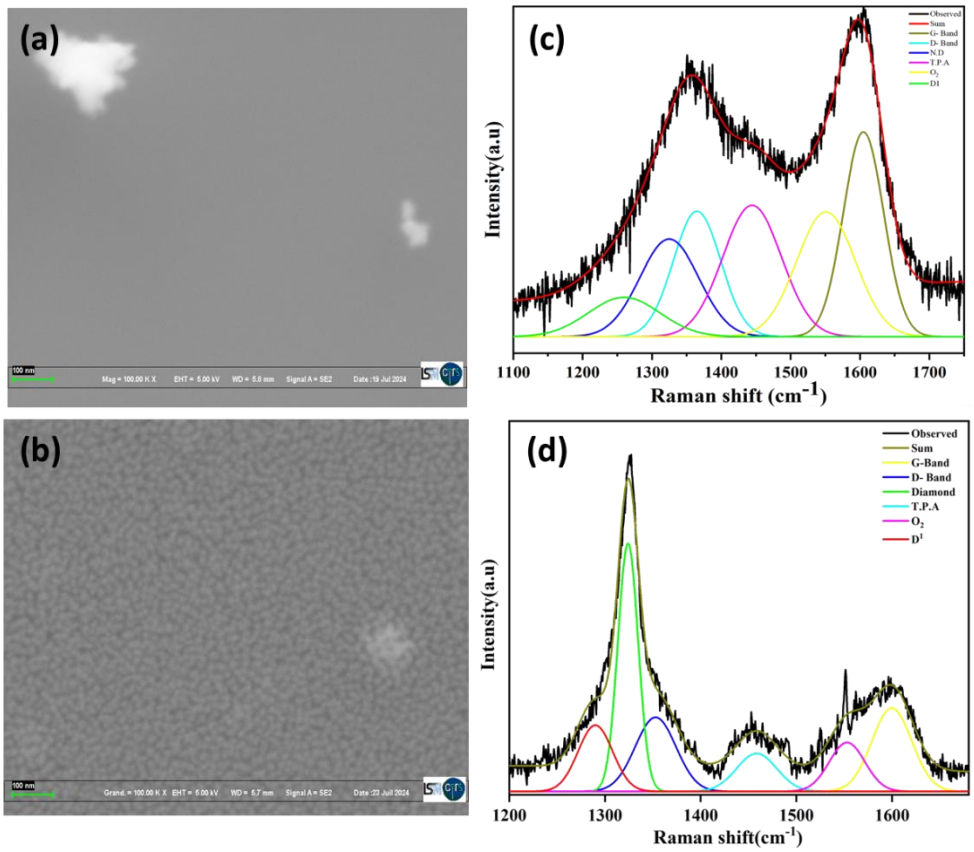

Fig. 1. SEM of (a) Nanodiamond particles (before growth) and (b) NCD film (after growth). Raman spectra of (c) Nanodiamond particles (before growth) and (d) NCD film (after growth).

Nanodiamonds were synthesised at 45 W power which was less than half the power previously used to generate nanodiamond [2] with the help of argon injection. The size of Nanodiamond seeds along with other forms of carbon ranges from 30-40 nm. Homogenous NCD film of grain size 15-25 nm with 15± 2 nm thickness and purity of 98.5% was developed [3,4]. This could be a possible cost-effective, *in-situ* alternative to the industrial diamond seeding for development of NCD film. This process should be further optimized to find the best operating condition to develop NCD film using the seeds from MWMP torch.

4. Acknowledgement

We acknowledge the French Agence Nationale de la Recherche (ANR), under grants ANR-22-CE51-0013 (project NANODIAPLAS) for their doctoral funding.

5. References

[1]Georgakilas V, Perman J A, Tucek J, and Zboril R 2015 *Chem. Rev.* **115** 4744–4822.
[2] Z. Jia et al. 2023 *Plasma Processes and Polymers* **20** 2200180.
[3] B. Baudrillart et al. 2017 *Diamond and related materials* **75** 44-51.
[4] Klauser F, Steinmuller-Nethl D, Kaindl R, Bertel E, and Memmel N 2010 *Chemical Vapor Deposition* **16** 127–135.

INVESTIGATING THE COMBINED ANTIYEAST EFFICACY OF PLASMA-ACTIVATED WATER AND NATURAL PHENOLICS ON PLANKTONIC DEBARYOMYCES HANSENII

Bernard Gitura Kimani[1], Ramin Mehrabifard[1], Oleksandr Galmiz[1], and Zdenko Machala[1]

[1]*Division of Environmental Physics, Faculty of Mathematics, Physics and Informatics, Comenius University in Bratislava, Mlynská dolina, 842 48 Bratislava, Slovakia*

E-mail: kimani1@uniba.sk

Plasma-activated water (PAW) has gained attention as a potent antimicrobial agent, demonstrating its capacity to regulate the growth of microorganisms. The production of PAW entails exposing water to cold atmospheric plasma (CAP) which introduces short and long-lived reactive oxygen and nitrogen species (RONS) such as H_2O_2, O_3, NO_2^-, NO_3^- and OH radicals. The reactive species in PAW interfere with the structural integrity and functional capabilities of microbial cells. Phenolic compounds are secondary metabolites in plants known for their health-promoting and antimicrobial properties. The combination of PAW with natural compounds as an antiyeast strategy could potentially yield additive or synergistic effects. Such an approach may broaden the antimicrobial spectrum and delay the development of microbial resistance.

This study involved the use of 1 kHz transient spark (TS) discharge PAW combined with cinnamic acid, vanillin, gallic acid and *p*-coumaric acid separately to create phenolics concentration of 2 or 1 mg/mL, and incubated with 10^6 CFU/mL of yeast *Debaryomyces hansenii* SZMC 8045Mo for 24 hours at 30 °C. In addition, 10^6 CFU/mL of *D. hansenii* in sterile tap water was directly treated with TS for 10 min and incubated with each of the four natural compounds under similar conditions. The efficacy of the PAW-phenolics was evaluated through agar plated colony counts. The results of this study suggest that the integration of PAW with natural phenolics constitutes an effective approach for combating yeast.

1. Introduction

Non-Thermal Plasma (NTP) technology serves as a green alternative that may be instrumental in the progress of agricultural production, biomedical innovations, food industry, water purification, air decontamination, and soil remediation, along with a wide array of other uses [1, 2, 3, 4, 5].

The control of fungi in agricultural, industrial and medical environments is fraught with challenges, stemming from their resilience and the multifaceted nature of these contexts [6]. Yeasts are exceptionally adaptable, able to endure extreme environmental conditions, such as low pH and high concentrations of sugar or salt, as well as surviving in cold storage [7]. Emerging technologies, including NTP and the incorporation of bioactive compounds such as phenolics, have shown substantial effectiveness in mitigating pathogenic and non-pathogenic microbes [8]. These contemporary approaches provide advantageous alternatives to traditional chemical interventions.

The utilization of plasma-activated water (PAW) in conjunction with bioactive compounds such as natural phenolics offers a promising avenue for microbial management [9]. PAW contains short-lived reactive species such as nitric oxide (NO), superoxide (O_2^-), ozone (O_3), hydroxyl radical (OH), peroxynitrate ($OONO_2^-$) and peroxynitrite ($ONOO^-$), and long-lived species such as nitrates (NO_3^-), nitrites (NO_2^-) and hydrogen peroxide (H_2O_2) [10]. These reactive species can disrupt the cellular integrity of yeasts, resulting in cell death [11]. The antifungal action of natural bioactive compounds, including phenolics, is primarily due to their ability to compromise cellular and membrane structures, denature proteins, and disrupt fungal metabolic processes [12, 13]. By integrating plasma with phenolics, it is possible to target yeasts through multiple pathways, thereby improving efficacy and reducing the potential for antifungal resistance. Furthermore, this combined approach can lead to a reduction in the concentrations of phenolics needed, which may help to minimize adverse effects on non-target organisms.

2. Methods

The transient spark (TS) discharge was generated through a power electrode connected to a high voltage DC power supply through a 10 MΩ resistor. A metal ring as a grounded electrode was submerged in the tap water/yeast-containing water. The treatment time for the transient spark was 10 min/10 mL. The schematic diagram of the TS plasma setup is shown in Figure 1.

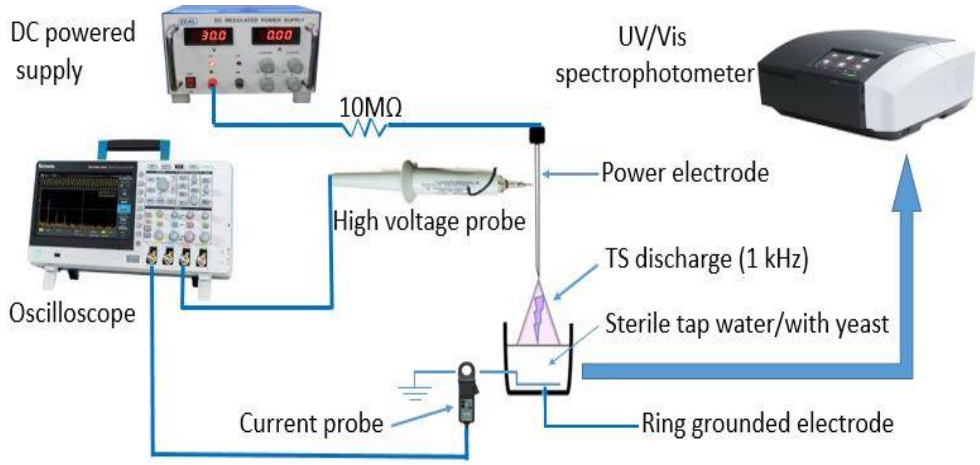

Fig. 1. The experimental setup of the transient spark discharge generating system

Two approaches to antiyeast treatment were investigated: (1) the direct application of TS discharge to 10 mL of *D. hansenii* suspension at a concentration of 10^6 CFU/mL, followed by incubation with either 2 or 1 mg of phenolic compounds; and (2) an indirect method in which transient spark PAW was used to dissolve 2 or 1 mg of phenolics, which were then incubated with 10^6 CFU/mL of yeast. The effectiveness of the plasma-phenolics treatment was evaluated by counting the number of yeast colonies on agar plates after a 24-hour incubation at 30°C.

3. Results and discussion

In the context of directly treating yeasts with TS discharge followed by the incubation with natural phenolics, it was observed that plasma-cinnamic acid displayed the highest level of antiyeast activity, followed by plasma-vanillin, plasma-gallic acid, and plasma-*p*-coumaric acid, respectively (Figure 2). Plasma-cinnamic acid showed a complete growth inhibition at both 2 and 1 mg/mL phenolic concentration (Figure 2). Plasma-vanillin resulted in growth inhibition values of 3.16 and 2.21 log at 2 and 1 mg/mL, respectively (Figure 2). Additionally, plasma-gallic acid and plasma-*p*-coumaric acid produced growth inhibition of 1.46 and 1.35 log at a concentration of 2 mg/mL, respectively (Figure 2).

In an indirect treatment scenario where PAW was used to dissolve phenolic substances at concentrations of 2 or 1 mg, followed by incubation with 10^6 CFU/mL of yeast, PAW-cinnamic acid completely inhibited growth at a concentration of 2 mg/mL and achieved a growth inhibition of 3.2 log at 1 mg/mL (Figure 3). PAW-vanillin demonstrated growth inhibition of 2.1 log and 1.6 log at 2 mg/mL and 1 mg/mL, respectively (Figure 4). Additionally, PAW-gallic acid produced growth inhibition of 1.2 log at 2 mg/mL and 1.1 log at 1 mg/mL, while PAW-*p*-coumaric acid resulted in growth inhibition of 1.4 log at 2 mg/mL and 1.0 log at 1 mg/mL (results not shown).

The combination of plasma and phenolics generally exhibited varying growth inhibitory effects on *D. hansenii* SZMC 8045Mo, with direct plasma treatment showing a higher antiyeast activity than the indirect treatment. Cinnamic acid, gallic acid, and *p*-coumaric acid, identified as hydroxybenzoic acids, exhibited varying levels of antiyeast activity when combined with PAW. These variations may be explained by the distinct chemical properties of each compound [12]. The dynamics between RONS

and phenolic functional groups, together with the antiyeast efficacy of the individual compounds, could have been pivotal in determining the final results. The presence of RONS in PAW may have augmented the effectiveness of phenolics by altering their chemical structure, enhancing solubility, and promoting effective penetration into yeast cells. In cases where antiyeast activity was notably high, such as with plasma-cinnamic acid, the combined oxidative stress from RONS and phenolics may have effectively compromised the yeast's defense mechanisms.

The plasma-phenolics antiyeast strategy holds promise in applications such as agriculture and food safety, where fungal contamination is a significant challenge [14]. Research continues to explore the optimization of PAW treatment and phenolic compound concentrations for maximizing their antiyeast efficacy [15,16,17].

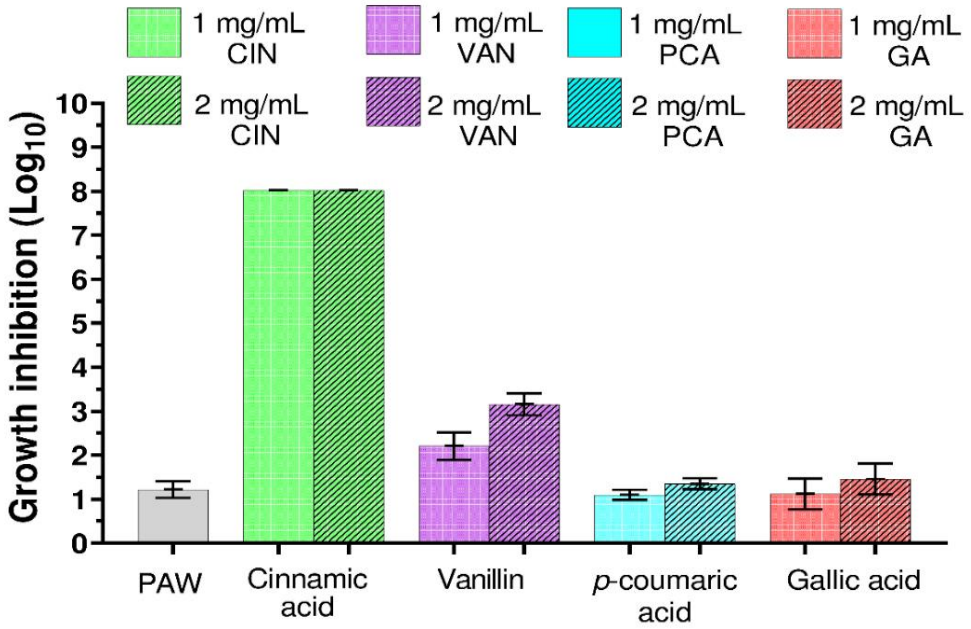

Fig. 2. Growth inhibition of direct transient spark treatment on 10 mL of 10^6 CFU/mL *D. hansenii* SZMC 8045Mo, followed by a 24-hour incubation in phenolics.

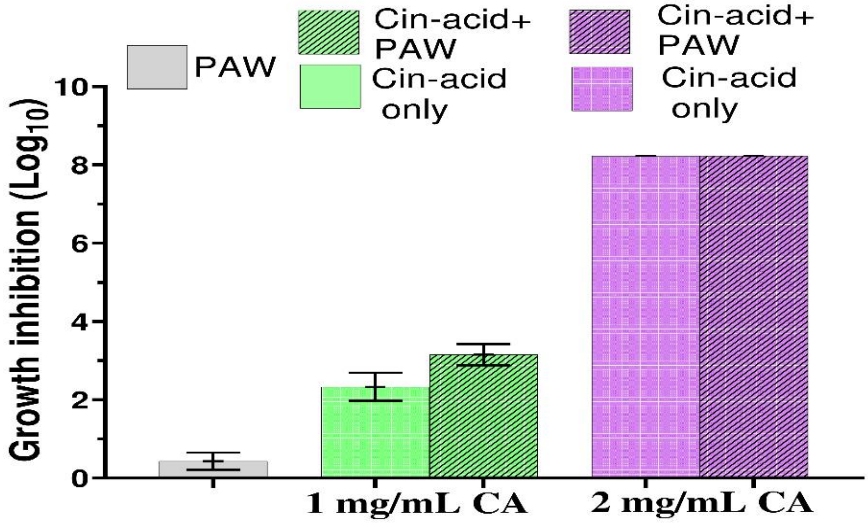

Fig. 3. Growth inhibition of transient spark PAW combined with cinnamic acid (CA) on *Debaryomyces hansenii* SZMC 8045Mo.

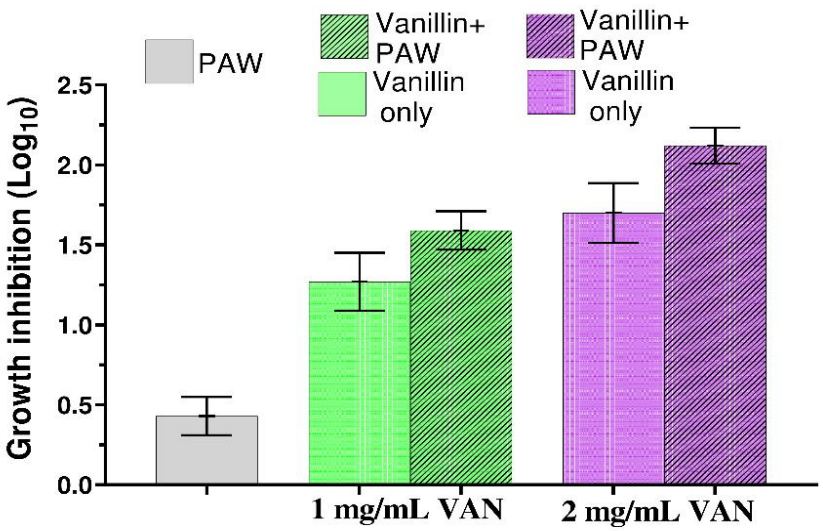

Fig. 4. Growth inhibition of transient spark PAW combined with Vanillin (VAN) on *Debaryomyces hansenii* SZMC 8045Mo.

4. Acknowledgement

This research was funded by the Slovak Research and Development Agency APVV-22-0247 grant and the EU NextGenerationEU through the Recovery and Resilience Plan for Slovakia under the project No. 09I03-03-V03-00033 EnvAdwice. Dr. Miklos Takó provided *Debaryomyces hansenii* SZMC 8045Mo from the University of Szeged Microbiological collection.

5. References

[1] Giardina A, Lofrano G, Libralato G, Siciliano A, Marotta E, and Paradisi C 2024 *Front. Environ. Chem.* **5** 1416702.
[2] Xu Y and Bassi A 2024 *Biotechnol. Prog.* e3511.
[3] Maccaferri C, Gherardi M, and Laurita R 2024 *Front. Phys.* **12** 1399720.
[4] Kooshki S, Pareek P, Mentheour R, Janda M, and Machala Z 2023 *Environ. Technol. Innov.* **32** 103287.
[5] Hatzisymeon M, Tataraki D, Tsakiroglou C, Rassias G, and Aggelopoulos C 2021 *Sci. Total Environ.* **786** 147420.
[6] Davies C R, Wohlgemuth F, Young T, Violet J, Dickinson M, Sanders J, Vallieres C, and Avery S V 2021 *Fungal Biol. Rev.* **36** 15-26.
[7] Segal K C, Romero A L Alcaraz L D, López O G, Torres R N, Sandoval G, and González J 2022 *Microorganisms* **10** 794.
[8] Matan N, Puangjinda K, Phothisuwan S, and Nisoa M 2015 *Food Control* **50** 291-296.
[9] Gustavo J, El Kadri H, Wantock T, Harle T, Seggiani M, Danti S, Di Stefano R, and Velliou E 2020 *Molecules* **26** 1890.
[10] Pareek P, Kooshki S, Tóth P, and Janda M 2024 *Chem. Eng. J.* **493** 152583.
[11] Polčic P and Machala Z 2021 *Inter. J. Mol. Sci.* **22** 2247.
[12] Kimani B G, Kerekes E B, Szebenyi C, Krisch J, Vágvölgyi C, Papp T, and Takó M 2021 *Foods*, **10** 1652.
[13] Kimani B G, Takó M, Veres C, Krisch J, Papp T, Kerekes E B, and Vágvölgyi C 2022 *Foods* **12** 1338.
[14] Liu X, Li Y, Wang S, Huangfu L, Zhang M and Xiang Q 2021 *LWT* **146** 111447.
[15] Kimani BG, Ramin M, Zdenko M 2024 *ICPM. IWPCT* **10** 127.
[16] Ramin M, Kimani BG, Zdenko M 2024 *ICPM. IWPCT* **10** 94.
[17] Oleksandr G, Kimani BG, Zdenko M 2024 *ICPM. IWPCT* **10** 97.

STUDY OF DIRECT AND INDIRECT PLASMA APPLICATION ON ONION SEEDING BULBS

Lenka Krejsová[1], Zdenka Kozáková[1], Ludmila Mravcová[1], Jana Šimečková[2], František Krčma[1]

[1] *Faculty of Chemistry, Brno University of Technology, Purkyňova 118/464, 612 00 Brno, Czech Republic*

[2] *Faculty of AgriSciences, Mendel University in Brno, Zemědělská 1752, 613 00 Brno, Czech Republic*

E-mail: Lenka.Krejsova@vut.cz

This paper deals with the analysis of fragrances in onions treated with plasma before planting. The treatment was carried out to see if it would improve onion growth while maintaining or increasing the fragrance content. The experimental part was carried out over a period of three years at 22 sites. The procedures for treating bulbs before planting with corona discharge and plasma-activated water are described. In total, four treatment variants were carried out and bulbs from the fifth variant were left untreated. Saturated vapors of liquid samples were analyzed by proton transfer reaction time-of-flight mass spectrometry (PTR-TOF-MS). Thanks to this analysis, the concentrations of volatile substances were determined. Some samples were analyzed by gas chromatography with mass spectrometer as a detector to identify the compounds. From the results obtained, it is evident that plasma treatment can be useful for the treatment of onions in agriculture, because it provided harvest increase without decrease of fragrances concentrations.

1. Introduction

One of the major current problems in agriculture is soil and water contamination caused by the use of synthetic pesticides, herbicides, and fertilisers. Pesticides benefit agricultural production by protecting crops from diseases and pests, while at the same time having negative environmental impacts. Their application over large areas not only negatively affects the targeted organisms but also affects other species, including birds, aquatic organisms, and other animals. Contamination of food with pesticides and fertilisers can also have serious health consequences for humans. Therefore, more environmentally friendly methods are being sought.[1]

One of the new research directions is the use of low-temperature plasma in the field of agriculture, a method known as "plasma agriculture". This approach focuses on using plasma to treat seeds, plants, or water to increase agricultural production while maintaining food quality and safety.[2]

Plasma can be characterized as the fourth state of matter. It is a quasi-neutral ionized gas in which particles exhibit collective behavior. It is composed of three types of particles, neutral molecules, negatively charged particles (electrons and anions), and positively charged particles (cations).

The reactive oxygen and nitrogen species (RONS) formed in the plasma have stimulatory and antibacterial properties for plants. When water is treated with plasma, RONS from the plasma penetrate the water surface, resulting in the formation of plasma-activated water (PAW). This water is enriched with nitrogen, which helps plants to grow, and hydrogen peroxide, which with a lower pH gives the water antibacterial properties.

Over the last few decades, cold plasma generated under atmospheric pressure has become a subject of intense interest for the scientific community and industrial applications. For example, it can interact with foods, polymers, seeds, and living tissues. The application of direct (corona discharge) and indirect (PAW) plasma treatment of bulbs, in order to increase the yield (weight), was used in research. At the same time, it was important not to reduce the concentration of volatiles in the onion.[3]

2. Experimental

In the experimental part of the work, bulbs were treated with plasma (using corona discharge, and plasma-activated water) and then, planted at different locations. The cultivated bulbs (for 5 months under field conditions) were transferred to the liquid sample, which was analyzed by reactive

ionization mass spectroscopy (PTR-TOF-MS) and tandem gas chromatography-mass spectroscopy (GC-MS) techniques. Onion planting was carried out in the years 2021, 2022 and 2023. During each year, soil samples were taken before and after the planting and characterized in the laboratory. Analyses included soil grain composition, soil exchange reaction, organic carbon content, and available nutrient analysis.

2.1. Treatment of bulbs

Four treatment variants were carried out before the planting as they are outlined in Table 1. The last variant was left untreated as a control sample. Each treatment was planted in four replicates, with ten bulbs each.

Tab. 1. Types of onion seeding bulbs treatments.

Variant	Type of treatment
1	Corona discharge 2x 10 seconds
2	Corona discharge 2x 40 seconds
3	Distilled water 24 hours
4	Plasma-activated water 24 hours
5	References

A multi-pronged system was used to treat the bulbs using corona discharge, as illustrated in Figure 1. The setup consisted of a bipolar pulsed voltage source, several spiked stainless steel electrodes charged positively, and a flat stainless steel electrode serving as the ground. After setting up the instrument, the bulbs were placed on the flat electrode, and corona discharge was initiated. The plasma treatment was performed in two repetitions. First from one side, and then from the other side, lasting either 10 or 40 seconds (corresponding to the treatment variants 2 and 3, as shown in Table 1).

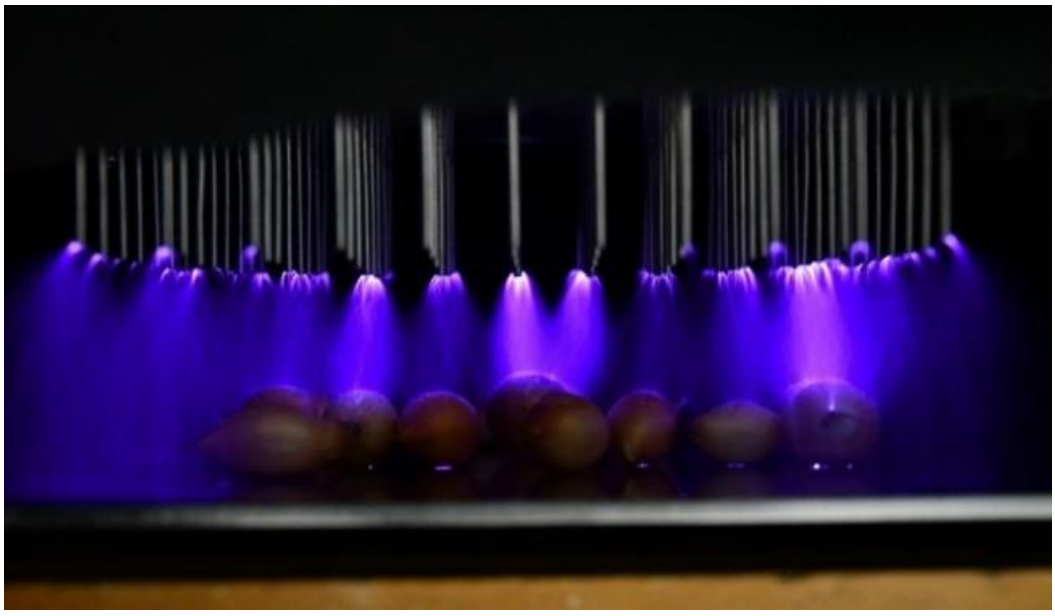

Fig. 1. Modification of bulbs by corona discharge.

A dielectric barrier discharge (DBD) with the liquid electrode system was used to prepare plasma-activated water (PAW), as shown in Figure 2. The system comprised a Petri dish with a graphite outer electrode at the bottom of the Petri dish and a second electrode placed on top of the Petri dish. This upper electrode is made of a ceramic plate on which a silver electrode has been deposited. The distilled water (75 mL) in the Petri dish was treated with the discharge, applied in 15-second intervals for eight

repetitions. The PET bottle was filled with bulbs up to its neck and topped up with plasma-activated water. This treatment was carried out for 24 hours. The next day, the bulbs were removed and immediately planted in the designated locations. The distilled water treatment was similar to the plasma-activated water treatment described above.

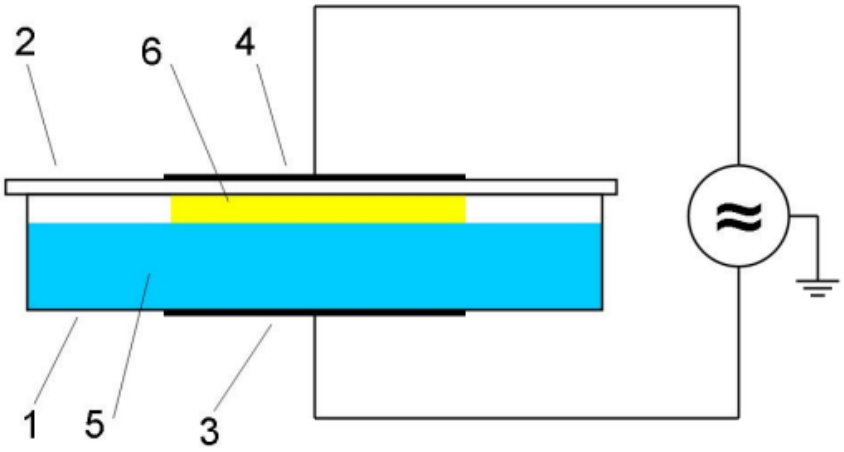

Fig. 2. Schema of PAW production: 1 – Petri dish, 2 – aluminium oxide plate, 3 – graphite electrode, 4 – silver electrode, 5 – plasma-activated water, 6 – plasma zone.[4]

2.2. Preparation and analysis of onions

The weighed, numbered and labelled bulbs were transported to the laboratory and converted to a liquid sample. The cleaned onion was cut in the middle and the thin slice approximately 4 cm wide was prepared. The onion slice was placed in a non-woven bag, which acted as a filter for the solid fibres of the onion. The bag was then placed in a polyethylene bag. The onion slice, prepared in this manner, was crushed and pressed using a roller. The liquid obtained was pipetted into pre-prepared tubes. These were immediately sealed with parafilm to prevent volatile compounds from escaping into the surrounding area. Measurement of the prepared sample was carried out using two analytical methods. Gas chromatography-mass spectroscopy (GC-MS Pegasus IVD (LECO)) was used for the qualitative analysis of volatiles in onions. The parafilm on the sample tube was pierced with a metal needle fitted with quartz fiber. A polydimethylsiloxane and divinylbenzene (PDMS/DVB) sorbent was coated on the fiber. Adsorption of the gaseous sample was carried out for 15 minutes. Subsequently, thermal desorption of the analytes into the carrier gas was followed. The sample was separated in the Rxi-5Sil MS capillary column and detected by mass spectrometer. Chromatograms were processed using the ChromaTOF program (Leco), which plotted the peaks for each volatile component of the sample. Then, these chromatograms were compared with the spectral library NIST v2.2.[5]

Mass spectroscopy with proton-transfer reaction ionization and a time-of-flight analyzer (Ionicon PTR-TOF-MS mass spectrometer) was used for the quantitative analysis of volatiles in onion. Initially, a background measurement without the sample was taken for 30 seconds. Subsequently, the gaseous substances from the liquid sample tube were analyzed and after 90 seconds, the tube was removed. In the last step, the spectrometer was relaxed for 60 seconds. The spectrum recording was stopped. The individual measurement steps are illustrated in Figure 3. Each set contained a maximum of 20 prepared samples. All measured mass spectra were processed using the PTR-MS Viewer 3 software. The data were calibrated, and the concentrations were exported for all masses to a text file for further work.

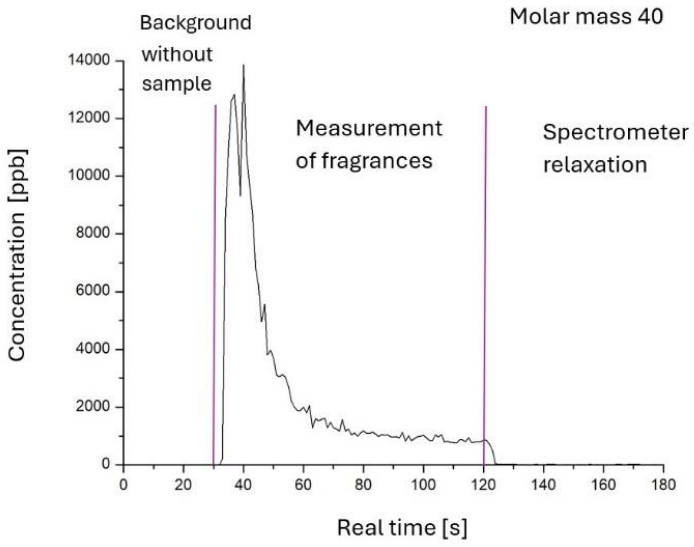

Fig. 3. Example of time recording of a measured sample from location 27, treatment variant 1, 1st. repetition, molar mass 40.

3. Results and discussion

Each location has its own specific soil characteristics that have a major impact on the plant growth and development. Soil analyses were conducted each year.

Thanks to the data obtained from qualitative analysis of the compounds (GC-MS), the fragrant compounds in the sample were identified. From these, three characteristic compounds (propanal, 2-methyl-2-pentenal, 2,4-dimethyl-thiophene) were selected. The agreement of the measured spectra with the spectrum library always involved several different substances with some similarity. Individual substances were identified by comparing the spectra from the library with the measured spectra. An example can be seen in Figure 4, which shows the measured mass spectrum and the NIST library spectrum for 2-methyl-2-pentenal.

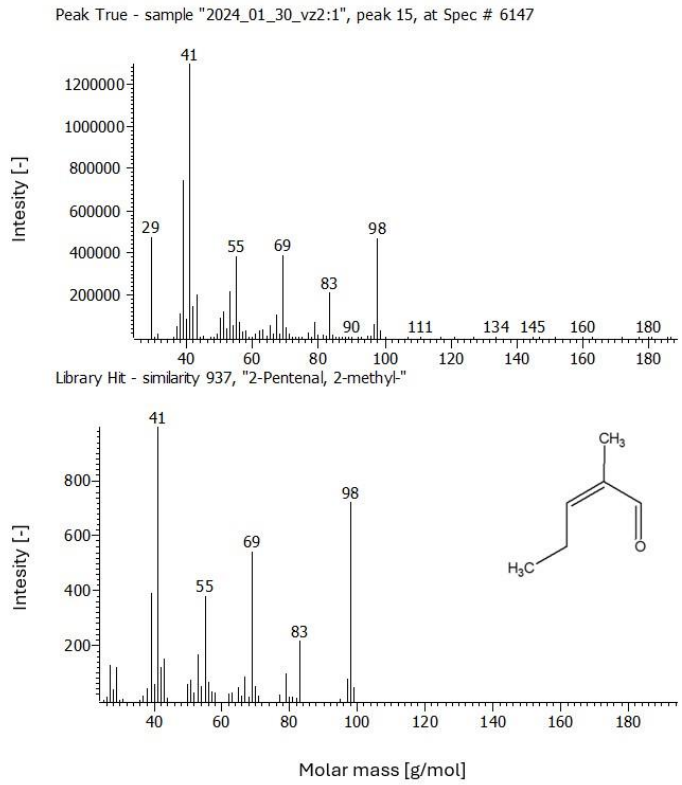

Fig. 4. Measured mass spectrum (above) and NIST spectrum (below) for 2-methyl-2-pentenal.

In all three years, the largest (heaviest) onion bulbs were grown across treatments at the site with moderately heavy soil. Onions prefer slightly acidic to neutral pH levels (specifically between 6.2 and 7.5), which this location fulfilled, with pH values ranging between 7 and 7.2. Additionally, the site had a sufficient quantity of organic carbon and moderately humic soil. In terms of nutrient content, it exhibited very high levels of phosphorus, potassium, calcium, and magnesium, making it well-suited for cultivation. Repeatedly, the highest weight yields over three years were obtained from seedlings treated with distilled water and also from the PAW-treated bulbs (Table 2). Yields increased by 26% compared to untreated bulbs. Lower yields were seen in bulbs that were treated twice with corona discharge for 10 seconds.

Tab. 2. Percentage yield variation compared to reference bulbs (Option 1) across years (average values).

Year	Bulbs treatment option				
	References	Corona 10 s	Corona 40 s	Distilled	PAW
	Deviation from reference [%]				
2021	0	-11	7	15	11
2022	0	8	0	-2	10
2023	0	-18	9	13	5
Total	0	-21	16	26	26

Based on the mass spectrometry data, graphs were created to show the average sample concentrations for each treatment variant. The effect of plasma treatment on the fragrance content of onions was evaluated using these graphs. For example, the graph corresponding to the concentration of propanal in the 2023 samples is shown in Figure 5. The average concentrations were calculated mostly from 4 samples, as some onions were rotten or completely spoiled. The different

treatment options are color-coded according to the legend in the upper left corner. Each graph shows the average concentration of the fragrance corresponding to the indicated molar mass, which is shown in the upper right corner alongside the year of planting. The numbered locations on the x-axis represent the sites where cultivation took place.

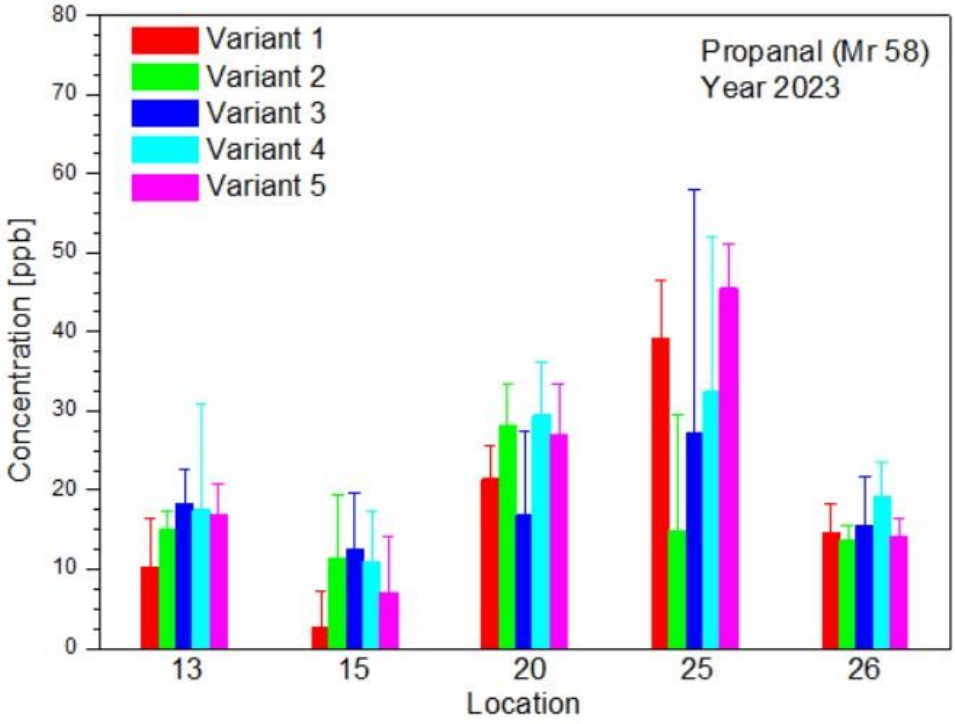

Fig. 5. Average propanal concentrations in 2023 samples.

The evaluation was performed using plots for all molar masses and locations discussed in this paper. Onions treated with 2x corona discharge for forty seconds repeatedly (18 times) had the highest concentration and were also the samples with the lowest concentration (10 times). The most frequent occurrence (18 times) of the lowest concentration was observed in the second treatment, where bulbs were treated with 2x corona discharge for 10 seconds.
It is important to keep in mind that the results are interpreted for a small, selected number of bulb samples. For clearer conclusions, instead of using 4 bulbs for one treatment variant, it would be necessary to measure preferably with 1000 bulbs. From the results obtained, it is evident that the plasma treatment can be useful for the treatment of bulbs in agriculture. An improvement in yield, while maintaining the fragrance content was confirmed. Also, a positive effect of the plasma treatment on the fragrance content of onions was observed.

4. Acknowledgements

This work was carried out within the frame of COST Action CA19110 (PlAgri).

5. References

[1] Mahmood I et al 2016 Plant, soil and microbes. (Springer)
[2] Judée F et al 2018 Water Research **133**
[3] Pauč N; Gherardi M, Shiratani M 2018 Plasma Processes and Polymers **15** 1700174
[4] Šimečková J, Krčma F, Klofáč D, Dostál L, Kozáková Z 2020 Water **12**
[5] NIST Standard Reference Database, Mass Spectral Library

EFFECT OF PLASMA-ACTIVATED WATER ON PHYSIOLOGICAL PARAMETERS IN BEAN PLANTS (*PHASEOLUS VULGARIS*)

Adriana Mišúthová[1], Zuzana Lukačová[2], Mustafa Ghulam[3], Ramin Mehrabifard[1], Božena Šerá[3], Zdenko Machala[1]

[1] *Division of Environmental Physics, Comenius University Bratislava, Slovakia*
[2] *Department of Plant Physiology, Comenius University Bratislava, Slovakia*
[3] *Department of Environmental Ecology and Landscape Management, Comenius University Bratislava, Slovakia*
E-mail: adriana.misuthova@fmph.uniba.sk

Our study explores the effects of plasma-activated water (PAW) used for seed priming, foliar application, and their combination on key physiological parameters of bean plants *Phaseolus vulgaris* (hybrid Petronilla) cultivated over three months under field conditions. The findings reveal that PAW treatments significantly enhanced the leaf area, the chlorophyll concentration, and the activity of selected antioxidant enzymes, demonstrating its potential to improve plant growth and stress resilience. These results highlight the effectiveness of PAW as a sustainable agricultural intervention to optimize crop performance in field conditions.

1. Introduction

The growing global population highlights the urgent need for sustainable food production. Modern agriculture heavily relies on commercial fertilizers, with nitrogen being a critical nutrient for plant growth [1, 2]. However, emerging physical methods like static magnetic fields, pulsed electric fields, and cold atmospheric gas plasmas offer innovative and potentially sustainable solutions, though their effects on plants require further investigation [3, 4]. One promising development a source of nitrogen is plasma-activated water (PAW), generated by electrical discharges in contact with water. Its chemical composition, including reactive oxygen and nitrogen species (RONS) like hydrogen peroxide (H_2O_2), nitrites (NO_2^-), and nitrates (NO_3^-), varies based on the plasma discharge type, interaction method, and water buffering capacity [5]. Hydrogen peroxide enters plant cells via facilitated diffusion through aquaporins, playing a crucial role in plant cells and tissues signalling, while NO_2^- and NO_3^- act as essential nitrogen sources, transported through specific transporters [6–9]. These properties position PAW as a sustainable, eco-friendly alternative to traditional fertilizers. This study explores the effects of different PAW applications, such as seed priming and foliar treatments, on bean plants. We examined its impact on key morphological and physiological parameters, including leaf area, concentration of chlorophylls, soluble phenolics, and selected antioxidant enzymes activity in young leaves of adult plants.

2. Methodology

Bean plants were cultivated over a three-month period in 90-liter pots located in the open-air atrium of the Faculty of Natural Sciences at Comenius University Bratislava. Each pot contained nine plants, and the study included the following experimental treatments: the control, seeds primed with PAW, the foliar application of PAW, and the combination of seed priming and foliar application. For priming, seeds were immersed in PAW for 8 hours. Bean seeds were soaked in plasma-activated water under controlled conditions, then air-dried before sowing. After drying seeds were sown directly into the pots. This treatment aimed to enhance germination and early plant growth. Foliar treatments were applied weekly, with each seedling receiving 3 mL of PAW per application. PAW was sprayed on Bean plants, starting when plants had three true leaves and continuing until flowering. Applications were done in early morning using a hand pump pressurized bottle to ensure even coverage.
PAW was prepared by batch treatment of regular tap water (pH=7.9) with multiple parallel transient spark (TS) discharges [10], typically 170 ml of tap water was treated by 17 discharges during 10 min.

Schematic diagram of TS plasma is shown in Fig 1. Each TS was set at approximately 1 kHz repetition frequency of the pulses and 1 cm distance of the power high voltage electrodes from the water surface. The PAW was applied to the plants fresh, within 10 min from the treatment. In such conditions its chemical characteristics were typically as follows: pH=7.5, concentrations of H_2O_2 = 452 µM , O_3=10 µM, NO_2- = 980 µM, NO_3- = 1.7 mM.

After three months, young leaves were sampled to evaluate the effects of plasma-activated water (PAW) on various physiological parameters. Leaf area was measured using the Image J software. Chlorophyll concentration was determined following the protocol described by Lichtenthaler [11]. Soluble phenolic content was quantified using the method outlined by Ainsworth and Gillespie [12]. In addition, the activity of the key antioxidant enzymes, including superoxide dismutase (SOD) [13], ascorbate peroxidase (APX) [14], guaiacol peroxidase (G-POX) [15] and catalase (CAT) [16] was monitored. Statistical analysis was conducted using Statgraphics Centurion XV version 15.2.05 (StatPoint, Inc., Warrenton, VA, USA) and Microsoft Excel (Microsoft Office). Treatment effects were assessed via analysis of variance (ANOVA), with single-step multiple comparisons performed, and the least significant difference (LSD) test applied at a significance level of $P < 0.05$.

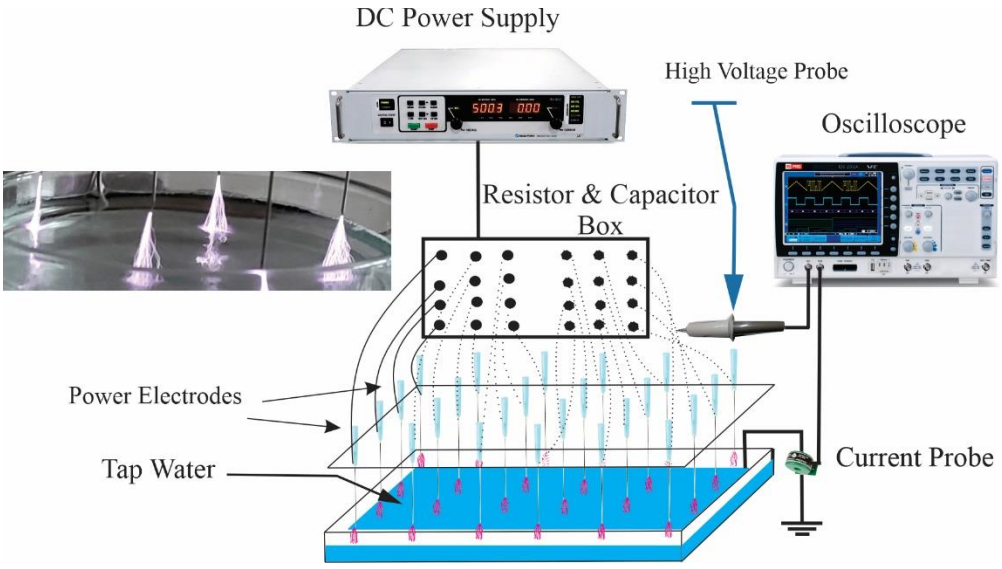

Fig. 1. Schematic diagram of transient spark discharge.

3. Results and Discussion

The foliar application of PAW significantly enhanced the leaf area of young bean plants, with a notable increase compared to the control. The combination of seed priming and foliar application resulted in the most pronounced differences, producing the largest leaves. A positive effect of PAW was also observed in chlorophyll concentration, a key indicator of photosynthetic activity, with a significant increase observed across all treatments compared to the control (Fig. 2). However, in the priming & spraying treatment, chlorophyll *a* concentration was significantly lowered compared with other PAW treatments. PAW acts as a nitrogen source for plants. Nitrate, essential for photosynthesis, supports chlorophyll synthesis in leaves contributing to their growth and development. This highlights the potential of PAW to enhance both physiological and biochemical parameters critical for plant productivity.

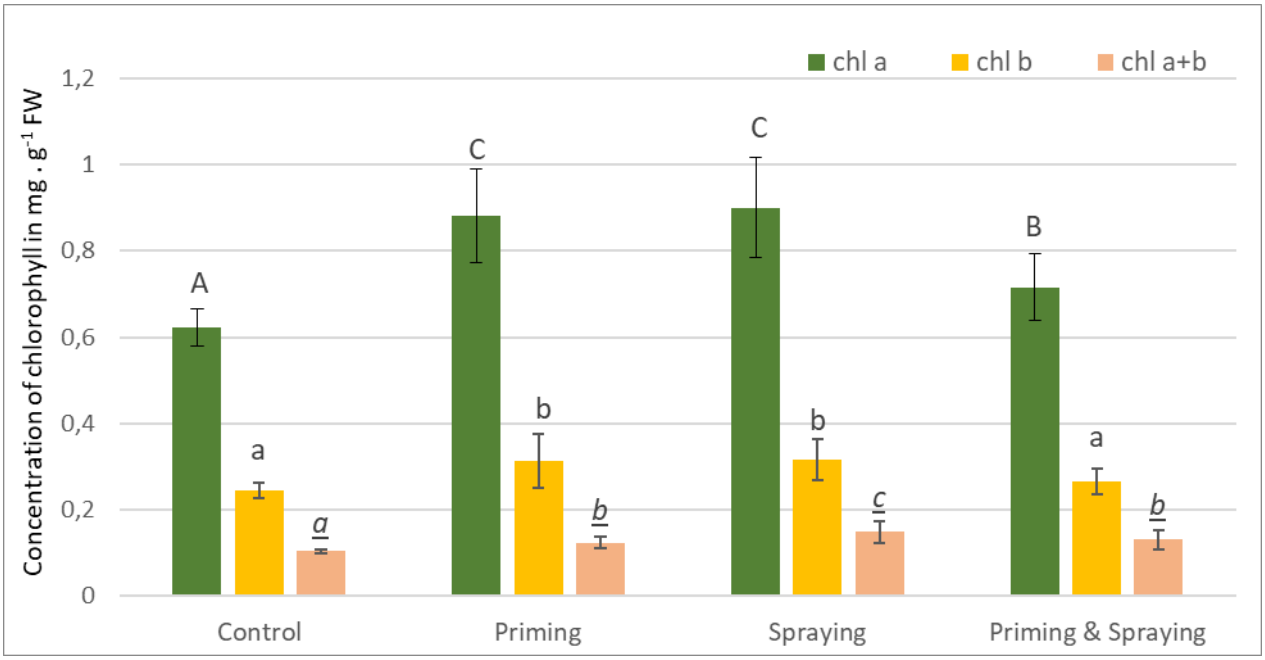

Fig. 2. Chlorophyll concentration in mg . g^{-1} fresh weight (FW) in young bean leaves. Different letters represent statistically significant differences among the treatments at $P \leq 0.05$.

Antioxidant enzymes are essential components of a plant's defence mechanism against environmental stresses. Superoxide dismutase is an essential enzyme in plant defence mechanisms against oxidative stress. Superoxide dismutase catalyses the dismutation of superoxide radicals into H_2O_2, which must subsequently be reduced to water to prevent oxidative damage. This critical step is facilitated by other enzymes in the antioxidant system, such as APX, G-POX and CAT, which exhibit high substrate affinity for H_2O_2. All three applications of PAW resulted in increased SOD activity compared to the control (Fig. 3A). While H_2O_2 plays a signalling role in stress responses, its excessive concentrations result in oxidative damage, compromising cellular integrity. Peroxidases are critical enzymes in detoxifying ROS, catalysing the conversion of H_2O_2 into water through electron donation, thereby protecting cells from oxidative stress [17]. A notable increase in APX activity was observed in seeds primed with PAW, and in the treatments combining seed priming with foliar application (Fig. 3B). Conversely, the foliar application alone did not significantly affect APX activity. In this case, the G-POX enzyme demonstrated the highest activity, suggesting a compensatory mechanism to manage ROS levels under this treatment condition (Fig. 3C). The differing reactions of these two peroxidases can be attributed to their distinct roles and locations: G-POX is a secretory extracellular enzyme, whereas APX is intracellular. Consequently, they operate in different environments and participate in distinct pathophysiological processes. Similarly, CAT activity was elevated in every PAW treatment relative to the control (Fig. 3D), likely due to its role in scavenging the oxidative effects of H_2O_2 present in PAW. Chen et al. [18] previously demonstrated that appropriate nitrogen application enhances the concentrations of SOD and CAT in sweet potato, findings consistent with the results of this study. The elevated levels of these antioxidant enzymes in this experiment suggest an improved tolerance to oxidative stress induced by ROS. During the vegetative stage, plants experience an increased demand for nitrogen to support their rapid growth. The application of PAW during this critical phase may effectively meet this nitrogen requirement, as PAW contains high concentrations of nitrite (NO_2^-) and nitrate (NO_3^-). This nitrogen supply likely contributes to the observed increase in chlorophyll content (Fig. 2) and the enhanced activity of antioxidant enzymes (Fig. 3), which can be attributed to the reactive nitrogen species (RNS) delivered through PAW treatments.

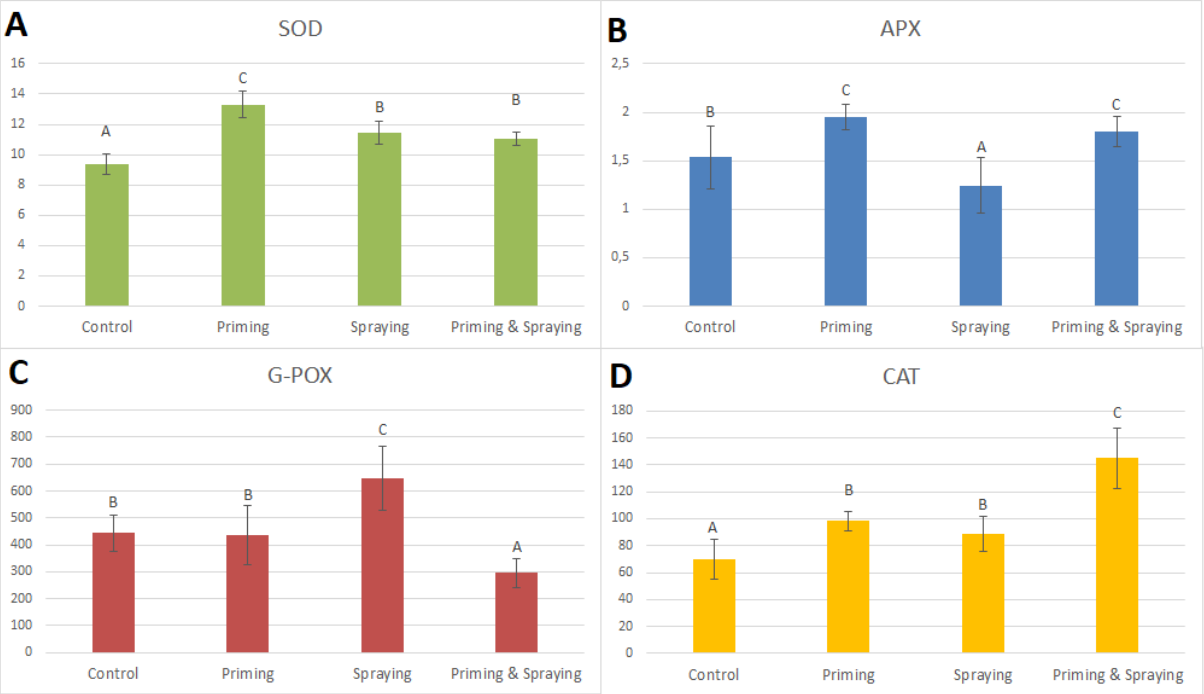

Fig. 3. Activity of SOD (A), APX (B), G-POX (C) and CAT (D) antioxidant enzymes in young leaves of beans plants. Different letters represent statistically significant differences among the treatments at $P \leq 0.05$.

4. Conclusion

Our study demonstrates that PAW significantly enhances adult bean plant growth and oxidative stress tolerance. Plasma activated-water treatments increased the leaf area and chlorophyll content in young bean plants, with the combination of seed priming and foliar application yielding the most significant effects. Furthermore, different application of PAW elevated the activity of almost all monitored key antioxidant enzymes, enhancing the plants' ability to mitigate oxidative damage. By providing reactive nitrogen species (RNS) and nitrates, PAW effectively meets nitrogen demands during critical vegetative growth stages, thereby improving physiological performance and stress resilience.

5. Acknowledgements

The research was supported by the EU project NextGenerationEU through the Recovery and Resilience Plan for Slovakia under the projects No. 09I03-03-V02-00036, Environmental applications of electrical discharges for water, air cleaning, and agriculture No. 09I03-03-V03-00033(EnvAdwice) and by the Grant Slovak Research and Development Agency No. APVV-22-0247.

6. References

[1] Masclaux-Daubresse C, Daniel-Vedele F, Dechorgnat J, Chardon F, Gaufichon L and Suzuki A 2010 *Annals of Botany* **105**, 1141–1157.
[2] Sharma A 2017 *International Journal for Research in Applied Science and Engineering Technology* **5**, 677–680.
[3] Reina F.G, Pascual L.A and Fundora I.A 2001 *Bioelectromagnetics* **22**, 596–602.
[4] Sonoda T, Takamura N, Wang D, Namihira T and Akiyama H 2014 *IEEE Transactions on Plasma Science* **42**, 3202–3208.
[5] Zhou R, Zhou R, Wang P, Xian Y, Mai-Prochnow A, Lu X, Cullen P.J, Ostrikov K and Bazaka K 2020 *Journal of Physics D: Applied Physics* **53**, 303001.
[6] Kučerová K, Henselová M, Slováková L, Bačovčinová M and Hensel K 2021 *Applied Sciences* **11**, 1985.

[7] Bienert G.P, Schjoerring J.K and Jahn T.P 2006 *Biochimica et Biophysica Acta (BBA) - Biomembranes* **1758**, 994–1003.
[8] Goyal S.S and Huffaker R.C 1986 *Plant Physiology* **82**, 1051–1056.
[9] Kotur Z, Siddiqi Y.M and Glass A.D.M 2013 *New Phytologist* **200**, 201–210.
[10] Machala Z, Tarabová B, Sersenová D, Janda M, Hensel K 2019 *Journal of Physics D: Applied Physics* **52**, 034002.
[11] Lichtenthaler H.K 1987 *Methods in Enzymology* **148**, 350.
[12] Ainsworth E.A and Gillespie K.M 2007 *Nature Protocols* **2**, 875–877.
[13] Garcia-Limones C, Hervás A, Navas-Cortés J.A, Jiménz-Díaz R.M and Tena M 2002 *Physiological and Molecular Plant Pathology* **61**, 325–337.
[14] Nakano Y and Asada K 1981 *Plant and Cell Physiology* **22**, 867–880.
[15] Frič F and Fuchs W.H 1970 *Journal of Phytopathology* **67**, 161–174.
[16] Hodges D.M, Andrews C.J, Johnson D.A and Hamilton R. I 1997 *Journal of Experimental Botany* **48**, 1105–1113.
[17] Zhou R, Zhou R, Zhang X, Zhuang J, Yang S, Bazaka K and Ostrikov K 2016 *Scientific Reports* **6**, 32603.
[18] Chen X, Kou M, Tang Z, Zhang A, Li H and Wei M 2017 *PLOS ONE* **12**, e0189715.

INFLUENCE OF APPJ ON PRIMARY TEETH ENAMEL

Joanna Pawłat[1], Michał Kwiatkowski[1], Piotr Terebun[1], Dawid Zarzeczny[1] Elżbieta Grządka[2], Agnieszka Starek-Wójcicka[3], Marta Krajewska[3], Monika Machoy[4], Agnieszka Mazur-Lesz[5]

[1]Department of Electrical Engineering and Smart Technologies, Lublin University of Technology, Nadbystrzycka Street 38A, 20-618 Lublin, Poland
[2]Faculty of Chemistry, Institute of Chemical Sciences, Maria Curie-Skłodowska University, M. Skłodowskiej - Curie 3 Sq., 20-031 Lublin, Poland
[3]Department of Biological Bases of Food and Feed Technologies, Faculty of Production Engineering, University of Life Sciences in Lublin, 20-612 Lublin, Poland
[4]Department of Periodontology, Faculty of Medicine and Dentistry, Pomeranian Medical University, Powstańców Wielkopolskich 72 Street, SPSK 2, 70-111 Szczecin, Poland
[5]Private Dental Office, Witkiewicza 49u/14 Street, 71-124 Szczecin, Poland
E-mail: j.pawlat@pollub.pl

The impact of plasma treatment duration on primary tooth enamel was investigated. A dielectric barrier discharge (DBD) plasma jet was used to generate plasma, and primary teeth were exposed for intervals of 5, 10, or 20 minutes. Enamel properties—such as colour, contact angles, surface roughness, surface topography, and elemental composition—were analysed before and after treatment. Results indicate that plasma exposure time is a critical factor in achieving desired effects like whitening and enhanced wettability. However, extended plasma treatment may lead to irreversible enamel damage. Plasma treatment for teeth presents promising potential as an alternative method for whitening or as a preparatory step before other dental procedures.

1. Experimental set-up

The research material consisted of primary teeth of six children. DBD plasma jet reactor [1,2] was powered by a high-voltage power supply with the following output parameters: VRMS = 3.25 kV, f = 28.5 kHz. The flow of the gas mixture of 0.013 dm3/min of oxygen with 1.667 dm3/min of helium was controlled by gas flow controllers. The plasma treatment time was 5, 10, and 20 minutes, respectively. The schema of the set up are presented in the Fig. 1A.
Following exposure to the plasma for specified durations, parameters including colour, surface roughness and topography, water contact angles (WCA) and elemental composition were assessed.

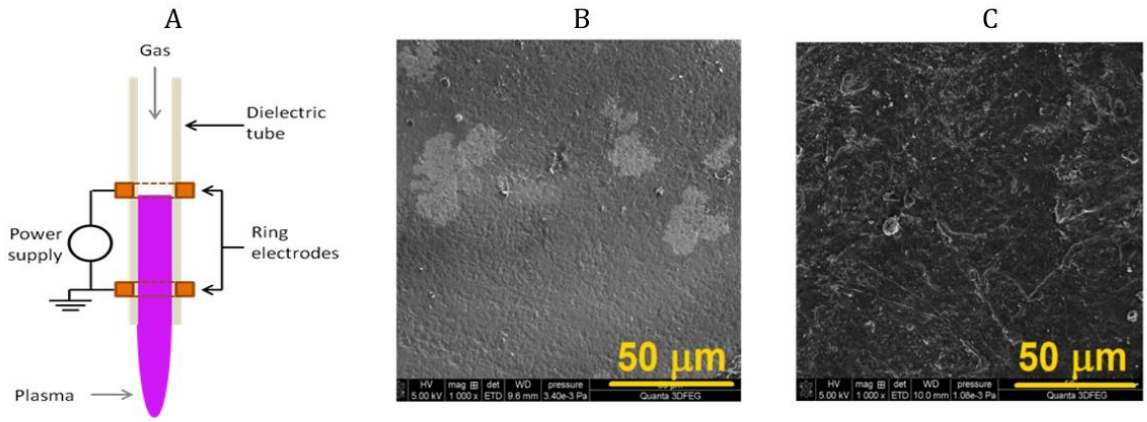

Fig. 1. Experimental set-up (A), micrographs of teeth surfaces before (B) and after 10 min CAP treatment (C).

2. Results and conclusions

The examined primary teeth display variations in the brightness parameter (L*) based on tooth type and individual characteristics. Notably, samples treated with cold atmospheric plasma (CAP) exhibit a higher L* value, indicating a lighter colour compared to untreated teeth. The chromatic colour parameters for all tested samples show a negative a* value (indicating a greener hue than red) and a negative b* value (indicating a bluer hue than yellow). Untreated teeth show higher b* values, suggesting a greater presence of yellow. Additionally, plasma treatment has been shown to enhance the hydrophilicity of tooth surfaces (Fig. 2), making them considerably more heterogeneous and rougher, with larger height variations, which become more pronounced with longer treatment times.

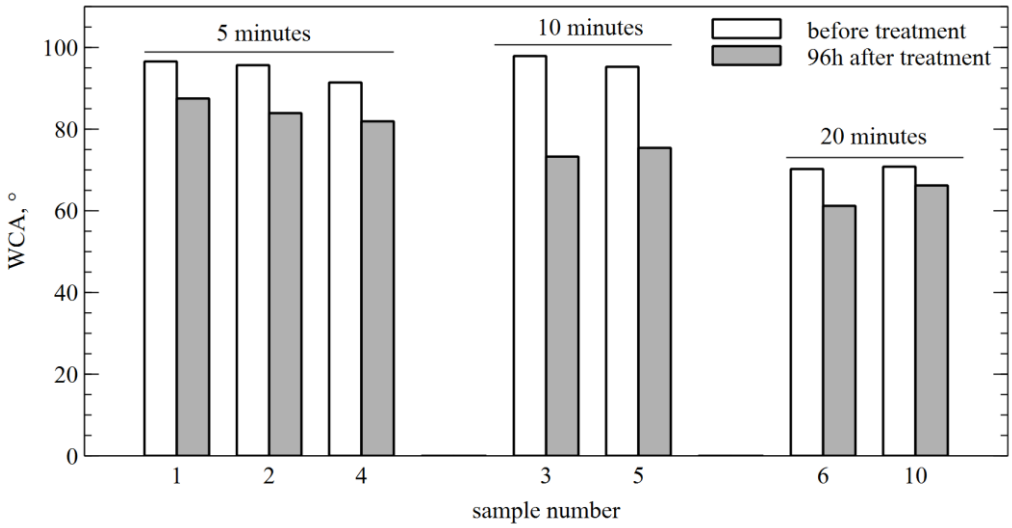

Fig. 2. WCA of individual samples before and after plasma treatment for different times.

SEM micrographs (Fig. 1B,C) confirm that CAP treatment disrupts the homogeneity of the primary tooth surface. Elemental analysis reveals only minor changes post-treatment, implying that the morphological changes observed in the enamel surface are predominantly physical rather than due to chemical interactions with plasma components. Overall, a treatment duration of 5–10 minutes appears optimal for achieving tooth whitening, enhanced hydrophilicity, and increased surface roughness without compromising enamel integrity.

Acknowledgement

We acknowledge fruitful discussions and scientific cooperation with members of CEEPUS CIII-AT-0063, COST Action PlAgri CA19110 and COST Action PlasTHER.

3. References

[1] Kwiatkowski M, Terebun P, Kučerová K, Tarabová B, Kovalová Z, Lavrikova A, Machala Z, Hensel K, Pawłat J 2023 *Materials*, **16(3)**, 1167.

[2] Kwiatkowski M, Terebun P, Mazurek P, Pawłat J 2018 *Sensors and Materials*, **30** 1207–1212.

APPLICATION OF NON-THERMAL PLASMA GENERATED BY PIEZOELECTRIC DIRECT DISCHARGE ON SEEDS AND STUDY OF ITS EFFECT

Petra Šrámková[1], Dominik Kostoláni[2], Stanislav Kyzek[3], Sahila Gahramanli[1], Monika Stupavská[4], Ali Jamaati Kenari[4], Eliška Gálová[3], Renáta Švubová[2], Anna Zahoranová[1]

[1] *Department of Experimental Physics, Faculty of Mathematics, Physics and Informatics, Comenius University Bratislava, Mlynská dolina, 842 48 Bratislava, SR*

[2] *Department of Plant Physiology, Faculty of Natural Sciences, Comenius University Bratislava, Mlynská dolina, Ilkovičova 6, 842 15 Bratislava, SR*

[3] *Department of Genetics, Faculty of Natural Sciences, Comenius University Bratislava, Mlynská dolina, Ilkovičova 6, 842 15 Bratislava, SR*

[4] *Department of Plasma Physics and Technology, Faculty of Science, Masaryk University, Kotlářská 2, 611 37 Brno, Czech Republic*

E-mail: petra.sramkova@fmph.uniba.sk

The use of various plasma sources in agriculture is a hot topic in the portfolio of plasma applications today. In this context, basic research on new plasma sources under laboratory conditions is crucial to consider their future application on an industrial scale. In this study, we investigate the potential of the commercial piezoelectric plasma discharge Piezobrush PZ3 for seed treatment. This portable plasma source generates a non-thermal plasma in ambient air. We monitored changes in surface wettability and chemical composition of pea seeds (Saxon var.) after treatment in the plasma exposure time range of 5-240 s. We also investigated the effects of this plasma source on the germination potential and possible DNA damage of model seeds. Preliminary results showed a positive effect on seed and seedling vigour. In addition, the Piezobrush PZ3 does not cause any DNA damage. Based on these positive results, our next step is to analyse and understand in detail the relationship between the nature of the plasma and the improvement of germination.

1. Introduction

In recent years, non-thermal plasma has attracted attention in agricultural research due to its positive effect on seed germination and viability and its decontaminating effect on undesirable microorganisms present on the seed coat [1,2]. Many different plasma sources for seed treatment have been investigated so far, but they all have one thing in common: they generate non-thermal plasma (NTP), which is crucial for the treatment of sensitive biological material.

The Piezobrush PZ3 is a commercially available portable device that generates NTP at atmospheric pressure in ambient air. It is a type of piezoelectric direct discharge (PDD) maintained by a high-performance piezoelectric transformer [3]. Due to its compactness, efficiency and versatility, this plasma source has been already studied for treatment of polymer substrates [4,5] or for biomedical applications [6].

Since Piezobrush PZ3 is a quite new plasma source commercialized in 2020, our aim is to investigate its effect on seeds in order to further expand its application in agriculture. In the present study, the Piezobrush plasma source was applied to pea seeds (Saxon var.) and the effect of exposure time in a wide range of values on the physicochemical properties of the seed coat and the physiological characteristics of seeds and seedlings was investigated.

2. Methods

Plasma treatment was performed by the Piezobrush PZ3 (Relyon plasma GmbH, TDK Group Company, Germany), which was fixed in the special holder in the vertical stable position. In order to treat the seeds evenly, a specially designed rectangular container with dimensions of 3 × 2 cm, which

can comfortably hold 10 pea seeds, was fabricated by 3D printer. By manually shaking the container during the treatment process, the PDD ensured thorough exposure of all sides of the peas. Based on the preliminary results, the distance of the seeds from the piezoelectric tip was adjusted to 3 and 5 mm. The seeds were treated with a maximum input power of 8 W operating at a resonant frequency (second harmonic) of 50 kHz. We investigated plasma exposure times in the range of 5-240 s. Surface wettability and chemical composition were analysed by measuring the water contact angle (WCA), X-ray photoelectron spectroscopy (XPS) and attenuated total reflection Fourier transform infrared spectroscopy (FTIR–ATR). In addition, the germination potential, the vitality indices of seeds and seedlings as well as DNA damage were analysed.

3. Results

The changes in wettability on the surface of the pea seeds monitored by WCA measurements showed that the WCA values decreased from the reference value of 103.2° to the lowest value of 33° at a 60-s treatment at a distance of 3 mm (see Fig. 1a). Extending the exposure time (90 and 120 s) did not lead to a further reduction in the WCA values. The very high standard deviation and the very uneven treatment at 5 s indicate low homogeneity at the lower exposure times, as the movement of the seeds was imperfect and therefore the treatment was not accurate. Considering the chemical changes on the pea surface using XPS measurements, the exposure times of 30 s and 60 s resulted in only negligible changes in the atomic content. The C content decreased from the reference value of 82 % to 78 and 76 % and the O content increased from 15 % to 17 and 20 % at 30 s and 60 s, respectively. At a treatment time of 90 s, the changes were more pronounced, as the carbon content decreased to 60 % and the oxygen content even increased to 35 %. The deconvoluted C1 spectra also confirmed the highest oxidation after 90 seconds of plasma treatment (see Fig. 1b). Plasma application leads to an increase in wettability, which is driven by the oxidation of the non-polar molecules that form the seed coat (lipidic and aromatic molecules). This leads to a higher hydrophilicity of the coat and a higher proportion of polar functional groups, as demonstrated by XPS measurements.

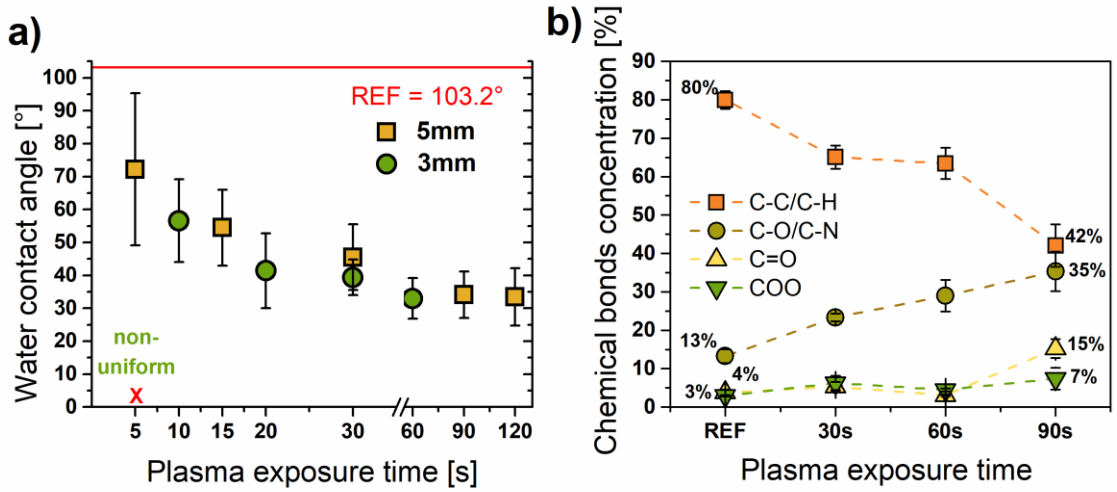

Fig. 1. a) Dependence of WCA on plasma exposure time for 3 mm and 5 mm distance of seeds from the piezoelectric tip; b) Concentration of chemical bonds observed from deconvolution of C1s peaks of reference sample and plasma treated seeds.

The application of the Piezobrush PZ3 plasma source on pea seeds has also affected the growth parameters of seeds and seedlings, and at the moment we have some preliminary results. Since we used pea as a model seed with an initial excellent germination of about 100 %, germination could not be further improved. However, we were able to achieve faster germination and an increase in the vigour of seeds and seedlings after the plasma treatment. The threshold for a positive effect of

plasma treatment was 240 s, when germination dropped to 80 %. In addition, the Comet assay showed no DNA damage even after 240 seconds and at all lower exposure times.

Based on these positive results, our next step is to analyse and understand in detail the relationship between the nature of the plasma and the improvement of germination. These promising results along with the already published industrial upscaling opportunity[7] open the new possibilities for utilization of Piezobrush PZ3 also in agriculture.

4. Acknowledgements

We would like to thank our colleague Martin Kuťka for the fabrication of rectangular container for keeping the seeds under the plasma source. We would also like to thank our former colleague Juliána Tomeková, who carried out the OES measurements.
This work was supported by the Slovak Research and Development Agency under the Contract no. APVV-21-0147.

5. References

[1] Waskow A, Howling A and Furno I 2021 *Front. Phyiscs* **9** 1–23.
[2] Bilea F, Garcia-vaquero M, Magureanu M *et al.* 2024 *Crit. Rev. Plant Sci.* **43** 428-486.
[3] Korzec D, Hoppenthaler F, Burger D *et al.* 2020 *Plasma Process. Polym.* **17** e2000053.
[4] Korzec D, Andres T, Brandes E and Nettesheim S 2021 *Polymers (Basel)* **13** 2711.
[5] Korzec D, Hoppenthaler F *et al.* 2022 P*lasma* **5** 111–129.
[6] Muslim R N and Majeed M A 2024 *J. Int. Dent. Med. Res.* **17** 962–975.
[7] Korzec D, Hoppenthaler F, Shestakov A et al. 2021 *Plasma* **4** 281–293.

INFLUENCE OF PLASMA ACTIVATED WATER ON THE PLANT GROWTH AND VITALITY

Tomáš Vozár[(1,*)], Ludmila Čechová[(1,2)], Kristína Trebulová[(1)], František Krčma[(1)], Zdenka Kozáková[(1)]

[1]*Faculty of Chemistry, Brno University of Technology, Purkyňova 118/464, 612 00, Brno, Czech Republic*

[2]*Central European Institute of Technology, Brno University of Technology, Purkyňova 123, 621 00, Brno, Czech Republic*

E-mail: Tomas.Vozar1@vut.cz

In this work, we investigated the effect of plasma activated water (PAW) prepared by pin hole electrode generating plasma directly in liquids with synthetic air flowing into the discharge on plant vitality and growth [1,2,3]. Distilled as well as tap water was treated by plasma discharge. Content of reactive oxygen and nitrogen species in PAW was determined colorimetrically by using UV-Vis spectrophotometer. We used pot experiment with radish (*Raphanus sativa* L.) plants to investigate the effect of long-term treatment with PAW on vitality and growth. The effect on the growth was observed through determination of fresh weight and dry matter content, the effect on vitality was assessed through chlorophyll fluorescence and the NDVI index. The results show positive effects of plasma activated water on the plant growth. The results further show that PAW does not adversely affect plant vitality.

1. Introduction

Nitrogen is the main element of plant nutrition. Major source of the inorganic nitrogen taken up by the roots of plants is nitrate. Sources of nitrate are generally derived from inorganic minerals by a high energy-consuming and not verry environmentally friendly chemical process [4]. Current research in this field is focusing on finding new alternative ways of preparing fertilizers. Promising opportunity brings to the table treating water with plasma. Nitrogen available in the air is fixed into the water using plasma. The treatment of water with plasma produces a mixture of nitrate, nitrite, and hydrogen peroxide as its major constituents. This way it was prepared so called plasma activated water (PAW).

2. Experimental setup

Plasma activated water was prepared by pin hole electrode generating plasma directly in liquids with synthetic air flowing into the discharge (nitrogen and oxygen in a 4:1 ratio, total air flow rate of 0.5 l/min) (fig. 1.). 500 ml of water was treated for 8 minutes with discharge [1,2,3]. After treatment physicochemical properties of PAW were analysed by measuring pH, conductivity and concentration of H_2O_2, NO_2^- and NO_3^- was determined colorimetrically and by UV-Vis spectrophotometry [5]. Optical emission spectroscopy was used for diagnostics of generated plasma.

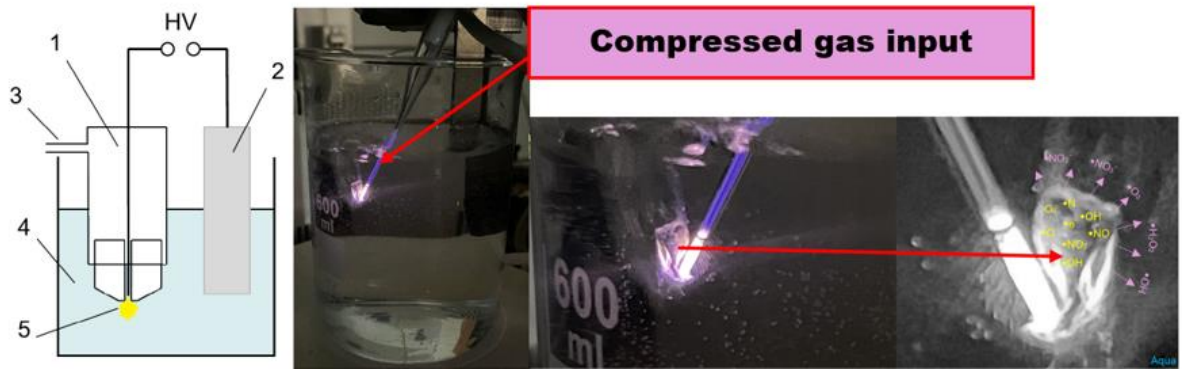

Fig. 1. System for plasma activated water preparation [1,2,3].

Soil was placed in pots (approximately 1400 g of soil into each pot), in total 120 pots were prepared. The pots were placed in grow boxes with artificial lighting (ViparSpectra PRO 600/100W, 16/8 h light/dark). The pots were divided into four variants based on the application of PAW, with 30 pots in each variant:

- Pots irrigated with PAW prepared from distilled water (PAW DW)
- Pots irrigated with PAW prepared from tap water (PAW TW)
- Pots irrigated with untreated tap water with application of PAW as a foliar spray (TW/PAW DW)
- Control variant irrigated with tap water (TW)

The whole experiment lasted for 30 days from the day of sowing. Pots were irrigated every 2 days, with PAW prepared on the day of irrigation. The experiment was carried out three times over the period of 12 months to ensure the reproducibility. Fluorescence parameters were measured on the 29th day (the day before the end of the experiment) using FluorPen FP 110 instrument. At the end of the experiment, radishes were carefully taken out of pots, without damaging the roots. They were washed with water and separated into two parts (leaves and roots). Both parts were weighed on scales. To determine the dry matter, the samples were placed in a vacuum drying oven, and they were dried at 60 ˚C for 24 h. After drying was completed, the samples were cooled and then weighed in on scales. Subsequently, the dry matter (DM) mass was calculated in percentage as shown in the formula 1, where m_D is weight of dried matter, m_E is weight of empty Petri dish and m_F is weight of fresh matter.

$$DM = \frac{m_D - m_E}{m_F} \cdot 100 \quad (1)$$

3. Results

Optical emission spectroscopy results showed us that initially intensity of emission of ·OH radicals and molecular nitrogen are decreasing, in contrast intensities of atomic hydrogen, oxygen and nitrogen lines are increasing. After some time, these processes stabilize. In the case of tap water, it stays constant throughout the whole treatment.

Results obtained from optical emission spectroscopy showed us initiated production of reactive species in discharge. This was verified by measuring its concentration in plasma activated water. Composition of PAW (table 1) prepared with system generating discharge directly in water showed us that in relatively short time the water is enriched with large amount of nitrates and nitrites. This is quite useful in agricultural applications of plasma activated water. Tap water already contains ions that are causing higher conductivity, which is important for easier ignition of the discharge, which leads to higher production of RONS. The presence of RONS in PAW further increases conductivity. pH of PAW DW was adjusted to 5.5 with PBS as 3.3 could be harmful to plants.

Tab. 1. Physicochemical properties of PAW used in experiment

Type of water	H_2O_2 [mg/L]	NO_2^- [mg/L]	NO_3^- [mg/L]	pH [-]	Conductivity [µS/cm]
Tap water	<LOD*	<LOD*	31.8±1.4	7.5±0.2	485±6.8
Distilled	<LOD*	<LOD*	<LOD*	6.7±0.4	1.6±0.2
Plasma activated distilled water (PAW DW)	3.0±0.6	20.2±0.4	65.3±3.7	3.3±0.1	260±6.0
Plasma activated tap water (PAW TW)	4.8±0.5	26.9±0.5	110.5±6.3	7.4±0.2	650±3.5

**LOD = limit of detection*

The effect of irrigation and foliar application of PAW on the fresh matter of radish plants was observed. According to results presented in table 2 both irrigation and foliar application had significant positive effect on fresh matter of roots. In the case of leaves the effect of PAW was significant in second and third repetition. In conclusion there was an overall increase in the weight of the plant and no preference of certain part growth was observed.

Tab. 2. Fresh matter of radishes

Variant (Root)	1st repetition (g)	2nd repetition (g)	3rd repetition (g)
PAW DW	46.8±17.1	16.9±7.1	27.2±10.7
PAW TW	44.6±11.7	17.6±6.9	21.1±8.2
TW/PAW DW	42.3±17.3	22.6±11.2	24.8±8.6
TW	32.2±13.2	12.3±7.3	19.6±9.4
Variant (Leaves)	1st repetition (g)	2nd repetition (g)	3rd repetition (g)
PAW DW	21.8±5.2	14.4±3.6	18.1±3.6
PAW TW	22.1±4.9	14.4±3.4	13.1±2.9
TW/PAW DW	24.7±6.7	15.8±2.5	11.2±2.3
TW	21.8±6.0	11.6±2.5	10.4±1.9

The effect of irrigation and foliar application of PAW on the dry matter of radish plants was also observed. According to results presented in table 3 both irrigation and foliar application did not have significant effect on dry matter of roots. In the case of leaves the effect of PAW was also not significant. In conclusion there was not observed significant lowering of dry matter content in comparison with control group, so we can say PAW did not affected negatively dry matter.

Tab. 3. Dry matter of radishes

Variant (Root)	1st repetition (%)	2nd repetition (%)	3rd repetition (%)
PAW DW	4.38±0.40	5.40±1.24	5.46±0.97
PAW TW	5.14±1.48	4.57±0.63	7.17±0.90
TW/PAW DW	4.28±1.31	4.70±0.76	8.32±1.28
TW	4.66±1.37	4.98±0.61	6.57±0.90
Variant (Leaves)	1st repetition (%)	2nd repetition (%)	3rd repetition (%)
PAW DW	5.19±0.49	6.92±0.84	6.24±0.60
PAW TW	5.43±0.79	6.64±0.39	8.26±0.86
TW/PAW DW	4.78±0.86	6.72±1.01	8.69±1.18
TW	4.61±0.87	6.50±0.63	7.74±0.78

Fluorescence measurement results showed no significant effect on maximum quantum yield on plants treated with PAW in comparation with control group. That means plants treatment with PAW did not affect the overall vitality of plants. Also, NDVI index measurements showed that plants health was not affected by PAW, as index was not lowered by PAW treatment compared to control group. As is widely known most of the fertilizers used in agriculture contain nitrogen. As we expected higher content of nitrates and nitrites in PAW positively affected growth of radish. That's why we can say promising PAW is alternative source of nitrogen for agriculture that is prepared by a more environmentally friendly way than inorganic fertilizers.

4. Acknowledgements

This work was carried out within the frame of COST Action CA19110 (PlAgri).

5. References

[1] Krčma F et al 2018 *Plasma Sourc. Sci. and Technol.* **27** 065001

[2] Krčma F 2019 European Patent EP3122161B1.

[3] L. Čechová, F. Krčma, M. Kalina, O. Man and Z. Kozáková, *Journal of Applied Physics*, 2021**129**233304.

[4] N. Punith, R. Harsha, R. Lakshminarayana, M. Hemanth, M. S. Anand and S. Dasappa, *Advanced Materials Letters*, 2019**10**700-704.

[5] Z. Kozáková, L. Čechová, K. Lišková, K. Šindelková, S. Korečková and F. Krčma, *PLASMA PHYSICS AND TECHNOLOGY*, 2024**11**1-6.

QUALITY TEST OF FRESHLY PRESSED CARROT JUICE AFTER COLD ATMOSPHERIC PLASMA TREATMENT

Dawid Zarzeczny[1], Joanna Pawłat[1], Piotr Terebun[1], Michał Kwiatkowski[1], Agnieszka Starek-Wójcicka[2], Agnieszka Sagan[2], Zbigniew Kobus[2], Barbara Chudzik[2], Dariusz Andrejko[2], Elżbieta Grządka[3]

[1] *Department of Electrical Engineering and Smart Technologies, Lublin University of Technology, 20-618 Lublin, Poland*

[2] *Department of Biological Bases of Food and Feed Technologies, University of Life Sciences in Lublin, 20-612 Lublin, Poland*

[3]*Faculty of Chemistry, Institute of Chemical Sciences, Maria Curie-Skłodowska University, 20-031 Lublin, Poland*

E-mail: d.zarzeczny@pollub.pl

The steadily growing consumer interest in consuming minimally processed food rich in bioactive components has created a need to investigate the impact of a novel low-temperature preservation method on the quality characteristics of freshly pressed carrot juice (Nerac variety). The conducted research analyzed the effects of plasma gas (air) generated in a Glide-arc reactor operating under atmospheric pressure on the microbiological, physicochemical, and structural changes of product samples.

1. Material and research methods

The study material consisted of juice obtained from Nerac variety carrots, extracted using a slow-juicer by Hurom (Model HZ, Owadów, Sławno). Part of the juice was treated with cold plasma for 10, 20, or 30 minutes, while the untreated juice served as the control. The samples were stored in a refrigerator at 6°C for 3 days.

For the treatment with non-equilibrium plasma, a single-phase gliding arc discharge reactor operating under atmospheric pressure was used. It consisted of a system with two profiled copper electrodes, each 78 mm in length, with a divergence angle of 12°. To minimize gas leakage from the system, the electrodes were enclosed in a glass shield with a diameter of 60 mm. The power supply system provided high-voltage pulses with a maximum value of 3.5 kV and an apparent power of 60 VA.

A glass container with an internal diameter of 63 mm was filled with 25 ml of freshly pressed carrot juice and positioned so that the liquid surface was 10 mm away from the electrode surface. Compressed air was used as the working gas at a flow rate of 440 l/h, regulated using a table-mounted glass rotameter (Zakłady Automatyki "ROTAMETR," Poland). Due to the forced gas flow, the generated electric arc moved along the electrodes toward the liquid, where it extinguished and then re-ignited in the ignition zone. To ensure uniform exposure to active factors, the juice was stirred during treatment using a magnetic stirrer and Teflon-coated stirring bars (Figure 1). A DT-847U temperature meter (Yu Ching Technology) with a K-type thermocouple was used to monitor the liquid's temperature after treatment. The maximum observed temperature for the longest treatment time did not exceed 39°C.

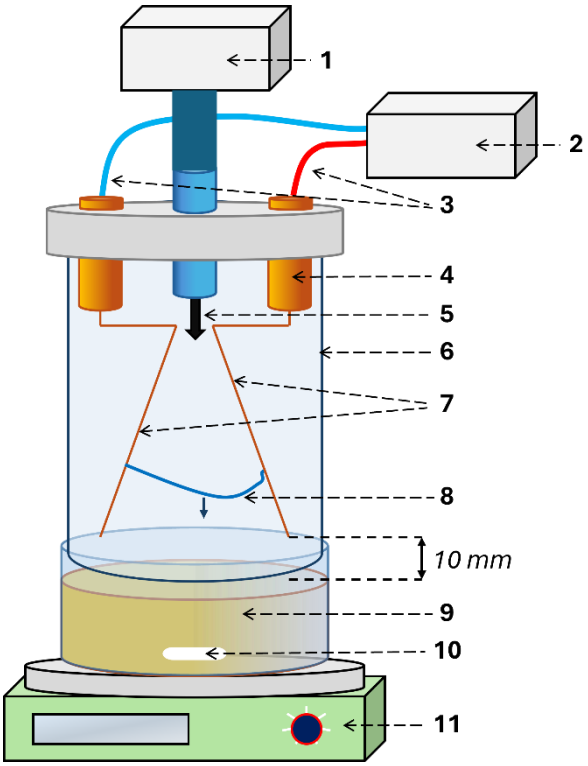

Fig. 1. Schematic diagram of the plasma treatment system: 1–Working gas source; 2–Power supply; 3–Power supply cables; 4–Electrode holder; 5–Forced flow of working gas; 6–Glass tube; 7–Copper electrodes; 8–Electric arc; 9–Vessel with juice; 10–Magnetic stir bar; 11–Magnetic stirrer.

2. Conclusions

1. The application of cold plasma treatment to carrot juice improved its microbiological quality compared to the control sample. Treating the juice with plasma for 20 and 30 minutes resulted in a product that met the requirements outlined in the Codex Standards regarding the total count of aerobic mesophilic microorganisms in edible juice.
2. Cold plasma treatment of the juice for 30 minutes produced a product with better colloidal stability and higher carotenoid and polyphenol content than the control sample.
3. The results indicate that a 30-minute cold plasma treatment using the Glide-arc reactor can extend the shelf life of carrot juice. Additionally, the treated juice exhibits enhanced colloidal stability and nutritional value, suggesting its potential for practical application in the industrial production of juices and other beverages.

Multiscale time evolution of C_2H_2+Ar mixture decomposition in low-pressure inductively coupled plasma

Jozef Brcka

Tokyo Electron America, Inc.

2400 Grove Boulevard, Austin, TX-78741-6500, U.S.A.

jozef.brcka@us.tel.com

This contribution presents results from the numerical simulation of the gas-phase chemical kinetics in C_2H_2+Ar low pressure inductively coupled plasma. These plasmas are used in the formation of graphene film or single-wall carbon nanotubes. CVD graphene film deposited using high density plasma has several applications in next generation LSI technology. Graphene films need to sustain the property through integration processes and be inert against the interactions or impact of the chemicals, radicals, ions, etc. The chemistry in plasma simulation requires a sensitive assessment of the dominant reactions and species [1] that are contributing to graphene growth. Simulation of complex reaction mechanisms helps to test hypothesis *in silico* and enable further innovation.

In plasma, it is anticipated that a vertical growth of carbon structure occurs when an extensive supply of carbon, chemisorption, grain boundary, high pressure, high fluxes, and imperfect surface are imposed. Deposition over >30 layers will form graphite. On the other side, a horizontal growth (graphene monolayer) is controlled by factors such as lower temperature (physisorption only to eliminate chemisorption), low reactant feed, lower pressure, low fluxes, and perfect surface. Fragmentation of acetylene C_2H_2 in plasma and neutral-neutral collisions are produced by primary electron collisions and process temperature.

We demonstrated by numerical simulation using a 2D fluid model with axial symmetry, the production and transport of reactive species can be affected under the changes in the spatio-temporal situation. As a consequence, the operation modes have the potential to control the reaction chemistry. Here, the gas pressure has an impact on time evolution and sustaining C_2H_2 chemistry. The time evolution pattern is revealing that C_2H_2 decomposition is developing through three phases, see Fig. 1. First phase consists of the ionization wave producing ions from parent molecules C_2H_2 by primary electron collisions (electron formation of plasma up to several tens μs). Subsequently, the production of new neutrals, radicals, e.g. heavy-species reactions phase starts during phase two, lasting up to hundreds of ms. The third phase is exhibiting a pattern of multiscale interaction, i.e. quenching or depletion of the charged species due to either electron energy loss, and plausibly other factors such as dimensional scale of reactor configuration, the RF power level, or other factors. This pulsed mode pattern is observed within the seconds range. A good example of a similar pattern in the time evolution of plasma chemistry could be the dielectric barrier discharge in molecular gases where plasma is formed within a fibral structure at atmospheric pressure [2].

From the point of view of technological applications, for example, surface cleaning in oxygen plasma, etching in fluorine chemistry, and deposition of silicon dioxide or titanium dioxide in chloride plasmas, the electronegative plasmas are playing an important role. In C_2H_2 plasma, we observed a substantial impact of the hydrogen created as a by-product or due to the inflow into the reactor during the third phase. Specifically, adopting the formation of the negative ion H^- by a two-steps process [3,4,5] initiated by vibrational excitation of parent H_2 molecules and followed by dissociative electron attachment (DEA) led to the pattern observed in the 3rd phase. Further investigation of the H^- formation by the multistep mechanism of DEA and destruction of the H^- ions plasma exposed high sensitivity of competing reactions. We believe the mechanism of lateral graphene layer vs. vertical nanotube walls is triggered by pressure with a transition around 6-7 Pa. Extension of the simulation by controlling

other parameters exposed the posibility to modulate process chemistry. RF power modulation was investigated to control plasma chemistry. Simulation results exhibited highly decomposed C_2H_2 molecules and the formation of dominant high-C_nH_m chains, C_2 dimer, and release of a significant amount of hydrogen. Separation of charged species and neutrals due to transition in the third phase offers an opportunity for reaction chemistry to control and assist to graphene growth mechanism. Exploring this approach enabled us to determine dominant charged and neutral species in C_2H_2 dense plasma and to suggest the graphene growth mechanism on the surface.

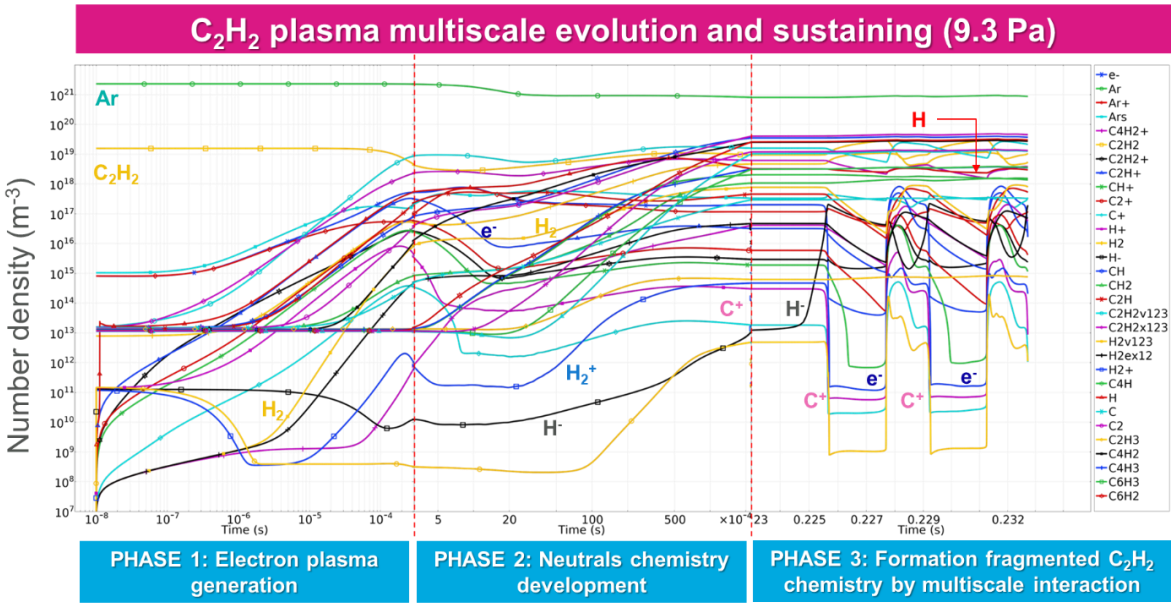

Fig. 1. Time evolution of the C_2H_2+Ar decomposition in an inductively coupled plasma reactor with total pressure 9.3 Pa and dual ICP coils at 13.56 MHz and 100/600 W, respectively.

Keywords: inductively coupled molecular plasma; acetylen decomposition; chemical kinetics; plasma time evolution.

1. Reference

[1] R. K. Janev, and Reiter, Physics of Plasmas 11(2), 780-829 (2004).
[2] R, Barni, P. Alex, and C. Riccardi, Plasma 2023, 6, 735-752, MDPI.
[3] L. Schiesko, Presentation (*https://www.mipse.umich.edu/files/iops*) CNRS, Universite Paris-Saclay (2021).
[4] M. Bacal, Phys. Scripta 2/2 467 (1982).
[5] C. W. Schmidt, Proc. Linear Accelerator Conf., Albuquerque, New Mexico, USA (1990).

DISSOCIATIVE IONISATION OF PENTAFLUOROPHENYL TRIFLATE, A POTENDIAL PHOTO ACID GENERATOR FOR CHEMICALLY AMPLIFIED EXTREME ULTRAVIOLET LITHOGRAPHY RESISTS

Mónica Mendes[1], Pedro Guerra[1], Filipe Ferreira da Silva[1], Robert Richter[2]
Fabian Holzmeier[3] and Oddur Ingólfsson[4]

[1] *CEFITEC, Department of Physics, NOVA School of Science and Technology, NOVA University Lisbon, 2829-516 Caparica Portugal*
[2]*Elettra-Sincrotrone Trieste, 34149 Trieste, Italy*
[3]*IMEC, Kapeldreef 75, 3001 Leuven, Belgium*
[4]*Science Institute of the University of Iceland, Department of Chemistry, Dunhagi 3, 107 Reykjavík, Iceland*
E-mail: odduring@hi.is

In the current contribution, preliminary experimental data on dissociative ionisation of pentafluorophenyl triflate is presented and compared to photoinisation of this compound at the EUVL wavelength of 13.5 nm. The DI processes are analysed with respect to the respective thermochemistry and discussed in context to the potential functionality of this compound as photoacid generator in chemically amplified resist materials for extreme ultraviolet lithography.

1. Electron driven chemistry in extreme ultraviolet lithography

Currently extreme ultraviolet lithography (EUVL), operating at the very short wavelength of 13.5 nm, is being established at the side of the conventional deep ultraviolet lithography (DUVL, typically 248 or 193 nm) in the high-volume manufacturing of computer chips.[1] Though the technical aspects of printing with this short wavelength are very challenging, it is considered worth the while as the resolution gain is directly proportional to the wavelength, enabling significantly higher transistor density with this approach. The chemical aspect of the transition to such short wavelengths is, however, also challenging. While the conventional DUVL is based on conversion of the resist materials through photochemistry, 13.5 nm light constitutes ionizing radiation with a photon energy of 92 eV, and the chemistry within the exposed photoresist materials is thus expected to be at large electron-, rather than photon-driven [2,3].

At this high photon energy, photoelectrons are produced within the exposed resist materials, leading to secondary ionisation processes alongside other inelastic scattering processes. This results in a dynamic secondary electron energy distribution that is nonnegligible at the 0 eV threshold, peaks at few eV and tails of towards the initial photoelectron energy [2,3]. Thus, the initial processes, triggering the respective resist chemistry, may be dissociative electron attachment (DEA), dissociative ionization (DI), dipolar dissociation (DD), and/or neutral dissociation (ND). These are different processes that are bound to initiate different chemistry (see ref [4] and refs therein). Thus, funded understanding of their nature and extent within the respective resist materials is a key element in the design of new high-performance platforms.

In general resist materials may be based on very different approaches to the chemical path of the transformation to be achieved, including chemically amplified resists (CARs), polymeric non-CARs, hybrid resists materials, metallic oxo-clusters among other (see e.g., ref [5-8] and refs therein). In the commonly used chemically amplified resists, a strong acid is generated in the light exposure of an added photo acid generator (PAG), which in turn drives the respective chemistry. Among such PAGs are aryl and allyl triflates that are used for generation of the strong triflic acid, and in the gas phase it was shown that DEA at low incident electrons energies leads to formation of the triflic anion [9].

In the current effort of better understanding the electron induced chemistry within potential EUVL resist materials, and possibly identify potential pathways to performance enhancement, we have extended this work and conducted comprehensive studies on pentafluorophenyl triflate as a potential candidate for triflic acid generation upon exposure. Specifically, pentafluorophenyl triflate is chosen for the current studies as the perfluorination may be expected to significantly enhance the DEA cross section and direct the fragmentation channels. However, despite the expected increased DEA cross section, EUV exposures of an epoxy-based cross-linking photoresist with perflorinated phenyl triflate as a PAG showed no enhancement of the degree of polymerization [9].

To better understand the fundamental chemical processes initiated in pentafluorophenyl triflate up on EUVL exposure and to further explore its potential as PAG in CARs intended for EUVL, we have conducted a comprehensive, comparative study on this compound, exploring its fragmentation in the electron induced processes of dissociative electron attachment (DEA) and dissociative ionization (DI) as well as direct photon induced fragmentation under EUV exposure.

In the current contribution, prelaminar experimental data on dissociative ionization of this compound is presented, compared to photofragmentation mass spectra recorded at 13.5 nm and discussed in context to the thermochemistry of the respective dissociation processes within the framework to the potential functionality of pentafluorophenyl triflate as a PAG in EUVL CARs.

2. References

[1] Kazazis, D., Santaclara, J.G., van Schoot, J., Mochi, I. and Ekinci, Y. 2024 *Nat Rev Methods Primers* ***4,*** *84*.

[2] Kostko, O., McAfee, T.R., Han Son Ma, J., Blackwell, J.M., and Naulleau, P.P., 2024 *J. Micro/Nanopatterning Mater. Metrol.* **23**(1), 014602

[3] Torok, J., Del Re, R., Herbol, H., Das, S., Bocharova, I., Paolucci, A., Ocola, L.E., Ventrice Jr., C., Lifshin, E., Denbeauxa G. and Brainarda, R.L., 2013 *J. Photopolym. Sci. Technol.* **26** (5) 625-634

[4] Ingólfsson, O. (Ed) 2019 *Low-Energy Electrons Fundamentals and Applications*; Pan Stanford Publishing Pte. Ltd.:, The Republic of Singapore

[5] Cen, J., Deng, Z.Y., and Liu, S.Y. 2024 Polym. Chem. **15** (45) 4599-4614

[6] Yeo Kyung Kang, Y.K., Lee, S. J., Eom, S., Kim, B. G., Hwang C.-C., and Kim, M.-G. *2024 J. Mater. Chem. C* ***12*** *15855-15887*

[7] Takahiro Kozawa 2024 *Jpn. J. Appl. Phys.* **63** 050101

[8] Wang, X., Tao, P., Wang, Q., Zhao, R., Liu, T., Hu, Y., Hu, Z., Wang, Y., Wang, J., Tang, Y., Xu, H., He, X., 2023 *Materials Today* **67** 299-319,

[9] Ptasińska, S., Gschliesser, D., Bartl, P., Janik, I., Scheier, P., Denifl, S., 2011 J. *Chem. Phys*. **135** 214309

[10] Torti, E., Dr. Protti, S., Bollanti, S., Flora, F., Torre, A., Brusatin, G., Gerardino, A., Businaro, L., Fagnoni, M., 2018 *ChemPhotoChem* **2**(5) 425-432

DISSOCIATIVE ELECTRON ATTACHMENT TO PENTAFLUOROPHENYL TRIFLATE, A POTENDIAL PHOTO ACID GENERATOR FOR CHEMICALLY AMPLIFIED EXTREME ULTRAVIOLET LITHOGRAPHY RESISTS

Mónica Mendes[1], Pedro Guerra[1], Reza Tafrishi[2] Filipe Ferreira da Silva[1], Fabian Holzmeier[3] and Oddur Ingólfsson[2]

[1] CEFITEC, Department of Physics, NOVA School of Science and Technology, NOVA University Lisbon, 2829-516 Caparica Portugal

[3]Science Institute of the University of Iceland, Department of Chemistry, Dunhagi 3, 107 Reykjavík, Iceland

[2]IMEC, Kapeldreef 75, 3001 Leuven, Belgium

E-mail: odduring@hi.is

In the current contribution, preliminary experimental and theoretical data on dissociative electron attachment to pentafluorophenyl triflate are presented and discussed in context to the underlying resonances and the thermochemistry of the respective processes as well as its potential functionality as a photoacid generator in chemically amplified resist material for extreme ultraviolet lithography.

1. Electron driven chemistry in extreme ultraviolet lithography

Currently extreme ultraviolet lithography (EUVL), operating at the very short wavelength of 13.5 nm, is being established at the side of the conventional deep ultraviolet lithography (DUVL, typically 248 or 193 nm) in the high-volume manufacturing of computer chips.[1] Though the technical aspects of printing with this short wavelength are very challenging, it is considered worth the while as the resolution gain is directly proportional to the wavelength, enabling significantly higher transistor density with this approach. The chemical aspect of the transition to such short wavelengths is, however, also challenging. While the conventional DUVL is based on conversion of the resist materials through photochemistry, 13.5 nm light constitutes ionizing radiation with a photon energy of 92 eV, and the chemistry within the exposed photoresist materials is thus expected to be at large electron-, rather than photon-driven [2,3].

At this high photon energy, photoelectrons are produced within the exposed resist materials, leading to secondary ionisation processes alongside other inelastic scattering processes. This results in a dynamic secondary electron energy distribution that is nonnegligible at the 0 eV threshold, peaks at few eV and tails of towards the initial photoelectron energy [2,3]. Thus, the initial processes, triggering the respective resist chemistry, may be dissociative electron attachment (DEA), dissociative ionization (DI), dipolar dissociation (DD), and/or neutral dissociation (ND). These are different processes that are bound to initiate different chemistry (see ref [4] and refs therein). Thus, funded understanding of their nature and extent within the respective resist materials is a key element in the design of new high-performance platforms.

In general resist materials may be based on very different approaches to the chemical path of the transformation to be achieved, including chemically amplified resists (CARs), polymeric non-CARs, hybrid resists materials, metallic oxo-clusters (see e.g., ref [5-8] and refs therein). In the commonly used chemically amplified resists, a strong acid is generated in the light exposure of an added photo acid generator (PAG), which in turn drives the respective chemistry. Among such PAGs are aryl and allyl triflates that are used for generation of the strong triflic acid, and in the gas phase it was shown that DEA at low incident electrons energies leads to formation of the triflic anion [9].

In the current effort of better understanding the electron induced chemistry within potential EUVL resist materials, and possibly identify potential pathways to performance enhancement, we have extended this work and conducted comprehensive studies on pentafluorophenyl triflate as a potential

candidate for triflic acid generation upon exposure. Specifically, pentafluorophenyl triflate is chosen for the current studies as the perfluorination may be expected to significantly enhance the DEA cross section and direct the fragmentation channels. However, despite the expected increased DEA cross section, EUV exposures of an epoxy-based cross-linking photoresist with perflorinated phenyl triflate as a PAG showed no enhancement of the degree of polymerization [9].

To better understand the fundamental chemical processes initiated in pentafluorophenyl triflate up on EUVL exposure and to further explore its potential as PAG in CARs intended for EUVL, we have conducted a comprehensive, comparative study on this compound, exploring its fragmentation in the electron induced processes of dissociative electron attachment (DEA) and dissociative ionization (DI) as well as direct photon induced fragmentation under EUV exposure.

In the current contribution, prelaminar experimental and theoretical data on dissociative electron attachment to this compound are presented and discussed in context to the underlying resonances and the thermochemistry of the respective dissociation processes within the framework of the potential functionality of pentafluorophenyl triflate as a PAG in EUVL CARs.

2. References

[1] Kazazis, D., Santaclara, J.G., van Schoot, J., Mochi, I. and Ekinci, Y. 2024 *Nat Rev Methods Primers **4**, 84*.

[2] Kostko, O., McAfee, T.R., Han Son Ma, J., Blackwell, J.M., and Naulleau, P.P., 2024 *J. Micro/Nanopatterning Mater. Metrol.* **23**(1), 014602

[3] Torok, J., Del Re, R., Herbol, H., Das, S., Bocharova, I., Paolucci, A., Ocola, L.E., Ventrice Jr., C., Lifshin, E., Denbeauxa G. and Brainarda, R.L., 2013 *J. Photopolym. Sci. Technol.* **26** (5) 625-634

[4] Ingólfsson, O. (Ed) 2019 *Low-Energy Electrons Fundamentals and Applications*; Pan Stanford Publishing Pte. Ltd.:, The Republic of Singapore

[5] Cen, J., Deng, Z.Y., and Liu, S.Y. 2024 Polym. Chem. **15** (45) 4599-4614

[6] Yeo Kyung Kang, Y.K., Lee, S. J., Eom, S., Kim, B. G., Hwang C.-C., and Kim, M.-G. *2024 J. Mater. Chem. C **12** 15855-15887*

[7] Takahiro Kozawa 2024 *Jpn. J. Appl. Phys.* **63** 050101

[8] Wang, X., Tao, P., Wang, Q., Zhao, R., Liu, T., Hu, Y., Hu, Z., Wang, Y., Wang, J., Tang, Y., Xu, H., He, X., 2023 *Materials Today* **67** 299-319,

[9] Ptasińska, S., Gschliesser, D., Bartl, P., Janik, I., Scheier, P., Denifl, S., 2011 J. *Chem. Phys*. **135** 214309

[10] Torti, E., Dr. Protti, S., Bollanti, S., Flora, F., Torre, A., Brusatin, G., Gerardino, A., Businaro, L., Fagnoni, M., 2018 *ChemPhotoChem* **2**(5) 425-432

ACCURATE REFERENCE DATA FOR MONITORING OF AMMONIA

P. Čermák[1], P. Cacciani[2]

[1]*Department of Experimental Physics, Faculty of Mathematics, Physics and Informatics, Comenius University, Mlynská dolina F2, 842 48 Bratislava, Slovakia*

[2]*Laboratoire de Physique des Lasers, Atomes et Molécules, CNRS, UMR 8523 Université Lille, 59655 Villeneuve d'Ascq Cedex, France*

E-mail: cermak@fmph.uniba.sk

The present contribution provides an overview of our recent progress in completing a precise experimental line list for the ammonia molecule in the infrared range from 3900 to 6350 cm^{-1}. This knowledge is an important prerequisite for accurate NH_3 retrievals, like the plasma reactors studying the production of green ammonia.

1. Introduction

The shift from fossil fuels to renewable energy sources is one of the primary objectives in addressing climate change. Ammonia (NH_3) is an important candidate for such an environmentally friendly synthetic fuel [1]. It has a high energy content and can be easily liquefied for efficient transport. Unfortunately, practical technologies for efficient and environmentally clean ammonia production are currently lacking. One promising approach for this purpose is using non-thermal plasma to dissociate N_2 molecules into reactive atomic nitrogen, which can produce ammonia via subsequent reactions with hydrogen-containing species. The efficiency and specificity of the process must be significantly enhanced to be practical from both the technological and economic points of view to enable its viability.

Real-time and in-situ monitoring of the chemical processes involved in ammonia production using non-thermal plasma is one of the key capabilities needed both in laboratory and industrial environments for process optimization. Such diagnostics should also be remote to ensure they do not interfere with the plasma chemical environment. Sensing through optical spectroscopy provides an ideal tool for such a purpose. It is a highly specific and remote sensing technique, capable of distinguishing individual species, including short-lived reactive intermediates directly in the plasma environment and determining other important characteristics, such as the level of their internal excitation and local temperature.

The aim of our work is the development of high-resolution spectroscopy techniques for the monitoring of ammonia in the gas phase or plasma. Our goal is to provide a better understanding of the structure of the visible spectra through a detailed analysis of the infrared absorption spectra of the primary ammonia isotopologues. To that end, a comprehensive and accurate line list for $^{14}NH_3$ and $^{15}NH_3$ was prepared in the range from 3900 to 6350 cm^{-1} [2]. Overall, 99.2 % of the total measured room temperature absorption was assigned to corresponding ro-vibrational transitions [3, 4], resulting in the most comprehensive experimental ammonia list within this region.

2. The line list.

Multiple Fourier transform absorption spectra at room temperature were accurately fitted and assigned by comparison with an ab initio line lists [2]. The assignments were systematically validated by lower state combination difference relations (LSCD) and compared with intensities deduced from the theoretical dipole-moment surfaces [3,4]. In total (Fig. 1), over 30000 ammonia transitions were identified (~21000 for $^{14}NH_3$ and ~9000 $^{15}NH_3$), out of which approximately 20000 transitions were given ro-vibrational assignments. Compared to our original publication [2], the current work focuses on the validation of these results (further verification by LSCD from different sources) and making the $^{115}NH_3$ assignments compliant with the C2018 dipole moment list [4], so they are ready for the upcoming HITRAN database [5] update.

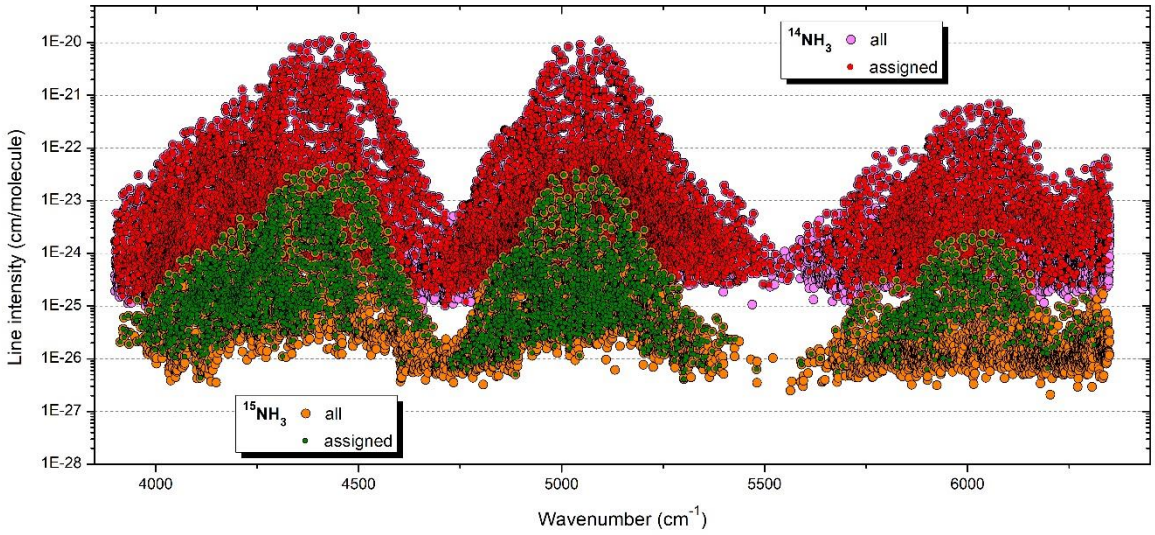

Fig. 1. Overview of the $^{14}NH_3$ and $^{15}NH_3$ line lists included in our recommended line list for natural ammonia between 5650 and 6350 cm^{-1}. Different colours are used for the assigned and unassigned transitions. The $^{15}NH_3$ line list has intensity scaled according to the $^{15}NH_3$ natural abundance.

3. Conclusion

In summary, we believe that the ammonia line list elaborated in this study represents a significant improvement over the HITRAN2020 list. These improvements include greater completeness, enhanced accuracy of the line parameters, and an expanded set of rovibrational assignments. The latter is crucial for capturing the temperature dependence of line intensities and improving the theoretical models for visible range ammonia spectra.

4. Acknowledgement

This research was supported by the Slovak Research and Development Agency (APVV-23-0522) and Scientific Grant Agency (VEGA-1/0710/24).

5. References

[1] Green Ammonia | Royal Society". https://royalsociety.org/topics-policy/projects/low-carbon-energy-programme/green-ammonia/.
[2] Cermak P and Cacciani P, 2024 Journal of Quantitative Spectroscopy and Radiative Transfer **329** 109148. https://doi.org/10.1016/j.jqsrt.2024.109148
[3] Coles PA, Ovsyannikov RI, Polyansky OL, Yurchenko SN, Tennyson J, 2018 Journal of Quantitative Spectroscopy and Radiative Transfer **219** 199-212. https://doi.org/10.1016/j.jqsrt.2018.07.022
[4] Yurchenko S et al, 2024 Monthly Notices of Astronomical Societies **533** 3442–3456. https://doi.org/10.1093/mnras/stae1849
[5] Gordon I E et al., 2022 Journal of Quantitative Spectroscopy and Radiative Transfer **277** 107949. https://doi.org/10.1016/j.jqsrt.2021.107949

MEASUREMENT OF ION CURRENT FROM MULTI-HOLLOW SURFACE DIELECTRIC BARRIER DISCHARGE

Martin Kuťka, Michal Stano, Anna Zahoranová

Department of Experimental Physics, Faculty of Mathematics, Physics and Informatics, Comenius University Bratislava, Mlynská dolina F1, 842 48, Bratislava, Slovakia
E-mail: martin.kutka@fmph.uniba.sk

This work investigates ion current at different distances from a multi-hollow surface dielectric barrier discharge. Single- and double-grid configurations were utilized to measure ion currents in air and oxygen under various conditions. In the single-grid configuration, the ion current was found to increase with the applied grid voltage until saturation was reached. The saturation current decreased with increasing distance from the plasma source. In the double-grid configuration, all ions were captured by the first grid in oxygen, while a residual current was observed on the second grid in air. To further explore this residual current, a modified double-grid configuration was employed. Measurements revealed that some of the current originated from photoemission of electrons induced by UV radiation from the plasma.

1. Introduction

The multi-hollow surface dielectric barrier discharge (MSDBD) is an innovative DBD geometry that combines the benefits of both volume and surface DBDs. In this design, all the working gas is fed through holes where surface micro-discharges are generated. The arrangement of the holes ensures that the plasma spreads across the surface of the holes, while the flow of the working gas carries the active particles away from the active plasma zone [1]. In recent years, various applications of MSDBD have been studied in fields such as material surface modification, biodecontamination, and agriculture. In material surface modifications, MSDBD has been shown to be effective for fast cleaning and activation of silicon wafers, significantly enhancing their surface characteristics and enabling improved adhesion for subsequent processes in microelectronics [2]. MSDBD has also been successfully used to modify the surface properties of glass, where plasma treatment has resulted in improved surface energy and enhanced adhesion for coating applications [3]. In biodecontamination, MSDBD has been proven effective in inactivating microorganisms, including bacterial biofilms, offering potential for sterilization in healthcare and food safety by inactivating pathogens and improving sterilization procedures [4,5]. In agriculture, plasma treatment has been shown to improve seed germination and growth, reducing the need for chemical treatments. In studies [6–8], MSDBD plasma treatment has led to boosted seed vitality and early plant development, making it a promising tool for increasing crop yields and promoting sustainable farming practices.

In various applications, plasma induces a wide range of reactions that are triggered by different plasma constituents, including charged particles. For experimental purposes, it would be interesting to assess the effect of ions that are produced by plasma and interacting with the sample. The aim of this study is to investigate the ion current generated by MSDBD at various distances from the plasma source. To achieve this, an electrical grid was designed and constructed, capable of capturing ions of both polarities.

2. Experiment

For our experiments, we selected the commercial RPS30 multi-hollow device (ROPLASS, Czech Republic) as the MSDBD plasma source, with an input power of 30 W. The electrode system consists of two plane-parallel electrodes separated by a gap of 0.5 mm, fully embedded in alumina ceramic and perforated with 105 holes (Kyocera, Japan). The total active area of the generated plasma is 18 × 19 mm. A photograph of the MSDBD plasma source is shown in Fig. 1 (left), while a more detailed description of the MSDBD system is available in other studies [1,2]. Ambient air and oxygen (purity >99.995%) were used as working gases, both supplied at a flow rate of 6 l/min.

The electrical grid was powered by a DC power supply (Heinzinger electronic, Germany) operated within a voltage range of 0 – 200 V, as illustrated in Fig. 1 (right). To attract ions of both polarities, a voltage divider was employed to symmetrically split the voltage between the negative and positive wires of the grid. The electrical current, generated by the recombination of ions attracted to the grid, was measured using an ammeter.

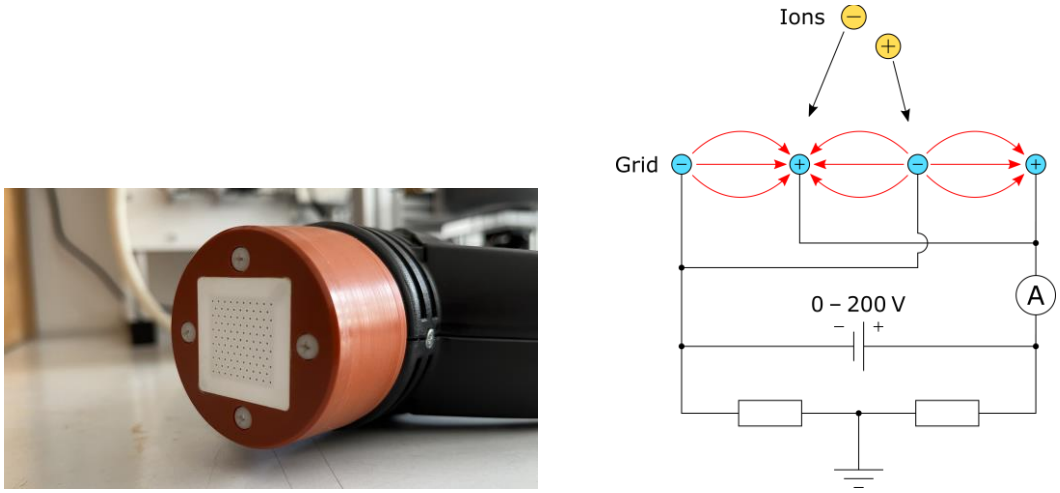

Fig. 1. MSDBD plasma source (left) and diagram of electrical grid (right).

The grid has a total area of 25 × 25 mm and consists of 32 parallel tungsten wires coated with graphite. Each wire has a diameter of 50 µm, with a uniform spacing of 0.8 mm between adjacent wires. The grid was mounted onto a custom MSDBD holder, which also included a distance frame. By using distance frames of different heights, the grid could be positioned at different distances *d* from the MSDBD plasma source. A schematic of the described experimental setup is shown in Fig. 2 a). In the second experimental setup, illustrated in Fig. 2 b), the first grid was positioned at a distance of 6 mm from the MSDBD. Below the first grid, a second identical grid was mounted at a distance of 10 mm from the MSDBD. This setup was designed to determine whether the first grid captures all ions generated by the plasma. If any ions pass through the first grid, they would be detected as an ion current on the second grid, providing insight into the efficiency of ion capture by the first grid. In the third experimental setup, shown in Fig. 2 c), the grids were positioned at the same distances as in the previous setup. However, the second grid in this configuration was modified so that every second wire (corresponding to one polarity of the wires) was covered. This design was implemented to investigate the occurrence of photoemission of electrons from the wires of negative polarity under exposure to UV radiation emitted by the plasma. If photoemission occurs, the current detected when only the negative wires are exposed to UV light would be greater than the current detected when only the positive wires are exposed. This configuration thus enables the assessment of whether photoemission is a contributing factor to the measured ion currents under the influence of UV radiation from the plasma.

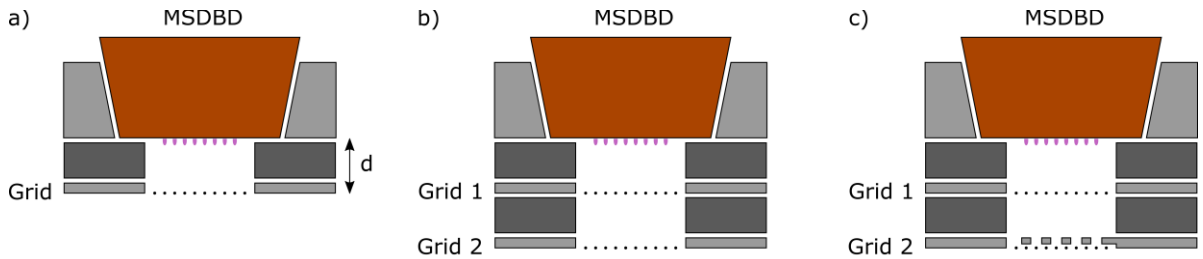

Fig. 2. Schematics of experimental setups: a) single-grid configuration with adjustable distance *d* from the MSDBD plasma source, b) double-grid configuration, c) modified double-grid configuration, where every second wire of Grid 2 is covered.

3. Results and discussion

The ion current as a function of the applied grid voltage for the single-grid configuration at distances *d* ranging from 4 to 10 mm is shown in Fig. 3. The graph for air is presented on the left, while the graph for oxygen is on the right. In all cases, the ion current increases with the applied voltage, but this increase gradually slows down until it reaches a saturated ion current. This behaviour can be explained by the increasing strength of the electric field as the voltage rises, which enhances the attraction of ions to the grid. As the electric field becomes stronger, more ions are captured by the grid. However, beyond a certain voltage, the grid captures all the ions generated by the MSDBD reaching the given location, leading to the observed saturation of the ion current. Additionally, it is evident that as the distance *d* increases, the value of the saturated ion current decreases. Similarly, the voltage at which the ion current reaches saturation also decreases with increasing distance. This trend is attributed to the fact that the density of ions decreases with distance from the MSDBD, leading to a reduced number of ions available for capture by the grid.

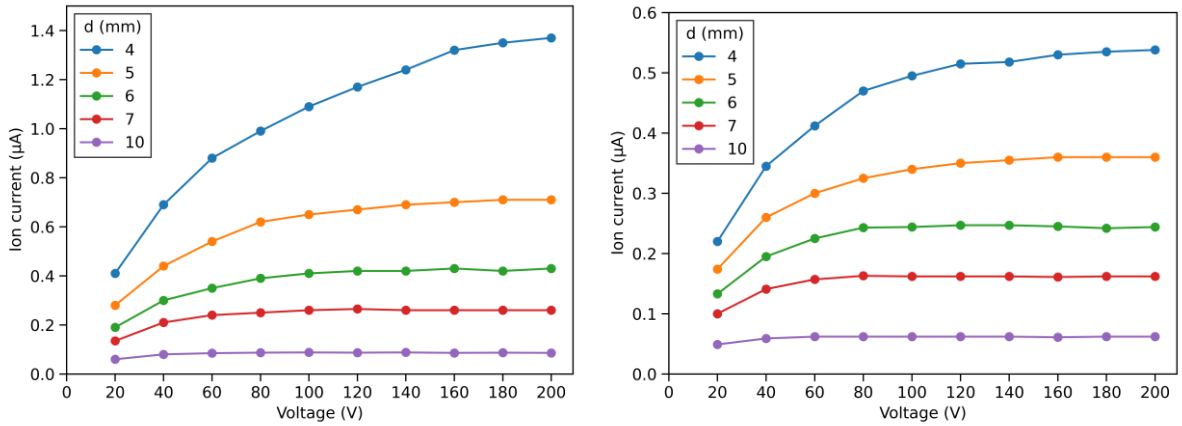

Fig. 3. Ion current as a function of the applied grid voltage for air (left) and oxygen (right).

The saturated ion current as a function of *d* for both gases is shown in Fig. 4. For both gases, the saturated ion current decreases exponentially with increasing distance from the MSDBD. Furthermore, the ion current values for air are higher than those for oxygen, and this difference becomes more pronounced as the grid is placed closer to the MSDBD. For comparison, at *d* = 10 mm, the saturated ion current is 0.09 μA for air and 0.06 μA for oxygen, while at *d* = 4 mm, the saturated ion current is 1.37 μA for air and 0.54 μA for oxygen.

Assuming that the ions produced by the plasma are predominantly singly ionized, the ion pair density *n* can be determined from the measured saturated ion current as

$$n = \frac{I}{e\,Q} \tag{1}$$

where *I* is the saturated ion current, *e* is the elementary charge, and *Q* is the gas flow rate.

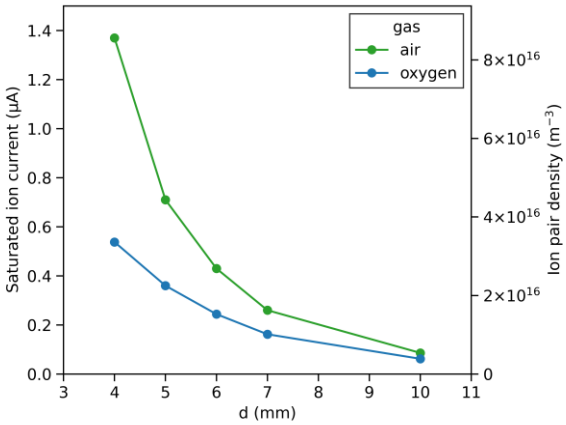

Fig. 4. Saturated ion current and ion pair density as a function of distance *d* from the MSDBD plasma source.

The results for the double-grid configuration are shown in Fig. 5, with air on the left and oxygen on the right. In both cases, the voltage on Grid 2 was 100 V. For both gases, it can be observed that as the ion current on Grid 1 increases, the current on Grid 2 decreases. In the case of oxygen, the ion current on Grid 2 decreases to zero, indicating that all ions produced by the MSDBD are captured by Grid 1. However, for air, the ion current on Grid 2 decreases to approximately 0.5 nA at a voltage of 100 V on Grid 1, and it does not decrease further with increasing voltage on Grid 1.

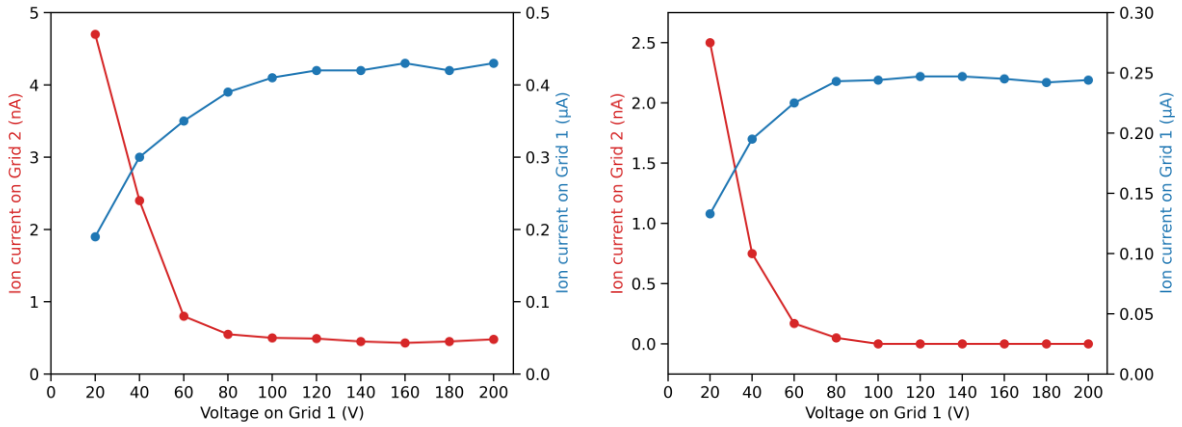

Fig. 5. Ion currents on both grids as a function of the voltage on Grid 1 for air (left) and oxygen (right).

Based on the results for air in the double-grid configuration, additional measurements were performed in the modified double-grid configuration with voltages of 100 V and 200 V applied to Grid 1. When the polarity of the illuminated wires was switched from negative to positive, a decrease in the ion current on Grid 2 by 0.3 nA was observed in both cases. This current can be attributed to photoemission of electrons induced by UV radiation from the plasma. The results are summarized in Table 1. The remaining ion current of 0.25 nA could not be attributed to a specific phenomenon. However, it could potentially be caused by insufficient coverage of the wires or by a small fraction of ions that were not captured by Grid 1.

Tab. 1. Results for air in the modified double-grid configuration.

Voltage on Grid 1 (V)	**Polarity of illuminated wires**	**Ion current on Grid 2 (nA)**
100, 200	negative	0.55
	positive	0.25

4. Conclusions

The ion current was measured in different experimental configurations using an MSDBD plasma source in air and oxygen. In the single-grid configuration, the ion current increased with the applied voltage and reached saturation. The saturated ion current decreased with increasing distance from the plasma source. In the double-grid configuration, all ions were captured by the first grid in oxygen, while a residual current of approximately 0.5 nA was observed on the second grid in air. Measurements in the modified double-grid configuration revealed that 0.3 nA of this residual current was caused by photoemission of electrons from the illuminated wires due to UV radiation from the plasma. These findings provide valuable insights into the behaviour of ions from MSDBD, which could aid in optimizing plasma experiments where ions play a significant role.

Acknowledgment: This work was supported by the Slovak Research and Development Agency under the contract No. APVV-21-0147.

5. References

[1] Homola T, Prukner V, Hoffer P, Šimek M. 2020 Multi-hollow surface dielectric barrier discharge: an ozone generator with flexible performance and supreme efficiency. *Plasma Sources Sci. Technol.* **29**, 095014. (doi:10.1088/1361-6595/aba987)

[2] Krumpolec R, Richter V, Zemánek M, Homola T. 2019 Multi-hollow surface dielectric barrier discharge for plasma treatment of patterned silicon surfaces. *Surfaces and Interfaces* **16**, 181–187. (doi:10.1016/j.surfin.2019.01.014)

[3] Sihelník S, Krumpolec R, Kelar Tučeková Z, Kelar J, Stupavská M, Černák M, Kováčik D. 2023 Atmospheric-pressure air plasma sources for cleaning and activation of float soda-lime glass: Effects and comparison. *Surfaces and Interfaces* **40**, 103080. (doi:10.1016/j.surfin.2023.103080)

[4] Mošovská S, Medvecká V, Valík Ľ, Mikulajová A, Zahoranová A. 2023 Modelling of inactivation kinetics of Escherichia coli, Salmonella Enteritidis and Bacillus subtilis treated with a multi-hollow surface dielectric barrier discharge plasma. *Sci Rep* **13**, 12058. (doi:10.1038/s41598-023-38892-2)

[5] Kelar Tučeková Z, Vacek L, Krumpolec R, Kelar J, Zemánek M, Černák M, Růžička F. 2021 Multi-Hollow Surface Dielectric Barrier Discharge for Bacterial Biofilm Decontamination. *Molecules* **26**, 910. (doi:10.3390/molecules26040910)

[6] Slavíček P, Štěpánová V, Fleischer M, Kelar J, Kelar Tučeková Z, Jurmanová J, Pazderka M, Prášil V, Prášil J. 2023 The multi-hollow surface dielectric barrier discharge usage for the seeds' treatment aimed to the dustiness decrease of free-floating particles from agrochemicals. (doi:10.21203/rs.3.rs-3053633/v1)

[7] Ďurčányová S, Slováková Ľ, Klas M, Tomeková J, Ďurina P, Stupavská M, Kováčik D, Zahoranová A. 2023 Efficacy Comparison of Three Atmospheric Pressure Plasma Sources for Soybean Seed Treatment: Plasma Characteristics, Seed Properties, Germination. *Plasma Chem Plasma Process* **43**, 1863–1885. (doi:10.1007/s11090-023-10387-y)

[8] Tunklová B, Šerá B, Šrámková P, Ďurčányová S, Šerý M, Kováčik D, Zahoranová A, Hnilička F. 2023 Growth Stimulation of Durum Wheat and Common Buckwheat by Non-Thermal Atmospheric Pressure Plasma. *Plants* **12**, 4172. (doi:10.3390/plants12244172)

DUAL-CHANNEL ABSORPTION SPECTROSCOPY

Filip Pastierovič[1], Shamaila Manzoor[1], Peter Čermák[1]

[1]*Department of Experimental Physics, Faculty of Mathematics, Physics and Informatics, Comenius University in Bratislava*
E-mail: cermak@fmph.uniba.sk

Radicals are an important component of many chemical reactions, specifically NO_x, which play a significant role in atmospheric chemistry and significantly affects the formation of reactive nitrogen. In the present work, we focused on the detection of short-lived NO_3, which is challenging to detect using common spectroscopy techniques such as Fourier transform absorption spectroscopy. For this purpose, we build a robust optical system for the rapid detection of nitrogen dioxide (NO_2) over a wide dynamic range. The system integrates two absorption spectroscopy techniques: direct absorption for the detection of higher concentrations (10-100 ppm) and incoherent broadband absorption spectroscopy with optical resonator (IBB-CEAS) for the detection of lower concentrations.

1. NO_2, NO_3 and plasma

NO3 and NO2, play a role in a chemistry of atmospheric plasma discharges. There are many applications of atmospheric plasma discharges. The possibilities offered by non-thermal plasma are currently in practice and continue to be explored. The temperature of heavy particles (neutrals and ions) is low. Only electrons get thermalized and these electrons with high energies are responsible for the chemical activity. This facilitates the formation of highly reactive particles such as radicals. In last decades, several plasma-based technologies were successfully developed such as flue gas cleaning, water purification, plasma assisted combustion, or hazardous liquid waste processing. Or the rapidly growing field of plasma applications in biomedicine in recent years [1].
Nitrogen dioxide and Nitrate radical are involved in the formation of reactive nitrogen. Reactive nitrogen is an essential component for all living organisms. Atmospheric nitrogen N_2 is predominantly global nitrogen, making up 78 % of the atmosphere. To make N_2 reactive and available to living organisms, the non-reactive nitrogen must be transformed or modified in compounds such as ammonia NH_3 or nitrogen oxides NOx by reaction with molecules such as H_2 or O_2 in a process called N_2 fixation [1]. However, the Haber-Bosch process for N_2 fixation is energy and environmentally demanding. Therefore, various types of non-thermal plasma are currently being investigated for nitrogen fixation. For example, Patil et al. [2] use a compact dielectric barrier discharge (DBD) reactor for NOx production.

Detection of highly reactive species, especially NO3, using common techniques such as FTIR, is challenging. Like in the [Trunec et al., 2022] paper, where the NO3 concentration was included the model, but NO3 was not actually measured. For this purpose, we used the IBB-CEAS technique, which is based on absorption spectroscopy and employs a detector developed by our research team.

2. Dual-channel absorption spectroscopy

Absorption spectroscopy is a technique used to measure the absorption of electromagnetic radiation by a sample as a function of wavelength or frequency. When a beam of light passes through a sample, the molecules of the sample absorb certain wavelengths, causing transitions between energy levels. This absorption results in an attenuation of light intensity at specific wavelengths that can be measured to produce an absorption spectrum. This spectrum provides valuable information about the molecular composition and structure of the sample, making absorption spectroscopy an important tool in fields such as analytical chemistry, molecular physics, and astronomy.
Incoherent broad band absorption spectroscopy belongs to a family of techniques using an optical cavity to extend the effective path of light with a sample, similar to CRDS. The primary advantage of IBB-CEAS over other techniques is the use of an incoherent source, which transmit a large number of

resonator modes at once versus only one as in traditional CRDS, for example. Thus, with an acceptable decrease in sensitivity, we obtain an optical scheme much more immune to mechanical inaccuracies or particles directly inside the resonator, a critical feature for the success of future research where we will test the calibrated dual-channel detector for resistance to plasma and liquid in the form of microdroplets present directly in the optical resonator.

The combination of direct absorption and IBB-CEAS results in a detector with a high dynamic range. The IBB-CEAS channel is used to measure low concentrations, which will give us an effective path in the order of hundreds of meters, even with a small reactor (on the order of tens of centimeters). On the contrary, for large concentrations, the signal drop in the IBB-CEAS channel is too high, leading to low signal to noise ratio. In this case, the direct absorption channel is used. Concentrations at which it is possible to use both channels simultaneously were used for system calibration.
At present we have a detector for low NO_2 concentrations using the IBB-CEAS technique. This detector uses as light source a red LED with a maximum emitted intensity at 660 nm, two mirrors from LAYERTEC with high reflectivity (R>99%). In this system, we have implemented, using optical and optomechanical components, a second channel operating on the principle of direct absorption, which uses as a light source a so-called Blue LED emitting over a wide spectral range. In particular, the local maximum at 450 nm will be used in the experiment.

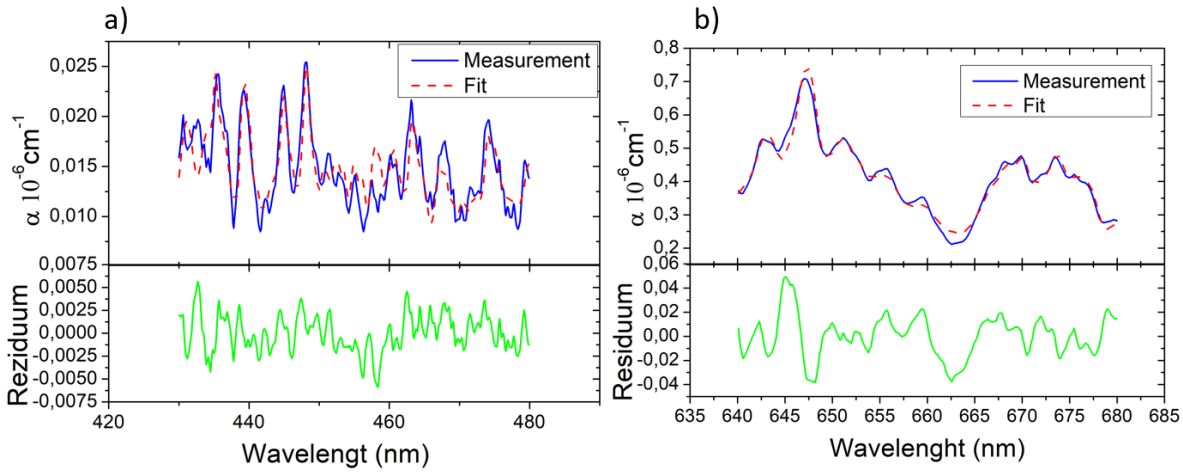

Fig. 1. Comparison of measured spectra with fit for a) direct absorption, b) IBB-CEAS system.

3. Conclusion

We were able to perform calibration measurements with dual-channel system where we used 100ppm of NO_2 as reference sample. The effective length of our optical cavity was found around 120 m with for a cavity length of 0,18 m. The calibrated detector will be used in future projects to analyse reactive particles in plasma, particularly NO_3.

4. Acknowledgement

This work was supported by the Scientific Grant Agency of the Slovak Republic (VEGA-1/0710/24) and (VEGA-1/0668/22).

5. References

[1] Lei X et al. 2022 *Plasma Chemistry and Plasma Processing* pages 1–17.
[2] Patil B 2017 *PhD thesis, Chemical Engineering and Chemistry*.
[3] Trunec D et al. 2022 **Plasma Sources Science and Technology**, **31** 11.

EMISSION SPECTRA OF TRANSIENT SPARK WITH ELECTROSPRAY

Peter Tóth[1], Mário Janda[1], Sergei Smirnov[1]

[1]*Faculty of Mathematics, Physics and Informatics, Comenius University Bratislava*
E-mail: peter.toth@fmph.uniba.sk

Transient spark (TS) discharge, generate low-temperature plasma rich in ions and electrons, initiating a chain of reactions that produce gaseous molecules like NO, NO_2, and HNO_2. When these gases dissolve in water, they form reactive species, including NO_2^-, NO_3^-, H_2O_2, and $ONOO^-$/ONOOH, which have potential applications in environmental processes. The solvation of these gases is enhanced by converting bulk water into electrospray (ES) microdroplets directly within the TS discharge zone. Moreover, the simultaneous production of TS and ES increases the concentration of iron ions due to electrode sputtering. This study investigates the precursor ions and atoms involved in reactive species generation using emission spectroscopy.

1. Introduction

The transient spark (TS) is a DC driven self-pulsing discharge characterized by a short-duration, high current pulses [1–4]. TS generates high-energy electrons, which collide with air molecules and atoms, causing ionization and excitation. The resulting ionized and excited species interact to form new molecules collectively referred to as reactive oxygen and nitrogen species (RONS). These gaseous RONS can dissolve upon contact with water, rendering the water "activated."

TS is able to operate in contact with water in a form of microdroplets. These microdroplets are generated by pumping the water through the electrode, on which simultaneously the transient spark is generated. Strong electric fields leads to the formation of water micro-droplets. This method of contacting the water with plasma ensures an efficient transfer of RONS into the water. [8, 9]

The primary objective of the presented study is to investigate the short lived precursors of stable RONS (such as NO, NO_2, and HNO_2) and to better understand the processes involved in their formation. To analyse the evolution and lifetimes of the relevant ions, atoms, and excited molecules, we employed both time integrated and time-resolved optical emission spectroscopy.

Although TS without ES was already studied [1-4], recent findings suggests, that the TS operated with ES might enhance the electrode erosion, introducing Fe+/Fe species into the treated water [5]. For this reason we focused here Fe+/Fe emission lines. Besides, we also studied the Hα line at 656nm, influenced by the Stark-broadening. This line can be used to determine the electron density of plasma. [3], [6] For this purpose, the FWHA of the Hα line was used according to Gigosos et al [6]. The electron density of the plasma is a key parameter for the assessment of the plasma reactivity. [3]

2. Experimental methods

Figure 1 presents a simplified schematic of the experimental setup. A stainless steel dispensing needle, serving as the anode, was connected to a high-voltage (HV) power supply delivering 12–15 kV. The grounded electrode consisted of an M5 stainless steel screw, with the electrode gap set at 9 mm. Electrospray (ES) was produced by continuously injecting deionized water through the HV needle at a flow rate of 500 µL/min using a syringe pump. A synthetic air flow rate of 1 L/min was maintained throughout the experiment. The anode voltage and discharge current were monitored using an HV probe and a current probe, respectively, with electrical signals recorded by a digital oscilloscope (Tektronix MDO34 500 MHz). Time-integrated optical emission spectra were collected using a compact

two-channel spectrometer (Ocean Optics SD2000), while time-resolved spectra with high spectral resolution were captured using a 2 m spectrometer (Carl Zeiss) coupled to an iCCD camera (Andor iStar).

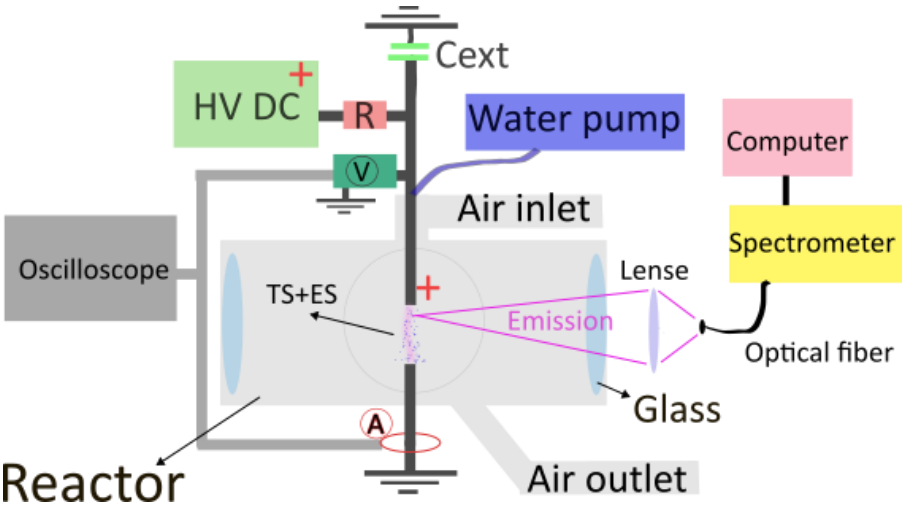

Fig. 1. A simplified schematic of the experimental setup

3. Results and Discussion

Figures 2 and 3 show the normalized emission spectra of TS with and without ES, recorded with the two-channel spectrometer. The prevalence of N^+ and O^+ lines in the spectra indicates a high degree of ionization during the high-current pulse of the TS. Alongside the N/N^+ and O/O^+ lines, the spectra also feature the Hα line and emission bands from the second positive system (SPS) of molecular nitrogen. The differences in the relative intensities of the oxygen and nitrogen lines in these figures between the TS with and without ES can be explained by the effect of frequency change. The generation of TS current pulses with ES is influenced by random droplet accumulation on the electrodes, causing more chaotic discharge behaviour, with lower frequency at the same mean discharge current (1.5mA). As it was shown by *Janda et al.* [4], the frequency of TS can have an impact on the emission spectra. However to correlate the influence of the ES on these emission spectra, further research is needed.

Figure 2. demonstrates a notable increase in the intensities of Fe^+/Fe emission lines in the TS with ES compared to TS without ES, supporting the hypothesis that electrospray enhances electrode erosion. [5] The presence of iron in the water can initiate Fenton-like reactions, leading to the gradual depletion of dissolved H_2O_2. While this reduction in H_2O_2 concentration may impact PAW composition, it could offer advantages for biomedical applications. [7] However, to fully understand the reactions, or the presence of these iron ions (or its oxides), further investigations of the PAW content is necessary, while also investigating the relevance and/or potential benefits on antibacterial properties.

We also examined the evolution of Hα line in time. Figure 4 shows example time-resolved spectra synchronized with the rising slope of the TS current pulses, measured by the Carl Zeiss spectrometer with the iCCD camera. From multiple samples, using python fitting program to fit the Voigth profile function, we obtained the FWHA and electron density from the following equation [6]:

$$\Delta\lambda_{FWHA}^{H\alpha} = 0.549\ nm\ \left(\frac{n_e}{10^{23} m^{-3}}\right)^{0.67965}, \quad (1)$$

where $\Delta\lambda_{FWHA}^{H\alpha}$ is the FWHA (in nm) of the Hα line and n_e is the electron density.

As can be seen on Figure 5., the calculated electron density decreases over time. The first measured spectrum is approximately 20ns delayed compared to the start of the current rise, due to delay of the triggering signal sending to the iCCD camera. That means, the electron density of the first few ns can be higher. Nonetheless, these obtained results of high electron density (≈10^{18} cm^{-3}) prove a high degree

of ionization and high reactivity of the plasma generated by the TS discharge, showing that there is no significant difference between with and without ES, from this point of view.

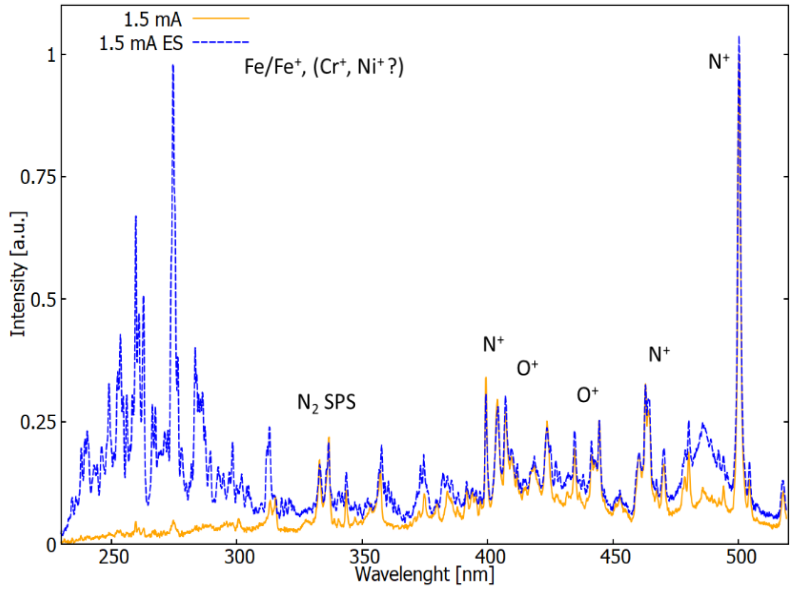

Fig. 2. Normalized time-integrated UV-VIS emission spectra of TS w/wo ES at mean current of 1.5 mA.

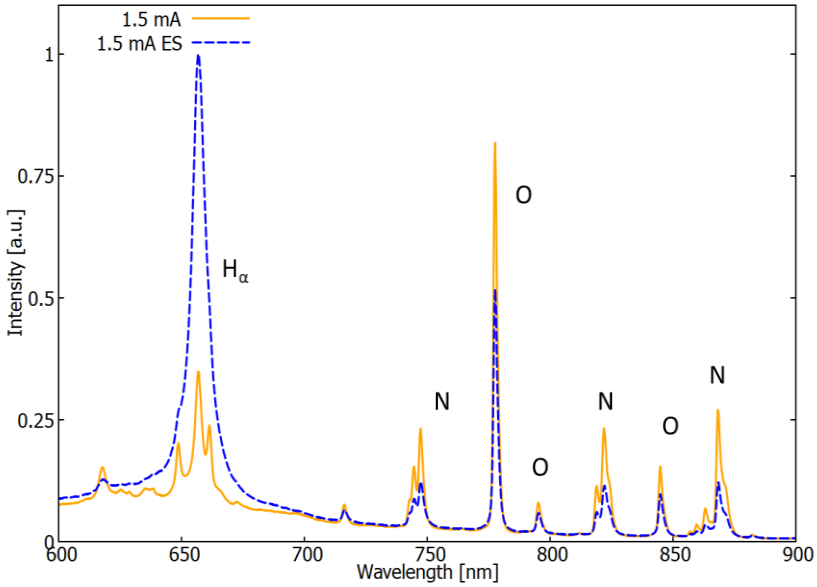

Fig. 3. Normalized time-integrated UV-VIS emission spectra of TS w/wo ES at mean current of 1 mA.

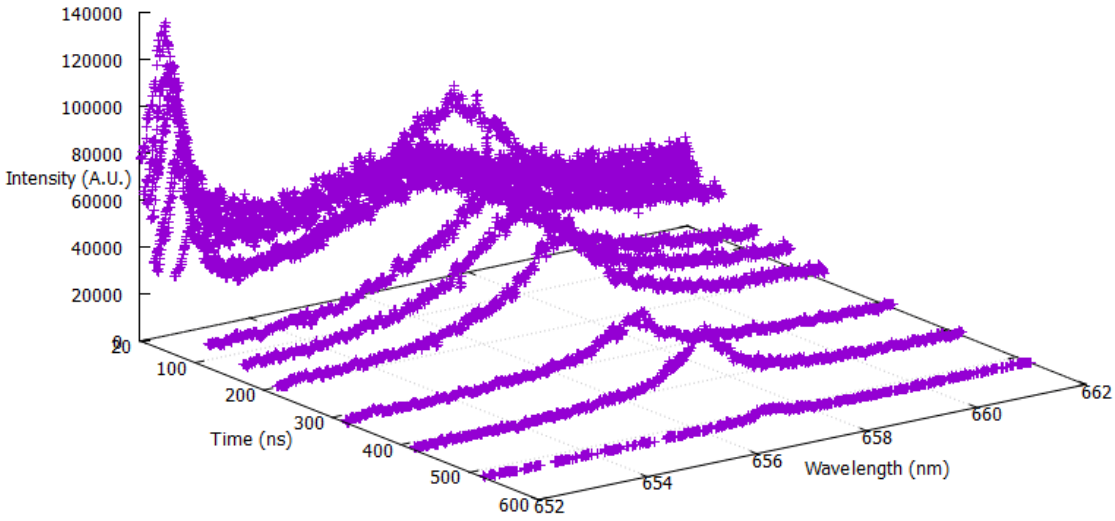

Fig. 4. Time-resolved emission spectra of TS with ES, showing Hα line evolution

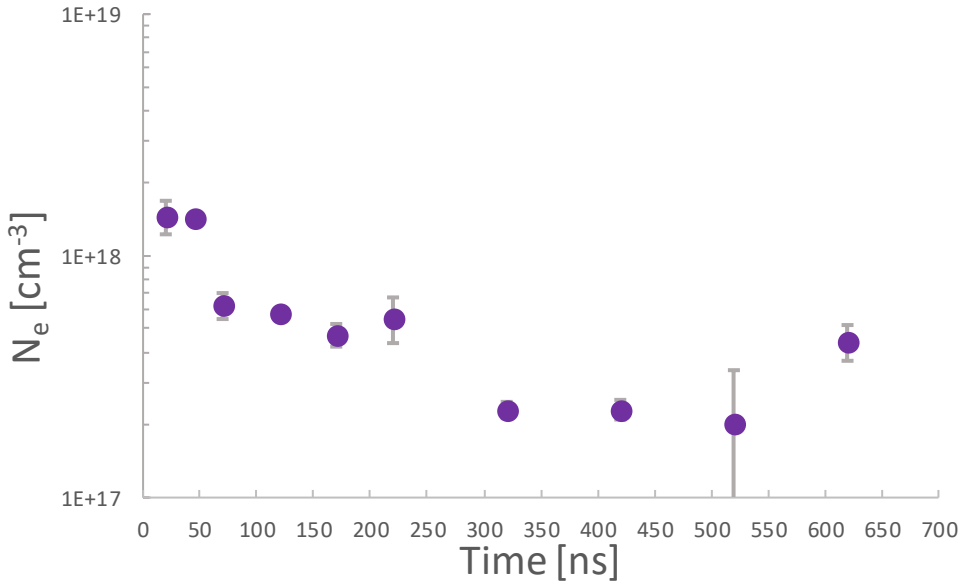

Fig. 5. Evolution of electron density in time for TS with ES, derived from the Stark broadening of the Hα emission line.

4. Conclusions

The emission spectra of TS discharge w/wo ES were dominated by N^+ and O^+ lines, as well as N, O atoms, and N_2 SPS emissions. These findings confirm the high degree of ionization and dissociation in the plasma, however the specific influence of ES on the emission spectra warrants further detailed investigation. Time-resolved spectra of the Hα line, were used to calculate the electron density, again confirming the plasma's high ionization level and reactivity. In the presence of ES, a marked increase in iron ion emission line intensities was detected, attributed to enhanced electrode sputtering.

In further research, we plan to investigate the time resolved spectra of the nitrogen, oxygen and iron ions observed in the integrated emission spectra. These studies aim to elucidate the processes and reaction pathways of plasma chemistry. Additionally, we plan to examine the influence of various parameters and conditions, such as electrical parameters or air- and water flowrate, on the emission spectra. Further research is also needed to identify the types of iron species from electrode erosion, as well as to evaluate the relevance in bio-chemistry of the PAW, and possibly examine other metallic materials as electrode.

Acknowledgements:

This research was funded by the Slovak Research and Development Agency APVV-22-0247 grant, Comenius University grant GUK 2024 - UK/1095/2024, and EU NextGenerationEU through the Recovery and Resilience Plan for Slovakia under the project No. 09I03-03-V03-00033 EnvAdwice

5. References

[1] Machala, Z., Janda, M., Niklová, A., & Martišovitš, V. (2011). Time-resolved emission spectroscopy and imaging of transient spark in atmospheric air. ISPC 20, Philadelphia, USA

2] Wang, S., Liu, F., Yang, D., Wang, W., & Fang, Z. (2019). *Characteristic study of a transient spark driven by a nanosecond pulse power in atmospheric nitrogen using a water cathode. Journal of Applied Physics, 125(4), 043304.* doi:10.1063/1.5050259

[3] Janda, M., Martišovitš, V., Hensel, K., Dvonč, L., & Machala, Z. (2014). *Measurement of the electron density in Transient Spark discharge. Plasma Sources Science and Technology, 23(6), 065016.* doi:10.1088/0963-0252/23/6/065016

[4] Janda, M., & Machala, Z. (2008). *Transient-Spark Discharge in $\hbox{N}_{2}/\hbox{CO}_{2}/\hbox{H}_{2} \hbox{O}$ Mixtures at Atmospheric Pressure. IEEE Transactions on Plasma Science, 36(4), 916–917.* doi:10.1109/tps.2008.917172

[5] Pankaj Pareek, Saeed Kooshki, Peter Tóth, Mário Janda, Tuning composition of plasma activated water generated by transient spark discharge with electrospray, Chemical Engineering Journal, Volume 493, 2024, 152583, ISSN 1385-8947, https://doi.org/10.1016/j.cej.2024.152583.

[6] Gigosos, M. A., González, M. Á., & Cardeñoso, V. (2003). *Computer simulated Balmer-alpha, -beta and -gamma Stark line profiles for non-equilibrium plasmas diagnostics. Spectrochimica Acta Part B: Atomic Spectroscopy, 58(8), 1489–1504.* doi:10.1016/s0584-8547(03)00097-1

[7] Winterbourn, C. C. Toxicity of iron and hydrogen peroxide: the Fenton reaction, Toxicol. Lett. 82 (1995) 969–974.

[8] Janda, M., Hensel, K., Tóth, P., Hassan, M. E., & Machala, Z. (2021). *The Role of HNO2 in the Generation of Plasma-Activated Water by Air Transient Spark Discharge. Applied Sciences, 11(15), 7053.* doi:10.3390/app11157053

[9] Hassan, M.E., Janda, M. & Machala, Z. Comparison of the Transport of Reactive Nitrogen Plasma Species into Water Bulk vs. Aerosolized Microdroplets. *Plasma Chem Plasma Process* (2024). https://doi.org/10.1007/s11090-024-10511-6

MASS SPECTROMETRY OF DIELECTRIC BARIER DISCHARGE WITH WATER ELECTRODE

Neda Babucić[1], Nenad Selaković[1], Oleksandr Galmiz[2], Mário Janda[2], Olivera Jovanović[1], Nevena Puač[1], Nikola Škoro[1]

[1]*Institute of Physics, University of Belgrade, Pregrevica 118, 11080 Belgrade, Serbia*
[2]*Division of Environmental Physics, Faculty of Mathematics, Physics and Informatics, Comenius University in Bratislava, Mlynská dolina, 842 48 Bratislava, Slovakia*
E-mail: nedab@ipb.ac.rs

This paper presents the results of an investigation into the generation of reactive species in two setups of a dielectric barrier discharge (DBD) plasma source, using a water target with different vessels. By analyzing both neutral mass spectra and MID-scan spectra, we explore the concentrations of reactive oxygen and nitrogen species (NO, NO_2 and O_3) under varying plasma conditions and mass spectrometer configurations.

1. Introduction

In the past decade, a lot of interest has been drawn to atmospheric pressure plasmas (APPs) because of their unique properties and wide range of applications in fields such as material processing, agriculture, food industry and biomedicine [1, 2, 3, 4]. Since they do not require costly vacuum systems and operate at atmospheric pressure, APPs have the advantage of being accessible and versatile. Lately, atmospheric pressure plasma in contact with water has attracted significant interest due to its potential to generate reactive species and drive advanced chemical processes for various applications.

The behaviour and chemistry of APPs are greatly affected when they come into contact with water, either as an electrode or as a target. Reactive oxygen, nitrogen and hydrogen species are found in water and are essential for a variety of processes, such as biomedical treatments, sterilization, and water purification. Water forms a dynamic interface where plasma-induced reactions take place, producing reactive species like ozone (O_3), hydrogen peroxide (H_2O_2), hydroxyl radicals (OH), nitrates (NO_3^-), nitrites (NO_2^-) etc. These species play an essential role in enhancing the efficacy of plasma-based processes [5].

Also, higher humidity introduced in feeding gas of APPs has been demonstrated to increase the generation of reactive species, such as OH radicals, which are necessary for surface modification and decontamination [6]. The interaction, however, is complex and depends upon a number of variables, including ambient circumstances, water composition, and plasma characteristics. To optimize plasma processes and customize them for particular applications, it is essential to comprehend these interactions.

Dielectric barrier discharges (DBDs) are widely used for surface activation in atmospheric-pressure plasma applications. However, treating sensitive materials like polymers can be challenging because high-density plasma may cause damage, such as pin-holing. This issue often occurs in volume barrier discharges or coronas, where the plasma moves perpendicular to the treated surface. A practical solution is to generate plasma that travels parallel to the surface. This approach minimizes the risk of damage while maintaining effective treatment. One promising method is the surface dielectric barrier discharge (SDBD), where the plasma spreads along the surface of a dielectric plate. This setup not only protects the material but also improves the efficiency of the process.
In our earlier work [7, 8, 9] we introduced a novel plasma discharge reactor for efficiently activating polymers at the gas/liquid interface. This design uses liquid electrodes to ignite the SDBD directly from the liquid surface. Although the plasma-water interaction is limited to the edge of the dielectric tube, the system is both scalable and flexible, making it suitable for a wide range of applications.

Mass spectrometry is an analytical technique that measures the mass-to-charge ratio of ions to identify and quantify molecules in a sample. Primary advantage of atmospheric pressure mass spectrometry lies in its ability to rapidly and accurately analyse a wide range of chemical species [10]. These instruments are equipped with specialized pumping systems that create a pressure gradient, enabling the effective intake of gases from atmospheric plasmas. For neutral species, the mass spectrometer incorporates an ionization chamber that converts neutrals into ions, enabling their detection and analysis. The mass analyser which filters and detects neutral species or positive and negative ions, generating detailed mass spectra for all components. The technique provides real-time measurements of reactive species, ions, and neutral molecules, which are essential for understanding plasma processes and optimizing plasma-based applications.

When it comes to plasma in contact with water, due to technical challenges, mass spectrometric analysis of the plasma has so far been conducted by introducing water vapour into the working gas [11]. In this paper, we tackled the technical challenge and developed a setup where the mass spectrometer inlet was positioned in close proximity to the plasma-water interface, allowing us to successfully record mass spectra.

In this paper, we will present the results of our investigation into the reactive species generated by the dielectric barrier discharge (DBD) setup, but with two different water vessel configurations. The analysis includes both neutral mass spectra and MID-scan spectra, offering insights into the concentrations of key reactive oxygen and nitrogen species, such as NO, NO_2, CO_2 and O_3, as well as the detailed composition of the plasma obtained under these conditions.

2. Experimental set up

The schematic of the DBD at atmospheric pressure and HIDEN HPR60 mass-energy spectrometer is given in Figure 1. The DBD device is in the triple-phase interface (plasma-liquid-solid) plasma system consisting of a thin glass test tube with a 10 mm diameter and a 0.5 mm wall thickness was used. The liquid inside the test tube served as the high-voltage electrode and was connected to a power supply generating a sinusoidal voltage waveform. The Petri dish bath, which grounded the system, completed the circuit. Tap water with an electrical conductivity of approximately 0.3 mS/cm was used as the liquid electrode. The water was electrically insulated both inside and outside the test tube to ensure stability. The discharge operated in ambient air at atmospheric pressure. The high-voltage sine waveform had an amplitude range of 0 to 20 kV and could be adjusted to frequencies between 23 and 30 kHz. Power was delivered to the liquid electrodes through a high-voltage resonance generator (Lifetech-300W) paired with a function generator (FY3200S-24M).

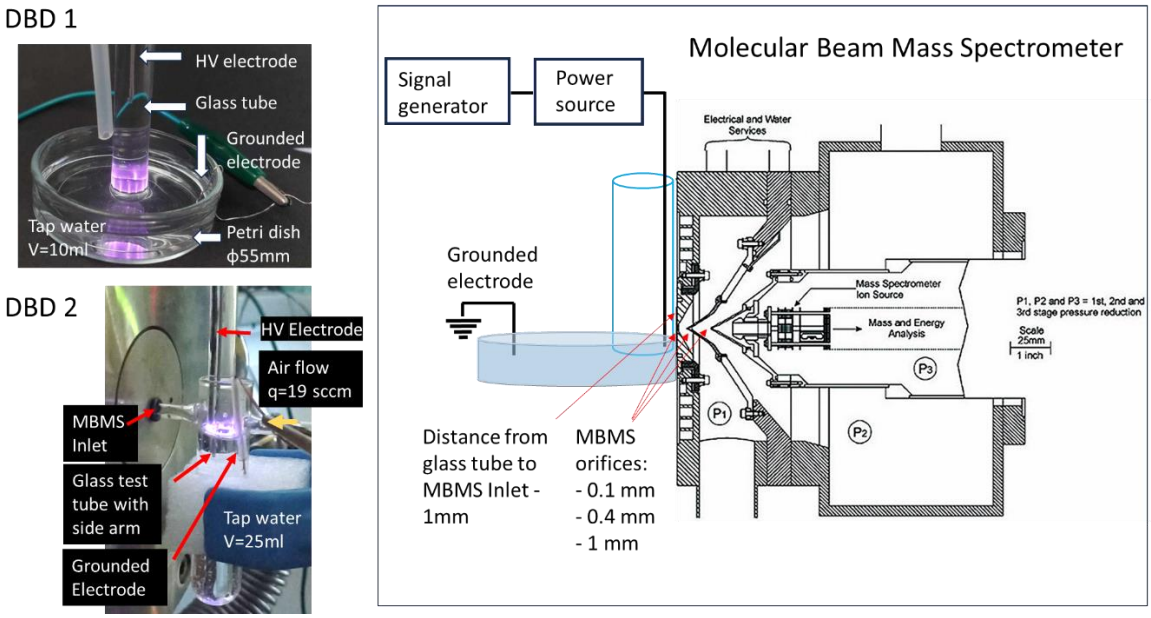

Fig. 1. DBD device in two configurations (DBD1 and DBD2) with a schematic representation of mass spectrometry measurements. In DBD1 setting, the device was immersed in 10ml of tap water placed in a Petri dish (ϕ55mm). In DBD2 setting, the device was placed in a glass test tube filled with 25ml of tap water, equipped with a side arm for gas sampling and a hole for synthetic air intake (q = 19 sccm).

Mass spectrometry measurements were performed by using MBMS (Molecular Beam Mass Spectrometer) HIDEN HPR60. To ensure the formation of a molecular beam, the geometry of the MBMS HPR60 system consists of a centralized combination of the orifice, cone1, and cone2 (P1 vacuum section is formed between the orifice and cone1, P2 vacuum section is formed between cone1 and cone2, and P3 vacuum section is formed after cone2 in the region of the mass analyzer). The orifice had an opening diameter of ⌀0.1 mm, cone1 ⌀0.4 mm, and cone2 ⌀1 mm, accompanied by the following voltages for DBD setups (the orifice was grounded, Vcone1 = 0 Vand Vcone2 =0 V).

During all experiments for DBD setups, the regions within the vacuum section of the mass spectrometer responsible for generating the pressure gradient had the following pressure values: $P_1 = 3.3 \cdot 10^{-1}$ Torr, $P_2 = 7.5 \cdot 10^{-6}$ Torr, and $P_3 = 2.4 \cdot 10^{-7}$ Torr. To identify the species of interest, we first recorded the mass spectra of neutrals (0–100 amu) using the RGA (Residual Gas Analyzer) mode, during which the ionization chamber was active. Within the ionization chamber, the electron emission current from the filament was for DBD1 = 5 µA and for DBD2 =10 µA. In both cases, the electron energy was 70 eV.

After that, we used MID-scan to monitor the temporal changes of selected species for different formation conditions: without plasma, with plasma at specific applied powers for DBD1 (5W and 15W) and DBD2 (15W), with Swagelok open, and with swagelok closed. Swagelok open represents the sum of foreground and background species, while swagelok closed corresponds to background species only.

3. Results and discussion

In this study, we have measured the neutrals mass spectra by using a mass spectrometer for two different configurations of Dielectric Barrier Discharge (DBD) system. In both configurations, titled DBD1 and DBD2, discharge was in contact with water during mass spectrometry measurements. The analysis of neutral species was performed in two different measurement modes of HPR60: RGA mode for neutral mass spectra and MID-scan mode for track in time changes of specific neutral species. These modes provide a comprehensive overview of the ionization processes and chemical compositions

present in the plasma generated by each DBD system. The neutral mass spectra revealed the types and relative concentrations of neutral species, the MID-scan measurement provided insight into the temporal evolution of these species.

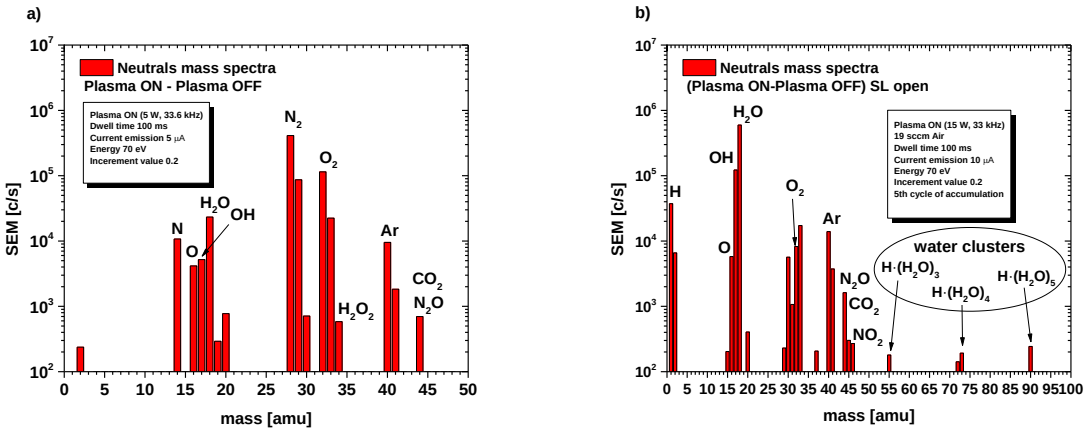

Fig. 2. Neutral mass spectra for a) DBD1 setting and b) DBD2 setting at an operating frequency of 33.6kHz. In the case of the DBD2, an airflow of 19sccm was added. The graphs were obtained by passing the raw results through a MatLab script to integrate the obtained lines for specific mass number.

Figure 2(a) and (b) present Neutral mass spectra for configurations DBD1 and DBD2, respectively. The presented spectra show the difference of Plasma ON mass spectra and Plasma OFF mass spectra. Plasma ON/OFF mass spectra represent the foreground signal i.e. the difference of total signal (swagelok open) and background signal (swagelok closed). The spectra in Figure 2 clearly show that the dominant species in the discharge are nitrogen and oxygen compounds (N, O_2, H_2O_2, N_2O, H, H_2O) which is to be expected because it is a discharge at atmospheric pressure where the target is water. Atomic nitrogen and atomic oxygen are present as a result of plasma reactions, along with the NO radical. The OH radical is also present, resulting from both plasma reactions and water dissociation in the MBMS. In Figure 2(b), water clusters can also be observed at mass numbers 53, 73 and 91, which appear in neutral mass spectra due to water vapor from the bottle containing the discharge. The high humidity in the DBD2 configuration and the plasma conditions promote cluster formation unlike in the case of DBD1 configuration where we did not detect any water clusters of mass above 50 amu.

While the mass spectra results provided an overall view of the main species present in the discharge chamber, nitrogen oxides and ozone can impact the industrial environment even at much lower concentrations (below the detection limit of the mass spectra used). Therefore, more sensitive measurements were conducted specifically for the important species NO, NO_2, N_2O, and O_3, as represented here. It was recorded for different conditions, Plasma ON and OFF with background only (BG), as well as Plasma ON and OFF with foreground and background (FG+BG). Unlike the case of BG, where only the inner part of the MS is considered in the measurement, in the case of FG+BG, the mass spectrometer is open so outside ambient air is also evaluated.

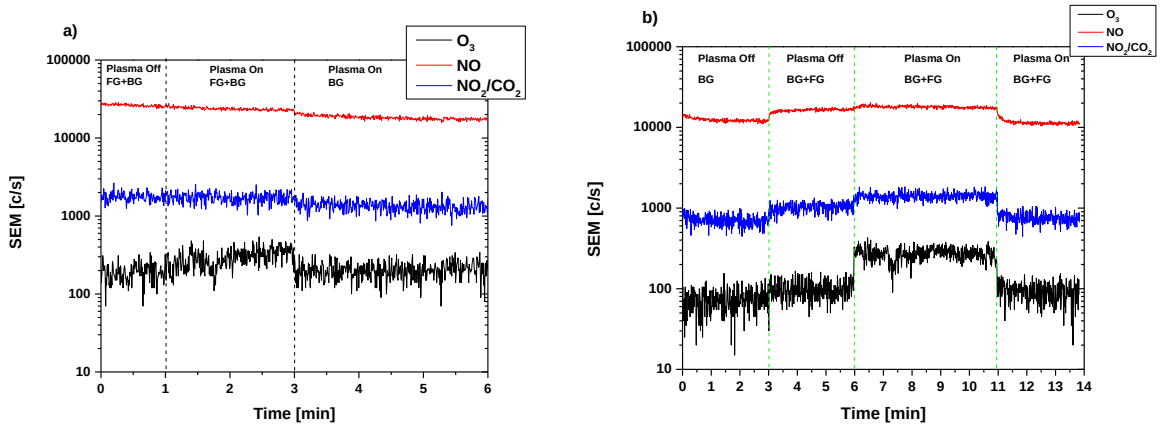

Fig. 3. The mid-scan provides constant tracking of selected species, with different stages of the experiment marked by labels: plasma on and off, foreground (FG) and background (BG); (a) DBD1 Setup, ionization filament current set to 5 µA at 70 eV, and (b) DBD2 Setup, ionization filament current set to 50 µA at 70 eV.

The MID-scan for DBD1 setup (Figure 3(a) starts with Plasma OFF and swagelock open (1st minute), both the foreground (outside the spectrometer) and background are measured. The discharge is ignited in minute 1 and swagelok is open. Here we can see that NO continues to decrease slightly, NO_2 remains constant, and O_3 increases, indicating plasma-driven production of O_3. After the 3rd minute, with the plasma still on but swagelock closed, all species (NO, NO_2, and O_3) decrease as expected (only background inside device is measured).

The Figure 3(b) shows MID-scan spectra for DBD2 configuration. In the first three minutes, with the plasma off and the swagelock closed, only the background signal is measured. After opening of the swagelok (3-6 minutes), the increase in NO and NO_2 suggests the influence of ambient air, while O_3 remains unchanged. Between 6 and 11 minutes, with the plasma on and the swagelok open, NO and NO_2 rise slightly, but O_3 increases significantly, indicating plasma-driven O_3 production. Finally, from 11th minute, with the plasma on and the swagelok closed, all species decrease due to limited external interaction (only background is measured).

4. Conclusion

Mass spectrometry analysis of two setups of a DBD source with a water electrode, generated at atmospheric pressure was performed. Despite the difference in the water vessel used in each setup, in both setups similar trends in the behavior of reactive species were shown, indicating strong influence of plasma on water target. In both cases, plasma activation leads to the generation of reactive oxygen and nitrogen species, such as NO, NO_2, CO_2, and O_3, with notable increases in O_3 concentration when the plasma is on. Differences in the water vessel may affect the plasma's efficiency in producing reactive species, but both setups demonstrate that the plasma's interaction with the water is crucial for modulating the levels of reactive species. These findings highlight the importance of the plasma-water system in applications such as water treatment and agriculture, where reactive species generated in plasma-activated water could have significant biological and chemical effects.

Acknowledgments: The research was supported by the project of bilateral cooperation between Republic of Serbia and Republic of Slovakia 2024-2025 (project no. 337-00-3/2024-05/07), grant of the Ministry of Science, Technological Development and Innovations no. 451-03-68/2024-14/200024 and by the EU NextGenerationEU through the Recovery and Resilience Plan for Slovakia under the project No. 09I03-03-V04-00094.

5. References

[1] Penkov, O. V., et al. "A Review of Recent Applications of Atmospheric Pressure Plasma Jets for Materials Processing."*Journal of Coatings Technology and Research*, vol. 12, 2015, pp. 225-235.

[2] Puač, N., et al. "Plasma Agriculture: A Rapidly Emerging Field." *Plasma Processes and Polymers*, vol. 15, no. 2, 2018, p. 1700174.

[3] Bilea, F., et al. "Non-Thermal Plasma as Environmentally-Friendly Technology for Agriculture: A Review and Roadmap." *Critical Reviews in Plant Sciences*, vol. 43, no. 6, 2024, pp. 428-486.

[4] Machala, Z., et al. "Emission Spectroscopy of Atmospheric Pressure Plasmas for Bio-Medical and Environmental Applications." *Journal of Molecular Spectroscopy*, vol. 243, no. 2, 2007, pp. 194-201.

[5] Machala, Z., et al. "Chemical and Antibacterial Effects of Plasma Activated Water: Correlation with Gaseous and Aqueous Reactive Oxygen and Nitrogen Species, Plasma Sources and Air Flow Conditions." *Journal of Physics D: Applied Physics*, vol. 52, no. 3, 2018, p. 034002.

[6] Sainct, F. P., et al. "Temporal Evolution of Temperature and OH Density Produced by Nanosecond Repetitively Pulsed Discharges in Water Vapour at Atmospheric Pressure." *Journal of Physics D: Applied Physics*, vol. 47, no. 7, 2014, p. 075204.

[7] Galmiz, O., et al. "Study of Surface Dielectric Barrier Discharge Generated Using Liquid Electrodes in Different Gases." *Journal of Physics D: Applied Physics*, vol. 49, no. 6, 2016, p. 065201. https://doi.org/10.1088/0022-3727/49/6/065201.

[8] Galmiz, O., et al. "Hydrophilization of Outer and Inner Surfaces of Poly(vinyl Chloride) Tubes Using Surface Dielectric Barrier Discharges Generated in Ambient Air Plasma." *Plasma Processes and Polymers*, vol. 14, no. 9, 2017. https://doi.org/10.1002/ppap.201600220.

[9] Galmiz, O., et al. "Plasma Treatment of Polyethylene Tubes in Continuous Regime Using Surface Dielectric Barrier Discharge with Water Electrodes." *Journal of Physics D: Applied Physics*, vol. 51, no. 19, 2018. https://doi.org/10.1088/1361-6463/aabb49.

[10] Rees, J. A., et al. "Mass and Energy Spectrometry of Atmospheric Pressure Plasmas." *Plasma Processes and Polymers*, vol. 7, no. 2, 2010, pp. 92-101.

[11] Willems, G., et al. "Absolutely Calibrated Mass Spectrometry Measurement of Reactive and Stable Plasma Chemistry Products in the Effluent of a He/H2O Atmospheric Plasma." *Journal of Physics D: Applied Physics*, vol. 50, no. 33, 2017, p. 335204.

RAPID DETECTION OF VOLATILE ORGANIC COMPOUNDS EMITTED FROM PLANTS BY MULTICAPILLARY COLUMN-ION MOBILITY SPECTROMETRY

Vahideh Ilbeigi*, Ladislav Moravsky, Stefan Matejcik
Department of Experimental physics, Comenius University, Bratislava, Slovakia.
E-mail: vahideh.ilbeigi@fmph.uniba.sk; matejcik@fmph.uniba.sk

This study presents a novel rapid analytical method for the detection of volatile organic compounds (VOCs) emitted from blueberry leaves using Tenax adsorbent followed by separation using a multicapillary column (MCC) and Ion Mobility Spectrometry (IMS) detection. The emitted VOCs including caryophyllene, benzene acetonitrile, linalool, ocimene, and methyl salicylate initiated by different stress factors including mechanical damage (punching), herbivore attack (aphids) and methyl jasmonate (MeJA) spraying were detected and quantified. This new cost-efficient method provided a simple and direct detection of the emitted VOCs form plants without any sample pretreatment.

1. Introduction

Plants produce a wide range of volatile organic compounds (VOCs) in different tissues and release them into air, environment, and their surroundings [1]. Some of the VOCs are produced at different developmental stages such as flowering, ripening, or maturation [2], while many of the plant VOCs are emitted as a defence mechanism [3]. The VOCs are released from plants upon exposure to mechanical, biotic (herbivores, pathogens, viruses) and abiotic (temperature, humidity, radiation) stresses and act as airborne signals to induce defence in the neighbouring plants [4]. To understand the defence mechanism and the biological information transmitted by the plant VOCs, the types of VOCs and their amount must be determined.

In this work, we employed ion mobility spectrometry for detection of the emitted VOCs from blueberry leaves upon exposure to different stress factors including mechanical damage (punching), herbivore attack (aphids) and methyl jasmonate (MeJA) spraying. A glass chamber was designed and constructed to collect the emitted VOCs using a Tenax®TA adsorbent. The collected VOCs were desorbed thermally and separated by a MCC column before detection by IMS.

2. Methods

The glass chamber for collecting VOCs from plants was designed and constructed in-house (Fig. 1). It includes a Teflon base with a hole in its center to put the plant into it and a glass cylinder (2L) which was sealed around the blueberry plant to avoid leakage of the emitted chemicals. A stream of zero air with flow rate of 100 ml/min was used to sweep up the emitted volatiles and were released through the outlet at the top of the glass cylinder. To the outlet of the glass cylinder a Tenax® trap was connected and was used to collect the exhaled VOCs. A small membrane pump (Piezoelectric Disc Pump, Lee Co.) was maintained the stream of the air through Tenax trap at flow rate of 100 ml/min. The sampling and collecting time were set to 30 min in all measurements. The VOCs emitted from the blueberry plants were collected 48 h after three different treatments of the plants: (i) mechanical punching of the blueberry leaves; (ii) spraying MeJA on the leaves; and (iii) herbivore attack. The desorption of adsorbed compounds from the Tenax trap was achieved using a thermal desorption system at 230 °C. The desorbed compounds were transferred to the MCC (as a pre-separation technique) by a carrier gas (zero air) with a flow rate of 70 mL min^{-1}.The measurements were replicated four times for each treatment.

Fig. 1. Experimental setup for collecting the emitted VOCs from blueberry leaves including (a) a Teflon guillotine-like base, (b) Tenax trap as an adsorbent, (c), a small pump and (d) the final assembled setup including a glass cylinder and a blueberry branch in it.

3. Results

The blueberry plants were exposed to the different stress factors including mechanical (punching), aphids, and methyl jasmonate (MeJA) spraying. Figures 2a, 2b, and 2c present the retention time integrated ion mobility spectra and 2D plots of the VOCs emitted from blueberry leaves, recorded 48h after exposure to aphids, application of MeJA, and punching. Different stress factors resulted in the release of different VOCs with different intensities. In the case of aphids (Figure 2a), higher levels of MeSA and BeCN and lower intensities of linalool and caryophyllene were detected. The treatment by MeJA, and mechanical damage (punching) resulted in low level of MeSA (in accordance with previous studies [5]). Application of MeJA produced high amount of linalool, and also induced considerable amount of caryophyllene and BeCN (Figure 2b). In mechanical damage (punching) higher concentration of ocimene, linalool and caryophyllene were detected compared to other stress factors (Figure 2c). MeJA was observed only for samples treated by this compound (Figure 2b).

In addition to studied VOCs substances, additional unidentified substances are present in the 2D plots which are indicated by X1 and X2 in the corresponding ion mobility spectra (Figure 2a-2c). These peaks may be due to other VOCs emitted from blueberry leaves with high concentrations like cadinene, myrcenone, or eucalyptol [5].

The amounts of emitted VOCs measured by the Tenax-MCC-IMS are summarized in Table 1 in ng per g of dry leaves per hour. These amounts are comparable with those obtained by Super-Q adsorbent-GC-MS [5]. For example, the emitted linalool and MeSA measured by Super-Q adsorbent-GC-MS after mechanical damage are 434 and 67 ng/g per hour [5] which are in accordance with those measured in this work (494 and 58 ng/g per hour) by the Tenax-MCC-IMS method.

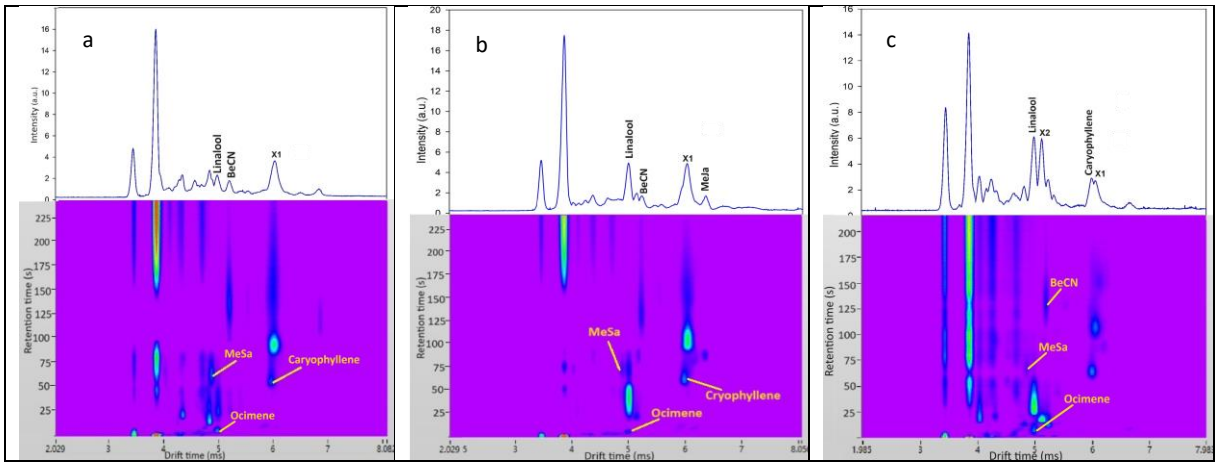

Fig. 2. Typical ion mobility spectra and the 2D plots (retention time vs drift time) for the VOCs emitted from blueberry leaves 48 h after (a) exposure to aphids, (b) MeJA spraying, and (c) punching.

Tab. 1. The amount emitted VOCs (ng per g of dry leaves) measured by the Tenax-MCC-IMS method 48 h after different treatments (4 replicates).

	treatment		
VOC	Aphids	MeJA (1.0 mM)	Mechanical (punch)
Linalool	245±74	430±165	494±112
Ocimene	65±29	44±15	82±23
MeSA	104±36	81±24	58±21
Caryophyllene	125±57	186±26	287±65
Benzene acetonitrile	456±44	398±42	340±79

4. Conclusions

A novel Tenax-MCC-IMS method was developed, optimized, and applied for the detection of the VOCs emitted from blueberry leaves. Using this method, in-vivo detection of linalool, MeSA, caryophyllene, BeCN, and ocimene was carried out in response to different stress factors applied to blueberry plant. It was found that the mechanical damage and MeJA caused emission of high amount of linalool while in case of aphids, emission of MeSA was preferred. Generally, the substances, as well as the measured quantities detected using the Tenax-MCC-IMS method are in reasonable agreement with those reported in literature using GC-MS, indicating the acceptable reliability of the present method. In addition, MCC-IMS has affordable price and provides a fast analysis (1-2 minutes) compared to GC-MS (> 10 min). Because of the use of the head-space extraction by a Tenax trap of the VOCs emitted from blueberry, there was no need of sample pre-treatment or using of the solvents. We applied the Tenax-MCC-IMS method for the analysis of the emitted VOCs from blueberry leaves, however, this method can be used for other plants as well, provided they can be housed in the integrated device. As there are different (commercial) portable IMS instruments, we hope that this method can be modified further for in-site measurements in green-houses and farms.

5. Acknowledgement

The research presented in this paper received funding from the European Union's Horizon 2020 research and innovation program under the Marie Sklodowska-Curie grant agreement No. 101031538 and the EU NextGenerationEU through the Recovery and Resilience Plan for Slovakia under the project No. 09I01-03-V04-00025. It was partially supported by Slovak Research and Development Agency under projects no. APVV-22-0199 and APVV-23-0522 and Slovak Grant Agency VEGA project no. 1/0372/24.

6. References

[1] Liu Z., Wang M., Wu M., Li X., Liu H., Niu N., Li S. and Chen L., *TrAC Trend Anal. Chem.* 2023, **158**, 116872.
[2] Vivaldo G., Masi E., Taiti C., Caldarelli G. and Mancuso S., *Sci. Rep.* 2017, **7**, 11050.
[3] Kigathi R. N., Weisser W. W., Reichelt M., Gershenzon J. and Unsicker S. B., *BMC Plant Biol.* 2019, 19, 58.
[4] Baldwin IT., Halitschke R., Paschold A., Von Dahl C. C. and . Preston C. A, *Science,* 2006, **311**, 812-815.
[5] Rodriguez-Saona C. R., Rodriguez-Saona L. E. and Frost C. J., *J. Chem. Ecol.,* 2009, **35**,163-175.

STUDY OF PLASMA-ASSISTED REACTION OF PENTANE AND AMMONIA BY ATMOSPHERIC PRESSURE CHEMICAL IONIZATION ION MOBILITY-MASS SPECTROMETRY (IMS-MS)

Priyanka Kumari, Vahideh ILbeigi*, Stefan Matejcik *

Faculty of Mathematics, Physics and Informatics, Mlynska dolina F2, 84248 Bratislava, Slovak Republic

Email: vahideh.ilbeigi@fmph.uniba.sk, matejcik@fmph.uniba.sk

The plasma-chemical processes of an alkane (pentane) initiated by Corona Discharge (CD) with and without NH_3 dopant at atmospheric pressure were studied using ion mobility spectrometry (IMS) and mass spectrometry (MS). A Corona Discharge Reactor (CDR) was designed to study the reaction mechanism of pentane in the presence of NH_3, and effects of the operational parameters such as discharge current, composition atmosphere in the reactor, pentane concentration, humidity, and discharge polarity were investigated. The IMS and MS spectra were recorded in the absence and presence of NH_3 dopant to analyze CDR's neutral products. The standard reactant ion (RI) in atmospheric pressure chemical ionization (APCI) is $H^+(H_2O)_n$ and the product ions of $[M+O-3H]^+$, $[M+O-H]^+$, $[M+O-H]^+H_2O$, and $[(M+O-H)_2-CO]H^+$ were identified indicating formation of pentanone and hydroxy-pentanone in CDR. In the presence of NH_3, $NH_4^+(H_2O)_n$ is the main RI in APCI-IMS, and the adduct ions $[M+O-3H]^+NH_3$, and $[M+O-H]^+NH_3$ were produced. It was found that humidity changes the distribution of the products in CDR so that at low humidity (0.1%), hydroxy-ketones are the main products, while with increase in the humidity to 32%, more ketones are produced. In addition, NH_3 enhances the ionization efficiency via ammonia attachment and consequently increases sensitivity of IMS for quantitative analysis of pentane.

1. Introduction

Ion mobility spectrometry (IMS) and mass spectrometry (MS) are effective tools for analyzing gas-phase samples, including volatile and non-volatile substances. IMS operates at ambient pressure, while MS requires a vacuum, with ionization achieved using sources like corona discharge (CD) or electrospray [1]. Alkanes, key components of fuels and natural gas [2], are challenging to analyze due to their high ionization energy and low proton affinity [3], rendering conventional methods like APCI and ESI ineffective [4]. Non-thermal plasma (NTP) facilitates alkane transformations, producing oxidation products with sufficient proton affinity for APCI detection [5]. Studies using plasma-based ionization have identified regioselective oxidation and carbenium ion formation in alkanes, enabling improved analysis [6,7].

In this work, an external corona discharge reactor (CDR) was designed and constructed to functionalize pentane. The pentane products were then monitored using ion mobility-mass spectrometry. The effect of NH_3 on the ionization of the pentane product is also investigated.

2. Experimental setup

2.1 Instrumentation

The IMS and IMS combined with the time-of-flight mass spectrometer (IMS-TOFMS) used in this work are equipped with a point-to-plane CD-APCI ionization source. They are a homemade instrument constructed at the Department of Experimental Physics of Comenius University. A detailed description of the instruments can be found elsewhere [8,9]. The IMS drift tube operates at sub-ambient pressure (600 mbar) and a temperature of 110 ± 2 °C (temperature of the drift gas at exit), with a Faraday cup as the IMS detector at the end of the drift tube. The flow rate of the drift gas (purified ambient air) was 600 ml.min-1. A voltage of 8.5 kV was applied across the IMS cell (12.5 cm) to provide a drift field of 680 $V.cm^{-1}$. The CD ion source was supplied by a potential difference of 3 kV between the needle and the planar electrode.

2.2 Corona discharge reactor (CDR)

The external corona discharge reactor (CDR) was designed and connected to IMS and IMS-MS. It was in point-to-plane geometry (Fig. 1-a) in a T-junction stainless steel element. The point electrode was made of tungsten wire (diameter 50 µm) mounted in a ceramic tube located in the axis of the discharge chamber. T- connector was connected to the ground of high voltage power supply to create a strong electric field around the point electrode. The distance between the tip of the wire (point electrode) and the ground electrode was around 5 mm and can be adjusted by moving the ceramic tube along the axis of the discharge chamber. A limiting resistor of 5 MΩ was used to prevent sparks. The alkanes and NH_3 dopant fed in the CDR (Fig. 1-b) with air carrier gas and the ionized products were introduced to IMS and IMS-MS. The experiments were performed in the positive polarity of CDR and positive polarity of IMS and IMS-MS. The polarities of CDR and IMS, and IMS-MS can be set independently.

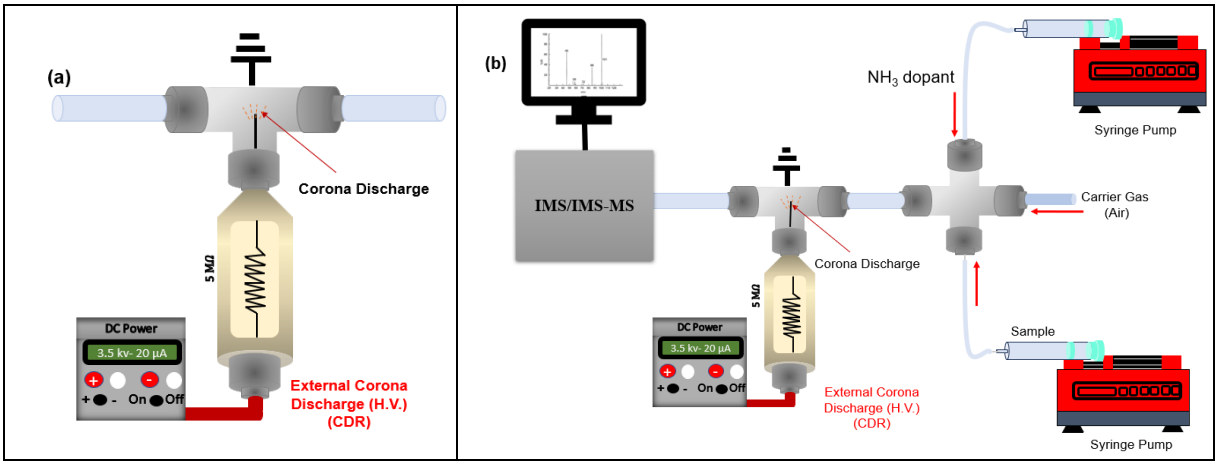

Fig. 1. a) Schematic view of external corona discharge reactor, b) experimental setup for ionization of alkanes with NH_3 dopant.

3. Result and discussion

The products of the chemical transformation of pentane in CDR and their ionization in APCI are studied using IMS technique. No signal was observed for pentane when it was directly injected into the ion source of IMS without pre-treatment by CDR. This is due to the low proton affinity of pentane (PA(M)=721±20 kJ/mol [10]; it cannot be ionised by RI ($H^+(H_2O)_n$) in reaction region of IMS. After pentane pre-treatment in CDR, several peaks appeared in the IMS spectrum (pink spectrum in Fig. 2-a), due to ionization of the neutral products generated in CDR. In IMS spectrum, the peaks appear at drift times 4.3 ms, 4.6, 4.8 ms, 5.45 ms, and 5.98 ms with corresponding mobilities 2.08 $cm^2V^{-1}s^{-1}$, 1.91, 1.90 $cm^2V^{-1}s^{-1}$, 1.65 $cm^2V^{-1}s^{-1}$ and 1.49 $cm^2V^{-1}s^{-1}$. The recorded mass spectrum in Figure 2b shows that the IMS peaks are due to ions with m/z of 85, m/z 87, m/z 105, m/z 145, and m/z 173. Hence, the ions were assigned to $[C_5H_{12}+O-3H]^+$ or $[M+O-3H]^+$ (m/z=85), $[M+O-H]^+$ (m/z=87), $[M+O-H]^+H_2O$ (m/z=105), and $[(M+O-H)_2-CO]H^+$ (m/z=145). The ion $[M+O-H]^+$ is a protonated ketone, 2-pentanone, or/and 3-pentanone and $[M+O-3H]^+$ can be attributed to protonation of hydroxy-pentanone followed by a water elimination. The effect of humidity on the formation of the products in the CDR was also investigated and it was found that at low humidity (0.1%) more 5-hydroxy-2-pentanone is produced, whereas, at higher humidity levels (32%), ketones (2-pentanone and 3-pentanone) are the predominant products (the results are not shown).

In the presence of ammonia, where $NH_4^+(H_2O)_n$ is the main reactant ion [11], the pentane products (pentanones and hydroxy-pentanone) are ionized via NH_4^+ attachment. The ion mobility spectrum of pentane in presence of NH_3 dopant shows a single peak (blue spectrum in Fig. 2a). In other words, using the ammonia dopant simplifies the IMS spectrum of pentane which is of importance practically from an analytical chemistry point of view. The mass spectrum in Fig. 2b confirms that this single broad

IMS peak is due to NH_4^+ attachment to pentanone and hydroxy-pentanone produced in CDR, and formation of $[M+O-4H]NH_4^+$ (m/z=102) and $[M+O-2H]NH_4^+$ (m/z=104) ions.

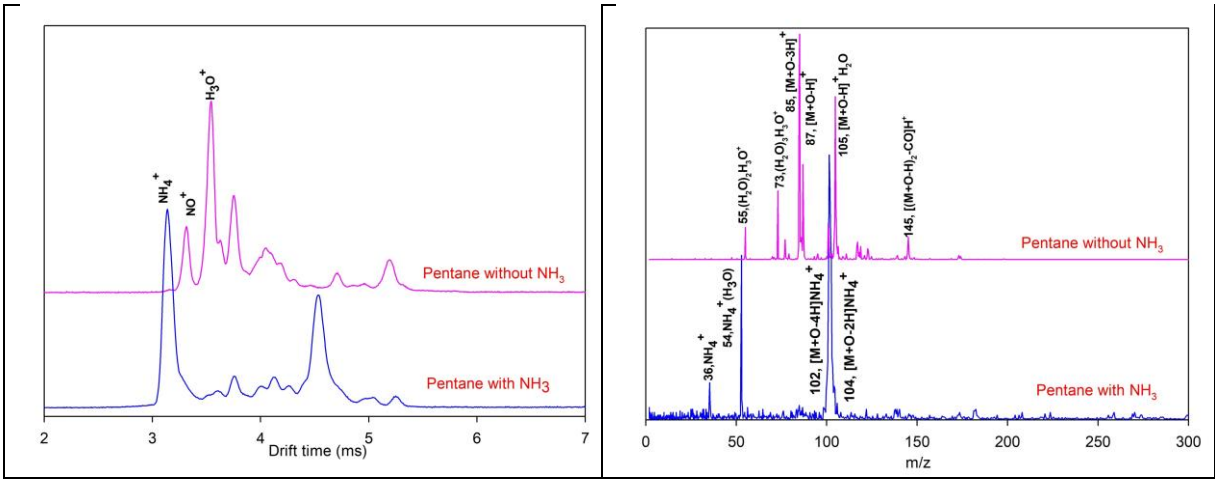

Fig. 2. a) Ion mobility spectra of pentane with and without NH_3 dopant chamber b) Mass spectra of pentane with and without NH_3 dopant

4. Conclusion

In this study, we successfully demonstrated the application of a custom-designed Corona Discharge Reactor (CDR) for the transformation and ionization of pentane in an air-pentane mixture at atmospheric pressure. The experiments were performed using Ion Mobility Spectrometry (IMS) and IMS combined with mass spectrometry (IMS-MS), which allowed the identification and quantification of the chemical products generated from pentane in the CDR. It was found that the main products were 5-hydroxy-2-pentanone, 3-pentanone, and 2-pentanone in the CDR. To increase sensitivity of IMS for detection of pentane, ammonia dopant was used. The results show that without NH_3, the primary reactant ion was $H_3O^+(H_2O)_n$, producing oxidized product ions such as $[M+O-3H]^+$ and $[M+O-H]^+$. In the presence of NH_3, $NH_4^+(H_2O)_n$ was the reactant ion, forming ammonia-adduct ions like $[M+O-H]^+NH_3$. The study highlights the role of humidity in influencing product distribution, with hydroxy-ketones formed under low humidity and ketones predominating at higher humidity levels. This work advances understanding of plasma-chemical processes, providing insights into the regioselective oxidation and ionization of alkanes, with potential applications in energy production, pollution monitoring, and analytical chemistry.

5. Acknowledgement

The present studies were supported by the Slovak Research and Development Agency under project Nr. APVV-19-0386 and Nr. APVV-22-0133. The studies were also funded by the EU Next Generation EU through the Recovery and Resilience Plan for Slovakia under project No. 09I03-03-V02-00036 and 09I01-03-V04-00025.

6. References

[1] Zhang, Ting, Zi-Yu Li, Mei-Qi Zhang, and Sheng-Gui He. The Journal of Physical Chemistry A 120, no. 25.

[2] Hillel, D., & Hatfield, J. L. (Eds.).: Encyclopedia of Soils in the Environment (Vol. 3). Amsterdam, The Netherlands: Elsevier. (2005)

[3] Dagan, S., & Amirav, A. Journal of the American Society for Mass Spectrometry. 6(2), 120-131 (1995).

[4] Kiontke, A., Billig, S., & Birkemeyer, C. *International Journal of Analytical Chemistry*.

[5] Usmanov, D. T., Chen, L. C., Hiraoka, K., Wada, H., Nonami, H., & Yamabe, S. Journal of Mass Spectrometry. 51(12).
[6] Ayrton, S. T., Jones, R., Douce, D. S., Morris, M. R., & Cooks, R. G. Angewandte Chemie. 130(3).
[7] Sekimoto, Kanako, Motoshi Sakakura, Takatomo Kawamukai, Hiroshi Hike, Teruhisa Shiota, Fumihiko Usui, Yasuhiko Bando, and Mitsuo Takayama. Analyst 141, no. 16.
[8] Stano, M., Safonov, E., Kucera, M., & Matejcik, S. Analytical chemistry. 102(16).
[9] Sabo, M., Páleník, J., Kučera, M., Han, H., Wang, H., Chu, Y., & Matejčík, Š. International Journal of Mass Spectrometry. 293(1-3).
[10] Yue Fu, Wanru Li, Jeremy M. Manheim, Jacob Milton, Gozdem Kilaz, Hilkka I. Kenttämaa. Proton Affinities of Alkanes. Journal of the American Society for Mass Spectrometry **2022**, *33* (10), 1850-1857.
[11] Valadbeigi, Y., Ilbeigi, V., Michalczuk, B., Sabo, M., & Matejcik, S. The Journal of Physical Chemistry A, 123 (1).

PERFORMANCE OF TWO-FIELD LINEAR TIME-OF-FLIGHT MASS SPECTROMETER

Catalina McLaughlin[1], James Ellis[2], Thomas Field[1]

[1] *School of Mathematics and Physics, Queen's University Belfast, Belfast BT7 1NN, UK*
[2]*Oxford Instrument Plasma Technology, Bristol, BS35 4GG, UK*
E-mail: cmclaughlin101@qub.ac.uk

Space focusing in linear time-of-flight mass spectrometry has been investigated. This work presents an updated condition for achieving second-order space focusing with two accelerating fields, along with simulations of recommended geometries. The relationship between first-order space focusing using a single accelerating region and second-order space focusing with two accelerating regions is also explored.

1. Introduction

Time-of-flight mass spectrometers (TOFMSs) are well-established and commercially available tools. A key paper in the development of these instruments was published by Wiley and McLaren in 1955 [1] describes a linear TOFMS with two electric fields and first-order space focusing. The goal of space focusing is to make the arrival time of ions at the detector independent of their initial displacement, x, from the centre of the ion source. In first order space focusing the time of flight is independent of x, but second-order (x^2) and higher-order (x^3, x^4 etc.) effects still contributed to peak broadening in the mass spectra, along with the initial velocity of the ion.

The resolution of TOFMSs was further advanced by Mamyrin et al. [2], who introduced the reflectron design, which incorporates an electrostatic mirror to compensate for the kinetic energy spread of ions originating from the source of TOFMSs. The reflectron redirects ions along the same flight path before detection, resulting in significantly improved resolution. Reflectron mas resolutions generally exceed 1000 whereas resolutions of 100 to 200 are more typical for Wiley McLaren linear TOFMSs [1] . Linear TOFMS systems are less complex and generally smaller than reflectron TOFMSs.

Re-examinations of linear TOFMSs by Eland [3] and Piseri et al. [4] described second-order space focusing, where ion times-of-flight are independent of first- and second-order spatial dispersion effects. This approach, and similar approaches [5-6], provide a more precise correction for variations in ion position, resulting in improved resolution compared to first-order systems.

We present simple geometrical relationships for construction of second-order TOF systems, supported by simulations. This study also provides new insight into the relationship between second-order space focusing with two accelerating regions and first-order space focusing with a single accelerating region.

2. References

[1] Wiley, W.C. and McLaren, I.H., 1955. Time-of-flight mass spectrometer with improved resolution. *Review of scientific instruments*, *26*(12), pp.1150-1157.
[2] Mamyrin, B.A., Karataev, V.I., Shmikk, D.V. and Zagulin, V.A., 1973. The mass-reflectron, a new nonmagnetic time-of-flight mass spectrometer with high resolution. *Zh. Eksp. Teor. Fiz*, *64*(1), pp.82-89.
[3] Eland, J.H.D., 1993. Second-order space focusing in two-field time-of-flight mass spectrometers. Measurement Science and Technology, 4(12), p.1522.
[4] Piseri, P., Iannotta, S. and Milani, P., 1996. Parameterization of a two-stage mass spectrometer performing second-order space focusing. *International journal of mass spectrometry and ion processes*, *153*(1), pp.23-28.
[5] Even, U. and Dick, B., 2000. Computer optimization for high-resolution time-of-flight mass spectrometer. Review of Scientific Instruments, 71(12), pp.4415-4420.
[6] Even, U. and Dick, B., 2000. Optimization of a one-dimensional time-of-flight mass spectrometer. *Review of Scientific Instruments*, *71*(12), pp.4421-4430.

DESIGN AND CONSTRUCTION OF AN ION MOBILITY SPECTROMETER BASED ON ELECTROSPRAY

Ondrej Cvičela[1], Ladislav Moravský[1] and Štefan Matejčík[1],

[1]*Department of Experimental Physics, Comenius University in Bratislava, 84248 Bratislava, Slovakia*
E-mail: ladislav.moravsky@fmph.uniba.sk

Ion mobility spectrometry (IMS) is an analytical technique characterized by high sensitivity and rapid analysis of gaseous ions at atmospheric pressure. This technique measures the mobility of ions generated from the sample in a gaseous medium with an electric field. Ionization and introduction of liquid samples into the spectrometer are made possible by using electrospray ionization (ESI). ESI allows the formation of ions directly from liquid samples using high voltage, minimizing the thermal degradation of molecules. This work shows the design and construction of an ion mobility spectrometer based on electrospray ionization (ESI-IMS). An important part of the work is the measurement and analysis of electric current carried by electrospray depending on the voltage at the capillary tip under different conditions.

1. Introduction

A large part of the samples under investigation can be introduced into the IMS apparatus by direct aspiration with subsequent ionization of gaseous particles, naturally evaporating from the substance under investigation, or dusted from the surface of a solid. Also, most substances that can be dissolved in non-polar solvents have sufficient vapor pressure to allow their presence to be examined in this way [1-2]. However, these methods still do not allow the investigation of many biological, as well as environmentally and industrially important non-volatile compounds commonly dissolved in polar solvents such as water. All organisms, many biological processes, and various human activities operate based on substances soluble in water. Therefore, the development of electrospray ionization (ESI) as a method of introducing a liquid sample into a spectrometer has significantly expanded the scope of IMS as an analytical method. The possibilities of ESI-IMS include the detection of non-volatile pesticides and other hazardous substances [3], the monitoring and investigation of polymers, peptides, and proteins [4-6], as well as many other complex compounds for analytical, medical, and bioanalytical purposes [7].

2. Experimental part

This work aimed to create a proposal for an ESI-IMS spectrometer, based on the design of the apparatuses operating at our faculty. The constructed apparatus will be used to analyze substances dissolved in liquids, which cannot be normally analyzed due to their insufficient saturated vapor pressure. The ESI process depends on many parameters, often specific to the apparatus, and capillary type. Therefore, it is necessary to investigate electrospray operation by measuring the current carried by the sprayed liquid as a function of external parameters. The parameters (Table 1) investigated by this method include capillary nature, the magnitude of the electric voltage between the capillary and the counter electrode, distance d between the capillary and the counter electrode, solvent flow rate, organic component content in the solvent, and acetic acid content in the solvent.

Tab. 1. Parameters of ESI used in the experiment.

Operating Parameters	Unit
Capillary nature	Glass and Metal
Electric voltage	0-6.5 kV
Distance	6-20 mm
Solvent flow rate	0.3 – 3 µL.min^{-1}
Organic component	90/10 and 80/20 methanol/water
Acetic acid content	0-0.5%

By measuring the dependence of the electric current on individual parameters, we subsequently tried to identify the optimal values of the electric voltage for the electrospray operation in cone-jet mode. All the used chemicals including HPLC-grade water and HPLC-grade methanol, along with glacial (≥ 99%) acetic acid, were supplied by Sigma-Aldrich. During the development of the spectrometer itself, we used the apparatus schematically shown in Figure 1.

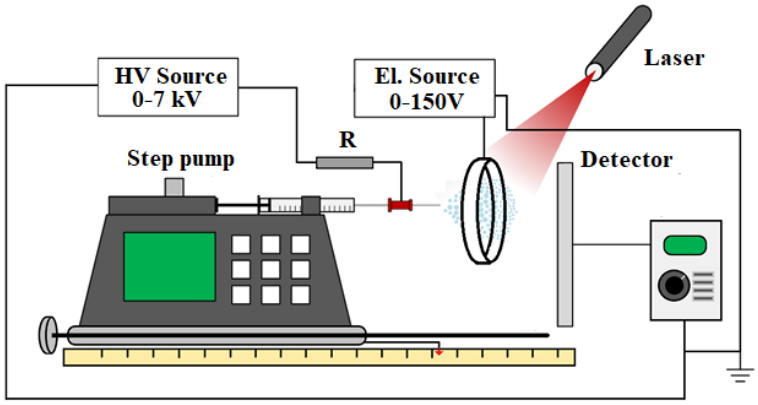

Fig. 1. Schematic view of the experimental apparatus.

The sprayed liquid was introduced into the capillary through a flexible tube with an internal diameter of 0.030", connected to the spray capillary using a stainless-steel coupling supplied with the capillary. Electrical voltage was applied to the conductive coupling, which served as a holder for the spray capillary. The entire capillary holder was placed on a movable base and the distance d between the counter electrode and the capillary could be varied by turning the threaded screw. The counter electrode, mounted on a non-conductive pad, was then connected to a picoamp meter from Ionicon Analytik. For visual inspection of the electrospray, we used a portable USB microscope 1600x from Sunnyside connected to a PC, along with illumination of the capillary tip with a red LED laser against a dark background (Figure 2).

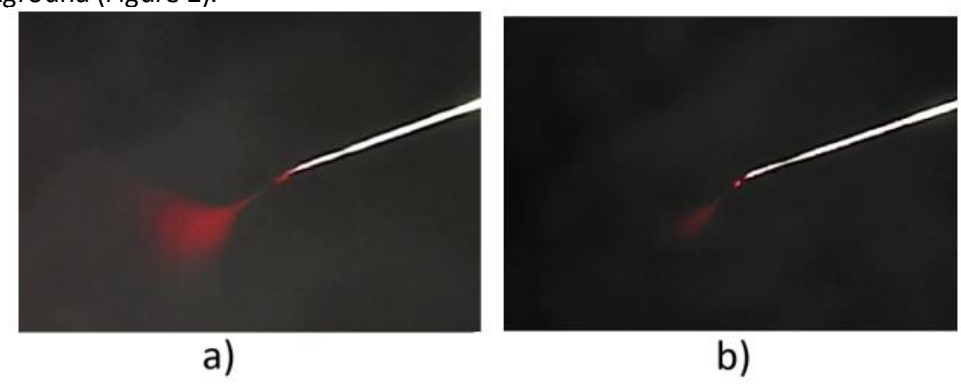

Fig. 2. Comparison of the visual flow regime a) 3 µL min^{-1} and b) µL min^{-1} at electric voltage 1.6kV

At flow rates greater than 1 µL/min, we could observe changes in the flow character for the development of electrospray. The dripping of visible droplets at voltages below 1.3 kV gradually accelerated with increasing electrical voltage, until electrospray initiation occurred. This regime was maintained even with further increasing electrical voltage. Only with further increasing voltage above the threshold of 2.1 kV on average did the optical division of the streamer into multiple sprays subsequently occur. A significant change was observed for the breakdown voltage value with varying distances (Figure 3). At a distance d = 6 mm, the breakdown voltage value was around 2.3 kV for the 90/10 solvent composition and 2.1 kV for the 80/20 methanol to water solvent composition. The change in the breakdown voltage value proved less significant with increasing distance above 20 mm for the 90/10 composition, and above 10 mm for the 80/20 composition. The attached graphs also show the dependence after adding 0.1% acetic acid, further reducing the breakdown voltage value. This fact limits the distance when using this type of stainless-steel capillary to a distance greater than 6 mm, since achieving a stable electrospray is crucial for the correct ionization of the sample present later.

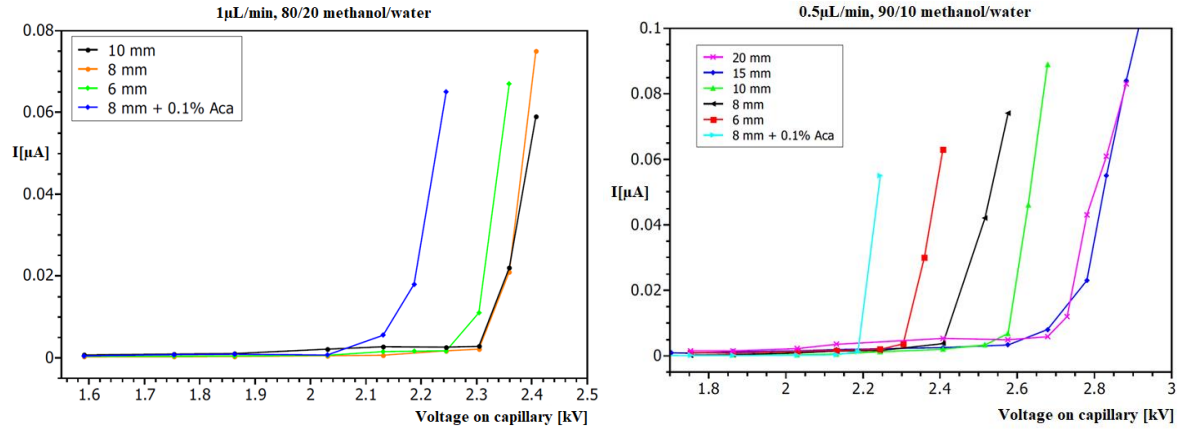

Fig. 3. Dependence of the current transmitted by the electrospray on the voltage on the capillary at different distances of the capillary from the electrode.

Under the same conditions, reducing the concentration of methanol from 90 to 80% reduces the voltage by an average of 0.1 kV without the addition of acetic acid and by almost 0.2 kV with acetic acid.

After replacing the metal capillary with a glass capillary, we continued with the measurements, however, the dependence of the electric current on the electric voltage on the capillary was more linear. We changed the electric voltage from the onset of stable electrospray to the limit of 6.5 kV. Based on the smaller inner diameter, we examined the solvent flow rate from 0.3 to 0.7 µl/min, where 0.3 was determined as the flow rate where the stepper pump still had a sufficiently continuous flow (Figure 4).

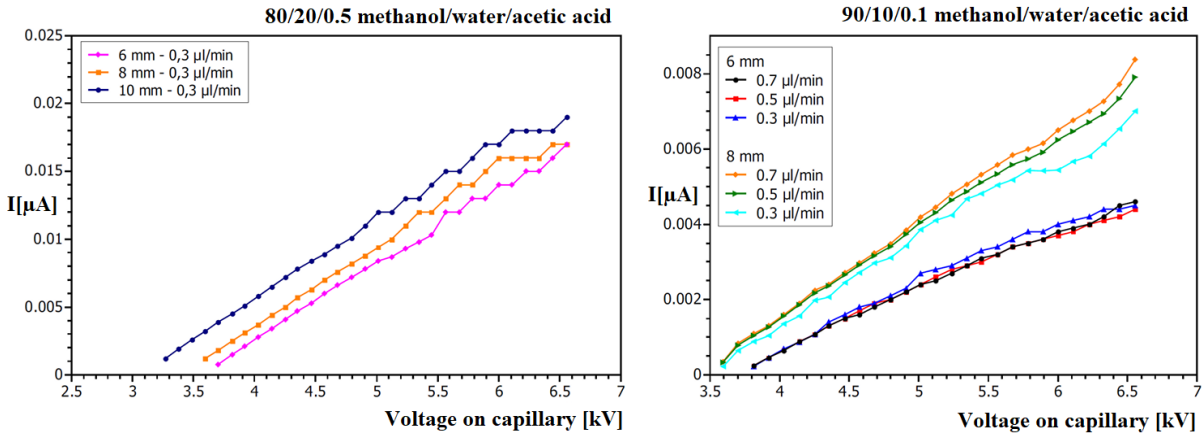

Fig. 4. Dependence of the current transmitted by the electrospray on the voltage on the Micromics capillary at different distances.

We observed much more linear dependences with the glass capillary than the stainless-steel capillary when the el. current increases linearly with increasing voltage, and no sharp increase in current was observable. The change compared to previous measurements occurred in the need for a longer flow of solvent through the capillary (10-15 minutes) before the actual increase in the el. voltage, to observe a stable electrospray after increasing the voltage on the capillary. Otherwise, even after increasing the voltage above 6 kV, the electrospray was neither visually observable nor detectable by current. This fact was probably also related to the lower degree of conductive contact with the solvent than with the stainless needle, which itself was an electrical conductor.

The stainless-steel capillary demonstrated higher stability at higher flow rates and easier electrospray start-up without the need for acetic acid, while the glass capillary showed more linear current-voltage dependencies, but required the addition of higher concentrations of acetic acid. With the stainless-steel capillary, it was important to optimize the solvent composition and the distance of the capillary from the electrode to achieve stable and efficient electrospray without achieving microdischarges. For this reason, we decided to apply the Micromics glass capillary to the design of the ESI-IMS spectrometer.

Acknowledgement:

This work was supported by the Slovak Research and Development Agency APVV-19-0386, APVV-22-0133, APVV-23-0522 and the Slovak Grant Agency for Science (contract no. VEGA 1/0553/22).

3. References

[1] L. Arce, M. Menéndez, R. Garrido-Delgado, and M. Valcárcel, *TrAC Trends in Analytical Chemistry*, vol. **27**, no. 2, pp. 139–150, 2008.

[2] J. Hrdá, Diploma theses. FMFI UK, 2019.

[3] W. Liu, Y. Chen, X. Yin, F. Liu, W. Li, J. Yu, G. Jing, and W. Liu, *Microchemical Journal*, vol. **182**, p. 107919, 2022.

[4] J. A. Tufariello, K. Grows, E. J. Davis, C. S. Harden, W. W. Siems, and H. H. Hill, *International Journal for Ion Mobility Spectrometry*, vol. **18**, pp. 95–104, 2015.

[5] P. Kebarle and U. H. Verkerk, *Mass spectrometry reviews*, vol. **28**, no. 6, pp. 898–917, 2009.

[6] P. Dwivedi, B. Bendiak, B. H. Clowers, and H. H. Hill, *Journal of the American Society for Mass Spectrometry*, vol. **18**, no. 7, pp. 1163–1175, 2007.

[7] C. Thoben, C.-R. Raddatz, A. Tataroglu, T. Kobelt, and S. Zimmermann, *Analytical Chemistry*, vol. **95**, no. 21, pp. 8277–8283, 2023

APPLICATION OF ATMOSPHERIC COLD PLASMA TO PESTICIDE DEGRADATION

Angel Pardo[1], Matej Klas[1] and Štefan Matejčík[1].
[1]*Comenius University in Bratislava, Faculty of Mathematics, Physics and Informatics.*
E-mail: matej.klas@fmph.uniba.sk

This study aims to evaluate the degradation of Chlorpyrifos in the gas phase using Corona Discharge (CD) and Chlormequat in water solution using Plasma Activated Water (PAW) prepared by air Plasma Jet (PJ). The degradation efficiency was quantified, and the degradation products were identified using Ion Mobility Spectrometry (IMS) and its combination with Mass Spectrometry. For Chlorpyrifos, 3,5,6-trichloro-2-pyridinol ions were the dominant ions used to monitor the degradation of Chlorpyrifos vapours by CD in air. In the case of Chlormequat, 2-dimethylaminoethyl ions were identified as the key ions for monitoring. The degradation of Chlorpyrifos of 50% was achieved at discharge power of 27 mW and 90% at 125 mW. In the case of Chlormequat, 90% degradation was achieved with PAW prepared by exposing water to a DC plasma jet.

1. Introduction

According to World Health Organization estimates, the global population is expected to increase by around 20 percent by 2050 [1], requiring an increase in crop productivity to meet food demand, therefore, the use of pesticides cannot be reduced despite their health risks, and they will continue to play a critical role in preventing crop losses due to pests and diseases.

After applying pesticides to crops, some may be found in food at a residue level due to their low solubility in water and stability under environmental conditions, which makes them resistant to degradation. Currently, one of the challenges is to develop technologies that effectively eliminate pesticide residues without causing damage to the nutritional content of the food. Cold plasma technology is a promising tool for pesticide removal because of its ability to degrade organic molecules through reactive oxygen and nitrogen species, radicals, and UV radiation that constitute the plasma. Several configurations of cold plasma, including dielectric barrier discharges, plasma jets (PJ), and corona discharges (CD), have been successfully applied to degrade air, water, and food matrix contaminants [2–8]. Plasma-activated water (PAW) has shown particular promise for degrading pesticides due to its high concentrations of reactive species, such as hydroxyl radicals, ozone, nitrate, nitrite, nitric acid, and peroxynitrite, which interact with the chemical structures of pesticides, leading to oxidative cleavage [6]. For example, research has highlighted the degradation of organophosphates, carbamates, and neonicotinoids using plasma-based methods [9].

Chlorpyrifos and Chlormequat, whose structures are shown in Figure 1, are widely used agrochemicals. Chlorpyrifos is an organophosphate pesticide banned in the EU since 2020, whereas Chlormequat, a quaternary ammonium salt still authorized as an herbicide, has recently been associated with fertility issues [10].In this study, the selection of these pesticides was based on their frequent detection in recent results from the Multiannual National Control Program for pesticide residue monitoring, conducted by the European Food Safety Authority [11]. Chlorpyrifos was selected due to its frequent detection in monitoring data and known risks to human health, including developmental neurotoxicity and genotoxicity [12].

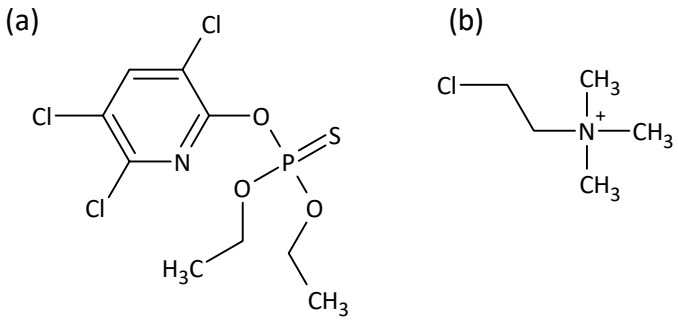

Figure 1. Structure of (a) Chlorpyrifos and (b) Chlormequat

2. Methods

The vapour phase of Chlorpyrifos was degraded using a positive DC corona discharge (CD) in dry air as working gas at room temperature and at 100 mL/min. The vapour phase of Chlorpyrifos was taken off from the headspace of analytical standards (Sigma-Aldrich, >99,0%) using a 20 mL syringe. The vapours were introduced into an external CD source coupled to the ion mobility spectrometer (IMS) using a syringe pump at a flow rate of 20 mL/min as shown in Figure 2 (a). The corona discharge configuration consists of a tungsten wire coated with Teflon, measuring 56 mm in length and 75 µm in thickness. The wire is connected to a resistor, which is then connected to a high-voltage source (FuG HCP 35-200000). A 5 mm section of the tungsten wire is positioned inside the stainless steel T-shape, which serves as the ground electrode and is the active region of the plasma where the corona discharge occurs. Through the T-shaped structure flows a mixture of Chlorpyrifos vapour and air, enabling interaction with the corona discharge. The external CD was operated using different electric power (2, 27 and 125 mW). The degradation was qualitatively evaluated using the IMS. Due to the challenge of accurately determining the mass introduced into the IMS, degradation estimates were calculated by comparing the percentage of the peak area before and after plasma treatment.

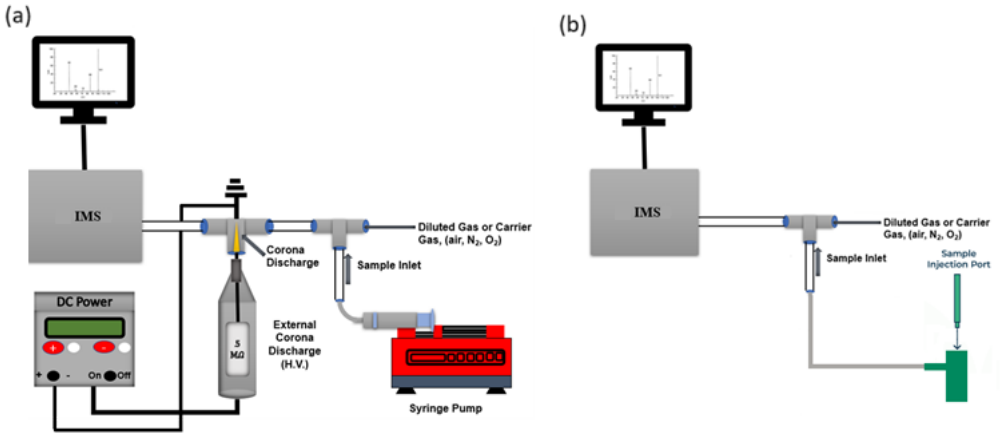

Figure 2. (a) Corona discharge degradation configuration. (b) Injection of liquid into IMS

The degradation of Chlormequat (Sigma-Aldrich, >99,0%) was performed by preparing a stock solution of 1000 ppm in distilled water, which was subsequently diluted in plasma-activated water (PAW) to final concentrations of 100 ppm and 10 ppm. The PAW was prepared by exposing 200 mL water to the bubbling of PJ exhaust gases for 10 minutes. The plasma was produced using a PJ system operated with filtrated air as the working gas at a flow of 300 mL/min. The air arc PJ was generated between two electrodes, with a copper-neutral electrode placed between them. The copper cathode, which contains a hafnium insert, is connected to the negative terminal of the high-voltage DC power supply, which includes current feedback. The discharge was sustained with an average power consumption of 400 W as described in [13].

Chlormequat degradation was quantified using a calibration curve (1, 10, 20, 100 ppm) prepared in water. The samples were injected into a gas chromatography injector port heated to 220°C, using dry air as the carrying gas at a flow of 100 mL/min for analysis with the IMS, as shown in Figure 2 (b).

Identification of the ions responsible for the detected signal in the IMS was carried out using an IMS connected to an orthogonal time-of-flight mass spectrometer (o-TOFMS). The operational parameters of the IMS are detailed in Table 1. Ammonium generated from ammonium carbonate (Sigma-Aldrich, >99,0%) was used as a dopant to improve the detection of Chlorpyrifos.

Table 1. IMS operating parameters

IMS drift tube length:	11.9 cm
IMS operating pressure:	600 mbar
Drift gas flow:	600 mL/min
Sample gas flow:	100 mL/min
CD current:	10 µA
Shutter grid pulse width:	10 µs
Shutter grid frequency:	120 Hz

3. Results

The presence of Chlorpyrifos in the air is visible in the IMS spectrum by the appearance of the ion with reduced ion mobility of 1.55 $cm^2/V{\cdot}s$ (6.5 ms) as it is shown in Figure 3, which corresponds with the protonated form of 3,5,6-trichloro-2-pyridinol ion (m/z of 199). This ion is a product of Chlorpyrifos ionization in the IMS. The intensity of this ion decreases as the power of CD discharge increases. Degradation of Chlorpyrifos vapours of approximately 50% was achieved using a DC CD power of 27 mW, and degradation of more than 90% was reached for a power of 125 mW.

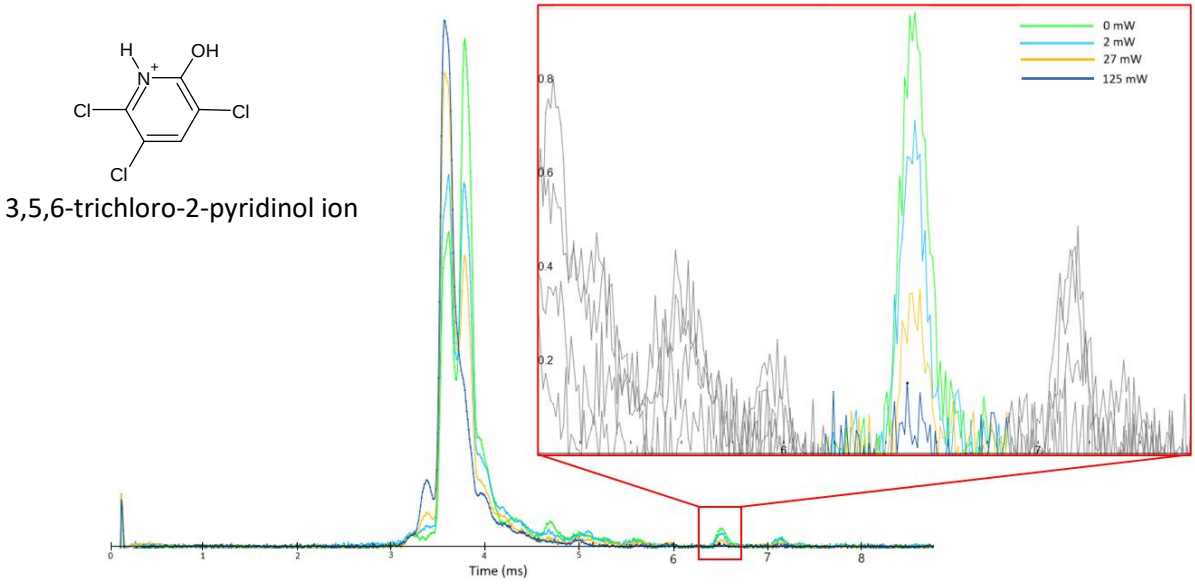

Figure 3. Ion mobility spectrum of Chlorpyrifos after CD degradation at different electric power. The green spectrum represents the untreated Chlorpyrifos spectrum.

In the Chlormetaqaut experiment, 100 ppm Chlormequat solution was diluted with PAW. This dilution resulted in changes in the IMS spectrum, compared to the dilution using a distilled water sample (Figure 4). The initial peak of Chlormequat disappeared and four new peaks corresponding to degradation products (2.14, 1.78, 1.66, and 1.57 $cm^2/V{\cdot}s$) were observed. Using IMS-oTOFMS, it was

possible to identify some of the degradation products, such as tetramethylammonium. The identification of other products is still subject to studies.

The degradation of Chlormequat using PAW exceeded 90%. After mixing the Chlormequat solution of 10 ppm with diluted PAW, the signal area of the 2-dimethylaminoethyl ion associated with Chlormequat (1.90 cm²/V·s) was found to be lower than the detection limit (1 ppm).

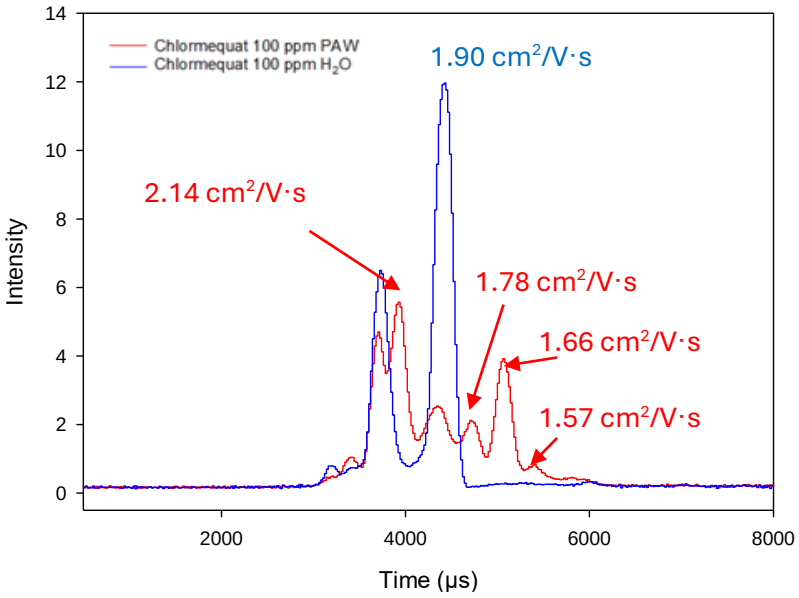

Figure 4. Ion mobility spectrum for Chlormequat before (blue) and after PAW treatment (red).

4. Acknowledgment

The present studies were supported by the Slovak Research and Development Agency under project Nr. APVV-19-0386 and Nr. APVV-22-0133.

5. References

[1] *World population prospects 2022: summary of results*, United Nations, New York, **2022**.
[2] R. Anbarasan, S. Jaspin, B. Bhavadharini, A. Pare, R. Pandiselvam, R. Mahendran, *LWT* **2022**, *159*, 113193.
[3] S. Li, X. Ma, Y. Jiang, X. Cao, *Ecotoxicology and Environmental Safety* **2014**, *106*, 146.
[4] R. Moutiq, S. K. Pankaj, Z. Wan, A. Mendonca, K. Keener, N. N. Misra, *Plasma Chem Plasma Process* **2020**, *40*, 1291.
[5] F. E. Rodrigues Júnior, F. A. N. Fernandes, *Journal of Environmental Chemical Engineering* **2024**, *12*, 111539.
[6] B. Rakesh, R. Anbarasan, B. Kamalapreetha, R. Purushothaman, B. R. Ashutosh, R. Mahendran, *Journal of Food Processing and Preservation* **2024**, *2024*, 1.
[7] H. Shen, H. Yuan, J. Liang, X. Zhou, P. Ge, Y. Liu, T. Gao, K. Yang, D. Yang, *Water* **2023**, *15*, 1562.
[8] S. Yuan, F. Yang, H. Yu, Y. Xie, Y. Guo, W. Yao, *Food Chemistry* **2022**, *383*, 132550.
[9] P. Sojithamporn, K. Leksakul, C. Sawangrat, N. Charoenchai, D. Boonyawan, *Foods* **2023**, *12*, 4386.
[10] A. M. Temkin, S. Evans, D. D. Spyropoulos, O. V. Naidenko, *J Expo Sci Environ Epidemiol* , DOI:10.1038/s41370-024-00643-4.
[11] European Food Safety Authority (EFSA), L. Carrasco Cabrera, G. Di Piazza, B. Dujardin, E. Marchese, P. Medina Pastor, *EFS2* , DOI:10.2903/j.efsa.2024.8753.

[12] C. L. Wilson, D. M. Huber, Eds., *Synthetic pesticide use in Africa: impact on people, animals, and the environment*, CRC Press, Boca Raton, First edition., **2021**.
[13] V. Medvecká, S. Omasta, M. Klas, S. Mošovská, S. Kyzek, A. Zahoranová, *Plasma Sci. Technol.* **2022**, *24*, 015503.